AD-A084 938 SCIENTIFIC SYSTEMS INC CAMBRIDGE MA F/G 20/4
GLOBAL STABILITY AND CONTROL ANALYSIS OF AIRCRAFT AT HIGH ANGLE--ETC(U)
AUG 79 R K MEHRA, J V CARROLL N00014-76-C-0780
UNCLASSIFIED ONR -CR215-245-3 NL

1 OF 4
AD
A084938

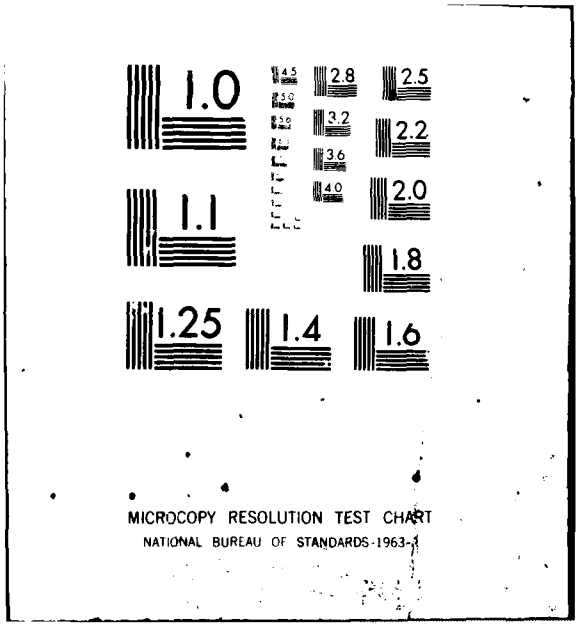
1.0
1.1
1.25
1.4
1.6
1.8
2.0
2.2
2.5
2.8
3.2
3.6
4.0
MICROCOPY RESOLUTION TEST CHART
NATIONAL BUREAU OF STANDARDS-1963-A

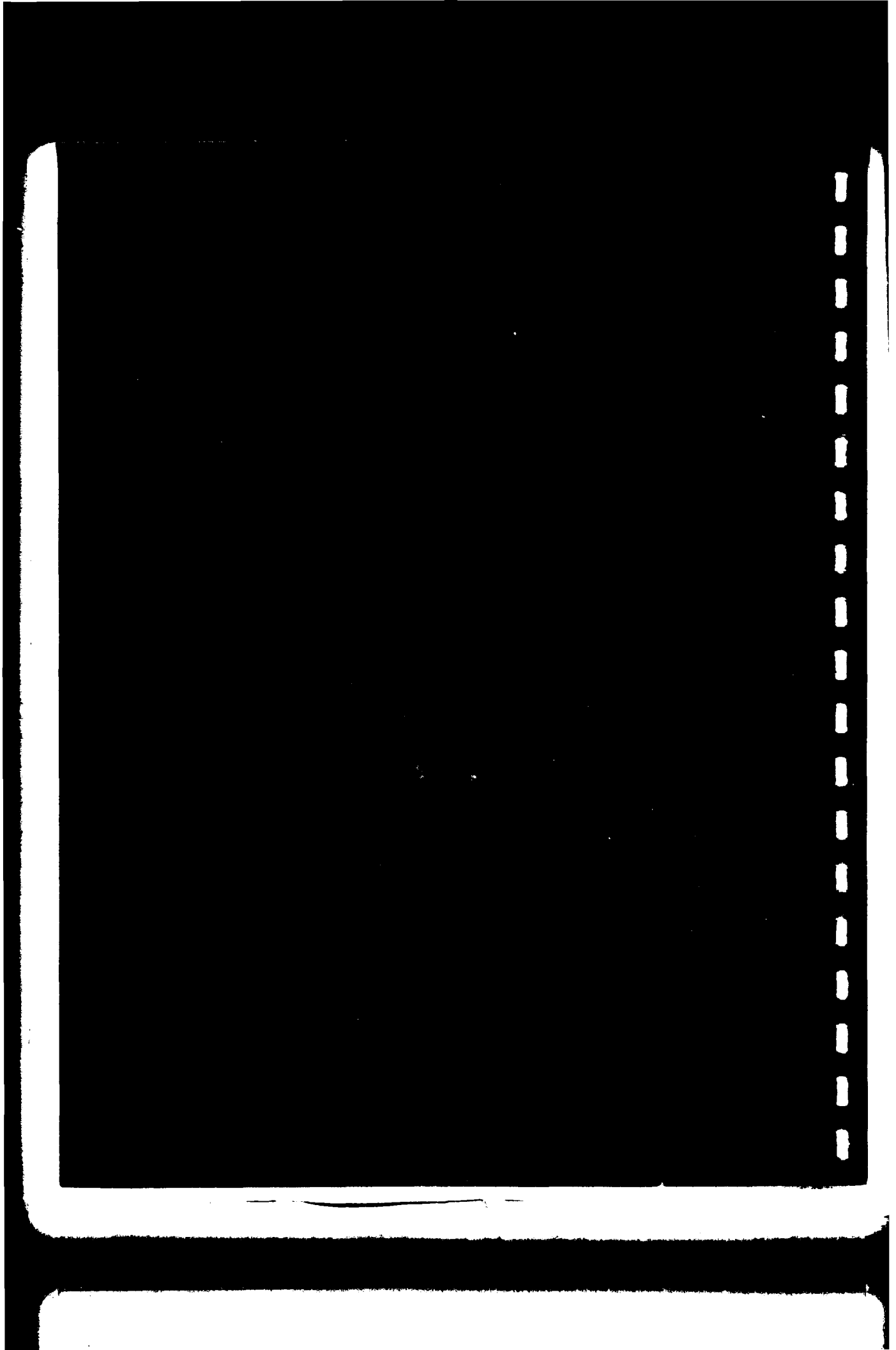

SECURITY CLASSIFICATION OF THIS PAGE (When Data Entered)

REPORT DOCUMENTATION PAGE

READ INSTRUCTIONS BEFORE COMPLETING FORM

1. REPORT NUMBER: ONR/CR-215-248-3	2. GOVT ACCESSION NO.: AD-A084 938
3. RECIPIENT'S CATALOG NUMBER:	
4. TITLE (and Subtitle): Global Stability and Control Analysis of Aircraft at High Angles-of-Attack.	5. TYPE OF REPORT & PERIOD COVERED: Annual Technical Report. no. 3, 1 June 1978—31 May 1979
	6. PERFORMING ORG. REPORT NUMBER:
7. AUTHOR(s): Raman K. Mehra, James V. Carroll	8. CONTRACT OR GRANT NUMBER(s): N0014-76-C-0780
9. PERFORMING ORGANIZATION NAME AND ADDRESS: Scientific Systems, Inc., 186 Alewife Brook Parkway, Cambridge, MA 02138	10. PROGRAM ELEMENT, PROJECT, TASK AREA & WORK UNIT NUMBERS:
11. CONTROLLING OFFICE NAME AND ADDRESS: Office of Naval Research, Technology Projects Division, Code 211, Arlington, VA 22217	12. REPORT DATE: 31 August 1979 13. NUMBER OF PAGES: 329
14. MONITORING AGENCY NAME & ADDRESS (if different from Controlling Office): 354	15. SECURITY CLASS. (of this report): Unclassified 15a. DECLASSIFICATION/DOWNGRADING SCHEDULE:

16. DISTRIBUTION STATEMENT (of this Report)

Approved for public release; distribution unlimited

17. DISTRIBUTION STATEMENT (of the abstract entered in Block 20, if different from Report)

18. SUPPLEMENTARY NOTES

19. KEY WORDS (Continue on reverse side if necessary and identify by block number)

Aircraft Stability and Control, Bifurcation Analysis, Catastrophe Theory, Atmospheric Flight Mechanics, Nonlinear Systems, High Angle-of-Attack Phenomena

20. ABSTRACT (Continue on reverse side if necessary and identify by block number)

High angle-of-attack phenomena have been of interest to aerodynamicists, aircraft designers, pilots and control system analysts ever since the advent of modern high performance aircraft. Due to the concentration of inertia along the fuselage, the modern jet fighters are highly susceptible to post-stall departures and spin. In spite of extensive design effort, modern aircraft still inadvertently enter spins which sometimes result in loss of life and/or property. Extensive wind-tunnel testing and radio-controlled flight testing has been done over the last 20 years to gain a better under-

DD FORM 1 JAN 73 1473 EDITION OF 1 NOV 65 IS OBSOLETE S/N 0102-014-6601

373341

20. (cont.)

standing of the dynamic instabilities at high angles-of-attack. A basic problem has existed in interpreting these data and in making predictions of aircraft dynamic behavior so as to achieve close agreement with flight test data.

Aircraft dynamic behavior at high angles-of-attack is highly nonlinear and in the past there has been a lack of suitable techniques for analyzing the global behavior of nonlinear systems. Under a previous project with the Office of Naval Research, Scientific Systems, Inc. has developed a new approach based on Bifurcation Analysis and Catastrophe Theory Methodology (BACTM). The approach has been applied to specific jump and limit cycle behavior such as roll-coupling, pitchup, post-stall departure, divergence, spin entry, developed erect spin, and spin prevention and recovery. The two aircraft used for the study of spin motions were selected because of the completeness of the aero data in the spin flight regimes, and because they are representative of modern fighters. These models were also used for studies of non-spin, high angle-of-attack behavior.

Under this project, the full six DOF aircraft model was implemented, and used not only for the above studies, but also for several new developments in the BACTM methodology. The new developments are basically in the area of generalizing and improving the numerical techniques for computing equilibrium and bifurcation surfaces, and in expanding the comprehensiveness of the physical model and environment.

The work on this project has included the application of BACTM to study the spin characteristics of a "variable sweep" fighter aircraft. The aerodynamic data for this model roughly corresponds to experimental data for the F-111, although modifications in some of the numbers, particularly C_n, are required to make simulation results agree with flight test data. We have designated this simulation model as Aircraft F.

Spin behavior is typically a post-stall phenomenon, and is characterized by angles-of-attack much in excess of the stall value of angle-of-attack. It is also possible that spin conditions will follow a roll departure motion. A certain type of spin, the erect flat spin, has been given particular emphasis in this work effort. This spin is featured by values of α (angle-of-attack) in the 75 - 85 degree ranges; a vertical body rotation rate, which is also constant over time, and center of mass motion which is basically helical, with the axis parallel to local vertical; and a noticeably prominent yaw rate.

Most of the work on this project involved a study of the second aircraft model, the F-4. A detailed description of modeling this aircraft, correlation time history runs, and a high angle-of-attack analysis utilizing equilibrium and bifurcation surfaces, is included in this report. The equilibrium spin regimes were found to be rather insensitive to aerosurface control deflections, a result consistent with observed performance. Studies were conducted as well in the stall/post-stall/spin entry regime, a control synthesis approach was initiated, and thrust effects were analyzed.

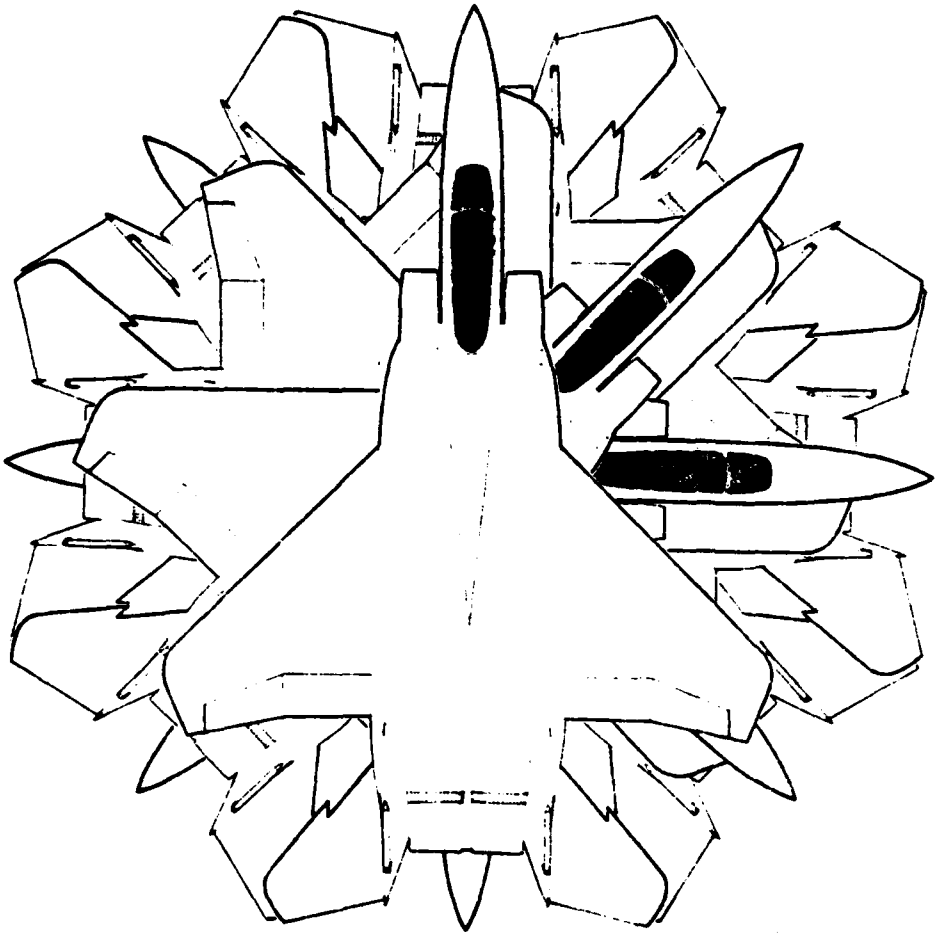

PREFACE

This investigation was conducted by Scientific Systems, Inc., Cambridge, Mass. from June 1, 1978 under contract N00014-76-C-0780 for the Office of Naval Research, Washington, DC. This report is the third annual technical report and includes results through May 31, 1979. The sponsoring office was the Vehicle Technology Program headed by Mr. David Siegel. Mr. Robert von Husen served as the Navy Technical Monitor for the program.

The principal investigator for the study was Dr. Raman K. Mehra. He was assisted by Dr. James V. Carroll, who wrote this report. Mrs. L. Washburn typed the final report.

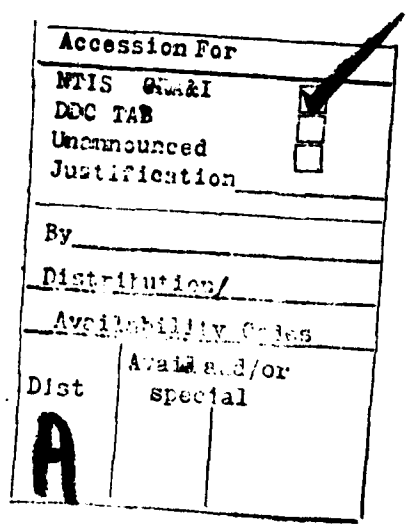

TABLE OF CONTENTS

LIST OF FIGURES

LIST OF TABLES

1. INTRODUCTION AND SUMMARY

1.1 Scope of Work Effort

Aircraft high angle-of-attack (α) phenomena are an ever-increasing item of interest to aerodynamicists, first, because the trends in aircraft design towards ever-expanding performance capabilities result, not surprisingly, in aircraft configurations highly susceptible to undesirable high-α behavior, such as spin; and second, because these phenomena are usually very nonlinear and the analysis tools available to the analyst have not been developed sufficiently enough to keep pace. As part of a continuing and broad-based effort to develop techniques capable of analyzing aircraft high-α flight behavior, Scientific Systems, Inc., under an ongoing project with the Office of Naval Research, has developed and applied to various simulator models a new approach based on Bifurcation Analysis and Catastrophe Theory Methodology (BACTM). The methodology has been developed specifically for high-α analysis, although other applications are feasible, and has been applied to specific jump and limit cycle behavior such as roll-coupling, pitchup, post-stall departure, wing rock, divergence, spin entry, steep spin, flat spin, inverted spin, oscillatory spin, and spin prevention and recovery. See Mehra et al. (1977) and Mehra and Carroll (1978) for details on BACTM theory and development, and its application to the high-α dynamics of nonlinear, albeit relatively simple, aircraft simulation models.

In the current project, the emphasis has lain in applying BACTM to

a realistic aircraft model. We have chosen the F-4 aircraft which, although not of the latest generation of fighter aircraft, nonetheless is a sufficiently modern aircraft; furthermore, it has a very comprehensive aerodynamic data base, collected over wide ranges of angles of attack and sideslip for static, forced oscillation, and rotary balance wind tunnel test configurations. During the process of developing the F-4 model, it became apparent that the results obtained by BACTM analysis would be made more emphatic if the simulation model of the F-4 adequately reproduced actual flight test motions. Thus, much emphasis has been given also to the problem of achieving adequate correlation between our simulation and the "real world."

Consistent with our recent high-α analysis efforts, spin behavior of the F-4 has received the most emphasis. We have found many of the high-α motions of the F-4, not unlike those of earlier models (aircraft F--see Mehra and Carroll, 1978), to be periodic in nature. This periodicity, or limit cycle behavior, is present in most steep spin conditions ($50° \lesssim \alpha \lesssim 75°$), but not in flat spin ($\alpha \gtrsim 80°$) when the controls are in a pro-spin setting (stick back, aileron opposite in sense to rudder). Limit cycle behavior is also prominent in the aircraft F model which, like the F-4 model, is described by means of tabular aerodynamic data, derived from wind tunnel measurements. As a consequence of these observations, it became important to expand BACTM to include methods capable of quantitatively investigating the existence, nature, and stability of limit cycles.

Much of the work reported on in this project involved completing the spin recovery analysis of the aircraft F model. The initial phases of

this effort are described in Mehra and Carroll (1978). Because the aircraft F model shares many essential features with the F-4 model, e.g., tabular aero data, and yet has a small, manageable data base, this aircraft has been very useful in the task of developing the various BACTM algorithms. With it, we were able to recognize potentially serious numerical computation problems associated with tabular data and the need to do much work analytically rather than numerically (e.g., partial derivatives). Aircraft F was thus the test model for the development of a more comprehensive and flexible bifurcation surface algorithm, and the limit cycle continuation algorithm. Both of these are discussed in this report.

The heart of many of the BACTM algorithms, in particular the algorithms which generate equilibrium and bifurcation surfaces, is an algorithm for parametric continuation. Parametric continuation is the means by which results are globalized. In this report, we describe how this basic algorithm is utilized in the upgraded BACTM algorithms, and in the new limit cycle continuation algorithm. As with the previous aircraft, BACTM analysis using the F-4 equilibrium surfaces shows regions of jump, limit cycle, hysteresis and other phenomena which are qualitatively similar to those earlier aircraft. One noteworthy difference between aircraft F and the F-4 which our analysis has detected is that, for the F-4, flat spin equilibria are uniformly stable with respect to allowable aerosurface control deflections. This is not so for aircraft F. This means that auxiliary spin recovery controls such as wing-tip thrusters or parachutes are necessary for the F-4, but that recovery from flat spin is possible for aircraft F using only the rudder, elevator, and aileron.

Two more items of interest, which are reported on here, to which BACTM has been applied successfully on the F-4, are a study of the effects of thrust on spin motion and a method of utilizing equilibrium and bifurcation surfaces, particularly the latter, for control system synthesis and/or definition of flight envelopes.*

1.2 Previous Work

Because so much of the results reported on here represent an extension of results reported on earlier, we refer the reader to these reports, Mehra et al. (1977) and Mehra and Carroll (1978). These references report extensively on previous work done both in the theoretical area and in the specific area of high-α flight dynamics. Our major effort has centered on analyzing the F-4 aircraft. To this end, it has been necessary to investigate how one assembles and uses the wind tunnel aero data, as well as key issues relevant to obtaining adequate correlation between simulation and flight test results. Three of several adequate references on these topics are Anglin (1978, 1977) and Chambers et al. (1969).

A final topic which is being presented here for the first time, and which offers much time- and money-saving potential, is that of limit cycle continuation. Our major reference here is Chua and Lin (1975). It will be noted that our application represents a significant extension of their ideas, which are well documented in their textbook.

1.3 Summary of Significant Results

The significant milestones achieved on this project are given below:

*Here, we must emphasize that we currently are assuming a rigid body, so that flutter and other structural phenomena which play a role in defining operational flight envelopes are not analyzed.

- Demonstration of the use of BACTM results to generate a control strategy for effecting complete recovery from equilibrium flat spin conditions.
- Improvement of the initial spin recovery strategy and definition of domains of attraction to stable limit cycles (steep spin), and to trim region, using time history simulations.
- Demonstration of the existence of special phenomena related to limit cycles and their stability, such as global bifurcations.
- Development of a realistic aircraft model (F-4) for simulation and analysis with the BACTM system, a model which utilizes a very extensive aerodynamic data base.
- Incorporation of the F-4 aero data into a hybrid aerodynamic model in which static, forced oscillation, and rotary balance data are combined under algorithms which reflect the latest thinking on utilization of hybrid models.
- Verification of the F-4 simulation model by means of a series of time history correlation runs.
- Incorporation of thrust effects in the F-4 model, and a determination that thrust influences are quite small if velocity is fixed and analysis is done in trim regions, and that, when velocity is allowed to vary, it and roll and pitch angles are highly sensitive to changes in control parameters, in the presence of thrust.
- Upgrading of BACTM algorithms by introducing a coupled set of dynamic equations valid for spin analysis (i.e., gravity effects included), in which velocity is solved for analytically, thereby

eliminating it as an explicit state variable from this system of equations.

- Upgrading of BACTM algorithms by restructuring the bifurcation surface algorithm to accomodate the increased computational demands required by aircraft models with an extensive tabular data base.
- Computation of extensive set of global equilibrium and bifurcation surfaces for the F-4 aircraft in several high angle-of-attack flight domains, including flat and steep spin, and stall and spin entry.
- Determination, based on the equilibrium surface results, that the F-4 model is highly stable with respect to control changes when in equilibrium spin; that limit cycle motions encountered in spin regions are similarly very stable; that spin recovery is consequently highly unlikely using aerosurface controls alone, unless they are aided by other devices. This is a confirmation of actual observed performance of the F-4.
- Determination, based on equilibrium surface results, that the high angle-of-attack regions associated with stall and spin entry conditions are sugject to varied nonlinear phenomena, such as jumps and Hopf bifurcations, which makes these regions attractive for BACTM analysis.
- Demonstration of the global capabilities of BACTM by means not only of the equilibrium surface algorithm, but also of the expanded bifurcation surface algorithm, which has been used with the F-4

model to aid in high angle-of-attack control system synthesis.

- Detection of a simple bifurcation point for the F-4 model in a high angle-of-attack, steep spin region; this situation offers the possibility that the condition may be exploited in this region, to achieve a recovery sequence.

1.4 Organization of the Report

The report is organized into two main chapters, 2 and 3. Chapter 2 contains a discussion of the techniques by which BACTM was modified and expanded to enable analysis to be done on a realistic aircraft model with an extensive aerodynamic data base, and to do quantitative limit cycle analysis. Chapter 3 describes how the upgraded BACTM programs have been applied to the analysis of nonlinear, high angle-of-attack phenomena of two aircraft. Included here are discussions of spin recovery, stall, spin entry, spin reversal, correlation studies, use of aerodynamic data extracted from wind tunnels, study of thrust effects, and use of bifurcation surfaces for control system synthesis. Conclusions and recommendations are stated in Chapter 4, and a list of symbols and nomenclature is included in Appendix A.

2. METHODOLOGY DEVELOPMENT

In this chapter, we discuss the various additions and improvements which have been made to the BACTM system during this period. These developments enable BACTM to analyze efficiently high-α behavior of aircraft models which consist of comprehensive aerodynamic data bases. In our context, high-α motion includes pre-stall buffeting, stall, post-stall, and spin recovery, as well as other nonlinear phenomena which have not been studied as extensively in this project. For further information on the structure and use of BACTM, see Mehra, et al. (1977).

2.1 Upgrading of BACTM

Considerable effort and progress has been made in this period to render BACTM capable, first, of successfully handling more complex aircraft models and more demanding flight conditions, such as post-stall departures and spin; and second, of performing the exacting task of computing the equilibrium surfaces, the time histories and the bifurcation surfaces for these models and flight conditions, with acceptable efficiency and accuracy.

The use of aircraft A, B and H (Mehra, et al., 1977) allowed for the construction of the BACTM system, and allowed us to establish and verify the usefulness of BACTM for the global analysis of aircraft in high-α regimes, particularly those where inertia coupling and roll departure phenomena were the prominent features. Aircraft F had been introduced (Mehra and Carroll, 1978) primarily for the study of spin motion, but also

because adequate study of spin behavior requires aerodynamic data to be functionally dependent on α and β, as well as the controls, velocity, dynamic pressure, and aircraft parameters. This is because of the extreme ranges of values these angles, particularly α, achieved in undergoing the transition from straight-and-level to spin conditions. More recently, the F-4 model uses larger sets of (α,β)-dependent aero data, as well as rotation balance data, which varies with spin rotation rate as well as α and β. These data, almost universally experimentally obtained, are typically in tabular form or plotted, interpolated curves. It has been, therefore, necessary to expand the dynamic model and to develop reliable and efficient algorithms for properly utilizing the aero data.

Additionally, BACTM has been modified in two other major ways in order for it to be able to complete the task of spin analysis with aircraft F, as well as to allow it to handle more efficiently the much larger and more complex aircraft models such as F-4. In Section 2.1.1, the organizational changes to the programs which comprise the BACTM system will be detailed, and in Section 2.1.2, some of the more prominent of the basic algorithmic changes will be described, with particular reference to the bifurcation surface algorithms. Section 2.1.3 discusses significant advances made in the area of detecting and quantitatively identifying nonlinear oscillatory, or limit cycle, motion, utilizing continuation techniques. Finally, Section 2.1.4 discusses the development of a reduced spin state equilibrium system.

2.1.1 New BACTM Program Structure

In order to assimilate larger data bases (the F-4 data base contains

up to 10 times the number of data points as does that of aircraft F), the BACTM programs were converted to a format which uses files for storage of the aero data. In addition, the programs which generate the solution surfaces and trajectories now have the capability of simultaneously buffering the generated data onto a disk. Thus, if some sort of system failure* occurs to interrupt the program, a second program can be automatically activated which transfers this data to permanent files on magnetic tape during the "grace period" of the system. In this way the data generated to that point are not lost. Because of the greater number of parameters of interest, as well as the increased dimensionality of the (spin) system, this is an important factor.

In addition, under routine operating conditions (i.e., no system interrupts), there is now a very large amount of data generated. With the old format, all of this had to be printed or plotted with each run, as there was no permanent storage capability. Again, in veiw of expanded size, this represents an impractical way of conducting spin studies. As seen in Table 2.1, there are up to 95 quantities of interest in the time history runs. See Appendix A for notation. To plot each of these for every run, even if they were all "production" runs, is clearly unwise. Thus, the system is arranged to dump all of the generated data onto magnetic tape or disk, while plotting only selected items of immediate concern. Each string of data on the tape is identified by its own file number, and all of the data, whether from equilibrium, bifurcation or time history runs has a similar format. This commonality allows for efficient post-processing.

*The most prevalent interruption is caused by excessive runtime.

TABLE 2.1

Current list of plot variables (all in degree, English units, except as noted)		
δa	$\dot{\theta}$	C_{ℓ}
δe	$\dot{\phi}$	C_m
δr	E	C_n
p	$\dot{E}$	C_L
q	u	C_D
r	v	$C_{n_{\beta_{DYN}}}$ (per radian)
α	w	$C_{n_{\beta}}$ (per radian)
β	V_{VERT}	$C_{\ell_{\beta}}$ (per radian)
V	h	$C_{m_{\beta}}$ (per radian)
$\dot{V}$	x_{NORTH}	{33 static, forced oscillation, and rotary balance aero data coefficients for the F-4 model}
θ	y_{EAST}	
ϕ	E_{SPIN} $(= I_V\dot{\psi}/2)$	LCDP1
$TURNS = \frac{1}{360}\int_{t_0}^{t_f}\dot{\psi}\,dt$	I_V (local vertical axis moment of inertia)	LCDP2
		D_{SPIN} $(\|\underline{x} - \underline{x}_{SPIN}\|/\|\underline{x}_{SPIN}\|)$
$\dot{p}$	Ω	{6 rotational aero and inertial moment terms--p,q,r}
$\dot{q}$	C_x	{9 translational gravity, aero and inertial terms--x,y,z}
$\dot{r}$	C_y	$\bar{q}$
$\ddot{\psi}$	C_z	t

As an example, it may require several runs to create a full equilibrium surface in some region of interest, although the BACTM continuation algorithms do reduce the total number of necessary runs. As each run generates its own file or files, a single post-processor run can collect the data from all of the relevant files and quickly produce the desired plots. In general, the post-processor plots are of better quality, containing more information and finer detail (some further refinements in this area are easily made) than the "engineering" plots produced by each run. Finally, there is now the capability to plot any variable from Table 2.1 against any other variable from that list. If this requirement were to be placed on the old run-time plotting system, the core requirements would be enormous.

2.1.2 Upgraded Continuation Algorithm; Bifurcation Surfaces

The algorithm works exceptionally well as coded for solving aircraft F and F-4 equilibrium surfaces, both in spin and non-spin regimes. There is consequently no need to discuss the algorithm per se with regards to these surfaces. However, the computation of bifurcation surfaces did necessitate more care in setting up the problem, and in the case of spin bifurcation surfaces, required in addition some modification to the algorithm itself. These points will now be discussed in more detail. More detailed disucssion of the basic BACTM algorithms may be found in Mehra and Carroll (1978).

Let $\underline{x}^*(\delta)$ represent a solution to $\underline{f}(\underline{x},\delta) = 0$. This is an equilibrium, or fixed, point for the dynamic system defined by $\dot{\underline{x}} = \underline{f}(\underline{x},\delta)$. It is

obvious that the variation of one element of $\underline{\delta}$ ($\underline{\delta} = (\delta a, \delta e, \delta r)$) will generate an equilibrium surface in the state-control space. A bifurcation point is a location at which the system experiences a basic structural change, caused by the continuation parameter (here, an element of $\underline{\delta}$) reaching some critical value. At this value, the structural stability has changed also. For example, the equilibrium limit points A and B are bifurcation points* in Figure 2.1, and the loci of their projection onto the control subspace is what we call a bifurcation surface. This locus is generated by varying

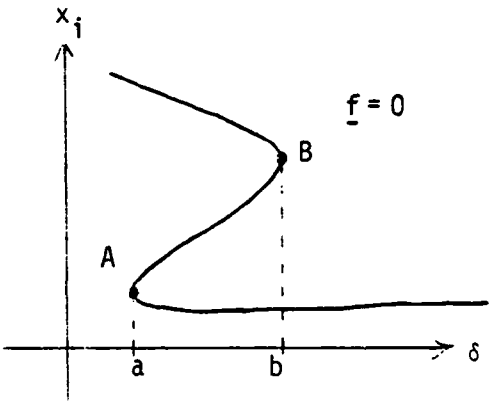

Figure 2.1
Equilibrium Surface

any two of the three controls, holding the third one fixed. It is obvious that all bifurcation points are equilibrium points, but the converse is not true. The mathematical criterion for a bifurcation point is made up of the equilibrium requirement $\underline{f}(\underline{x}, \delta) = 0$ and the constraint

$$\Delta \triangleq \det(F) = \det\left[\frac{\partial \underline{f}}{\partial \underline{x}}\right] = 0 \qquad (2.1)$$

*There is a disparity in the literature as to whether points A and B are properly bifurcation points. Abraham and Marsden (1978), for example, do include them, since a stable segment is "annihilated" by an unstable segment at such points.

(i.e., the Jacobian matrix F is singular). This condition arises from the fact that, if

$$\underline{f}(\underline{x},\delta) = 0 \tag{2.2}$$

is true, then

$$F \frac{d\underline{x}}{d\delta} + \frac{\partial \underline{f}}{\partial \delta} = 0 \tag{2.3}$$

and δ is one of the controls selected as a parameter. It is seen from Figure 2.1 that $d\underline{x}/d\delta$ is the slope of the $\underline{f} = 0$ locus for values of $\underline{x}$ and $\underline{\delta}$ on that locus. Also, points A and B are characterized by the fact that $d\underline{x}/d\delta$, the slope, is infinite. Hence, the continuation solution

$$\frac{d\underline{x}}{d\delta} = -F^{-1}\left[\frac{\partial \underline{f}}{\partial \delta}\right] \tag{2.4}$$

breaks down, and this is equivalent to saying that the inverse of the Jacobian F does not exist at $\delta = a$ or b; i.e., Eq. (2.1) holds.

Thus, standard continuation methods break down at such points, as these methods solve for $\underline{x}^*(\delta)$ by integration of (2.4). Kubicek's method, which is the basis of our BACTM algorithm, avoids this by introducing an arclength parameter and by augmenting the Jacobian with an extra column representing the continuation parameter, and eliminating (via Gaussian reduction) the one column which leaves the "most non-singular" square matrix (this amounts to interchanging the parameter δ with an x_k as necessary; x_k then becomes the parameter and continuation via an equation like (2.4) remains valid. See Mehra and Carroll (1978) for details.)

To summarize, Eqs. (2.2), evaluated for some starting value $\underline{x}_0^*$, and (2.4), which continues the solution from $\underline{x}_0^*$, generate equilibrium surfaces. Bifurcation surfaces--represented by points a and b in the control-space in Figure 2.1--are generated in a similar way, with the basic equilibrium system being enhanced by one dimension (representing the constraint (2.1)).

For equilibrium surfaces, one of the controls is selected as a parameter, leaving the other two fixed. For bifurcation surfaces, one of the controls is also a parameter, but one of the remaining two plays the role of an $(n+1)^{\underline{th}}$ state variable, needed because of the introduction of the $(n+1)^{\underline{th}}$ constraint (2.1); the final control is fixed, so that two dimensional bifurcation surfaces result at each value of this final control. In the context we have employed, bifurcation surfaces exist only in the control space. In Figure 2.1, these three-dimensional surfaces project to the points a and b along the one control space dimension shown in that figure. The bifurcation surfaces then are generated by the following system:

$$\dot{\underline{g}} = \frac{d\underline{g}}{ds} = \left[\frac{\partial g_i}{\partial y_i}\right] \frac{d\underline{y}}{ds} + \left(\frac{\partial \underline{g}}{\partial \delta_i}\right) \frac{d\delta_i}{ds} = 0 \tag{2.5a}$$

or

$$\dot{\underline{g}} = G\dot{\underline{y}} + \underline{g}_{\delta_i} \delta_i = 0 \tag{2.5b}$$

where we have introduced two (n+1)-dimensional arrays

$$\underline{g} \triangleq (\underline{f}^T, \Delta)^T \tag{2.5c}$$

$$\underline{y} \triangleq (\underline{x}^T, \delta_j)^T \tag{2.5d}$$

and the $(n+1) \times (n+1)$ matrix

$$G = \left[\frac{\partial \underline{g}}{\partial \underline{y}}\right] \tag{2.5e}$$

Eq. (2.5) is solved for the $(n+1)$ derivatives $\dot{\underline{y}}$ (the $(n+1)^{\underline{th}}$ element of $\underline{y}$ is δ_j), as functions fo the scalar δ_i. This latter derivative is then determined from the arc-length normalization relationship

$$\dot{\underline{y}}^T \dot{\underline{y}} + (\dot{\delta}_i)^2 = 1 \tag{2.6}$$

2.1.2.1 Non-Spin Bifurcation Considerations

In the non-spin case, $n = 5$ (gravity effects are neglected and V is assumed constant). However, even though this system is considerably smaller than the spin system (for which $n = 8$; see Section 2.1.4 for discussion of an $n = 7$ spin system), the Γ array (defined below) is still of size 6×7. Furthermore, because

$$\Delta = \det(G) = \det\left[\left(\frac{\partial f_i}{\partial x_j}\right)\right] \tag{2.7}$$

represents the $(n+1)^{\underline{th}}$ element of $\underline{g}$ (hence row $(n+1)$ of

$$G = \left[\frac{\delta g_i}{\delta y_j}\right] = \left[\begin{array}{c|c} F & \partial \underline{f}/\partial \delta_j \\ \hline \partial \Delta/\partial \underline{x} & \partial \Delta/\partial \delta_j \end{array}\right], \tag{2.8}$$

there are serious computational problems to consider.

These problems center on the computation of G and the $(n+1) \times (n+2)$ matrix

$$\Gamma = \left[G \;\vdots\; \frac{\partial \underline{g}}{\partial \delta_i} \right], \tag{2.9}$$

which is often more difficult than inverting the (n+1)-by-(n+1) submatrix of Γ, Γ_k. For example the bottom row of Γ is given by

$$\Gamma_{(n+1),\cdot} = \left(\frac{\partial \Delta}{\partial (\underline{y}, \delta_i)} \right) \tag{2.10}$$

It is of practical necessity to compute at least this row using a numerical differentiation algorithm. Thus, the last row of Γ in either the spin or the non-spin case is determined by numerical differentiation. The first column element in the bottom row of Γ, $\gamma_{(n+1),1}$ is given by $\partial\Delta/\partial p$. The numerical differentiation of this term involves five evaluations of $\Delta(p)$, with p varied in small increments from its value at $\underline{y}$, where Γ is to be computed, and all other variables fixed. This must be done altogether seven times for each of the last row elements of Γ, in the non-spin case. Thus, 29 evaluations of Δ are needed each time an evaluation of Γ is made. Only one evaluation $\Delta(\underline{y})$ is needed; this provides the central value of the five $\Delta(\underline{y} + \Delta y_i)$ needed to compute each $\partial\Delta/\partial y_i$. There can be several evaluations of Γ made for each point on the continuation solution, due to the iterative nature of the Newton-corrector steps. Every evaluation of Δ requires full evaluation of the matrix F. It is possible to do this using numerical differentiation, but there is obviously a tremendous saving in time to be had if the terms in F can be

analytically derived, as well as all other elements of Γ (F is a sub-matrix of Γ) for which this is feasible.

The above strategy for computing Γ, both in the spin and non-spin cases, is to use analytic expressions for the elements of Γ, γ_{ij}, as much as possible, using numerical differentiation only for the last row of Γ, Eq. (2.10). This modification provided the opportunity to compare the precision of the numerical differentiation results with the "exact" expressions, and the numerical adequacy of the former was verified.

Another modification made to run bifurcation solutions was to evaluate the aerodynamic coefficients only once for every point actually accepted as a solution point, and not every time $\underline{\Gamma}$, or worse, $\underline{f}$, is evaluated. This results of itself in considerable time savings, as the aero data for aircraft F requires interpolation routines. However, great care must be taken here not to overlook valid changes in aero coefficients resulting from changes in elements of $\underline{y}$.

The modifications mentioned above, when applied to the non-spin bifurcation system, can generate almost a solution point per CPU second, an improvement by about a factor of 50 on the unmodified system, which was used on simpler aircraft models. Results for the F-4 are discussed in Chapter 3.

2.1.2.2 Spin Bifurcation System

Here, the dimension for high-α aircraft is 8, with likely reduction to 7 due to elimination of V from the coupled system, as discussed in Section 2.1.4. For $n = 8$, the augmented Jacobian matrix Γ assumes the size 9×10, and this presents formidable dimensionality problems. We

have initiated development of this system but not with the vigor that the $n = 5$ system has received, for three reasons: (i) it is natural to initiate development on a smaller system; (ii) although the $n = 5$ system is relevant strictly for trim and near stall α values only, our previous work (Mehra and Carroll, 1978) indicates that high-α resutls using the "trim" ($n = 5$) system do not differ numerically by more than 25% from the "spin" ($n = 8$), which is more proper to use when $\alpha \gtrsim 30°$. Furthermore, qualitative features, including stability information, are preserved. See Section 3.1.1; (iii) finally, the F-4 model has yet to yield limit points within the control limits when in high-α or spin flight regimes. Although this is not the case with aircraft F, the latter model is used for development reasons only.

2.1.3 Limit Cycle Continuation Algorithm

A limit cycle is a nonlinear motion ("closed orbit") which is characterized by the return of the state $\underline{x}$ to a previous point at some fixed time later, T. The purpose of the limit cycle continuation algorithm is to generate those surfaces in the equilibrium state-control space for which periodic, or limit cycle, motions persist after transient motions become negligible. The mathematical constraint on such a surface is the requirement that there exists some $T \in [0, T_{max}]$, $T_{max} < \infty$, for which

$$\underline{x}(T;\underline{x}_0) \equiv \underline{x}_0 \tag{2.11}$$

where the general expression for $\underline{x}(T;\underline{x}_0)$ is given by

$$\underline{x}(t;\underline{x}_0) \triangleq \underline{x}_0 + \int_0^t \underline{f}(\underline{x},\underline{\delta};s)ds \tag{2.12}$$

Chua and Lin present an algorithm for one aspect of this problem, the "corrector," which is stated as (Chua and Lin, 1975, Sec. 17.6):

> Given the system $\dot{\underline{x}} = \underline{f}(\underline{x},\underline{\delta})$, find $\underline{x}_0$ and $T(\underline{x}_0)$ such that (2.11) is satisfied.

They present what is basically a Newton-Raphson-type scheme to solve (2.11) for T. The problem is, in essence, one of using the $n^{\underline{th}}$ order system of equations (2.11) to solve for T and $\underline{x}_0$, (n+1) unknowns. The control vector $\underline{\delta}$ enters as a fixed parameter, for the scope of problem to which they address their method.

Our modification is to find the subspace of points $X \triangleq (\underline{x}_0, T, \underline{\delta})$ for which (2.11) holds by using the BACTM continuation algorithms derived from Kubicek (1976), with an element of $\underline{\delta}$ being selected as the nominal continuation parameter. The modification, then, expands the scope of the problem by introducing "predictor" as well as "corrector" aspects. As a result, a smooth curve $T(\delta_i)$, where δ_i is the continuation parameter, is generated. The motivation for developing this expanded algorithm is to seek control changes which would move the system from a limit cycle region to one free of limit cycles (T = 0).

The method of Chua and Lin (1975) will now be discussed in detail, and changes needed to incorporate their basic method into the continuation system of BACTM will be pointed out:

Initial guesses for $\underline{x}_0$ and T, say $\underline{x}_0^{(0)}$ and $T^{(0)}$, are input, along with relevant control values, $\underline{\delta}$. One of the controls, say δr, is specified as the nominal continuation parameter. ("Nominal" in the sense that the Jacobian based on this parameter remains sufficiently well-conditioned; as the continuation process develops, the continuation parameter may change

from δr to one of the x_{0_i} --or even T-- if the Jacobian starts showing singular tendencies.) The problem of the underdetermined system is dealt with by selecting* and holding fixed one of the $\underline{x}_0^{(0)}$, viz.: $x_{0_k}^{(0)}$. This element then becomes an additional parameter. The n remaining unknown elements are ordered as follows:

$$\underline{y}' = (x_{0_1},\ldots,x_{0_{k-1}},T,x_{0_{k+1}},\ldots,x_{0_n}) \tag{2.13}$$

The method of Chua and Lin solves for (2.13) by using (2.11), with $x_{0_k}^{(0)}$ and $\underline{\delta}$ held fixed. (An iterate of the ultimate solution is defined as

$$\underline{y}^{(j)'} \triangleq (x_{0_1}^{(j)},\ldots,x_{0_n}^{(j)})) \tag{2.14}$$

In order to utilize the Kubicek continuation algorithm on this system, it is necessary to expand $\underline{y}'$ to an (n+1)-dimensional vector:

$$\underline{y} \triangleq (x_{0_1},\ldots,x_{0_{k-1}},T,x_{0_{k+1}},\ldots,x_{0_n},\delta_{ICNTL}) \tag{2.15}$$

where

$$\delta_{ICNTL} = \begin{cases} \delta a, & ICNTL = 1 \\ \delta e, & ICNTL = 2 \\ \delta r, & ICNTL = 3 \end{cases} \tag{2.16}$$

The continuation problem, an extension of the problem of (Chua and Lin, 1975), is now restated as:

> Given a "reasonable" initial guess, $\underline{y}^{(0)}$, and given x_{0_k}, find all $\underline{y}(\delta_{ICNTL}) \in Y$, where Y is some admissible set, such that

$$\underline{F}(\underline{y};\delta_{ICNTL}) \triangleq \underline{x}_0 - \underline{x}(T;\underline{x}_0) = 0 \tag{2.17}$$

*The selection method will be detailed below.

The Jacobian matrix of this system is now defined as

$$G \triangleq \left[\frac{\partial \underline{F}}{\partial \underline{y}'}\right]_{n\times n} \tag{2.18}$$

Note that $\underline{y}'$, of dimension n, is used here, not the (n+1)-vector $\underline{y}$. The Kubicek continuation algorithm uses a non-square "Jacobian" matrix

$$\Gamma = \left[\frac{\partial \underline{F}}{\partial \underline{y}}\right]_{n\times(n+1)} \tag{2.19}$$

and, by means of controlled pivoting, eliminates a column from Γ, leaving a square array, Γ_ℓ, where ℓ represents the eliminated column. ℓ also represents the index for the element in $\underline{y}$ which is the current continuation parameter. For example, if $\ell = n+1$, δ_{ICNTL} is the parameter and $\Gamma_\ell = G$. For each prediction in the continuation process, the value of ℓ may change. Also, as described below, the value of k in selecting $x_{0_k}^{(j)}$ for the $j^{\underline{th}}$ Newton correction iteration may change with each iteration. In each case, the desire is to have as well-conditioned a Γ_ℓ as possible.

The continuation algorithm is as follows:

1) Read in $\underline{x}_0^{(0)}$, $T^{(0)}$, $\underline{\delta}$; select a value for ICNTL;

2) Select k as follows:

Solve (2.12) for $\underline{x}_F(T^{(0)}) \triangleq \underline{x}(T^{(0)};\underline{x}_0^{(0)})$ and evaluate

$$\underline{f}_F \triangleq \underline{f}(\underline{x}_F,\underline{\delta}) \tag{2.20}$$

k is the value for which

$$|f_k(\underline{x}_F,\underline{\delta})| > |f_i(\underline{x}_F,\underline{\delta})|, \quad i \in (1,\ldots,n),\ i \neq k \tag{2.21}$$

is true. The reason for this selection scheme is that the

invertibility of the Jacobian matrix requires that $|f_k| \neq 0$;

3) With this value of k, replace $x_{0_k}^{(0)}$ with x_{F_k}: $x_{0_k} = x_{F_k}$ $\underline{x}_0^{(0)}$ is now updated

$$\underline{x}_0^{(0)} = (x_{0_1}^{(0)},\ldots,x_{0_{k-1}}^{(0)}, x_{0_k},x_{0_{k+1}}^{(0)},\ldots,x_{0_n}^{(0)} \tag{2.22}$$

(there is no iteration index on x_{0_k} to emphasize its new parametric role), and the continuation vector becomes

$$\underline{y} = (x_{0_1}^{(0)},\ldots,x_{0_{k-1}}^{(0)},T^{(0)},x_{0_{k+1}}^{(0)},\ldots,x_{0_n}^{(0)},\delta_{ICNTL}) \tag{2.23}$$

4) With the updated $\underline{x}_0^{(0)}$, determine an updated $\underline{x}_F$ from (2.12), where

$$\underline{x}_F = \underline{x}(T^{(0)},\underline{x}_0^{(0)}) \tag{2.24}$$

5) The Newton-Raphson iteration ("Corrector") involves updating $\underline{y}^{(j)}$ by $\underline{y}^{(j+1)}$ in a manner which drives $\underline{F}$ as given by (2.17) to zero. That is, first order information is used to update $\underline{y}^{(j)}$:

$$\underline{y}^{(j+1)} = \underline{y}^{(j)} - G^{-1}\underline{F}(\underline{y};\delta_{ICNTL}) \tag{2.25}$$

In (2.25), $\underline{F}$ is evaluated by subtracting (2.24) from (2.22), for the $j^{\underline{th}}$ iteration:

$$\underline{F}^{(j)} = \underline{x}_F - \underline{x}_0^{(j)} \tag{2.26}$$

If $|\underline{F}^{(j)}| \leq \varepsilon$, the corrector process ends; if not, $\underline{y}^{(j+1)}$ must be found, which requires first evaluating G (G is more correctly Γ_ℓ in terms of the overall problem. The distinction for the moment is not important.)

For ease later on, not only G but

$$\Gamma \triangleq \left[\underset{n\times n}{G} \;\vdots\; \left(\frac{\partial \underline{F}}{\partial \delta}_{ICNTL}\right)^{T}_{n\times 1} \right] \tag{2.27}$$

is computed using numerical differentiation when $j \neq k$:

$$G_{ij} = \begin{cases} -\underline{f}_{F_i}, & j = k \\ -\dfrac{(x^{+}_{F_i} - x_{F_i})}{(x^{+}_{0_j} - x_{0_j})}, & \begin{matrix} j \neq k \\ i \neq j \end{matrix} \\ 1 - \dfrac{(x^{+}_{F_i} - x_{F_i})}{(x^{+}_{0_j} - x_{0_j})}, & \begin{matrix} j \neq k \\ i = j \end{matrix} \end{cases} \tag{2.28}$$

This formula is justified in Chua and Lin (1975). It comes directly from the differentiation of the right side of (2.17) with respect to $\underline{y}$ using (2.12) and the Leibnitz Rule. In (2.28), $x^{+}_{0_j}$ is the $j^{\underline{th}}$ element of $\underline{x}^{+}_{0}$, defined as

$$x^{+}_{0_i} = \begin{cases} x_{0_k}, & i = k \\ y_i + \Delta, & i \neq k \end{cases} \tag{2.29}$$

With $\underline{x}^{+}_{0}$ given,

$$\underline{x}^{+}_{F} = \underline{x}^{+}_{0} + \int_0^{T^{(0)}} \underline{f}(\underline{x}^{+}_{0}; \underline{\delta})dt \tag{2.30}$$

In (2.29), Δ is set to 10^{-4}, and a quantity

$$\rho_i = \frac{\Delta}{|x^+_{F_i} - x_{F_i}|} \tag{2.31}$$

is generated.

If $|\log_{10}(\rho_i)| > 1$ for any i, then Δ in (2.29) is replaced by $\Delta \cdot \rho_i$, the integration (2.31) is repeated, and the above check is done; all until the test is satisfied or until an iteration limit is exceeded. The logic for sizing Δ represents one expansion on the method of Chua and Lin. It is based on our experience in evaluating numerical derivatives. There are other options which may be considered in the future. One would involve the evaluation of four additional $\underline{x}_F$'s about the basic $\underline{x}_F$, and then using spline function approximations to compute $\frac{\partial \underline{x}_F}{\partial \underline{x}_0}$. We are using the one presented, however, as it involves fewer integrations.

In a similar manner, the sixth column of Γ,

$$\Gamma(\cdot,6) = \frac{\partial \underline{F}}{\partial \delta}_{ICNTL}, \tag{2.32}$$

is evaluated numerically. The formula is

$$\Gamma_{i,6} = -(x^+_{F_i} - x_{F_i})/(\rho_i \cdot \Delta) \tag{2.33}$$

where, as for the G submatrix of Γ, $\rho_i = 1$ in (2.33) unless the ρ_i given by (2.31) violates $|\log_{10}(\rho_i)| > 1$.

6) $\underline{F}$ and $\underline{\Gamma}$ having been numerically evaluated, the Kubicek subroutine

GAUSE is called. This routine does inversion by Gaussian reduction using controlled pivoting to eliminate a column of Γ. It therefore finds ℓ and inverts the resultant submatrix Γ_ℓ. Then $\underline{y}^{(j+1)}$ is computed from (2.25), using Γ_ℓ for G. The column ℓ is controlled to some extent by the use of "preference" parameters. In this way, a favored element of $\underline{y}$, usually δ_{ICNTL}, remains the continuation parameter. If no ℓ is found, Γ_ℓ is singular and the problem aborts. See Mehra and Carroll (1978) for details of this method.

7) The tolerance

$$P = \sum_{i=1}^{n+1} W_i |y_i^{(j+1)} - y_i^{(j)}| \tag{2.34}$$

is computed next, where W_i is an (input) weighting element. This is used in step (11).

8) For the usual case ($\ell \neq k$), $\underline{y}^{(j+1)}$ will contain a new iteration for T, $T^{(j+1)}$, as well as (n-1) new iterates for $x_{0_m}^{(j+1)}$. The continuation parameter, typically δ_{ICNTL}, as stated above, is unchanged until (2.17) is satisfied to within an acceptable tolerance. It is possible to keep k, hence x_{0_k}, unchanged throughout. However, Chua and Lin (1975) show that $f_k(\underline{x}_F, \underline{\delta}) \neq 0$ assures an invertible matrix. Thus, using $|f_i(\underline{x}_F, \underline{\delta})|_{max}$ to determine k insures numerical robustness also. Therefore, for each $\underline{y}^{(j+1)}$, k should be reevaluated. As the solution converges, k should not change. The index k is found as follows:

   a) $\underline{x}_0^{(j+1)}$ is updated to reflect the new values in $\underline{y}^{(j+1)}$; the old x_{0_k} is unaffected; however, there is a new period,

$$T^{(j+1)} = y_k^{(j+1)}$$

b) a new $\underline{x}_F$ is found by integration:

$$\underline{x}_F = \underline{x}_0^{(j+1)} + \int_0^{T^{(j+1)}} \underline{f}(\underline{x}_0^{(j+1)}; \underline{\delta})dt \qquad (2.35)$$

c) $\underline{f}_F = \underline{f}(\underline{x}_F; \underline{\delta})$ is evaluated

d) k is chosen as before such that

$$\left|f_{F_k}\right| \geq \left|f_{F_m}\right|, \quad m = 1,\ldots,k-1,k+1,\ldots,n \qquad (2.36)$$

9) Currently, whether or not k changes, $x_{0_k}^{(j+1)}$ is replaced by x_{F_k} from (2.35). As more computational experience is gained, this step may be altered or completely avoided.

10) $\underline{x}_0^{(j+1)}$ with $x_{0_k}^{(j+1)}$ replaced by x_{F_k} as stated in Step (9) is used to generate a compatible $\underline{x}_F$ using (2.35).

11) Test P computed in Step (7). If P > some ε, increment j by 1 and go back to Step (5); if $P < \varepsilon$, convergence is assumed about the initial point $\{\underline{x}_0^{(0)}, \underline{\delta}^{(0)}\}$. In this case, $\underline{y}^{(j+1)}$ is the basis for another Newton evaluation (call to GAUSE). The subroutine GAUSE also returns the derivatives of the elements of $\underline{y}^{(j+1)}$ with respect to the continuation parameter. This information is used in the Kubicek algorithm ADAMS to "continue" the solution: i.e., the continuation parameter (y_ℓ, nominally δ_{ICNTL}), as an independent variable, is augmented by some (input) step size, and a new $\underline{y}$ is "predicted." Then the correction segment at the new point is initiated, by going to Step (5). The continuation process halts when any of the variables

in $\underline{y}$ exceeds a specified bound, or when the signularity in G is not caused by a limit point (in which case rank $(\Gamma) < n$).

A flowchart of this algorithm is shown in Figure 2.2. This algorithm has not yet reached operational status; however, testing has been completed to the extent that the basic algorithm has been verified and is known to perform adequately. Problem areas which remain are generally of a secondary nature and include the following:

i) CPU time remains high at this point, with about a hundred CPU seconds being required to complete on the order of five Newton corrector steps for iterating to a solution point. Some improvements can be made here, but these runs will be costly, due largely to the number of integrations required in computing the Jacobian matrix;

ii) the tolerance logic for the numerical differentiation algorithm needs improvement so that it can operate in a more closed loop manner. At this point, the logic is very problem-dependent and the tolerances often are changed in an open-loop manner.

We do emphasize here, however, that the method of Chua and Lin, Steps (2) to (5), is coupled to the highly robust continuation algorithm of BACTM; the result is a powerful tool for the quantitative global analysis of limit cycle behavior.

That the basic algorithm is working will be shown by presenting some numbers from a test example. The test case involves aircraft F with $V = 600$ fps, h fixed at 30,000 ft, $\delta a = 15°$, $\delta e = 0°$, and $\delta r = 28°$. From a plot of the trajectory thereby generated, the initial guesses for $\underline{x}_0$ and T were:

Figure 2.2 Limit Cycle Continuation Algorithm

PROBLEM: Find (n+1) values $\underline{x}_0, T$ for which $\underline{F} \triangleq \underline{x}(T;\underline{x}_0) - \underline{x}_0 = 0$

ALGORITHM:

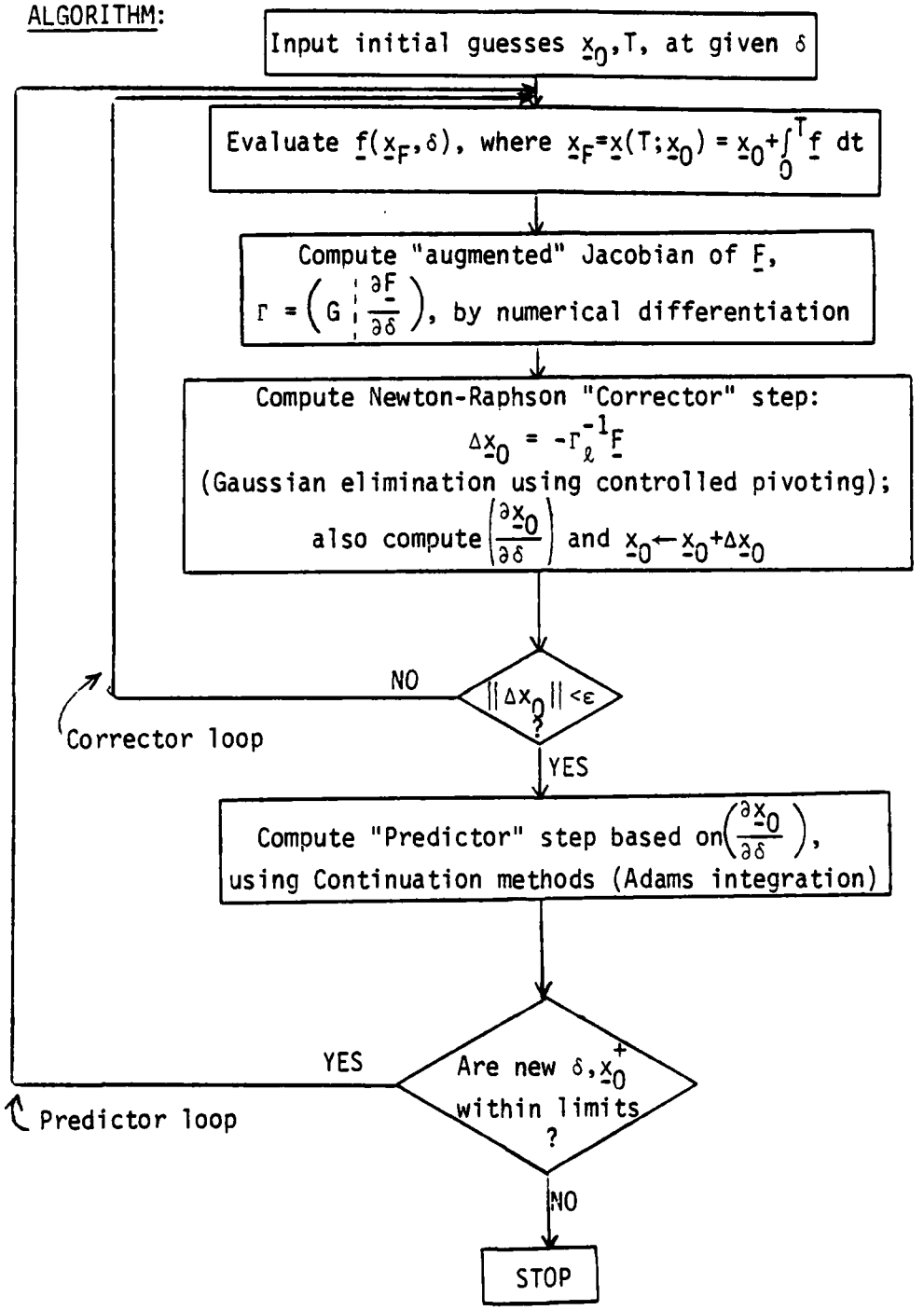

$$\underline{x}_0^{(0)} = (p_0, q_0, r_0, \alpha_0, \beta_0) = (79.9, 69, 14.6, 83.38, 58.66, -8.63)$$

$$T^{(0)} = 2.5$$

$T^{(0)}$ was estimated visually, and $\underline{x}_0^{(0)}$ was read from printout.

After only three Newton steps, we have

$$\underline{x}_0^{(3)} = (70.33, 18.62, 73.50, 50.54, 49, -7.24)$$

$$T^{(3)} = 2.487$$

Thus, integrating over $T^{(3)}$ from $\underline{x}_0^{(3)}$ should yield a state $\underline{x} \simeq \underline{x}_0^{(3)}$. In fact, $\underline{x}(t_0+T^{(3)}) = (70.36, 18.63, 73.50, 54.49, -7.23)$; this is certainly an acceptable result.

2.1.4 Reduced Spin Equilibrium System

A "reduced spin" equilibrium system has been developed for the F-4 model. This is potentially a very important result for the following reasons: i) dimensionality. Even a reduction by only one dimension (achieved here by eliminating V from the system) has a large impact on size, run-time and general computational efficiency; ii) scaling. With the removal of V, potential scaling problems are eliminated, because the remaining state variables have units of angles or angular rates. The computation and inversion of the Jacobian matrix therefore proceeds much more easily; iii) finally, this system should be the basis for a very efficient bifurcation surface program, because of features (i) and (ii).

The reduction was achieved by recognizing that the $\dot{V} = 0$ equation in the $\dot{\underline{x}} = \underline{f}(\underline{x},\underline{\delta})$ system is readily converted into a quadratic expression for V, when the functional relationship $\bar{q}(h,V)$ is explicitly stated. Thus, we can write

$$\dot{V} = 0 = A_V V^2 + B_V V + C_V \tag{2.37}$$

In this expression, the three coefficients are functions of $\underline{x}_R \triangleq (p,q,r,\alpha,\beta,\theta,\phi)$ and $\underline{\delta} \triangleq (\delta a, \delta e, \delta r)$, but not of V. Ignoring the physically impossible negative root, we have

$$V = \frac{-B_V + \text{sgn}(A_V)\sqrt{B_V^2 - 4A_V C_V}}{2A_V} \tag{2.38}$$

Using the reduced spin system, a run was made in which the starting equilibrium point was determined to be

$$\underline{x}_R = (37.56,\ 1.95,\ 154.6,\ 76.4,\ 0.26,\ -13.65,\ 0.72)$$

for

$$\underline{\delta} = (0.,\ 0.,\ -25.) \quad \text{and} \quad V = 381.74$$

The full spin system was used at this same point, with the result

$$\underline{x}_S = (37.57,\ 1.94,\ 154.6,\ 76.4,\ 0.26,\ 380.97,\ -13.65,\ 0.72)$$

A comparison shows excellent agreement, even for V, which differs only by 0.77 ft/sec.

At this time, the spin and reduced spin systems are not used at trim, because there are no equilibrium solutions for θ and ϕ if thrust is not

present in the model. The above equilibrium point was computed in a steep spin region; there was no rotary balance data in the model at the time of the run so that these results may not be realistic.

3. BACTM APPLICATION TO SPECIFIC AIRCRAFT PROBLEMS

In this chapter, we discuss results obtained using BACTM on two aircraft models with particular emphasis on spin motions and spin recovery. Section 3.1 describes results with aircraft F, and Section 3.2 presents results obtained to date with the F-4 model. For convenience, Figures 3.1 to 3.36 and 3.42 to 3.88 for this chapter occur at the end of the chapter.

3.1 Aircraft F Results

During the rather extensive BACTM system modification and upgrading effort, work nonetheless progressed on using BACTM to analyze the high-α behavior of aircraft F. Selected results from these efforts are presented below. The major result for aircraft F has been a demonstration that the BACTM methodology can be used to generate spin recovery control strategies. This is discussed in Section 3.1.4.

3.1.1 Equilibrium Surfaces

The reason for producing the equilibrium surfaces for spin analysis is to generate equilibrium branches which extend from the so-called "trim" region--where the controls are neutral--to the region of developed, equilibrium spin. The global picture thus obtained will thus aid in defining control strategies for achieving mission results of interest.

Figure 3.1 shows r,α,p contours, respectively, versus δr for zero elevator and δa = 15 degrees. The extreme asymmetry and highly nonlinear

nature of these contours highlight the aircraft's sensitivity to control changes in the roll departure region (extreme aileron). A companion set of plots seen in Figure 3.2, for which $\delta a = 15$ degrees, $\delta r = 0$ and δe is allowed to vary, again show very much the strength of the nonlinearities when δa is large. Comparing Figure 3.2a to 3.1a, we can expect a third branch in the former figure, in the $\delta e = 0°$ region, near $r = 45$ deg/sec. The same is true for the respective α,p plots in Figures 3.1, 3.2. (The presence of physical bounds on the controls, e.g., $\pm 30°$ for δr usually requires multiple runs in order to detect and compute all of the equilibrium surfaces in a given region. This apparent "limitation" on the globality of the BACTM approach is mitigated by two items: (i) each branch represents a continuum of equilibrium solutions, each one of which has heretofore been solved for essentially by some open loop hunting technique, at very high expense of time and money. On the other hand, each branch computed by BACTM is done so with no more than one quick and inexpensive run; (ii) it is quite often possible, as in the Figure 3.1 - 3.2 case just discussed, to exploit the results of one run in a second run; e.g., from Figure 3.2 alone, there is no specific information about the location of a third equilibrium at $\underline{\delta} = (15,0,0)$, $r = 45°$, and so searching for it would require more effort, had not the Figure 3.1 results, which clearly show such a point, been available.) Nonlinear coupling is very evident in Figure 3.2b, which shows angle-of-attack (A on the plot axis) vs. δe. $\alpha(A)$ decreases with increasing δe in a nicely linear, stable manner from $\delta e = -11°$ to $\delta e = 2°$. However, at this point, due to inertia coupling, α sharply changes slope from negative to positive.

In order to investigate spin behavior, we have selected a right pro-spin control setting ($\delta a = 15°$, $\delta e = -21°$, $\delta r = -25°$) as the reference spin condition. These exist other, non-spin equilibrium states for this particular setting; however, if the aircraft state is close enough to the equilibrium spin state,

$$\underline{x}_{SP} = (30., -4., 100.9, 73.53, -3.1) \tag{3.1}$$

where

$$\underline{x} = (p, q, r, \alpha, \beta), \tag{3.2}$$

associated with the particular spin control setting specified above, then spin equilibrium branches will result.

In our previous studies, the spin equilibrium surfaces were generated using the full spin system of dynamic equations. This system assumes the presence of gravity forces, which couples the orientation angles θ (pitch) and ϕ (roll) into the basic non-spin system (3.2). Velocity may or may not be included (see Section 2.1.4). The presence of θ and ϕ is an important requirement for realistic analysis of spin behavior. However, this does present an interfacing problem with the non-spin equilibrium region, in which zero gravity is a reasonable, workable assumption. With zero gravity, the coupled state variables are $\underline{x} = (p,q,r,\alpha,\beta)$ (the control set for either case, of course, is $\underline{\delta} = (\delta a, \delta e, \delta r)$). The spin system does not produce equilibria near trim conditions because gravity keeps θ and ϕ from achieving equilibrium values. The presence of thrust in the model tends to offset this gravity effect, as discussed in Sec. 3.2.5.

It was felt to be of interest to see if the $g = 0$ (non-spin) system can generate surfaces which retain basic features of the actual spin

system surfaces. A comparison of Figures 3.3 and 3.5 shows that, indeed, the essential features remain. There is less of a numerical disparity than anticipated, even for the α-plots, which reflect the (θ,ϕ)-coupling in a stronger manner than do the (p,r)-plots. A possible explanation for this is that θ_{SP} is small and ϕ_{SP} is almost 90°, and this restricts gravity's influence on the aircraft z-body (α) motions.

A stronger influence than gravity, in this regard, is seen by comparing Figure 3.4 to Figure 3.3. In the former, V = 600 fps, whereas V = 443 fps in the latter to afford better comparison with the $g \neq 0$ results of Figure 3.5. With V being the only difference between Figures 3.3 and 3.4, there is a noticeable difference in magnitude of the results, although again, the spin features remain. The non-zero gravity, or spin system, equilibrium plots are presented in Figure 3.5 for comparison.

The computation of the = 600 fps, g = 0 equilibrium surfaces in the spin region essentially demonstrates that it is now possible for one system--the non-spin, g = 0 system--to extend from non-spin regions into spin regions (where the g = 0 assumption is not as valid, but where the essence of the spin features nonetheless remain).

3.1.2 Bifurcation Surfaces

As reported elsewhere in this report, significant and substantial progress has been made to upgrade and "strengthen" the bifurcation surface solution algorithms. Also, because of the results reported in the above section regarding the extension of the g = 0 system (non-spin) into the spin ($g \neq 0$) region are relatively recent, the use of the non-spin (state dimension = 5) bifurcation system in the spin regime should help in

producing results. In any event, such an analysis would be followed by the more accurate spin bifurcation system (state dimension = 8).

At this time, only "developmental" versions of both the spin and non-spin bifurcation packages are available for aircraft F, so that no plots exist for any bifurcation runs. The non-spin version, however, has been more thoroughly checked out, and is essentially ready to generate and plot such solution curves. Furthermore, an F-4 version has been completely developed, the results of which are discussed in Section 3.2.7.

3.1.3 Time History Runs

As also described elsewhere, the aircraft F time history package has been incorporated into the expanded BACTM system package. Files have been made, and the preliminary results are now presented.

Figure 3.6 shows the time history of the aircraft F center-of-gravity in flat spin as seen in the reference horizontal frame. The top figure shows the time variation of altitude, from which it is easily determined that the rate of descent is fairly steady. The initial conditions for this run were $(\underline{x}_{SP}, \underline{\delta}_{SP})$, the stable, developed spin condition discussed above. The bottom figure shows the c.g. trace on the horizontal plane, in which x_{NORTH} points due north, and y_{EAST} east. There is a noticeable left-to-right drift in the spin spiral, probably due to the asymmetry of the lateral aero data of aircraft F with respect to sideslip. (The trajectories begin at the (0,0) point.) Note how tight the spiral is for this condition (the x-y coordinates are in feet).

In contrast to the equilibrium spin trajectory is the trajectory

presented in Figure 3.7, which represents a run beginning in trim conditions with neutral controls, and then stepping all of the controls simultaneously to $\underline{\delta}_{SP}$ at t = 2.0 seconds. The horizontal c.g. trace (Figure 3.7b) obviously has a much different scale, as the familiar spin spiral fails to develop. Altitude variation is not uniform, as a check of the velocity (VEL) trajectory would imply (Figure 3.7f). Finally, the other parameters exhibit a noticeably erratic behavior, indicating, first, that no equilibrium motion has been attained; and second, that the transition from trim flight into spin would involve a more complicated sequencing of the controls.

More extensive use of the equilibrium and time history BACTM programs is discussed in the following section, which features spin recovery analysis for aircraft F.

3.1.4 Application of BACTM to Spin Recovery and Spin Reversal

Much of the effort in this reporting period has been devoted to completing spin recovery studies with the aircraft F model. Based on an investigation of several relevant equilibrium surfaces, a spin recovery control sequence has been found by which aircraft F can recover from a stable, flat, erect spin equilibrium condition to a complete, non-oscillatory trim condition. This control strategy is noteworthy in that (i) is was derived primarily by BACTM analysis. Control recovery sequences for the same model implemented on a fixed base simulator (Moore, et al., 1971) have been tried with our model (Mehra and Carroll, 1978), but with inconclusive results. The reason is that is was difficult to obtain initial conditions or timing for the control changes from the figures presented

in Moore et al. (1971) with sufficient accuracy. As will be seen, spin recovery trajectories are highly sensitive to both initial conditions and control sequencing, because of their highly nonlinear nature; and (ii) the control history developed by BACTM nonetheless has many of the features of spin recovery control sequences which others have used, which are for the most part derived empirically. The main similarity is that the rudder is deflected from one limit position (pro-spin) to the opposite one (anti-spin), before being returned to trim.

The ($\delta a, \delta e, \delta r$) time histories and the recovery trajectory are shown in Figure 3.8. In this run, the elevator has been fixed at trim. The actual pro-spin control setting would be $\delta e = -21°$, the setting which would be responsible for inducing stall and spin entry. However, once the flat spin equilibrium condition is achieved, the elevator becomes ineffective as a control. Therefore the first control action for recovery, not shown in Figure 3.8, is to move δe from its pro-spin setting of -21° to trim.* Note in Figure 3.8 that all motion ultimately becomes steady-state. Notice also that very oscillatory, limit-cycle-type motions occur during the recovery. This is a consequence of converging the spin equilibrium from a stable one to an unstable one, by means of changing the controls. The limit cycle behavior typifies motion in the flight regime intermediate to the flat spin and trim regimes. The study, therefore, of limit cycle motions, Hopf bifurcations and the conditions under which limit cycle amplitudes decay to a steady state mean value is a very significant aspect of a better understanding of spin recovery dynamics.

*Young (1974), however, studies optimal and suboptimal recovery techniques on several models which show that oscillating the elevator at the limit cycle frequency enhances recovery. We hope in the future to investigate this approach using BACTM.

This observation motivates the development of the limit cycle continuation algorithm discussed in Section 2.1.3. The control sequence for effecting spin recovery, then, by changing the flight condition from a relatively mild limit cycle condition ($\delta r = -18°$) to a rather severe oscillatory condition ($\delta r = 28°$), is predicated on the knowledge, obtained primarily from the equilibrium surfaces, that returning δr to trim from -18° in this case does not change appreciably the limit cycle motions; however, the limit cycle amplitudes do decay when δr is trimmed from 28°, at the cost of very severe transient oscillations while $\delta r = 28°$. A final note on Figure 3.8: altitude and speed are free to vary. Initial velocity was 450 fps, initial altitude was 30,000 ft, and altitude when recovery was first attained ($t \simeq 60$ sec) is 8000 ft.

As stated above, the control sequence for spin recovery was derived largely via the BACTM equilibrium surfaces which pertain to the relevant equilibria (i.e., the spin equilibrium in which the motion begins and the desired trim equilibrium). Figure 3.9 shows a composite of these. In Figures 3.9 a,b respectively, $\bar{r}$ and $\bar{\alpha}$ (equilibrium r and α) are plotted against δr; and Figure 3.9 shows a plot of $\bar{r}$ vs. δa. For all of these figures, $\delta e = 0°$ and V is fixed at 350 fps. Holding V constant in the equilibrium surfaces is justified because, even when V is allowed to vary dynamically, it quickly assumes a steady-state value for motion confined to either the flat spin regime (Branch 1 in Figures 3.9a,b) or the non-spin regime (Branch 3). Branch 2, located between the flat spin and the non-spin branches, governs motion in the steep, or oscillatory, spin region ($\alpha \simeq 60°$). Aileron is 15° on Branch 1, and 0° on the other two.

However, while the basic shapes of the equilibrium surfaces are generally invariant to the value of V selected, the equilibrium values themselves do change significantly with V (cf. Figure 3.49 of Mehra and Carroll, 1978). This situation indicates that the value of V may play an important role in spin recovery dynamics, and results to be presented below confirm this. But useful results from equilibrium surfaces are not obscured by assuming constant V.

The major goal in spin recovery, referring to Figure 3.9, is to change the equilibrium state from the stable one (albeit a very undesirable one) at Point A to the trim equilibrium at Point E. From this figure, it is seen that moving δr to -18° will initiate a jump (Hopf bifurcation) to the vicinity of Point B, which is governed by limit cycle motion (Figure 3.9c). Point B is actually not on the non-spin equilibrium surfaces of Figures 3.9a,b, Branches 2 or 3, since δa is still 15°. Returning the aileron from 15° to trim causes the equilibrium to change from Point B to C. Limit cycle behavior remains, as can be seen in Figure 3.8, for t less than 30 sec.

We emphasize here that Point B, which has been associated with Branch 3 in Figure 3.9, may actually belong to Branch 2. At this setting of δr (-18°), the limit cycle motion includes both Branches 2 and 3; the distinction in this case is not important. The change from Point B to C occurs along the δa-axis, with $\delta r = -18°$, and Figure 3.9c shows that very little seems to change. Figure 3.10 shows Point B on its own branch, at a different projection from that shown in Figure 3.9c. In Figure 3.10, $\delta a = 15°$, and this non-trim setting is seen to cause a much more prominent limit

point on Branch 3. It extends fully to $\delta r = 18°$ for $\delta a = 15°$ (Figure 3.10), but only to about $\delta r = -6°$ when $\delta a = 0°$ (Figure 3.9c); in the latter case, it is thus easier to move toward trim conditions with large, positive δr.

With δa and δe now at trim, there remains only to sequence the rudder so that the oscillatory motion decays and the equilibrium condition at Point E is reached. However, it is known that, while the L-points on the equilibrium manifolds indicate possible limit cycle behavior (two imaginary eigenvalues with a positive real part of the system linearized about the (unstable) equilibrium point), the limit cycle amplitude does not, in general, decay as the control changes from, say, its value at Point C to Point E. In our case, the limit cycle amplitudes persist as δr increases from -18°, even through the stable region centered at trim (Point E). This is due to the influence of Branch 2, about which the transitory motion is centered. However, the limit cycle amplitude does decay when δr decreases from Point D to Point E. This indicates a likely global bifurcation, i.e., the annihilation of a stable limit cycle by an unstable one, as a parameter (here, δr) changes. The Branch 2 limit cycle is no longer an attractor when δr is large enough. This phenomenon has been discussed previously, in reference to aircraft H (Figures 3.48 and 3.49 from Mehra, et al., 1977), and will be discussed in more detail below.

It should be pointed out that other control sequences exist from which spin recovery may be achieved in this example. The one presented, furthermore, is not necessarily optimal in any sense, such as minimum time. Use of bifurcation surfaces will aid both in developing families of recovery strategies and in selecting more optimal strategies.

3.1.4.1 Velocity and Altitude Effects

In Figure 3.8, it can be seen that V is allowed to vary, and that it begins to increase sharply in conjunction with the decay of the dynamics to steady state values. The increase in V adds to control effectiveness through an increase in dynamic pressure at the point where anti-spin moments are being generated by the controls. Without this increase, these anti-spin moments do not reach the magnitudes required to offset the motions due to the spin, and so the limit cycle motions persist. This can be seen clearly in Figure 3.11, in which all of the conditions of Figure 3.8 are duplicated, except for fixing V at 450 fps (holding V constant simulates a thrust profile which instantaneously offsets drag effects). The motion is roughly similar at first, but diverges quite noticeably from the recovery trajectory of Figure 3.8 beginning at about 20 sec, when δa is trimmed. The expanding spiral of the center-of-mass locus in the horizontal plane, Figure 3.11c, indicates a condition from which further control action would likely effect recovery. But clearly, the effect of fixed V is pronounced.

3.1.4.2 Other Effects

The development of aerodynamic restoring control moments is similarly influenced by altitude or, more specifically, air density, the other constituent besides velocity in the dynamic pressure term (aero forces and moments are directly proportional to dynamic pressure). The spin equilibrium surfaces are generated under the assumption of constant altitude, so that they obviously correspond more closely to time histories in which

altitude remains fixed. Figure 3.12 shows such a run. As before, the only difference between the conditions here and those of Figure 3.8 is that altitude is maintained at 30,000 ft, which is the value for Figures 3.9 and 3.10. Unlike the case presented in Figure 3.11, recovery does occur here, although it is significantly delayed and the transient motions are more severe than those of the Figure 3.8 case. The reason for this is similar to the Figure 3.11 case: because altitude does not decrease, the control torques generated by the aerosurface controls have correspondingly less magnitude.

The existence of actual limit cycle motion when elevator and aileron are at trim and $\delta r = 28°$ is hard to discern in the basic spin recovery case (Figure 3.8), although the equilibrium surface (Figure 3.9) does predict such a motion. If the return of rudder to trim is delayed enough to allow for transient decay, limit cycle behavior does develop. This is indeed what happens, as Figure 3.13 shows. Here, the trajectory and control history duplicates that of Figure 3.8*, with the principal exception being that δr is held at 28° 20 seconds longer in Figure 3.13, before being trimmed. The two variables in the figure, p and Ω, both show the development of oscillatory behavior, although the Ω motion has yet to decay to a steady mean value. At $t = 60$ seconds, this oscillation is interrupted by the return of the controls, and also the motion, to trim.

If δr is not returned directly to trim from 28°, but stepped first to 14° for 30 seconds, and then to 0°, as seen in Figure 3.14, then recovery also occurs. There is an intermediate equilibrium condition

*except that $V(t=0) = 350$ fps.

corresponding to $\delta r = 14°$ which is featured by limit cycle motions of greatly reduced amplitude. The yaw rate at $\delta r = 14°$ is of opposite sign from that of the original equilibrium spin.

Another indication of both the general nonlinearity of the problem and the sensitivity of the system to changes in initial conditions or control sequencing is shown in Fig. 3.15. This figure represents a time history for which the basic recovery sequence, as well as initial conditions, was preserved; however, the time intervals between the control changes is reduced. In the case shown, the effect of reducing the time intervals is seen to cause the recovery effort to fail. In Fig. 3.15, the aileron is trimmed at 6 sec; the rudder is changed to 28° at 15 sec and trimmed at 20 sec. This case represents a 50% proportional scaling of the strategy which effects complete recovery.

As a result of inspecting several spin recovery runs, we have noticed certain situations which appear to bear directly on the issue of whether or not recovery may be achieved. By exploiting these situations in subsequent analyses, it has become apparent that control strategies based on the values of yaw rate (r) and angle-of-attack (α) can be developed which lead to spin recovery. Furthermore, spin reversal is a prominent feature of the recovery trajectories. Conditions which lead to reversal tend to be conditions which are favorable for recovery.

Our approach to this point has been to combine BACTM equilibrium and limit-cycle information with a series of time history runs whose "trim

initial conditions"--i.e., the value of $\underline{x}$, the state vector at the point in time at which the controls are returned to neutral or trim--are varied by several techniques over as much of the subspace as possible, thus defining in an ad hoc manner the domain of attraction of the trim equilibrium point. The domain of attraction, in fact, defines the recovery region for the aircraft.

For the most part the analysis has centered on the subspace depicted by the equilibrium curves shown in Figures 3.16a - 3.16d. These figures show two groups of equilibrium plots of r and α vs. δr; in one group, δr is increasing and in the other δr is decreasing. There are four equilibrium branches shown in each frame. Branch 1 includes the stable branch of the flat spin equilibrium for the case $\delta e = 0°$, $\delta a = 15°$, $V = 450$ fps. Branches 2, 3 and 4, the ones where the recovery emphasis lies, include the limit cycle branches associated with steep oscillatory spin (right and left) as well as the trim equilibrium branch (S). Superimposed on these equilibrium surfaces are projections along r and α axes of the limit cycle histories, generated as δr changes in steps between its limits. These projections are plotted in the figures as vertical bars. The height of each bar indicates the limit cycle amplitude at a given value of δr. This information will be much more readily available when the limit cycle continuation algorithm is applied to this problem.

It is clear from this figure that the direction of changing δr significantly influences the resultant motion. This is a hysteresis effect. Increasing δr from some value (Figures 3.16a,c) and then returning it to that value (Figures 3.16b,d) creates a hysteresis pattern out

of the time history projections. In the r vs. δr case, spin recovery does not occur in a direct manner; in fact, under increasing rudder (Figure 3.16), there is still very strong limit cycle activity when $\delta r = 0$. This limit cycle exists through $\delta r \approx 8°$; it is influenced by Branch 2, whose effect on the motion weakens steadily with increasing rudder, but does not vanish until $\delta r = 8°$. At this point the limit cycle disappears by merging with an unstable limit cycle (global bifurcation), and a jump occurs to a second (stable) limit cycle, governed by Branch 4. This second limit cycle family is shown for control values up to $\delta r \approx 20°$. Notice, however, as δr decreases from 20° (Figure 3.16b), the state remains strongly attracted to this left spin limit cycle family for almost the complete range of δr. Only when δr arrives at -30° does spin reversal reoccur, bringing the system to the original right spin cycle.

This lack of symmetry is also evident in another way. The equilibrium curve itself is not symmetric in terms of the stability character of equilibrium points. This is due to the fact that several of the lateral aero coefficients are not symmetric in β. C_y even lacks magnitude symmetry for all α, although one does expect anti-symmetry for this coefficient in sign. For example, at $\alpha = 30°$, $C_y(\beta = -30°) = 0.420$ and $C_y(\beta = 30°) = -0.323$. For most α, C_n is symmetric in magnitude and anti-symmetric in sign; but C_ℓ is like C_y. C_m, the remaining β-dependent coefficient (longitudinal), is sign-symmetric only in β, but the magnitude discrepancies are relatively small. Aero data asymmetries in β are the only realistic explanation for lack of symmetry in the equilibrium surfaces. The equilibrium surface asymmetries are naturally reflected in the time

history projections. If these were symmetric, for example, spin reversal for decreasing δr would have occurred by $\delta r \simeq -8°$, not at -30°. Also, the amplitudes of r (and α) clearly are different for the two limit cycle families.

The above observations pertain as well to the α-plots. Figure 3.16c shows the increasing δr case, and Figure 3.16d the decreasing case. Spin reversal at $\delta r = 8°$ (increasing) is highlighted here by a dip in the magnitude of α. Clearly, left spin is achieved for $\dot{\delta r} > 10°$ because by then, α has returned to very high spin values. The stable limit cycle for increasing rudder is not of the same size as that for decreasing rudder, because the magnitudes differ; of course, the distinction is clearer in the r-plots because of the sign change effected by spin reversal.

In the region $\delta r \in (0°,-20°)$, it can be seen that there are two stable limit cycle branches for a given δr. Furthermore, for any $\delta r \in (0°,-8°)$, there is a stable branch. Thus, one can postulate the presence of at lease three domains of attraction: two for the limit cycles sandwiching the asymptotically stable (or trim) domain. This is based on the equilibrium surface results shown in Figure 3.16. In addition, it is possible to state some qualitative things regarding the size of these three regions: we know, for example, that if $|r_0| \gtrsim 50°$ and $\alpha_0 \gtrsim 45°$, then return to trim conditions is not possible for $\underline{\delta} = 0$ (neutral controls)*. This is because such values would place the state outside of the trim

*The effect of the other variables has yet to be fully assessed; their values may possibly complicate this conjecture, but as yet no clear trend has been found.

domain of attraction. Also, we haven't done so, but it is possible to investigate motions beginning at high α_0 ($\approx$30°) and very high $|r_0|$ ($\gtrsim$150°/sec), at $\underline{\delta} = 0$, to see if there is still attraction to the known stable limit cycles.

Plots of r vs. α at two control points, $\delta r = 0°$ and $\delta r = -10°$, in the δr-region where two stable limit cycles exist are shown in Fig. 3.17. These figures represent another projection of the limit cycle time histories. They can be used for defining the r-α domains of attraction. For the $\delta r = 0°$ case, Figure 3.17a, there is a trim domain of attraction to be defined as well. The center of this domain is the trim equilibrium point for $\delta r = 0°$, i.e., $(r,\alpha) \approx (0,3°)$. By the time $\delta r = -10°$, Figure 3.17b, this domain has disappeared. The dotted lines in these figures represent conjectured domains of attraction, based on an incomplete study of the problem. The boundary between the trim domain and limit cycle domain is most likely an unstable limit cycle. The dots in the $\delta r = 0°$ case represent initial conditions of runs actually made, from which the domain of attraction has been determined approximately. These runs are described below.

The plots shown in Figures 3.16 and 3.17 thus add insight to the spin recovery picture for aircraft F which is of a global nature. Within the context of these figures, the relevance of the local time history results described below can be appreciated more. These runs are summarized in Table 3.1. Again, their purpose is both to define to some extent the boundaries of the domains of attraction, as well as to look more closely at how certain quantities and conditions affect spin recovery.

Run (File) Number/ Variable Trim Initial Conditions	164 (1)	220 (1)	221 (2)	222/232 (1)	223 (2)	224 (2)	229 (3)	230 (3)
p (deg/sec)	- 27.59	33.5	14.5	- 45.4	17.3	42.3	- 29	- 29
q (deg/sec)	3.89	13.97	21.1	48.1	66.17	73.96	17.75	17.75
r (deg/sec)	- 2.73	3.51	5.86	17.0	- 5.99	- 17.35	- 10.4	- 10.4
α (deg)	25.65	25.68	25.9	66.4	47.2	29.77	11.96	11.96
β (deg)	23.7	22.3	22.	30.8	48.90	58.74	8.08	8.08
V (fps)	364.5	358.3	411.0	344.8	388.	390.7	681.0	681.0
θ (deg)	- 50.87	-54	- 53	- 18.5	- 25.74	- 25.5	- 83.6	- 83.6
ϕ (deg)	44.3	46.7	42	34.0	59.68	74.37	76.3	76.3
t (sec) (last control change)	40.5	40.0	22.0	36.0	22.5	21.	0.	0.
RECOVERY (time)	Y (45)	Y (45)	Y (32)	Y (65)	N (-)	Y (45)	Y	Y
Figure No.	3.8	3.18	3.19	3.20	3.21	3.22	3.24	(none)

Table 3.1 Summary of A/C F Spin Recovery Runs;

Trim Initial Conditions

File/ Variable	231 (2)	233 (2)	234 (2)	236 (2)	237/241 (2)	240 (5)	242 (2)
p	52.15	111.2	60.12	- 6.44	114.2	0.	22.67
q	- 31.8	25.4	- 10.7	- 71.59	- 22.	0.	64.9
r	51.37	46.75	75.97	5.48	66.2	0.	48.2
α	42.77	25.37	48.5	60.59	37.06	90.	66.0
β	- 12.48	14.89	- 9.6	42.0	- 15.	0.	21.5
V	395.9	395.9	406.4	381.5	390.0	450.	392.0
θ	- 44.9	- 58.9	- 39.6	- 21.4	- 49.3	0.	- 22.
ϕ	- 14.6	39.2	- 11.3	48.88	- 20.3	0.	25.7
t (last control change)	0.	0.	0.	22.0	17.5	0.	18.5
RECOVERY (time)	N (-)	Y (10.)	N (-)	N (by 40 sec)	N (by 100 sec)	Y (8.)	N (-)
Figure No.	3.25	3.26	3.27	3.28	3.29	3.31	3.30

Table 3.1 (concluded)

All of the runs have the following features in common: aircraft F aero data model, $\delta e = 0°$, $V(t_0) = 450$ fps. The run numbers correspond to data files generated by the run, and are thus unique to every run. Numbers in parentheses below the file (run) number indicate commonality among the runs; i.e., two type 3 runs have more in common than a type 3 run and a type 2 run. Time histories of key variables for these runs are shown in Figs. 3.18 to 3.31. A summary of each of the runs of Table 3.1 and a description of their significance now follows.

File 220 (Fig. 3.18). The control logic duplicates File 164 run (not shown here; this run is the "basic" spin recovery run and is given in Fig. 3.8), except that the final control action of trimming the rudder ($\delta r = 0$) was initiated by means of the feedback logic

$$|r| \leq 10 \text{ deg/sec}$$

which was activated for $t > 30$ sec. Also, altitude (h) was allowed to vary from its initial value of 30000 ft. This run generates almost exactly the same trajectories as 164, as a result of $\delta r = 0$ occurring for both within 0.5 seconds of each other.

File 221 (Fig. 3.19). All conditions here duplicate those of runs 164 and 220 with the following changes in control strategy: $\delta r \rightarrow 28°$ and $\delta a \rightarrow 0°$ at 0.5 sec from their initial values of -25° and 15°, respectively; and, from 28°, $\delta r \rightarrow 0°$ when $|r| \leq 10$ deg/sec for any time t. This run clearly shows recovery, and at an earlier time that either 164 or 220. From Fig. 3.16, it can be seen that this control sequence readily produces spin reversal, and the rudder time condition would place the trim initial conditions within the trim domain of attraction, shown in Fig. 3.19a.

Files 222/232 (Fig. 3.20). Like 220 and 164, except that the "r trim window" is widened from 10 deg/sec to 20 deg/sec. This causes $\delta r \rightarrow 0$ 4 sec earlier than in the above two cases and can be seen to seriously jeopardize recovery. In fact, a follow-on run, file 232, is needed to confirm recovery. This run is an instance of trim initial conditions lying very close to the boundary of competing domains of attraction. Note in particular from Table 3.1 that α_0 (66.4°) is very high for a successful recovery.

File 223 (Fig. 3.21). This run is similar to 221, except that $\delta r \rightarrow 14°$ from -25° at t = 0.5 sec, and not 28°. Also, $\delta r \rightarrow 0°$ from 14° when $|r| \leq 15$ deg/sec. This is an early run which tries to benefit directly from the results shown in Fig. 3.16; however, α was not a factor in nulling rudder and it has an initial value (47.2°; Table 3.1) almost double the "typical" values for recovery runs. Also note that θ_0 is small and negative as opposed to successful recovery cases which typically show large and negative pitch. It is clear from Fig. 3.21 that recovery was not achieved.

File 224 (Fig. 3.22). This is a follow-on run to 223 above, in that it attempts to investigate effects of aileron on recovery; the run duplicates 223 except that $\delta a \rightarrow -15°$ at t = 0.5 sec, and not 0°. Aileron was trimmed (stick to neutral) in an open-loop manner at t = 25 sec. This value was chosen because it was expected that δr would be trimmed under its closed-loop strategy at about this time, based on the 223 results (Table 3.1). It is seen in Fig. 3.22 that this change indeed produces recovery. The reason for selecting -15° as the value for δa was motivated

by: (i) it produces an overall strategy very similar to those reported in the literature; and (ii) the BAC™-generated equilibrium surfaces for $\delta a = 15°, 0°, -15°$, as shown in Fig. 3.23, indicate likely improvement of recovery prospects, in light of the Fig. 3.16 situation for $\delta a = 0°$. Point (ii) will now be amplified further.

Fig. 3.23 shows plots of $\bar{r}$ vs. δr for $\delta e = 0°$, V = 450 fps and $\delta a = 15°$, 0° and -15° respectively. Fig. 3.23(b) is the same equilibrium plot as is seen in Figs. 3.16a,b, where $\delta a = 0°$. It was discussed earlier in some detail for the $\delta a = 0°$ case that δr had to increase beyond +8° to effect spin reversal, from initial conditions which place the motion on the stable limit cycle governed by the steep spin, positive-r, L-branch. The expected reversal or jump point is $\delta r \simeq -6°$. Based on the Fig. 3.16 results, a quick glance at both the $\delta a = 15°$ (Fig. 3.23(a)) and $\delta a = -15°$ (Fig. 3.23(c)) cases indicates clearly that recovery prospects from the flat right pro-spin condition are enhanced the more negative δa becomes. Figures 3.23a and 3.23b are the same as Figures 3.9 and 3.10. One feels secure in predicting failure to reverse in the $\delta a = 15°$ case (the pro-spin setting) because the equilibrium jump point moves from $\delta r \simeq -6°$ (when $\delta a = 0°$) to $\delta r \simeq 18°$ ($\delta a = 15°$). On the other hand, there is not even a jump in the -15° case to the asymptotic (S) branch. Moving the rudder to 14° for the $\delta a = -15°$ case most likely effects "escape" from the domain of attraction of the upper-left L-branch in Figure 3.23c. Presumably, the domain shifted to the middle L-branch in this figure ($\bar{r} \simeq 3$ deg/sec), from which recovery ensues when all controls are neutralized. We expect to generate Figure 3.16-like plots for the $\delta a = \pm 15°$

cases as well, to confirm these observations. This will be done with the limit cycle continuation approach.

File 229 (Fig. 3.24). This run attemots to use Fig. 3.16 results directly to effect spin recovery. By selecting trim initial conditions "appropriately" from the $\delta r = 8°$ trajectory which is projected onto Fig. 3.16(a), it is hoped that recovery ensues for δr set at 0°. This does happen, as Fig. 3.24 shows, indicating that the trim initial conditions for this run were "appropriate," and located the aircraft within the trim domain of attraction, as was hoped. The importance of this run lies in the fact that the strategy was derived directly from the BACTM-produced curve of Fig. 3.16, and represents an improvement over the more common "hunt-and-try" mothods of evolving recovery strategies.

File 230. This run repeats 229 exactly, except that altitude was maintained at 30000 ft. The only strongly noticeable difference was the more rapid pitch-up which results when altitude decreases (and air density increases); also the oscillations are a bit less sharp at lower altitudes. These observations are consistent with experimental results (Sallada et al., 1967). The overall effect is so negligible that the 230 plot is too similar to 229 to gain benefit from reproducing it here.

Files 231, 233, 234 (Figs. 3.25, 3.26, 3.27). This is a family of runs based on 221 and Fig. 3.16; in that run, $\delta r \rightarrow 0°$ at $t = 22$ sec based on $|r| \leq 10$ deg/sec. Favorable values at that time for α, θ and other variables caused eventual recovery. The runs shown in Figs. 3.25 through 3.27 try to improve on the recovery time of 221 by trimming δr at certain times prior to $t = 22$. The times selected were predicated upon trim

initial conditions "likely" to fall within the trim domain of attraction. These runs are an aid in defining this domain's boundaries, and Table 3.1 adequately summarizes the results.

Files 237, 241, 242 (Figs. 3.29, 3.30). This run attempts to achieve recovery from the failed 223 run, but by means of a different approach than the one tried in the 236 run. Here, $\delta r \rightarrow 0°$ in an open loop manner at $t = 17.5$ sec, with the trim initial conditions intended to fall within the trim domain of attraction. This attempt obviously failed in this particular case, although it is necessary to try other trim initial conditions, which would likely clarify more the role of the remaining variable in spin recovery. File 241 is merely another 50 sec extension of 237, which merely confirmed failure to recover. No plot for this run is shown. File 242, shown in Fig. 3.30, is like 237 except that $\delta r \rightarrow 0°$ at $t = 18.5$ sec. Again, recovery fails.

File 240 (Fig. 3.31). This run attempts to determine if it is possible for the (r,α)-point $(0°,90°)$ to lie within the trim domain of attraction: all other variables were set to zero, except $V_0 = 450$ fps, and all of the controls were set to neutral. During the obvious and rapid recovery, there was no lateral-longitudinal coupling of the motions.

Based on these runs, and with particular reference to Table 3.1, which summarizes them and also to Figs. 3.16 and 3.17, we can make these observations:

1. More development of BACTM and more analysis of current spin recovery runs needs to be done before a full, more comprehensive picture emerges which enables one to evolve a recovery control strategy in a

global manner. However, it should be evident that BACTM has already defined a procedure for doing this, i.e., based on generating bifurcation surfaces and figures such as Figs. 3.16 and 3.17, the latter with domains of attraction; and that the preliminary results presented in the progress of this investigation period already add in many ways to our understanding of the spin problem. Also, since conducting this particular study, new equilibrium branches have been found (see below). These aid greatly in understanding more about aircraft F in the spin recovery domain depicted in Fig. 3.16.

2. The variables r (yaw rate) and α (angle-of-attack) are the most significant ones in terms of analyzing spin and spin recovery motions. This is true at least of the aircraft F model, and needs emphasis because of a tendency of some researchers to overlook the importance of α. In addition, pitch angle (θ), roll angle (ϕ) and velocity (V) play prominent roles, and perhaps other variables are significant also; more study is required to define such roles adequately and to determine how model-dependent they are.

3. Introducing the limit cycle analysis, both as shown in the plots of Figs. 3.16 and 3.17 and by utilizing the limit cycle continuation algorithm, represents useful new BACTM tools for broadening our understanding of the intermediate spin and recovery flight regime, which for aircraft F and F-4 is characterized by highly oscillatory and limit cycle behavior.

4. We have obtained a qualitative idea of the size and boundaries

of the r-α domains of attraction for the aircraft F recovery cases investigated and discussed above. This task is incomplete, but shows promise of being quite worthwhile.

5. Altitude has been shown to have minimal effect on spin and spin recovery motions. This result is consistent with other work.

6. With particular reference to Table 3.1 we note:

i) the value of V is often not crucial when other factors enter the picture; i.e., compare V for run 223, which fails, and 224, which succeeds;

ii) roll rate (p) apparently is not a critical parameter, judging from the range of values given in Table 3.1 and their lack of correlation with recoveries and failures;

iii) α seems to have an important bearing on the speed of recovery (neglecting the well-controlled, "textbook" case 240), as can be seen by comparing its value in 222 with other runs in which recovery is successful;

iv) pitch (θ) may not be as critical as some (e.g., Bihrle, 1974) suggest, at least for aircraft F, but it does have at least a secondary role in enhancing or retarding recovery. A large and negative pitch angle, with roll (ϕ) and sideslip angle (β) being large and positive, may be a favorable recovery situation, but is neither necessary nor sufficient. This should be investigated more completely;

v) θ could be an indicator of recovery prospects, at least

based on run 221 near t = 30 sec (Fig. 3.19). In this regime, it is interesting also to note the sensitivity of θ to δr, as Fig. 3.19 again shows;

vi) if the "r trim window" is too "loose" or wide, spin recovery seems to deteriorate (compare 220 with 222);

vii) a more anti-spin aileron setting (e.g., 224 case) enhances recovery prospects; indeed, in the case studied, $\delta a = -15°$ obtained recovery where δa at trim failed.

3.1.4.3 Spin Reversal

For a discussion of aircraft F in spin reversal, we consider again Figure 3.16. In the course of effecting spin recovery from Point A, the aircraft enters an intermediate condition which is characterized by very oscillatory behavior. The motion is influenced by Branches 2 and 3, until rudder increases past 8°, at which point Branch 2 "disappears" as an attractor, and spin reversal occurs. This is very evident by the change in sign of yaw rate r shown in Figure 3.16a. At this point, the stable limit cycle associated with* Branch 2 disappears (global bifurcation), and the domain of attraction for the Branch 4 limit cycle (which remains stable) has now grown to include the right spin region ($r > 0$, high α). Thus the spin reverses, from positive r to negative, as the motion is attracted to the limit cycle associated with Branch 4 for $\delta r \lesssim 8°$. This is easy to see in the r-plots, but even the α-plot (Figure 3.16c) shows indications of spin reversal. In Figure 3.16c, the vertical bars

*That is, while points on the equilibrium Branch 2 do not represent stable equilibria, motions starting sufficiently close to them are attracted to a stable limit cycle, when $\delta r < 8°$.

for $\delta r < 8°$ represent limit cycles influenced by Branch 2. After the reversal ($\delta r > 8°$), the limit cycles are centered around Branch 4. It can be seen that their amplitudes are a bit smaller than those centered around Branch 2.

To confirm that Branch 2 no longer supports a stable limit cycle for $\delta r > 8°$, two time history runs were made with initial conditions on Branch 1, at $\delta r = 20°$. Specifically, $\underline{x}_0 = (25., 16.8, 67.2, 62.1, -0.5, 450., 0., 0., 0.) = (p_0, q_0, r_0, \alpha_0, \beta_0, V_0, \theta_0, \phi_0, \psi_0)$ for the case shown in Figure 3.32; for the second case, $\theta_0 = -50.$ and $\phi_0 = -40$ were the only changes (see Figure 3.33). Units are degrees and feet per second for V.

For the trim altitude case ($\theta_0 = \phi_0 = 0°$, Fig. 3.32), note that spin reversal has occurred; see the r(t) plot, and observe also that p and q are developing oscillatory, limit cycle behavior after the reversal. However, the new spin is an inverted one, as can be ascertained directly from the α and ϕ (roll angle) histories. Angle-of-attack actually is in a range for which the aero data are no longer valid, for $t > 24$ sec.* If r changes sign as ϕ goes to 180° from 0°, the direction of spin as seen from the ground remains the same; thus, TURNS $\triangleq \frac{1}{2\pi}\int_0^t \dot{\psi}\, dt$, Fig. 3.32d, continues to increase after the transients have lost influence ($t > 30$).

When $\theta_0 = -50°$ and $\phi_0 = -40°$, values which are typical in the oscillatory spin region,** the results (Fig. 3.33) are quite different from the trim attitude case. Here, a "clean" spin reversal has occurred, with the erect spin being retained but the direction (sgn(r)) reversed. The

*For this reason, and because rotation balance data are not yet in the model, we cannot associate this result with the F-4 aircraft.

**The equilibrium surfaces shown in Figure 3.16 were created with the reduced-state system, $\underline{x} = (p,q,r,\alpha,\beta)$. Time histories and the full equilibrium system, $\underline{x} = (p,q,r,\alpha,\beta,V,\theta,\phi)$ justify this statement.

variable TURNS clearly indicates this, and the r,α and ϕ plots confirm it. The Figure 3.33 case, then, represents the trajectory predicted by the Figure 3.16 Branches 2 and 4. From Figure 3.32 we learn to expect even more equilibrium branches based on different values of θ and ϕ. Such new branches, not yet found, are to be found by using the complete spin-equilibrium system of equations.

To summarize: Branches 2 and 4 of Figure 3.16 are seen to play a major role in the spin reversal and recovery dynamics which we have been investigating recently; furthermore, their presence adds greatly to our understanding of the dynamic phenomena which occur in the oscillatory spin region. Finally, time history results presented here make it clear that the influence of θ and ϕ--i.e., the aircraft attitude or gravity effects--must be given much attention in the oscillatory spin region. We will take this knowledge and put it to use in our investigation of the F-4 system by concentrating more on the full spin equilibrium system, especially in this critical flight regime.

3.2 F-4 Simulation Results

This section summarizes our progress to date on developing the BACTM system for the F-4 model.

3.2.1 F-4 Model

The mass, geometry and aero model for the F-4 aircraft has been successfully incorporated into the BACTM programs. These include the aero data setup program, which processes the basic tunnel data for use by the spline function interpolation routines; the time history program; three

equilibrium surface programs; and the fifth order (trim regime) bifurcation surface program. The equilibrium surface programs include: (i) the trim program (for a reduced state $\underline{x}_T = (p,q,r,\alpha,\beta)$. In the absense of thrust, no trim equilibrium is possible if θ and ϕ are coupled into the $\underline{x}_T$-system. Thus gravity is neglected, which decouples θ and ϕ from $\underline{x}_T$); (ii) the full spin program ($\underline{x}_S = (p,q,r,\alpha,\beta,V,\theta,\phi)$); and (iii) the reduced spin program. In the last, the dimension of the spin system is reduced by one by means of eliminating V from $\underline{x}_S$. This is discussed in more detail in Section 2.1.4.

The physical characteristics for the F-4 are presented in Table 3.2. This information was compiled from Chambers (1969) and Adams (1972).

Table 3.2 F-4 Mass, Inertia Properties

W	= 36328	lbf.
I_x	= 26108	slug-ft^2
I_y	= 116222	slug-ft^2
I_z	= 131625	slug-ft^2
I_{xz}	= 0	slug-ft^2

(the above assume center of gravity location ($\%\bar{c}$) of 33.9)

b (wing span)	= 38.41	ft.
$\bar{c}$ (M.A.C., wing)	= 192.50	in.
S (wing area)	= 538.34	ft^2

It is assumed that the aerodynamic data corresponds to the specified center of gravity location. Using the equations in Kroll (1976), it is possible to convert the aero coefficients to correspond to a given center of gravity location.

The aerosurface controls for the F-4 consist of the horizontal "stabilator" (subsequently to be called "elevator"), a rudder, ailerons, and upper surface spoilers. The elevator is the entire horizontal tail ("all-movable"), at 23° negative dihedral (droop); its range is (21°,9°). The rudder is standard, and has a range of ±30°. The ailerons deflect only downward while the upper surface spoilers deflect only upward from the wing; they operate in conjunction to generate lateral motions. Hence, the combined aileron/spoiler system will be considered as the ailerons, with a range of ±30°.

3.2.2 F-4 Aerodynamic Data

Aerodynamic data for the F-4 was sent to us by Mr. E. Anglin of NASA Langley. These data include static, forced-oscillation damping and rotation balance data. It has been emphasized (Anglin, 1977, Bihrle and Barnhart, 1974, Bihrle, 1976) that adequate simulation of aircraft in post-stall and particularly spin motions may be obtained only if rotation balance data are incorporated into the aero model. "Adequate simulation" in this context means a reasonable correlation with flight test data of the aircraft in spin. The simulation model which we have been using, aircraft F, has aero data which are adequate for simulating spin and other high-α motions. However, these data were "manufactured," particularly the C_n data, in order to achieve this goal; flat spin motions are simulated, but at the expense of realistic behavior in other flight regimes, including steep spin. Thus, aircraft F has no real world counterpart, although the F-111 aircraft is the basis for the data.

Use of aircraft F, however, has been important and insightful in its own right. By using aircraft F we have been able to construct the simulation package which can handle a tabular aero data base, as well as come to recognize some of the characteristics of developed spin motion and the problems which accompany simulating spin entry and spin recovery dynamics. In brief, aircraft F was an excellent working model to use for expanding the capabilities of BACTM to include spin analysis.

That having been said, continued use of aircraft F is a policy of dubious merit, precisely because it is not possible to gauge the effectiveness of any stall/spin-prevention control strategies derived from BACTM analysis on a real aircraft. Nor is the identification of control settings which lead to catastrophic high-α behavior of any real use beyond confirming their effect only on the aircraft F model. Thus, we have turned to the much more realistic model represented by the F-4 data. A brief description of the F-4 data will now be given.

3.2.2.1 Static Data

These data are classified according to control groups, as follows:

Table 3.3

F-4 Static Data Control Groups

Control Group	Control Settings (degrees)
A	Left pro-spin ($\delta e = -21$, $\delta r = 30$, $\delta a = -30$
B	neutral
C	$\delta e = -21$
D	$\delta r = 30$
E	$\delta a = -30$

Table 3.4

F-4 Static Aero Data Table Correspondence

Data Table #		Aero Coefficient
1		C_x
2		C_z
3		C_m
4		C_ℓ
5		C_n
6		C_y
7	(a)	$C_{x_{\delta e}}$
8		$C_{z_{\delta e}}$
9		$C_{m_{\delta e}}$
10		$C_{\ell_{\delta e}}$
11		$C_{n_{\delta e}}$
12		$C_{y_{\delta e}}$
13		$C_{\ell_{\delta a}}$
14		$C_{n_{\delta a}}$
15		$C_{y_{\delta a}}$
16		$C_{\ell_{\delta r}}$
17		$C_{n_{\delta r}}$
18		$C_{y_{\delta r}}$

a) These tables are non-zero only for Control Group B; in the other Control groups the effects of these coefficients are incorporated into the first six coefficients.

For the non-neutral control groups (A, C, D, E), each group contains six tables of coefficients: C_x, C_z, C_m, C_ℓ, C_n, C_y (see Table 3.4). Only in group B is the effect of control changes directly reflected in the values of the six major coefficients. The data for the non-neutral groups were collected at a fixed control setting, so that moving $\underline{\delta}$ from that setting results in no change in the dynamic condition. Thus, equilibrium surfaces, for example, are possible only using group B.

Each data table consists of 13 subtables, with each subtable representing data for the coefficient over the α points, for a given value of sideslip, β. The 13 β-tabular values are 0, ±5, ±10, ±15, ±20, ±30, ±40 degrees, sequenced minimum to maximum within each data table; and the α-sequence for each subtable is (-10, -5, 0, 5, 10, 12.5, 15, 17.5, 20, 22.5, 25, 27.5, 30, 35, 40, 45, 50, 55, 60, 65, 70, 75, 80, 85, 90, 100, 110, 120), representing 28 α-points for each value of β. (In this particular case, the $\alpha = 120°$ F-4 data are duplicates of the $\alpha = 110°$ data, but are carried along in order to standardize the format.) A visualization of these data is presented in Figure 3.34.

3.2.2.2 Forced-Oscillation Damping Data

These data have a slightly different arrangement. The data base is organized into damping groups, as specified in Table 3.5; and the data themselves cover data table numbers 19 through 27.

Table 3.5

F-4 Forced Oscillation Damping Group Organization

Damping Group	Amplitude (degrees)	Frequency (sec^{-1})	Corresponding Control Group
A	±5	.7	B
B	±5	1.0	
C	±5	1.3	
D	±10	.7	B
E	±10	1.0	
F	±10	1.3	
G	±5	.7	C (yaw oscillation only)
H	±5	1.0	
I	±5	1.3	
J	*	*	

The correspondence is given by Table 3.6. For each data table number, i.e., aero coefficient, there is a block of numbers which represent the α-point values of that coefficient. As with the static data, there are 28 of these numbers, covering the same α-points as the static data points. There is no tabular dependence of these damping coefficients on β. The forced oscillation data may be visualized as shown in Fig. 3.35.

Table 3.6

F-4 Forced Oscillation Data Table Correspondence

Data Table #	Aero Coefficient
19	C_{x_q}
20	C_{z_q}
21	C_{m_q}
22	C_{ℓ_p}
23	C_{n_p}
24	C_{y_p}
25	C_{ℓ_r}
26	C_{n_r}
27	C_{y_r}

Note that two "new" coefficients are presented in Table 3.6, which have not heretofore been used. These are C_{x_q} and C_{z_q}.

3.2.2.3 Rotation Balance Data

These data were furnished to us stored on a magnetic tape (the static and forced-oscillation damping data were supplied on cards). This is wind tunnel data, obtained by mounting a model of the F-4 onto a rotary balance and collecting data over a range of rotation rates (called "roll" rates, presumably because of the designation of the rotation axis of the rotary balance mount). The correspondence between the roll rates and the dimensionless angular velocity, ($\Omega b/2V$), is given in Table 3.7.

Table 3.7

F-4 Rotation Balance Roll Rate Correspondence

Roll Rate (RPM)	$\left(\frac{\Omega b}{2V}\right)$
0	0
12	.049
24	.098
36	.147
48	.196
60	.245
72	.294

Each record on the tape supplies the following quantities of interest: α, β, C_L, C_D, C_y, C_m, C_ℓ, C_n, (L/D), Roll Rate. In this list, (L/D) is the lift-over-drag ratio, and equals (C_L/C_D). Also note that for use on our BACTM package, the data for C_L and C_D will have to be processed in order to transform them into C_x and C_z. Finally, data are supplied for negative values of the roll rates presented in Table 3.7, as well as the positive values.

It is critical to select an Ω which is representative of the given flight condition, but there as yet exists no specific technique for this. In Section 3.2.4.2 we discuss typical choices of Ω.

3.2.3 F-4 Aero Data Spline Model: Considerations

As it was supplied to us, the F-4 model consisted of a large number of values for each of the aero coefficients described in Mehra and Carroll (1978). In general, the forces oscillation coefficients are functions of α (angle-of-attack) and the static coefficients are functions of both α and β (angle-of-sideslip). Rotary balance data has yet to be implemented. With regard to the spline function approximations to this data, there arise some questions:

(1) Are the interpolations obtained from the spline fits reasonable (e.g., are they similar to those that would be made by eye)?

(2) Is it really necessary to use all of the data in creating our spline interpolations?

To answer these questions, we developed a spline approximation program which has the option of selecting for knots the entire array of data points, or any subset of points, not necessarily original data points. This version plots an x at every data point before drawing the spline fit to the data. As the plots included in Fig. 3.36 show, the spline fits to the data almost always correspond to what one would like to see. One exception to this rule is at $\alpha \approx 33°$ in the graph of C_{y_p}. Note that the curve looks something like this:

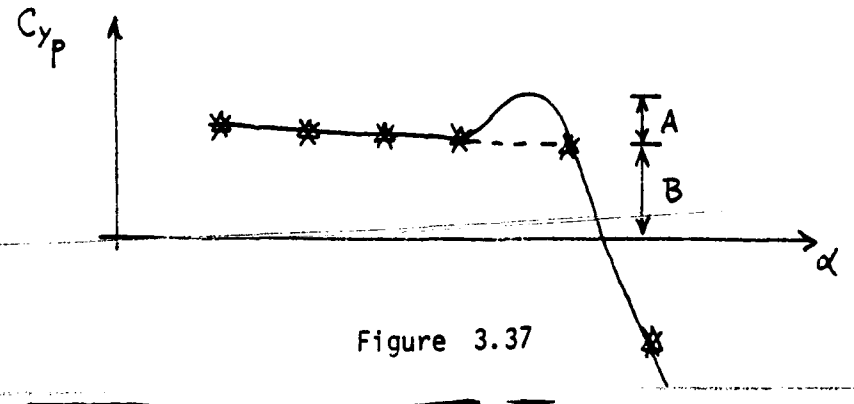

Figure 3.37

One would expect the dotted line, but sees instead the solid line. The maximum error (A/B) is about 25%, which is within the error bands given for forced oscillation data (see Section 3.2.4).

Errors of this type can be understood by considering the nature of the spline fitting algorithm used. Suppose the N+1 data points (knots)* are denoted by $C(\alpha_i)$, $1 \leq i \leq N+1$. The algorithm produces a set of N cubic polynomials $p_i(\alpha)$, $1 \leq i \leq N$, that satisfy the following two constraints:

(1) The composite curve passes through all of the knots continuously (e.g., $p_i(\alpha_{i+1}) = p_{i+1}(\alpha_{i+1})$).

(2) The composite curve is everywhere twice differentiable, implying that both the first and second derivatives of the polynomials must agree at the knots (e.g., $p_i'(\alpha_{i+1}) = p_{i+1}'(\alpha_{i+1})$; $p_i''(\alpha_{i+1}) = p_{i+1}''(\alpha_{i+1})$).

The second constraint requires that sudden changes in the direction of the composite curve are "propagated" to adjacent p_i's, introducing errors, such as the overshoot shown above.

Since this is the only fitting artifact found in the large forced oscillation database, one may conclude that: (1) this is the only type of problem we can expect to find with our spline fitting algorithm; (2) this problem will only occur when several knots lie along a straight line with an adjacent knot departing markedly from that line. Examination of the static data plots indicates that similar knot configurations do not occur.

We were initially concerned about the magnitude of the derivatives

*In general, a spline fit need not pass through any of the data points; however, one usually constrains the fit to pass through specific points called knots, which may or may not be data points. As a first approach, we chose all of the data points as the knots.

$C'(\alpha)$ in the spline fits. However, these were plotted in reciprocal radians instead of reciprocal degrees, introducing an extra factor of $180/\pi$ ($\approx 57.3°$) into their magnitude. Calculation of $\frac{C(\alpha_{i+1})-C(\alpha_i)}{\alpha_{i+1}-\alpha_i} \approx C'_{OBSERVED}(\alpha)$ for several "worst cases" is in good agreement with the spline fits.

We also revised our plotting program to fit the curves using the subset of the data plotted as ✱. We ran this program deleting data points for all curves at $\alpha = 12.5$, 17.5, 22.5, and 27.5 degrees. In general, the new fits agreed quite well with the fits using all of the data. This suggests that considerable simplification of the model is possible. However, we noted small absolute errors that would result in large percentage errors when $C(\alpha) \approx 0$. We conclude, therefore, that model simplification should proceed on a curve-by-curve basis.

Since the static data fits contain fewer "wiggles" than the forced oscillation data, we can extend this conclusion to the static data as well.

3.2.4 Use of the F-4 Data

The presence of three distinct groups of data obligates one to incorporate them with care into the simulation package dynamic equations. Even so, as Anglin (1977) points out, not all of the guesswork is removed. He has found that static and forced-oscillation data, which represent the typical forms of aero data, are adequate only in describing motions which do not involve steady, developed spin. The minimum data required for analysis of spin motions is forced-oscillation and rotary balance data; rotary balance data alone will not adequately simulate developed spin. Use of all three types of measured aerodynamics offers the best chance of

adequately simulating spin and high-α/post-stall motions; however, there are regions in the flight regime, typically low-α, for which the rotary balance data are not to be used. Typically, rotation aero data are not used below $\alpha = 55$, although for each individual configuration there will be some experimentation necessary to establish the most reasonable limit point. Some degree of artwork is also needed in combining the proper control group of the static aero data with the rotary balance data, as a function of α. Further discussion of this topic is given below.

When using all three types of measured aerodynamics simultaneously (the "hybrid"), each kind must be properly combined with the proper kinematic component. In essence, because spin is typified by large and persistent yawing motion, and because the rotary balance data represents aerodynamic forces and moments under some steady angular motion about a fixed axis, the $\dot{\psi}$ components in the angular velocity components are associated with the rotary balance data. Thus,

$$\begin{aligned} p &= p_0 + p_r \\ q &= q_0 + q_r \\ r &= r_0 + r_r \end{aligned} \tag{3.3}$$

where

$$\begin{aligned} p_r &= -\dot{\psi}\ \sin\theta \\ q_r &= \dot{\psi}\ \cos\theta\sin\phi \\ r_r &= \dot{\psi}\ \cos\theta\cos\phi \end{aligned} \tag{3.4}$$

and

$$\begin{aligned} p_0 &= \dot{\phi} \\ q_0 &= \dot{\theta}\ \cos\phi \\ r_0 &= -\dot{\theta}\ \sin\phi \end{aligned} \tag{3.5}$$

Eq. (3.3) represents the relation between the Euler angle rates $(\dot{\psi},\dot{\theta},\dot{\phi})$ and the body-axis rates (p,q,r) for a yaw-pitch-roll rotation sequence. With definitions (3.4) and (3.5), the aero force-moment coefficients expand as follows:

$$
\begin{aligned}
C_x &= C_x + C_{x_{\delta e}}\delta e + C_{x_{rot}} + C_{x_q}\left(\frac{\bar{c}}{2V}\right)q_0 \\
C_y &= C_y + C_{y_{\delta a}}\delta a + C_{y_{\delta r}}\delta r + C_{y_{\delta e}}\delta e + C_{y_{rot}} + \left(\frac{b}{2V}\right)\left(p_0 C_{y_p} + r_0 C_{y_r}\right) \\
C_z &= C_z + C_{z_{\delta e}}\delta e + C_{z_{rot}} + C_{z_q}\left(\frac{\bar{c}}{2V}\right)q_0 \\
C_\ell &= C_\ell + C_{\ell_{\delta a}}\delta a + C_{\ell_{\delta r}}\delta r + C_{\ell_{\delta e}}\delta e + C_{\ell_{rot}} + \left(\frac{b}{2V}\right)\left(p_0 C_{\ell_p} + r_0 C_{\ell_r}\right) \\
C_m &= C_m + C_{m_{\delta e}}\delta e + C_{m_{rot}} + C_{m_q}\left(\frac{\bar{c}}{2V}\right)q_0 \\
C_n &= C_n + C_{n_{\delta a}}\delta a + C_{n_{\delta r}}\delta r + C_{n_{\delta e}}\delta e + C_{n_{rot}} + \left(\frac{b}{2V}\right)\left(p_0 C_{n_p} + r_0 C_{n_r}\right)
\end{aligned}
\tag{3.6}
$$

In computing $C_{x_{rot}}$, $C_{y_{rot}}$, $C_{z_{rot}}$, $C_{\ell_{rot}}$, $C_{m_{rot}}$, $C_{n_{rot}}$ for Eq. (3.6), one may use, for example

$$
\Omega_{rot}^2 = p_r^2 + q_r^2 + r_r^2 \tag{3.7}
$$

Each of the six rotary balance derivatives are functions of α,β and $\left(\frac{\Omega_{rot}b}{2V}\right)$, for a given control setting. As written, the expansions in Eq. (3.6) are those used when the aircraft is near a post-stall or spin flight regime; in this case the first terms of each expansion (e.g., C_ℓ, $C_{\ell_{\delta e}}$,

$C_{\ell_{\delta a}}$ and $C_{\ell_{\delta r}}$) are static aero derivatives. The forced oscillation derivatives (Table 3.6) remain the same through all flight regimes. When the motion is reasonably close to a flight condition for which the mutual controls are appropriate, then p_0, q_0 and r_0 are replaced by p, q and r; also the rotary derivatives, $C_{(\cdot)_{rot}}$, are dropped. It is again to be emphasized that the resolution of the terms "near" and "reasonably close" of necessity awaits both simulation experience as well perhaps as establishment of a firm criterion of correlation (such as minimization of RMS error between simulation and flight test results).

In implementing the three types of aerodynamic data as outlined above for spin analysis, the conventional forced oscillation and static derivatives are used in such a way as to account only for the effects of oscillations superimposed on the steady rotational motion. The effects of these oscillations are added to the coefficients obtained from the steady rotation. Care also must be taken to assure that the data for steady rotations does not include static effects. Bihrle and Barnhart (1974) state that rotary balance data and static data are equivalent, when the "roll rate" is zero. If the rotary data include static effects, then obviously the static terms (e.g., C_ℓ, $C_{\ell_{\delta e}}$, $C_{\ell_{\delta a}}$, $C_{\ell_{\delta r}}$) are not used where the rotary terms (e.g., $C_{\ell_{rot}}$) are active. The F-4 data are of this nature.

In order to gain more insight into the use of the three types of aero data, we visited NASA Langley to talk to Mr. Ernie L. Anglin, who supplied us with these data. A summary of the main points discussed at this meeting is now presented below.

3.2.4.1 Static and Forced Oscillation Data

It is possible to obtain spin motions from an aero model which consists only of static (S) and forced oscillation (FO) data. Traditionally, static and forced oscillation data are sufficient to describe motions for which $\alpha \lesssim 40°$ or so; also, FO and rotary balance (RB) data are used in spin regimes. At this time, there is no fixed rule establishing the exact conditions for switching from one configuration to another. Indeed, the purpose of the Langley meeting was to become familiar with the current thinking, and with the as yet unsolved problems.

The analysis of spin motions without using RB data would not produce accurate representations of flight test results. For example, the aircraft F model uses only S and FO data (Moore, Anglin, 1971). These data suffice for tracking motions through stall, or when α (angle-of-attack) and $|r|$ (yaw rate magnitude) are "small;" however, their simulated spins are unrealistic. Indeed, it is usually not possible to obtain flat spin equilibria (α very high, usually in the 75°-85° range: $\alpha \in (75°,85°)$) when only S and FO data are used. If the data are altered, an equilibrium spin may be produced at a given value of α. But this process makes the model non-unique, and it is thus incapable of predicting non-equilibrium spin motions. For example, the number of turns required to effect recovery from an equilibrium spin using such a "massaged" model varies greatly from flight test results, depending on which of the coefficients were modified.

It is worthwhile to understand more about the way in which FO data

are modified to produce a model which can simulate flat spin equilibria. Usually, the coefficients C_{ℓ_r}, C_{ℓ_p}, C_{n_r}, C_{n_p} are the ones from the FO set which are altered. A subset of two from these four will actually suffice, but the equilibrium requirement ($\dot{\underline{\omega}} = 0$, where $\underline{\omega} = (p,q,r)$, the aircraft rotation rate) may well require new values for those two, values which fall outside the "scatter band" of the original data curve. By changing all four, their new values are typically still within or very close to the scatter band. Further, flight test results for equilibrium spin can be matched very closely. But it must be emphasized again that such a procedure causes recovery trajectories to be unreliable, as the data are no longer unique.

With regards to the scatter band widths, i.e., general confidence levels, of the wind tunnel data, we learned that the F-4 data results are repeatable to within 10% or so in trim and developed flat spin ($\alpha \approx 80°$) flight regimes. Oscillatory spin ($\alpha \in (50°,70°)$) results have a much wider scatter band--less repeatability, less confidence in the data--often with 100-200% variation. Also, forced oscillation (FO) data have a wide scatter band, poor repeatability. However, it is important to include even poor FO data in the model, rather than none at all. This is dramatically emphasized by examining Fig. 11 in Anglin (1978). In this figure, no damping (FO) data are used and the predicted flat spin motion diverges in a very short time from spin tunnel test results. When FO data are included, the oscillations die rapidly and agreement is very close.

The wide scatter bands associated with FO data are probably related to the manner in which it must be collected. The usual procedure involves vibrating the model in the wind tunnel at 5 or 10 degrees amplitude, at various values of α, about each of the body axes in sequence. This method, however, introduces effects due to $\dot{\alpha}$ and $\dot{\beta}$ (β is the angle-of-sideslip). For example, the measured quantity C_{n_r} is in actuality $(C_{n_r} - C_{n_{\dot{\beta}}}\cos\alpha)$; the other FO coefficients are similar. Ideally, these terms would be measured separately, since there is a distinction, based on the two variables r and $\beta(\dot{\beta})$; however, measured tunnel data rarely distinguishes between these terms.

Experimenters have in the past used a "plunging rig" (Fig. 3.38) to isolate r-$\dot{\beta}$ effects. This rig allows only for oscillatory translations, and no rotations; thus, $C_{n_{\dot{\beta}}}$ can be measured explicitly. This procedure

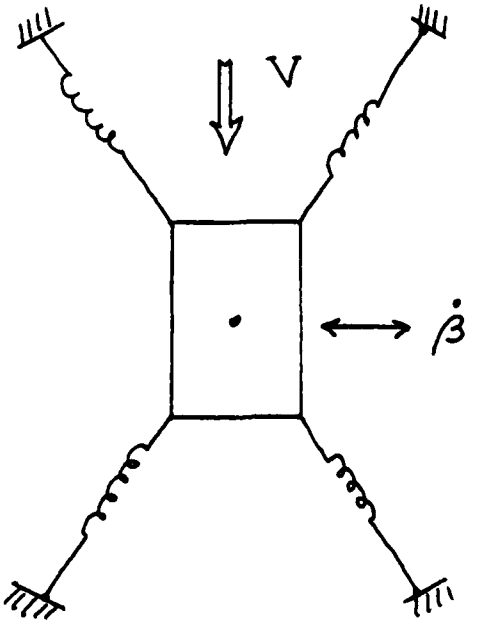

Figure 3.38

is not used extensively, however, because in the past results have been very irregular and uncertain. So much so, apparently, that the usual method, with its known fault of combining effects of two variables, is nonetheless preferable.

Both the static and forced oscillation data are collected for various control settings and forced oscillation amplitudes and frequencies. S data for the F-4 consist of data for five basic control settings:

A - left pro spin ($\underline{\delta} = (-30,-21,30)$)

B - neutral ($\underline{\delta}$ at trim)

C - δ_e at spin; others neutral

D - δ_r at spin; others neutral

E - δ_a at spin; others neutral

For all of the non-trim groups (i.e., all groups but B), the effect of the control setting is included in each of the six main static coefficients recorded: C_x, C_z, C_m, C_ℓ, C_n, C_y. The coefficients for these four groups, then, vary only with α and β. It is not possible to use them uniquely on BACTM because there is no means of evaluating the influence of changes in the controls on the aircraft response. It would be necessary to introduce some mixing logic based on using Group B, the neutral group. (In all cases, FO data adds in effects due to aerodynamic damping. For the F-4 model, there are nine such coefficients which are ultimately combined with the six major static coefficients: C_{x_q}, C_{z_q}, C_{m_q}, C_{ℓ_p}, C_{n_p}, C_{y_p}, C_{ℓ_r}, C_{n_r}, C_{y_r}.) For neutral controls with the F-4 model, in addition to the nine FO coefficients, the six major S coefficients are split into

a total of eighteen basic static coefficients: C_{x_0}, C_{z_0}, C_{m_0}, C_{ℓ_0}, C_{n_0}, C_{y_0}, $C_{x_{\delta e}}$, $C_{z_{\delta e}}$, $C_{m_{\delta e}}$, $C_{\ell_{\delta e}}$, $C_{n_{\delta e}}$, $C_{y_{\delta e}}$, $C_{\ell_{\delta a}}$, $C_{m_{\delta a}}$, $C_{y_{\delta a}}$, $C_{\ell_{\delta r}}$, $C_{n_{\delta r}}$, $C_{y_{\delta r}}$. Of this group, the last twelve are (linear) coefficients of the elements of $\underline{\delta}$, i.e., δa, δe or δr. When $\underline{\delta} = 0$ (trim), all five S control groups supply only the major S coefficients; but for Group B, if any of the controls move from 0°, there is a direct functional effect on the aero forces and moments.

The recommendation, therefore, is to use Group B static data as much as possible; indeed, unless control effects on the coefficients can be inferred into the other groups by some kind of mixing, it is impossible to use any other group but B to generate equilibrium and bifurcation surfaces. These data are of course used with FO and rotation balance data to complete the aerodynamic model. We are interested, however, in comparing time history trajectories between any of the other groups and Group B, with $\underline{\delta}$ set appropriately.

Another point of interest concerning the five S control groups is that there is no additivity relationship among them. For the F-4 case, this means that the pro-spin group A is not the sum of groups C, D and E. We do expect, however, that Group B ≈ Group A when $\alpha \geq 80°$ and $\underline{\delta}$ is set for left pro spin motions. It is possible to get an equilibrium point for Group A static data, in the flat spin regime at least*; we are told that $\bar{\alpha}$ at this point should be close to 83°.

FO data are distinguished in groups by the values of amplitude and frequency at which the model is oscillated in the tunnel. Amplitudes are

*Oscillatory spin equilibria, at lower α, are possible also.

AD-A084 938 SCIENTIFIC SYSTEMS INC CAMBRIDGE MA F/G 20/4
GLOBAL STABILITY AND CONTROL ANALYSIS OF AIRCRAFT AT HIGH ANGLE--ETC(U)
AUG 79 R K MEHRA, J V CARROLL N00014-76-C-0780
UNCLASSIFIED ONR-CR215-245-3 NL

2 OF 4
AD
A084938

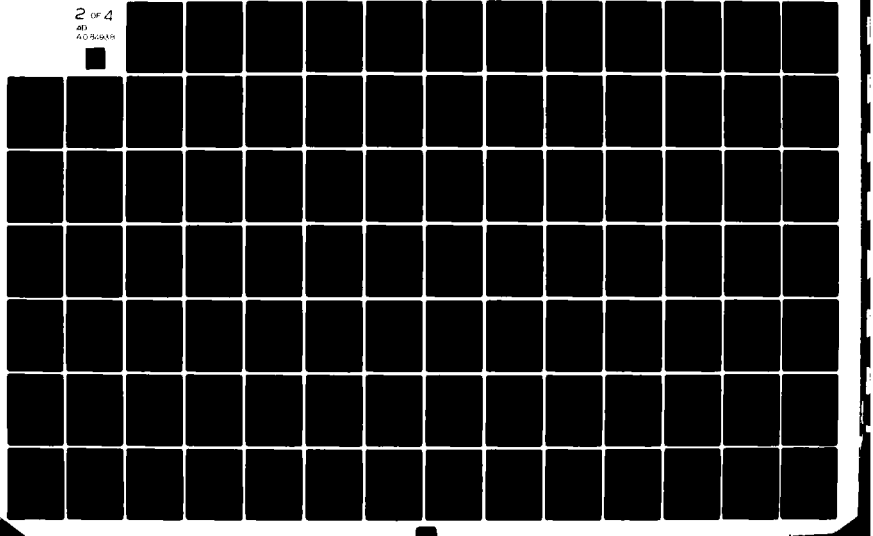

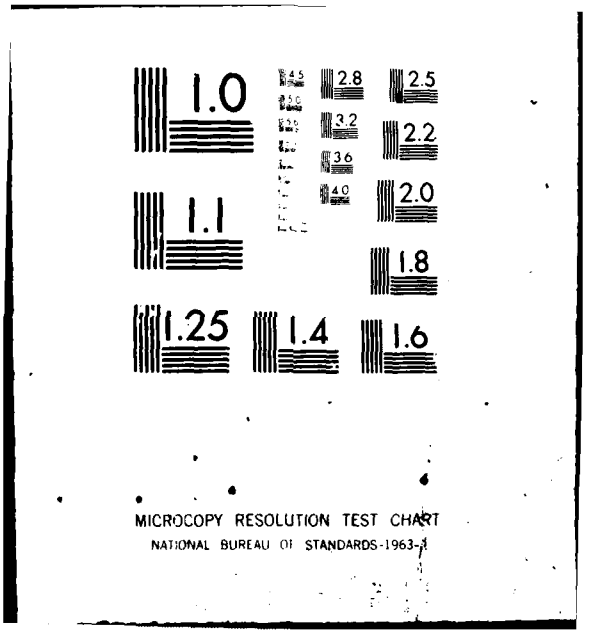
1.0
2.8
2.5
3.2
2.2
3.6
4.0
2.0
1.1
1.8
1.25
1.4
1.6
MICROCOPY RESOLUTION TEST CHART
NATIONAL BUREAU OF STANDARDS-1963-A

5° and 10° and these are each used for three different frequencies: 0.7, 1.0, 1.3 Hz. For the most part, these data were collected with $\underline{\delta}$ neutral; damping groups G, H and I were taken at $\delta e = -21°$. Group J were extracted directly from control model flights; these have no reference amplitude and frequency, therefore.

It is recommended that we use damping group D in our simulation. In this group, the amplitude is 10°, frequency is 0.7 Hz and controls neutral. This is the only group of the ten for which $C_{n_r} \leq 0$ at $\alpha \in (75°,85°)$; this means that the computed flat spin is stable, which would not be true if $C_{n_r} > 0$--an autorotational situation, and this agrees with flight test results. The other groups have $C_{n_r} > 0$ for high α, and so are less realistic. In addition to C_{n_r}, the effects on stability due to the signs (and magnitudes) of C_{ℓ_p} and C_{n_q} for the critical α are also important, because of inter-axis coupling. In fact, if rotation balance data are used in spin simulations (as it should be: see below), then a "bare minimum" FO data model for flat spin analysis requires only C_{ℓ_p}, C_{m_q}; two coefficients instead of nine (Williams, 1976). With these, the $\dot{\theta}$ and $\dot{\phi}$ oscillations would be damped, so that flat spin should result. C_n at flat spin can come only from S and rotation balance tables.

3.2.4.2 Rotation Balance (RB) Data

It is critical that RB data be part of the aero model if spin motions are to be described accurately (Chambers, 1969; Williams, 1976). This is even more true today than in 1964, when use of RB data was first successfully applied to high-performance aircraft susceptible to spin entry (Anglin and Scher, 1964), because of the trends in aircraft design over the past fifteen years. Until the late '60's,

developed spin conditions were less of a problem because the geometry of the aircraft invariably permitted rapid recovery by using only the standard aerosurface controls. Indeed, spin entry was often an evasion tactic in dogfights. The RB data in the earlier aircraft show much less variation in Ω (the spin angular velocity) than do today's aircraft, such as F-14, F-15 and F-18 (and also F-4).

RB data must be used with at least forced oscillation data or else there will not be stable spin equilibria. In actuality, static data is incorporated as well, since it is convenient to have all non-Ω-dependent effects associated with it. RB data, then, is meant for use in so-called "hybrid" situations. In these cases, $\alpha \in (55°,90°)$ for spin entry; for spin recovery, α must drop below about 30° before RB data is no longer useful. In the wind tunnel, RB data are measured over $\alpha \in (55°,90°)$.* Because of the manner in which the sting is fastened to the model, tail interference typically prohibits reducing α further. Sideslip is varied also; however, seldom greater than ±10°. This is because, given the degree of freedom requirements at the point of attachment of the sting to the model, a large hole would have to be cut into the top of the model fuselage if β were to be large. This would generate unrealistic flow patterns about the fuselage and produce spurious data. If $\beta \simeq 0°$ then, the sting can ride along a slit in the fuselage as α varies. (The sting must be fastened at the center of mass, which is usually inside the fuselage.) It should be noted that, although RB data are measured as functions of the two angles α and β, as well as (Ωb/2V), the angles

*To compute RB values for $\alpha = 30°$, it is suggested to hold constant the $\alpha = 55°$ tunnel results.

actually are Euler angles roll (ϕ) and pitch (θ) in tunnel coordinates. The exact relationships are $\tan\alpha = \tan\theta\cos\phi$ and $\sin\beta = \sin\theta\sin\phi$. However, if α is large and ϕ small, the usual situation, it is valid to assume $\alpha \simeq \theta$ and $\beta \simeq \phi$.

As mentioned earlier, there is a good bit of artwork required in the process of switching to and from the "hybrid" aero model (this model uses S + FO + RB data; the "non-hybrid" or standard model uses only S + FO aero data). The values of α for which this transition should occur are not clear-cut. In addition, the actual content of Ω, the rotational variable, is not fully resolved. In the tunnel, Ω represents the rate at which the model is rotated about the sting. In flight and simulation stiuations, it may or may not be realistic to use

$$\Omega^2 = p^2 + q^2 + r^2. \tag{3.8}$$

For example, in flat spin regions ($\alpha > 85°$), the above relationship is probably adequate for describing the model in equilibrium because $p,q \ll r$. But in oscillatory spin regions ($\alpha \simeq 65°$ for the F-4), much of Ω consists of components which contribute to FO-related forces and moments; there would therefore be redundancy, and consequently inaccurate results, if Ω were as given above. In such situations, an improvement usually results if $\dot{\psi}$ replaces Ω as one of the RB independent variables (the other two independent variables are α and β). FO data can be used with either S or RB data (or both) because it represents coefficients derived from oscillatory motion imposed on either the "steady-state" static or rotation condition.

Another difficulty with RB data is that they are unreliable near $\Omega = 0$. The prevalent technique for dealing with this problem is to set (using C_n, the most prominent aero coefficient for spin/rotation analysis)

$$C_{n_{RB}} = 0 \quad \text{for } \Omega = 0, \tag{3.9}$$

thereby incorporating all $\Omega = 0$ effects into C_{n_S}. Thus, for a given (α,β) pair,

$$C_n\Big|_{\Omega=0} = C_{n_S} + C_{n_{FO}} \tag{3.10}$$

The RB data for given (α,β) are usually plotted against $(\frac{\Omega b}{2V})$, a non-dimensional quantity. Because a different run is made for negative $(\frac{\Omega b}{2V})$ than for positive, there is not only a non-zero value for the <u>measured</u> $C_{n_{RB}}$ at $\Omega = 0$, but a mismatch, as seen in Fig. 3.39. For each of the two

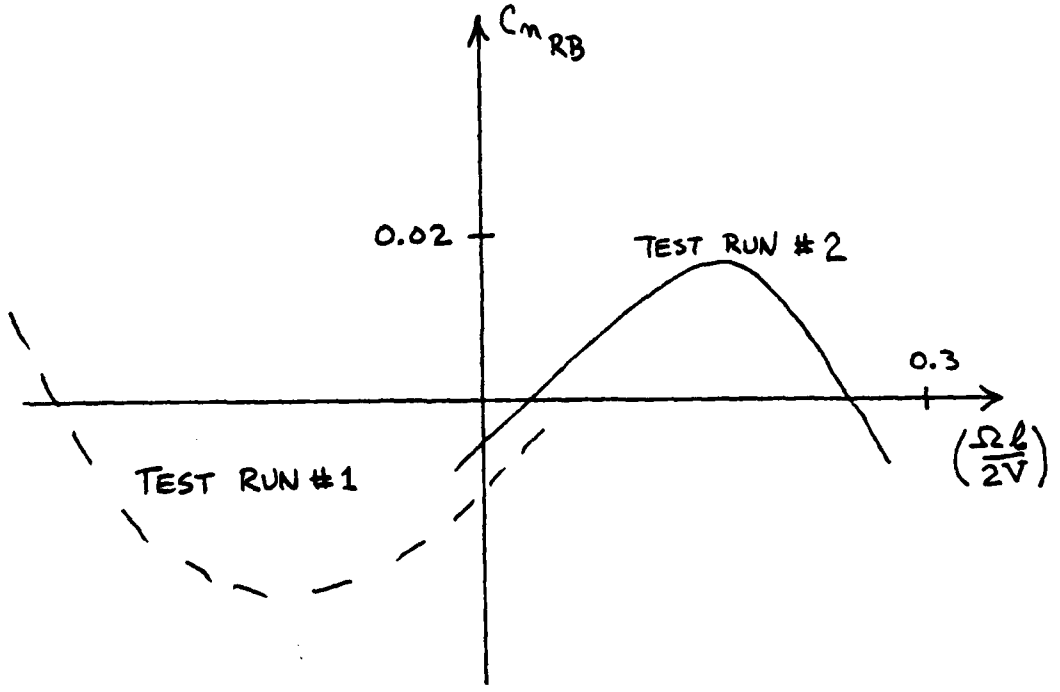

Figure 3.39

Representative Rotation Balance Data Runs (α,β fixed)

sets of data (two runs) shown in Figure 3.39, the $\Omega = 0$ value of C_n should be taken out of the $C_{n_{RB}}$ computed at any Ω, as it is reasonable to assume that this component has been incorporated in C_{n_S}.

Another comment on Figure 3.39 is that equilibrium spin occurs for values of $\Omega \neq 0$; C_{n_r} should be greater than zero in a small α-band near 60° in order to duplicate F-4 flight test results. No equilibrium spin is possible if $C_{n_r} = 0$ only at $r(\Omega) = 0$. Finally, C_{n_p} in equilibrium spin should be small, to minimize adverse autorotational coupling effects.

3.2.4.3 Summary of Discussions of Testing Techniques

The following comments concern aspects of data collection techniques which have some relevance to the set of F-4 aero data which we received from NASA Langley:

Aircraft with long, slender noses and $I_x \ll I_y, I_z$ (i.e., low axial moments of inertia) tend to produce non-repeatable wind tunnel data for certain ranges of α in the high-α regions. As α reaches some critical value, usually near 60°, divergence is possible. This can be seen by inspecting the $C_{n_r}(\alpha)$ curves, which show destabilizing (autorotational) values at this α. The problem is, that repeating the tunnel run, with all other conditions retained, often produces a C_{n_r} of the opposite sign at the same α*. Fortunately the F-4 data is quite repeatable, which makes this model a fine one for spin analysis purposes. The F-4 does not have a long nose. F-14, F-15, B-1 and F-111 do have long noses, however, and only F-14 displays any degree of repeatability in its data.

Even though F-4 has a shorter nose, so that the separation effects at high-α about it are not as critical, it nonetheless has tail geometry

*This is a bifurcational situation--which we are not studying--which is similar to the situation shown in the coupled roll-divergence equilibrium plots for aircraft H and F; the "pitchfork" bifurcation, in which one equilibrium solution (the handle of the pitchfork) branches off into three solutions.

which produces autorotational effects near $\alpha = 60°$. When $\alpha = 60°$, $\beta = 0°$ (Fig. 3.40a), a vortex pattern develops around the horizontal stabilizers which is essentially symmetric; however, if $\beta \neq 0$ (Fig. 3.40b), the negative dihedral (anhedral) of the horizontal stabilizers causes a vortex pattern which generates autorotational yaw rates.

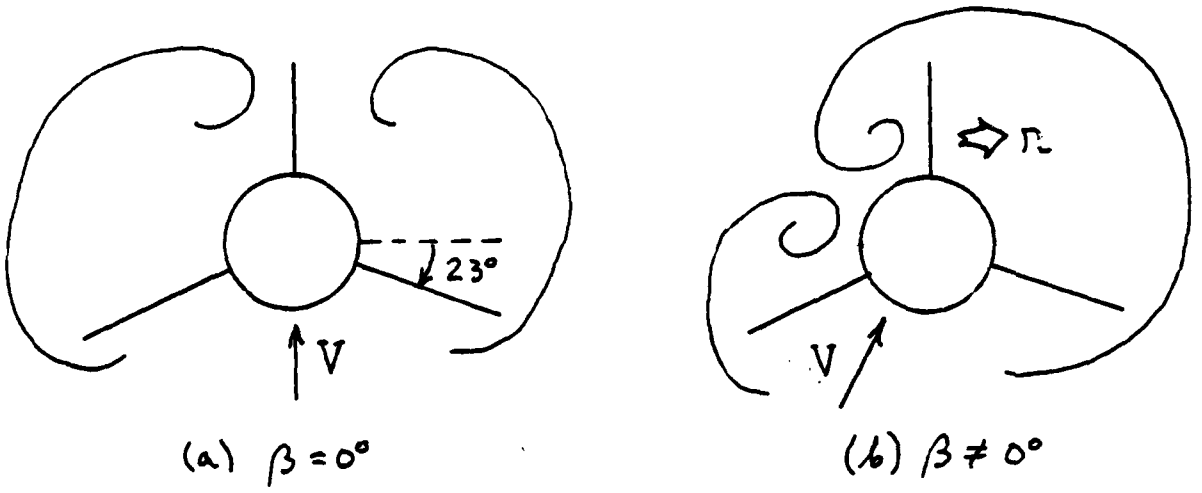

Figure 3.40 F-4 Tail Vortex Effects, $\alpha \approx 60°$

3.2.4.4 Hybrid Aero Data

A goal of this analysis is to have the same hybrid set of aero data (i.e., data which are some combination of S, FO and RB) accurately reproduce flight conditions in both the flat and oscillatory spin regimes. According to the people at NASA Langley, this would then result in a very worthwhile analysis tool, as now these must apparently be different sets of data for each spin regime. In any event, no aero data base which does not include rotation balance data can be exepected to be an accurate simulator of high-α and spin motions.

3.2.4.5 Comparison of F-4 Rotation Balance (RB) Models

Much of the work done related to the simulation model of the F-4 has been devoted to defining different models for utilizing RB aero data, and in making simulations for the purpose of comparing the models among themselves and with the results of others. The motivation for this concern with an accurate RB model lies in recognizing that RB data is crucial for describing accurately high-α motion in which there is an appreciable secular rotational component in the aircraft (i.e., rotation which persists in time, such as that caused by spin, as opposed to the oscillatory rotations cuased by wing rock or Dutch roll). After having made several preliminary runs, using a large class of models based on our correspondence with other researchers, and on other published reports, the models still being considered are now described (there remain other possibilities, not described here, which will be attempted if the models under consideration prove inadequate).

a) The basic wind tunnel data presents the rotary balance coefficients, denoted here by the general term C_{ROT}, as functions of α, β and $R \triangleq (\Omega b/2V)$. However, for the most part, the β-dependence of C_{ROT} is neglected (e.g., Anglin (1978)), and we do so here for the time being. Thus,

$$C_{ROT} = f(\alpha,R) \tag{3.11}$$

This allows for representation using bicubic splines, which is one interpolation algorithm which we have run. Additionally, we have set up a linear 2-D interpolation routine, which has been used for a majority of

the runs. We also have a 3-D linear interpolation RB data representation, which utilizes bicubic spline representations for α- and β-dependencies, and linear interpolation for R.

b) A second, and more important, aspect lies in the "proper" choice of Ω. On this issue, there has not been a strong consensus, at least with regard to research produced at NASA Langley. Ideally, Ω would represent a vehicle spin angular rotation. However, the difficulty which exists in obtaining a consistent set of high-α and spin wind tunnel data which can adequately model flight test results effectively precludes definitive definitions of Ω; some "artwork" is required. Again, because it was first (and easiest) implemented, we have made a majority of runs using

$$\Omega_1 \triangleq r \tag{3.12}$$

where r is the aircraft body axis yaw rate. The use of $\Omega = \Omega_1$ and linear (interpolated) RB data has persisted thus far largely because consistency among runs was desired for other, more elementary comparisons, and for checkout/verification of the BACTM F-4 system. The simulation runs being made now are being used to help resolve which RB interpolation method is the most favorable and which of the possible choices of Ω is best. We will discuss some of these results below.

Continuing with the possible Ω choices, another one being considered is

$$\Omega_2 = \dot{\psi} \tag{3.13}$$

where $\dot{\psi}$ is the vehicle heading rate of rotation. Anglin (1978) considers this choice to be as effective as any. A final version of Ω, from which

similar definitions may be extracted, is best presented by referring to Figure 3.41. In this figure, the body (aircraft) rotation rate vector $\underline{\omega}$ is decomposed into the vectors $\underline{\Omega}_3$ and $\underline{\omega}_\perp$; $\underline{\Omega}_3$ is parallel to $\underline{V}_{xz}$, which is the component of the velocity vector lying in the symmetric aircraft plane, $x_B z_B$.

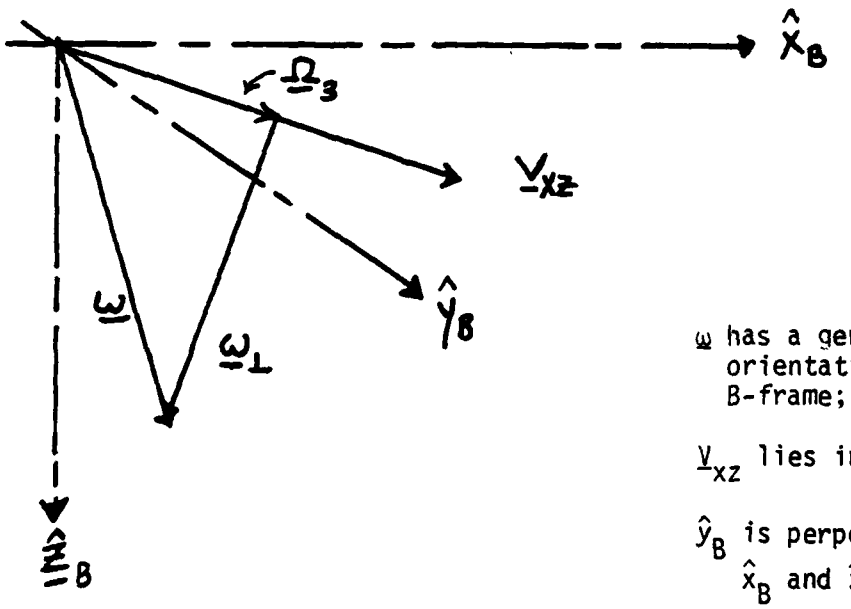

$\underline{\omega}$ has a general orientation in the B-frame;

$\underline{V}_{xz}$ lies in $x_B z_B$ plane

$\hat{y}_B$ is perpendicular to $\hat{x}_B$ and $\hat{z}_B$

Figure 3.41
Geometry for Ω_3

Given, then, that

$$\underline{\omega}^B \triangleq (p,q,r) \tag{3.14}$$

and

$$\hat{V}^B_{xz} \triangleq \frac{\underline{V}^B_{xz}}{|\underline{V}_{xz}|} = (\cos\alpha,\ 0,\ \sin\alpha) \tag{3.15}$$

where $(\ )^B$ denotes coordinatization in the aircraft body axis system shown in Figure 3.41, there results

$$\Omega_3 = \underline{\omega}\cdot\hat{V}_{xz} = (p\cos\alpha + r\sin\alpha) \tag{3.16}$$

The motivation for Ω_3 as defined above is based on two considerations:

i) the rotary balance wind tunnel apparatus at Langley is set up so that the rotation axis is parallel to the airstream (hence, $\underline{\Omega}_3$ parallel to $\underline{V}_{xz}$);

ii) because C_{ROT} is used for $\beta = 0°$ ($\beta \triangleq$ sideslip angle), only the $\beta = 0°$ part of the full velocity, or $\underline{V}_{xz}$ is used.

If (ii) were relaxed, and we were to use

$$C_{ROT} = f(\alpha,\beta,\Omega) \tag{3.17}$$

then the equivalent definition of Ω_3 would be

$$\Omega_3' \triangleq \underline{\omega}\cdot\hat{V} \tag{3.18}$$

As further runs are made using Ω_3, similar modifications may suggest themselves. The validity of each model for Ω depends on the flight condition under which it is used. For example, in flat spin where pitch angle (θ) is small and $\alpha\simeq 90°$, it is clear that all of the Ω_i are equivalent. In high-α, transitory motions, Ω_1 or Ω_2 may not be as good as Ω_3. Ω_1 would be acceptable in cases where the non-oscillatory rotation component is close to the z_B axis; this is not true in general for high-α transitory behavior. At this time, we are favoring Ω_3, but do not yet have a complete enough set of correlation runs to reject the other choices.

c) One of the issues closely connected with the RB aero model is the proper use of forced oscillation (FO) aero data in conjunction with RB data. For example, when Ω_3 is used for RB data, some inaccuracy would

be introduced in the form of redundancy if the full components of ω, p, q and r, were used as multipliers of the FO coefficients.* It is more proper to use the body axis components of ω_1, shown in Fig. 3.41, in the FO terms, since the force-moment effects due to Ω_3 are incorporated in the C_{ROT}. Similarly, when $\Omega_2 = \dot{\psi}$ is used, the FO angular rate multipliers should not consist of $\dot{\psi}$-terms, only those due to $\dot{\theta}$ and $\dot{\phi}$ ($\dot{\psi},\dot{\theta},\dot{\phi}$ are the Euler angular rates in yaw, pitch and roll respectively). As a final complement to the RB modeling philosophy of (b) and (c), all C_{ROT} data were readjusted from the original to assure that $C_{ROT} = 0$ when $\Omega = 0$.

d) A final aspect considered thus far with regard to RB modeling concerns the issue of when to use the RB data (when it is used with static (S) and FO aero data, the resultant aero model is called a hybrid model). There is no well-established formula for incorporating the hybrid model, but a scheme favored by Langley researchers--and used so far in our analyses--is to use the hybrid model when α exceeds about 55°, and to retain it until α drops below 30°. Although configuration limitations preclude taking RB data for the F-4 in the tunnel below $\alpha = 55°$, Langley results suggest that the $\alpha = 55°$ data is valid also at 30°, with interpolation over the interior 25° range. It is possible that a "hybrid" interpolation algorithm for the RB data may be the most realistic--i.e., linear interpolation for $\alpha \in (30°,55°)$, effectively producing a constant value, and spline approximation polynomials for $\alpha > 55°$. At this time, such a hybrid interpolation algorithm has not been tried; we are currently using fully linear or fully spline representations over the complete α ranges of

*Recall that a typical force-moment term arising from forced-oscillation effects would be $C_n = \ldots + (\frac{b}{2V})pC_{n_p} + \ldots$, where C_{n_p} is the FO coefficient. See Eqs. (3.3) to (3.6).

values. Two other issues concern smoothness of the total coefficients' values as the aero model transitions between hybrid (RB) and non-hybrid (no RB), and trying different "boundary" values for α than the above pair, (55°,30°). We are currently continuing our investigation of these issues as well.

In summary, several aspects of realistically modeling an aircraft model (F-4) with a hybrid aero data base have been discussed, and we have described several candidate models. Basically, the RB modeling issues reduce to two items: proper Ω-representation and whether or not spline-polynomial interpolation is sufficiently adequate. Several runs have been made using most of the models described above. In the next section, we will describe a sampling of these runs, as well as other runs which have served to define spin recovery capabilities of a particular F-4 model ($\Omega = r$, full linear interpolation of RB data). The ultimate purpose of the analysis reported in this section is:

i) to verify the accuracy of the algorithms as they are coded--i.e., to give confidence in the model;

ii) to establish an accurate "reference" model, against which a class of reduced or simplified models, presumably flight-condition-dependent, may be compared. Simpler models which are nonetheless sufficiently accurate for a given flight condition are needed in order to perform control system synthesis studies, and to construct spin prevention and recovery algorithms;

iii) to identify the regions over which more wind tunnel data are needed, or to identify other shortcomings with the current F-4 data base which may limit the accuracy of BACTM analysis.

In Sections 3.2.5.1 and 3.2.5.2, some of the aspects of the above RB modeling considerations are discussed in more detail.

3.2.5 F-4 Simulation Results

In this section, we shall report on the progress of our ongoing effort both to establish an adequate model from the F-4 data base for realistic spin recovery analysis, and to actually apply BACTM to such a model to determine globally its high-α properties. Therefore, the simulation results reported on here fall into two general categories, with possible overlapping:

i) runs made for the purpose of spin recovery analysis; at this time, since we have not completed our study which will allow us to define a complete F-4 model, we have used a preliminary RB model--linear interpolation for RB aero data and $\Omega = r$--for spin analysis;

ii) runs made for the purpose of developing an F-4 model which correlates most closely, given the aero data base, with flight test results.

Unless otherwise stated, the F-4 model used for the runs discussed below is that described in (i) above, and shall be called the "initial" model.

3.2.5.1 Equilibrium Surface Results

High-α and spin equilibrium surfaces generated so far for the F-4 initial model appear at first glance to be quite uninteresting. Their shapes are very plain, and reflect a general insensitivity of the equilibrium

point to control variations; another way of stating this observation is by saying that spin recovery using aerosurface controls alone is, for the cases investigated so far, not a feasible option. Figure 3.42 shows a typical result, one of several which have been made. Shown in this figure are plots of the state variables p (roll rate), r (yaw rate), and α (angle-of-attack) against aileron (δa). Point A in this figure depicts the stable flat spin equilibrium point for the left pro-spin control setting,

$$\delta_L = (-30., -21., 30.) \tag{3.19}$$

As δa moves from its pro- to the anti-spin region (near $\delta a = 30°$), one can notice some improvement in the prospects for recovery. As with aircraft F, the goal is to find control sequences which effectively convert a stable equilibrium into an unstable one. In that case, however, the spin equilibrium branches are much more amenable to recovery efforts made using aerosurface controls. In particular compare Branch 1 in Figure 3.9 with Figure 3.42b. The former is for a right pro-spin set of $\underline{\delta}$, but this basically affects the sign of r, not its magnitude or the shape of the equilibrium curves. In Figure 3.42, we see that a Hopf bifurcation occurs for $\delta a \simeq 2°$, and that oscillatory-type motion, possibly of a limit cycle variety, exists for $\delta a \gtrsim 2°$. Also, r and α values change in the "right" direction,* as δa increases. However, as time history runs

*The goal for recovery from spin, based on our aircraft F experience, is not only to convert a stable high-α or spin equilibrium condition into an unstable one, but also to observe the two major spin quantities: r and α. In our left pro-spin example, r is large and negative, and α is close to 80°. An effective recovery control sequence requires that the magnitudes of r and α become smaller.

discussed later will show, it turns out that, even with δa set to its maximum allowable anti-spin value of 30° (the ±60° limits shown in the figure were for the purpose of determining more global features of the curve), the oscillatory behavior is far too mild to admit transition to recovery conditions; that is, the oscillatory motions are quite stable. Figure 2.42d shows equilibrium α versus δe, with Point B the common one to all curves in Figure 2.42. As δe increases, the local instability does also; however, it does not do so severely enough to prevent the L-branch in Figure 2.42e from being a stable attractor.

The nonlinear nature of the high-α problem dictates that control sequences are not necessarily additive. From the $\delta a = 30$ point in Figure 3.42, δe was varied from its value there (-21°) to its anti-spin value of 9°. The resulting curves show that the magnitude of r remained almost totally insensitive to δe over its full range, retaining a value near -160 deg/sec. The equilibrium branch was classified as L over the whole curve also (indicating a complex pair of eigenvalues of the Jacobian matrix with a positive real part. The Jacobian would be the system matrix of the linearized system, so that only motions "sufficiently close" to the equilibrium curve are accurately described by eigenvalue analysis). However, the fact that the real part of the unstable mode increases with increasing δe, from 0.042 at -21° to 0.135 at 9°, while the imaginary part's magnitude is essentially unchanged, indicates perhaps that the amplitude of the oscillations would grow sufficiently. If so, and if α and r are in phase, then a judicious choice of time to trim the controls may produce recovery, as we have seen with aircraft F.

A run was made moving δr to -30° from $\underline{\delta} = (30, -21, 30)$. This run was motivated by the fact that some recovery sequences generated by optimal control (steepest descent) techniques require somewhat rapid oscillation of the elevator between its limits; also, δe has been shown to be somewhat insensitive as a control in this flight regime. The result of this run showed further improvement in r, from -160 to -140 deg/sec at $\delta r = -30°$, but also a transition to an asymptotically (in the neighborhood) stable equilibrium for anti-spin δr.

The above discussion centered on equilibrium solutions emanating from the stable, flat left spin control setting. For controls at trim, there not only exist "trim" (i.e., standard low-α, linear dynamics flight regime) equilibria, but also we have found high-α equilibria near $\underline{\delta} = 0$. One of these runs is shown in Figure 3.43. This is interesting because of the manner in which the locus of a complex pair of eigenvalues oscillates at small amplitude about the imaginary axis, as δa varies over ±30°. For this run δe was fixed near its upper limit of 9° and δr was fixed at 0°. For $(\delta a, \delta e, \delta r) = (0., 8.8, 0)$, there is a Hopf bifurcation point which is very definite as δe varies from 0° to 8.8° for $\delta a = \delta r = 0°$, as seen in Figure 3.44. The Figure 3.43 run shows that the Hopf bifurcation in δe remains about at 9° elevator over the full aileron control range.

The $\underline{\delta} = 0$ (trim) spin equilibrium solution point was "continued" to the left pro-spin point, $\underline{\delta} = \underline{\delta}_L$, showing that a second equilibrium branch exists at $\underline{\delta}_L$, one with large, positive r ($r = 210$ here, but is -210 deg/sec in Figure 3.42). This result again would indicate the difficulty of

effecting recovery using aerosurface controls alone, principally because equilibrium r at spin seems unaffected by δr. Figure 3.45 shows the last phase of the continuation sequence from $\underline{\delta}$ = trim to $\underline{\delta} = \underline{\delta}_L$, the left pro-spin setting. Point A in Figure 3.42 is the same as that in Figure 3.44. (No plots of some of the other runs discussed above are shown here, because of their overall similarity to those shown in Figure 3.42.)

From several high-α equilibrium surface runs, it is possible to assemble a small composite of the results analyzed thus far. Figure 3.46 shows a 3-D plot of equilibrium yaw rate, r, vs. aileron and elevator, with the rudder at trim, and Figure 3.47 shows r vs. δe and δr, with aileron at trim. There is a common point to these figures, Point B, where $\underline{\delta} = (0,0,0)$; each Point B from the two figures would coincide in a merged, 4-D plot--if we could draw one. Note again the scarcity of folds and interesting topological features. This tends to imply that equilibria in this undesirable region are quite persistent.

Effects of using different interpolation algorithms for RB data are shown in Figure 3.48. In this figure, $\Omega = r$ and aileron and elevator have left pro-spin settings. It is clear from this figure that differences are not inconsequential; as stated above, we are still analyzing which representation is most appropriate. Note that the linear branch in this figure could be combined with the branch in Figure 3.45, since δa, δe and the other conditions are the same.

It should be noted that not all regions in the high-α region of the F-4 model are as "tranquil" as the figures shown here would suggest. One of our runs, in fact, has found a bifurcation point near $\underline{\delta} = (\delta a, \delta e, \delta r) =$

(-30.,0.,11.5) degrees. This particular point seems to be the result of the intersection of more than one equilibrium branch.* Dynamic properties in the neighborhood of such points are usually quite interesting and may presage recovery possibilities. Such a point is not to be confused with a Hopf bifurcation point, in which a complex pair of eigenvalues crosses the imaginary axis, all other modes remaining stable. Nor is it a limit point, or fold, in the equilibrium surface, several examples of which have been identified in our previous work. The projections of limit points onto the control space generate bifurcation surfaces. The bifurcation point we have found here is a relatively rare occurrence; we did not find any in the aircraft F study.

We have found that the existence of this point, for the particular control setting $\underline{\delta} = (-30., 0., 11.5)$, is model-dependent. A run was made which was exactly similar to the one discussed above, except that the α-knot locations for the RB aero data were increased to nine from four, the value at which our runs are typically made. In this new run, no bifurcation point was encountered in the vicinity of the above $\underline{\delta}$. However, when the original run is duplicated in every way except for value of certain continuation parameters--i.e., no model changes--we are still able to encounter this bifurcation point. This happens even though the different tolerances, step sizes, etc., produce a slightly different series of equilibrium solutions points; as these points approach the critical value of $\underline{\delta}$, the solutions bifurcate.

*The point is most likely a simple bifurcation point, i.e., the intersection of only two branches, since the rank of the $n \times (n+1)$ "augmented" Jacobian matrix Γ (see Chapter 2) is (n-1). We shall discuss this in more detail in later reports. It is also important to point out that the projection of multi-dimensional surfaces onto the plane of the paper often causes intersections in the 2-D space. These are usually not bifurcation points.

Other equilibrium runs for the F-4 aircraft will now be discussed. The results presented thus far have been devoted primarily to the very high-α, flat spin regions. These results are seen to contrast greatly with results at similar flight conditions obtained with aircraft F (Section 3.1). The likelihood of there being F-4 spin regions with equilibrium sufraces which have features amenable to spin recovery strategies using aerosurface controls only--i.e., that these surfaces have folds or limit points--is very remote. However, the α domains from stall to spin entry do show very interesting features. We show some of these results here, and more results in Section 3.2.6, where F-4 bifurcation surface results are discussed, and in Section 3.2.7, where thrust effects are discussed. The following sets of equilibrium curves were generated for an altitude of 5000 feet and a velocity of 330 feet per second, using the five-state "trim" equilibrium system (results for the F-4 discussed above were generated on the 8-state "spin" equilibrium system. The reason for the chosen altitude and velocity was to investigate the dynamic environment which corresponds to that of certain drop model flight tests, which were a series of remotely piloted tests conducted at NASA Langley of a 0.13 scale model, free-fall version of the F-4 aircraft. The ultimate goal in achieving correlation between these flight tests and our simulation results is, of course, to develop a more realistic F-4 model.

Figure 3.49 shows results near the trim flight condition, extended over the δr range. The effect of the low speed and altitude seems to be that a very stable condition is created. One interesting aspect is that

roll rate (p) seems to be more sensitive to δr than yaw rate (r), at these conditions. In general, we have found that δr in our F-4 model is not a sensitive control unless sufficient aileron also exists. However, there is little question as to the control effectiveness of the aileron in this region, as the plot of p vs. δa in Figure 3.50 shows. The variables r and α remain close to zero for the full range of δa. Note that the $\delta = 0$ points in Figures 3.49c and 3.50 coincide.

If the values for δe and δr are offset slightly from trim, e.g., $\delta e = -3.5°$ and $\delta r = -6°$, aileron is less sensitive to p, but influences r and α more, as a comparison of p plots in Figures 3.51 and 3.50 shows. When δa is offset to $-6°$ and δe to $-3.5°$, we observe that, as stated above, δr becomes more control-effective (Figure 3.52). There are mild but unmistakable limit points, and the lateral/longitudinal coupling is strong even for these relatively small values of δa and δe, as evidenced by the α vs. δr plot, Figure 3.52a. This figure shows that decreasing rudder can induce stall, when $\delta a = -6°$ and $\delta e = 03.5°$. The $\alpha = 8°$ limit point was the initial condition for the bifurcation surface discussed in Section 3.2.6.

By starting at the $\delta r = -6°$ point in Figure 3.52 and continuing it in the δe direction, keeping $\delta a = -6°$ also, we see the very nonlinear effect that elevator has on the equilibria (Figure 3.53). Thus, both δe and δr can readily induce jump phenomena, if the controls are offset a bit from trim; however, δa in this region seems to be a linear control, influencing roll rate most noticeably, as expected, but over its full range. Elevator and rudder have a considerably smaller linear range.

It is clear that the stall and spin entry region for the F-4 model contains many interesting nonlinear features. Equilibrium values for α extend well beyond its stall value of about 12°, to above 30°, as δe is decreased. This control action provides more pitchup response, as Figure 3.53b verifies. These high-α equilibria, however, are unstable. Figure 3.53 is a "connecting" branch between the plane depicted in Figure 3.52, where $\delta e = -3.5°$ and $\delta a = -6°$, and the plane depicted in Figure 3.54, where $\delta e = -25°$. It would seem that more equilibrium surfaces exist in this region of negative δe (pitchup), particularly for spin values of α (i.e., $\alpha \gtrsim 50°$).

Other equilibrium surfaces will be introduced in later sections in support of topics relevant to those sections. In particular, see Section 3.2.6.

3.2.5.2 *Time History Results; Correlation Runs*

This section discusses highlights of F-4 time history runs made during this reporting period. In making these runs, the overall goal has been to try and match F-4 results obtained either in actual flight tests, or in other studies (e.g., Bihrle, 1976; Adams, 1974; Anglin, 1978). This correlation effort is, of course, aimed at defining a realistic simulation model for the F-4 aircraft; clearly, such an achievement would validate the BACTM results. We are therefore not making as many time history runs solely for the purpose of validating other BACTM results, e.g., equilibrium surfaces.

Figures 3.55 and 3.56 show the effect of using RB spline aero data (Figure 3.56) as opposed to linearly interpolated RB data. Although for a different flight condition here ($\underline{\delta}(t = 0) = (0,-21,30)$, with $\delta a = 28°$ at

$t = 15$ sec), the distinction in interpolation methods is not as pronounced as in the equilibrium surface result, Figure 3.48. A more pertinent aspect of these runs is that a sudden change of aileron to an anti-spin value, while retaining δe and δr at pro-spin settings, has negligible impact on the trajectory. Only roll and pitch angles experience even modest changes, although there is a noticeable buildup in oscillation towards a possible limit cycle, as predicted by the relevant equilibrium result, Figure 3.42 (see in particular Figure 3.42b, r vs. δa. Point B in that figure corresponds to the control condition for $t > 15$ sec in Figure 3.55.) However, such oscillations must be much more severe before recovery possibilities can be entertained. Any recovery effort clearly requires more than aileron activity, based on these results.

The importance of the choice of Ω (Section 3.2.2.3) may be understood better by comparing the results in Figure 3.57 with either of Figure 3.55 or 3.56. In Figure 3.57, $\Omega = \Omega_3$, given by Eq. (3.18), was used, while $\Omega = \Omega_1 = r$ (Eq. (3.12)) in Figures 3.55 and 3.56. The trajectory was otherwise the same (except that minor software problems caused a premature abort of the trajectory). If Ω_3 is indeed more realistic a choice, then Figure 3.57 shows a possibly enhanced likelihood for recovery, as the oscillation amplitudes are growing much more rapidly than in the $\Omega = r$ cases. In all of these runs (Figures 3.55 to 3.57), α remains near 84°; however, α is much less oscillatory for the $\Omega = r$ cases.

A preliminary correlation run is now discussed. Figure 3.58 shows recorder tracings of a drop-model flight test run conducted at NASA Langley. Our simulations are attempting to duplicate the trajectory between $t = 15$

and t = 45 sec. Figure 3.59 shows our simulation of this trajectory. There is fair agreement for some variables, although r and α are not in good agreement, and there is no clear tendency for developed spin or spin recovery. We are awaiting a magnetic tape from Langley which has the flight test results in digitized form. In this way, we can more accurately match initial conditions. In the run in Figure 3.59, $\delta a = 30°$, $\delta e = -21°$, $\delta r = 30°$, to match Figure 3.58. Figure 3.60 shows time history plots of the major aerodynamic force-moment coefficients, as well as C_{ℓ_β}, C_{m_β}, C_{n_β}, for the Figure 3.59 run. Analysis is continuing on all of these runs. We have found that there is little distinction in our results when altitude is allowed to vary, Figures 3.59 and 3.60, or when it is fixed. Figure 3.61 shows the Figure 3.59 - 3.60 case, but with h fixed at 30,000 ft. There is evidently no major difference, at these conditions.

Correlation with a second Langley scale model drop flight test proved to be much better, although still not adequate. Figure 3.62a - 3.62d show drop model flight test results for a second flight test with the scale model of the F-4 conducted at NASA Langley. When compared to our simulation results (Figures 3.62e - g), it can be seen that r, α, and β are reasonably close in agreement, although velocity is not too similar. Our conclusion at this point is to continue work at defining high-α conditions at which agreement is adequate, and to specify the changes needed in the model to assure better agreement where it is not adequate.

Another correlation run which didn't fare as well was an attempt to match the F-4 recovery results presented in Young and Adams (1972), reproduced here in Figure 3.63. We do not achieve recovery, in spite of

using a control sequence and initial conditions which match his as closely as can be done visually; it is felt that the major reason is that we are using RB aero data. See Figure 3.64, which shows a less oscillatory but very definite spin condition using our model.

Another correlation run attempts to duplicate Figure 8 from Anglin (1978). Anglin's Figures 8 and 13 are presented here in Figure 3.65. Judicious guesses were required for some of the initial values, but in the Figure 8 case our result seems to match the flight test result shown on that figure closer than it does his calculated result (Figure 3.66). However, the match is still poor, especially in r, although α and β display many similarities. A run to match Figure 13 from Anglin (1978) does somewhat better, especially in r and β, although again the overall match is lacking in close correlation. The BACTM result shows little variation in heading (TURNS variable), which is very much unlike Anglin's result. We get a higher mean value for α, 84°, than Anglin does (60°). See Figure 3.67 for the BACTM run, and Figure 3.65 for Anglin's Figure 13 run.

The following series of correlation runs is based on stall and spin entry studies done by Bihrle and Barnhart (1978). The basic flight condition for these results is 40,000 feet altitude, velocity near 800 feet per second, and straight and level flight. For the BACTM model, this yields an equilibrium (trim) α of 7.1°, at $\delta e = -3.5°$. For these runs, we have also incorporated logic which includes thrust effects. Normalized thrust parameters, $C_{x_{THR}}$ and $C_{z_{THR}}$ are added to the aerodynamic force coefficients along the axial and normal directions, respectively, as long as α is between -10° and 20° (thrust moment arm is

assumed zero in all cases). These limits were used by Bihrle in his studies, and such a strategy reflects the idea that, once stall has occurred, the engine is quickly brought to idle. Further discussion of the effects of adding engine thrust to the dynamics at high α may be found in Section 3.2.7.

Figure 3.68 shows a control sequence initiated from the trim condition described above, which is a stall and recovery maneuver. From the r, α, and ϕ plots, it is seen that a severe oscillatory motion combined with steady roll rate ensues while the controls are at their extreme setting, $\underline{\delta} = (45°,-25°,-30°)$. While growth to an oscillatory spin condition seems quite likely, this run is very interesting in that the motion can be returned to trim if the controls are neutralized quickly *enough*, as they are here. This run is being analyzed in more detail to study such aspects as the threshold. A more extreme motion (see r, α and ϕ for comparison) results when the sequencing of the controls is changed to a more realistic stall/entry sequence, as Figure 3.69 shows. Again, we are continuing to study this interesting run. At about t = 16.0 sec in Figure 3.69 (designated as t*), the dynamic state of the vehicle seems to be favorable for spin entry, induced by subsequent control action not shown in this figure. At $t = t^*$, the controls are $\underline{\delta} = (\delta a,\delta e,\delta r) = (0,-30,0)$. The runs discussed now describe some of the results which arise when different sets of $\underline{\delta}$ are applied at $t = t^*$ to the state at that time, which is

$$\underline{x}^* = (-106.16,27.64,-53.68,61.18,-15.18,641.5,-7.23,64.58)$$
$$= (p,q,r,\alpha,\beta,V,\theta,\phi) \qquad (3.20)$$

Figure 3.70 shows the case $\underline{\delta}(t^*) \equiv \underline{\delta}^* = (0,-30,30)$; i.e., the rudder is set to 30°, and this is the only difference from Figure 3.69, for $t > 16$ (=t*) sec. Thrust is on when $\alpha \in (-10°,20°)$. It can be seen that yaw rate becomes more responsive to δr, when $\delta e \neq 0$. The enhanced sensitivity of δr as a control, when δa or δe is nonzero, was discussed in Section 3.2.5.1. Equilibrium surface results presented in that section predicted such behavior as we are seeing in Figure 3.70. Inspection of Figure 3.70 also shows possible development of an inverted ($\alpha < 0°$), steep ($40° \lesssim |\alpha| \lesssim 75°$) spin. We cannot claim that such a condition is characteristic of the actual F-4, however, for two reasons: (i) our correlation studies are incomplete, and we haven't consequently refined our simulation model of the F-4; (ii) such F-4 aero data we have is limited to $\alpha > 10°$, so that motions in which $\alpha < -10°$ for more than a fraction of the time, e.g., Figure 3.70, are inherently unrepresentative of even a valid F-4 model. In our simulations, we assign $\alpha = -10°$ values to the aero coefficients for all $\alpha \leqq -10°$. Several of the runs made from the initial conditions given by Eq. (3.20) displayed the tendency for inverted spin, as seen in Figure 3.70, or for $\alpha < -10°$ for persistent periods. Because such results are less representative of F-4 aircraft, although valid in themselves, we are placing little emphasis on them in this report. Further, we do not generate equilibrium results for the conditions $\alpha < -10°$ or $\alpha > 120°$.

A motion starting at $\underline{x} = x^*$ (Eq. (3.20)) with $\underline{\delta} = (30,-30,30)$ is shown in Figure 3.71. In this figure, not only altitude is fixed as in the Figure 3.69 and 3.70 runs, but also thrust is fixed at zero. Here, we can see likely development of an erect, steep spin, although r must increase

somewhat before this is assured.

In Section 3.2.7, we shall continue our discussion of F-4 simulation results, with emphasis on how the presence of thrust affects high-α behavior. It is interesting, however, to show one thrust comparison here, since it deals with the series of runs we are discussing in this section. Figure 3.72 shows a thrust comparison result with Figure 3.71. In the former, thrust is on when $\alpha \in (-10°, 20°)$, while there is no thrust in the latter. It is seen that only minor differences arise in the plotted variables; here, this is due largely to the fact that $\alpha < 20°$ only briefly, hence turning on thrust, for $t > 4.0$ sec in Figure 3.71. It was felt, however, that more differences would result from the first, large dip in α, which occurs at $t = 3.0$ sec. Section 3.2.7 will analyze this further. The following section discusses results obtained thus far in generating bifurcation surfaces for the F-4.

3.2.6 Bifurcation Surfaces

Our definition of a bifurcation surface is that it is the projection of limit points into the control subspace, $(\delta a, \delta e, \delta r)$. Such surfaces, therefore, exclude Hopf bifurcations, global bifurcations, and bifurcations resulting from intersecting equilibrium branches. See Section 2.1.2 and Mehra and Carroll (1978) for a glossary and detailed discussion of the concepts of bifurcation surfaces. Section 2.1.2 describes how the algorithm was adapted to the F-4 aircraft.

At this time, only the high-α regions associated with the post-stall/spin entry flight regime ($\alpha \lesssim 35°$) have been found to possess the "folds" in the equilibrium surfaces (manifolds) which correspond to limit

points. As we have seen in Section 3.2.5.1, the developed spin regions typically produce flat equilibrium surfaces, monotonic in the controls. This feature of our F-4 model, while quite different from the aircraft F model, which displayed many folds and "jump features" in the spin regions, nonetheless is consistent with flight experience on the real aircraft. That is, spin recovery does not depend on jump phenomena associated with changing the aerosurface controls, as is possible with aircraft F; it is necessary to use such recovery aids as parachutes or wing-tip thrusters.

Our preliminary F-4 bifurcation surface results are now discussed. During this discussion, it should become evident how useful these surfaces are in achieving an understanding of the global high-α motion of aircraft. Our first curve, Figure 3.73, was derived from Figure 3.52. Here, V = 330 feet per second, altitude = 5000 feet, and $\delta e = -3.5°$. This figure shows δr vs. δa. Again, the curves in this control plane are projections of limit points of the equilibrium surfaces, and they form boundaries to regions which have different numbers of equilibria. Thus, the numbers seen in Figure 3.73 indicate the numbers of equilibria for the given region. It should be noted, however, that these numbers at this time exclude the spin equilibria at high, positive yaw rate, and at high, negative yaw rate. Further, there may be equilibria at values of α intermediate to the region depicted, and the spin region.

The number of equilibria in a given region in the bifurcation surface is found from the relevant bifurcation curve. The plane for the equilibrium surface of Figure 3.52, for example, which was used to provide initial conditions for the Figure 3.73 result, is depicted in Figure 3.73

by the vertical hatched line at $\delta a = -6°$, and points A and B from Figure 3.52 are located also on Figure 3.73. From this, we can deduce that the small region between points A and B in Figure 3.73 will always contain two more equilibria than the regions along the $\delta a = -6°$ line outside of these points.

Bifurcation surfaces greatly expand our knowledge of the nonlinear features of a given region. As evidenced by the mild nature of the limit points in Figure 3.52, our exploration of this particular region using only equilibrium surfaces nearly missed a very interesting region; for δa a few degrees more negative, we would have. Having found a case for which limit points exist, however, a bifurcation surface can be generated, and this surface will indicate specifically where further equilibrium surfaces may be generated. In this case, the bifurcation surface of Figure 3.73, generated from the somewhat unpromising $\delta a = -6°$ plane, yielded a region of much greater complexity (and interest) in the $\delta r = -30°$ region. The bifurcation branch emanating from point A did not generate the entire surface shown in Figure 3.73. However, it supplied enough information for us to realize that an equilibrium surface at $\delta r = -30°$, $\delta e = -3.5°$, indicated by the horizontal hatched line, would be worthwhile. This curve is shown in Figure 3.74. It indicated that there were several more limit points in this region than we had been aware of (a total of 8). These limit points of course provided initial conditions for new bifurcation surface branches; having generated these, it was possible to use equilibrium surfaces in new areas to seek yet more limit points. By proceeding in such a manner, that is, by using information from one program to add

to information from another, our total, global, information of a certain region expands greatly. About four iterations were needed for Figure 3.73, which is still not complete. There is a great deal of information to be obtained from such a series of runs, which are quick and inexpensive to make.

Bifurcation surfaces yield information on control system synthesis. That is, from curves such as the one shown in Figure 3.73, we can derive relationships governing the aerosurface controls which would safely perform some mission objective. For example, when $\delta e = -3.5°$, as in Figure 3.73, an aileron-rudder gain schedule which maintains the aircraft on one of the two stable branches in the larger five-equilibria region, might be drawn as shown in that region in Figure 3.73. If δa and δr always assume values which trace a locus along this curve, then no jump catastrophes will occur, and the pilot may feel free to perform whatever maneuvers this envelope allows him. The nonlinear curve shown here is clearly superior in this region to the standard linear command augmentor--i.e., $\delta r = k\delta a$. A straight line in this region does not expand the envelope as naturally to its actual limits as would a curve of the type shown. However, constant gains in the δa-δr plane may have practical advantages, when one takes into consideration effects due to δe. That is, we may be able to use relationships of the type

$$\delta r = k(\delta e)\delta a \tag{3.21}$$

A bifurcation surface of the complexity shown in Figure 3.73 is developed essentially from a single starting point, point A, and a strategy

which interchanges results from equilibrium and bifurcation surfaces to compound the number of branches (solutions). Indeed, this solution extends not only throughout the (δa,δr)-plane as we have seen, but can extend completely through the 3-D $\underline{\delta}$ space. This is because, at any point on a bifurcation surface, any one of three sets of control pairs may be chosen to generate a curve. From point A we used the (δr,δa) set to generate Figure 3.73. To get a similar curve, say, at $\delta e = 0°$, it is not necessary to scan previous equilibrium surface results at $\delta e = 0°$ for limit points. It is necessary only to select any point in Figure 3.73 and make a bifurcation surface run using either the (δe,δr) or (δa,δe) sets. Then, any solutions at $\delta e = 0°$ may be used as initial conditions for a (δr,δa) curve similar to Figure 3.73. We have done this for $\delta e = 0°$, and the result is shown in Figure 3.75. This figure is quite different from Figure 3.73, given that they represent a difference in δe of only 3.5°. The evolution of some of the regions can be traced, however, and it is clear that any gain derived from Figure 3.73 must change significantly at $\delta e = 0°$ in order to exploit the features of Figure 3.75. Thus, it appears as though traditional design approaches can be greatly enhanced by the BACTM methodology. Here we see a strong need to change the control gain with δe. One of the equilibrium surfaces generated in the process of developing Figure 3.75 is shown in Figure 3.76.

3.2.7 Thrust Effects

In Section 3.2.5.2, we discussed how the F-4 simulation was modified to allow for translational forces due to engine thrust. The thrust model allows only for thrust in the plane of symmetry ($x_B - z_B$ plane), and it

does not allow for thrust moments. The combined thrust magnitude of the two engines, and the angle the thrust vector makes with the x_B-axis, are input. These quantities do not change during a run (that is, thrust is strictly a parameter, not a control), nor is there any provision for showing the altitude dependence on thrust. It is the responsibility of the user to recognize, for example, that while the rated thrust of each F-4 engine at sea level is about 8,500 pounds, combined thrust at full throttle is usually below 9000 pounds at 40,000 feet. Finally, we note that thrust is "on" during the time history simulations only for $\alpha \in (-10°, 20°)$; there was no such restriction placed on equilibrium surface runs for which thrust was a factor.

The main effects due to the presence of thrust are: (i) for the "spin" equilibrium system of equations, V, θ, and ϕ are found to be highly sensitive to small control changes, for a given thrust magnitude and orientation in the aircraft. Figure 3.77 illustrates this observation. Here, thrust = 9000 pounds and altitude = 40,000 feet. There are two noteworthy aspects of this run, in addition to the general observation made above. First, this run shows that the addition of thrust to the n = 8 spin equilibrium system does allow for solutions in the trim, or low-α, regime. Undoubtedly this is due to the fact that thrust can be oriented against gravity in a manner so as both to prevent gravity from keeping θ and ϕ from equilibrium conditions, and to attain a valid equilibrium in the eight state variables: p, q, r, α, β, V, θ, and ϕ. Note that α and β have quite nominal, trim, values. Note also that changes in δa, α, and p are extremely minor with respect to changes in V. The second aspect of

this run is the lack of steadiness of the stability analysis results, as evidenced by the "fluctuation" between S (locally stable) and U (one positive, real root: locally unstable) points. Here, the eigenvalues of the Jacobian matrix F do not shift much at all with respect to the very large V variation. In particular, there is one real root whose magnitude remains less than 0.01 over the full V range shown; this root, probably due to numerical accumulation errors, may or may not be positive.

A time history run, however, does support the results presented in Figure 3.77. Taking initial conditions at point A in Figures 3.77a and 3.77b, with $\underline{\delta}(t_0) = (-0.221,-3.5,0.)$, a "stable" point, holding this setting for 25 seconds, and then changing only δa to -0.215 degrees, to an "unstable" region, we do see that the motions are locally stable and unstable at the correspondingly predicted points, as indicated by Figure 3.78. However, it seems as though allowing V, and perhaps θ and ϕ as well, to vary in the thrust equilibrium case causes an overly-sensitive, inherently unstable system. This is because, for a given thrust level, θ and ϕ apparently can adjust to values which orient thrust against gravity for equilibrium over very wide ranges in V. It therefore seems more reasonable to reduce sharply the V-variation, or indeed, to fix V altogether, in order to study thrust effects realistically. We thus are led to studying thrust effects with the $n = 5$ (trim) equilibrium system, for which V is fixed and θ and ϕ are decoupled from the major variables. This in turn, leads to the result. (ii) Thrust effects in the trim system, taken at low-α, are very small. There is a consistency between

this observation and (i), because none of the variables in the $n = 8$ system which are sensitive in the presence of thrust, i.e., V, θ, ϕ, are present in the trim system. Physically, the explanation for small effects lies in the fact that, when α is small, only a small component of thrust affects the trim state variables.

Figure 3.79 shows the trim equilibrium surface for the same conditions as depicted by Figure 3.77, except for the major difference that V is fixed at 875 feet per second in Figure 3.79. Fixing V allows the continuation parameter, δa, to extend to its full range in a "stable" manner; i.e., without a variable V free to assume physically impossible values. There do exist similarities, however, between Figure 3.77 and 3.79 results; the range of values for p and α, especially the latter, are the same, over the same range of δa values.

The contention that thrust effects are small if V is fixed is supported by the comparison shown in Figure 3.80. In this figure, the same general conditions as found in Figure 3.79 apply, except that δe is the continuation parameter. For Figure 3.80a, thrust is 9000 pounds, whereas there is no thrust in Figure 3.80b. Differences in the curves are indistinguishable; at $\delta e = -3.5°$, the state for 9000 pounds thrust is

$$\underline{x} = (p,q,r,\alpha,\beta) = (0.09,2.22,0.03,6.40,-1.42) \tag{3.22}$$

and for zero thrust:

$$\underline{x} = (0.11,2.16,0.02,6.41,-1.42) \tag{3.23}$$

That the $\delta a = 0°$ point in Figures 3.77 and 3.79 is stable is confirmed

by the time history run shown in Figure 3.81, in which $\underline{\delta}$ is fixed at (0.,-3.5,0.). The Hopf bifurcation to post-stall conditions, derived from Figure 3.80, is shown in Figure 3.82; note how long it takes for the limit cycle condition to establish. The motion begins at a stable point in Figure 3.80, $\underline{\delta}$ = (0,-5.2,0); at t = 15 sec, δe is set to -11.2°, causing the Hopf bifurcation (plus a mild jump), as the arrow in Figure 3.80 indicates. It is apparent that this flight regime is a highly interesting one, in view of such results as are seen in Figure 3.80, and it is therefore very worthwhile to develop a full set of bifurcation surfaces in this area. These would be most useful in devising control strategies which exploit the aircraft's capabilities to the fullest without encountering the difficulties which an open loop strategy such as seen in Figure 3.82 encounters.

3.2.8 Limit Cycle Analysis

This section is brief, chiefly because the limit cycle continuation algorithm is not yet operational for the F-4 simulation model. Section 2.1.3 discusses limit cycle continuation in more detail. We therefore show F-4 limit cycle results by using more basic methods, as presented in Mehra et al. (1977). In one method, initial conditions are obtained from an equilibrium solution in a region of interest whose local stability analysis indicates possible limit cycle behavior. Such a solution is designated by L in the equilibrium curves shown in this report, e.g., Figure 3.80. Ideally, this L-segment extends over a significant range of values for the control variable of interest. A time history solution is then initiated at this point, controls fixed, allowing enough time for

limit cycle motions to establish. Then the control variable of interest is incremented a small amount, typically 2°, and the controls are fixed at that position for time enough to eliminate transient motions. By proceeding in this way, bringing the control first to one limit in fixed increments, and then reversing direction from that limit, we can observe how limit cycles develop, how their amplitudes change, how stable they are, how they are annihilated, and how the domains of attraction change, all as the control variable of interest is changed. Typically, the direction of change of the control variable has an effect on the limit cycle motions, so that hysteresis effects are present.

This technique is typical of methods currently used in analysis today, yet it is considerably less efficient than the continuation approach. These problems are compounded for the F-4, because most of the regions of interest seem to be dominated by oscillatory modes of very light damping (positive or negative), creating large time constants. Thus, the cost of such time history runs, with long waits required at each control setting, can get very high. Nonetheless, we did make a few such runs for the F-4, and we discuss some of the results below. Limit cycle analysis can be expanded greatly for the F-4 once the continuation algorithm is operational.

We begin with a study based on the equilibrium surface shown in Figure 3.83. Here, $\delta a = 28°$, $\delta e = -21°$, δr is the continuation variable, and we have a flat spin condition, as the average values of r and α would indicate. This "curve" is typical of F-4 spin equilibria. It is of interest to learn how "post-transient" motions in this flight regime are affected by incremental changes in δr over $\pm 30°$. The reason for this

interest lies in the fact that the stability information given in Figure 3.83--in particular the unstable region, the L-segment--is based only on local, linear analysis. The actual motion in the vicinity of the L-segment of the branch may display interesting features; for example, stable limit cycles may exist in certain areas, but changing δr may weaken or lose stability. If the latter occurs, it is possible that the motion would be attracted to a regime from which recovery may occur. We have seen this with aircraft F (Section 3.1), but thus far there seems to be no similar situation with the F-4.

Figures 3.84 to 3.86 show the time history results corresponding to Figure 3.83. The results are typical of those spin regimes for the F-4 which we have thus far investigated. In Figure 3.84, δr is increased in 6° increments from -30° to 30°, and held for 30 seconds at each setting. Note that the motion is very oscillatory, even in the stable region (negative δr; see Figure 3.83). This is an expensive run, but in many cases even 30 seconds does not allow sufficiently for transient decay. That the stable region is poorly damped yet basically stable may be seen from Figure 3.85, in which the $\delta r = -30°$ setting from Figure 3.84 was held for 40 seconds. Here, we can see that there is definite decay to a steady state value. Returning to Figure 3.84, it is evident that all of the limit cycles obtained are stable, and have relatively small amplitudes centered close to the relevant equilibrium solution of Figure 3.83. The hoped-for instability of the spin limit cycle does not materialize here, for $\delta a = 28°$, $\delta e = -21°$, and δr increasing. The result for δr decreasing from 30° to -30° is shown in Figure 3.86. Again, no instability develops; on the other

hand, there is clearly a hysteresis effect, as we have seen with aircraft F.

As was done with aircraft F, it is often convenient to project the time history amplitudes in "post-transient" motion onto the equilibrium curve figure. This results in a series of vertical bars representing $x_i(\delta_j,t)$ vs. t, with δ_j held at a fixed value. Figure 3.87 shows such a result for the F-4. It is derived from the equilibrium conditions depicted in Figure 3.80b, i.e., h = 40,000 feet and zero thrust, trim to stall and spin entry. Again, hysteresis is very strong; when δe increases from a very unstable region (Figure 3.87b), the motion deteriorates badly, yet recovery does occur. Decreasing elevator, from stable to unstable (pitch up direction) shows a more orderly decay from stable to limit cycle motion (Hopf bifurcation). In Figure 3.87, each value of δe was held for 40 seconds. The corresponding time history runs are seen in Figure 3.88, part (a) for δe decreasing and part (b) for δe increasing. Note the close agreement with the equilibrium surface values, especially for stable values of δe.

3.3 Summary

This chapter has described the results of the application of the BACTM methodology to a wide range of high α aircraft flight conditions. We have made this application to two aircraft, aircraft F and the F-4, whose simulation models are featured by multi-variable tabular aerodynamic data. Using the aircraft F model, we have demonstrated that BACTM is capable of effectively predicting high-α phenomena; in particular, spin has been analyzed extensively with aircraft F, and recovery control

strategies developed.

Many aspects of F-4 high-α motion have been investigated in this chapter, including the selection and proper use of the different types of aerodynamic data, model definition by means of time history correlation runs, and the study of spin, spin entry, spin recovery, thrust effects, and limit cycle motion. The BACTM analysis has confirmed some results and identified several areas where more analysis would be useful. Analysis tools employed by BACTM, in particular the bifurcation surface algorithm, have been extremely useful in providing a global picture of F-4 dynamic behavior in high α regions of interest, and time history runs have been used extensively to support conclusions predicted by equilibrium and bifurcation surfaces.

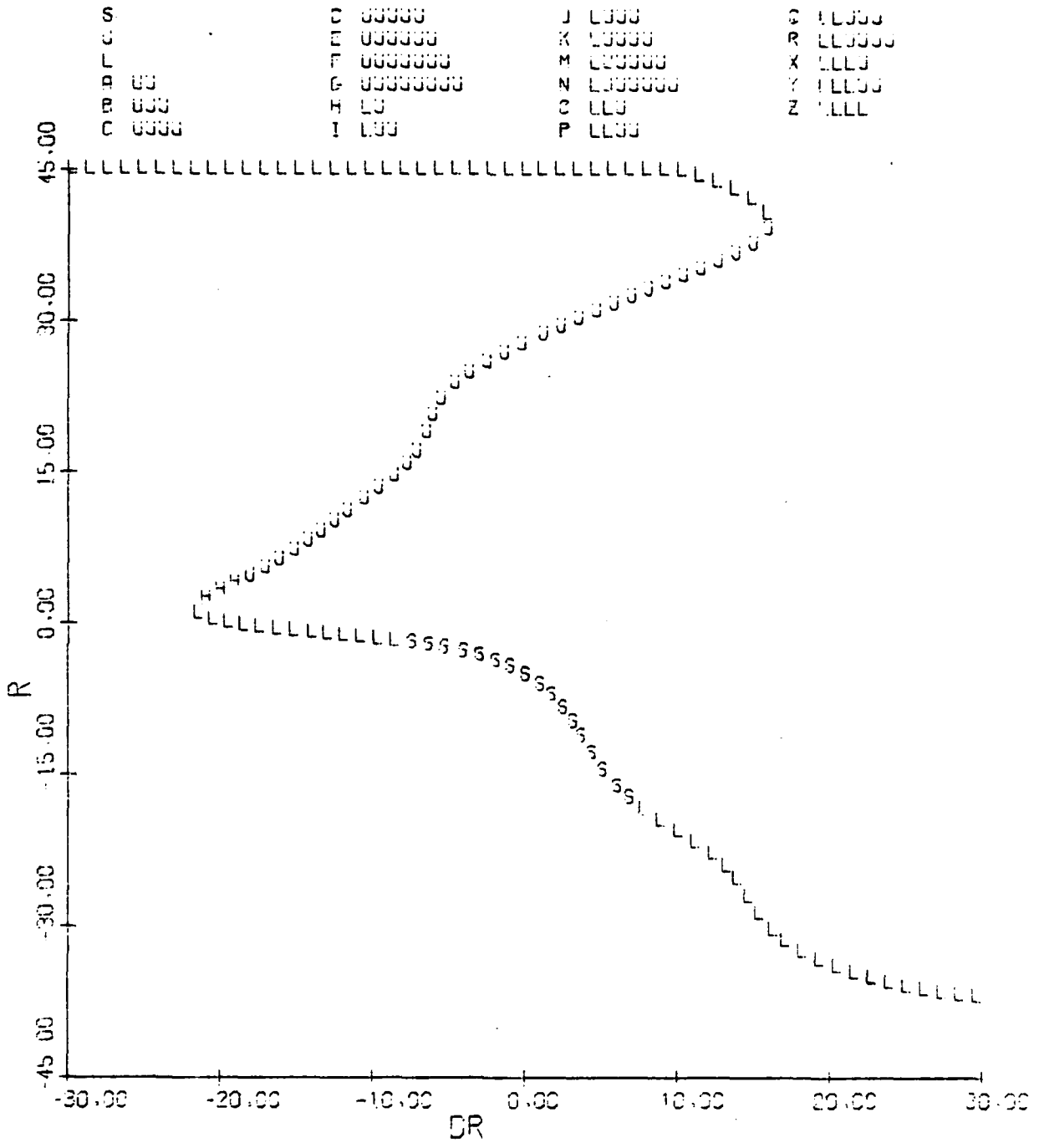

Figure 3.1: Aircraft F Equilibrium Surface - Non-Spin Regime:
$\delta a = 15°$, $\delta e = 0°$, $V = 600$ fps, $g = 0$
(a) Yaw Rate vs. Rudder Deflection

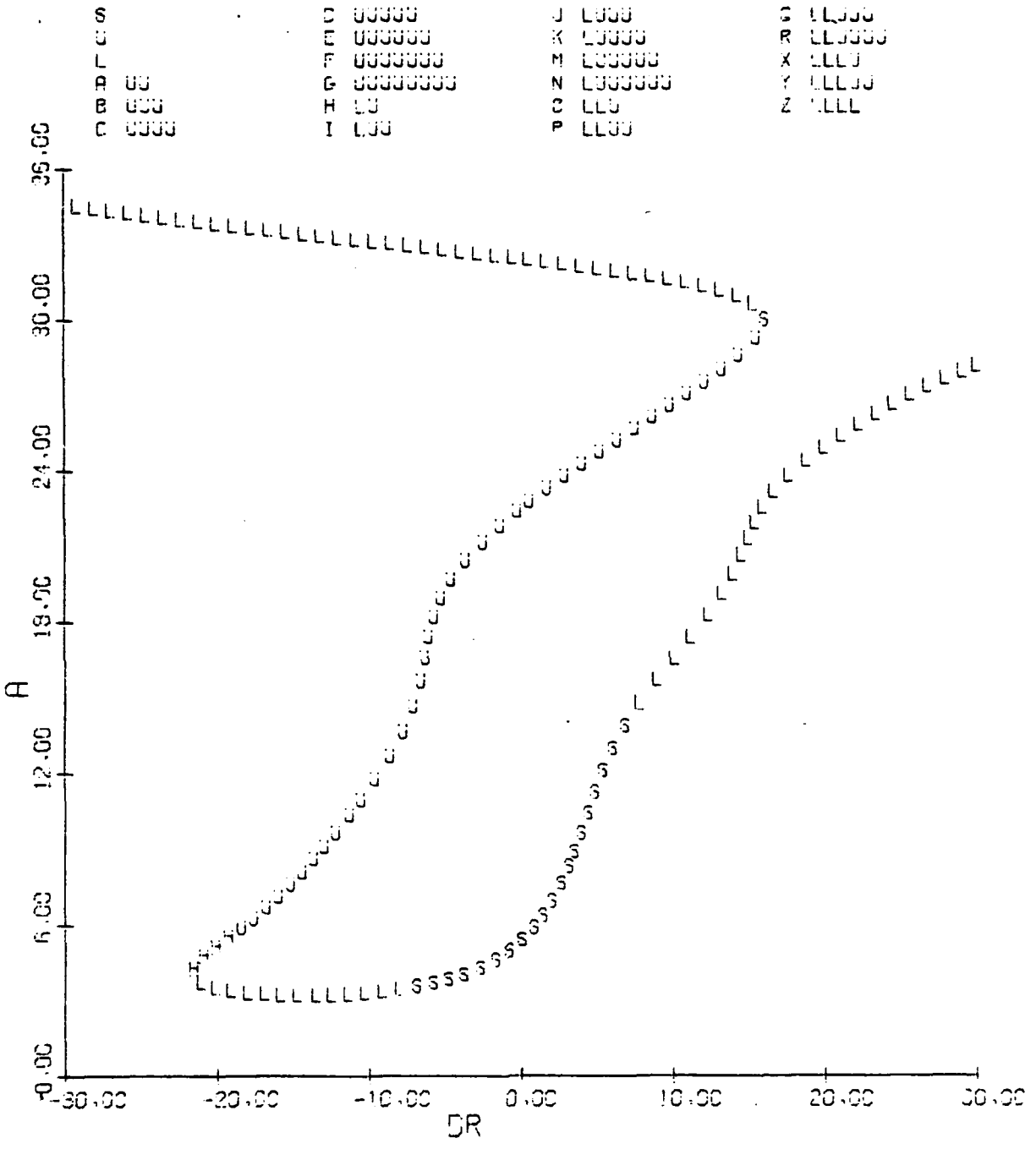

Figure 3.1(b): Angle-of-Attack vs. Rudder Deflection

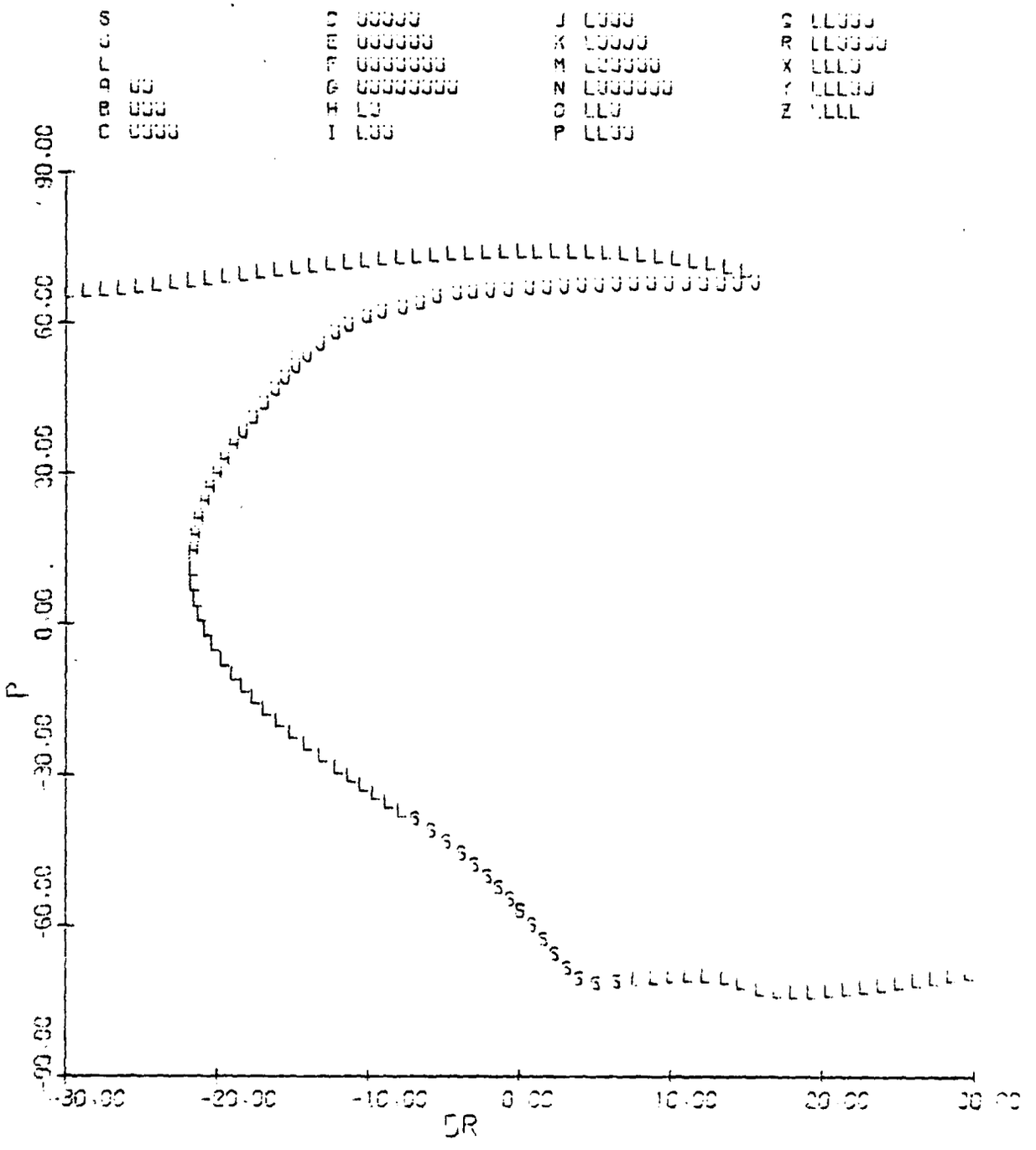

Figure 3.1(c): Roll Rate vs. Rudder Deflection

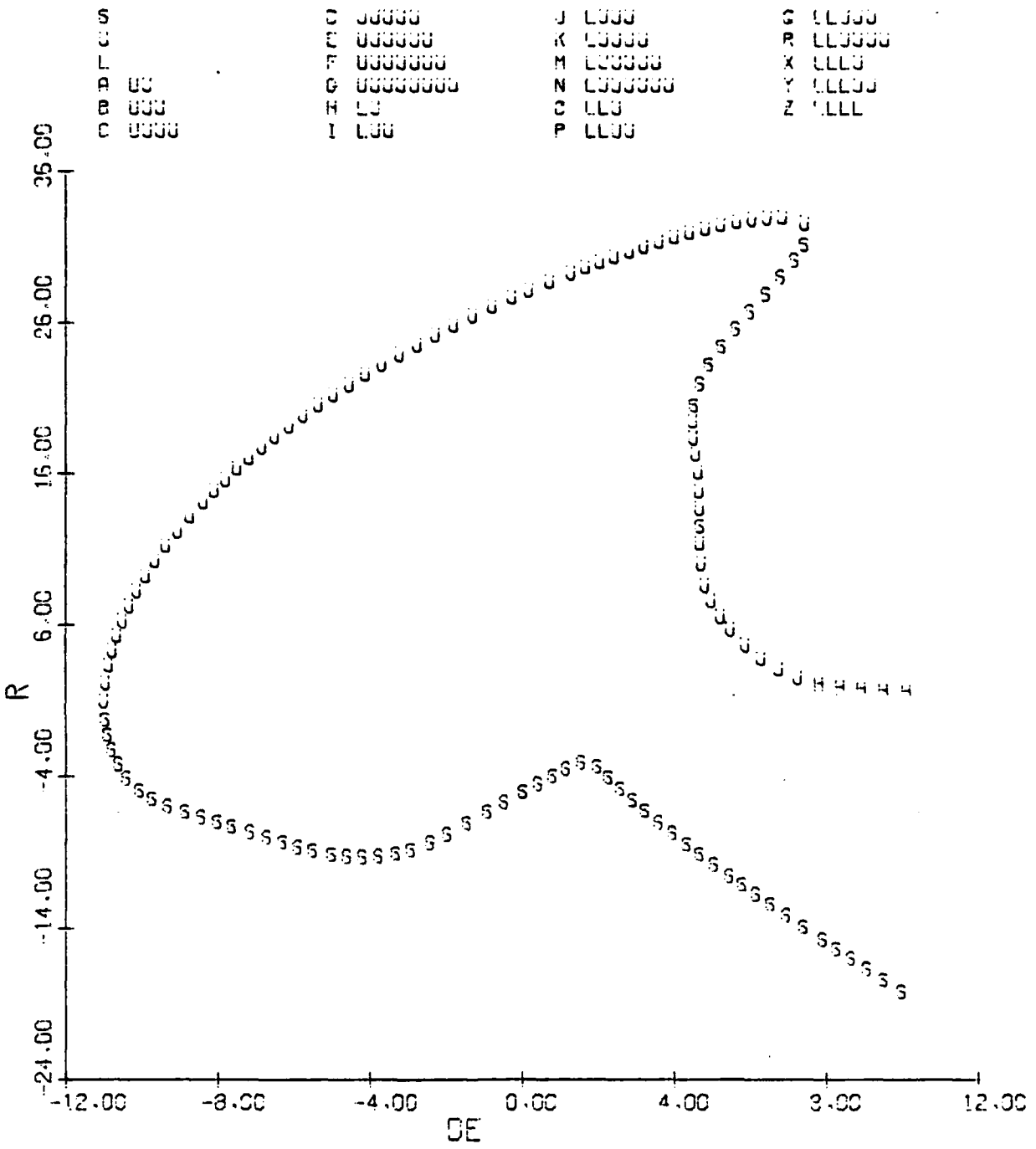

Figure 3.2: Aircraft F Equilibrium Surface - Non-Spin Regime:
$\delta a = 15°$, $\delta r = 0°$, $V = 600$ fps, $g = 0$
(a) Yaw Rate vs. Elevator Deflection

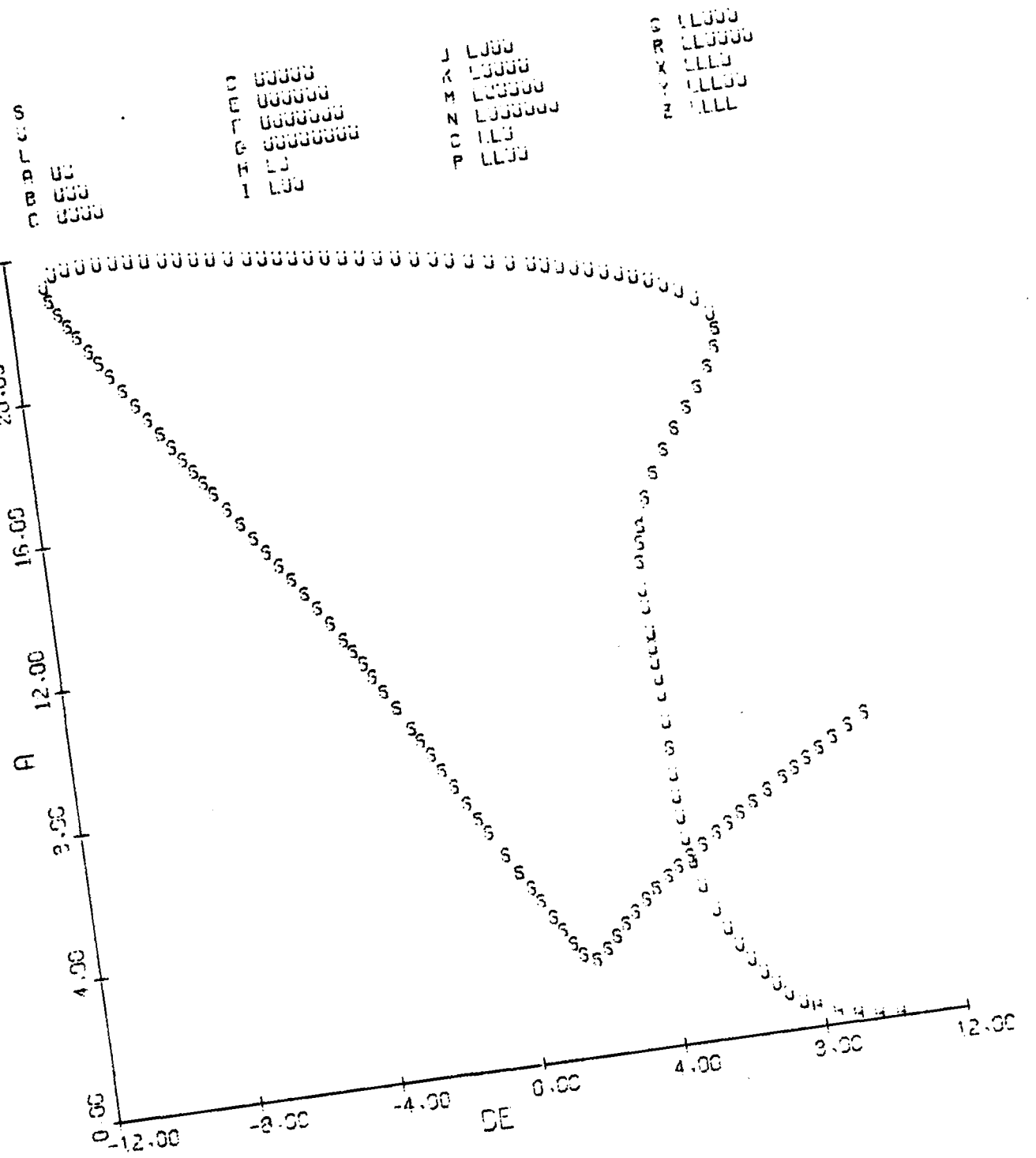

Figure 3.2(b): Angle-of-Attack vs. Elevator Deflection

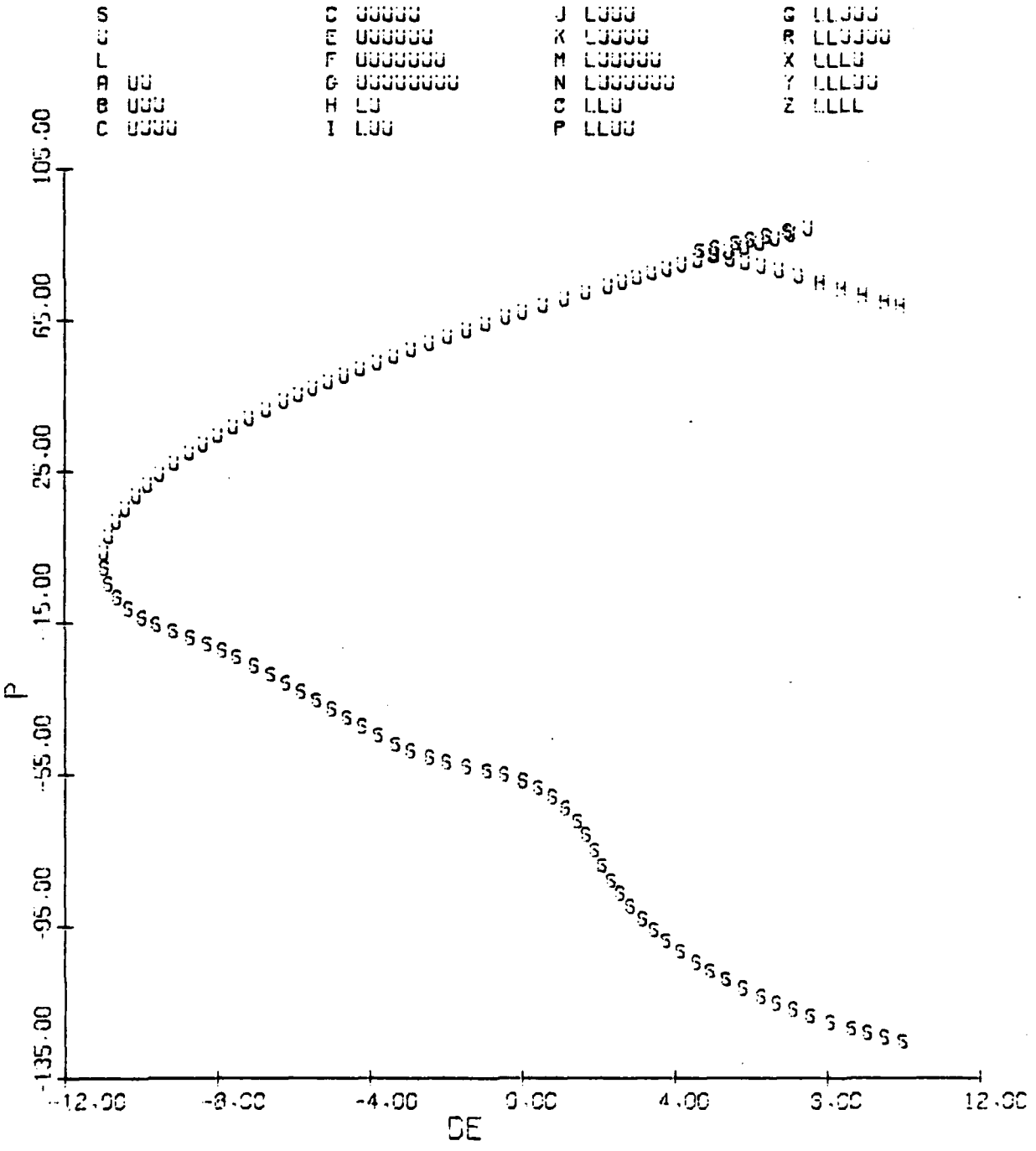

Figure 3.2(c): Roll Rate vs. Elevator Deflection

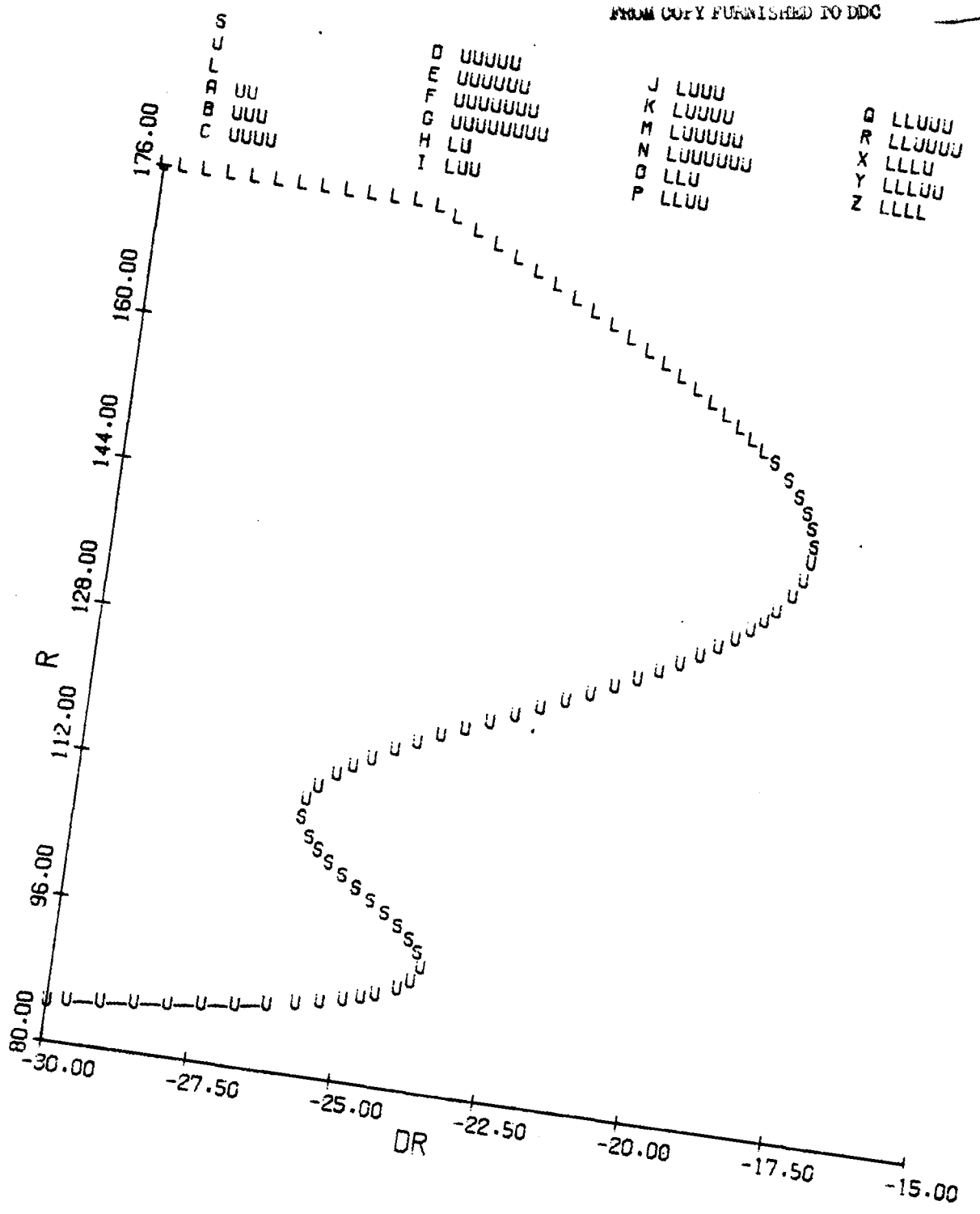

Figure 3.3(a): Aircraft F Equilibrium Surface - Spin Regime: $\delta a = 15°$, $\delta e = -21°$, $V = 443$ fps, $g = 0$
Yaw Rate vs. Rudder Deflection

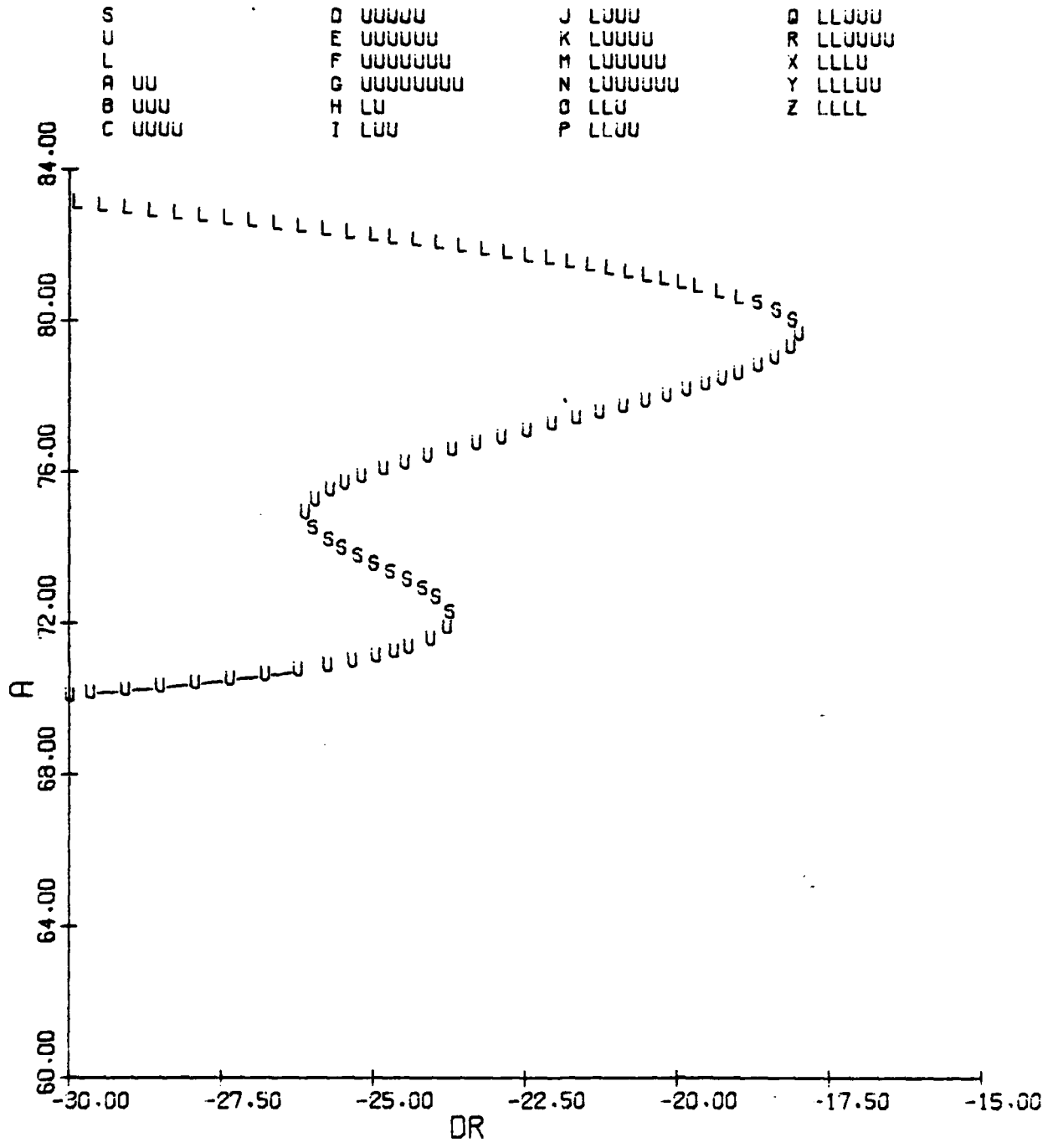

Figure 3.3(b): Angle-of-Attack vs. Rudder Deflection

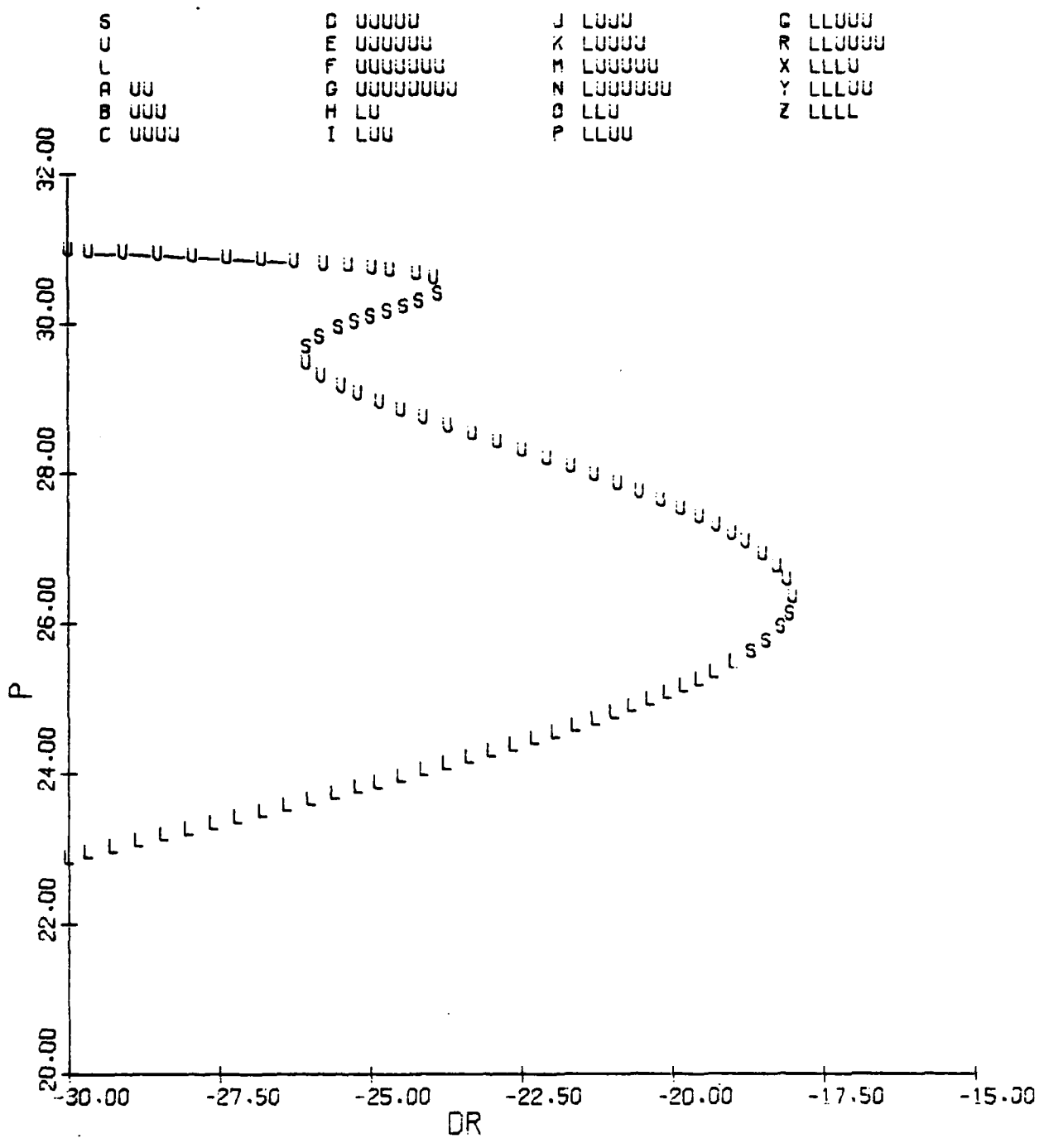

Figure 3.3(c): Roll Rate vs. Rudder Deflection

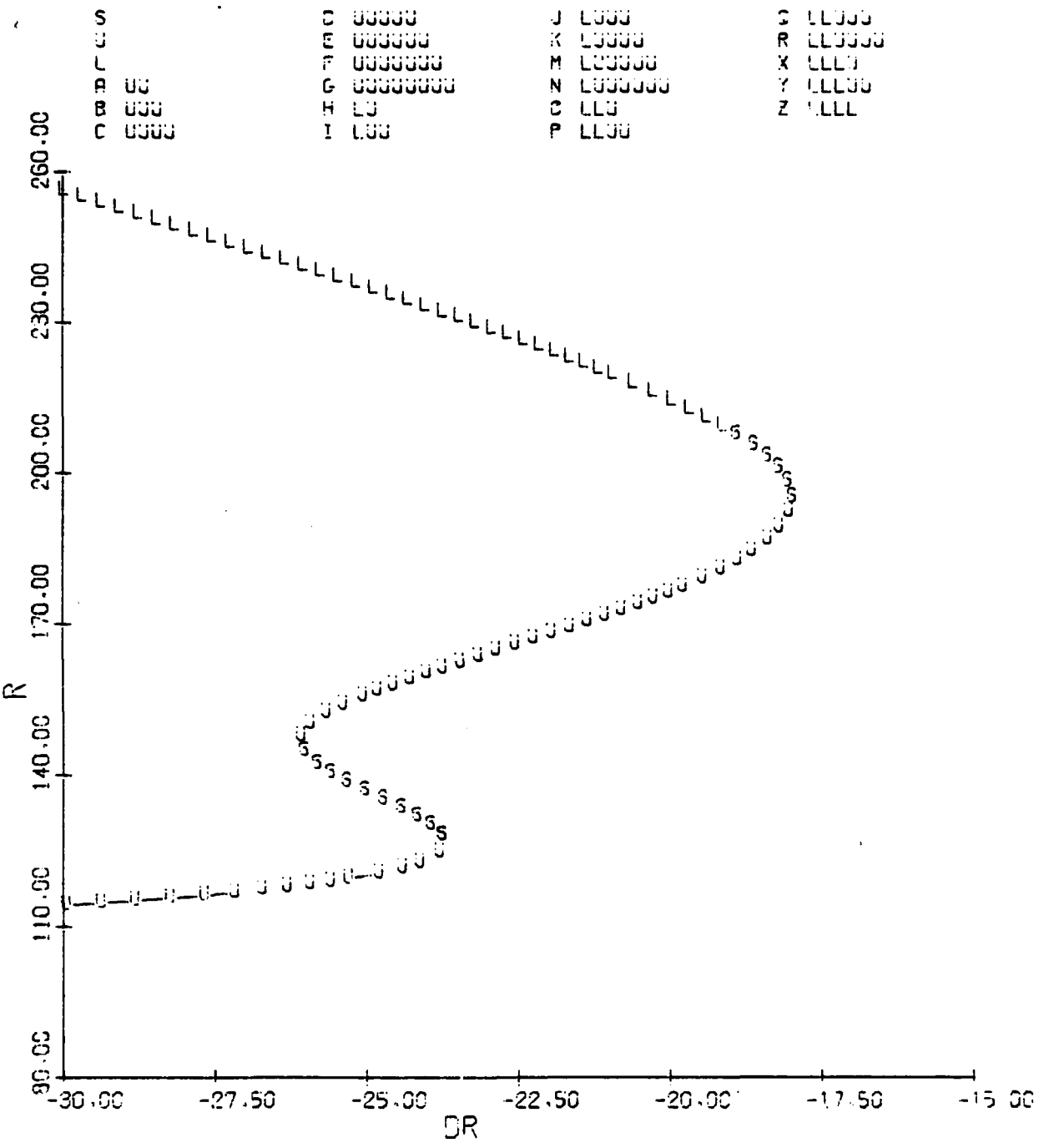

Figure 3.4: Aircraft F Equilibrium Surface - Spin Regime:
$\delta a = 15°$, $\delta e = -21°$, $V = 600$ fps, $g = 0$
(a) Yaw Rate vs. Rudder Deflection

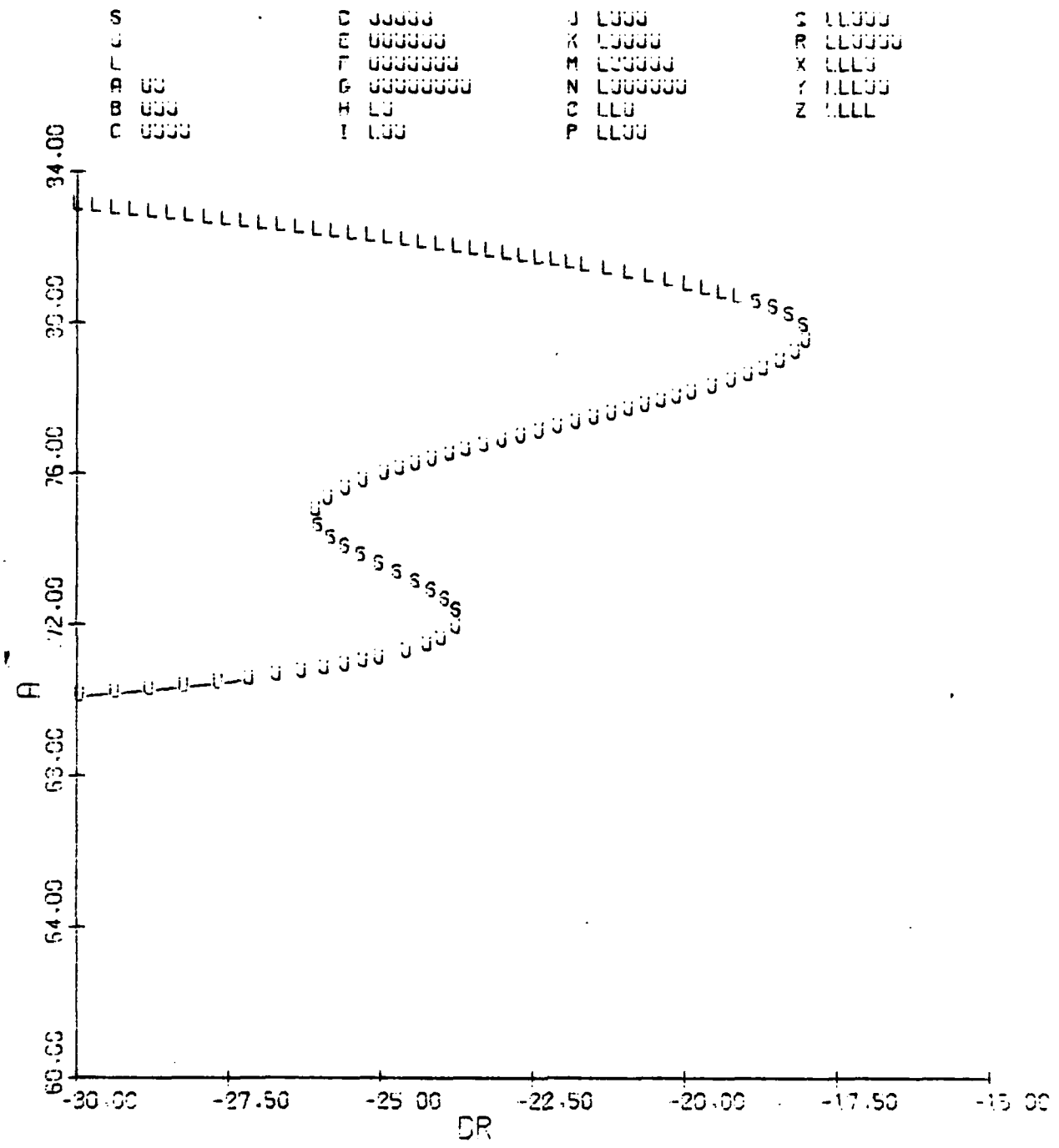

Figure 3.4(b): Angle-of-Attack vs. Rudder Deflection

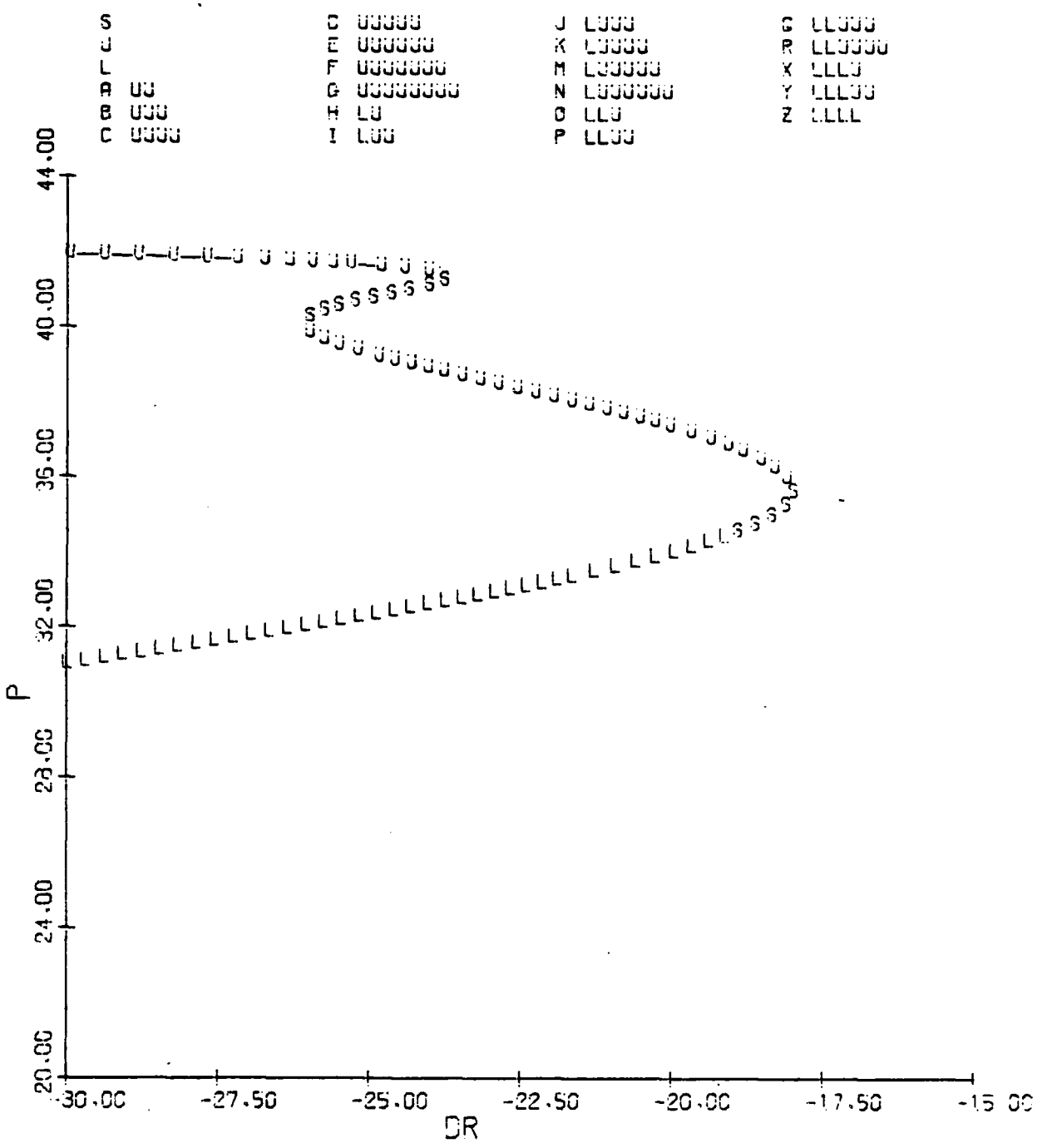

Figure 3.4(c): Roll Rate vs. Rudder Deflection

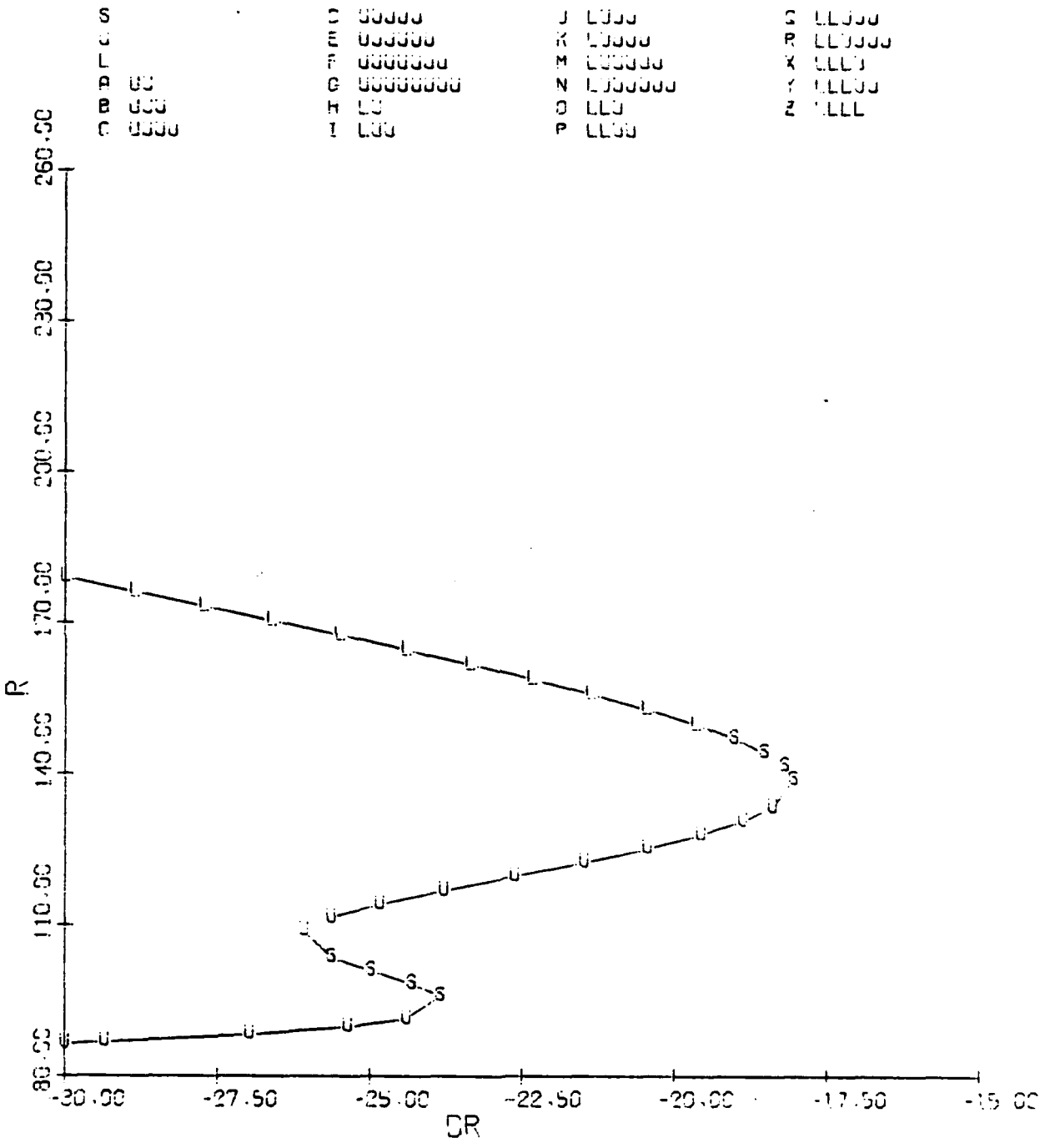

Figure 3.5: Aircraft F Equilibrium Surface - Spin Regime:
$\delta a = 15°$, $\delta e = -21°$, $V = 443$ fps, $g \neq 0$
(a) Yaw Rate vs. Rudder Deflection

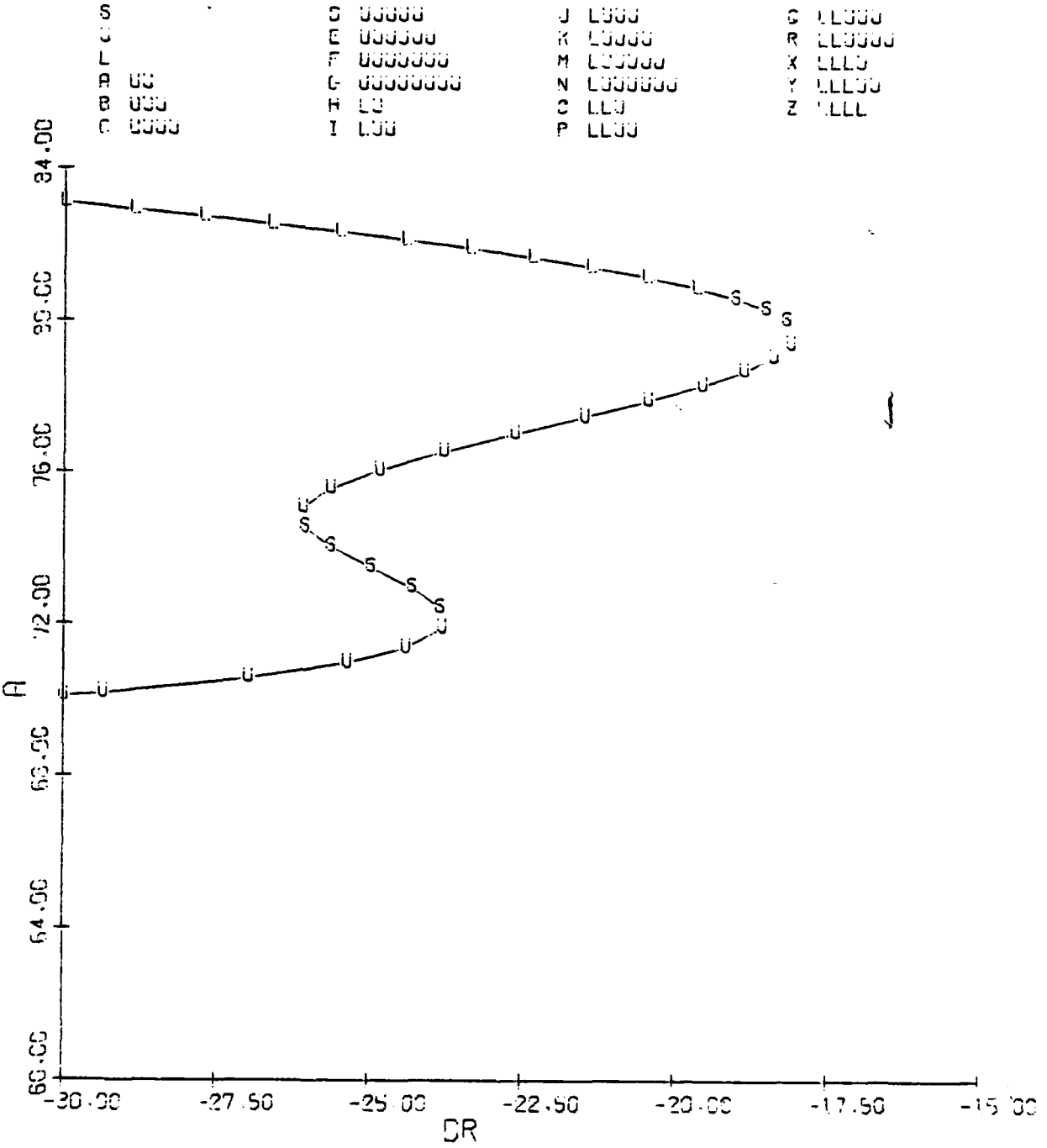

Figure 3.5(b): Angle-of-Attack vs. Rudder Deflection

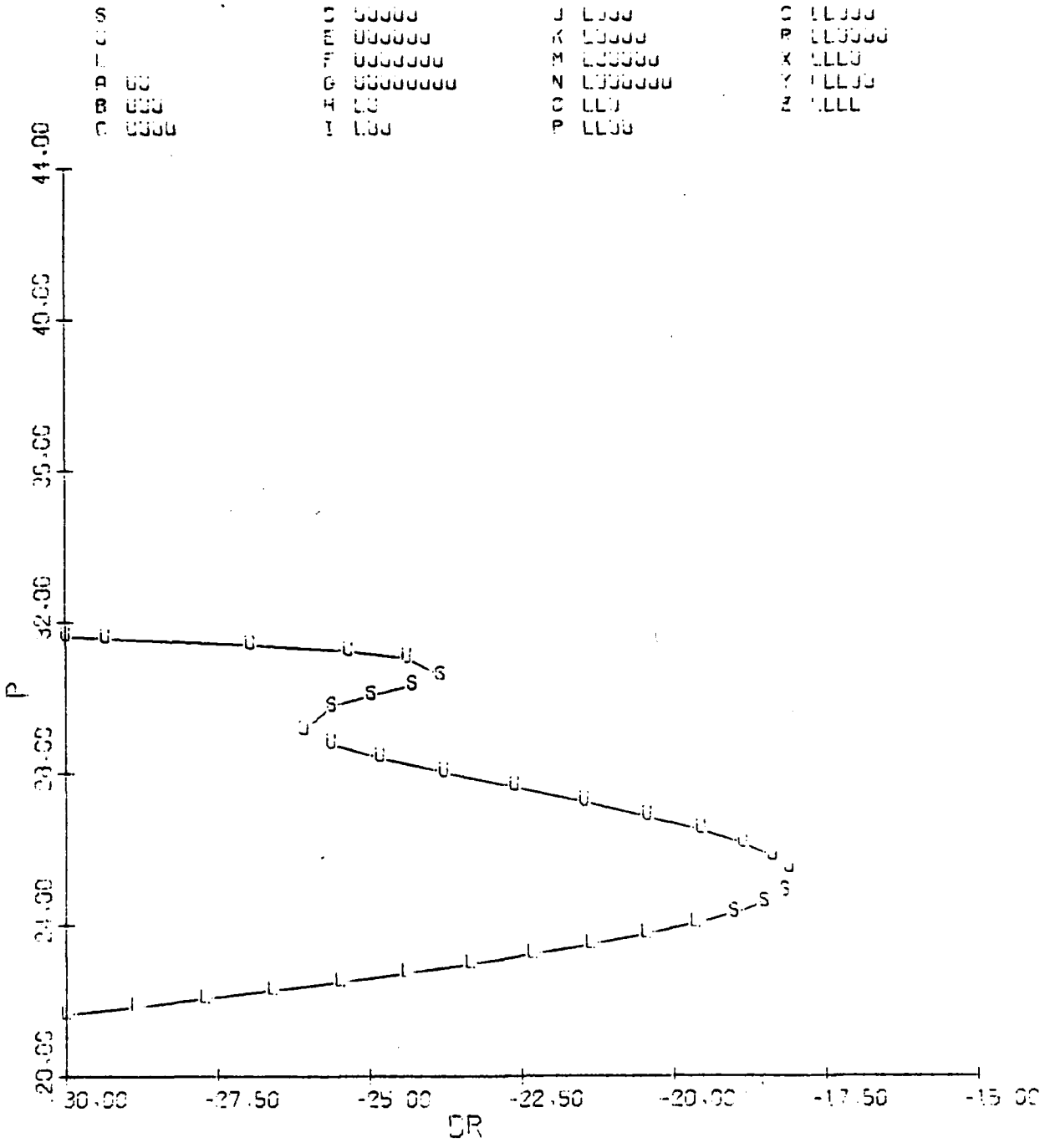

Figure 3.5(c): Roll Rate vs. Rudder Deflection

Figure 3.6: Aircraft F Time History; Developed, Stable Spin, V = 443 fps.
$\underline{\delta}_0 = (15,-21,-25)$; $\underline{x}_0 = (p_0,q_0,r_0,\alpha_0,\beta_0) = (30.,-4.,100.,74.,-3)$

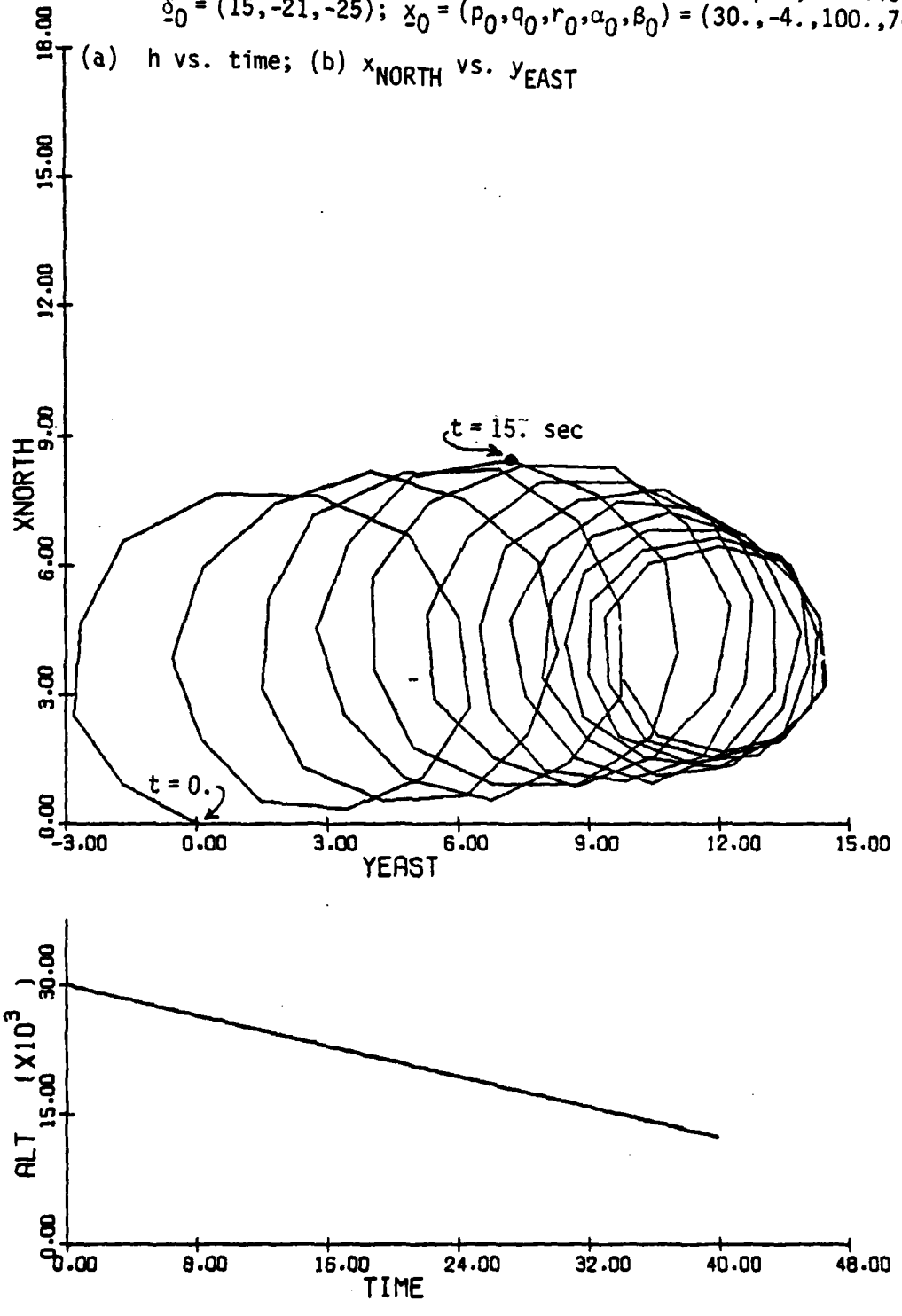

Figure 3.7

Aircraft F Time History; High-α Departure, V = 600 fps

$\underline{\delta}_0 = (0,0,0)$; $\underline{x}_0 = (p_0, q_0, r_0, \alpha_0, \beta_0) = (0,.9,0,3.2,0)$

$\underline{\delta} = (15,-21,-25)$ at t = 2 seconds

(a) TURNS vs. time

(b) x_{NORTH} vs. y_{EAST}

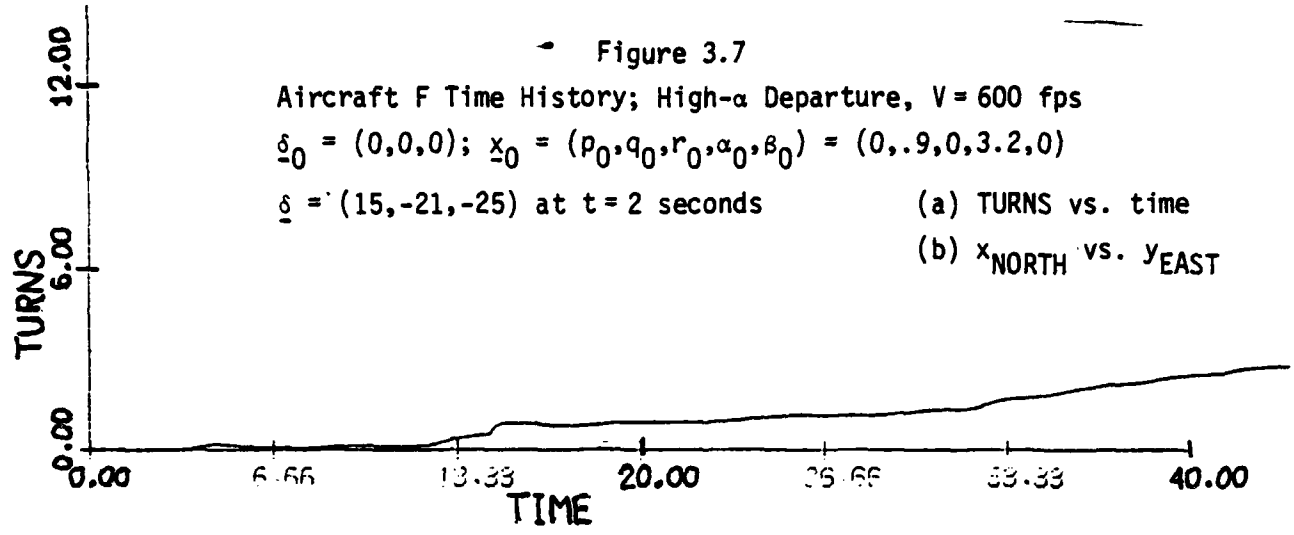

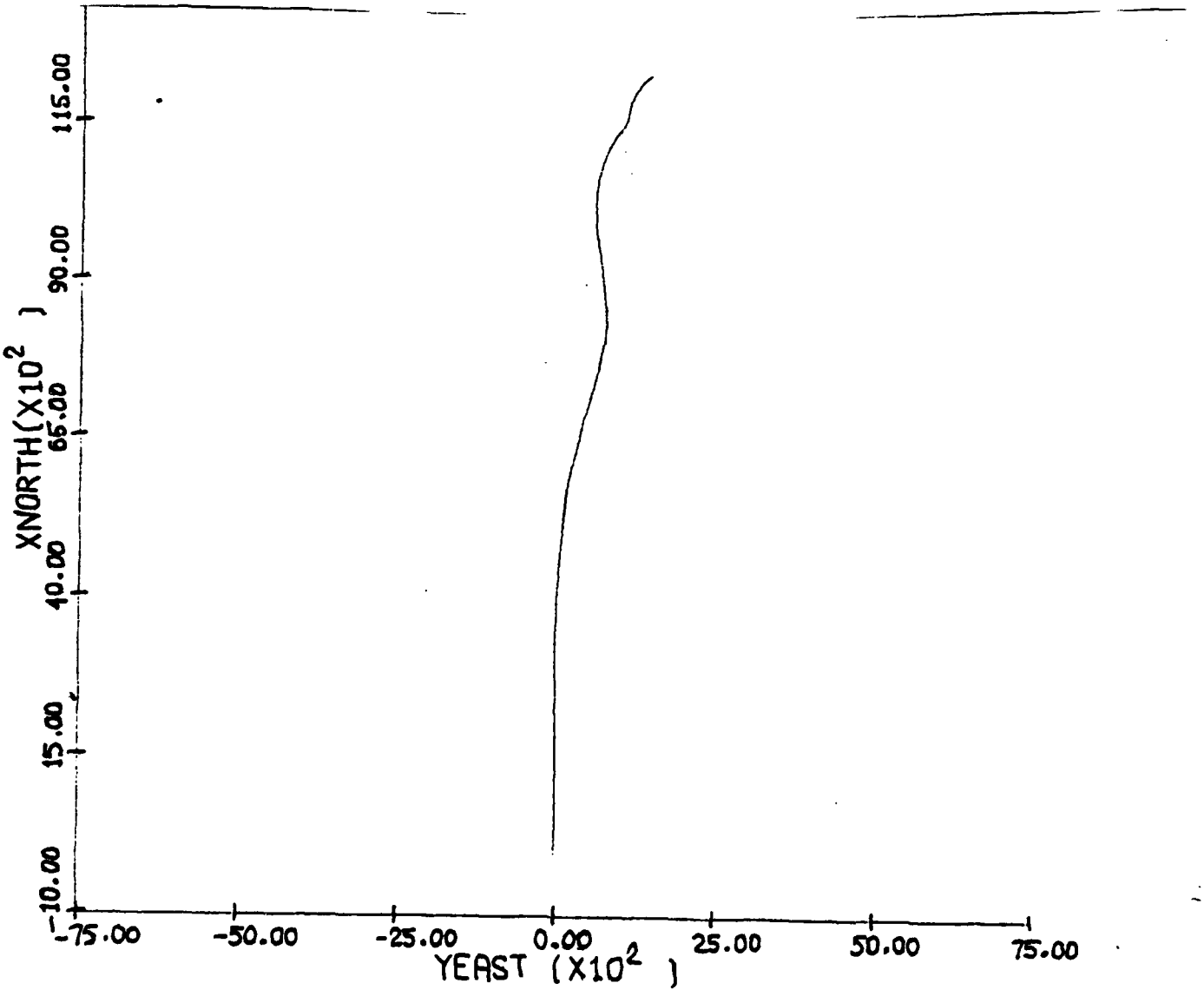

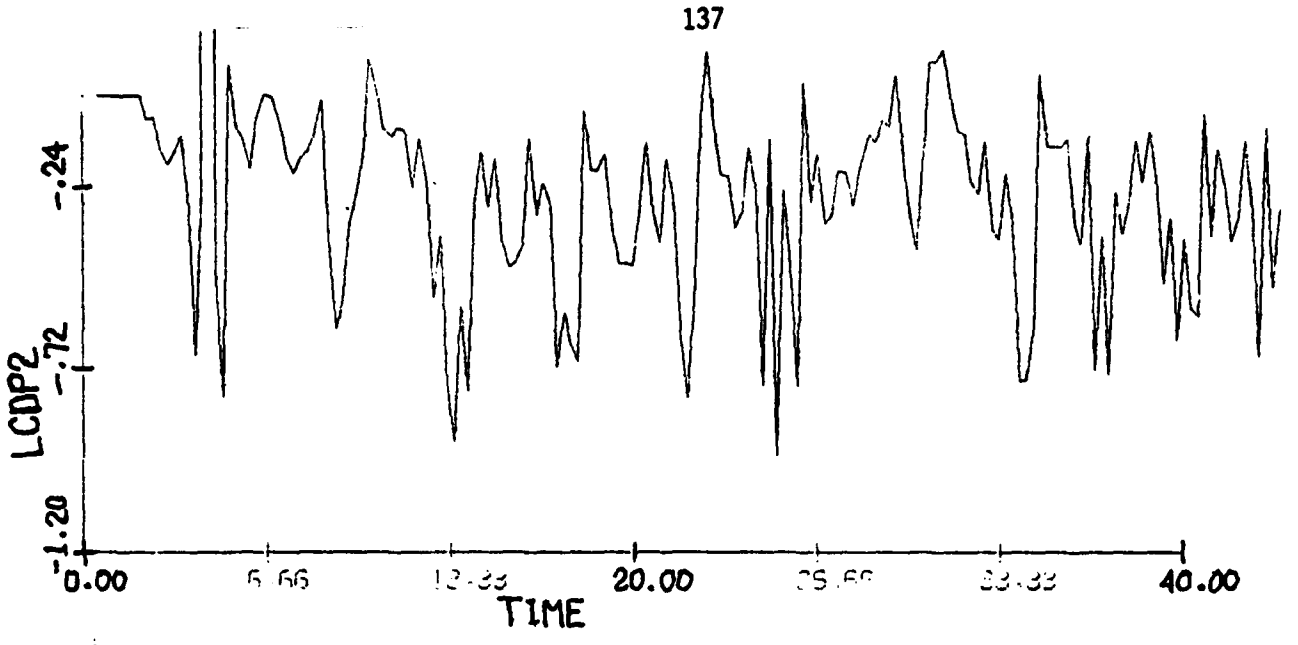

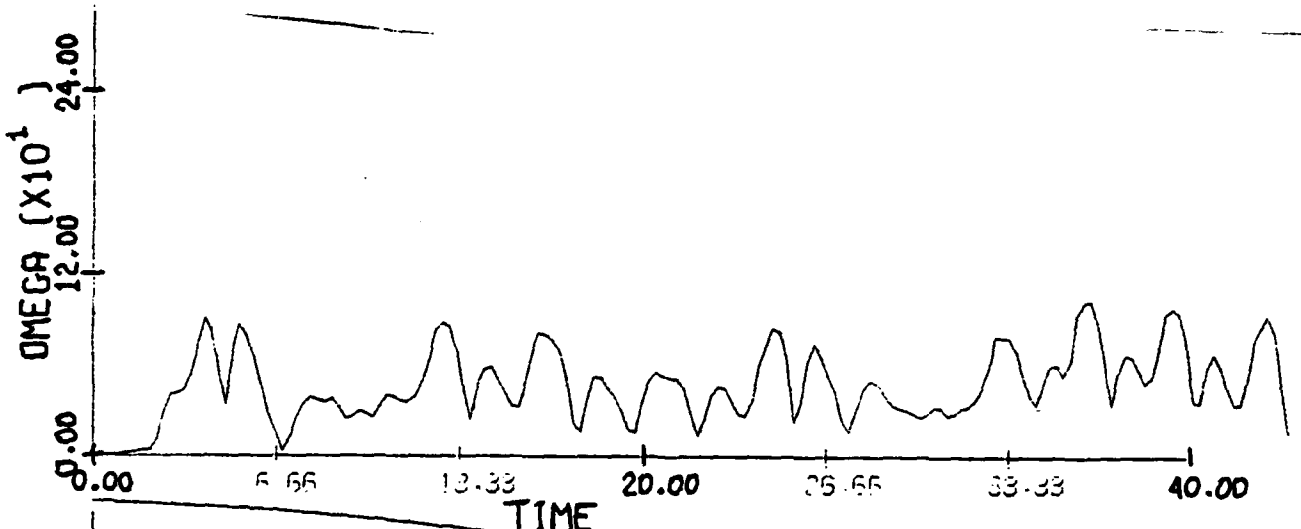

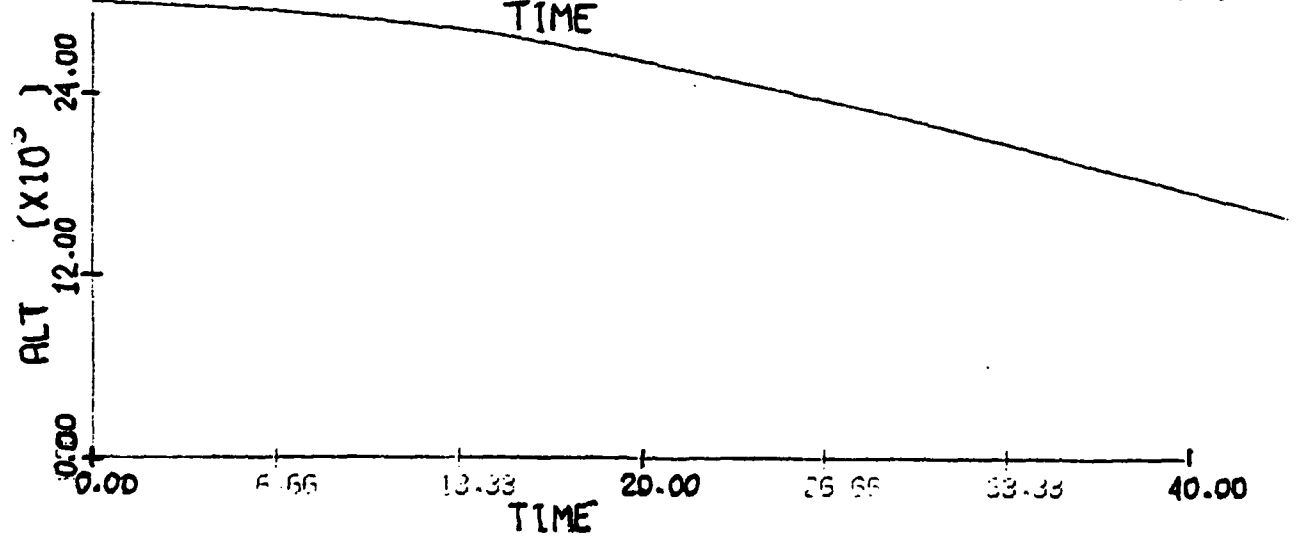

Figure 3.7

(c) CLDP2 vs. time (d) Ω vs. time (e) h vs. time

Figure 3.7

(f) V vs. time (g) ϕ vs. time (h) θ vs. time

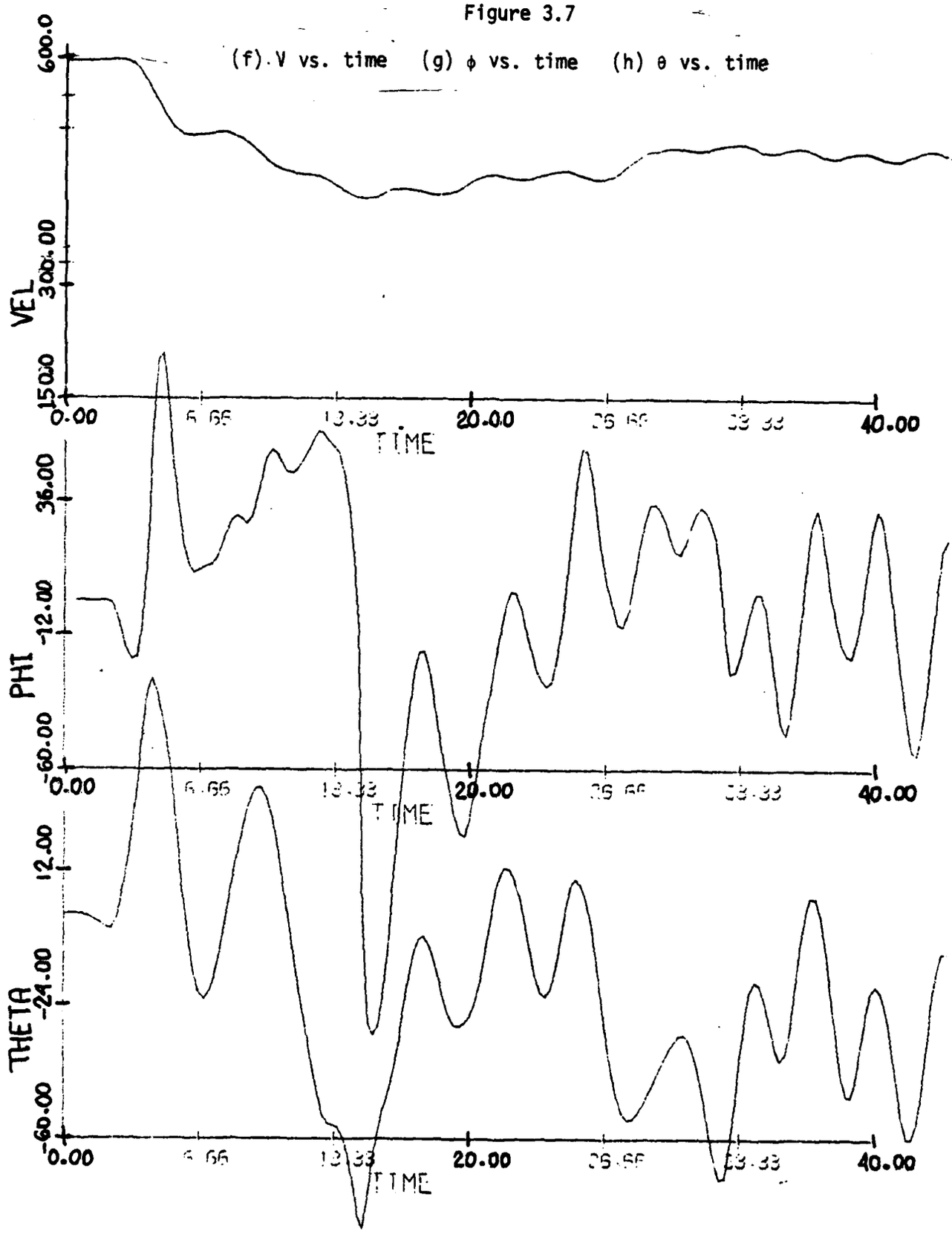

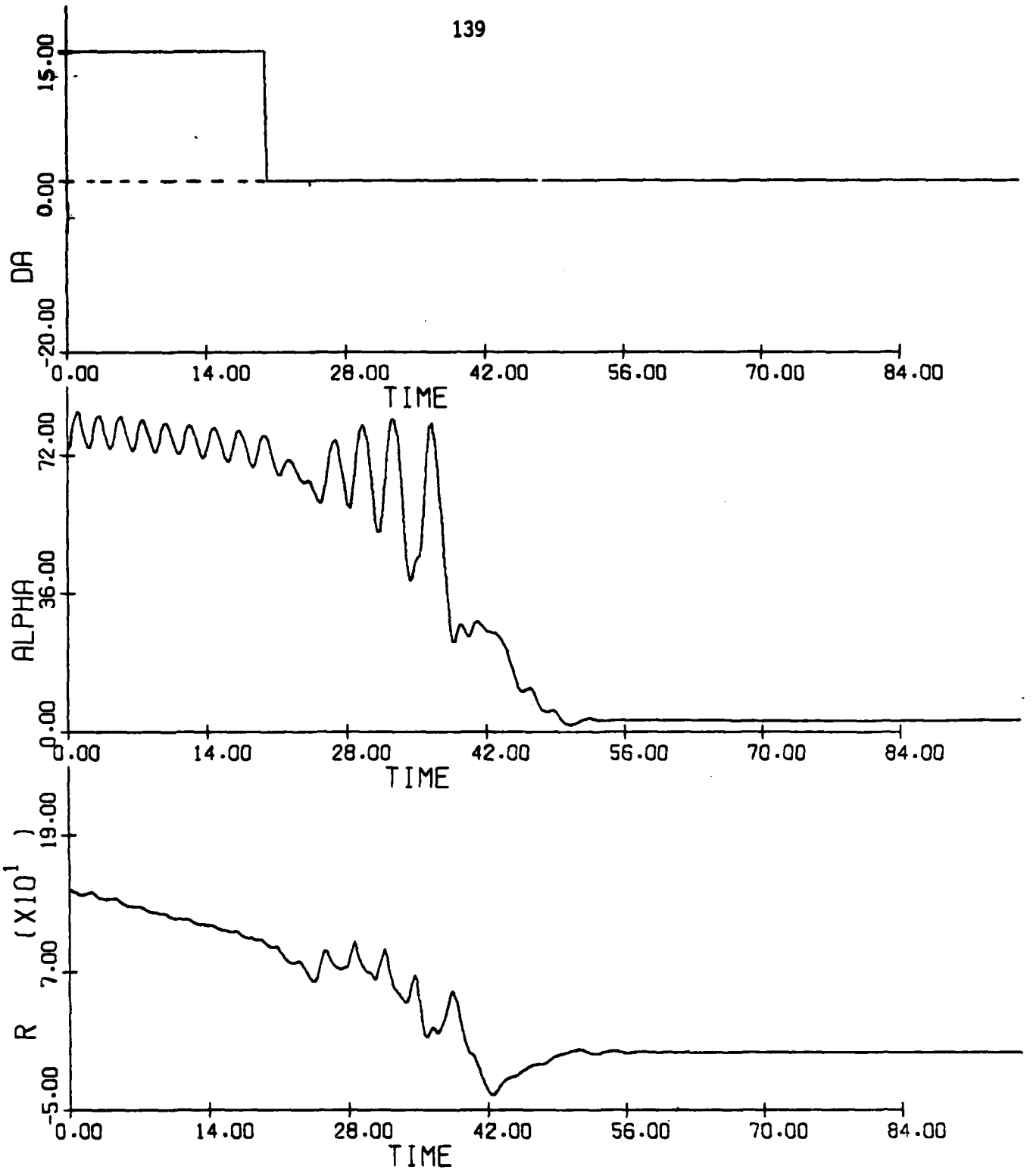

Figure 3.8(a): Aircraft F Spin Recovery; h = 30000 ft, $V(t_0)$ = 450 ft per sec, $\delta e = 0°$, $\delta a = 15°$, $0 \leq t \leq 20.$, $\delta a = 0°$, $t > 20$; $\delta r_0 = -28°$, $\delta r = -18°$, $1. \leq t \leq 30$, $\delta r = 28°$, $30 \leq t \leq 40$, $\delta r = 0$, $t > 40$.
r,α,δa vs. t

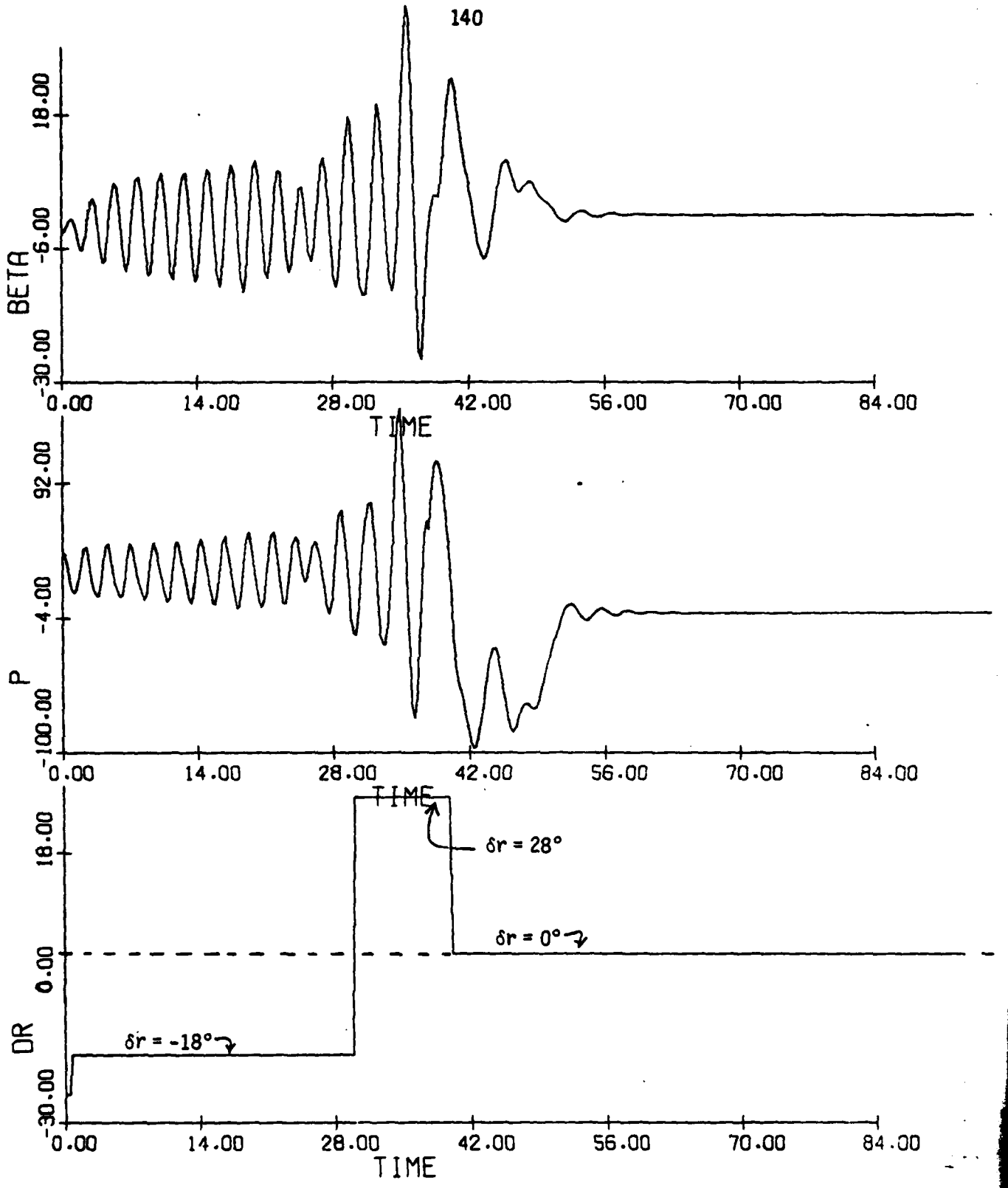

Figure 3.8(b) (cont.): δr,p,β vs. t

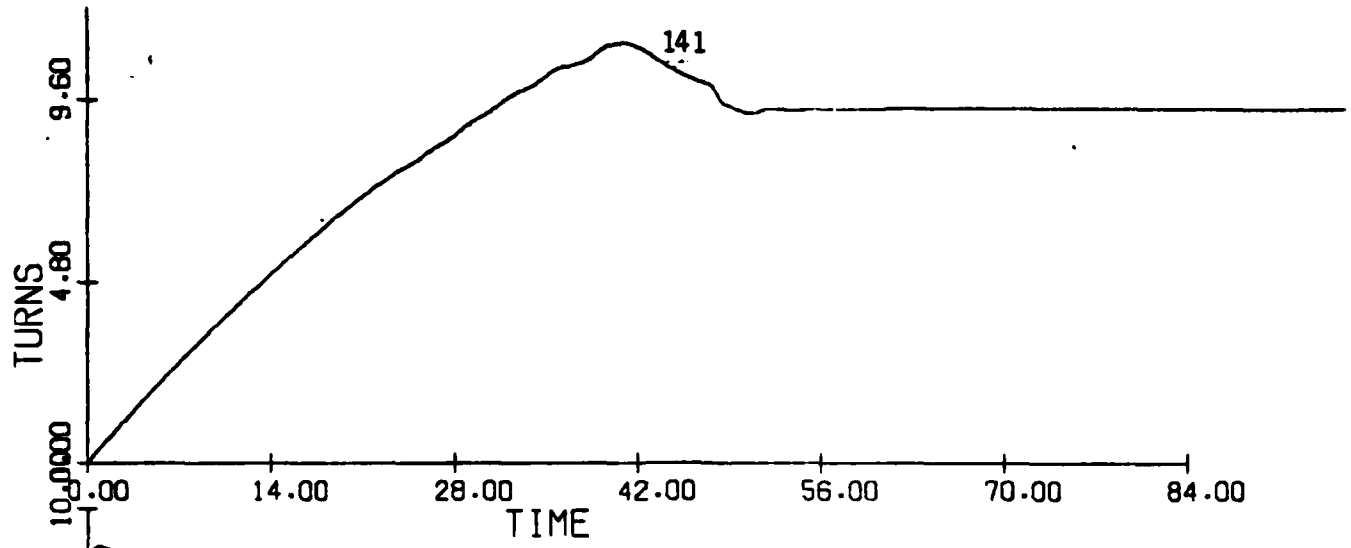

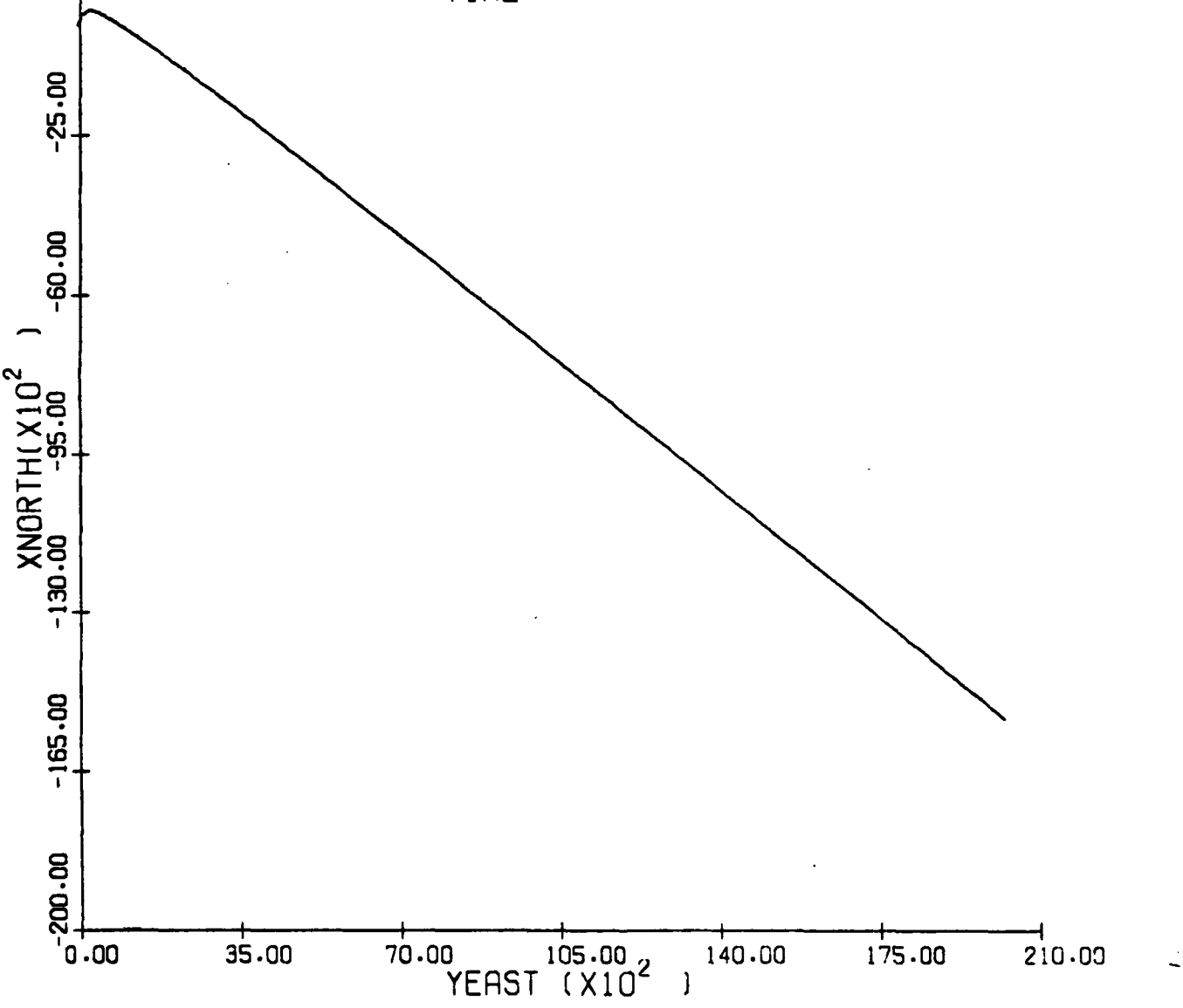

Figure 3.8(c) (cont.): x_{NORTH} vs. y_{EAST}; TURNS vs. t

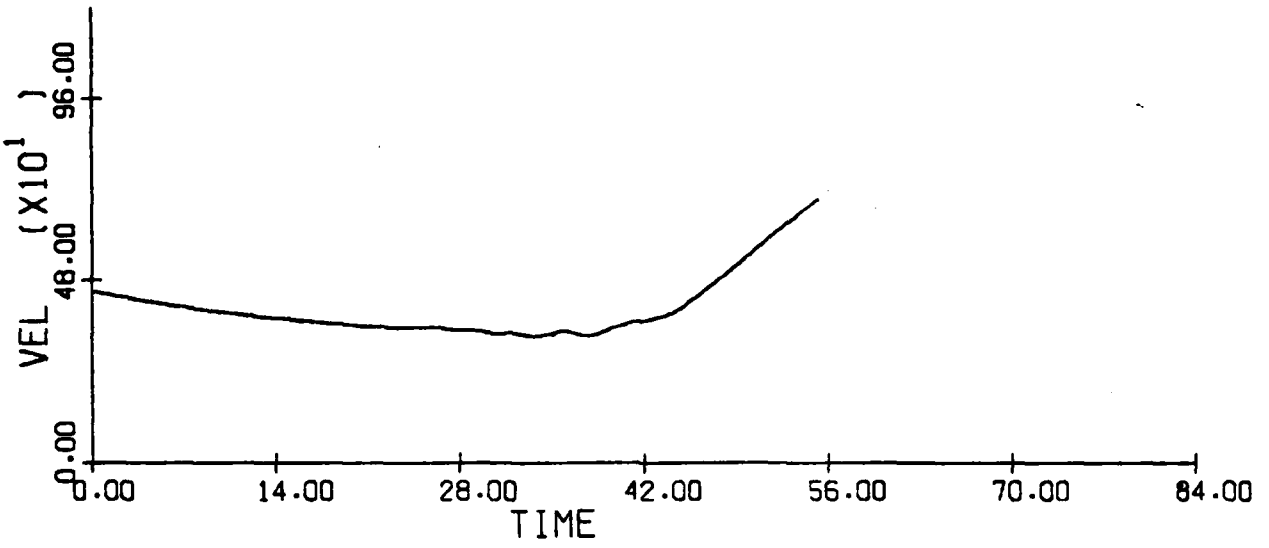

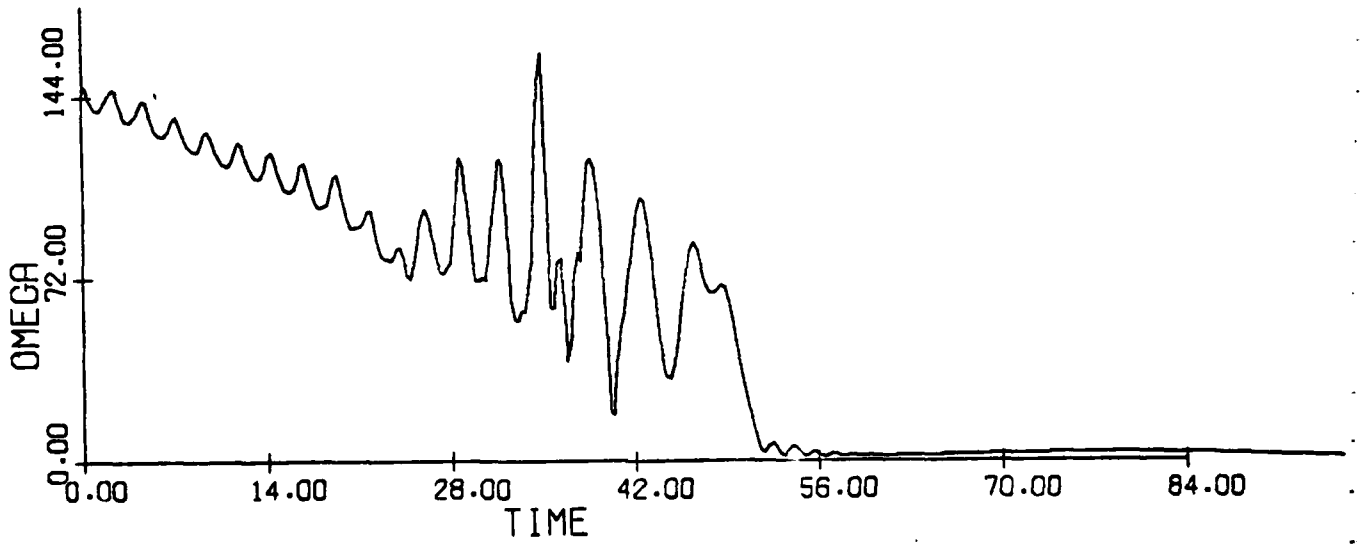

Figure 3.8(d) (concluded): Ω,V vs. t

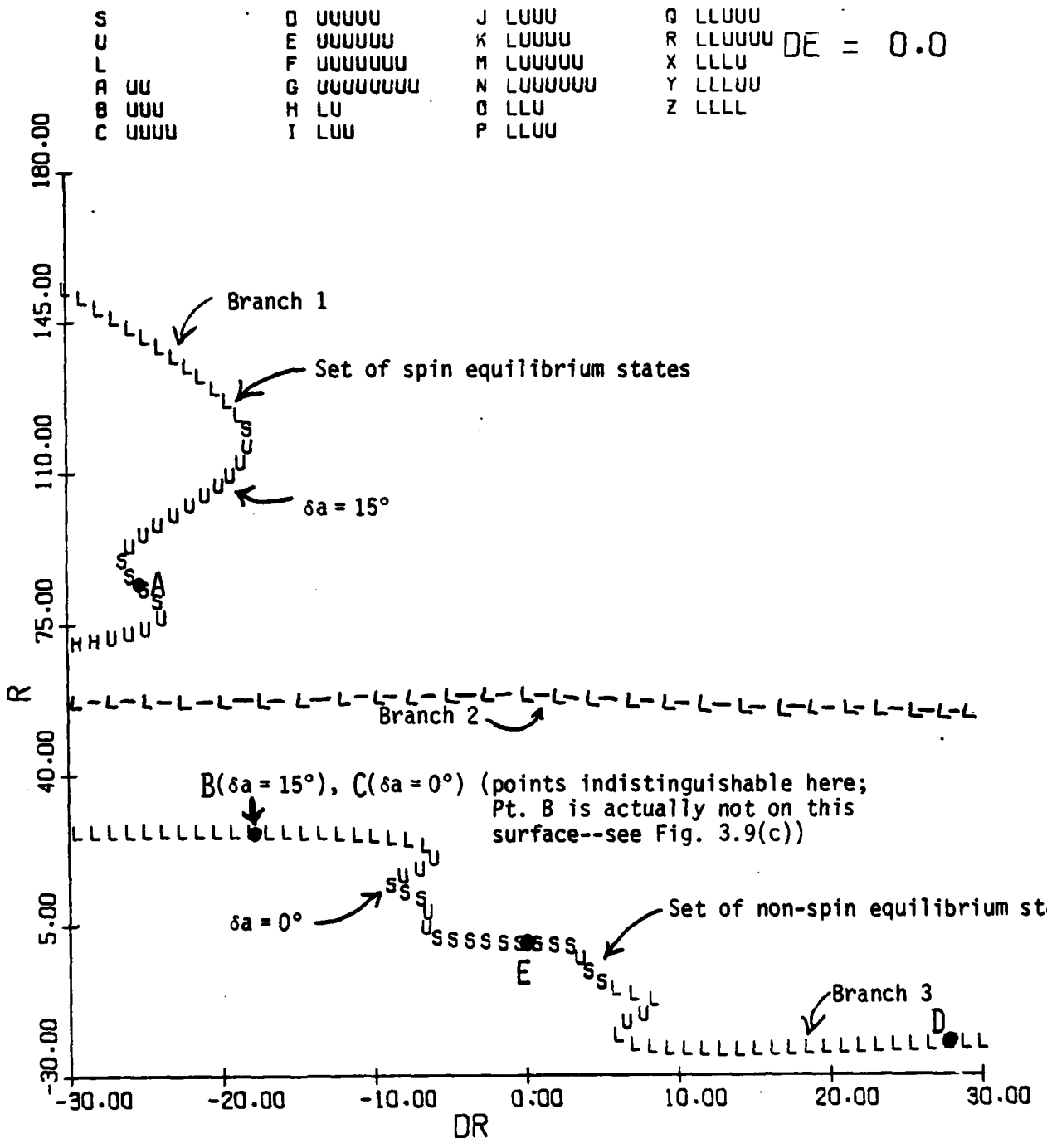

Figure 3.9(a): Aircraft F Equilibrium Surface for Spin Recovery
r vs. δr; δe = 0°, V = 350 fps, h = 30000 ft; δa = 0°,15°

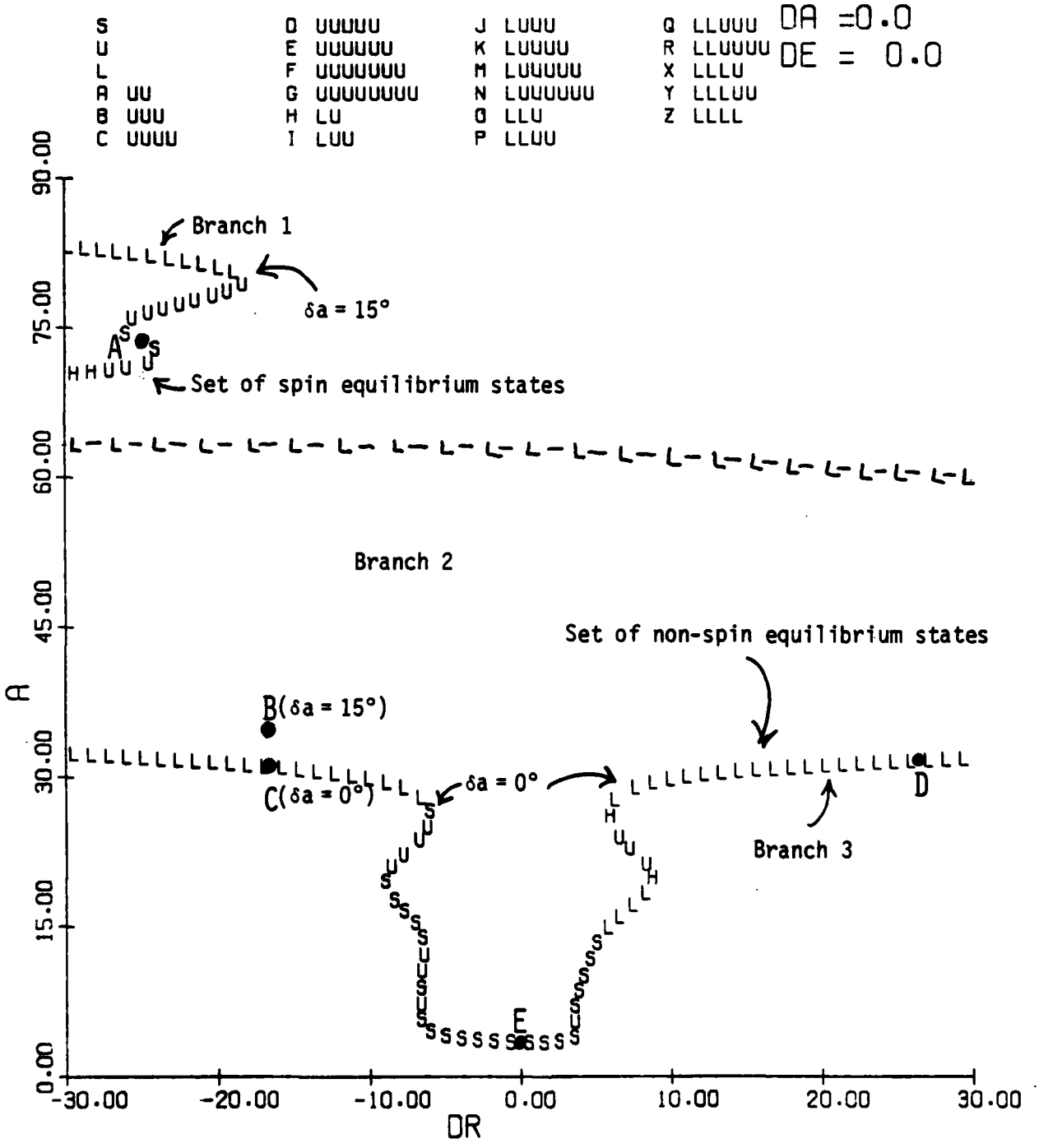

Figure 3.9(b) (cont.) α vs. δr; δe = 0°; V = 350 fps; δa = 0°,15°

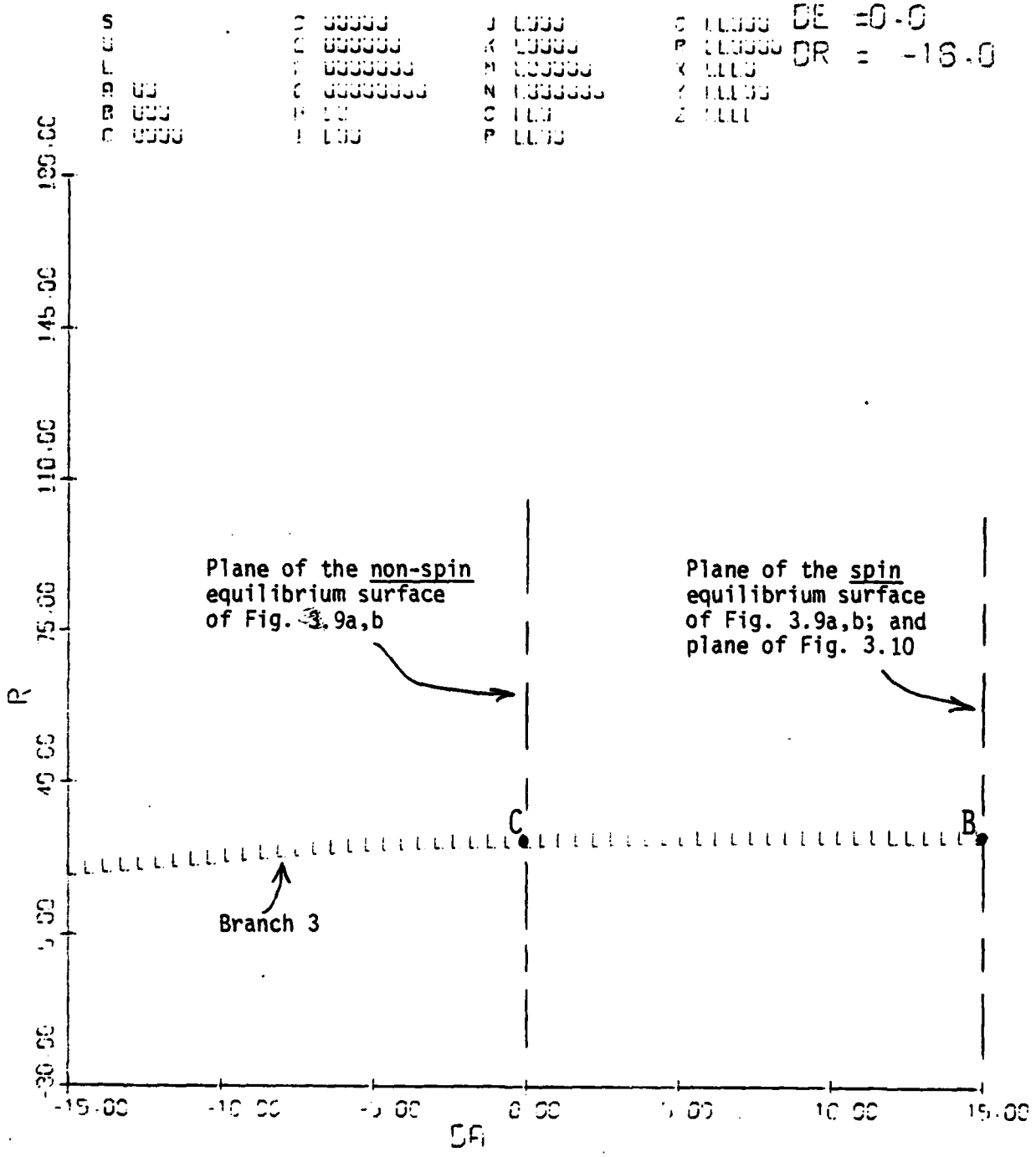

Figure 3.9(c) (concluded) r vs. δa; δe = 0°, δr = -18°, V = 350 fps

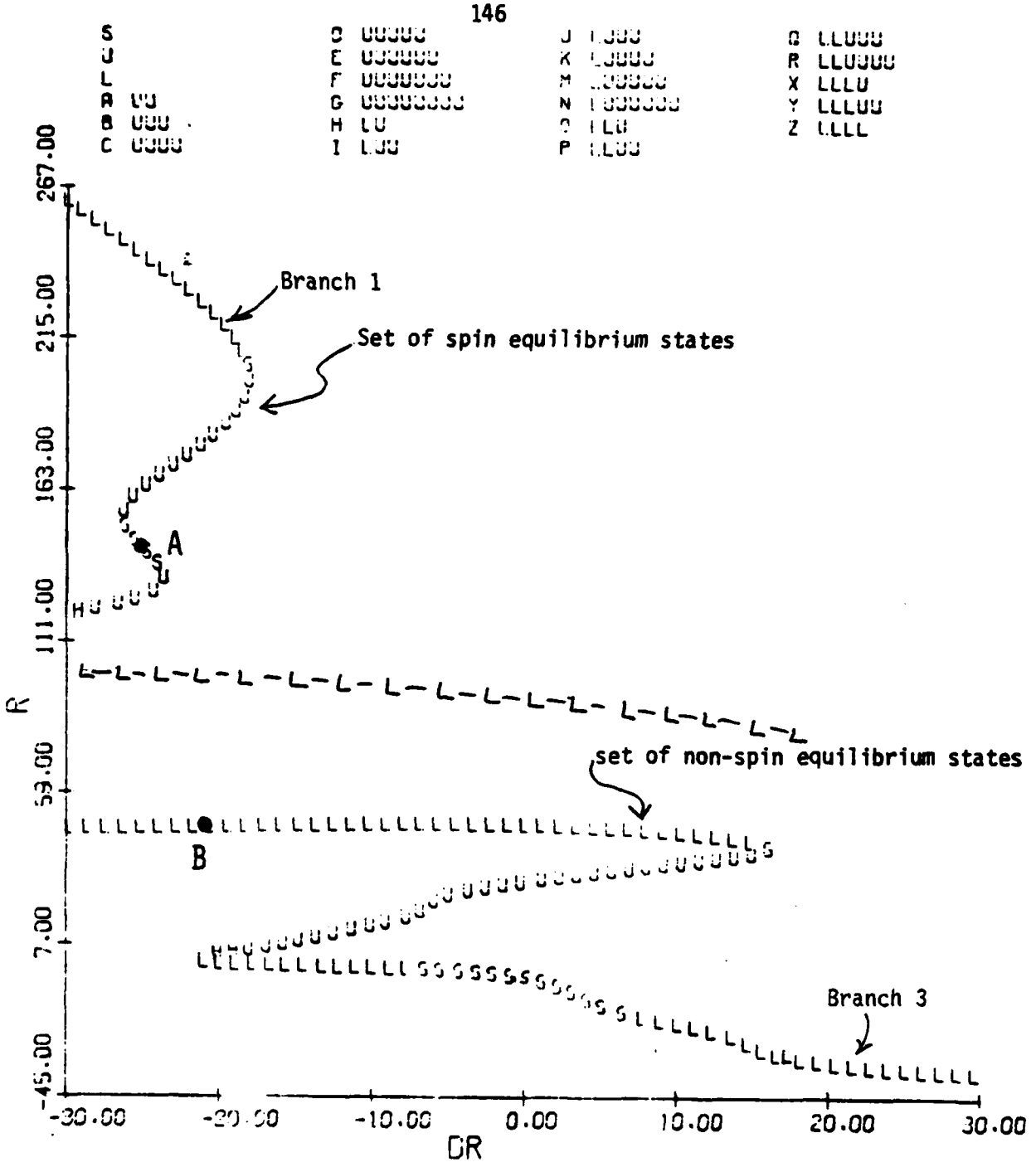

Figure 3.10: Aircraft F Equilibrium Surface: r vs. δr
$\delta a = 15°$, $\delta e = 0°$, V = 600 fps, g = 0, h = 30000 ft

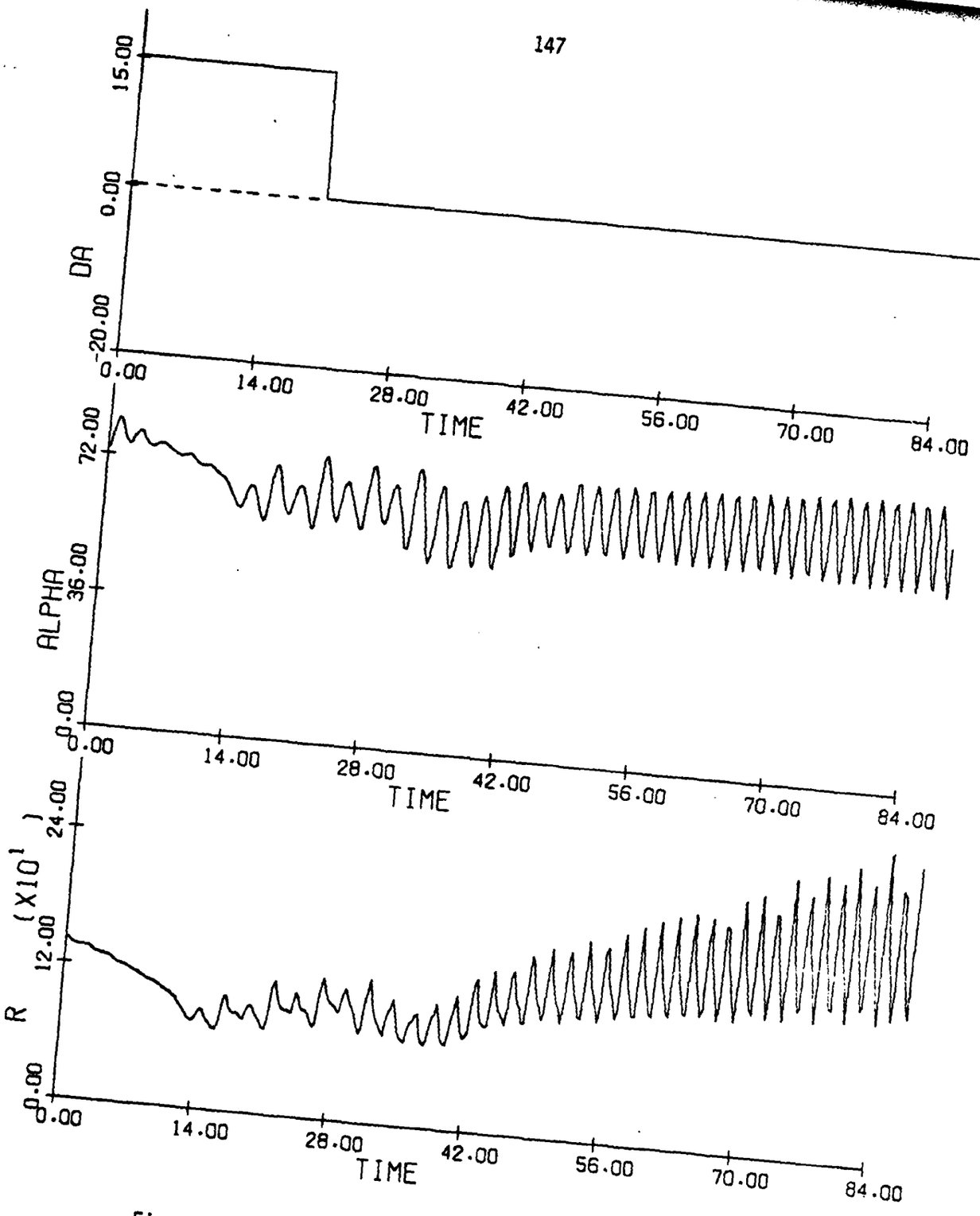

Figure 3.11(a): Aircraft F Spin Recovery; $h = 30000$ ft, V fixed at 450 feet per sec; control sequence as in Fig. 3.8 (p. 139).

$r, \alpha, \delta a$ vs. t

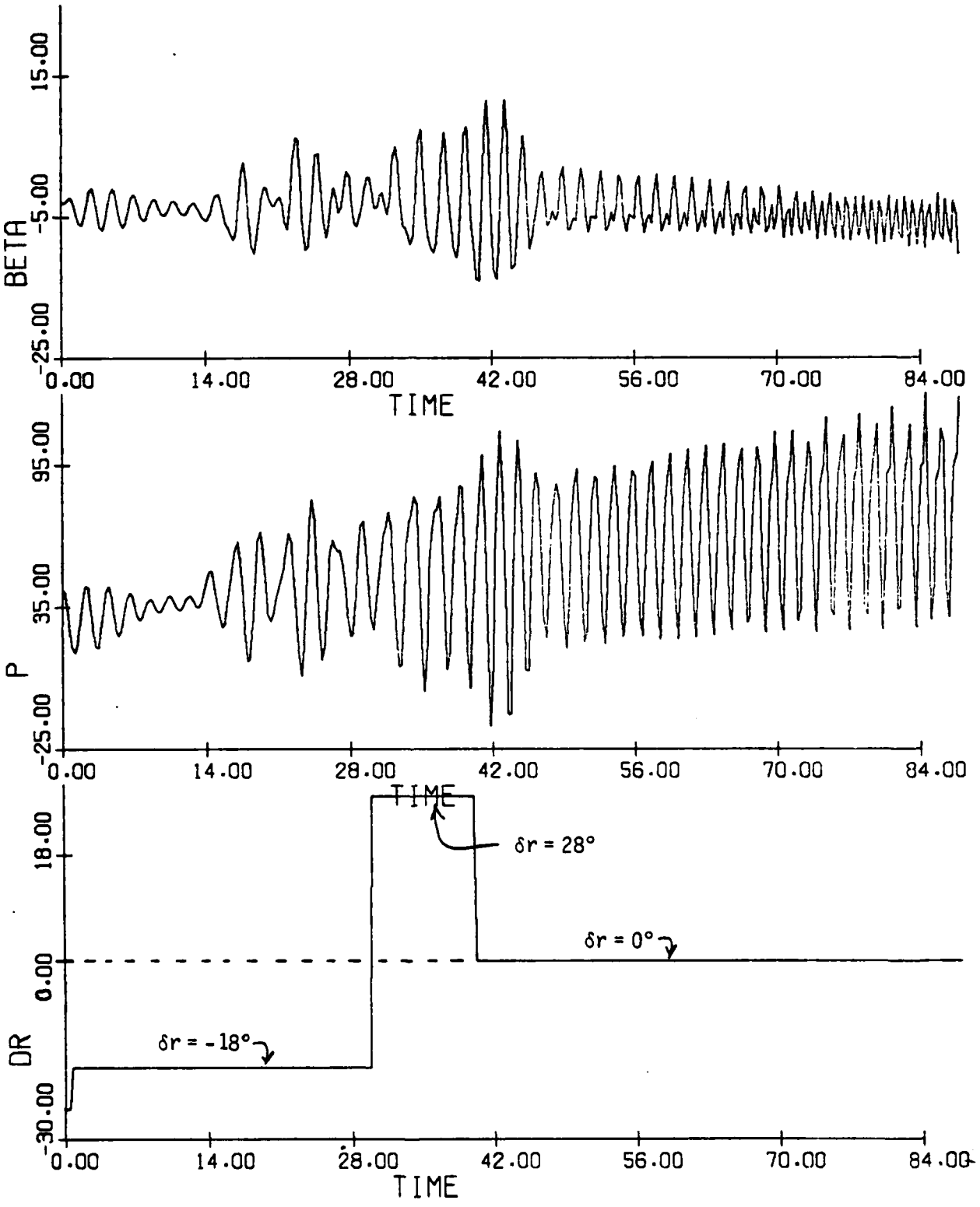

Figure 3.11(b) (cont.): $\delta r, p, \beta$ vs. t

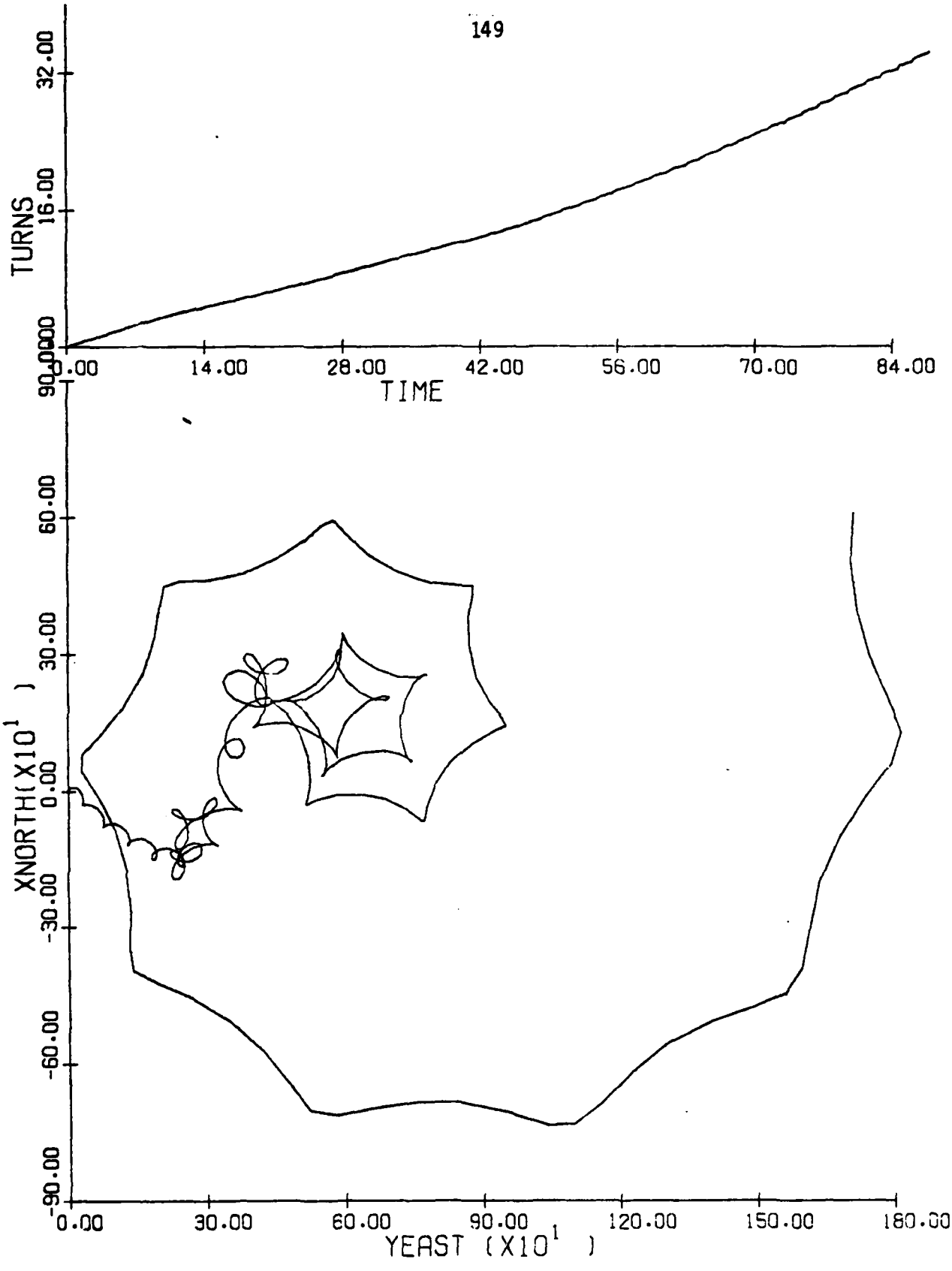

Figure 3.11(c) (cont.): x_{NORTH} vs. y_{EAST}; TURNS vs. t

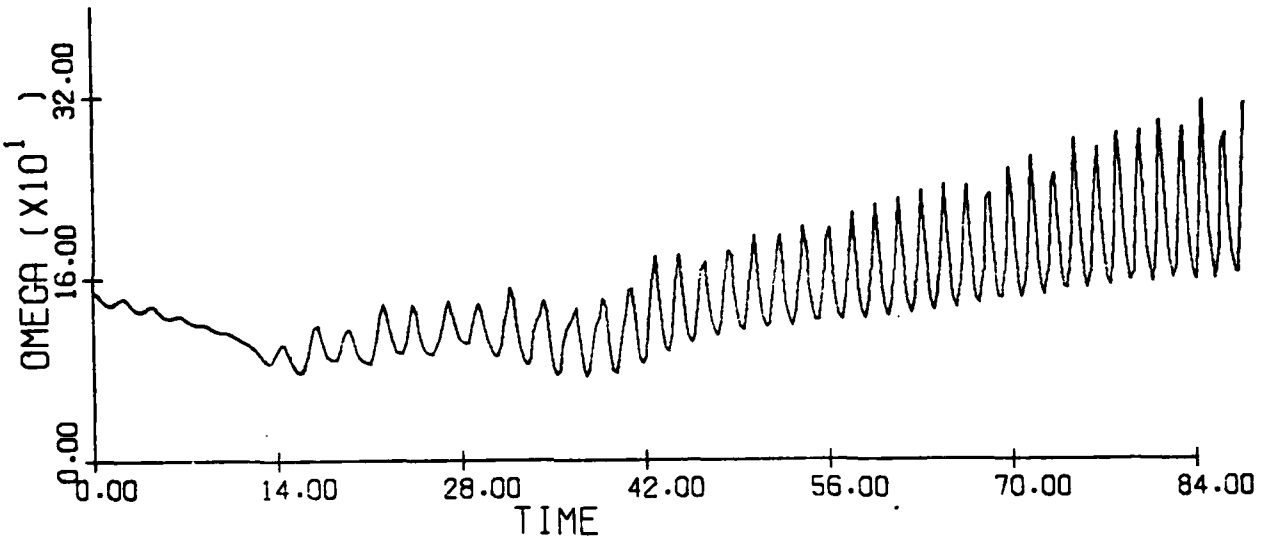

Figure 3.11 (d) (concluded): Ω vs. t

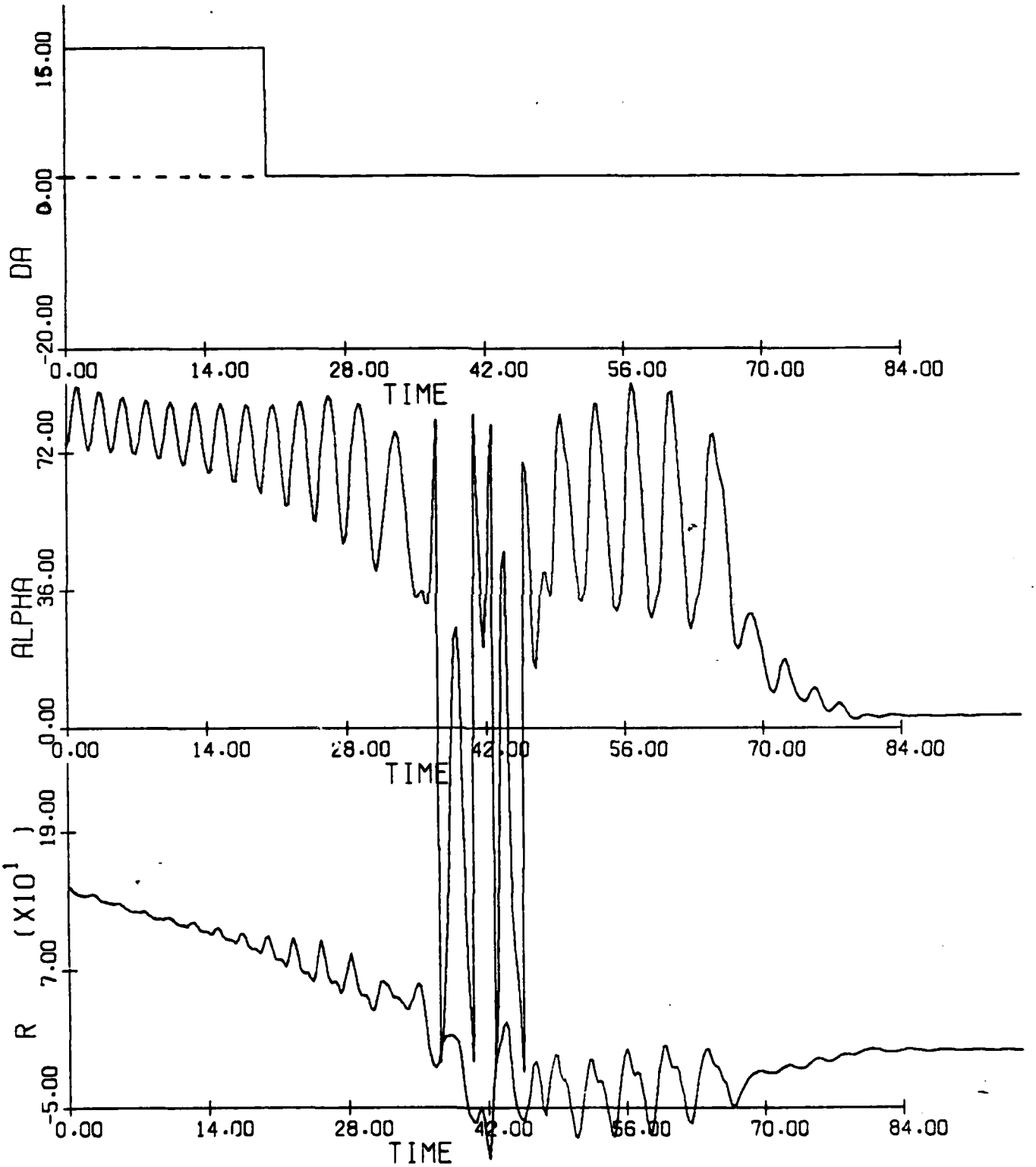

Figure 3.12(a): Aircraft F Spin Recovery; h = 30k ft; V free; all other conditions same as Fig. 3.8 (p. 139).

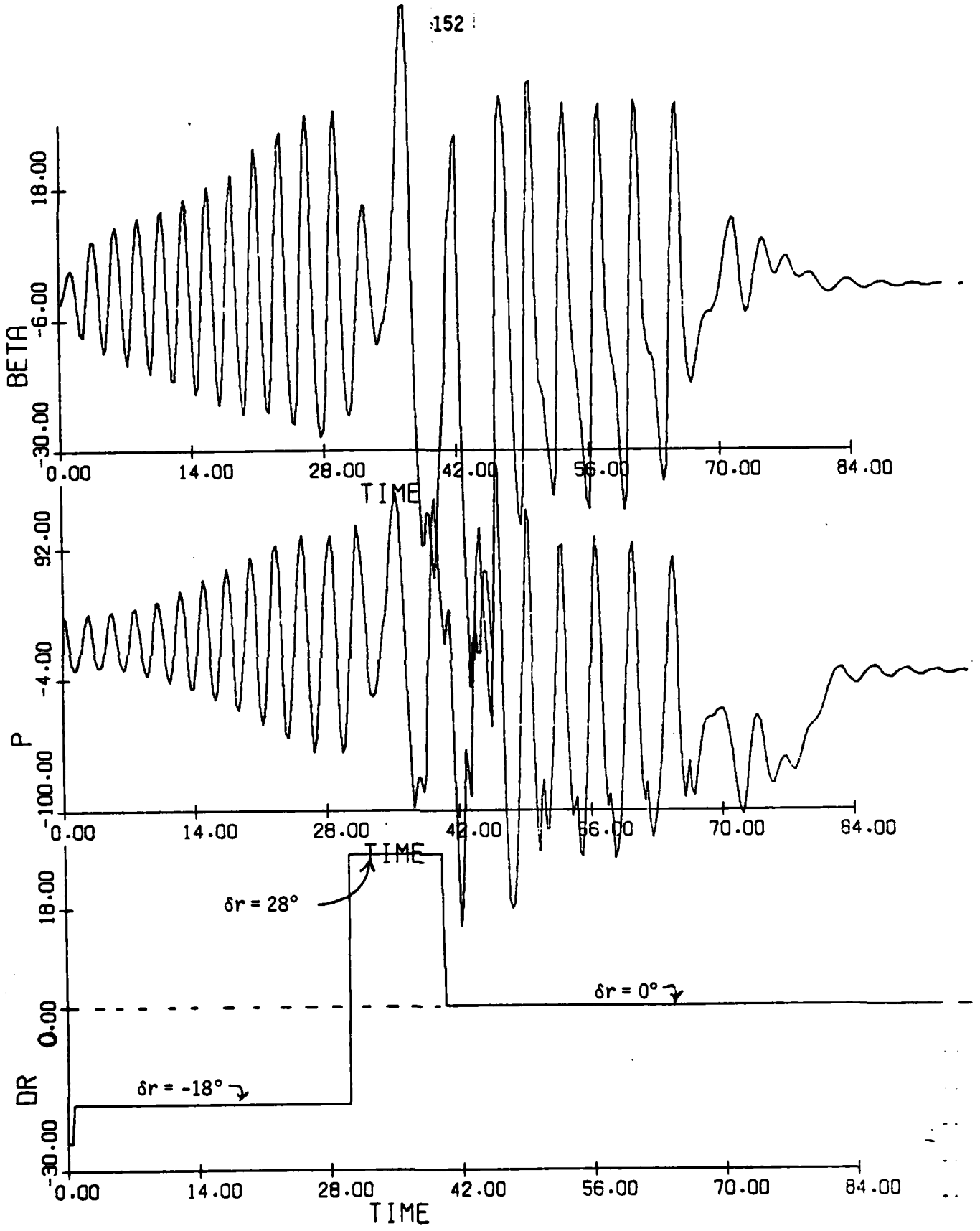

Figure 3.12(b) (cont.)

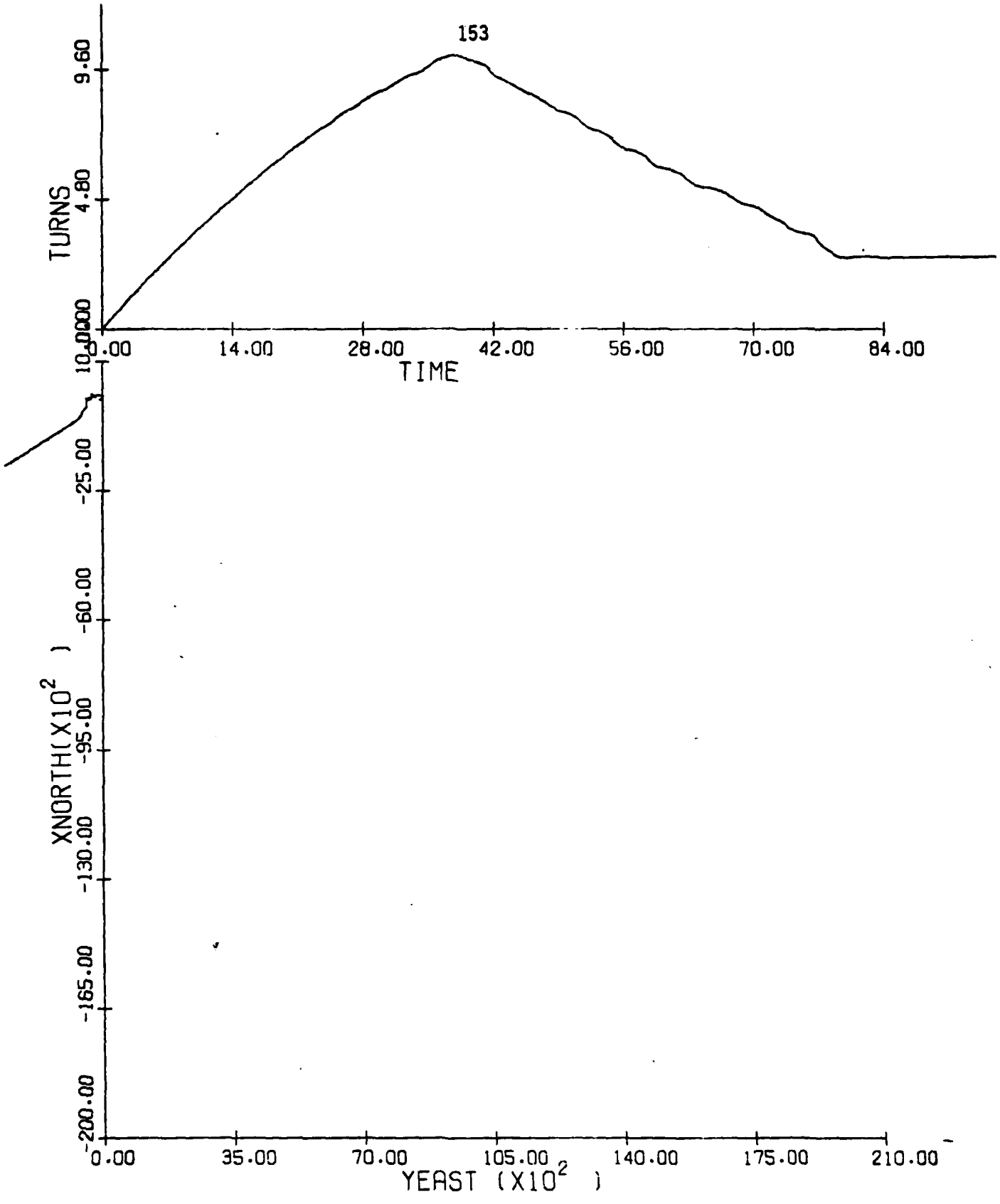

Figure 3.12(c) (cont.)

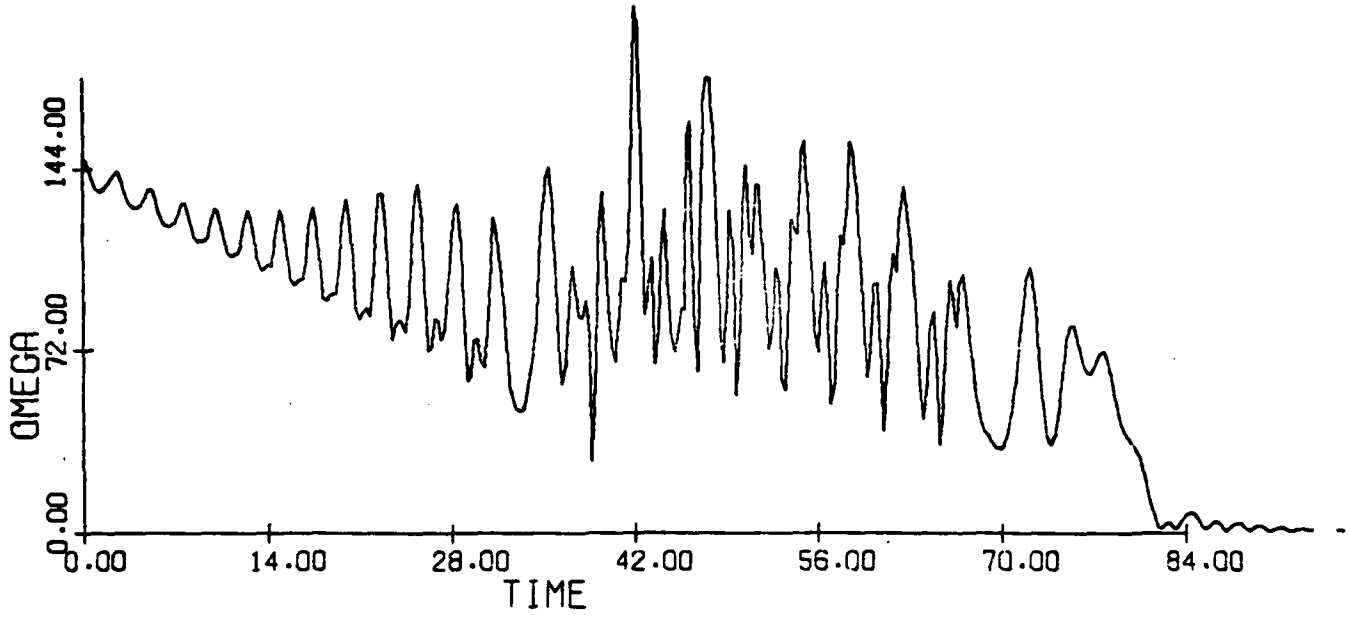

Figure 3.12(d) (concluded)

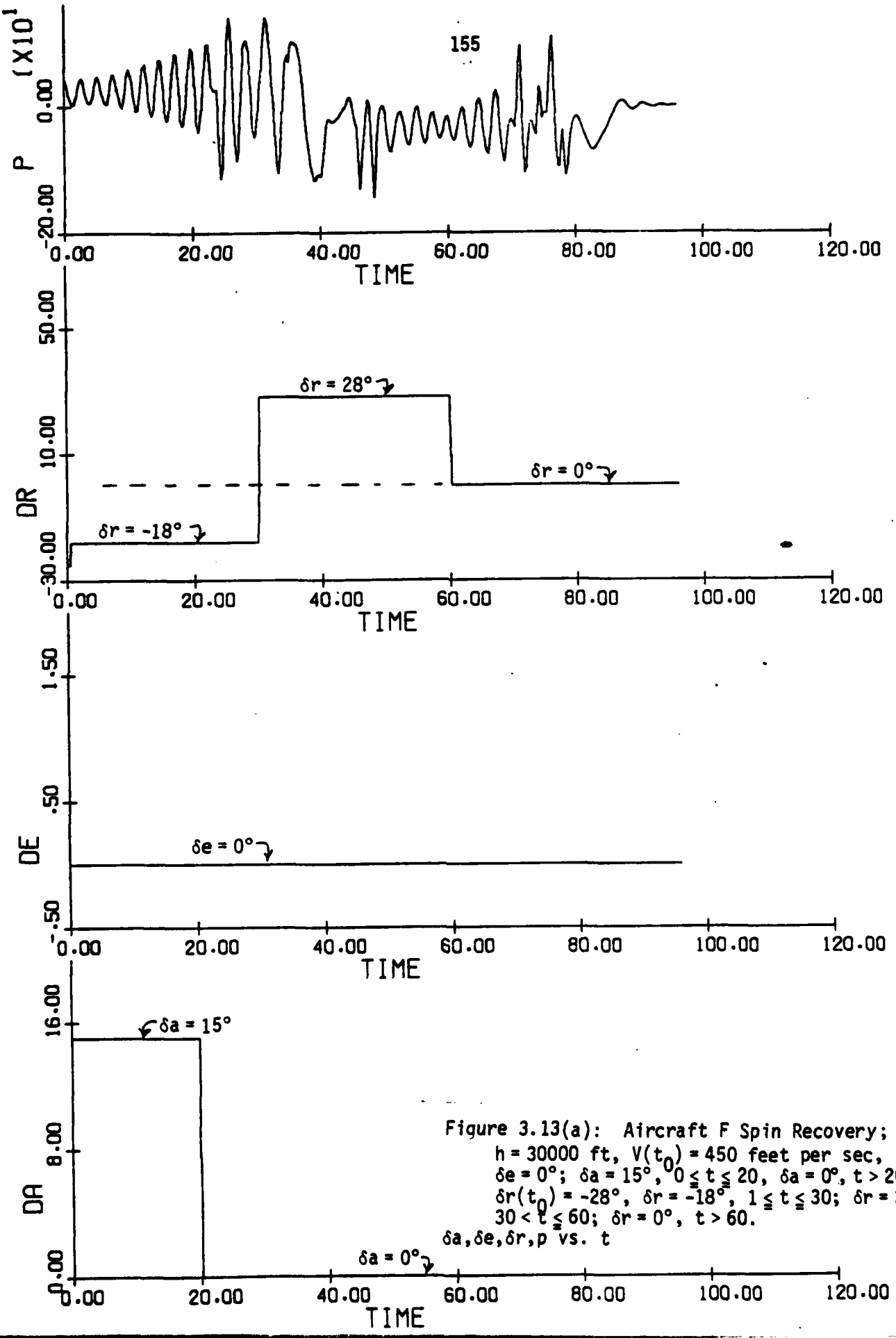

Figure 3.13(a): Aircraft F Spin Recovery;
h = 30000 ft, $V(t_0)$ = 450 feet per sec,
δe = 0°; δa = 15°, $0 \leq t \leq 20$, δa = 0°, $t > 20$;
$\delta r(t_0) = -28°$, δr = -18°, $1 \leq t \leq 30$; δr = 28°,
$30 < t \leq 60$; δr = 0°, $t > 60$.
δa, δe, δr, p vs. t

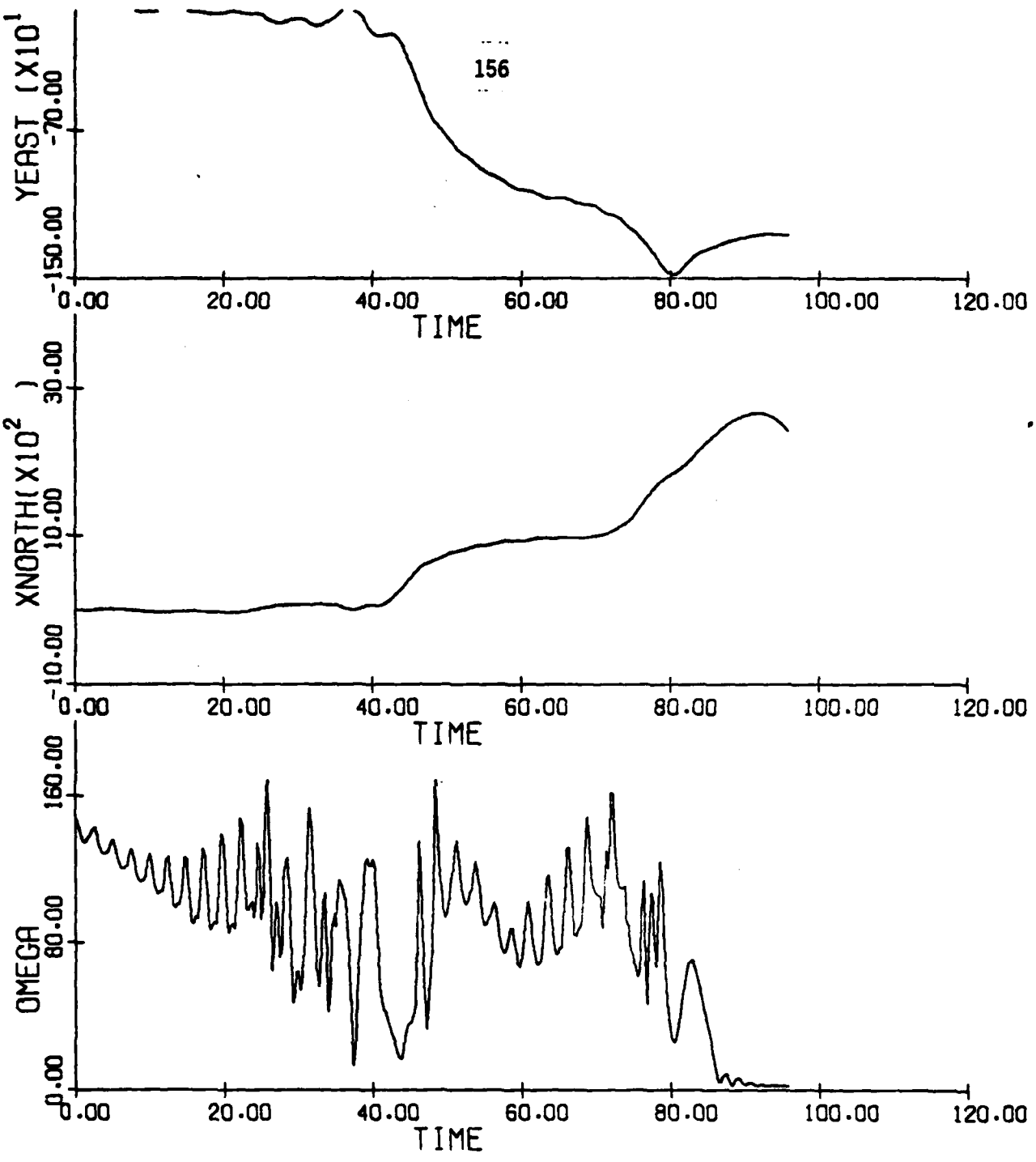

Figure 3.13(b) (concluded): $\Omega, x_{NORTH}, y_{EAST}$ vs. t

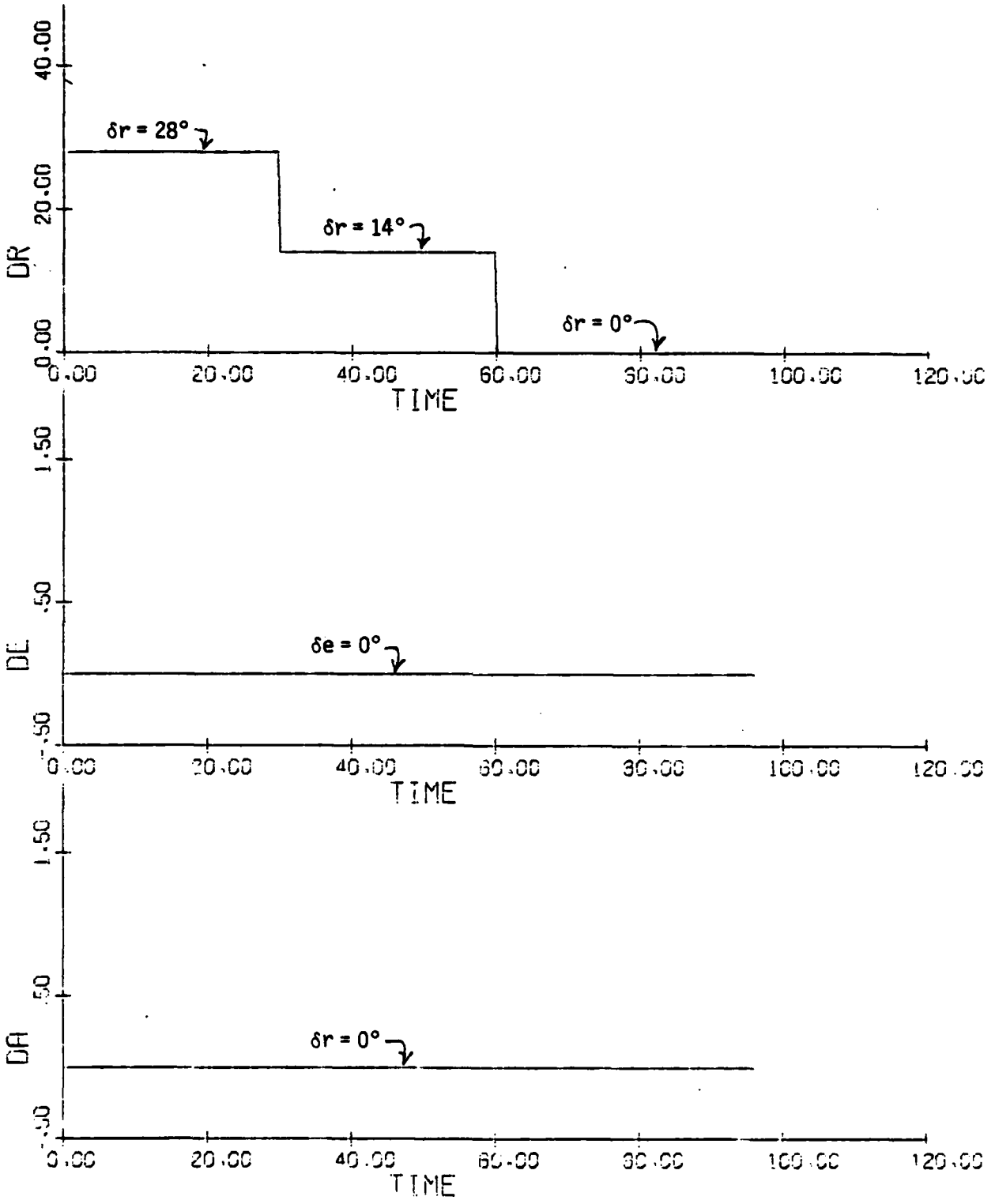

Figure 3.14(a): Aircraft F Spin Recovery; $h = 30000$ ft, $V(t_0) = 450$ fps; initial conditions from $t = 30.$ of Fig. 3.13 (pp. 155,156); $\delta a = \delta e = 0°$; $\delta r = 28°$, $0 \leq t \leq 30$; $\delta r = 14°$, $30 < t \leq 60.$; $\delta r = 0°$, $t > 60.$

$\delta a, \delta e, \delta r$ vs. t

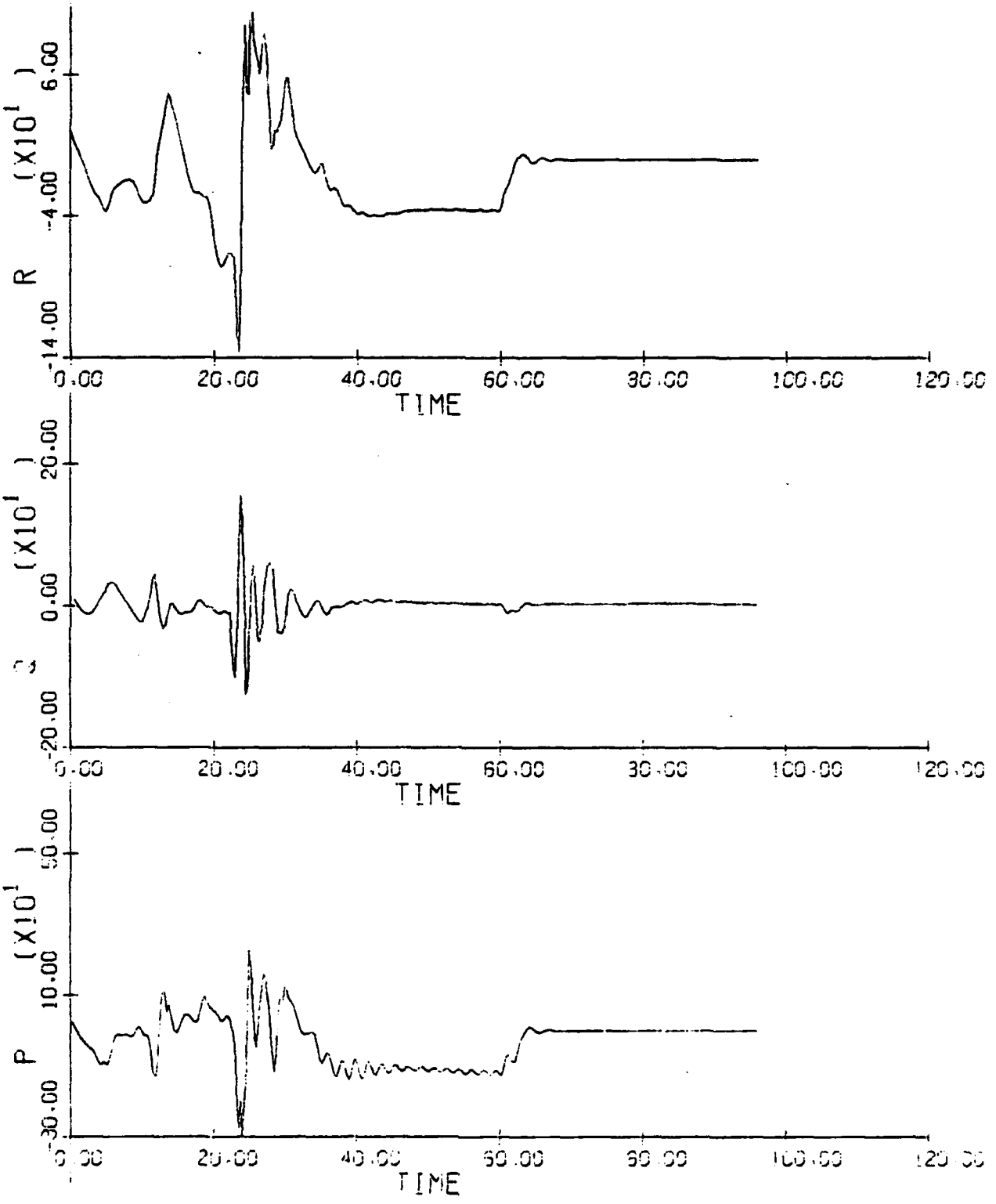

Figure 3.14(b): p,q,r vs. t

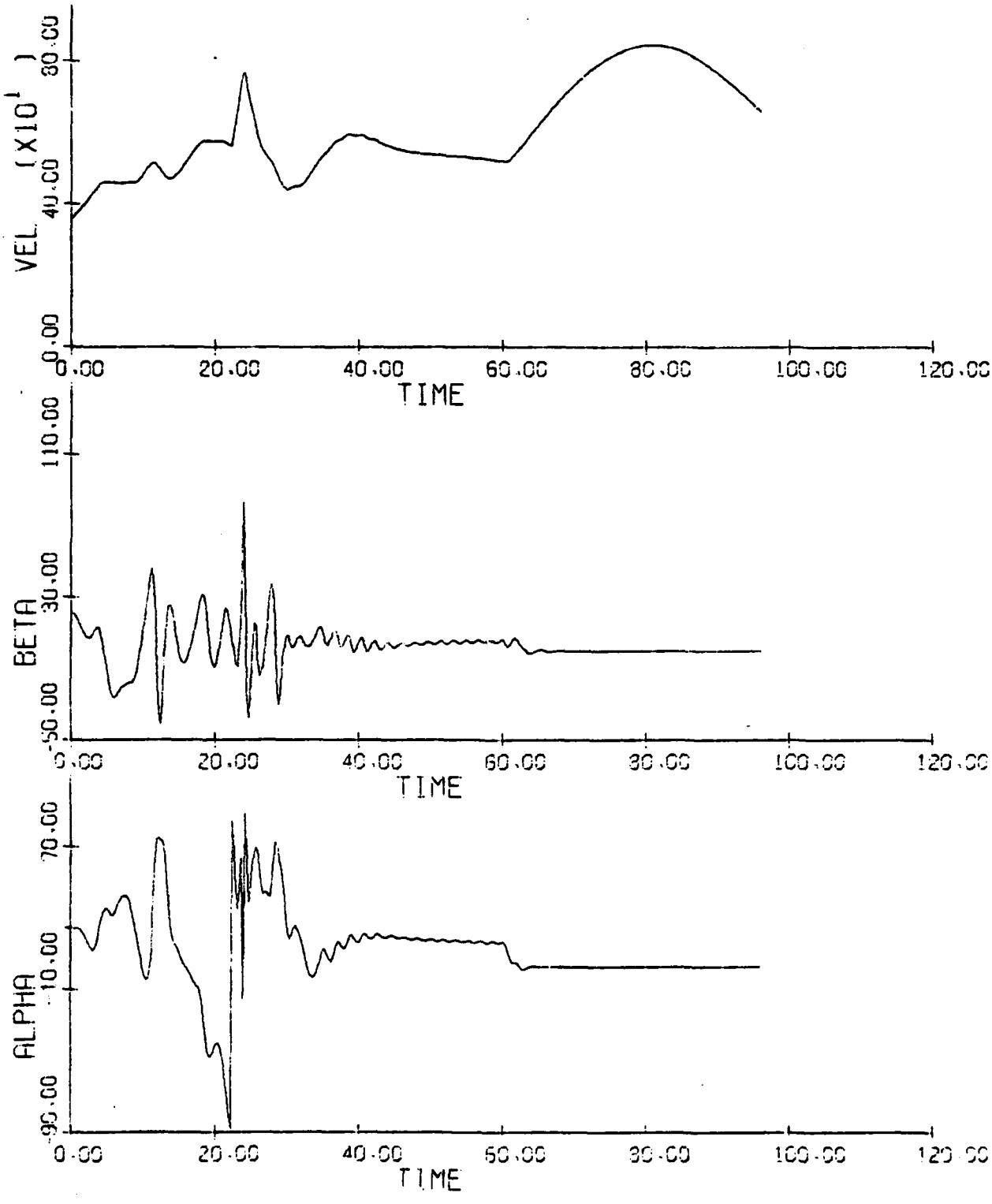

Figure 3.14(c): α,β,V vs. t

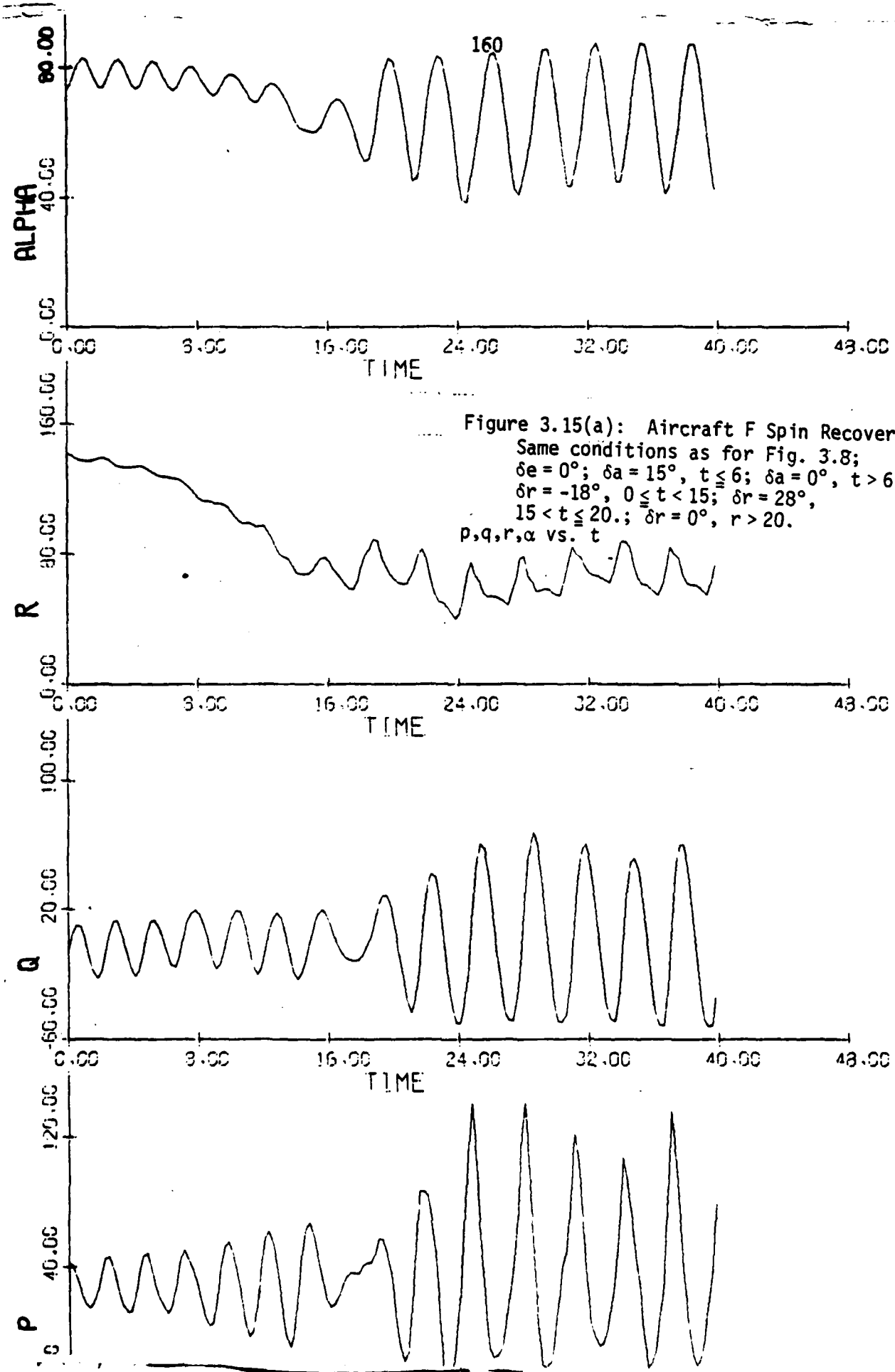

Figure 3.15(a): Aircraft F Spin Recovery;
Same conditions as for Fig. 3.8;
$\delta e = 0°$; $\delta a = 15°$, $t \leq 6$; $\delta a = 0°$, $t > 6$;
$\delta r = -18°$, $0 \leq t < 15$; $\delta r = 28°$,
$15 < t \leq 20.$; $\delta r = 0°$, $r > 20.$
p,q,r,α vs. t

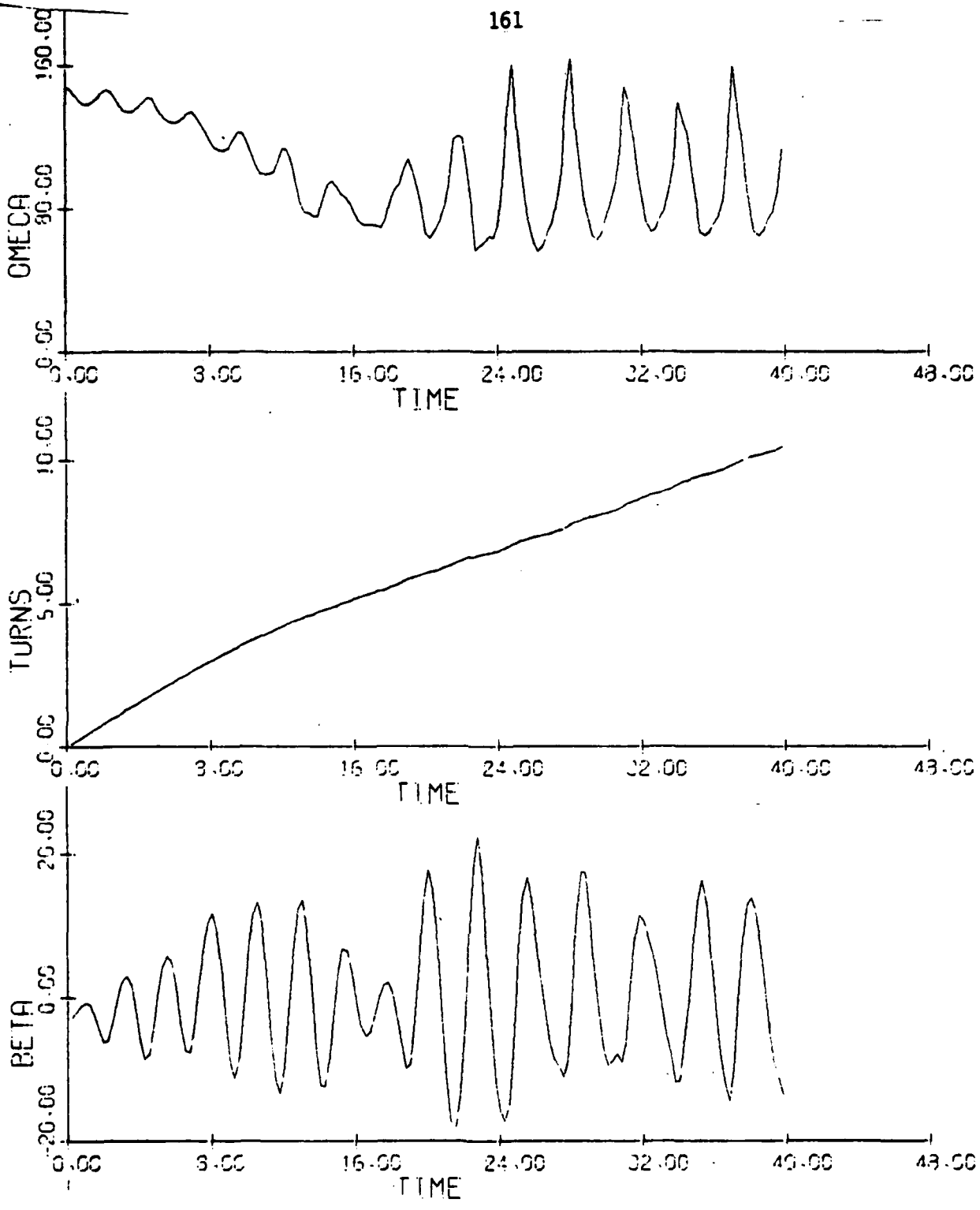

Figure 3.13(b) (concluded): β,TURNS,Ω vs. t

Figure 3.16: Aircraft F Equilibrium and Limit Cycle Trajectories for Spin Recovery; $\delta a = 0$, $\delta e = 0$; $V_o = 450$ fps., $h = 30{,}000$ ft.

(a) $\bar{r}$ vs. δr, δr increasing

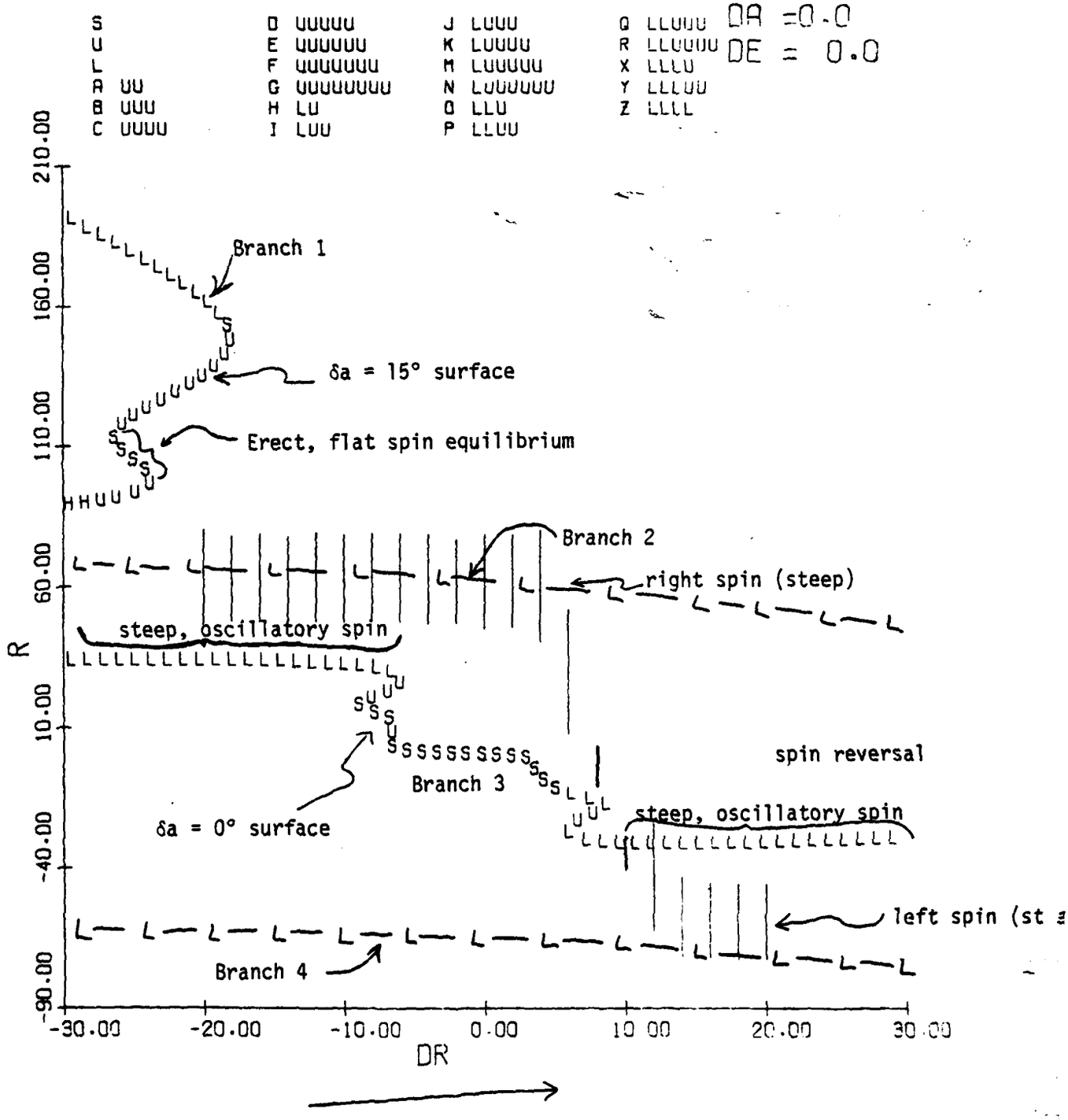

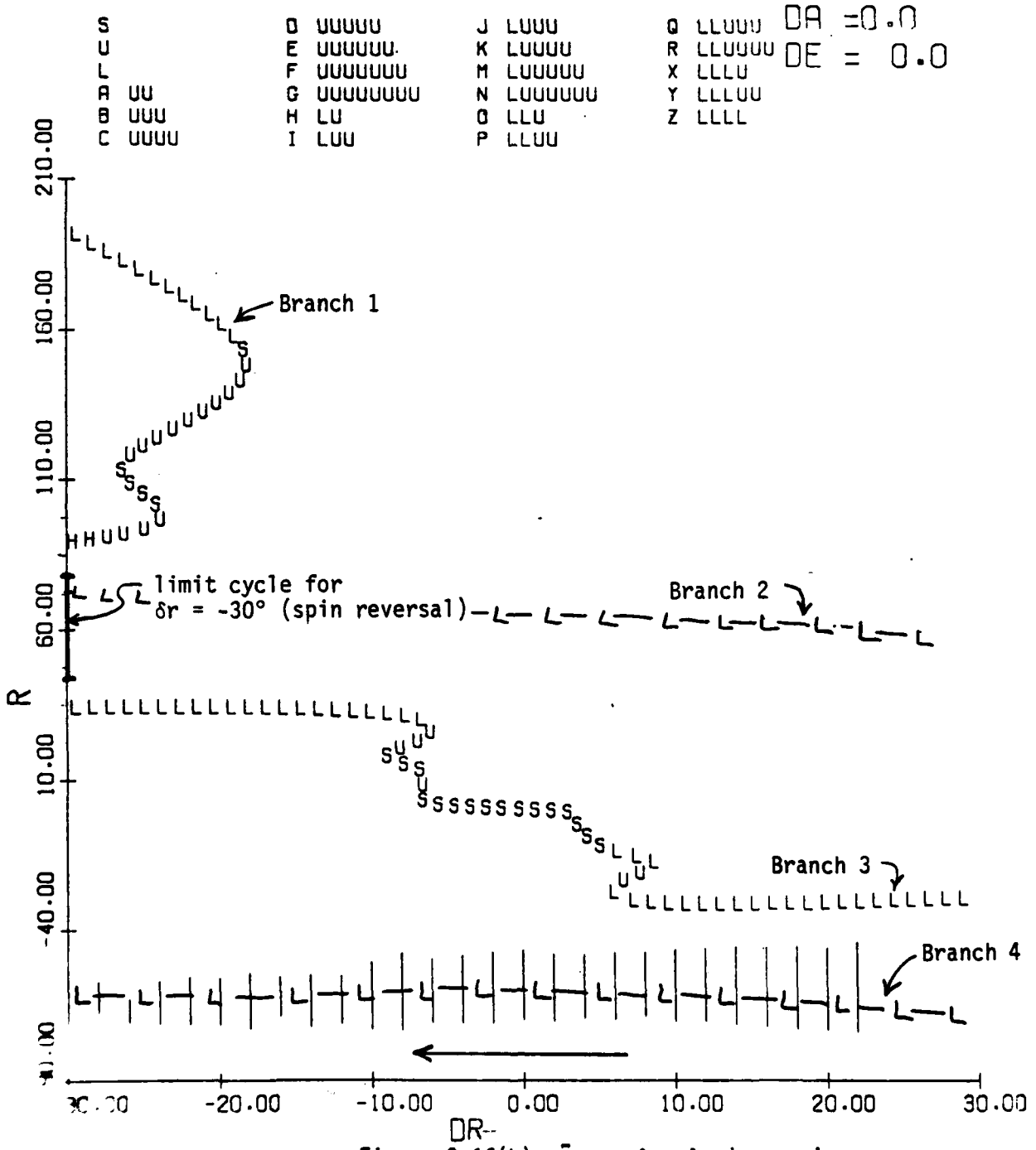

Figure 3.16(b) $\bar{r}$ vs. δr, δr decreasing

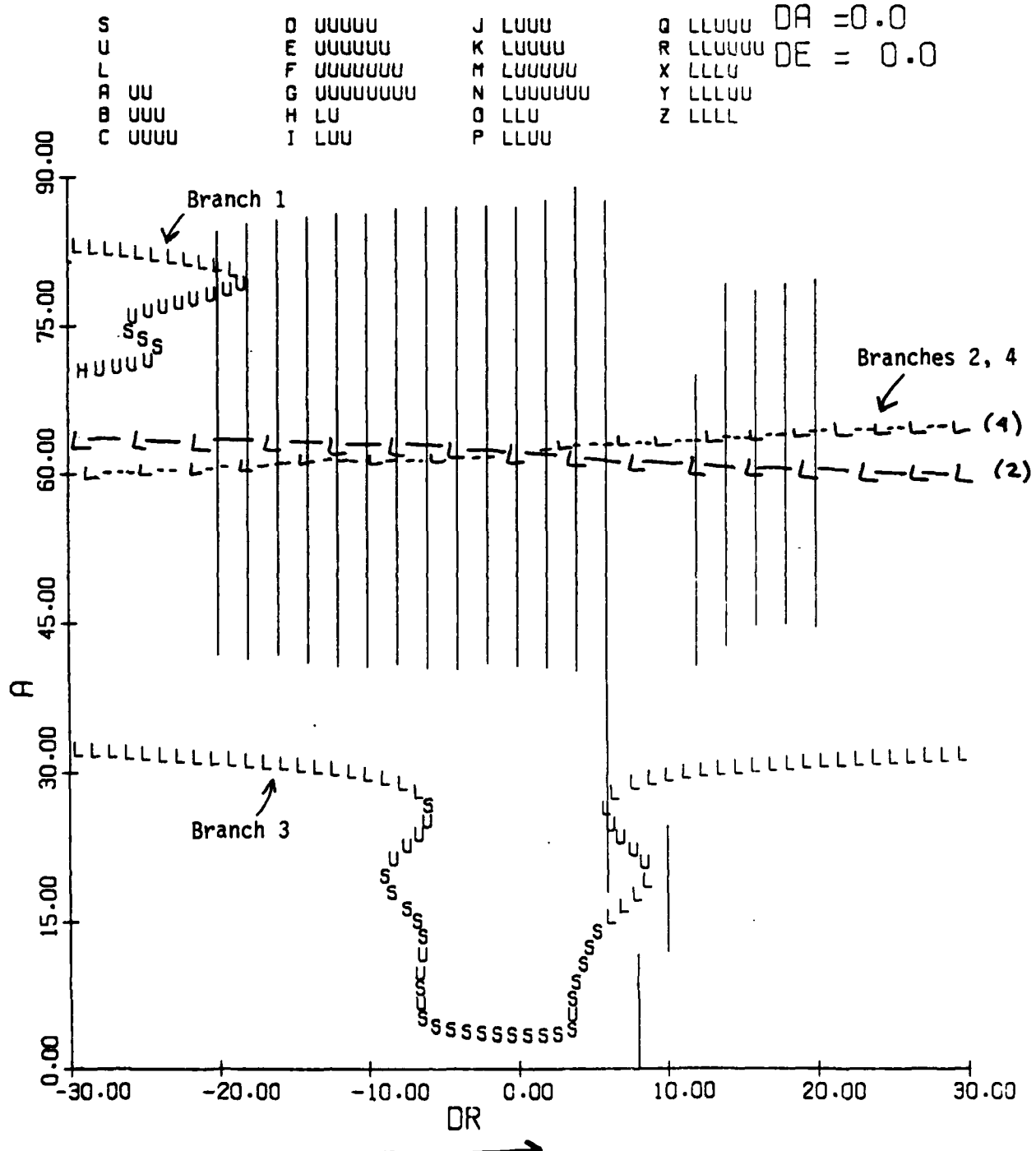

Figure 3.16(c) $\bar{a}$ vs. δr, δr increasing

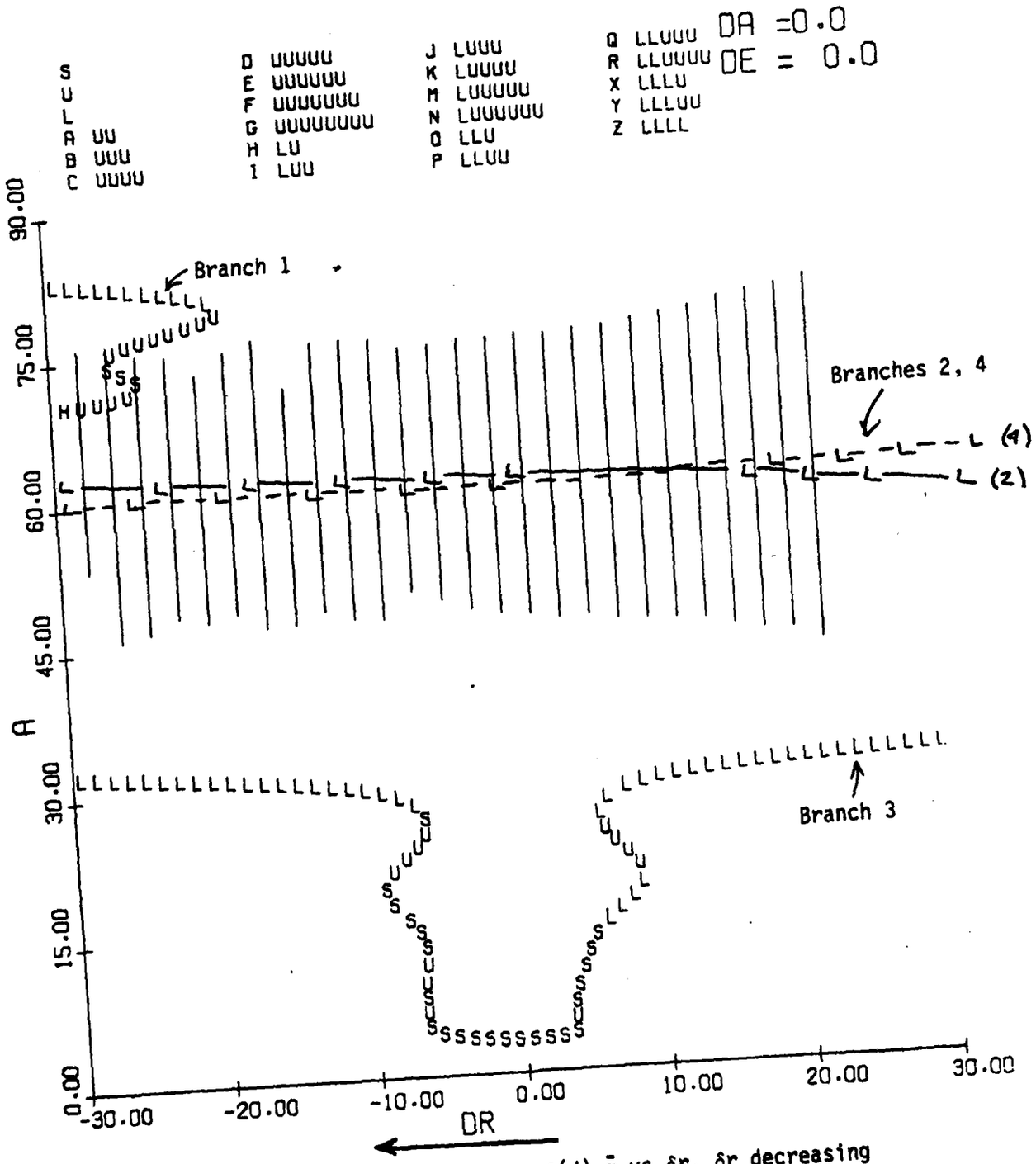

Figure 3.16(d) $\bar{\alpha}$ vs.δr, δr decreasing

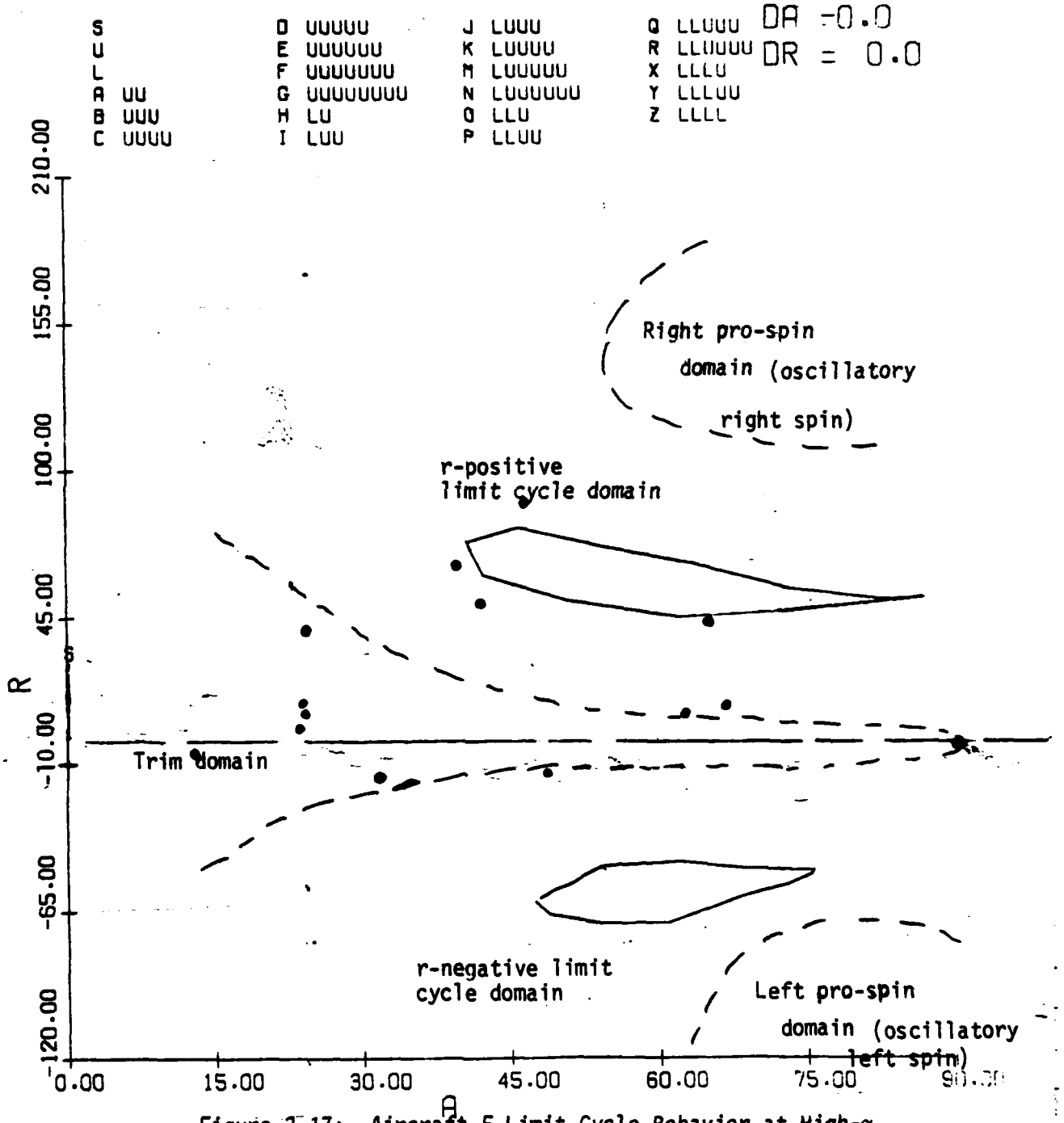

Figure 3.17: Aircraft F Limit Cycle Behavior at High-α
$\delta a = \delta e = 0°$, V = 450 fps., h = 30,000 ft.
(a) $\delta r = 0°$

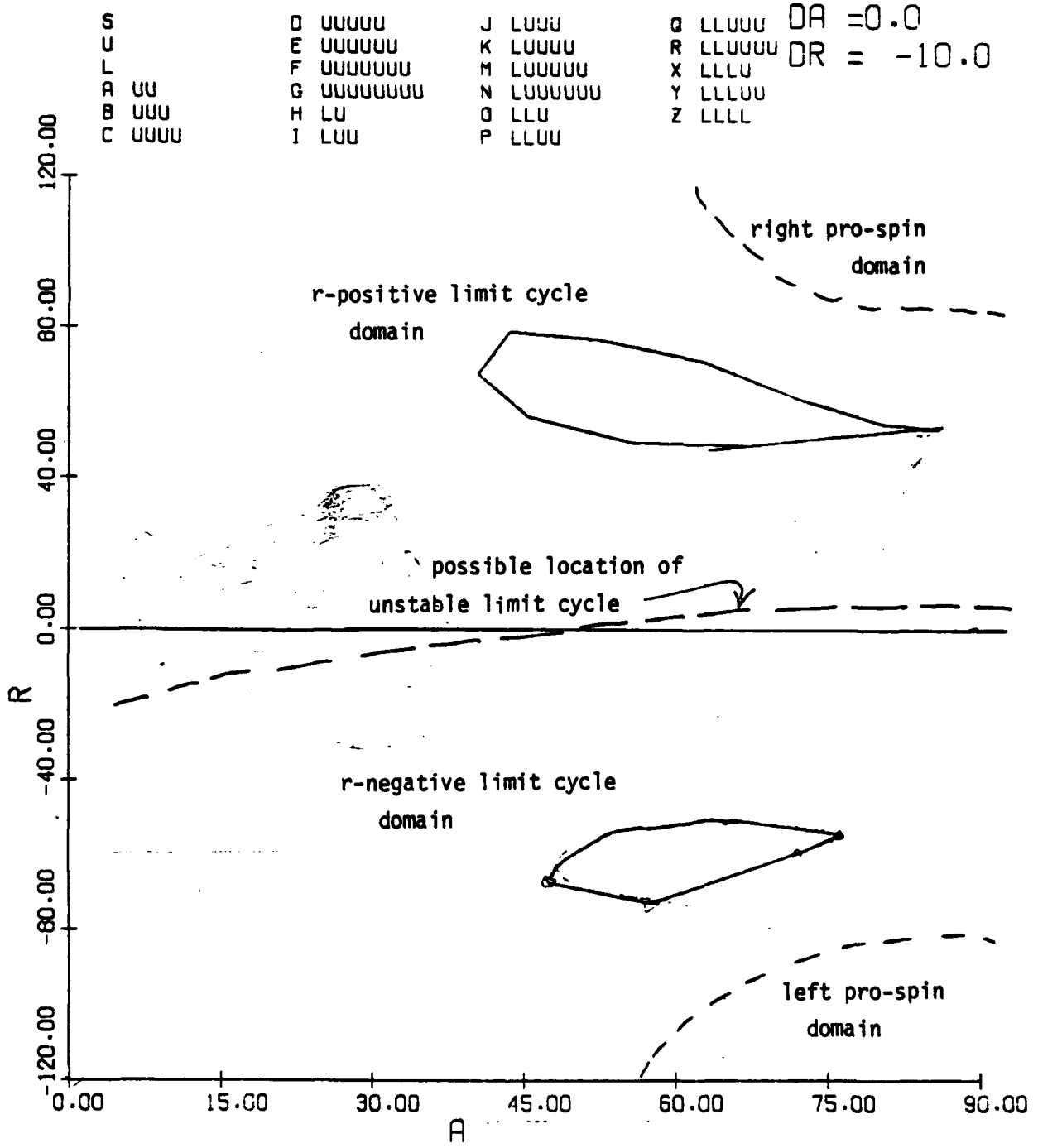

Figure 3.17(b) (concluded): $\delta r = -10°$

Figure 3.18(a): Aircraft F Time History, Spin Recovery Case 220

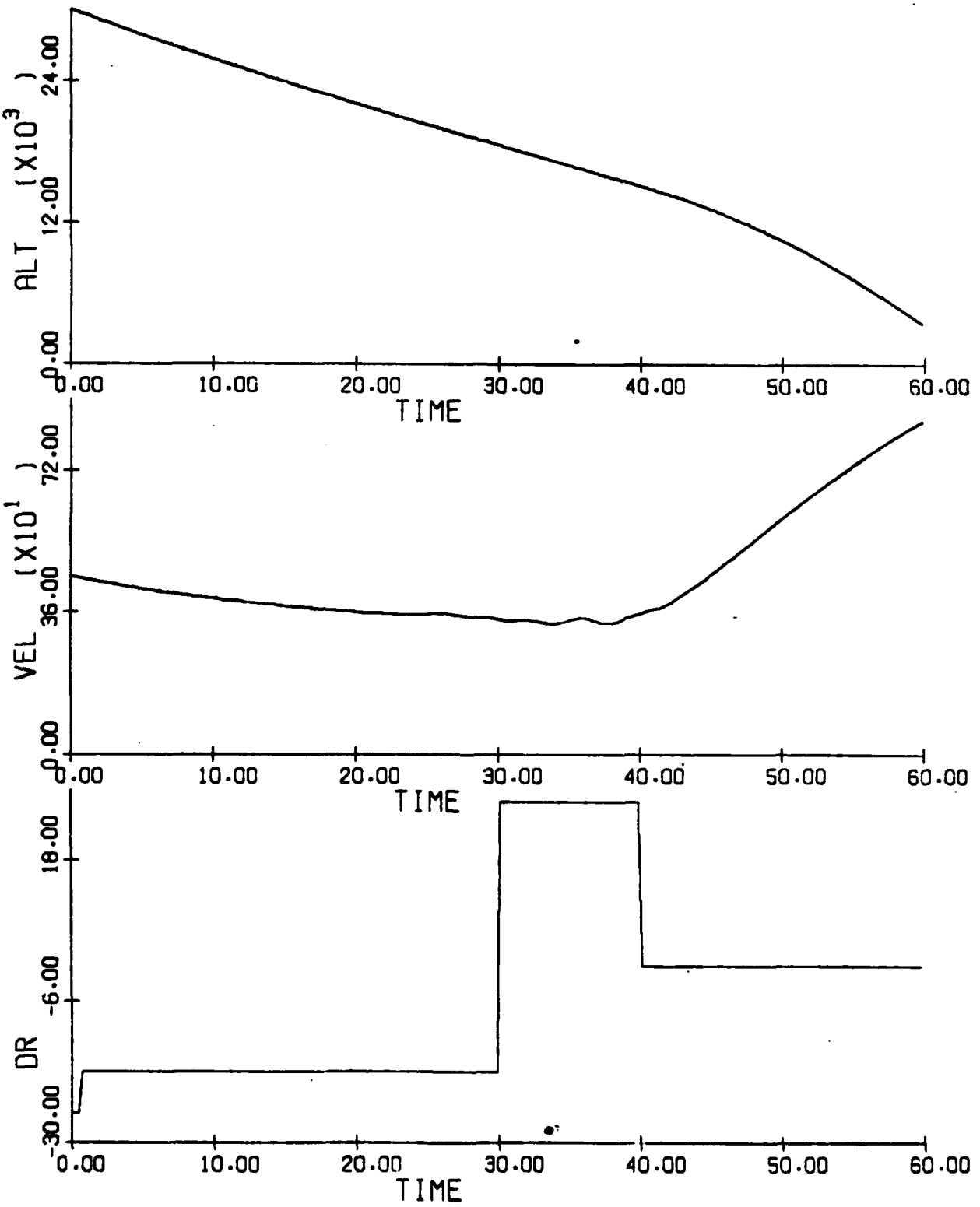

Figure 3.18(b) (concluded)

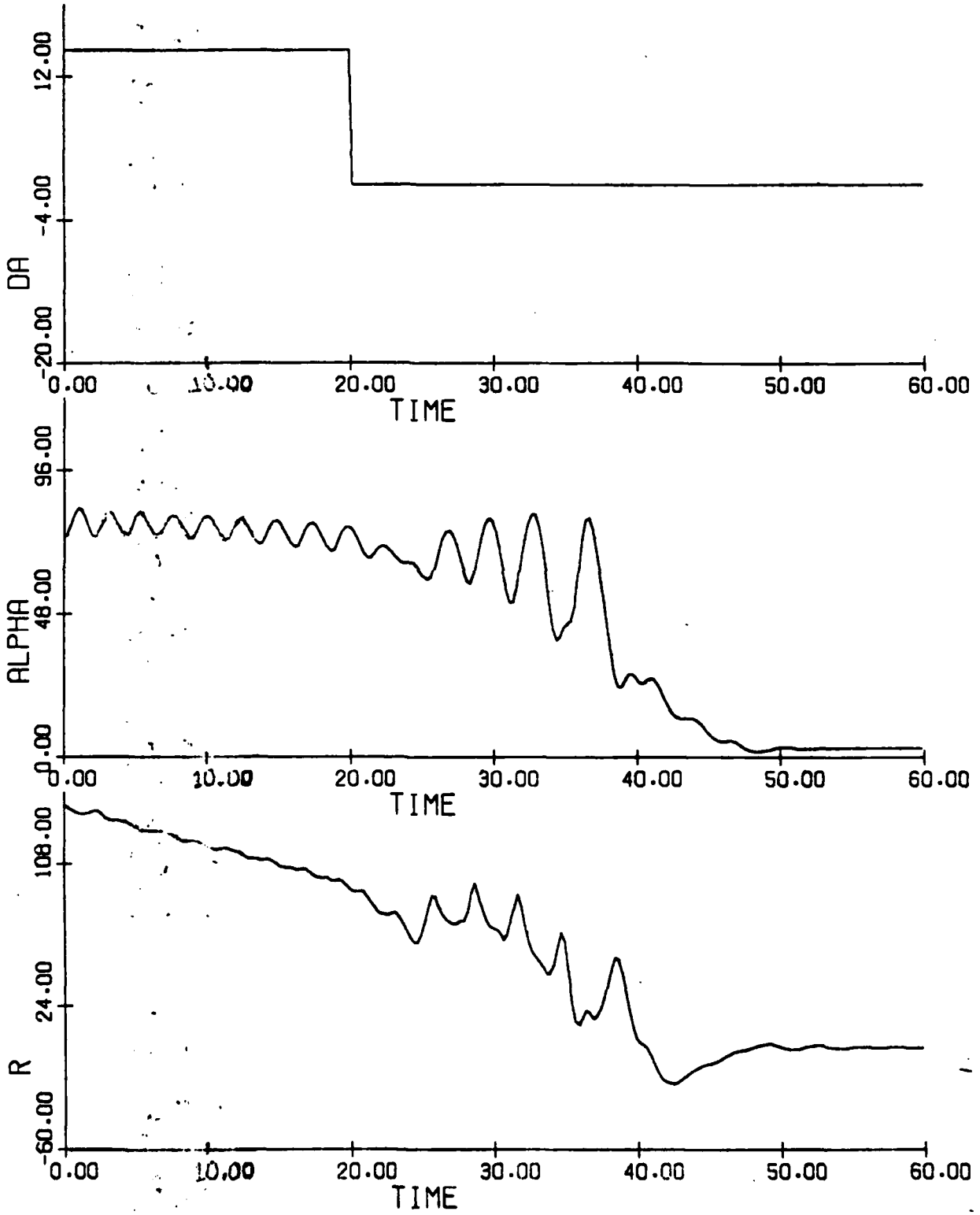

Figure 3.19(a): Aircraft F Time History, Spin Recovery Case 221

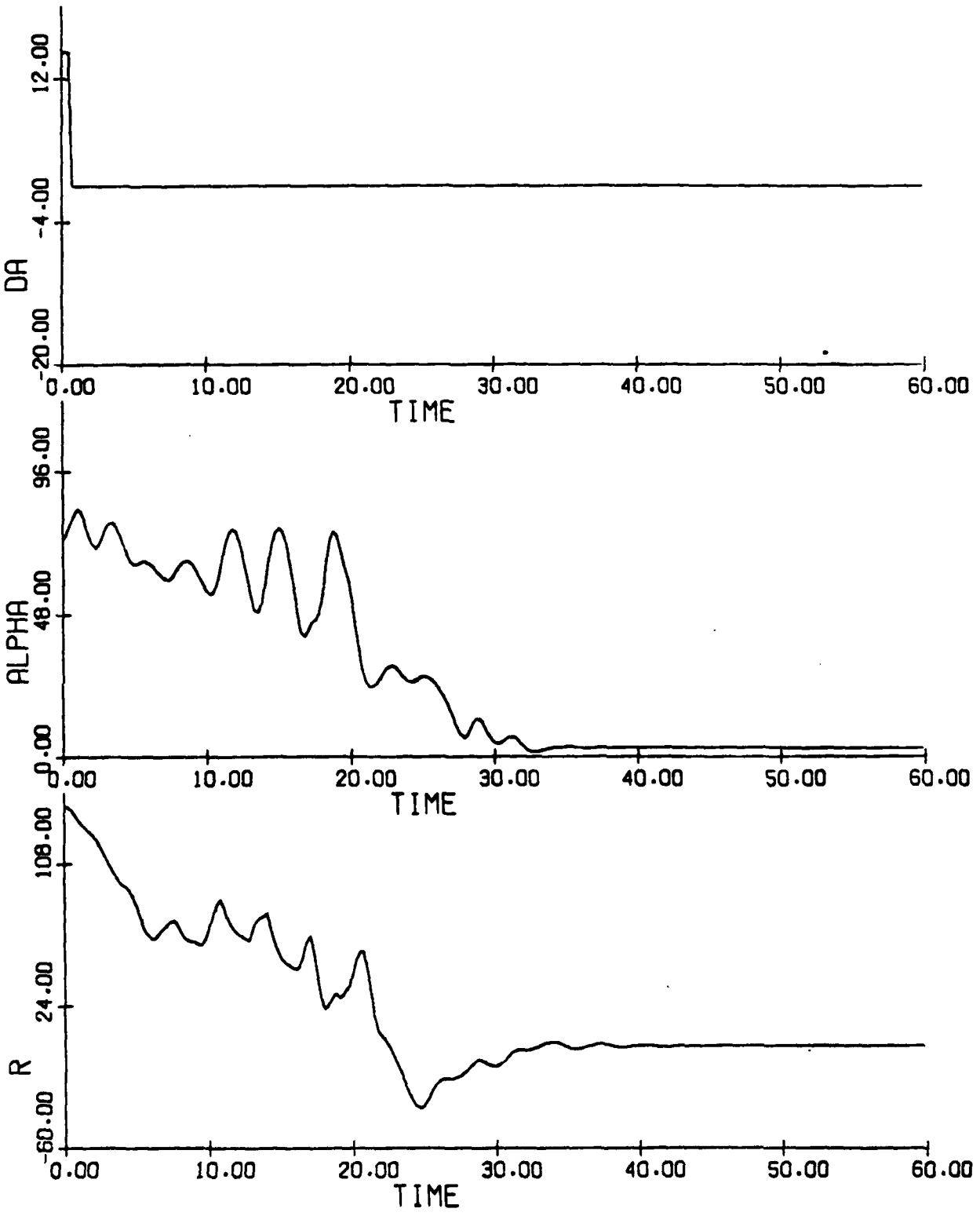

Figure 3.19(b) (concluded)

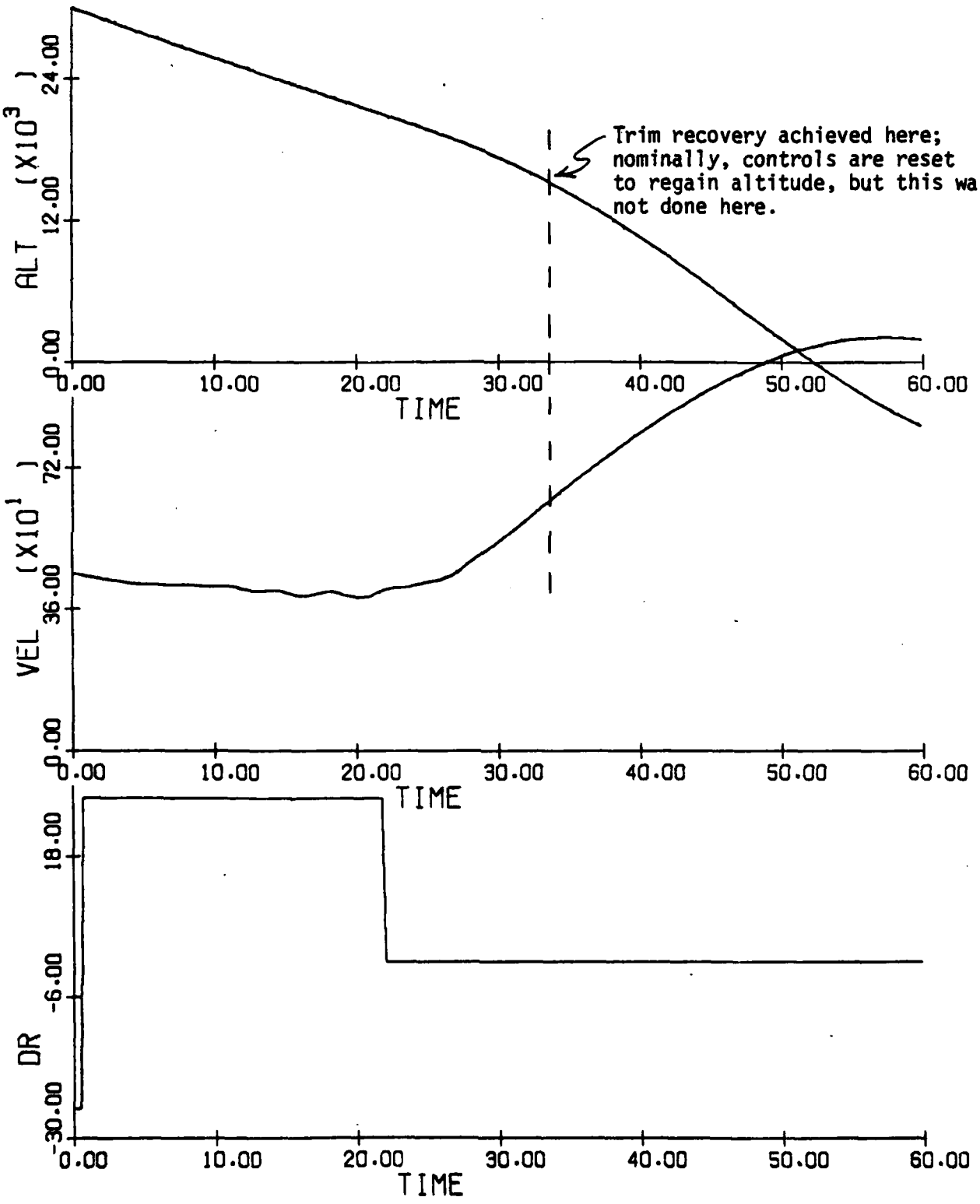

Figure 3.20(a): Aircraft F Time History, Spin Recovery Case 222/232

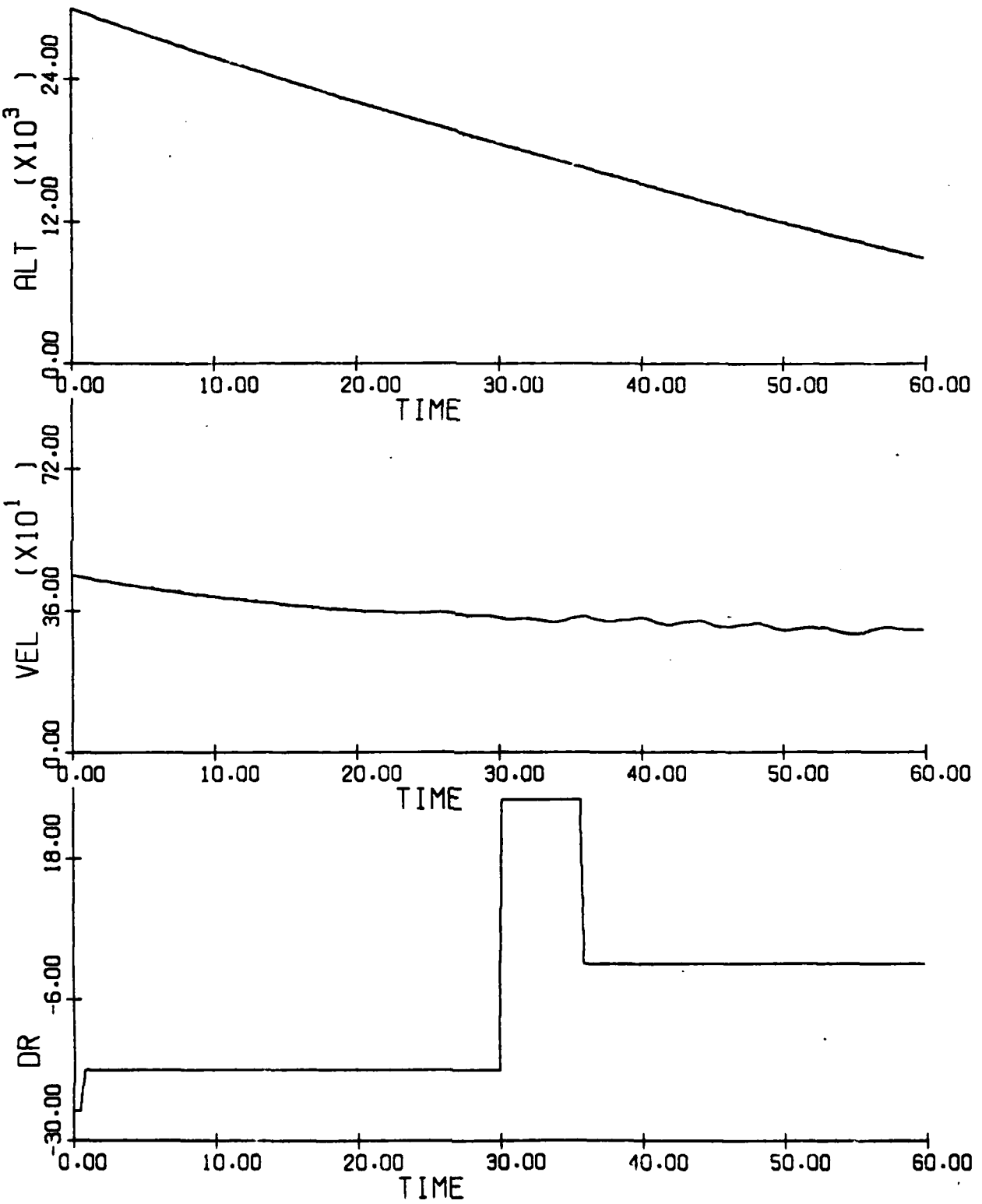

Figure 3.20(b) (cont.)

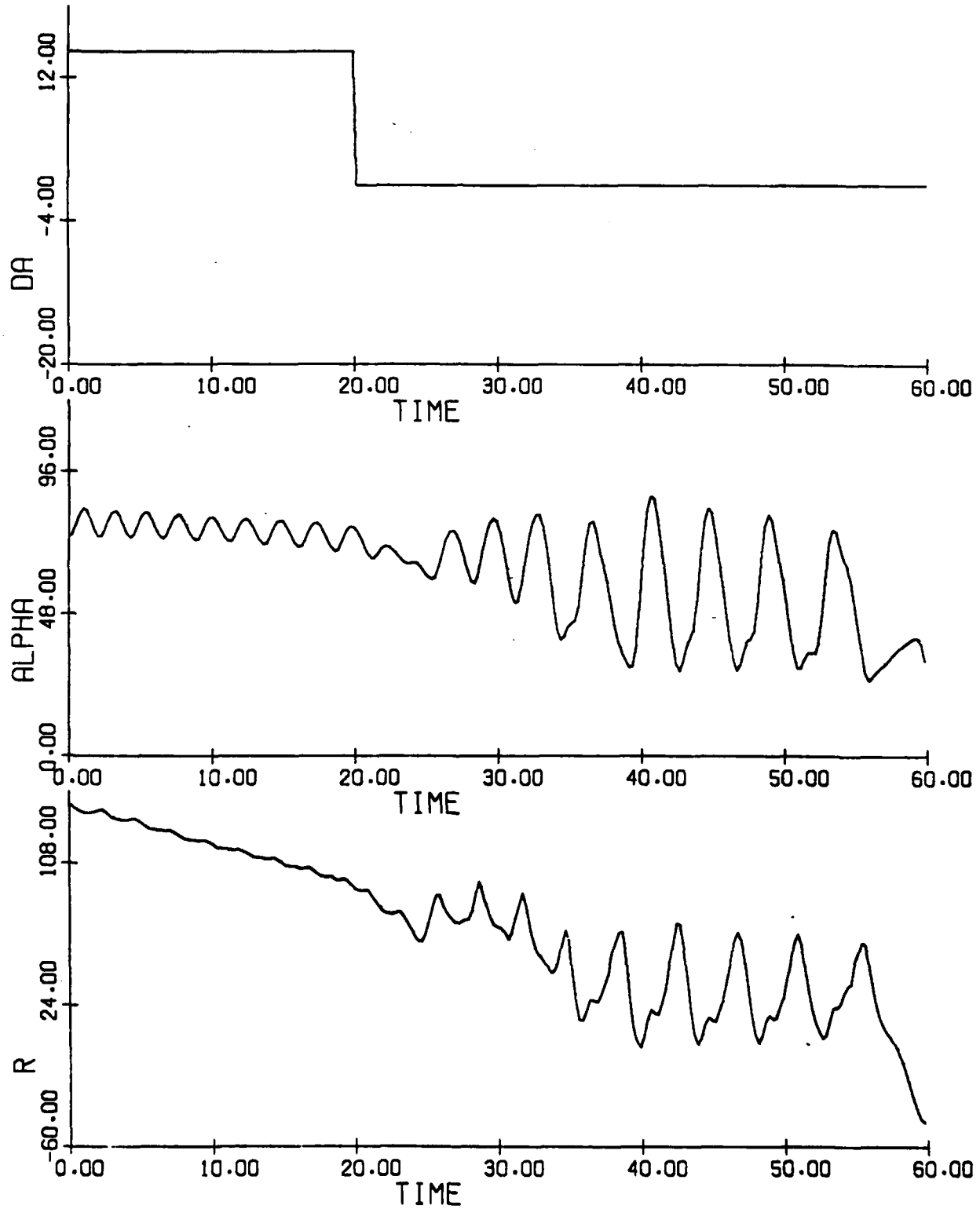

Figure 3.20(c) (cont.)

This and part (d) are follow-on runs to parts (a) and (b); they use the initial conditions at t=60. sec of (a),(b).

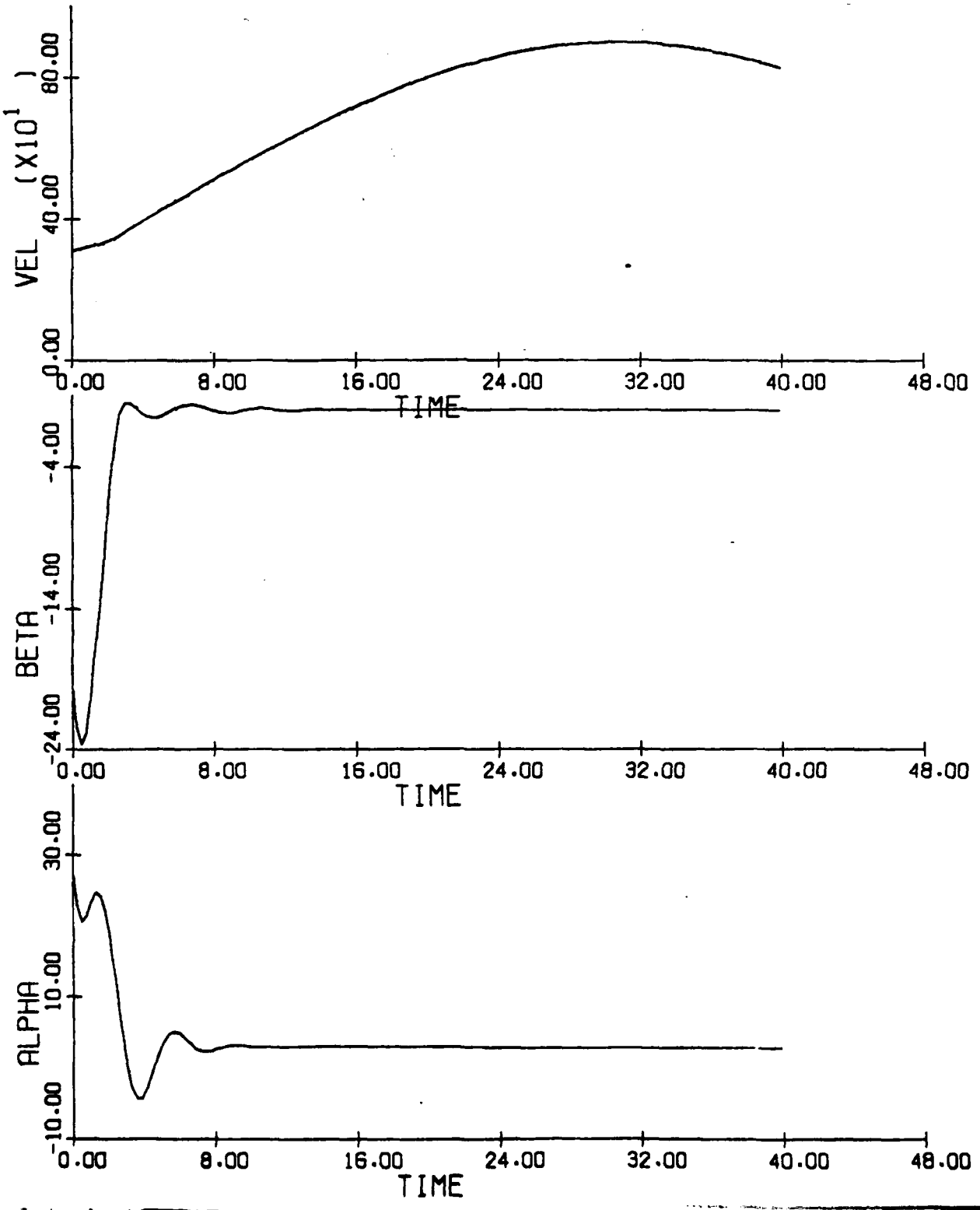

Figure 3.20(d) (concluded)

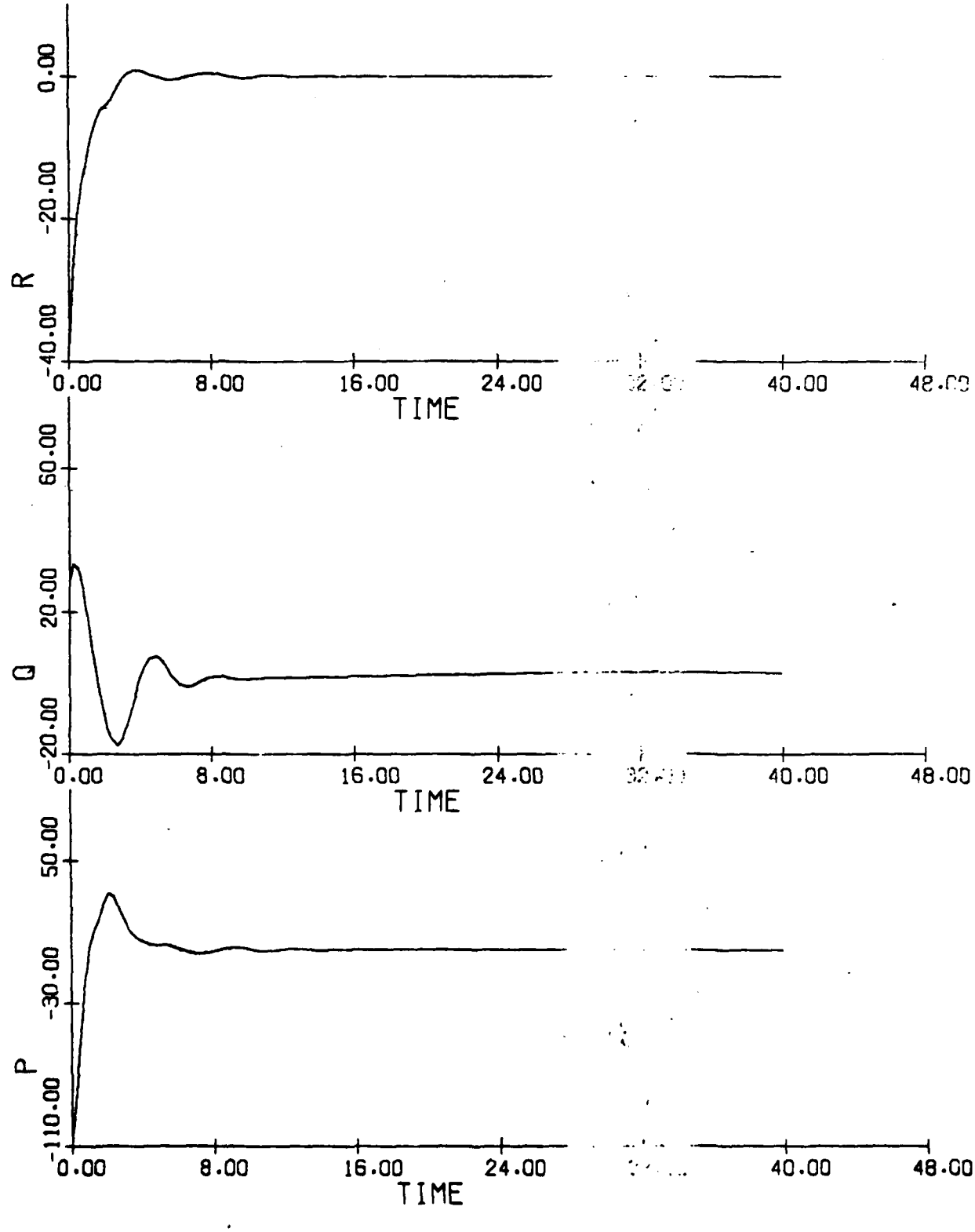

Figure 3.21(a): Aircraft F Time History, Spin Recovery Case 223

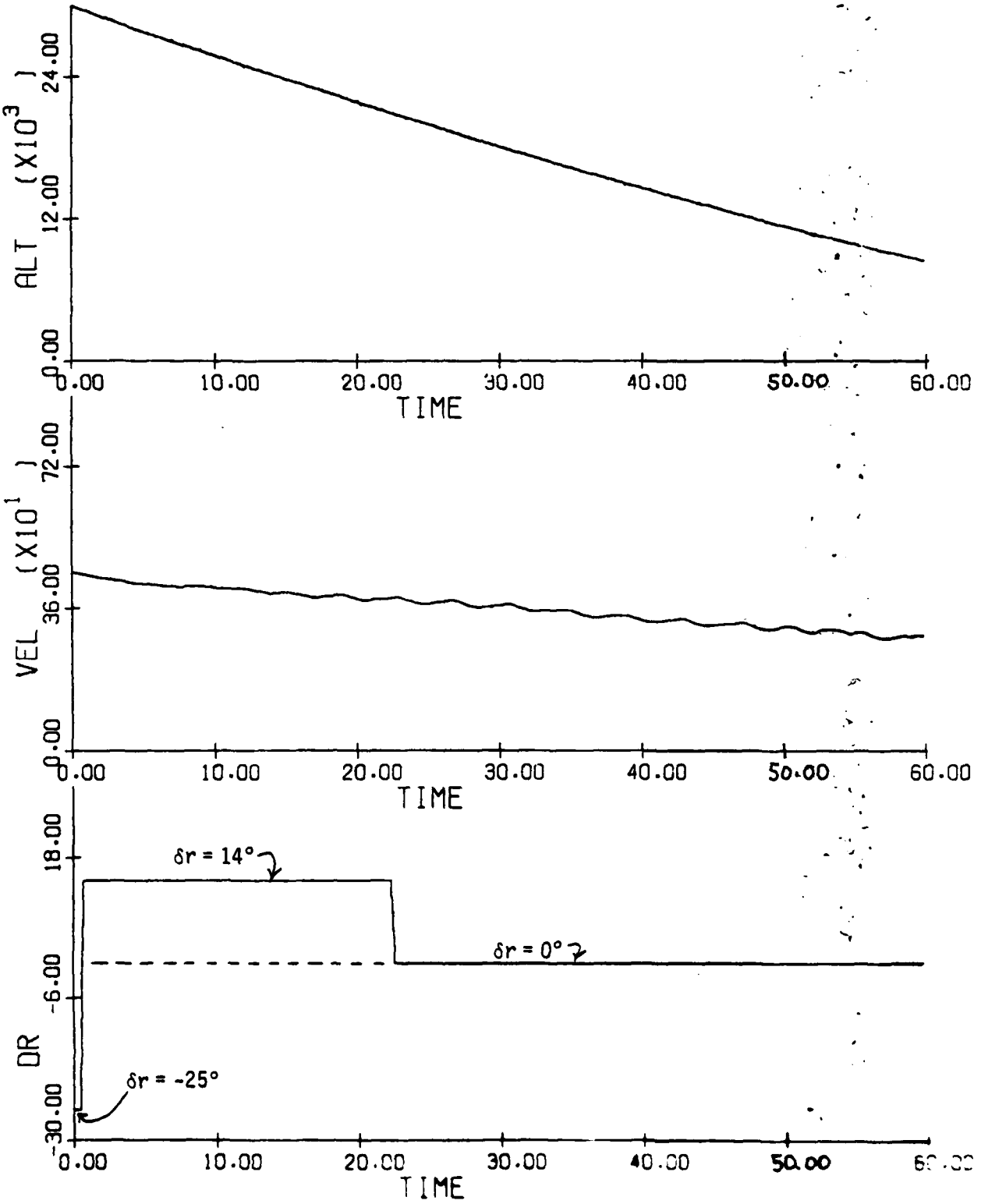

AD-A084 938 SCIENTIFIC SYSTEMS INC CAMBRIDGE MA F/G 20/4
GLOBAL STABILITY AND CONTROL ANALYSIS OF AIRCRAFT AT HIGH ANGLE--ETC(U)
AUG 79 R K MEHRA, J V CARROLL N00014-76-C-0780
UNCLASSIFIED ONR-CR215-245-3 NL

3 OF 4
AD
A084938

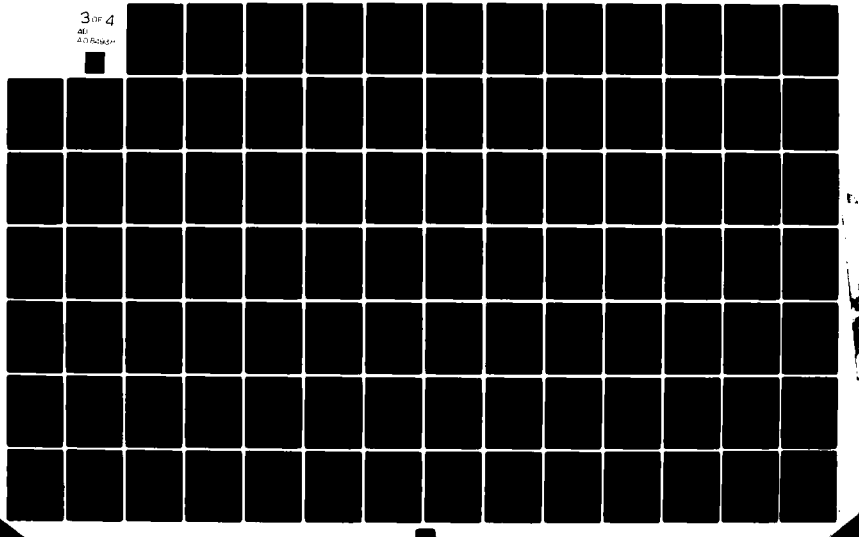

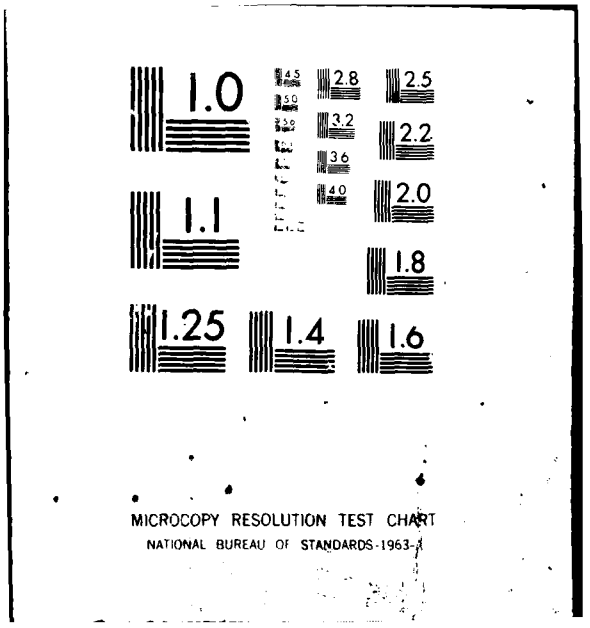
1.0
1.1
1.25
1.4
1.6
1.8
2.0
2.2
2.5
2.8
3.2
3.6
4.0
MICROCOPY RESOLUTION TEST CHART
NATIONAL BUREAU OF STANDARDS-1963-A

Figure 3.21(b) (concluded)

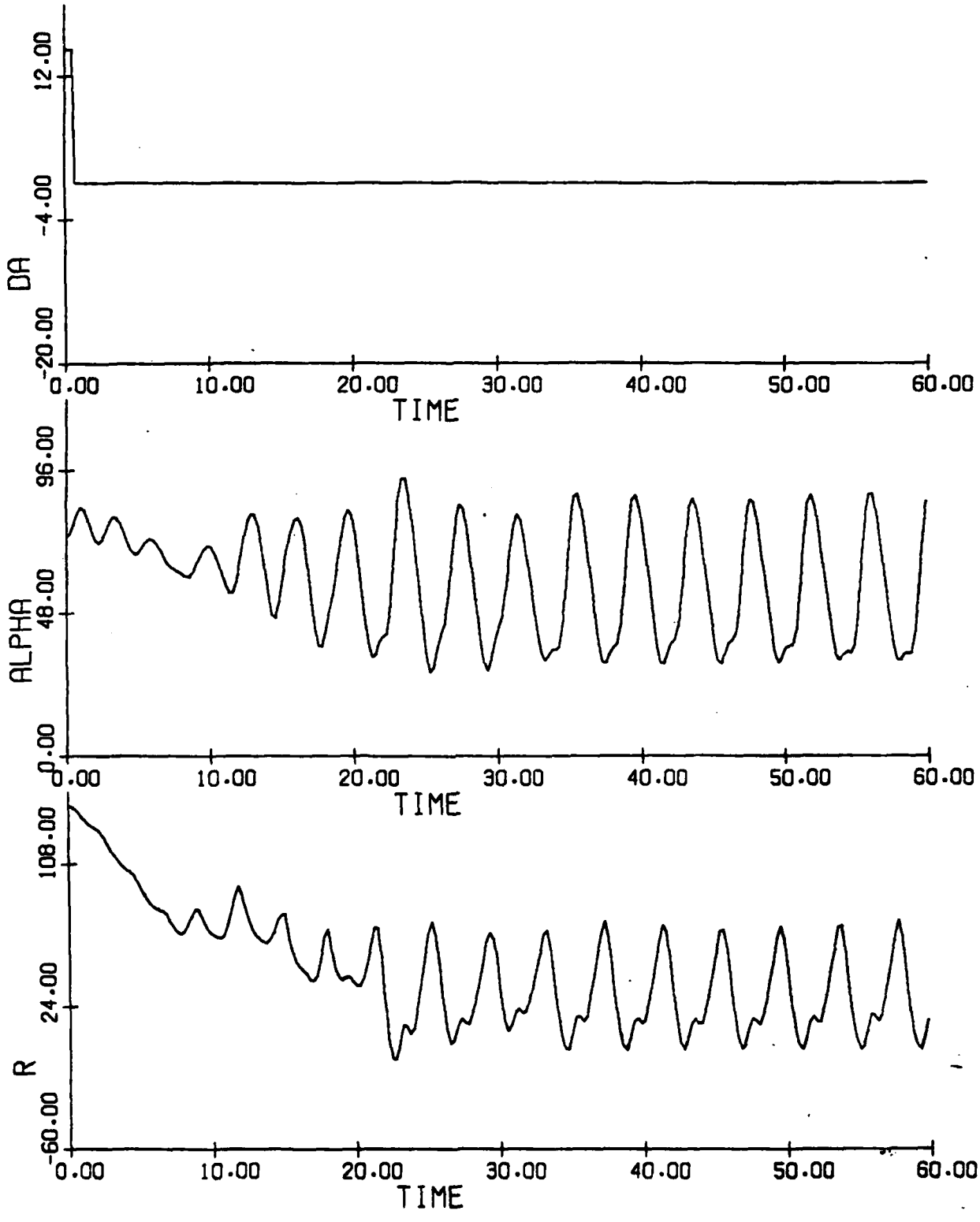

Figure 3.22(a): Aircraft F Time History, Spin Recovery Case 224

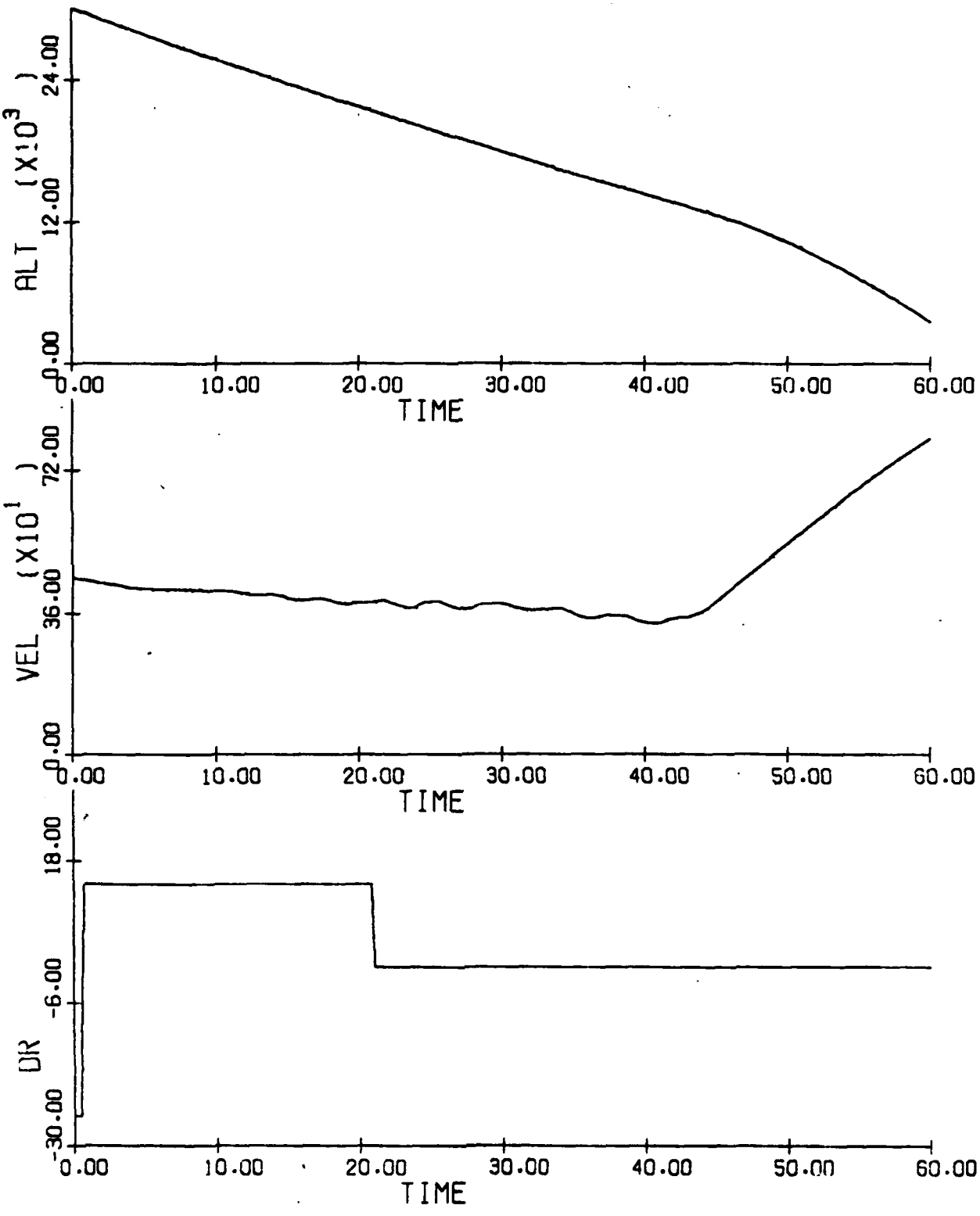

Figure 3.22(b) (concluded)

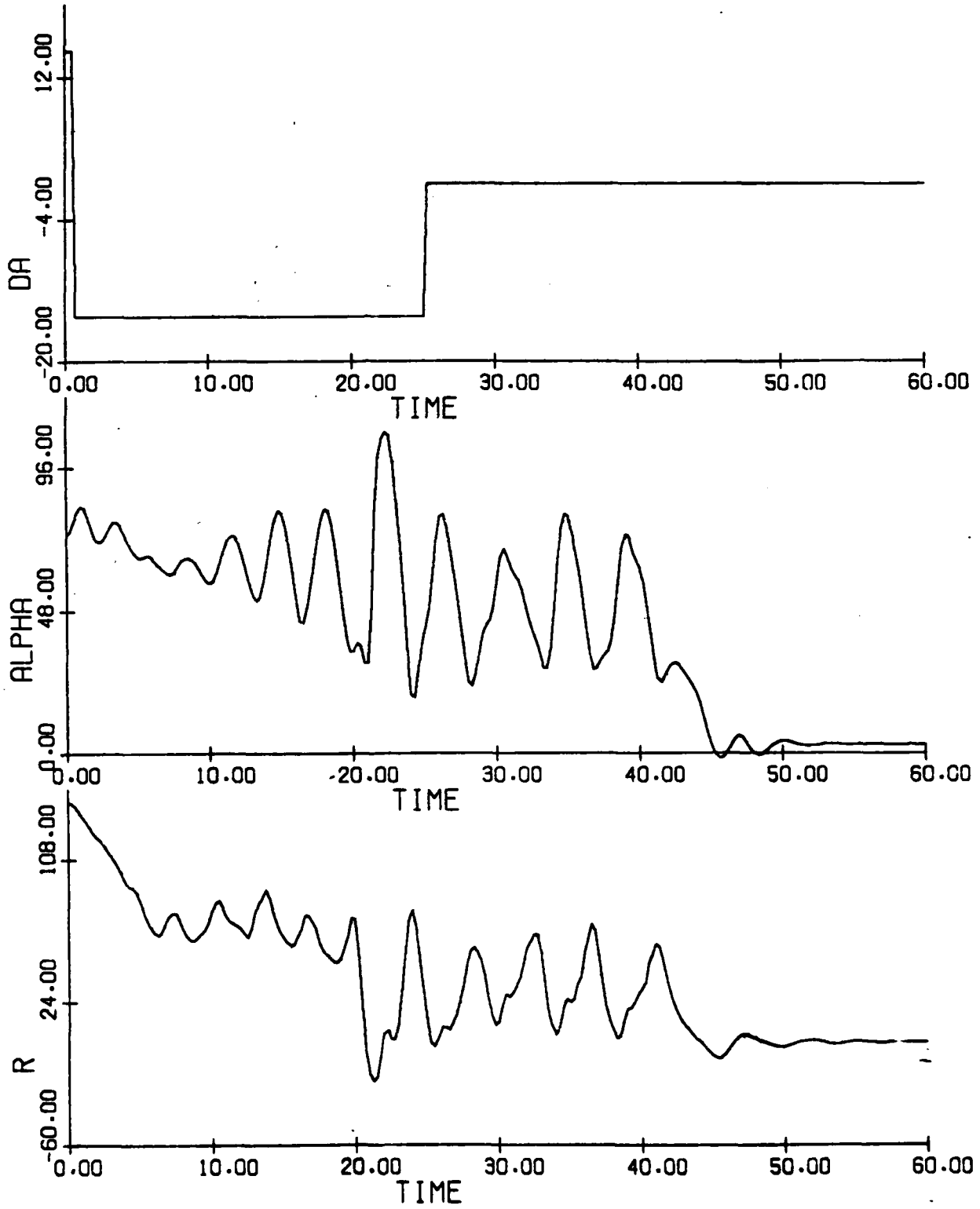

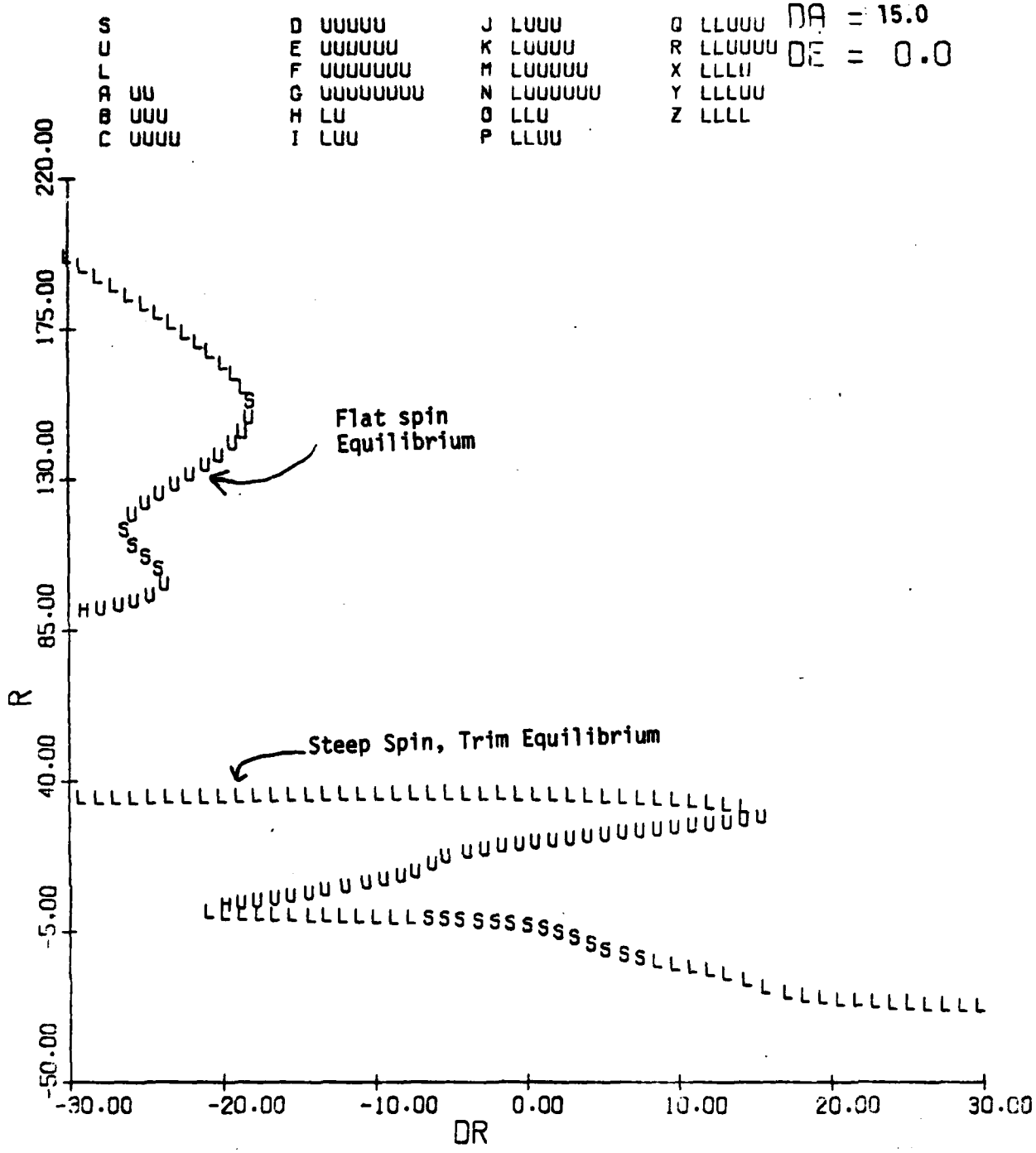

Figure 3.23: Aircraft F Equilibrium Surface; $\bar{r}$ vs. δr,
$\delta e = 0°$, V = 450 fps
(a) $\delta a = 15°$

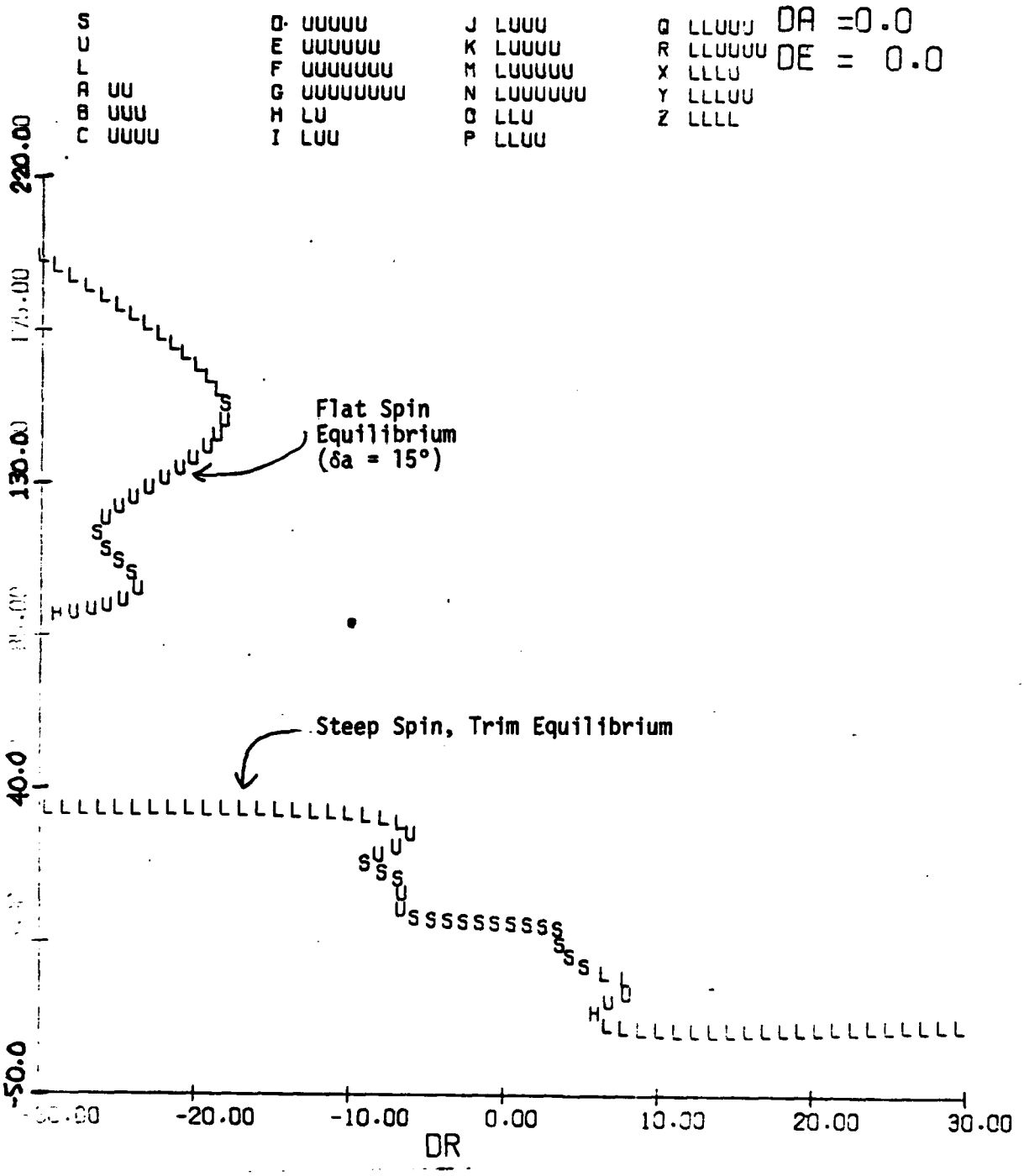

Figure 3.23(b): $\delta a = 0°$

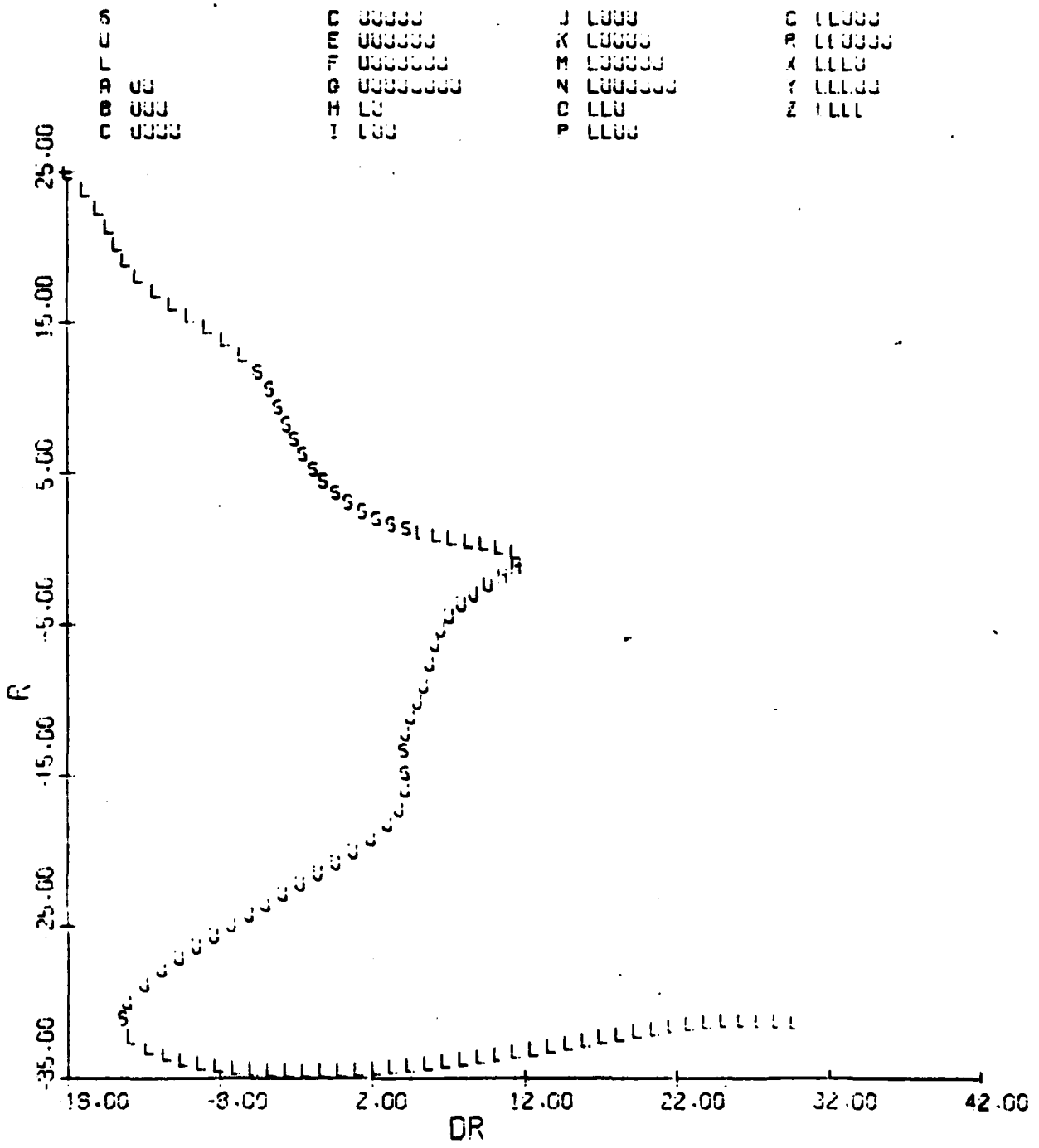

Figure 3.23(c): $\delta a = -15°$

Figure 3.24(a): Aircraft F Time History, Spin Recovery Case 229

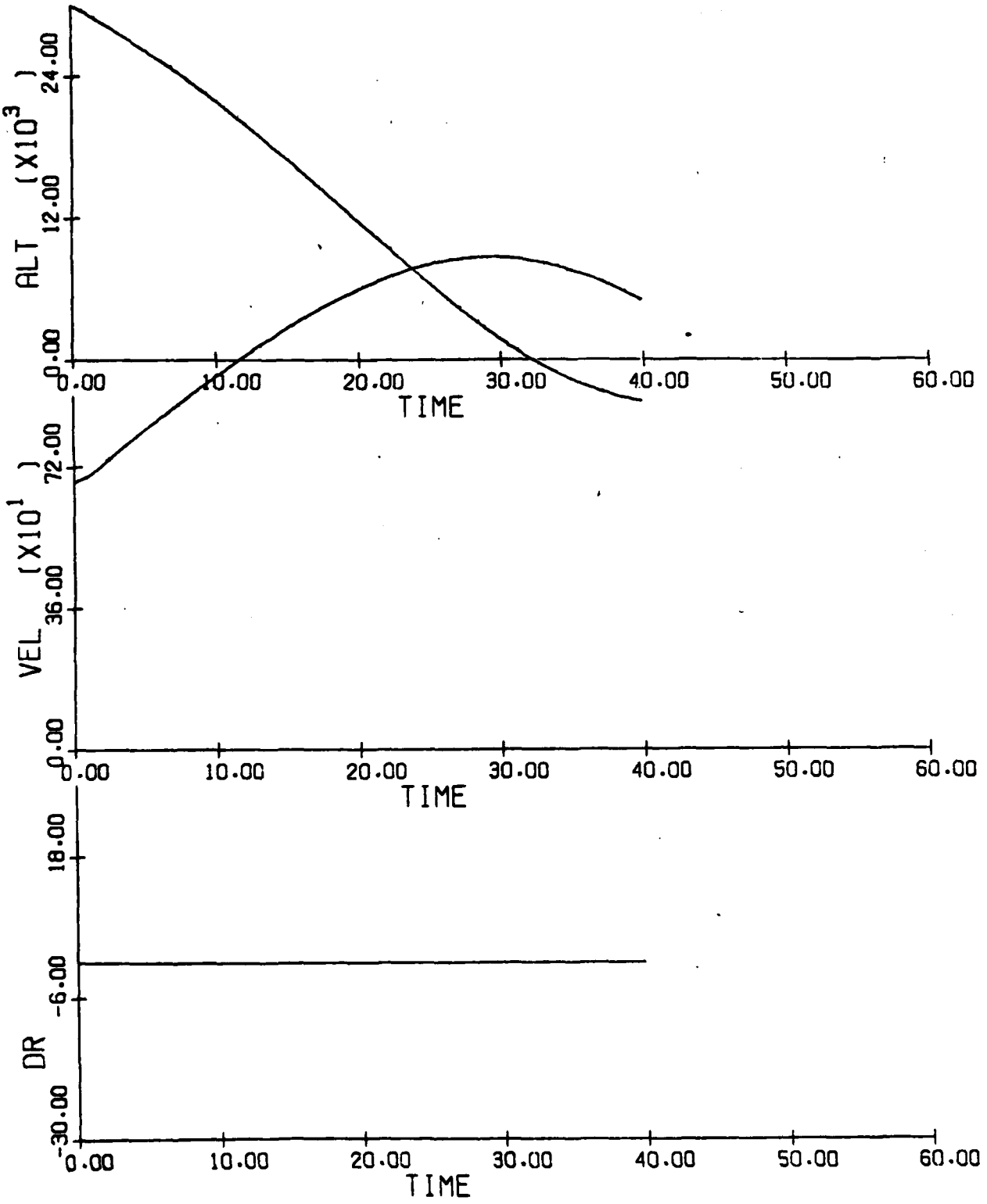

Figure 3.24(b) (concluded)

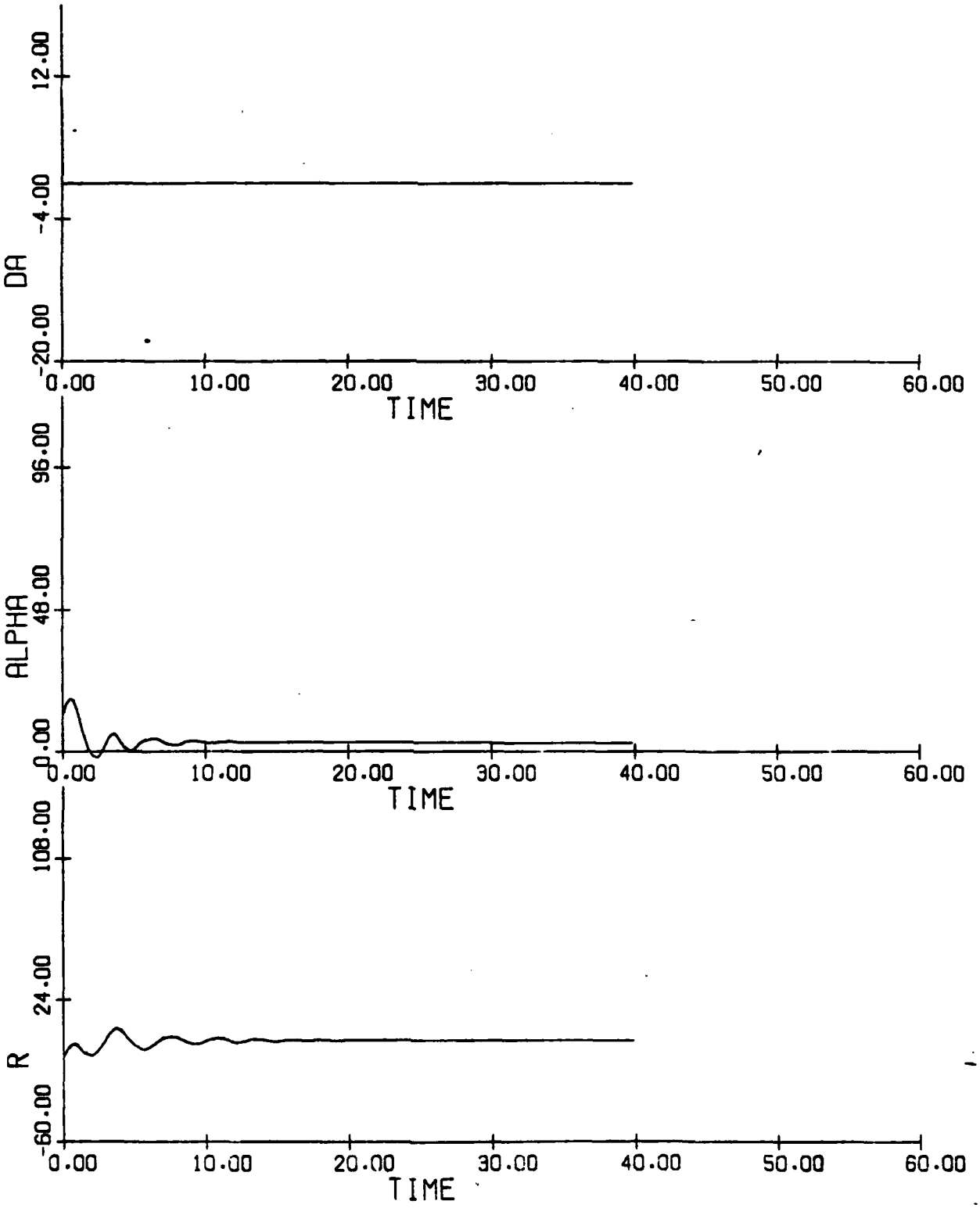

Figure 3.25(a): Aircraft F Time History, Spin Recovery Case 231; $\underline{\delta} = 0$

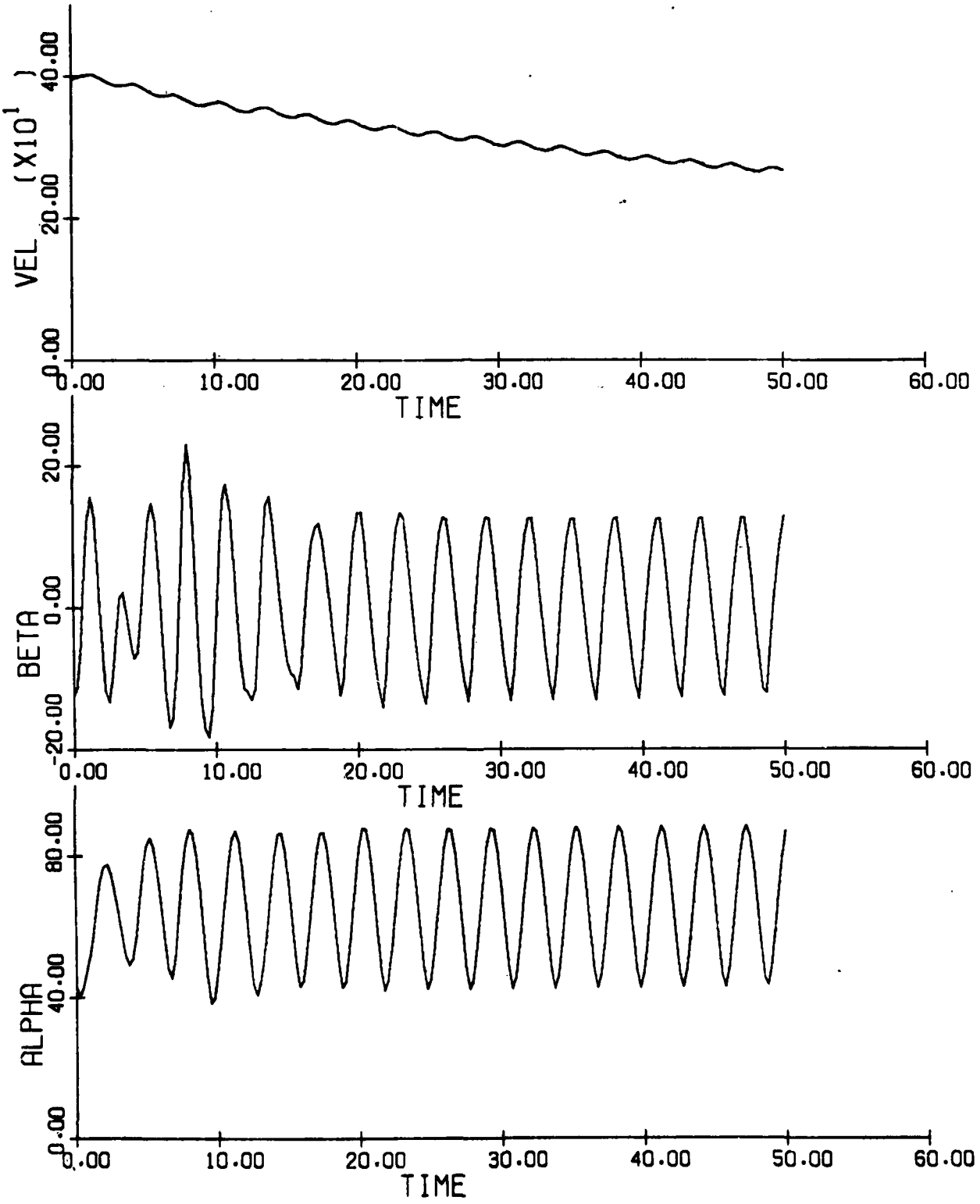

Figure 3.25(b) (concluded)

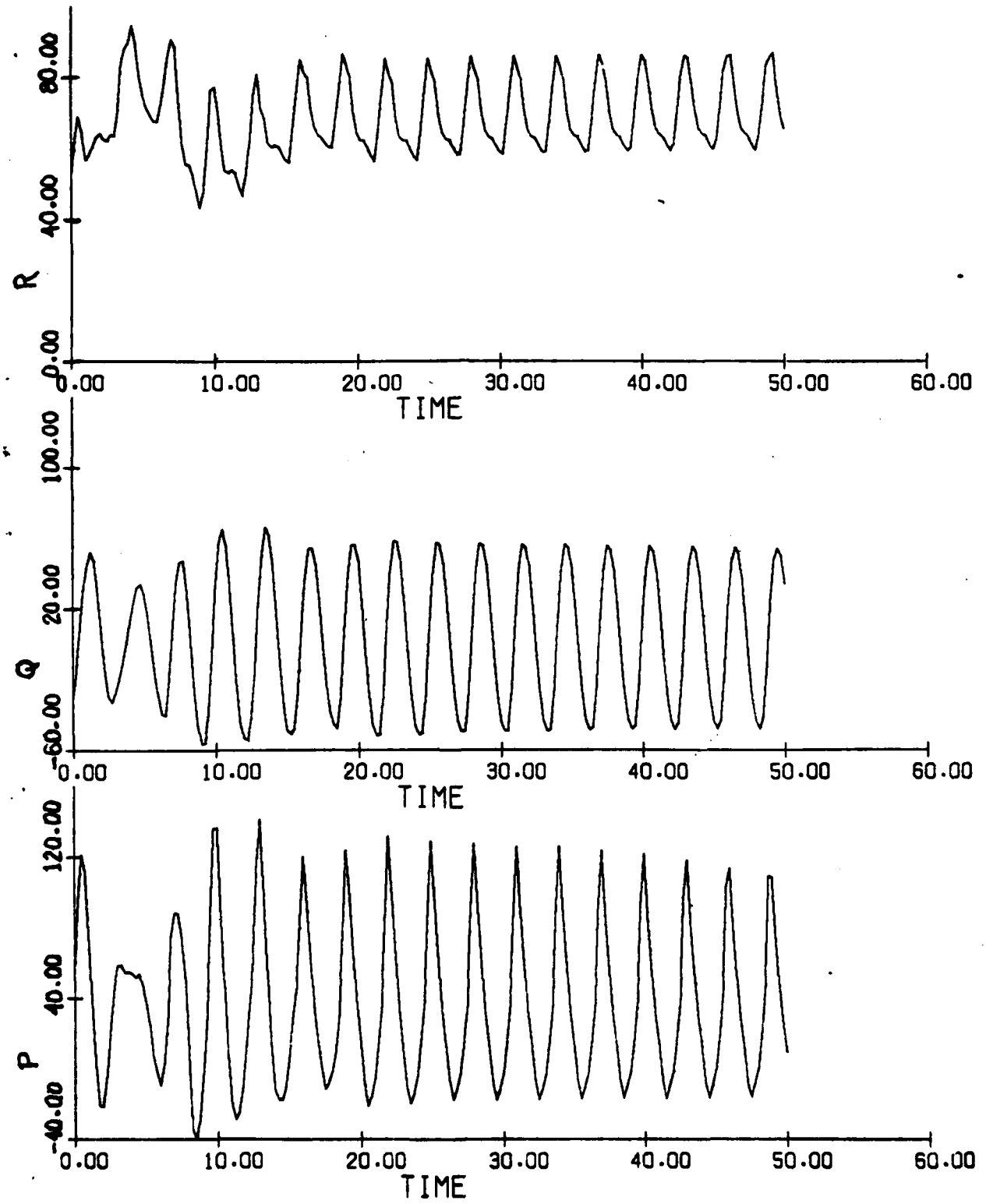

Figure 3.26(a): Aircraft F Time History, Spin Recovery Case 233; $\underline{\delta} = 0$

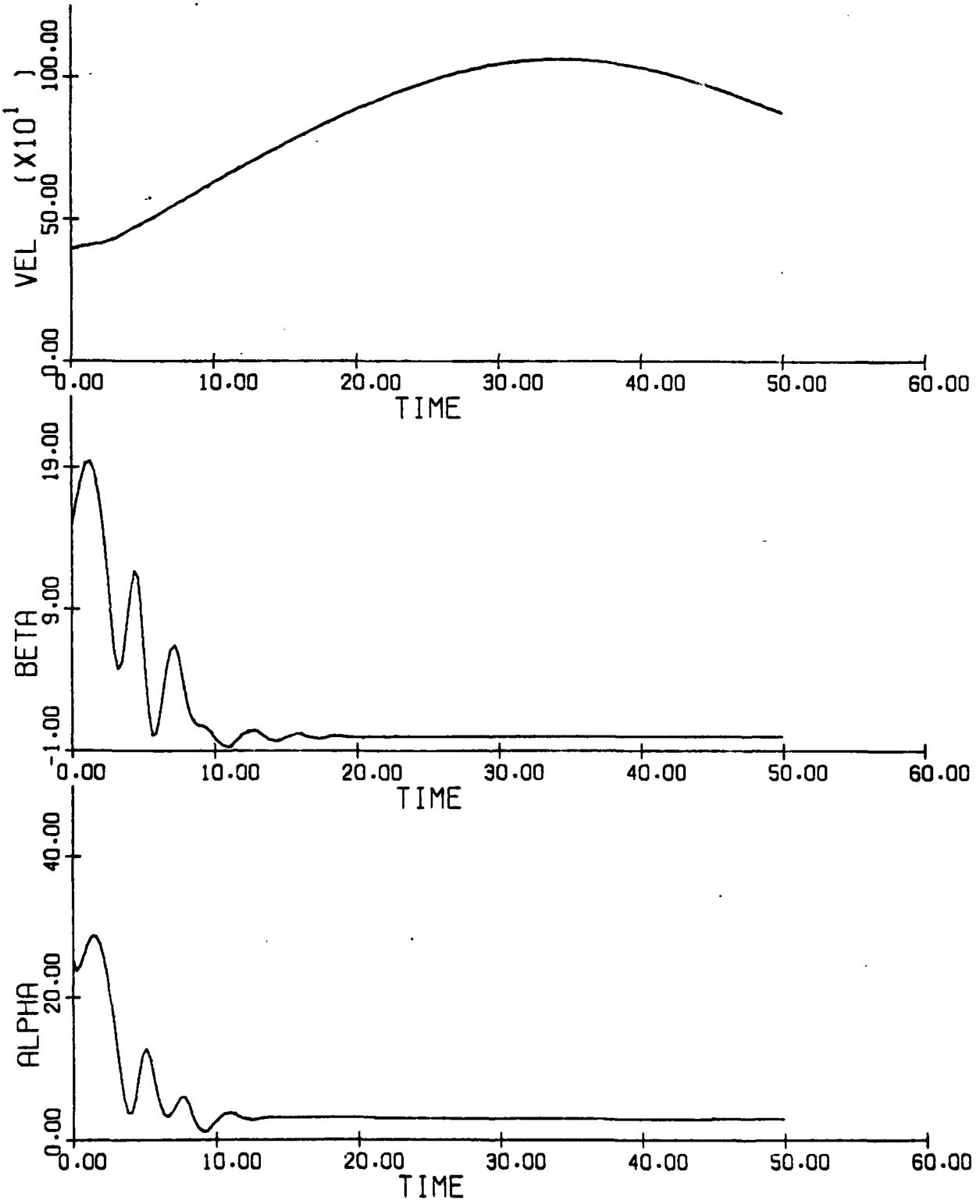

Figure 3.26(b) (concluded)

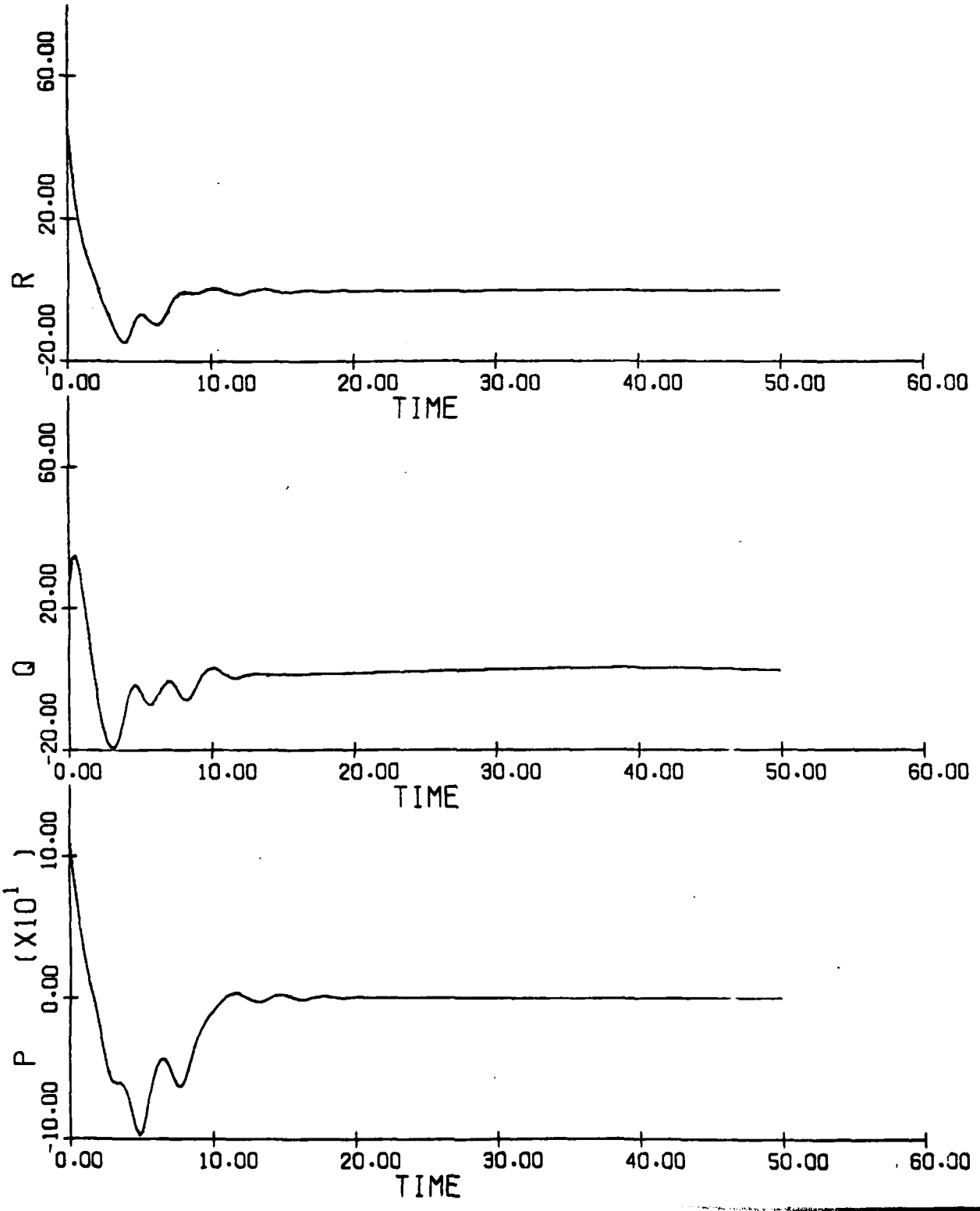

Figure 3.27(a): Aircraft F Spin Recovery Time History, Case 234; $\underline{\delta} = 0$

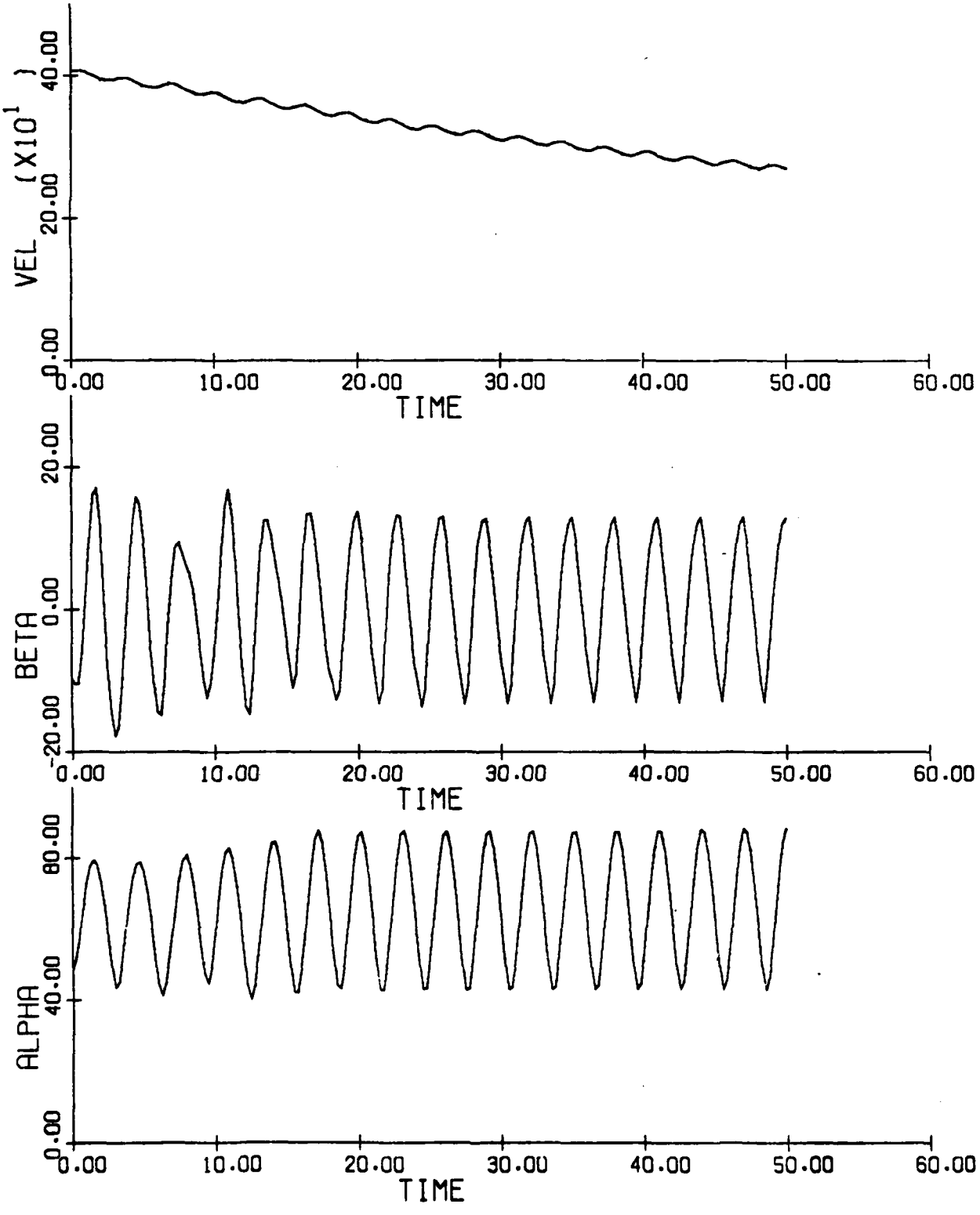

Figure 3.27(b) (concluded)

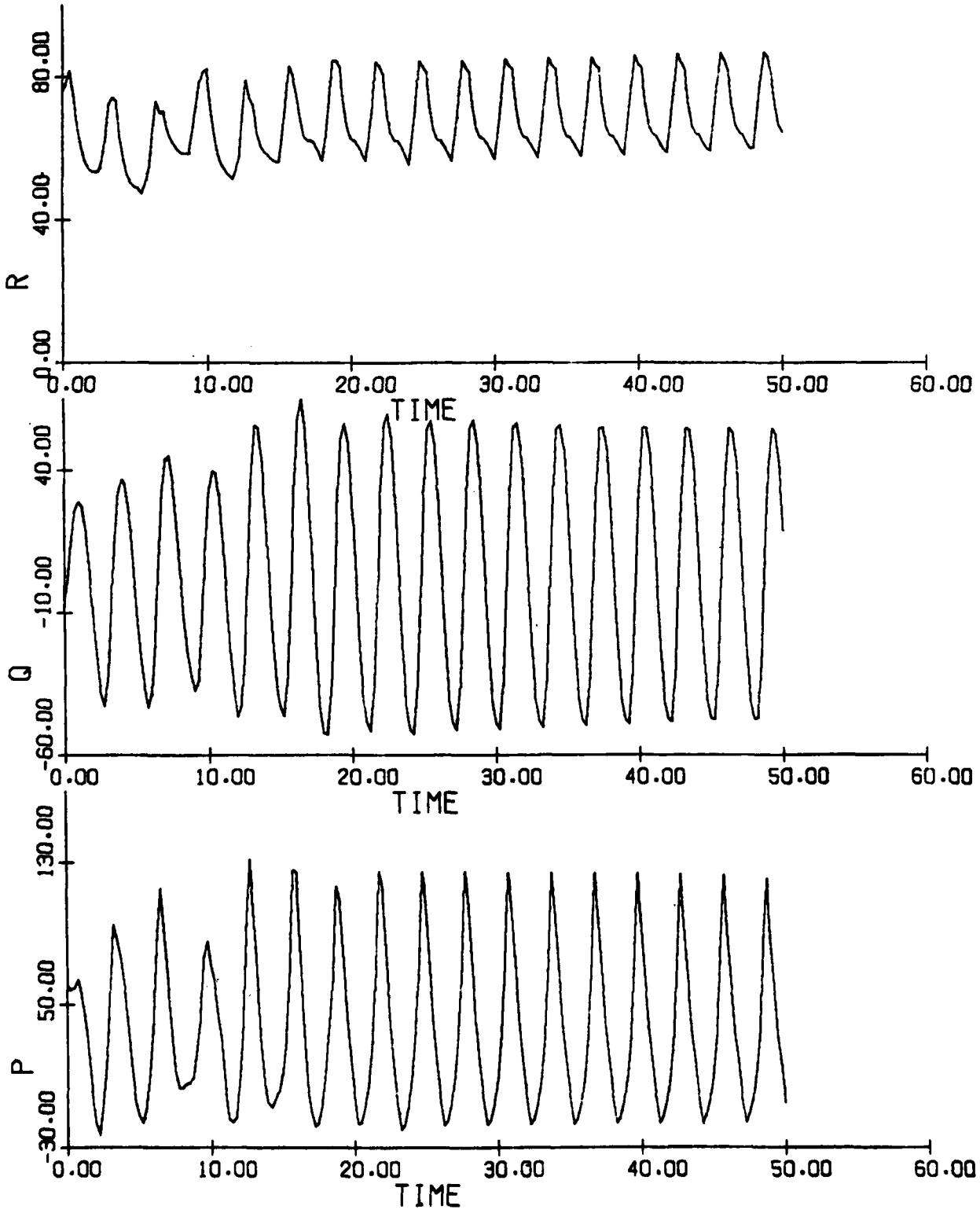

Figure 3.28(a): Aircraft F Time History, Spin Recovery Case 236; $\underline{\delta} = 0$

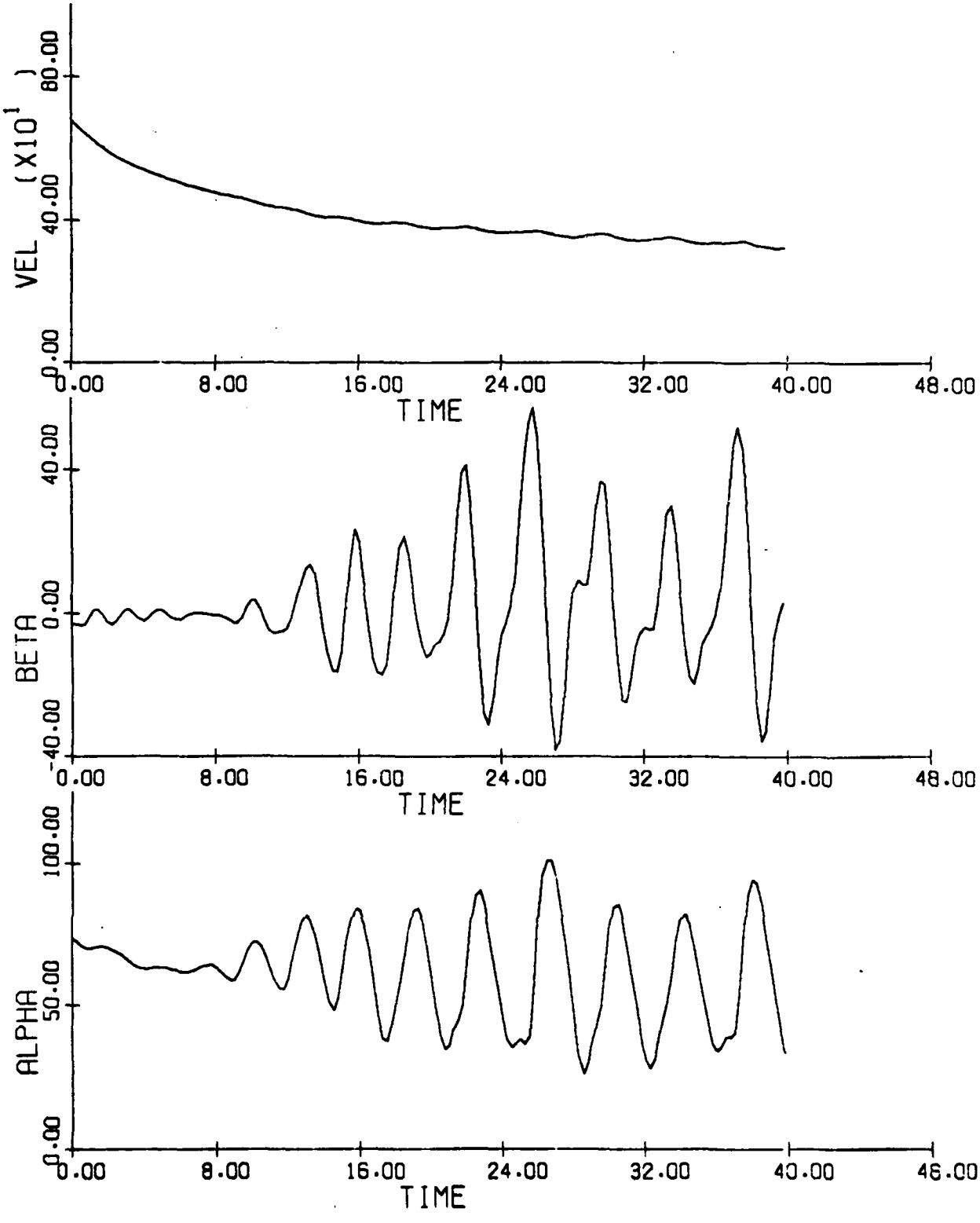

Figure 3.28(b) (concluded)

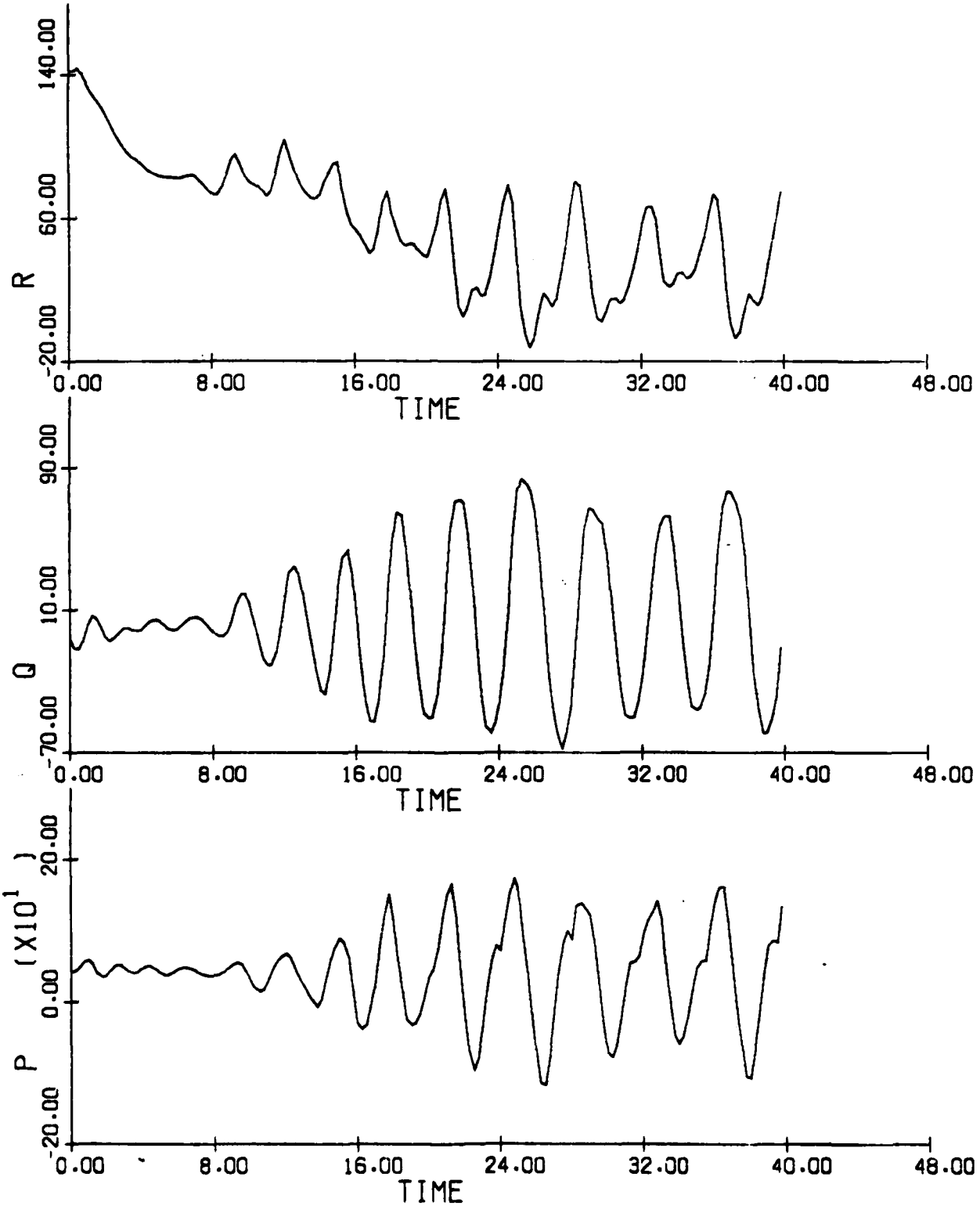

Figure 3.29(a): Aircraft F Time History, Spin Recovery Case 237

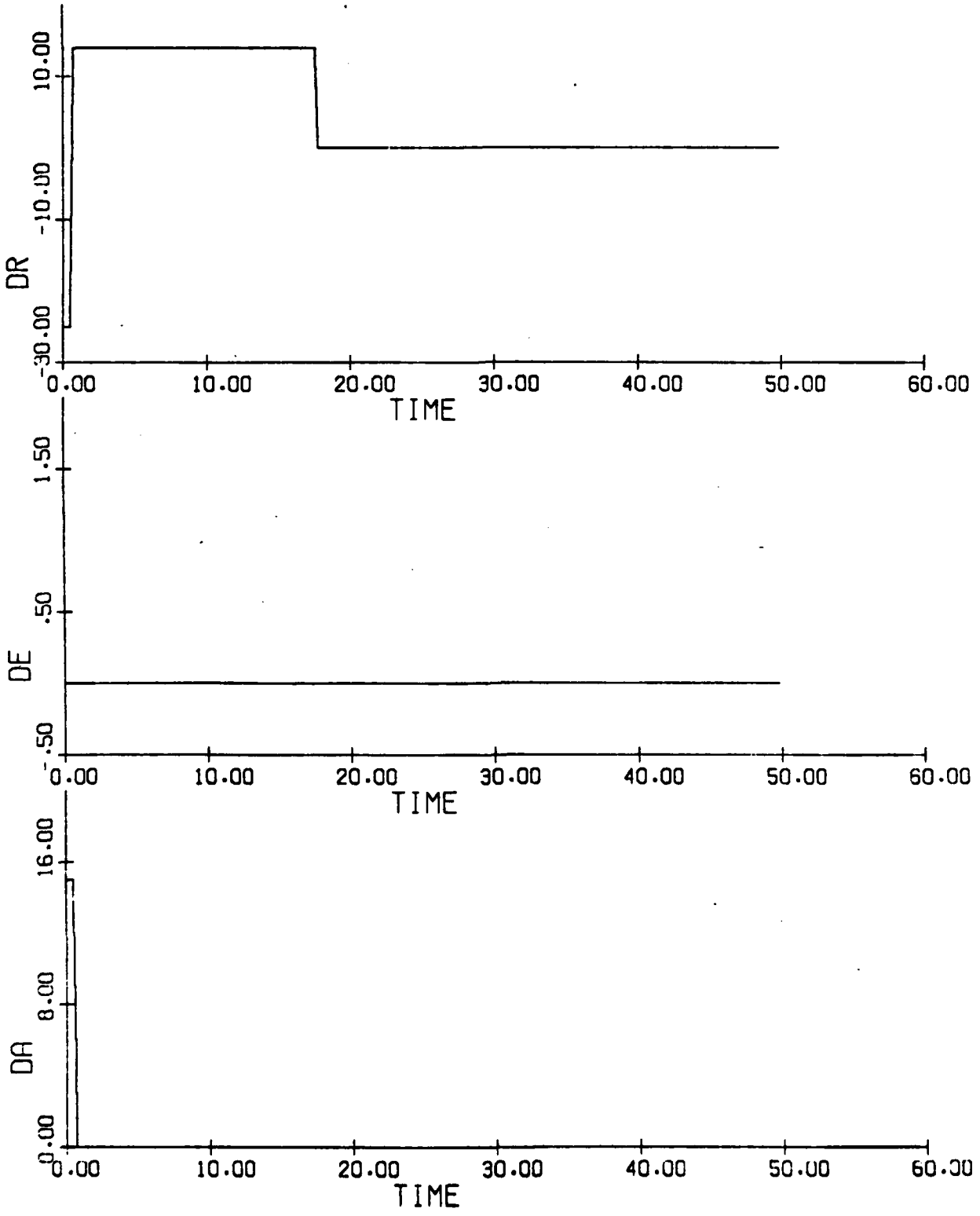

Figure 3.29(b) (cont.)

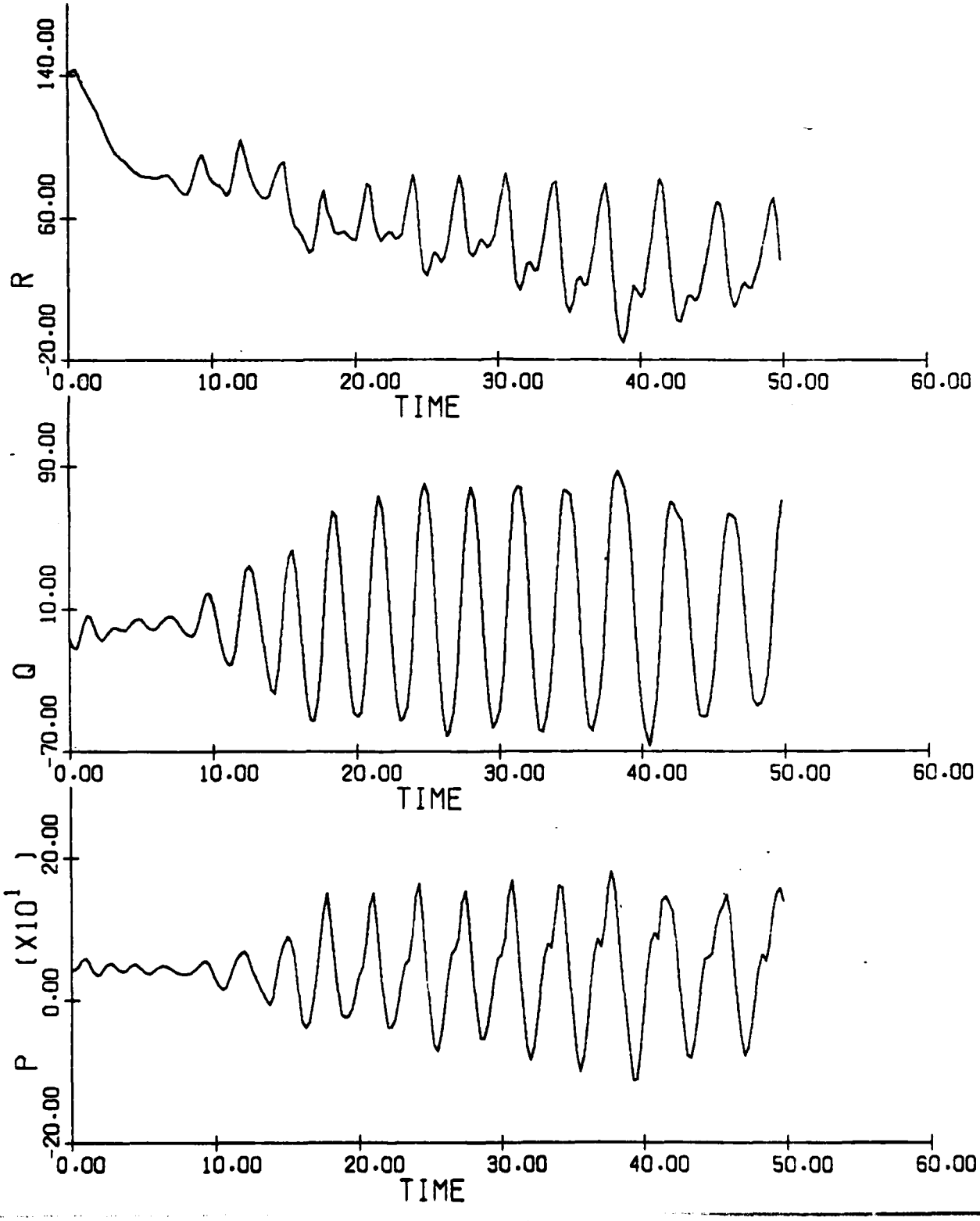

Figure 3.29(c) (concluded)

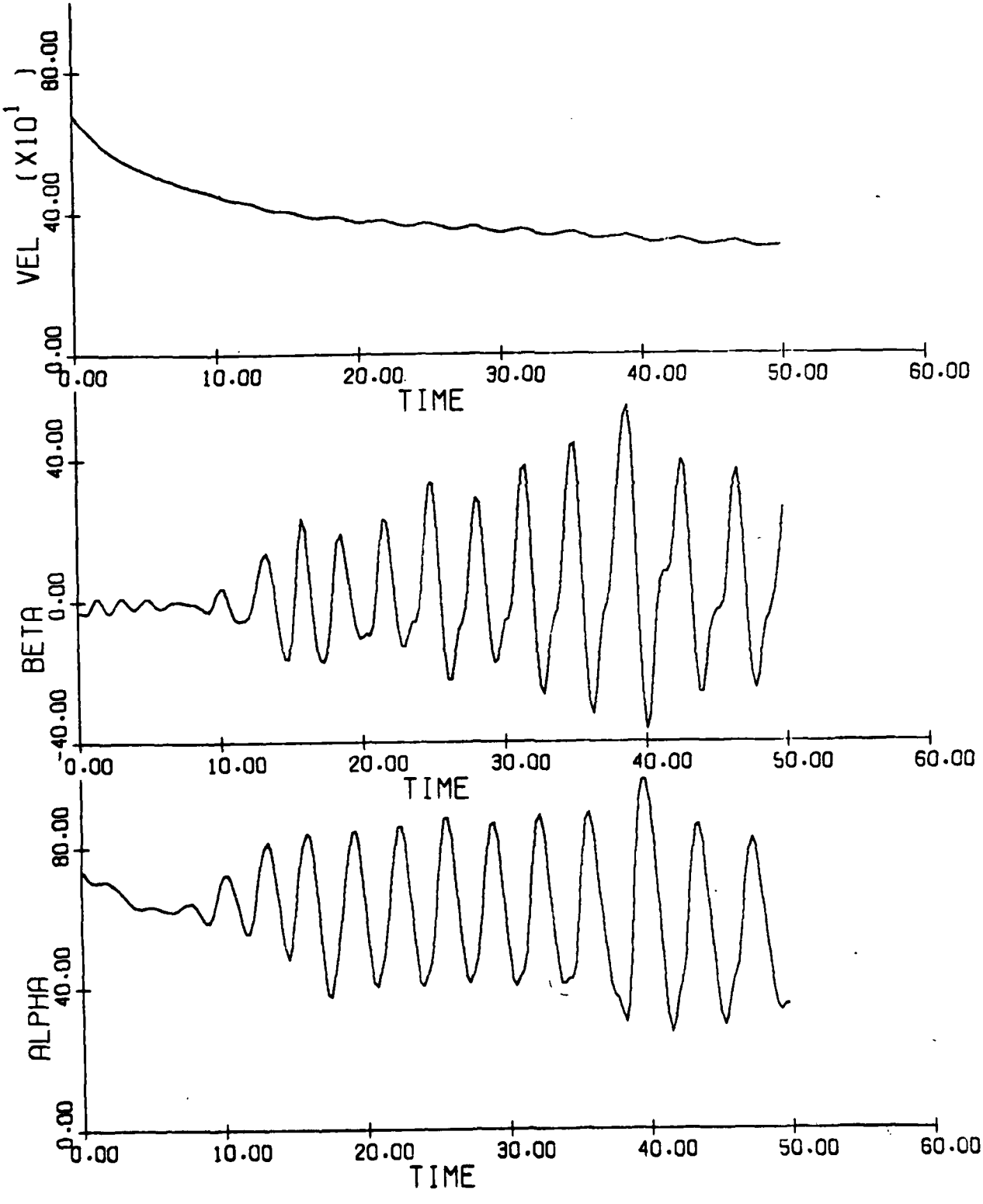

Figure 3.30(a): Aircraft F Time History, Spin Recovery Case 242

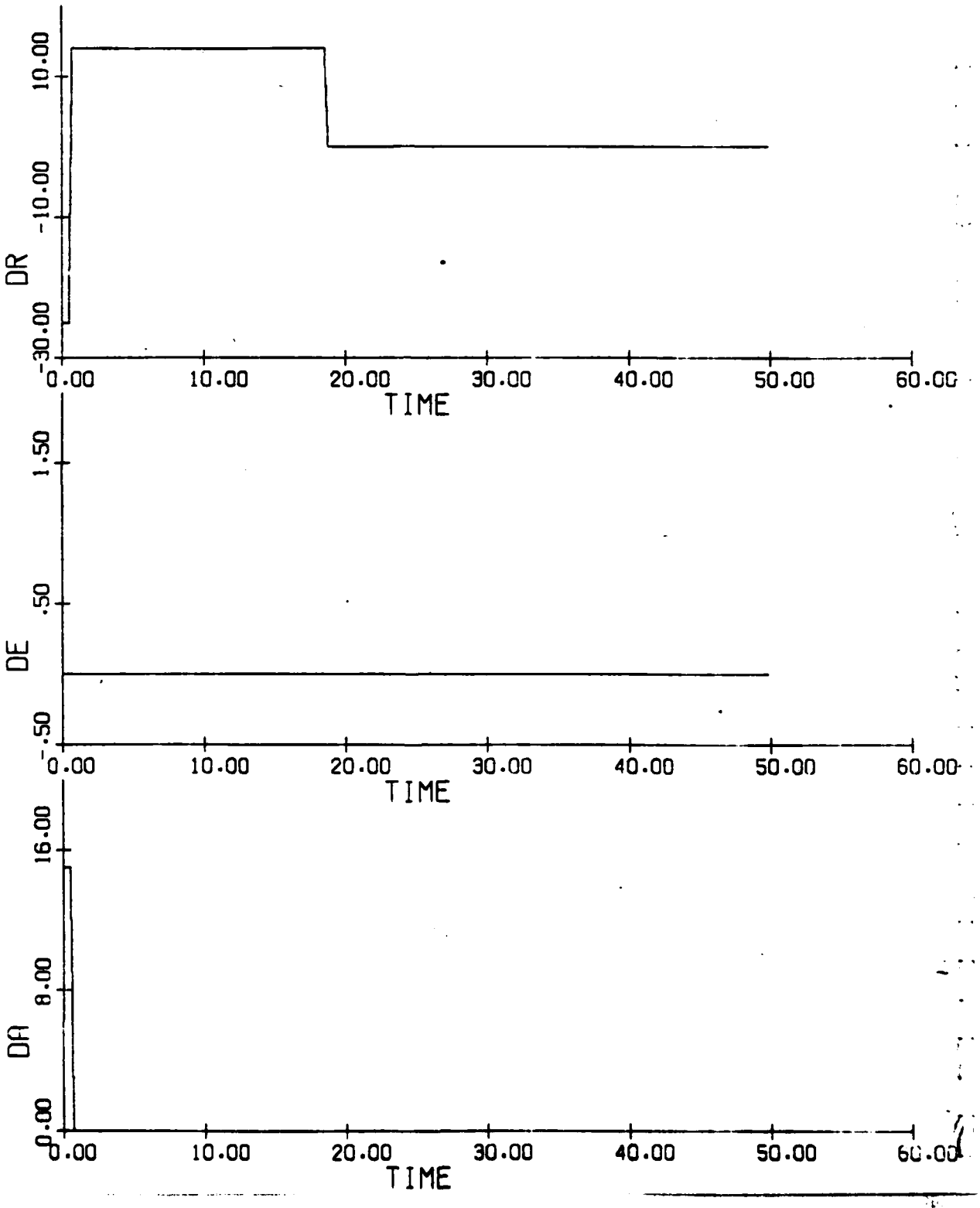

Figure 3.30(b) (cont.)

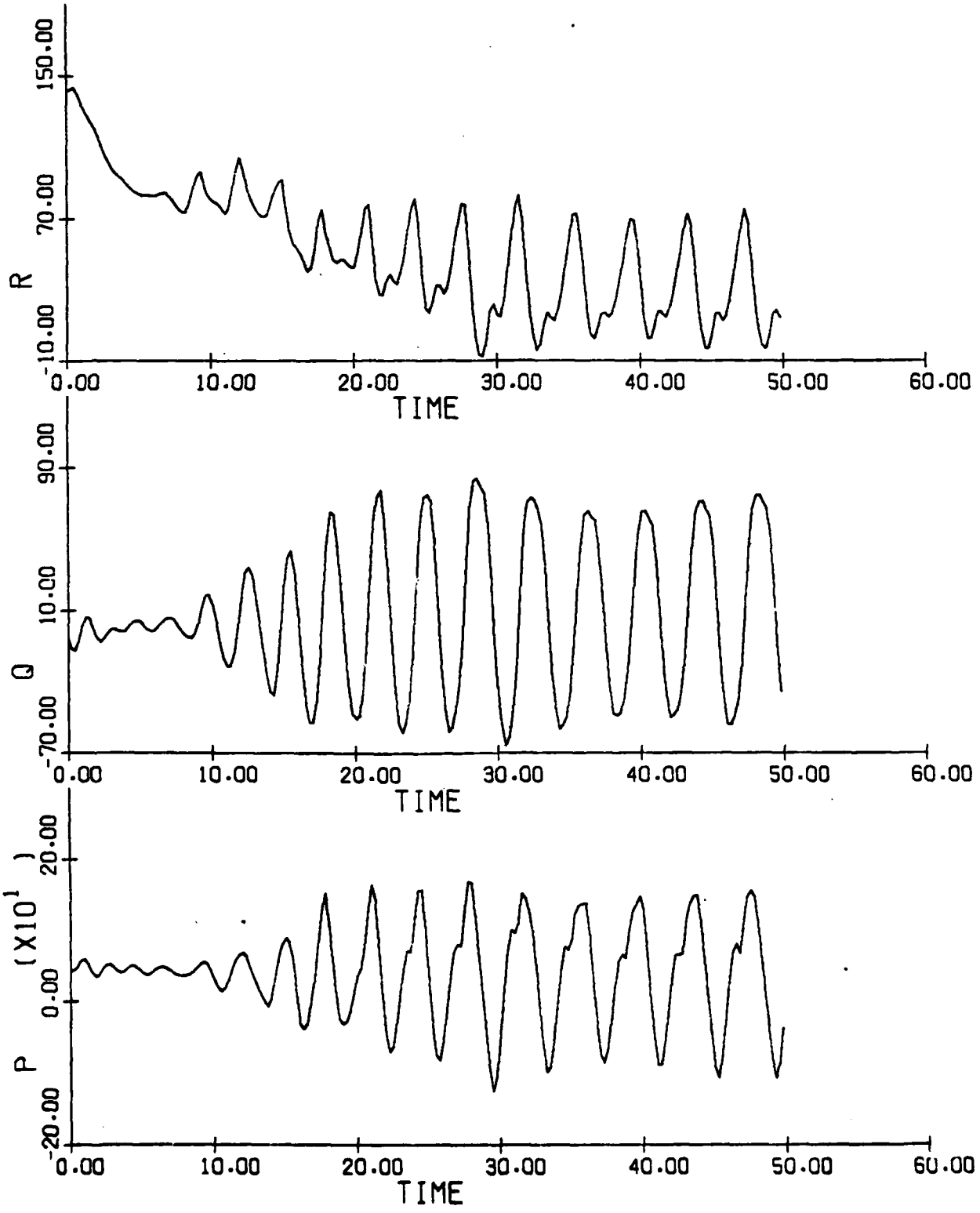

Figure 3.30(c) (concluded)

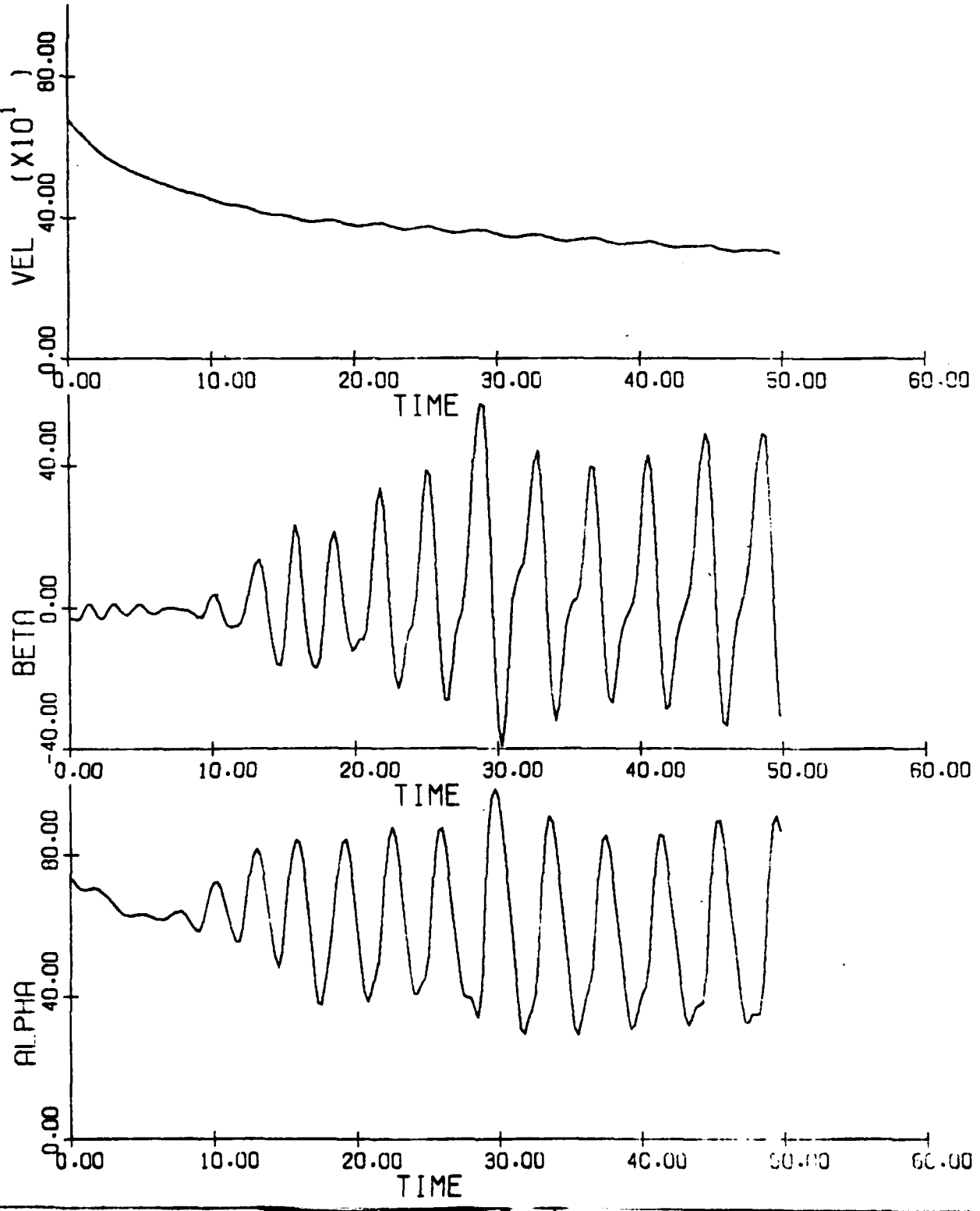

Figure 3.31(a): Aircraft F Time History, Spin Recovery Case 240; $\underline{\delta} = 0$

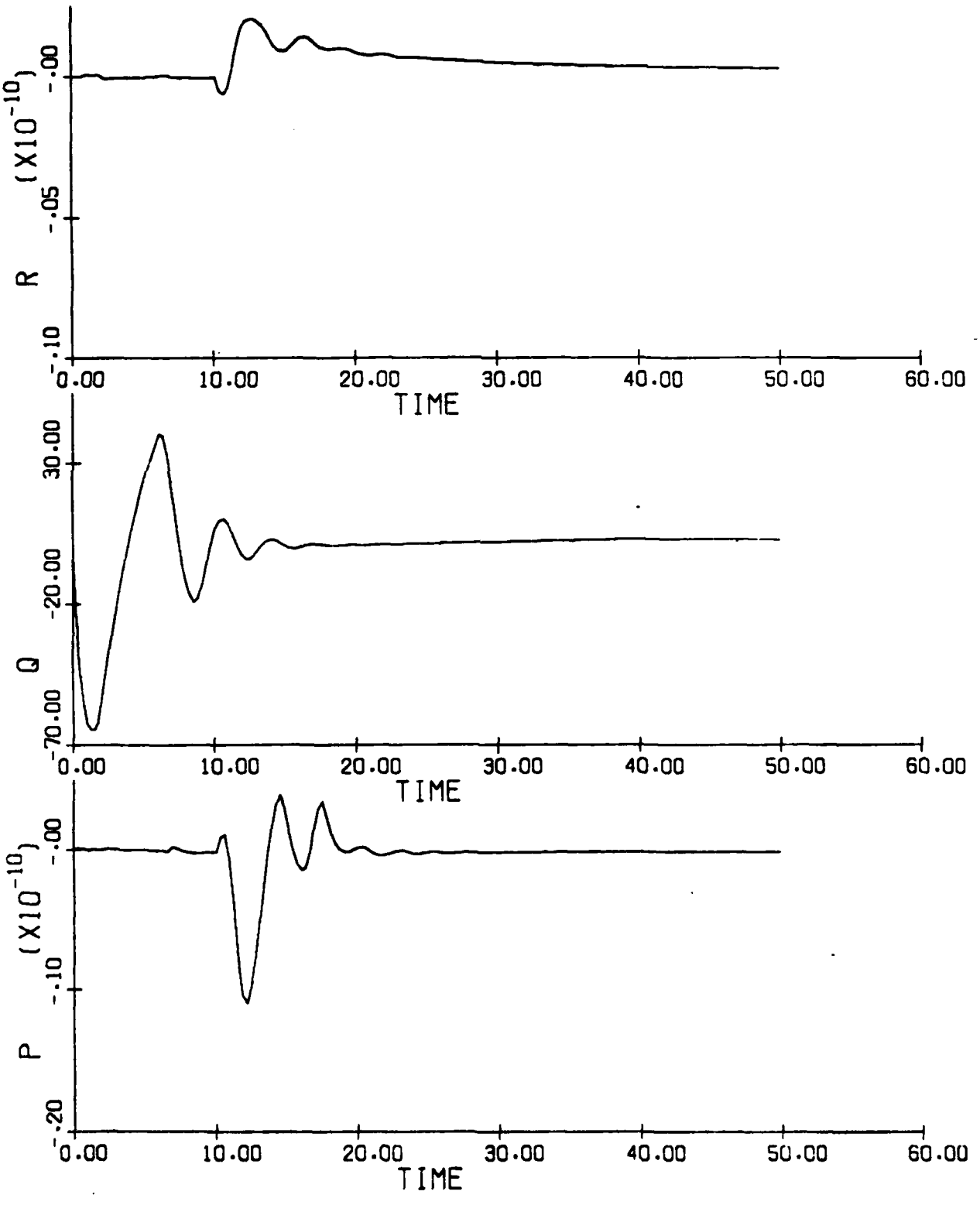

Figure 3.31(b) (concluded)

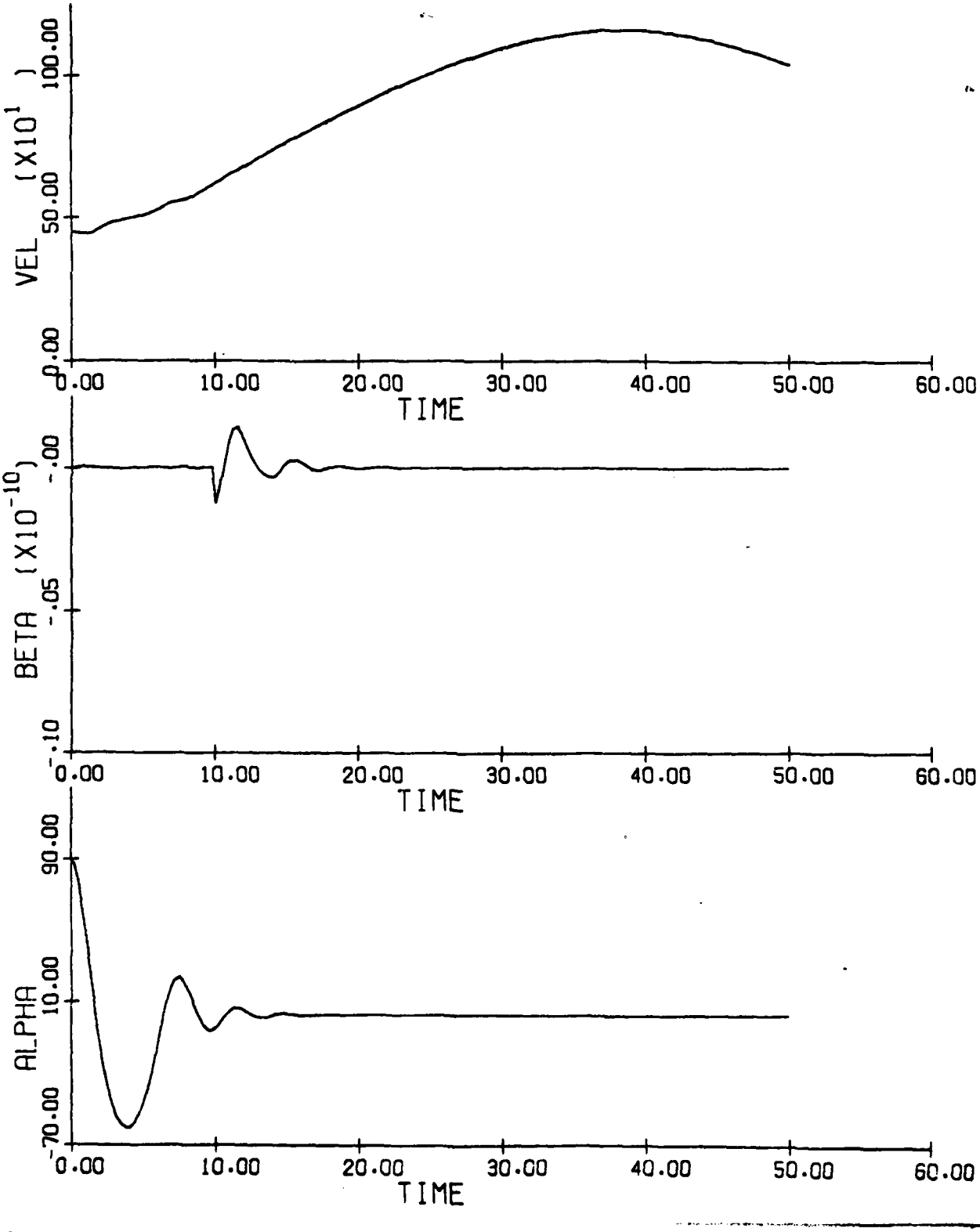

Figure 3.32(a): Aircraft F Spin Reversal

$(p_0, q_0, r_0, \alpha_0, \beta_0, V_0, \theta_0, \phi_0)$ = (35., 16.8, 67.2, 62.1, -0.5, 450., 0., 0.)

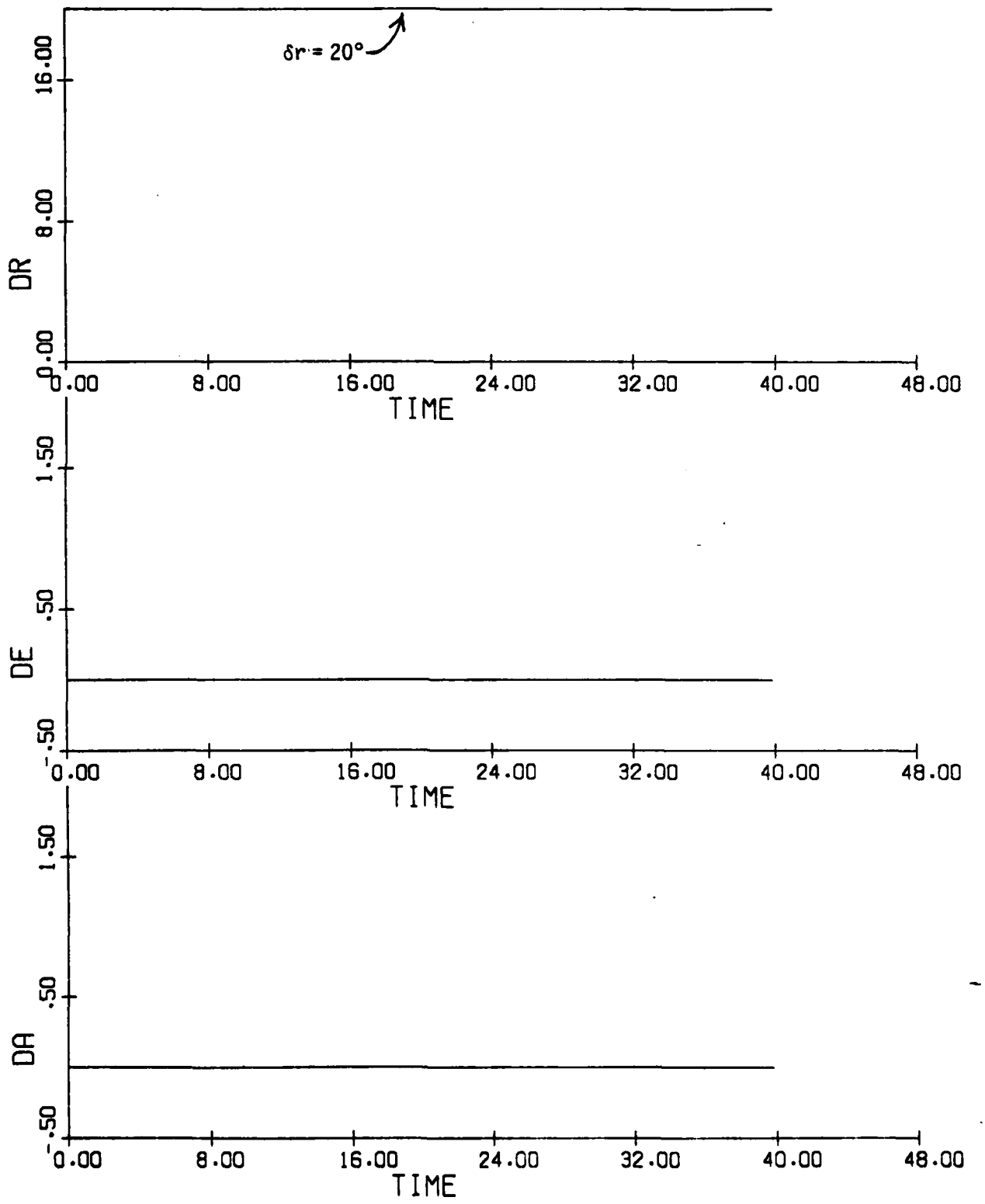

Figure 3.32(b) (cont.)

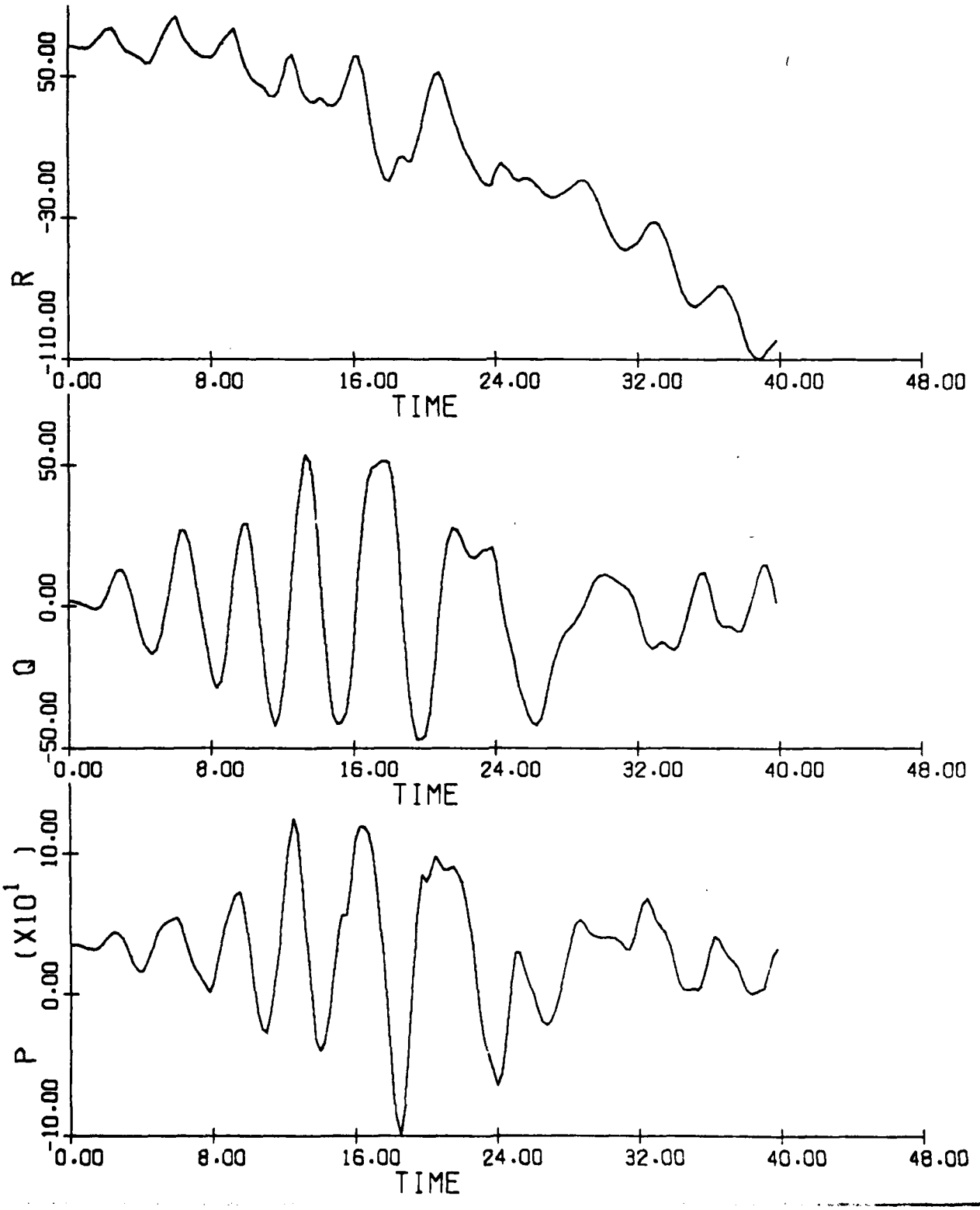

Figure 3.32(c) (cont.)

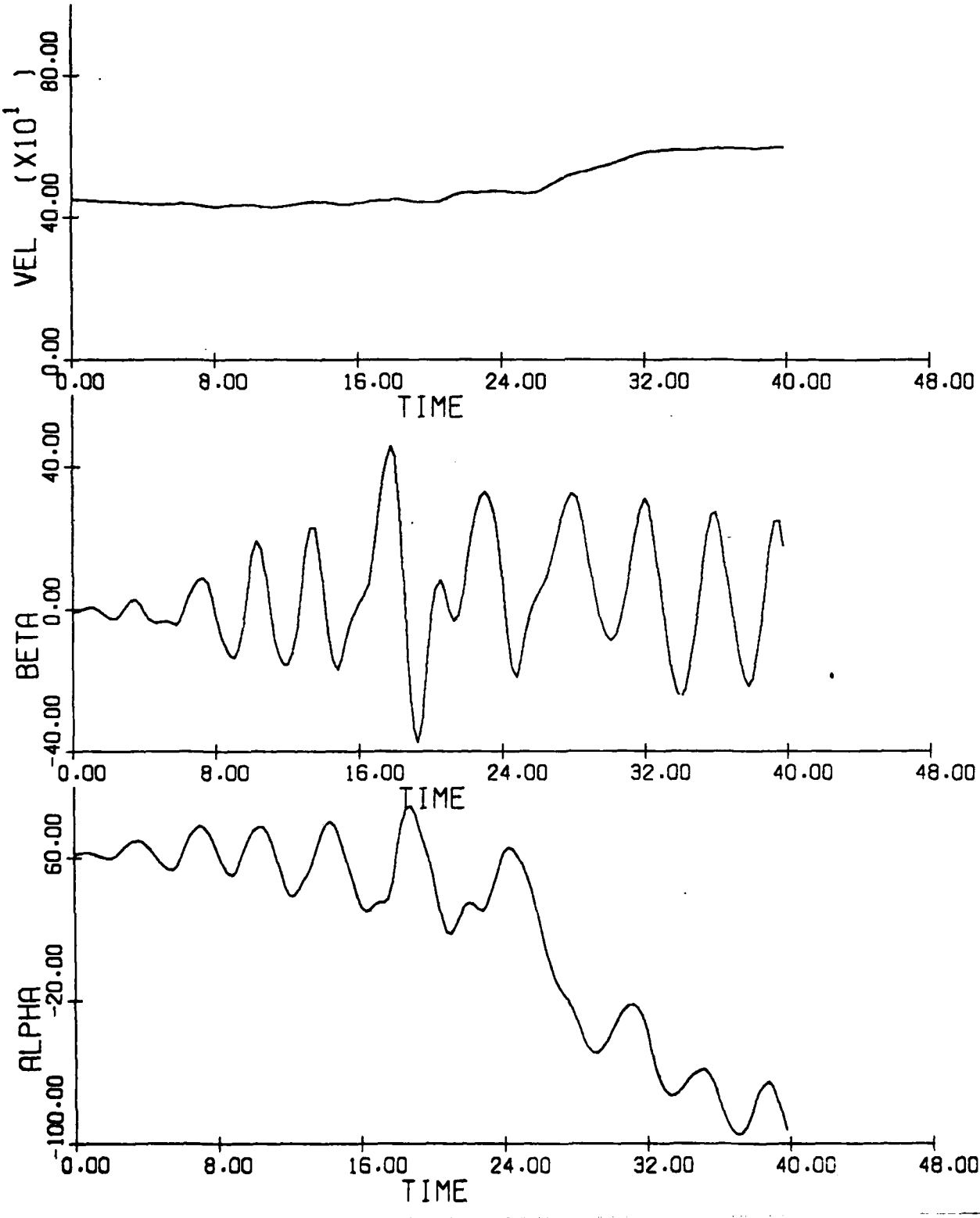

Figure 3.32(d) (cont.)

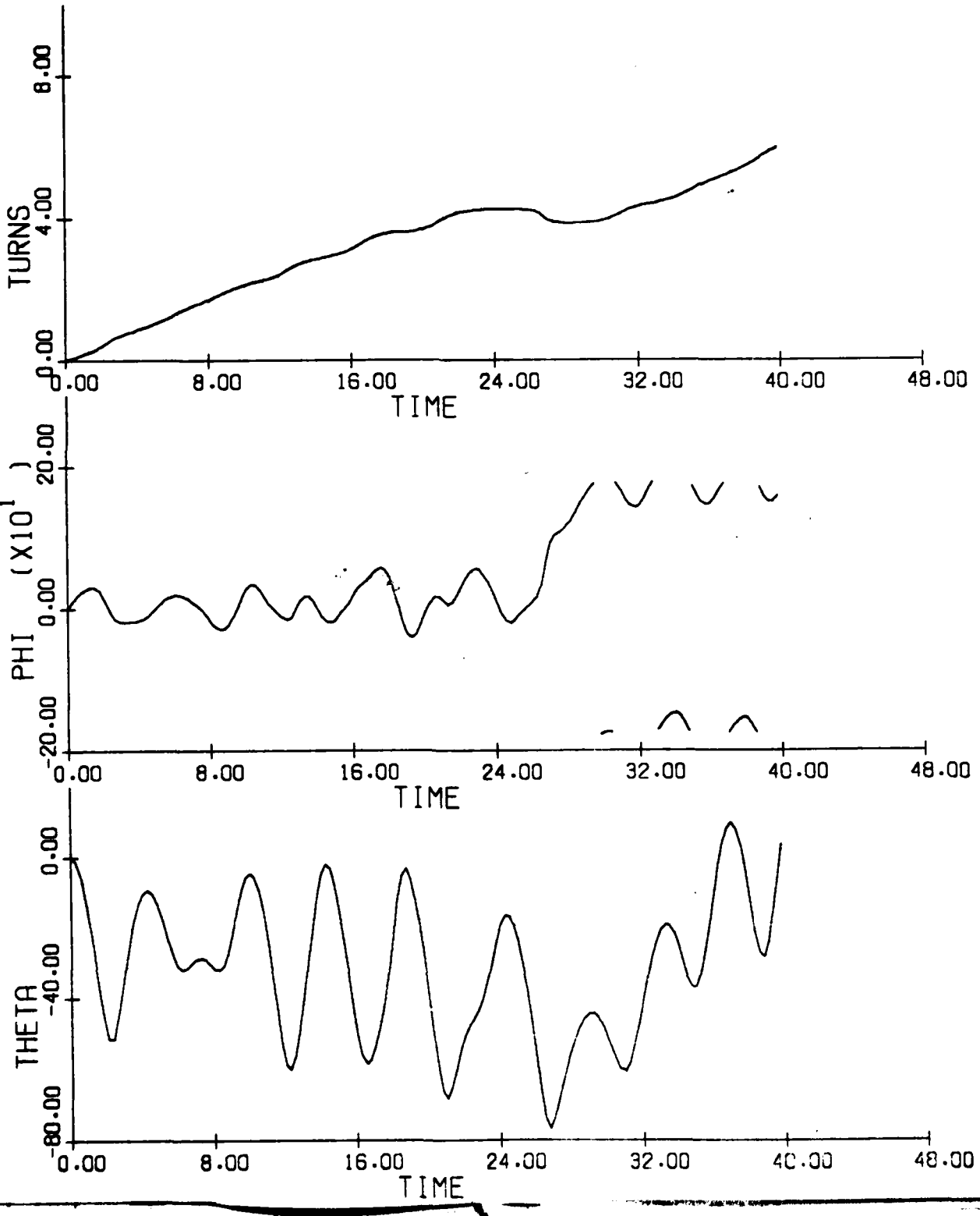

Figure 3.32(e) (cont.)

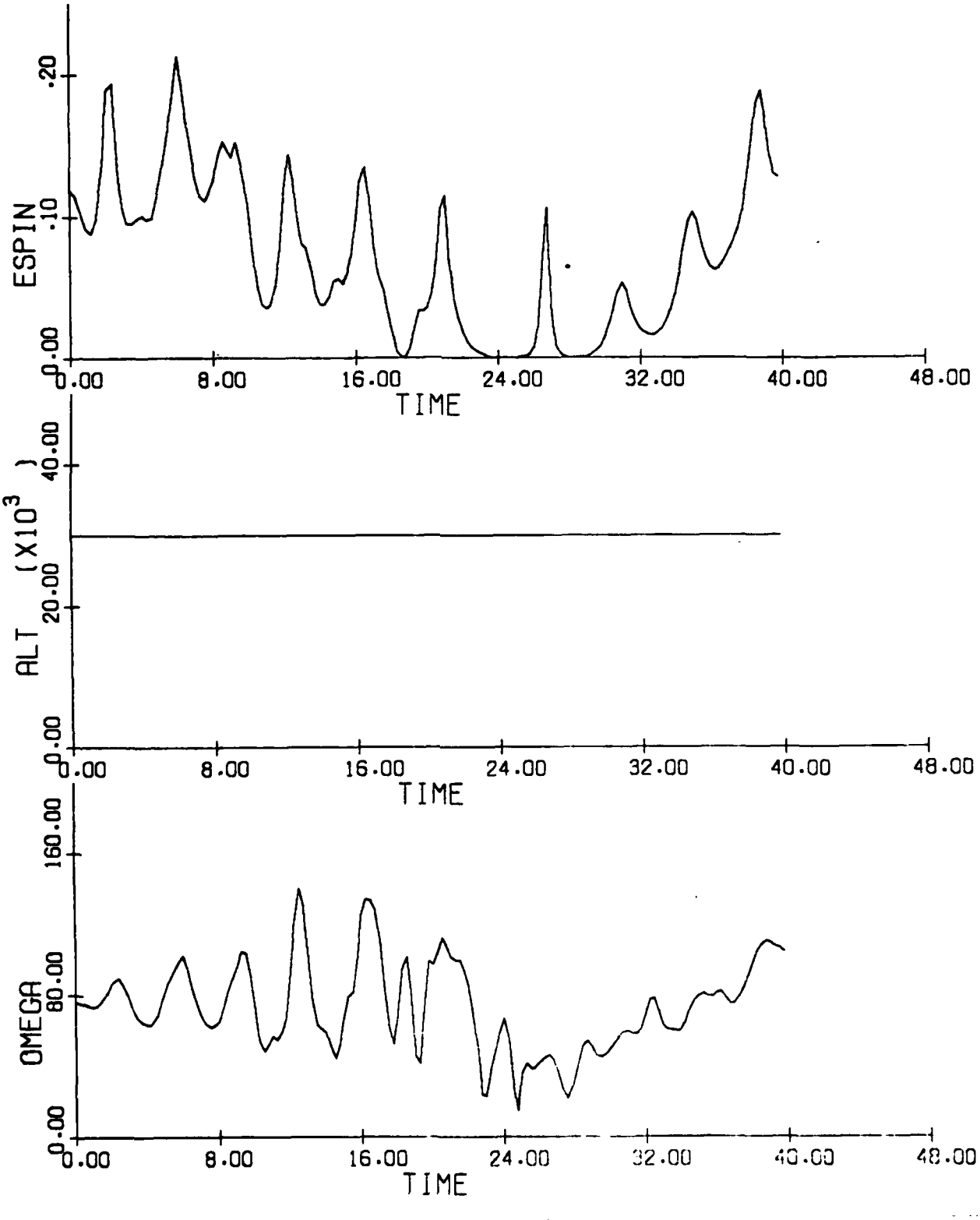

Figure 3.32(f) (cont.)

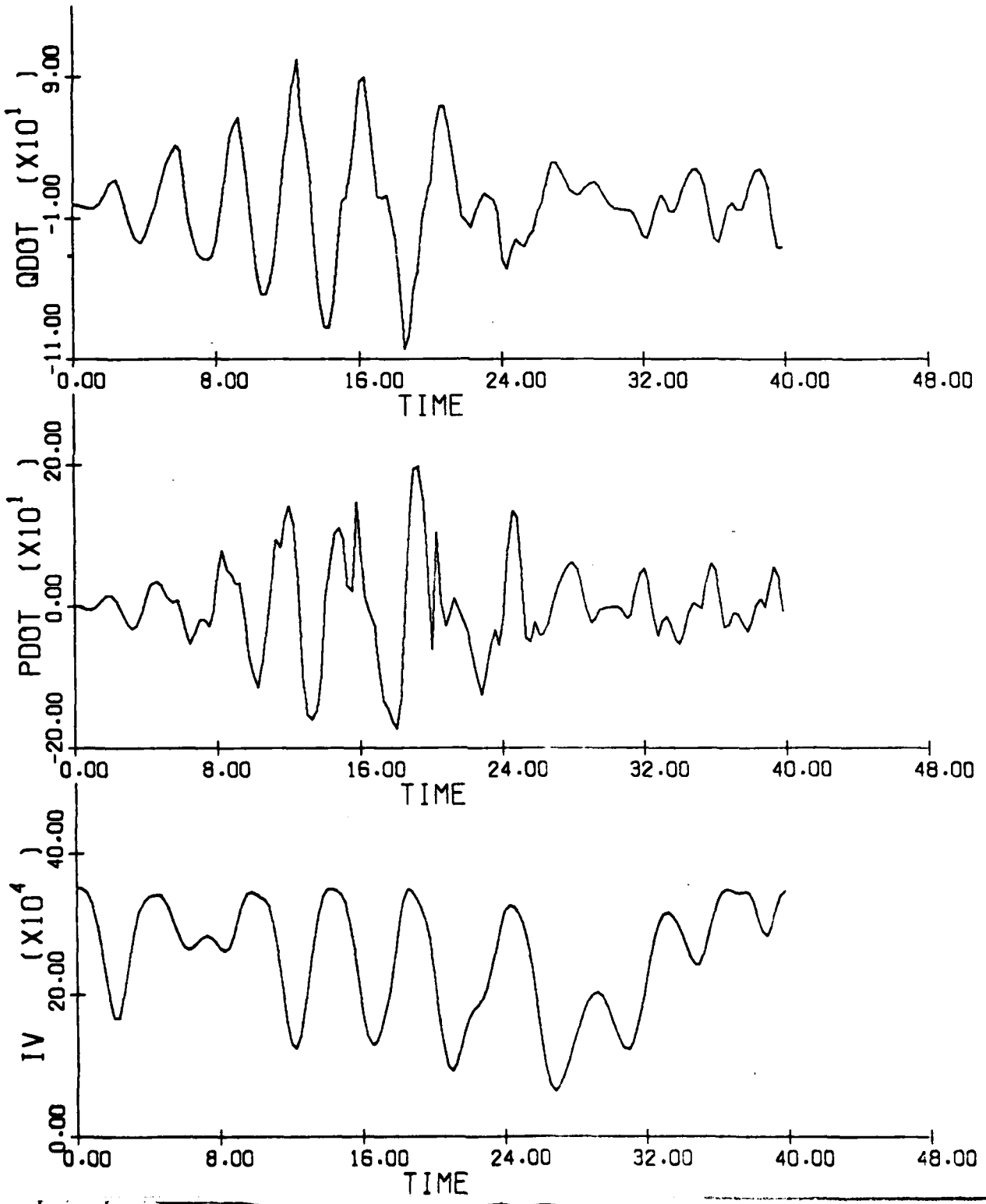

Figure 3.32(g) (concluded)

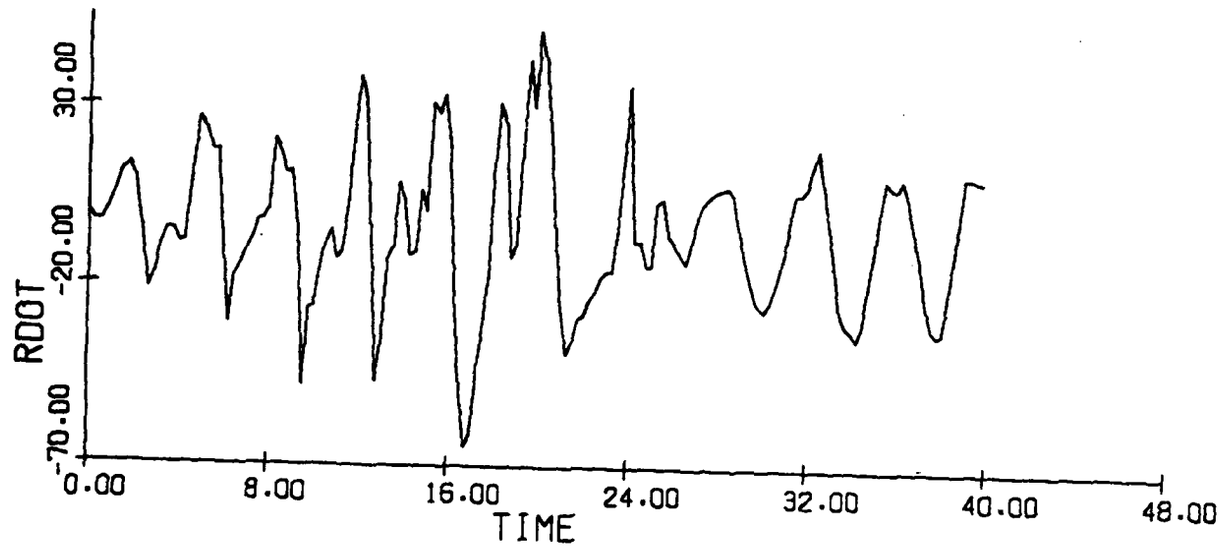

Figure 3.33(a): Aircraft F Spin Reversal

$(p_0, q_0, r_0, \alpha_0, \beta_0, V_0, \theta_0, \phi_0)$ = (35., 16.8, 67.2, 62.1, -0.5, 450., -50., -40.)

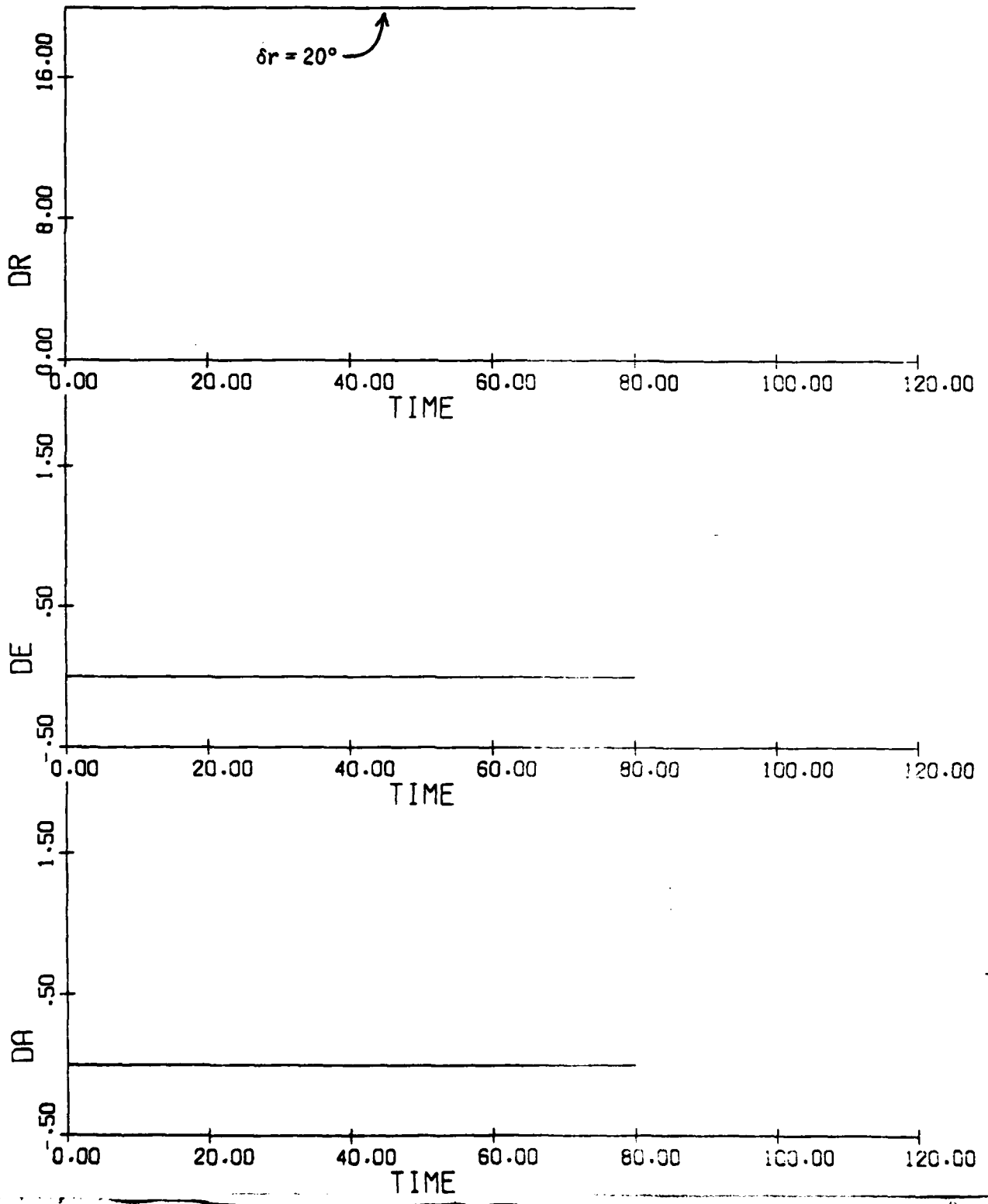

Figure 3.33(b) (cont.)

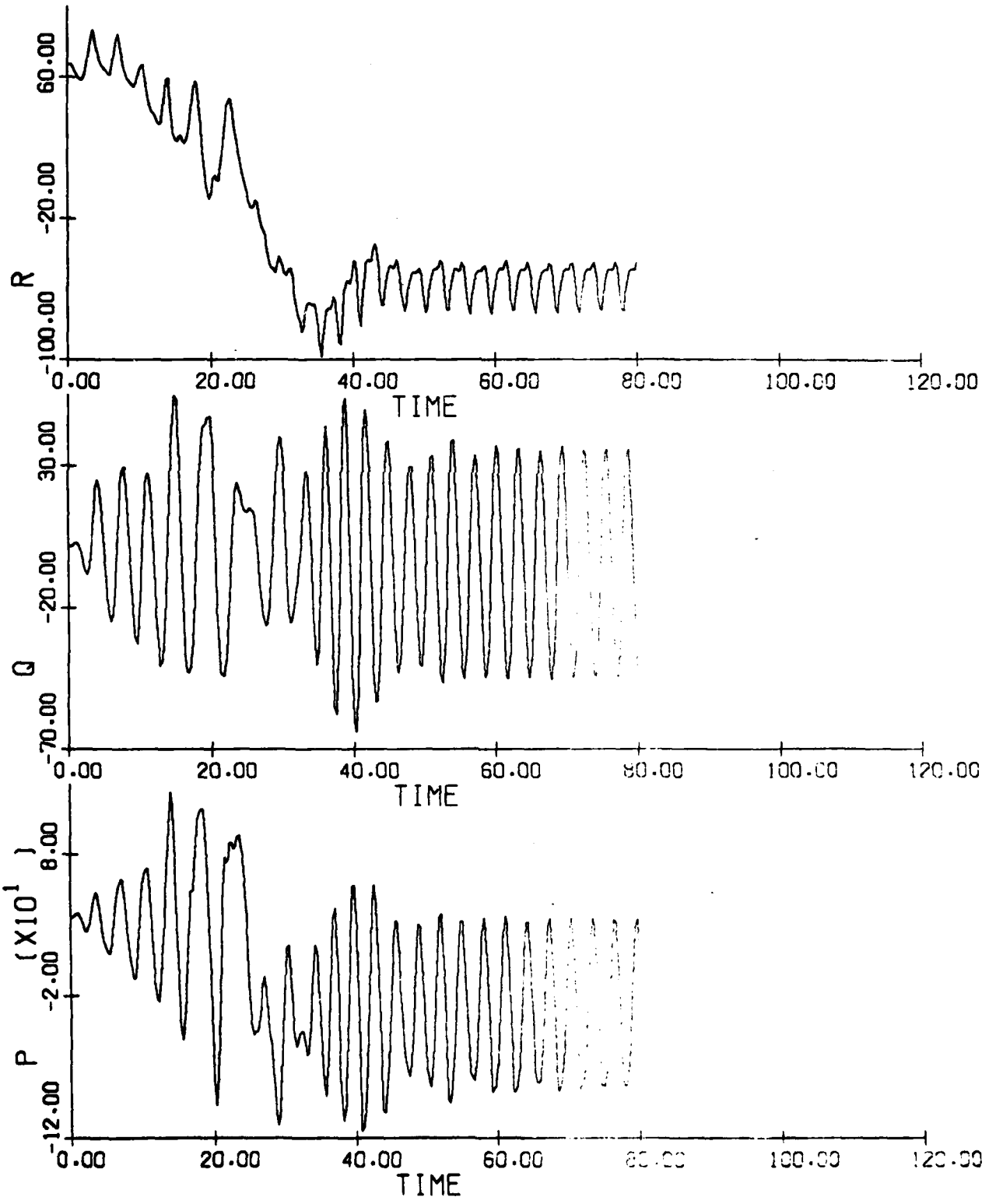

Figure 3.33(c) (cont.)

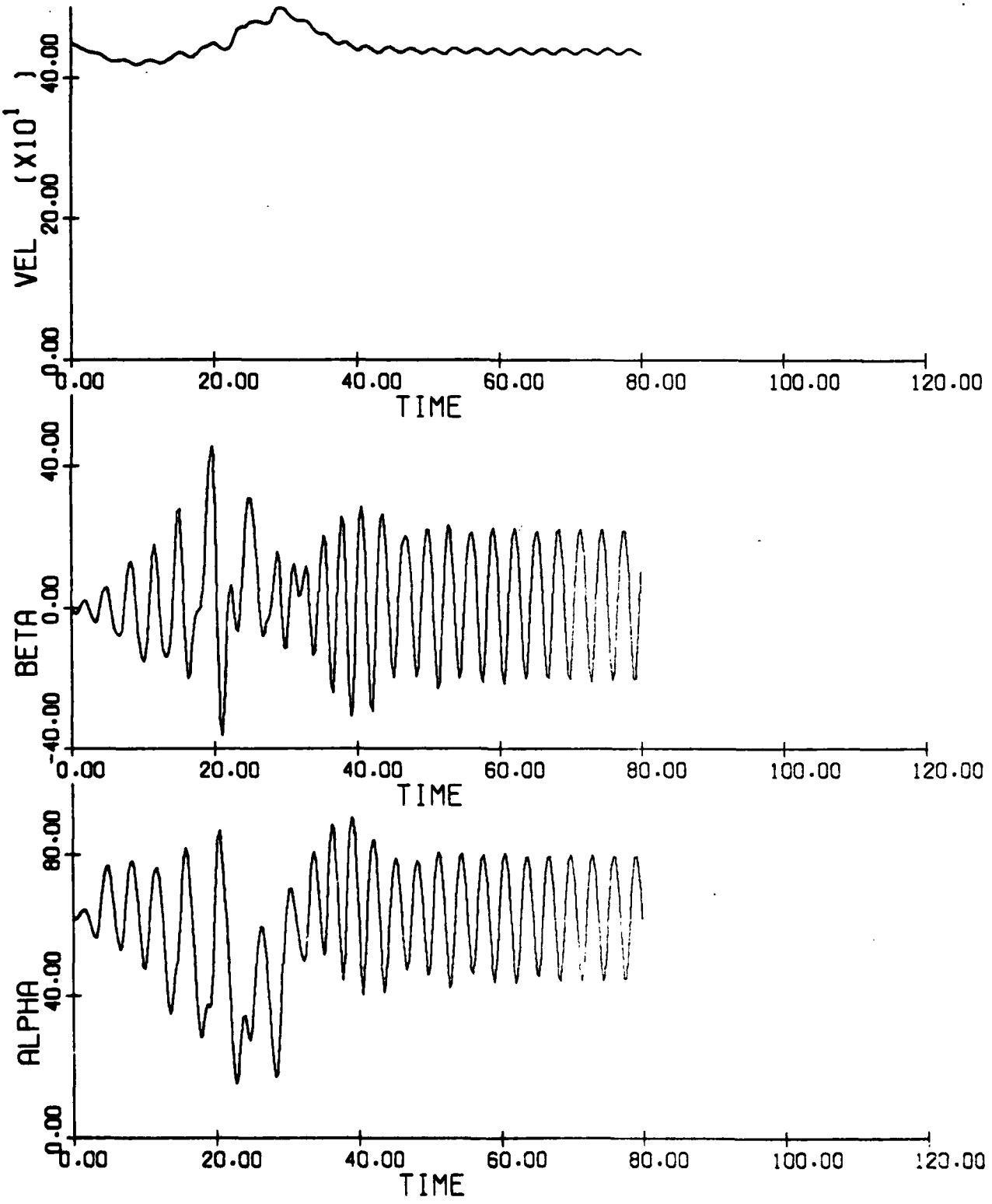

Figure 3.33(d) (cont.)

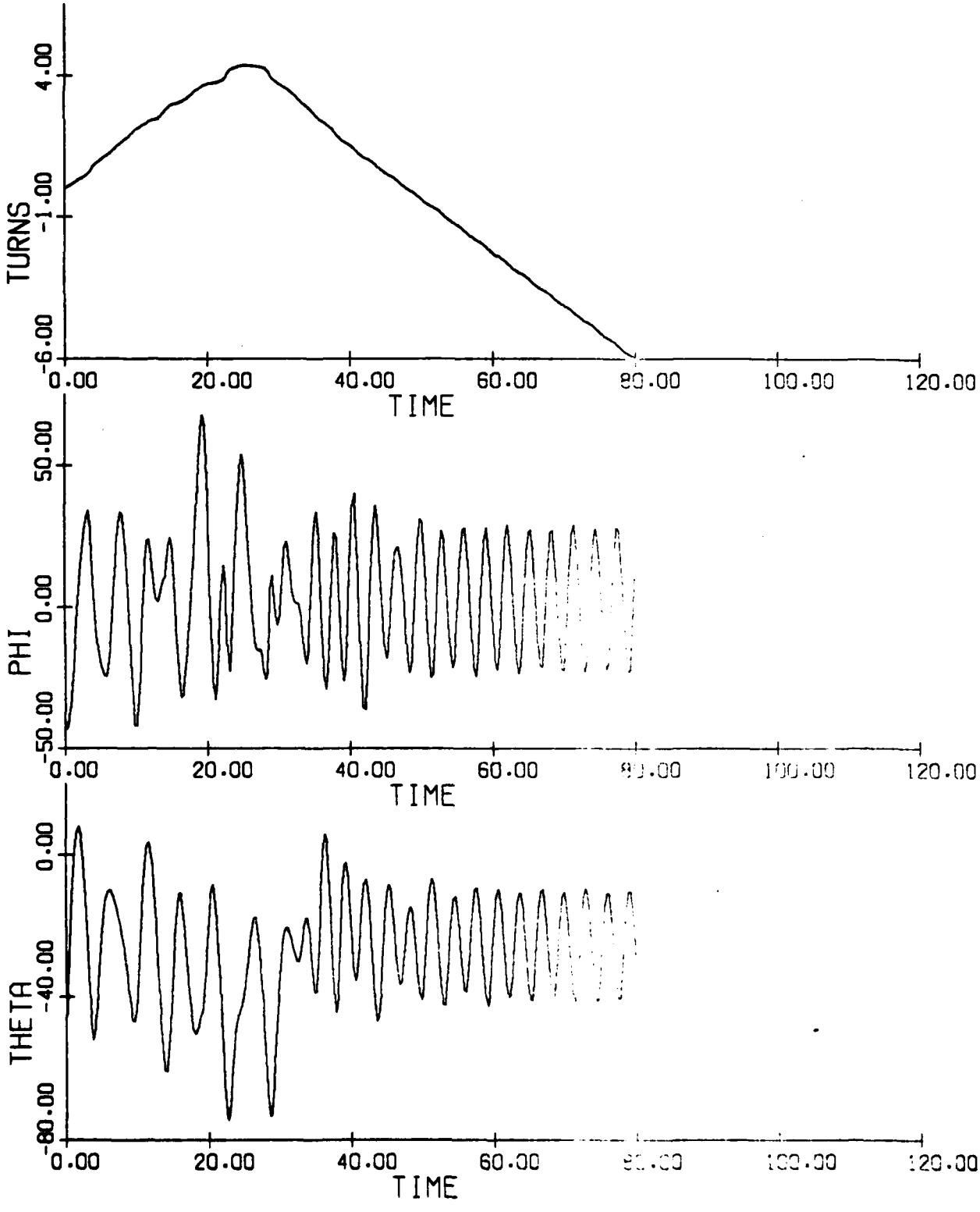

Figure 3.33(e) (cont.)

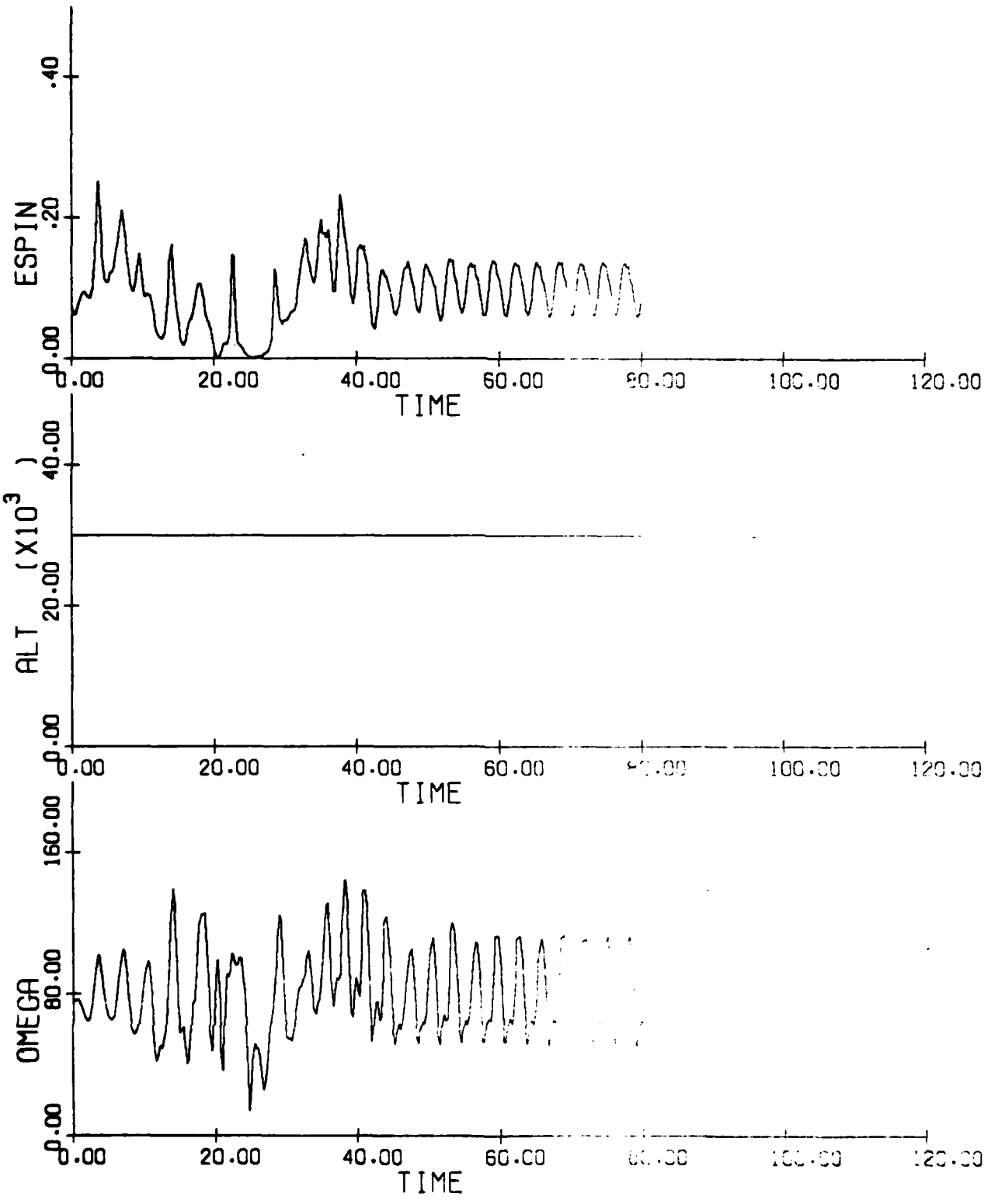

Figure 3.33(f) (cont.)

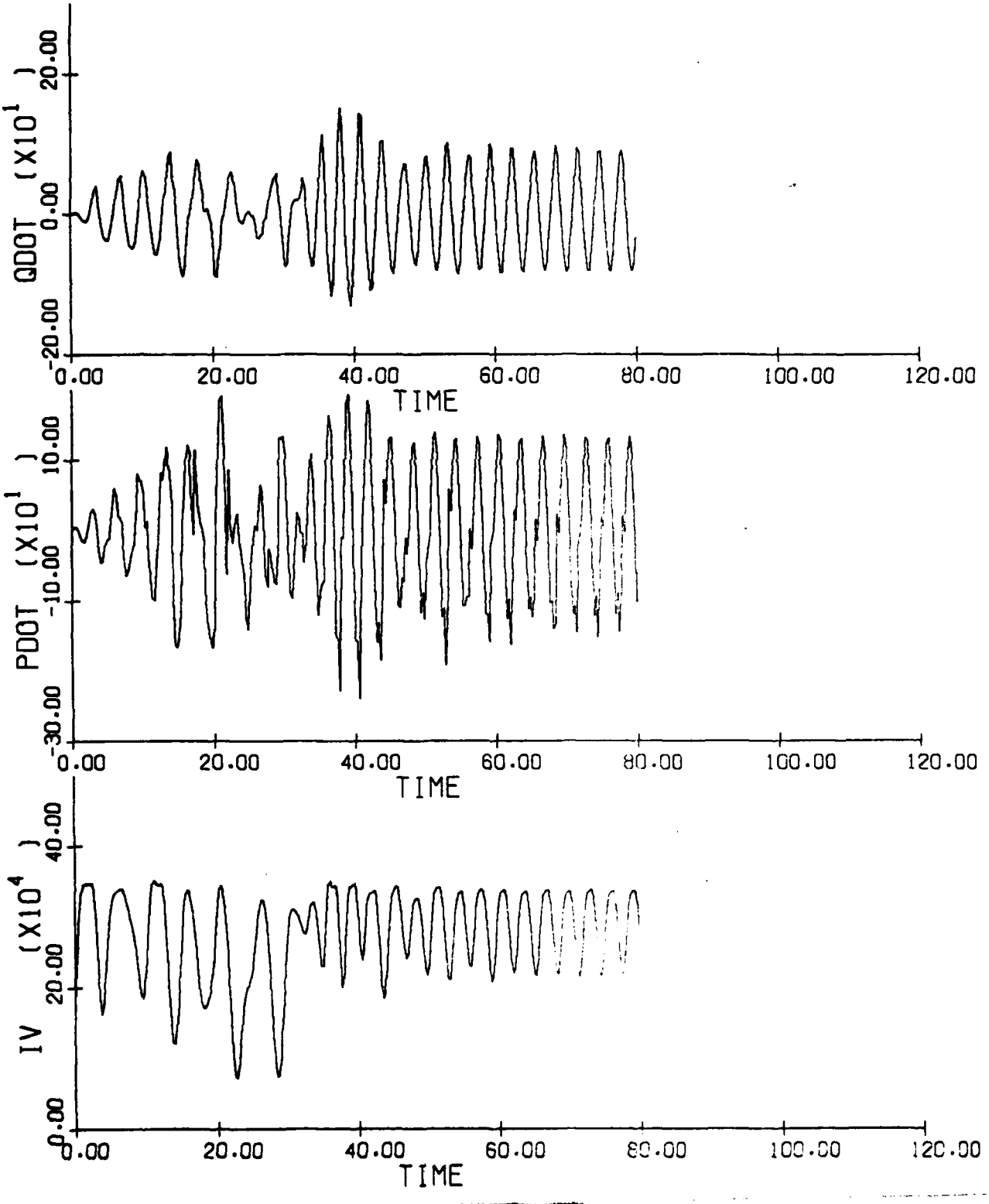

Figure 3.33(g) (concluded)

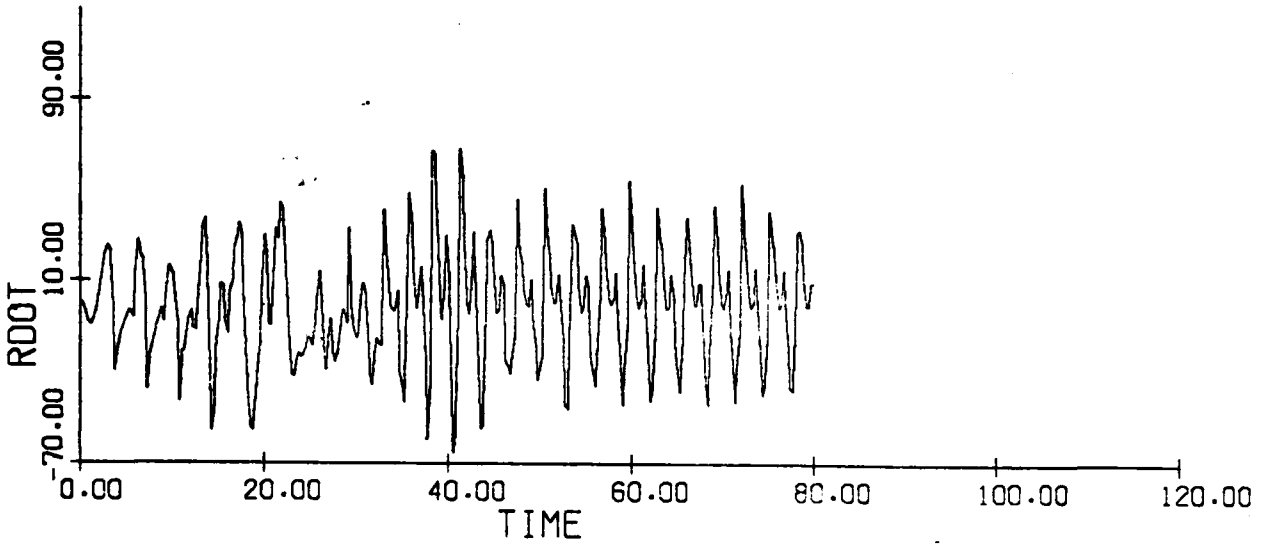

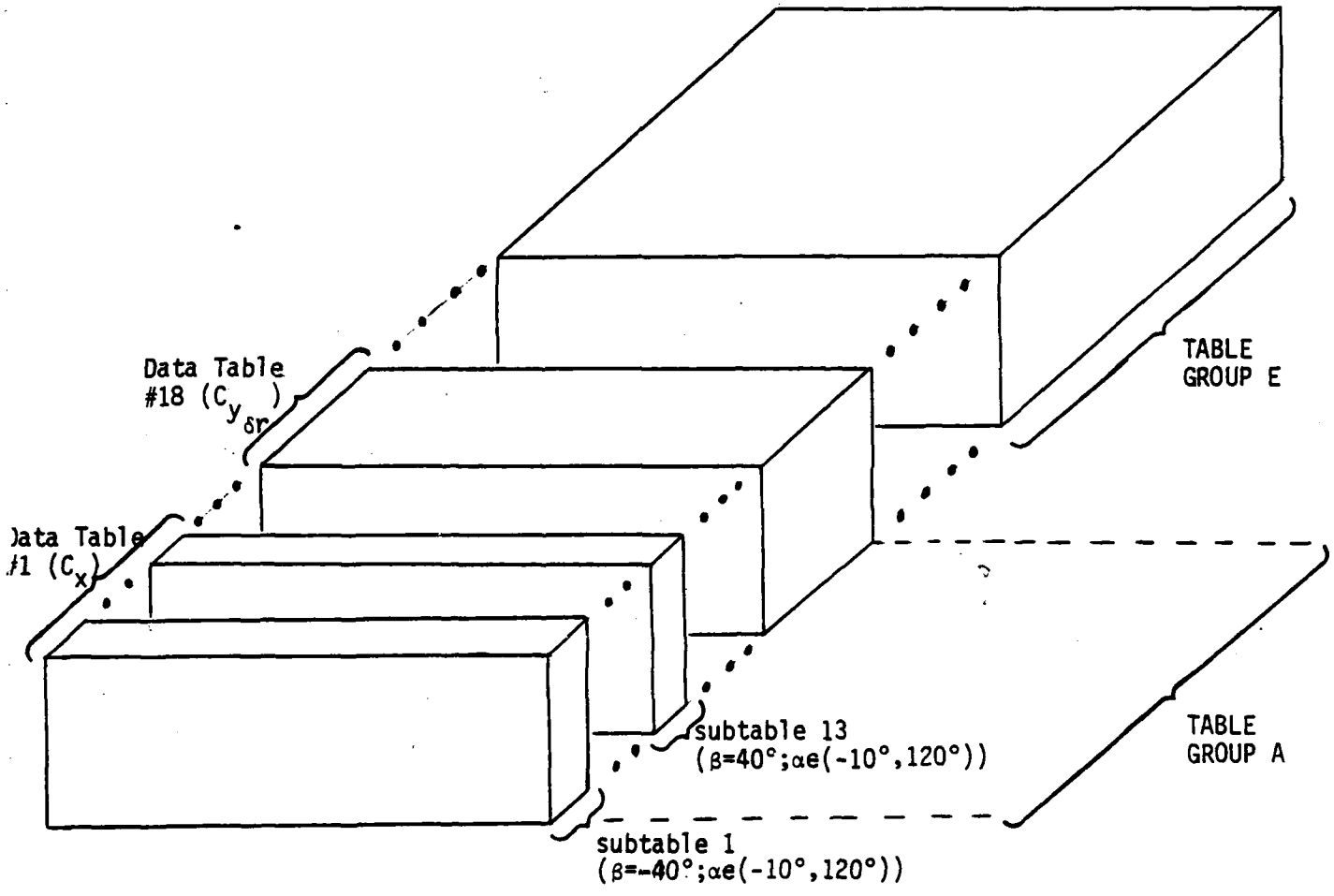

Figure 3.34: Organization of Aircraft F-4 Static Data

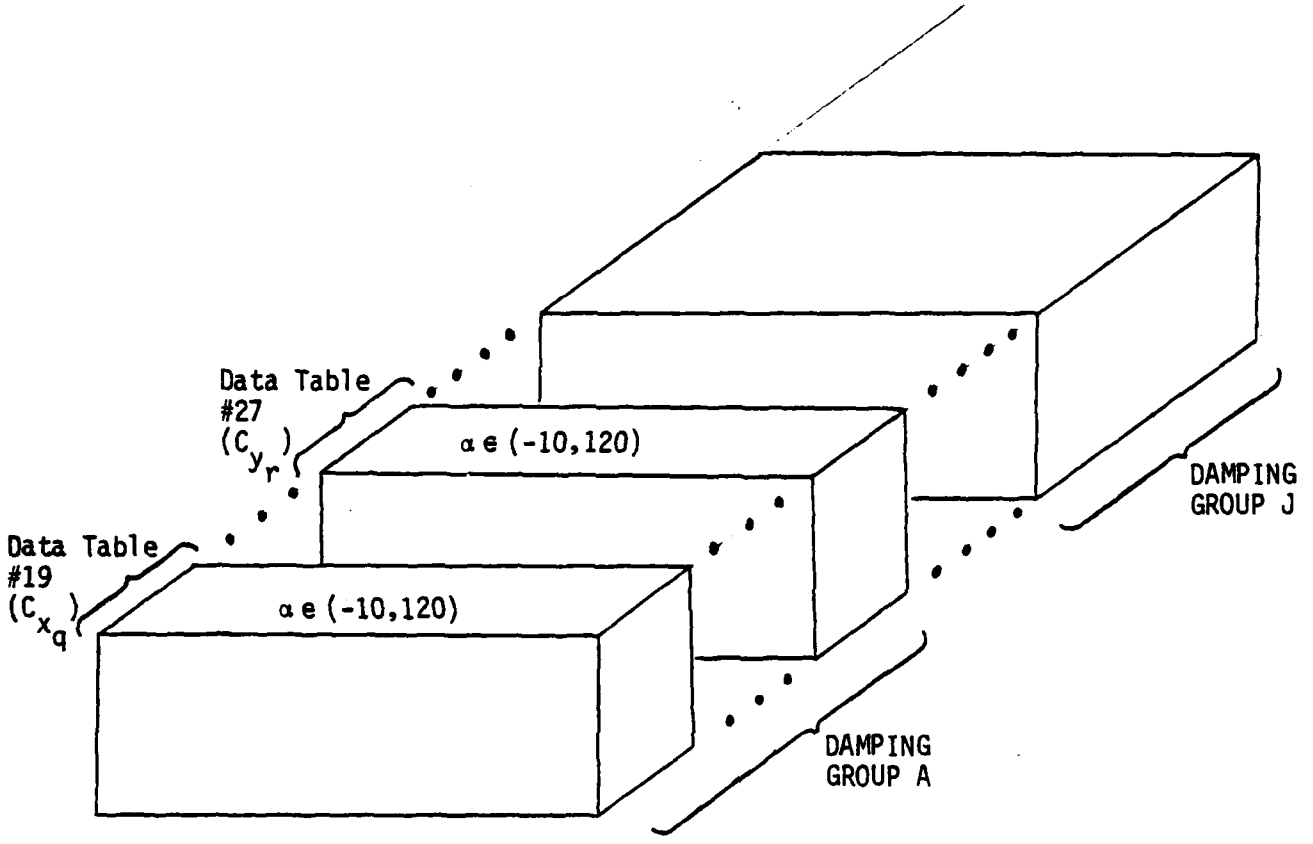

Figure 3.35: Organization of Aircraft F-4 Forced-Oscillation Damping Data

Figure 3.36: Spline Function Example, with Knots at all Data Points. Data is for F-4 Aircraft.

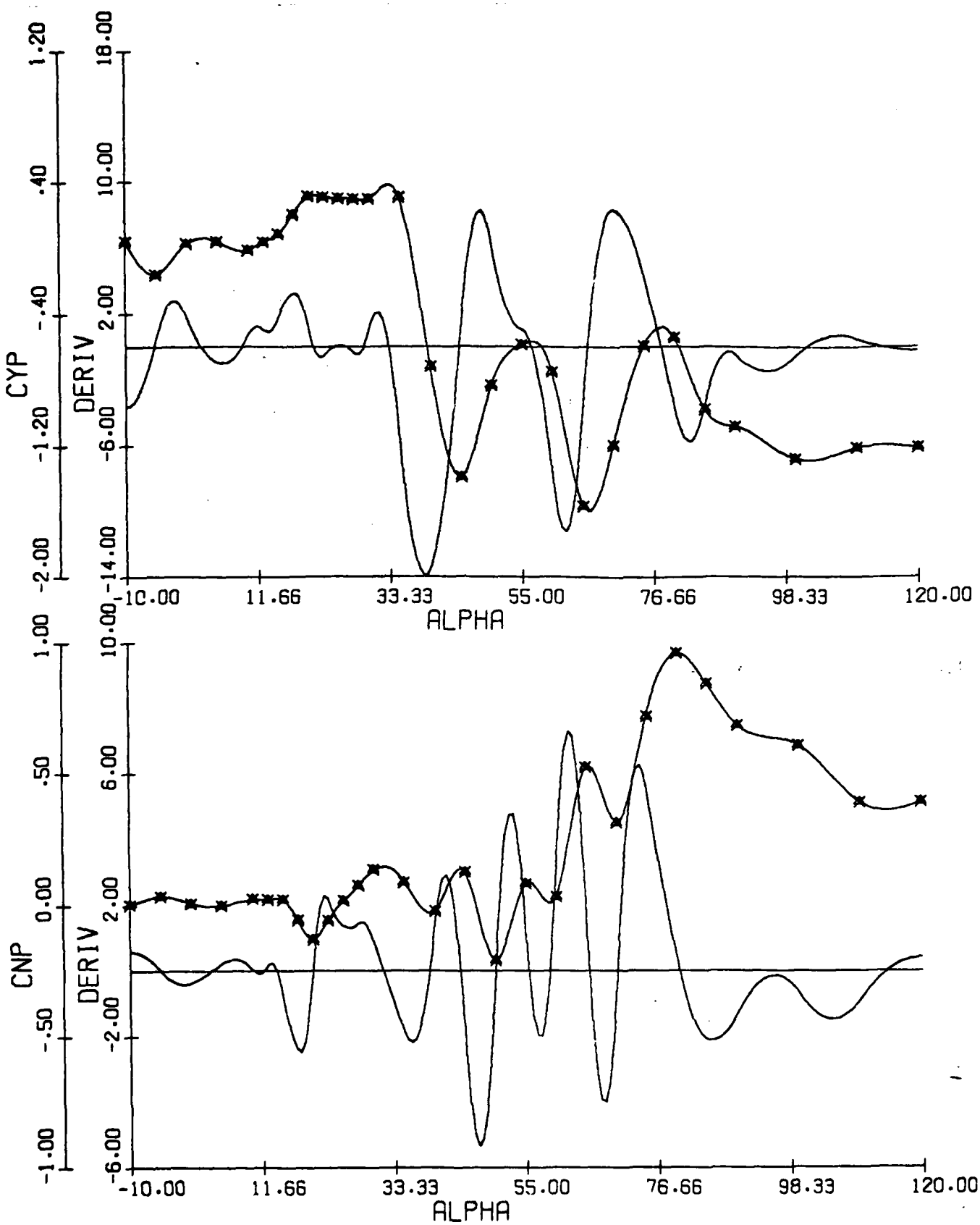

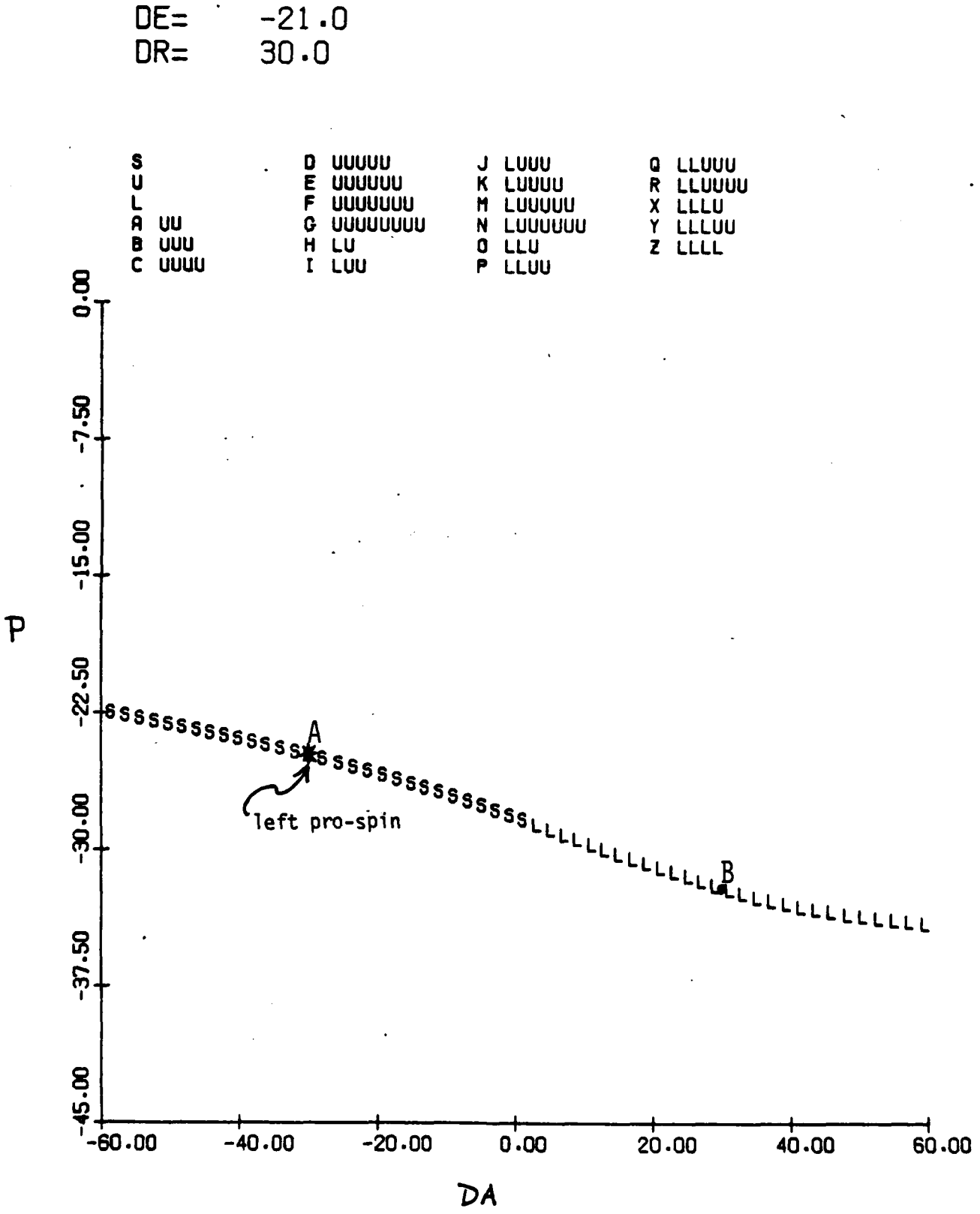

Figure 3.42: F-4 Equilibrium Surface, Spin Region
(a) p vs. δa

DE= -21.0
DR= 30.0

S
U
L
A UU
B UUU
C UUUU
D UUUUU
E UUUUUU
F UUUUUUU
G UUUUUUUU
H LU
I LUU
J LUUU
K LUUUU
M LUUUUU
N LUUUUUU
O LLU
P LLUU
Q LLUUU
R LLUUUU
X LLLU
Y LLLUU
Z LLLL

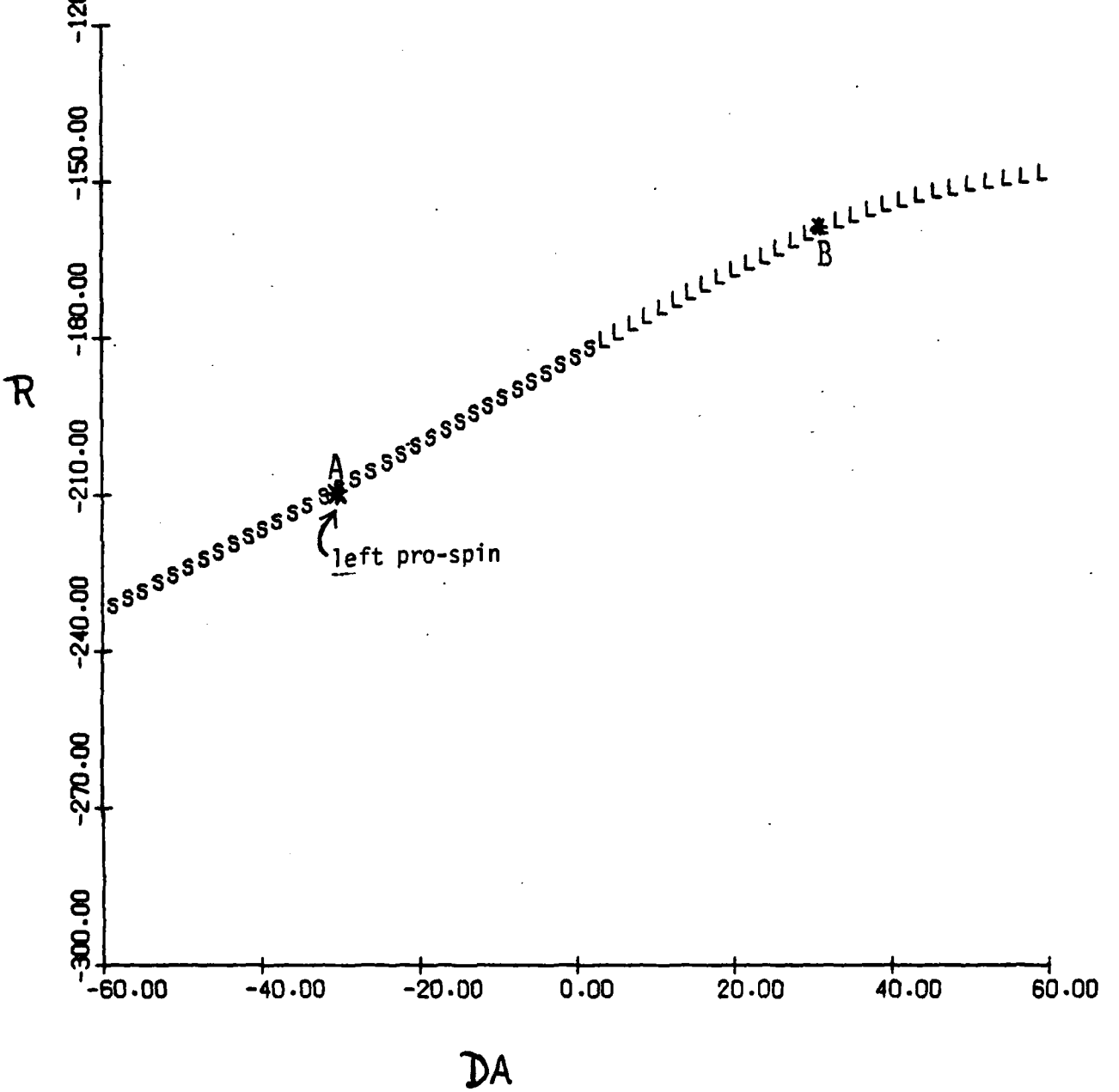

Figure 3.42(b): r vs. δa

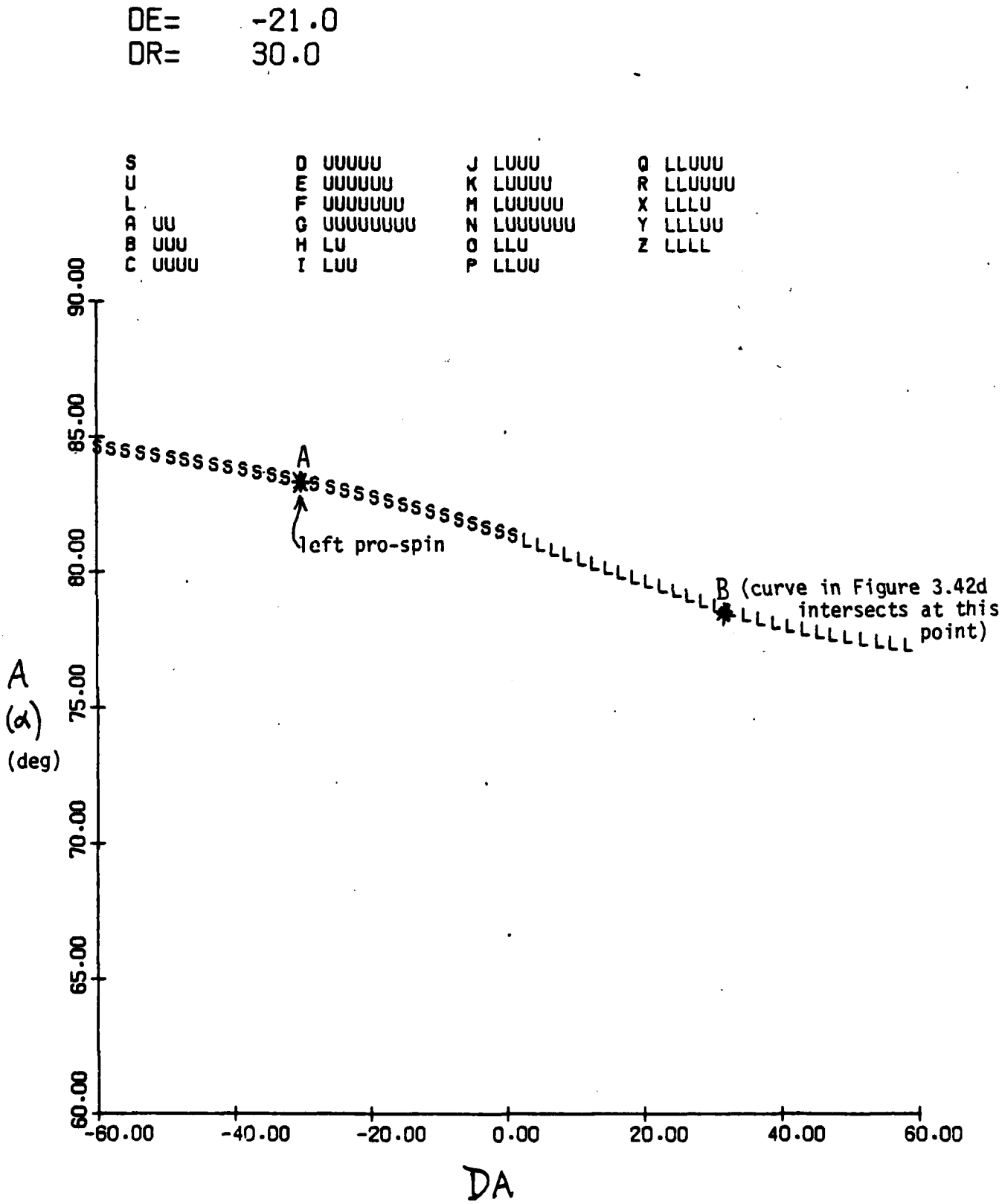

Figure 3.42(c): α vs. δa

DA= 28.0
DR= 30.0

S	D UUUUU	J LUUU	Q LLUUU
U	E UUUUUU	K LUUUU	R LLUUUU
L	F UUUUUUU	M LUUUUU	X LLLU
A UU	G UUUUUUUU	N LUUUUUU	Y LLLUU
B UUU	H LU	O LLU	Z LLLL
C UUUU	I LUU	P LLUU	

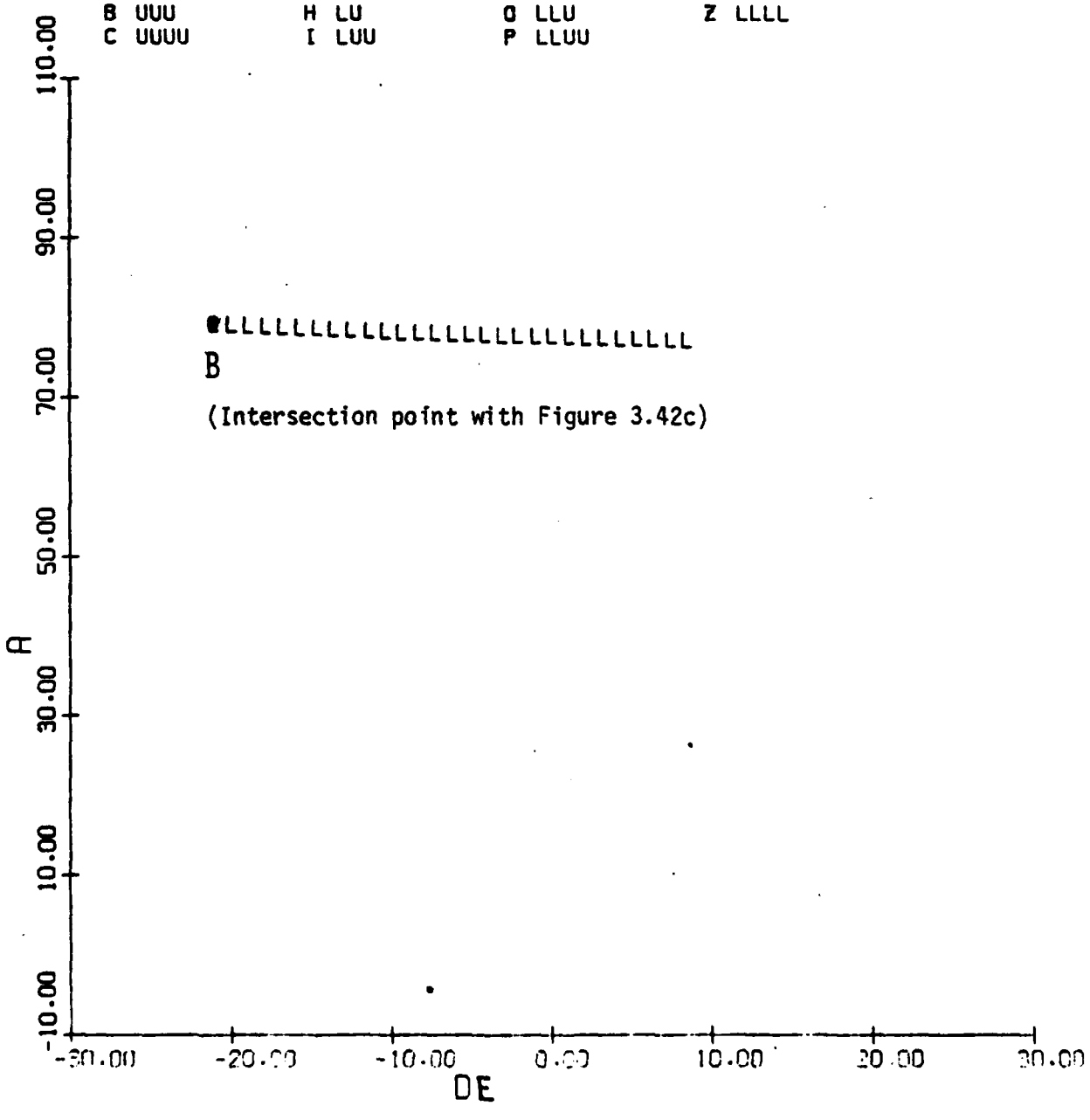

LLLLLLLLLLLLLLLLLLLLLLLLLLL
B

(Intersection point with Figure 3.42c)

Figure 3.42(d): α vs. δe

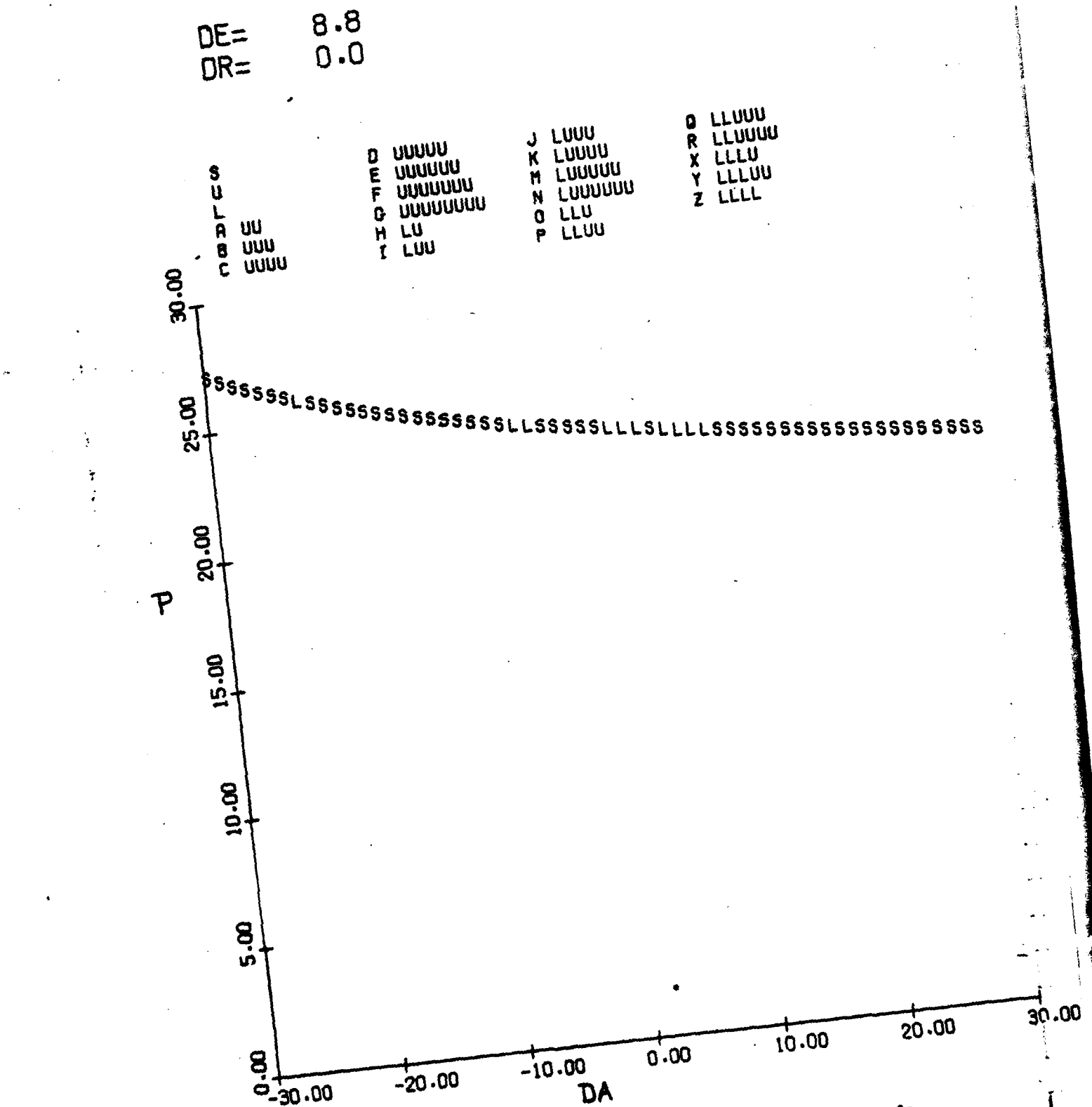

Figure 3.43: F-4 Equilibrium Surface, Spin Region; p vs. δa

S		D	UUUUU	J	LUUU	Q	LLUUU
U		E	UUUUUU	K	LUUUU	R	LLUUUU
L		F	UUUUUUU	M	LUUUUU	X	LLLU
A	UU	G	UUUUUUUU	N	LUUUUUU	Y	LLLUU
B	UUU	H	LU	O	LLU	Z	LLLL
C	UUUU	I	LUU	P	LLUU		

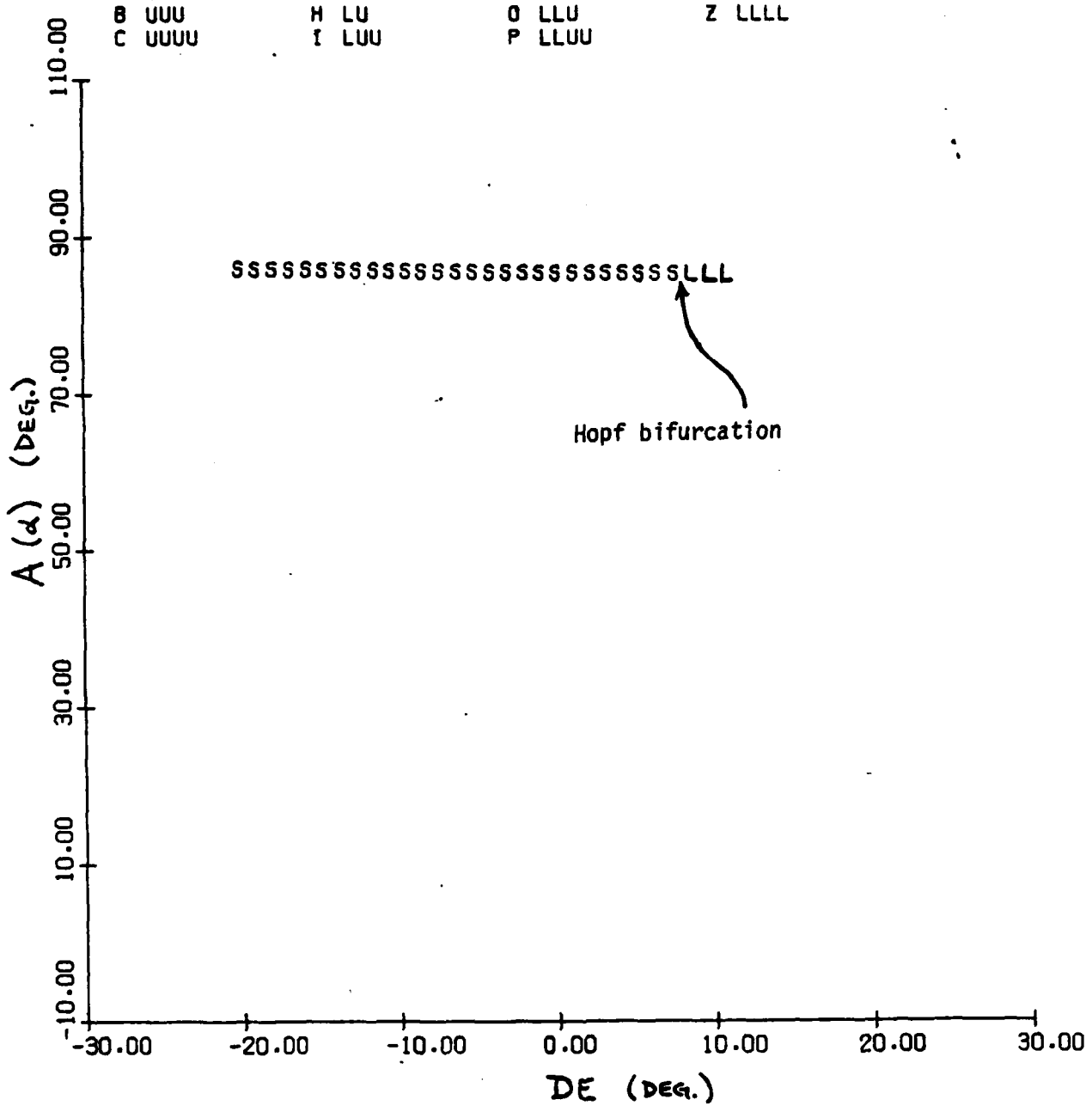

Figure 3.44: F-4 Equilibrium Surface, Spin Region; $h = 30000$ ft; $\delta a = \delta r = 0°$

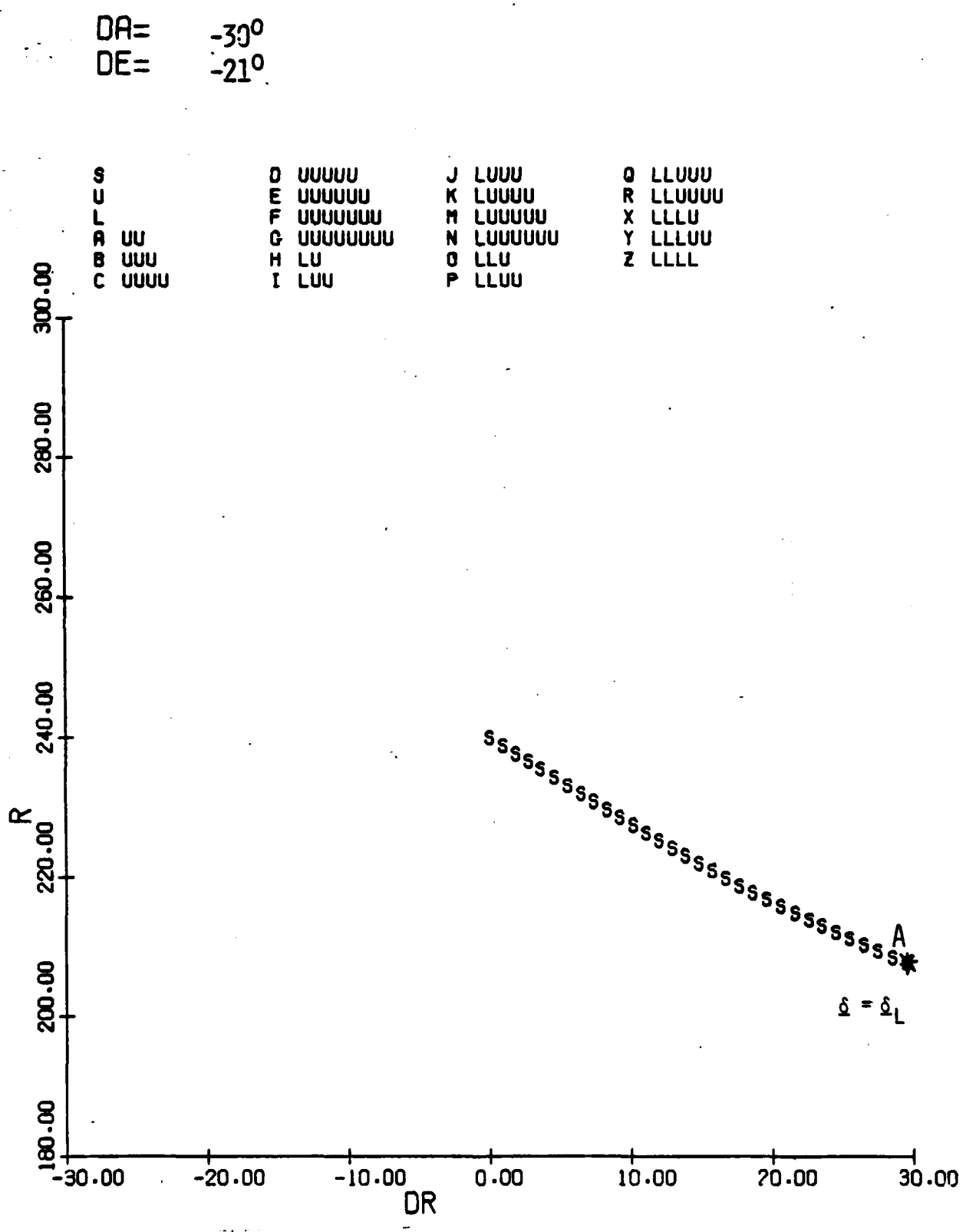

Figure 3.45: F-4 Equilibrium Surface, Spin Region; r vs. δr

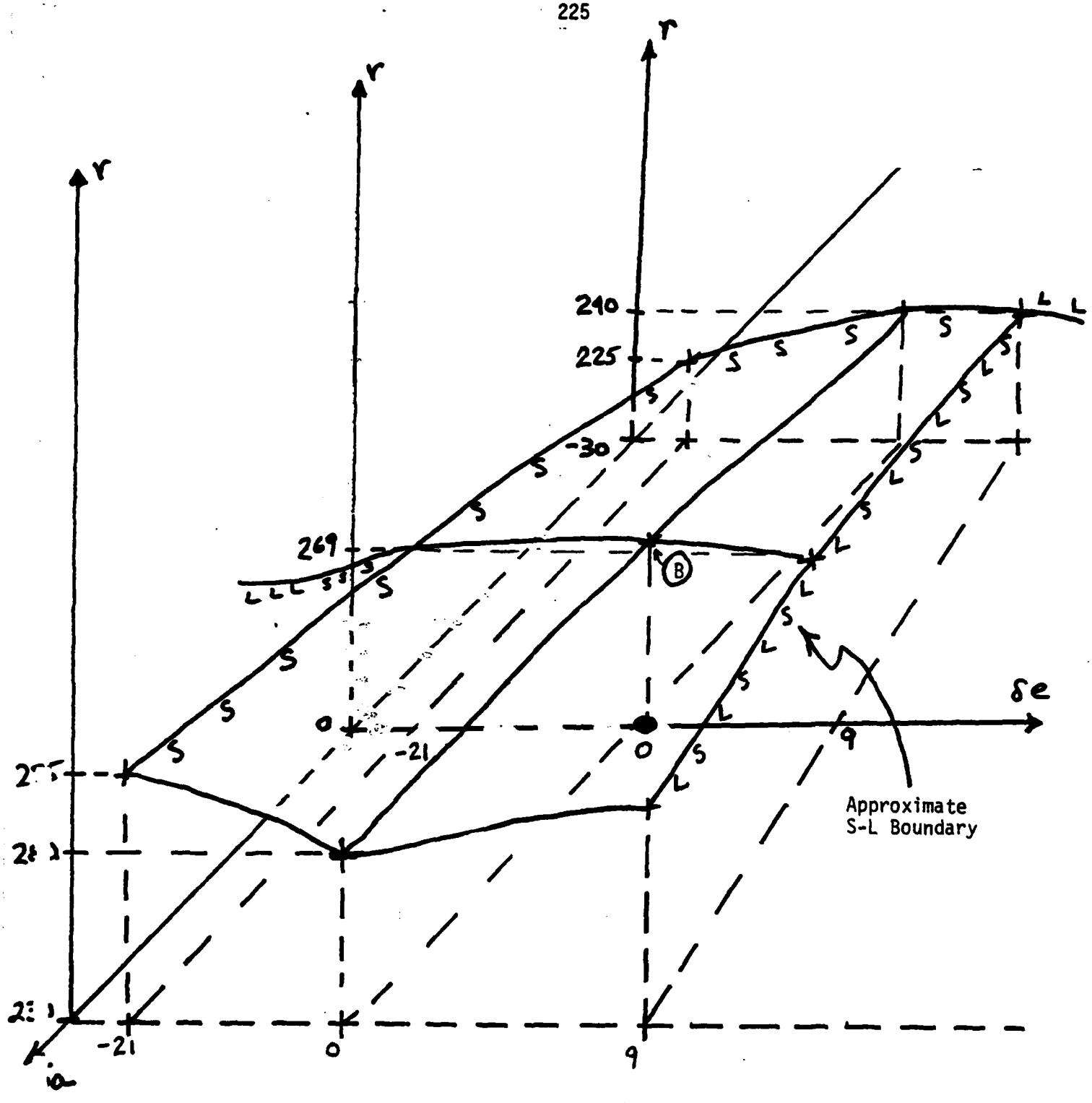

Figure 3.46: F-4 Equilibrium Surface, Spin Region; r vs. (δa,δe); δr = 0; entire surface shown is asymptotically stable (S).

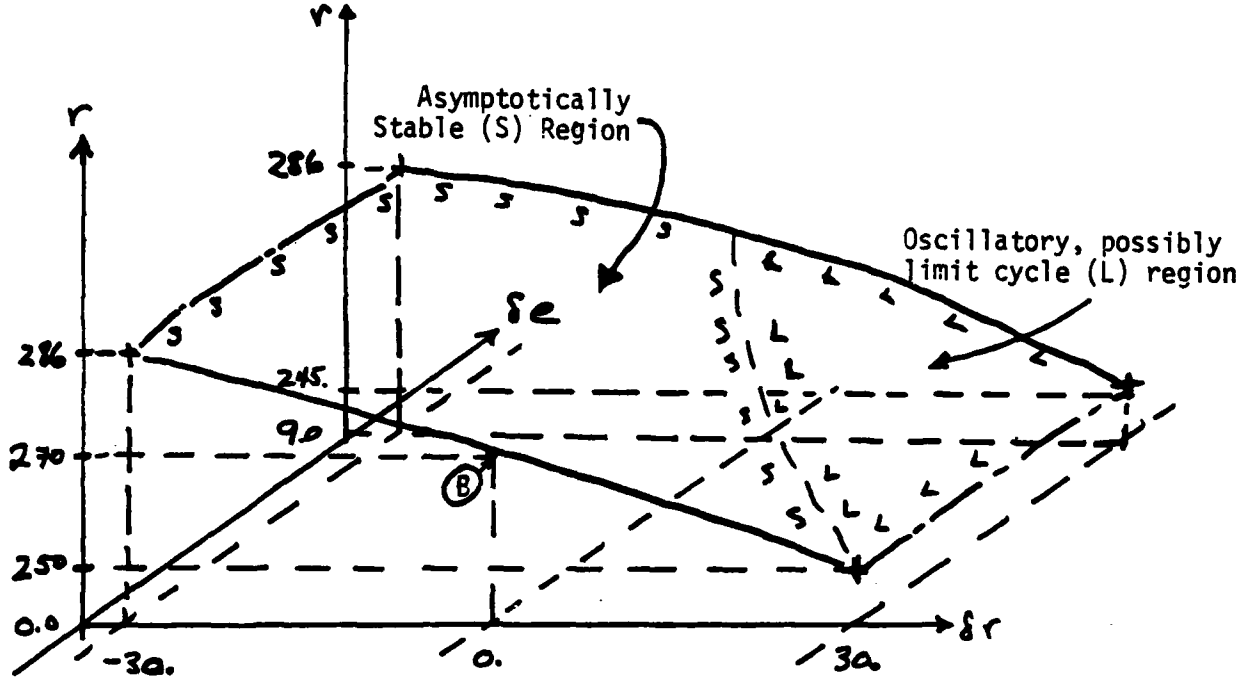

Figure 3.47: F-4 Equilibrium Surface, Spin Region
r vs. (δe,δr); δa = 0°

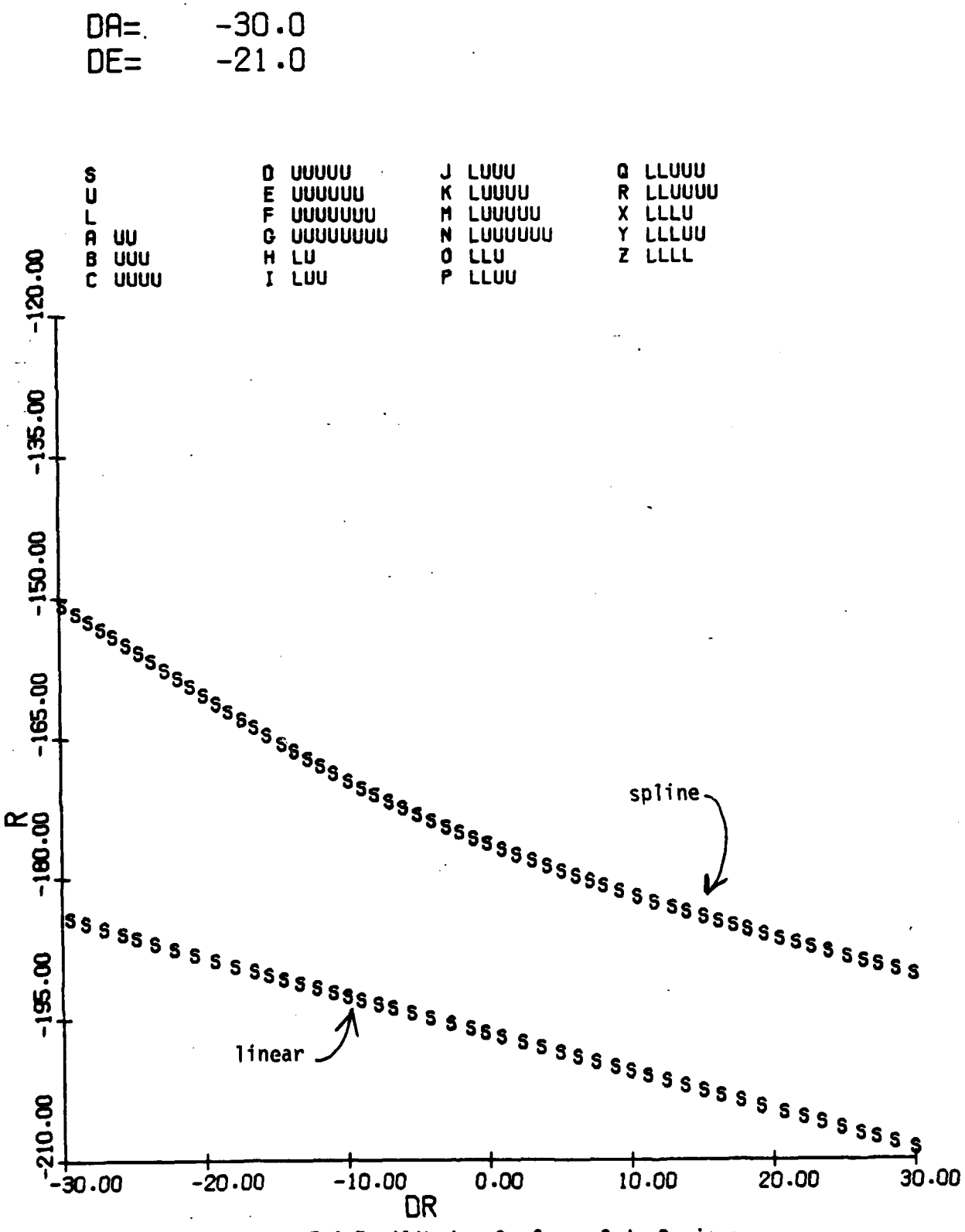

Figure 3.48: F-4 Equilibrium Surface, Spin Region;
Comparison of linear and spline fits of rotation balance data
(a) r vs. δr

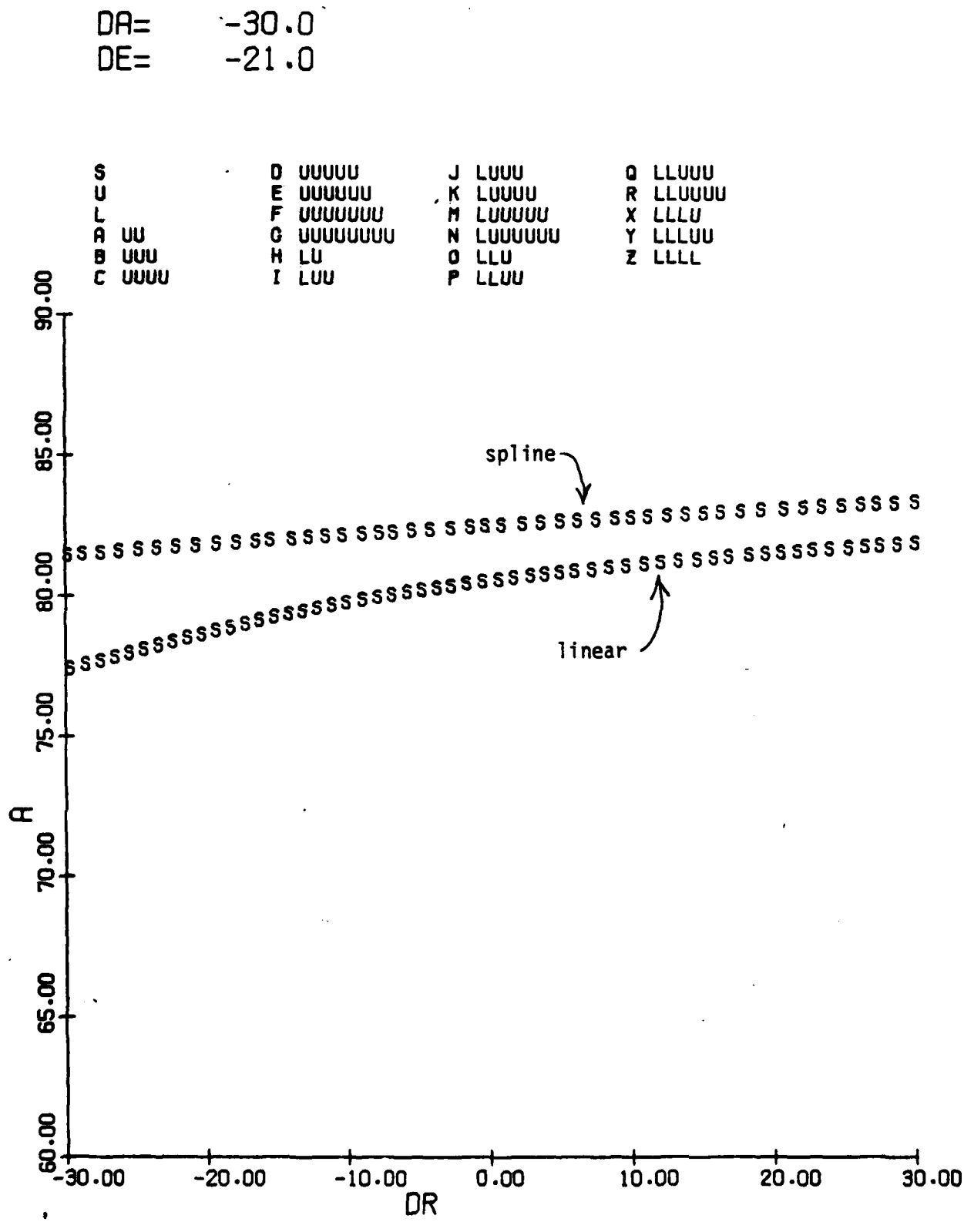

Figure 3.48(b) α vs. δr

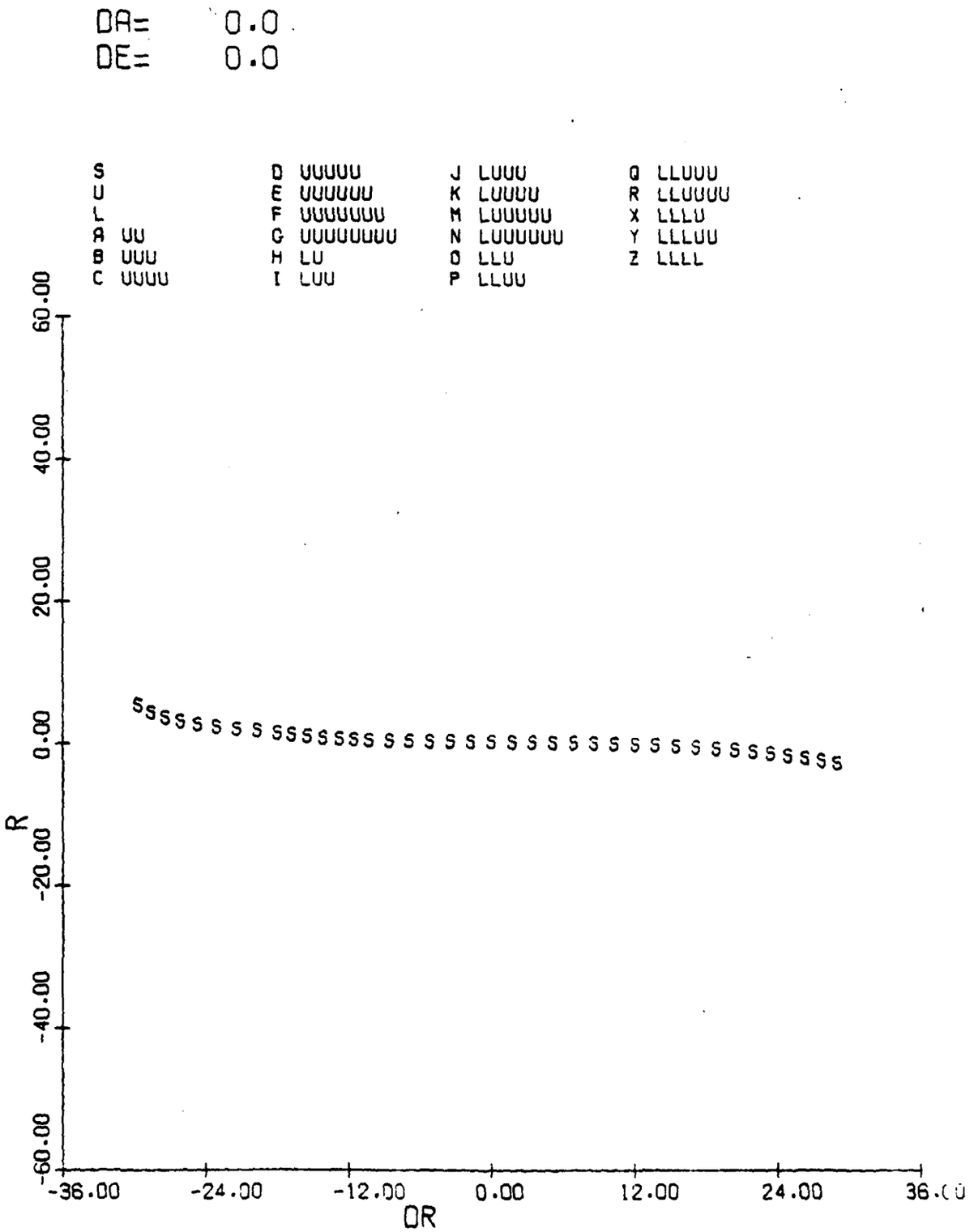

Figure 3.49: F-4 Equilibrium Surface, Trim Region;
h=5000 ft, V=330 fps, thrust=0
(a) r vs. δr

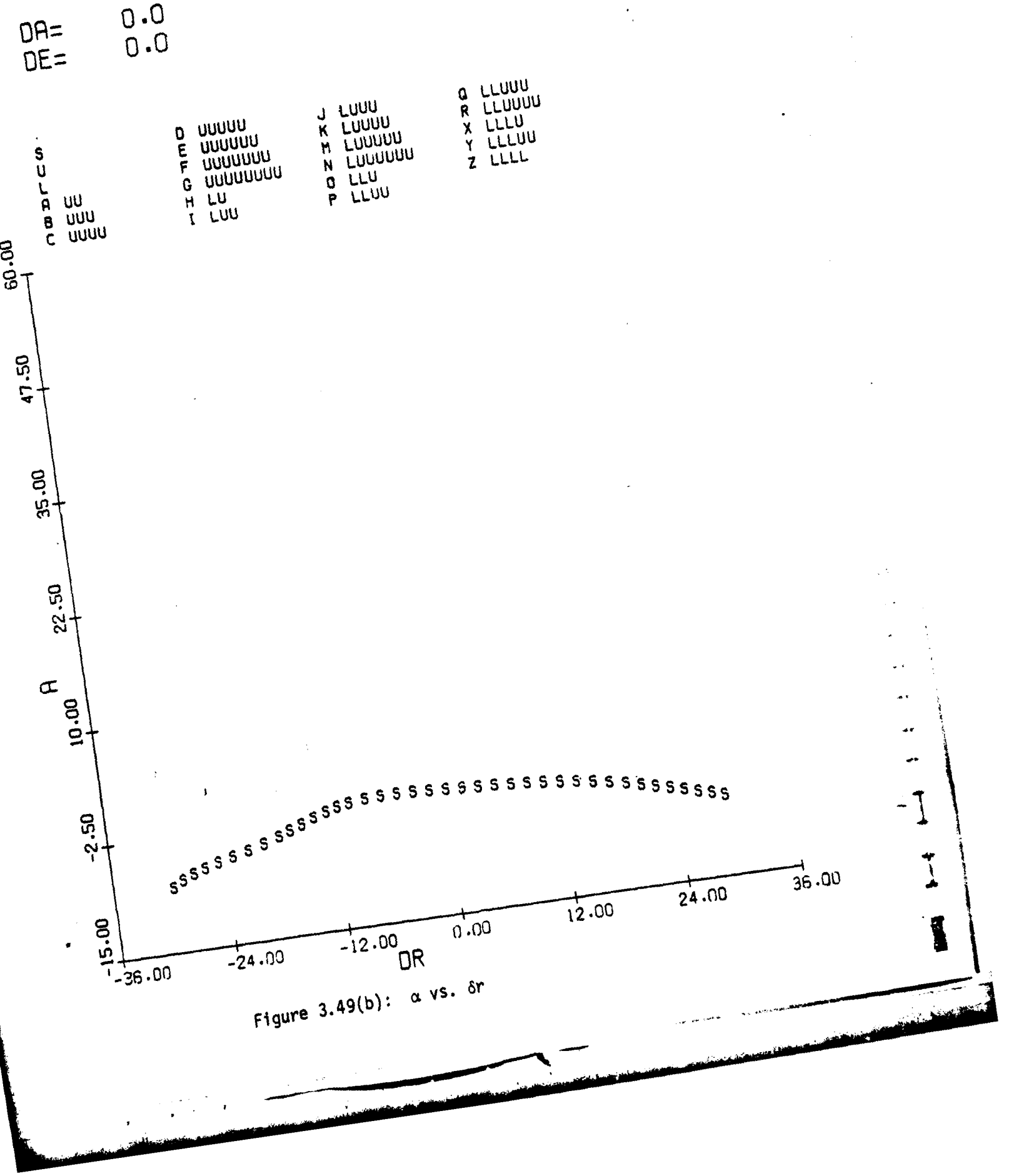

Figure 3.49(b): α vs. δr

DA= 0.0
DE= 0.0

S	D UUUUU	J LUUU	Q LLUUU
U	E UUUUUU	K LUUUU	R LLUUUU
L	F UUUUUUU	M LUUUUU	X LLLU
A UU	G UUUUUUUU	N LUUUUUU	Y LLLUU
B UUU	H LU	O LLU	Z LLLL
C UUUU	I LUU	P LLUU	

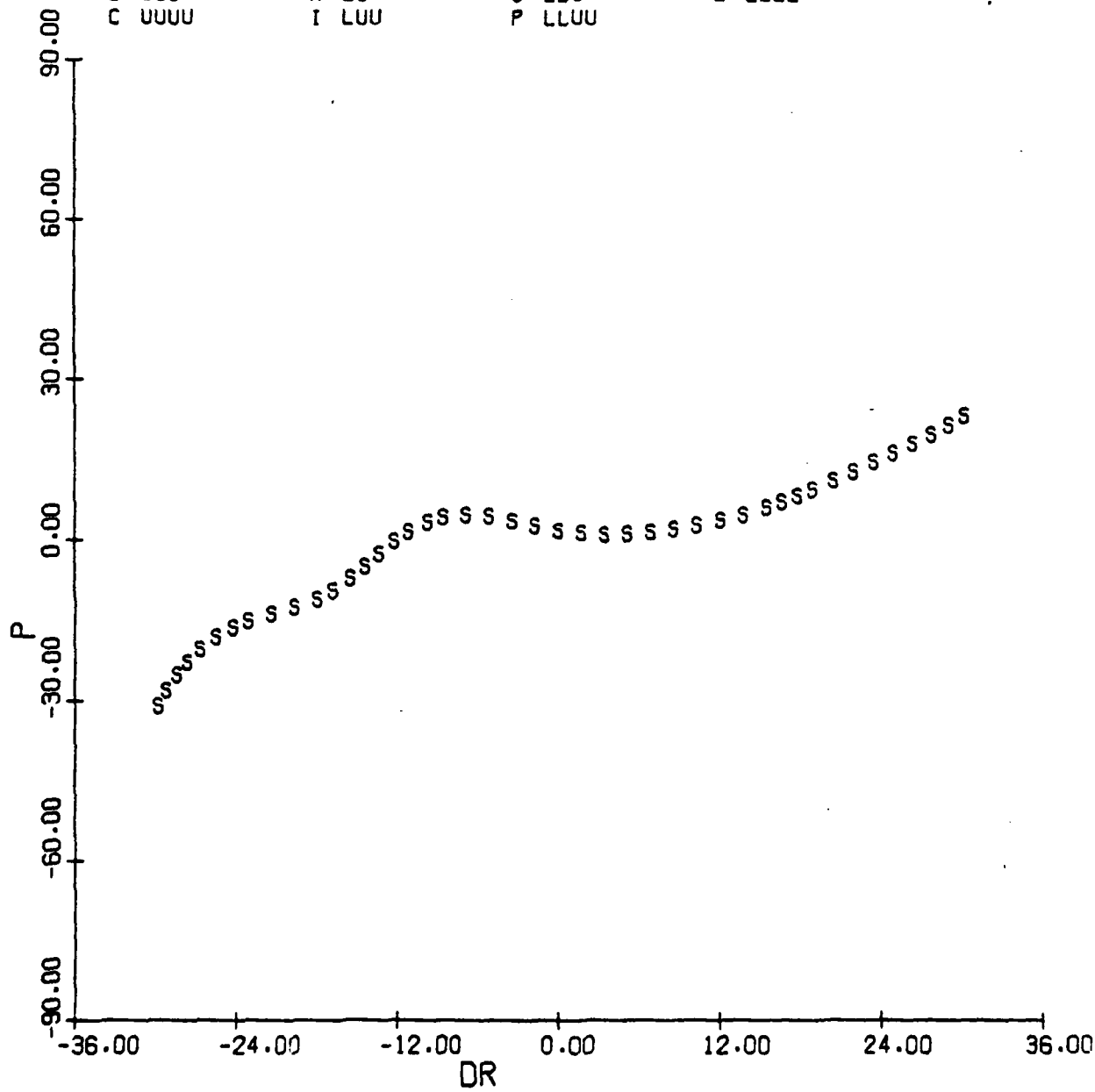

Figure 3.49(c): p vs. δr

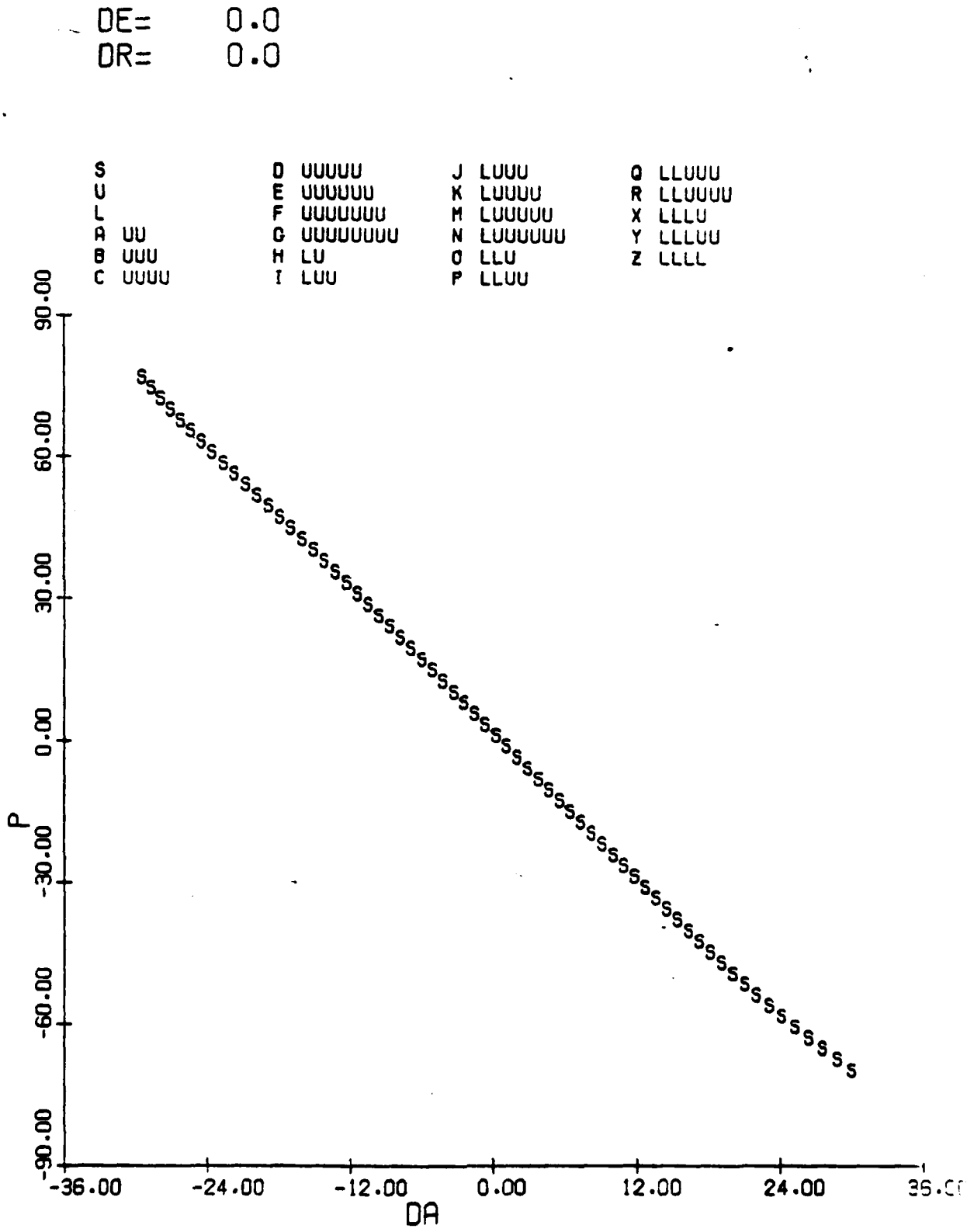

Figure 3.50: F-4 Equilibrium Surface Trim Region;
h=5000 ft, V=330 fps, thrust=0; p vs. δa

Figure 3.51: F-4 Equilibrium Surface, Trim Region;
h = 5000 ft, V = 330 fps, thrust = 0;
(a) r vs. δa

DE= -3.5
DR= -6.0

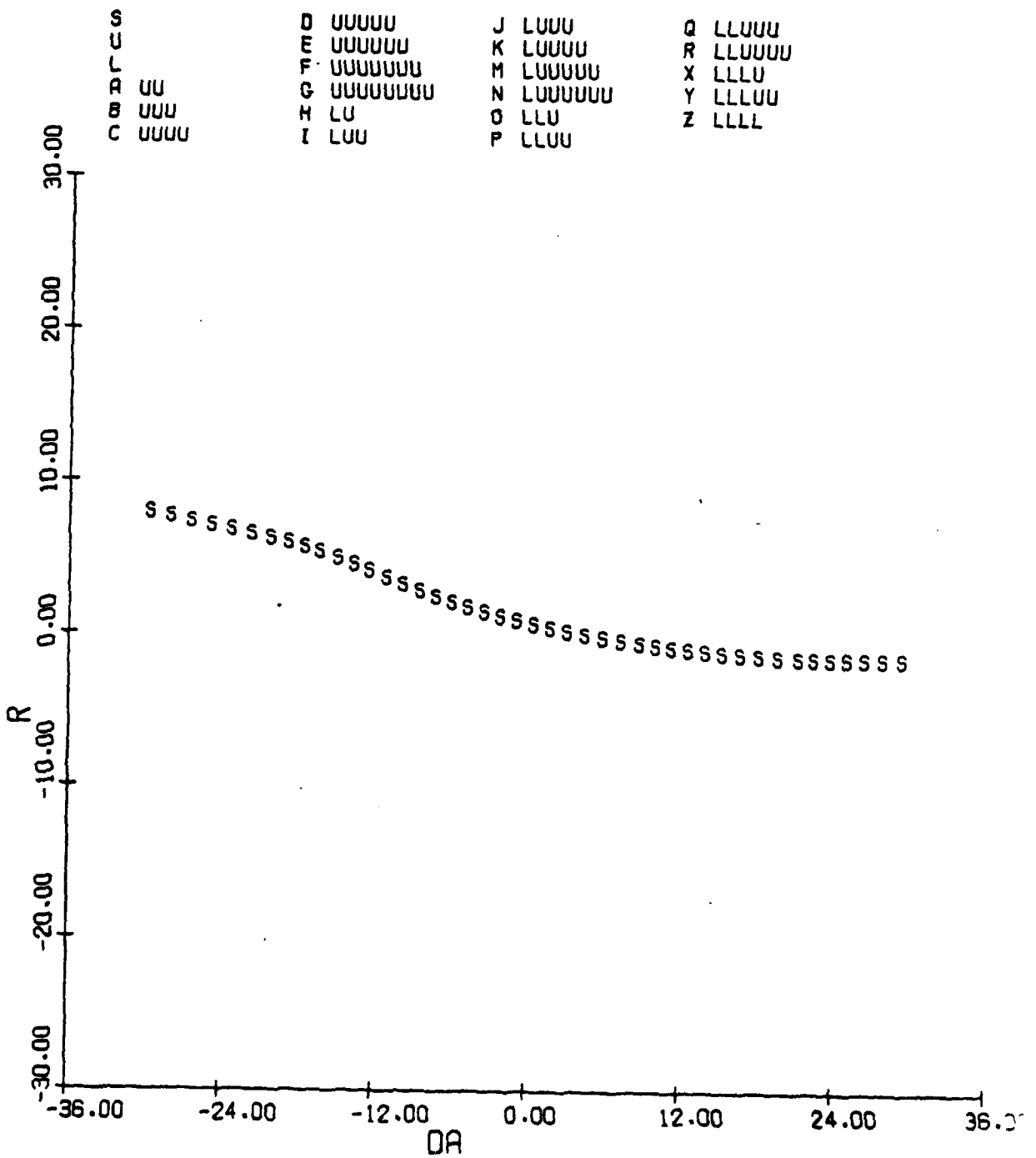

Figure 3.51(b): α vs. δa

DE= -3.5
DR= -6.0

S	D UUUUU	J LUUU	Q LLUUU
U	E UUUUUU	K LUUUU	R LLUUUU
L	F UUUUUUU	M LUUUUU	X LLLU
A UU	G UUUUUUUU	N LUUUUUU	Y LLLUU
B UUU	H LU	O LLU	Z LLLL
C UUUU	I LUU	P LLUU	

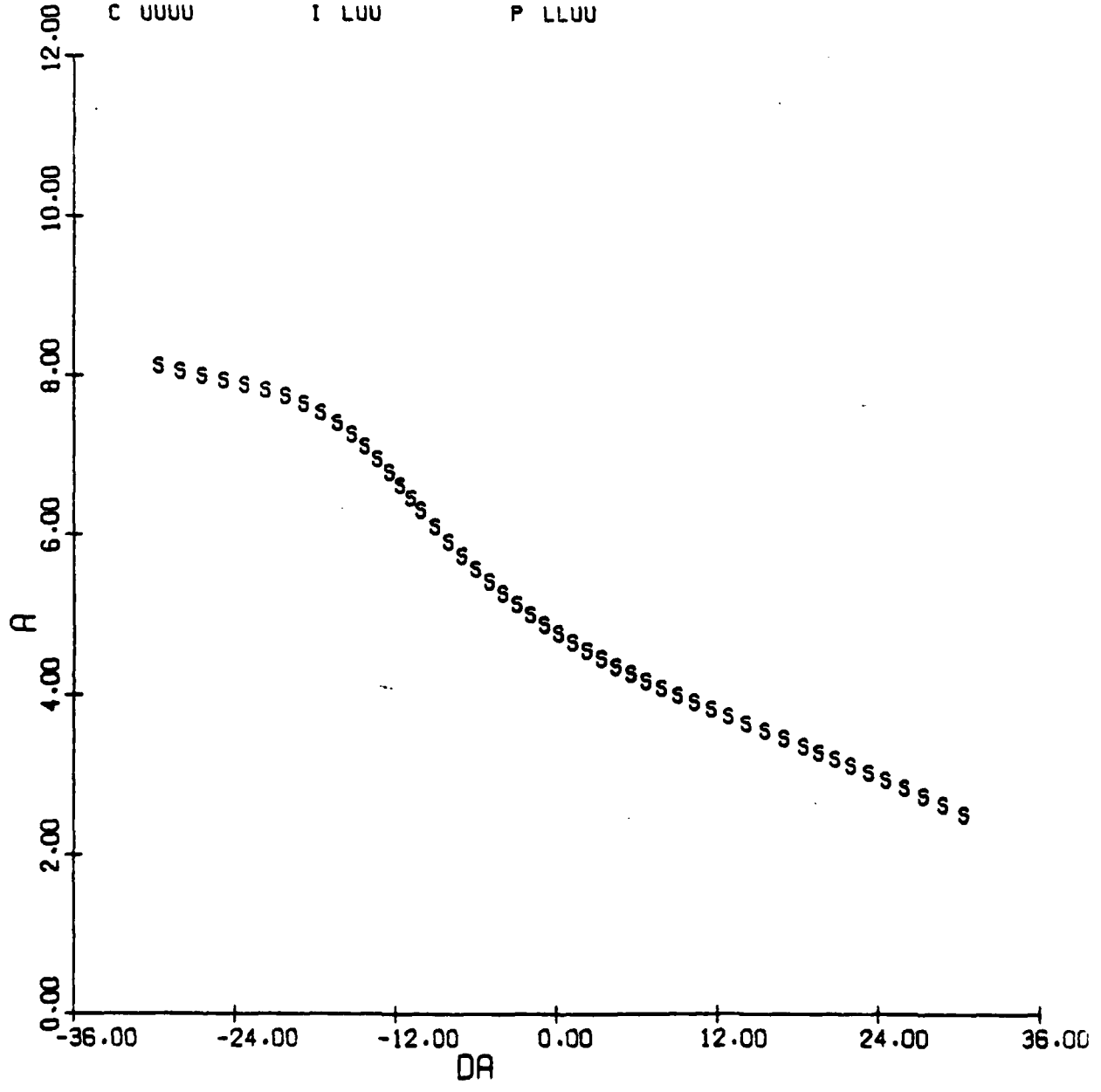

Figure 3.51(c): p vs. δa

DE= -3.5
DR= -6.0

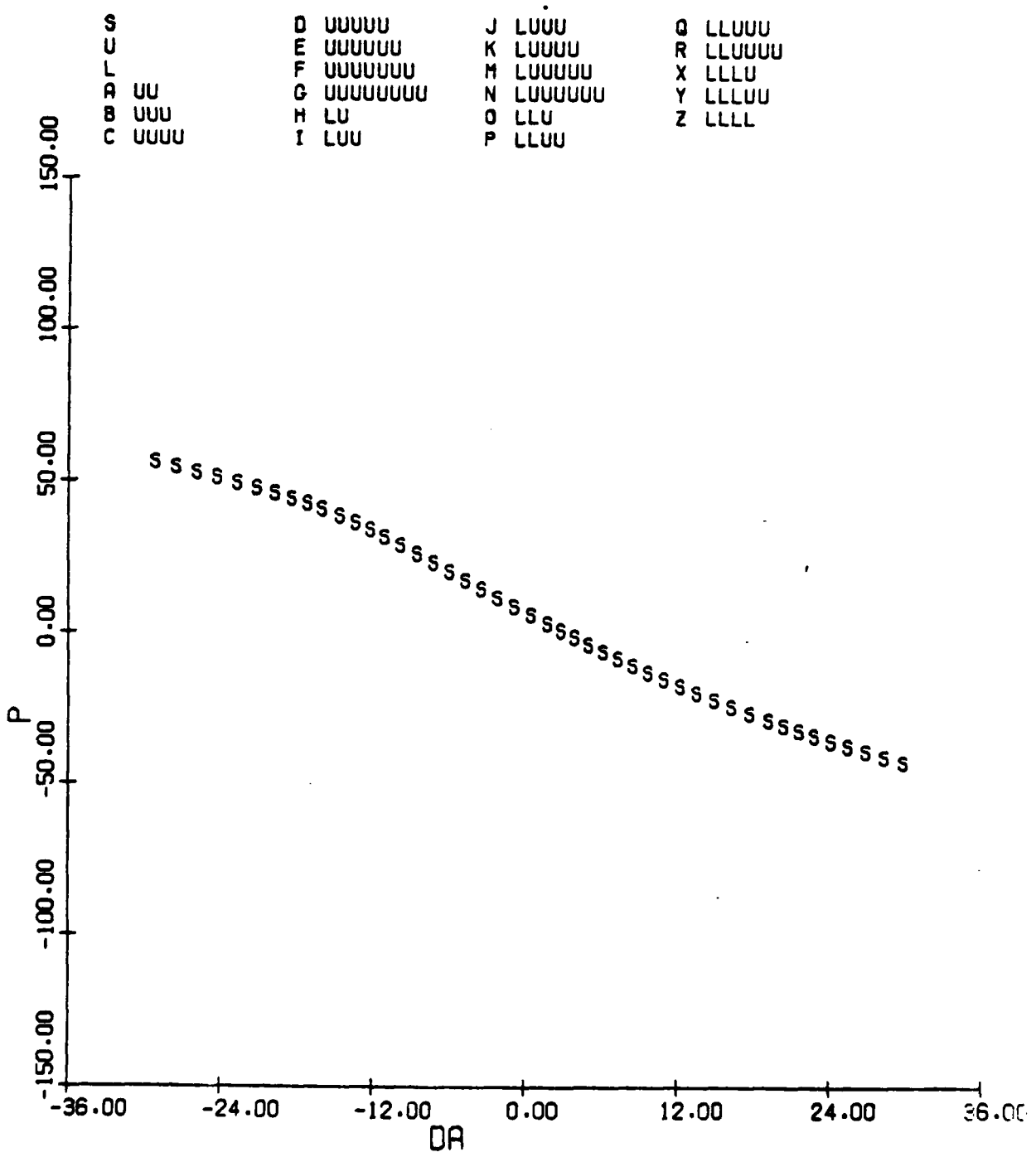

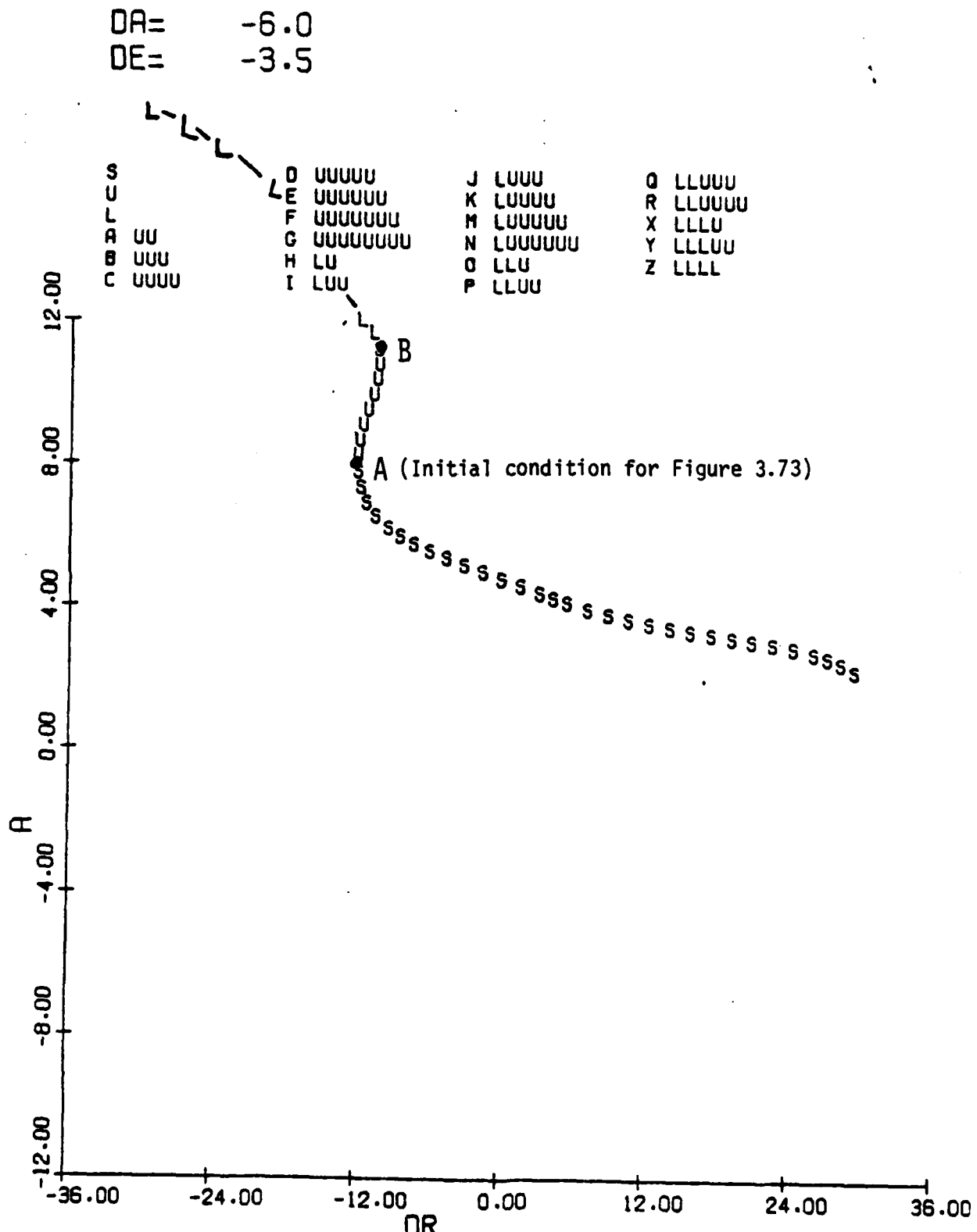

Figure 3.52: F-4 Equilibrium Surface, Trim Region;
h=5000 ft, V=330 fps, thrust=0
(a) α vs. δr

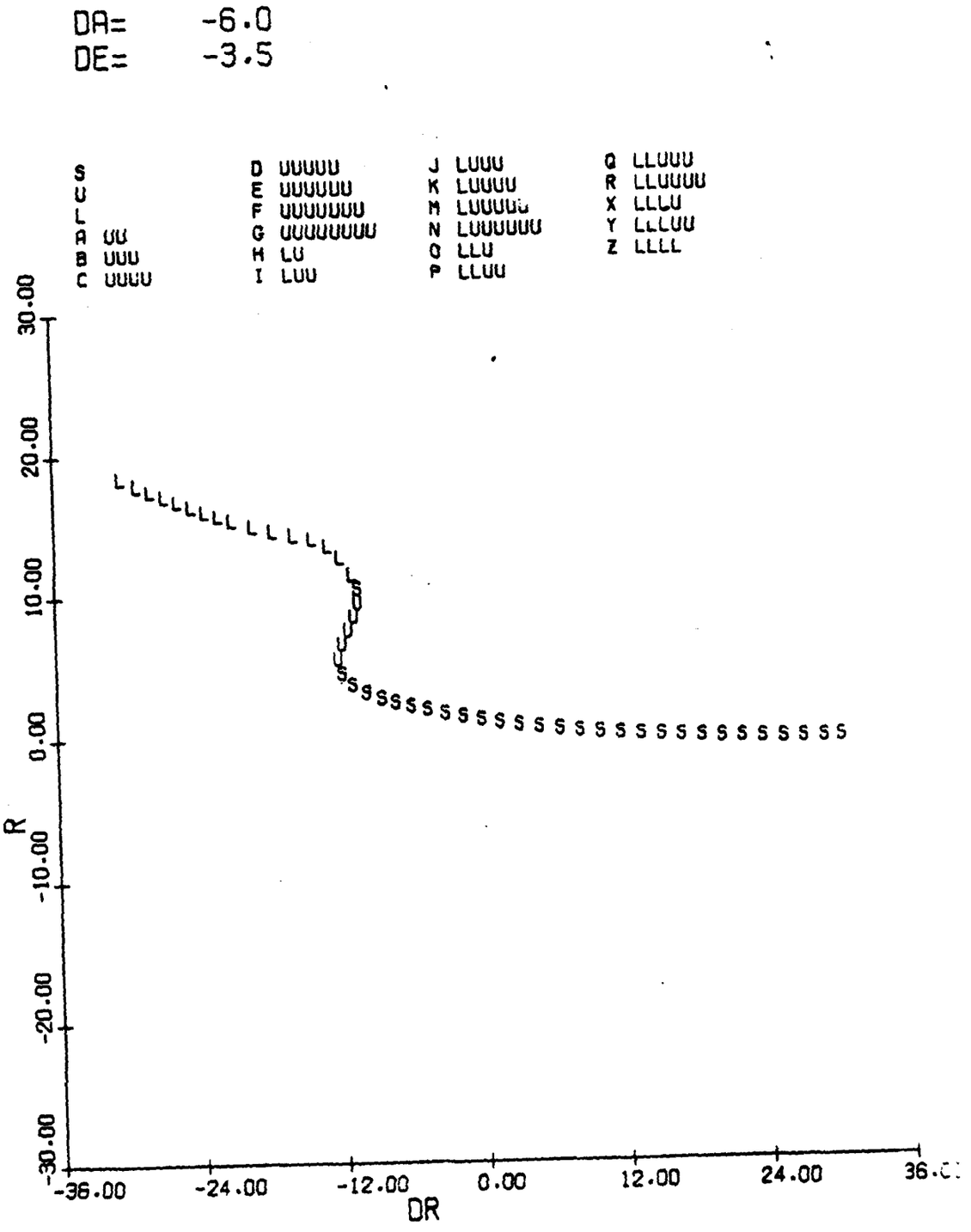

Figure 3.52(b): r vs. δr

DA= -6.0
DE= -3.5

S	D UUUUU	J LUUU	Q LLUUU
U	E UUUUUU	K LUUUU	R LLUUUU
L	F UUUUUUU	M LUUUUU	X LLLU
A UU	G UUUUUUUU	N LUUUUUU	Y LLLUU
B UUU	H LU	O LLU	Z LLLL
C UUUU	I LUU	P LLUU	

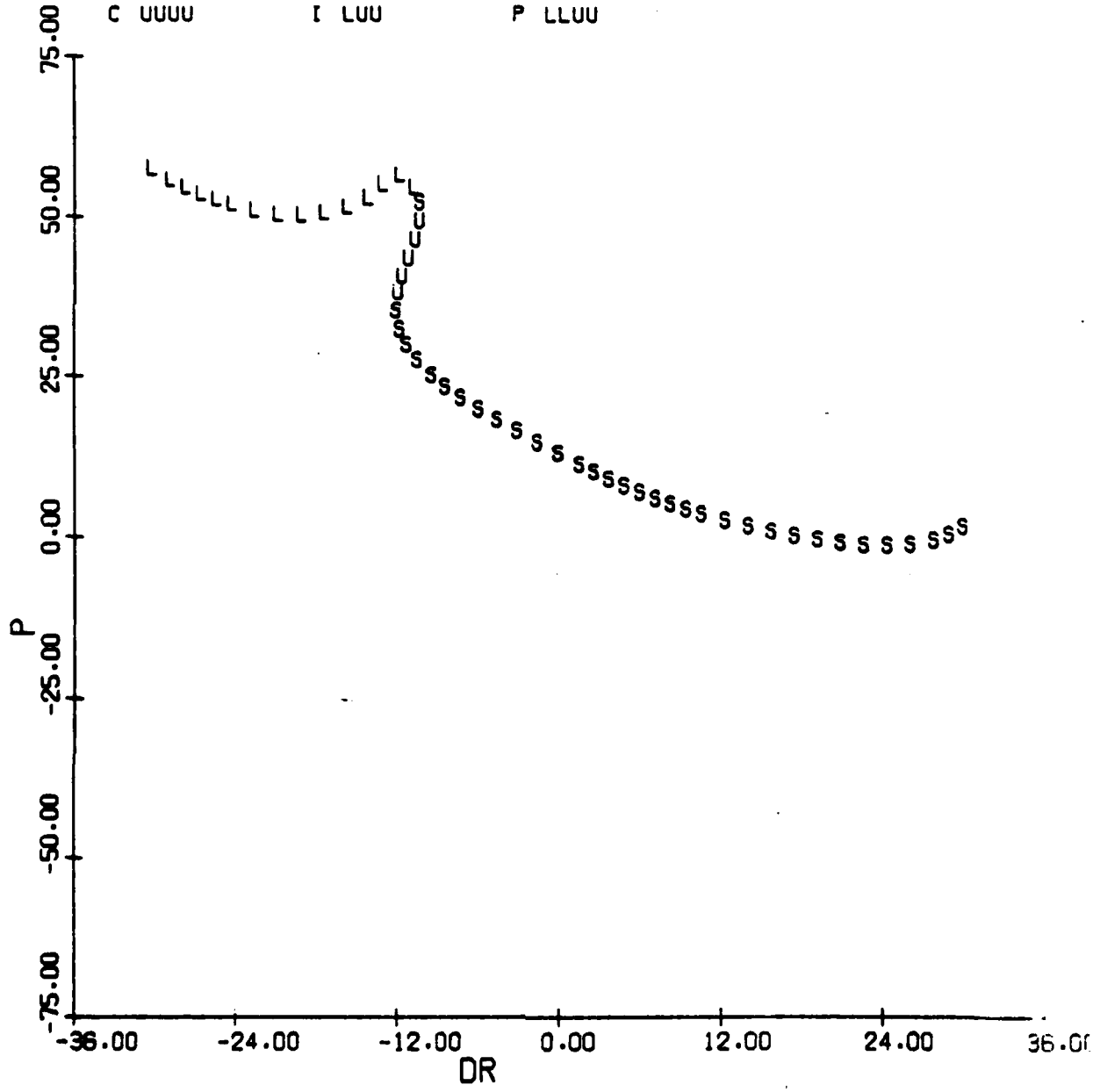

Figure 3.52(c): p vs. δr

Figure 3.53: F-4 Equilibrium Surface, Trim Region;
h = 5000 ft, V = 330 fps, thrust = 0
(a) r vs. δe

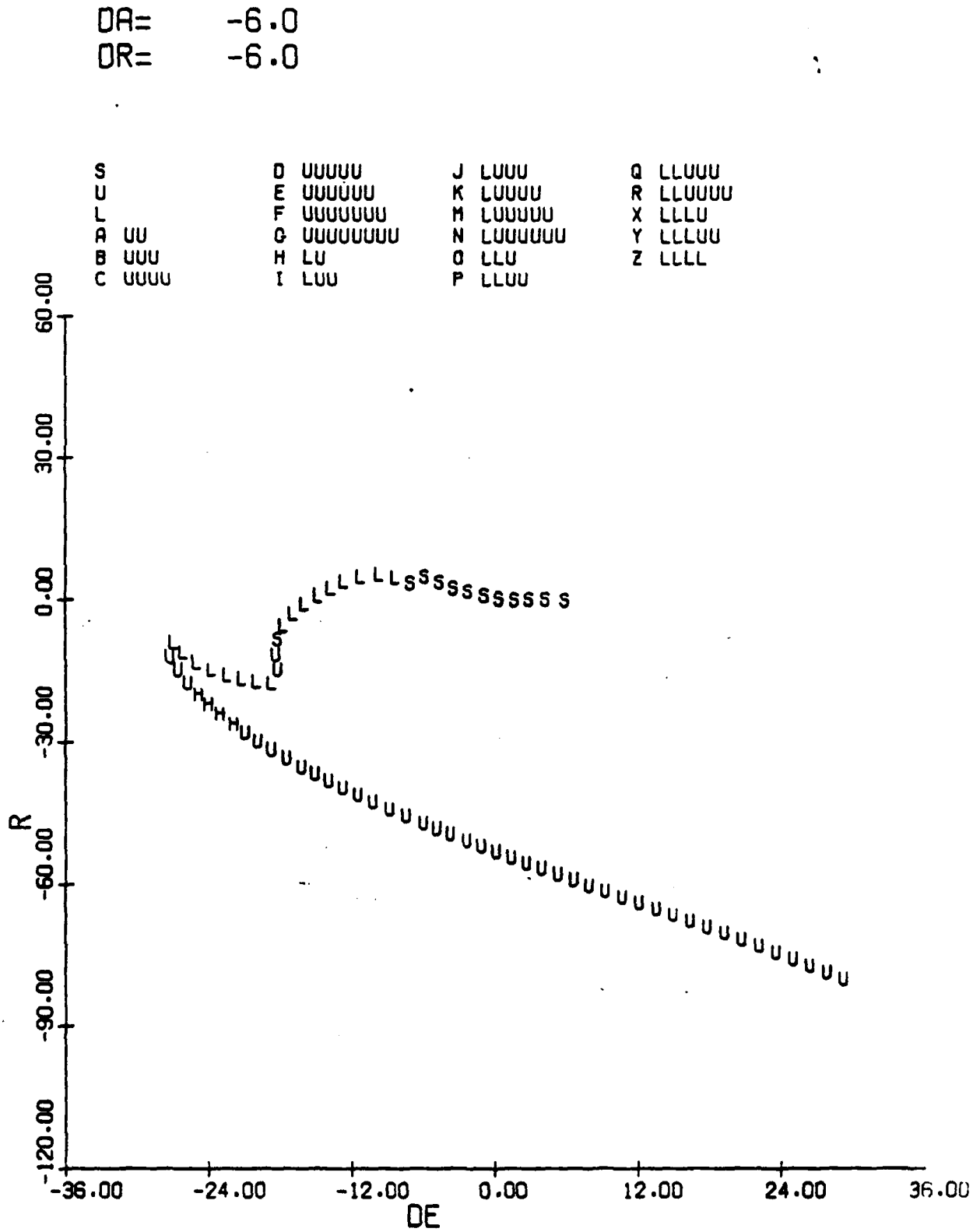

DA= -6.0
DR= -6.0

S
U
L
A UU
B UUU
C UUUU
D UUUUU
E UUUUUU
F UUUUUUU
G UUUUUUUU
H LU
I LUU
J LUUU
K LUUUU
M LUUUUU
N LUUUUUU
O LLU
P LLUU
Q LLUUU
R LLUUUU
X LLLU
Y LLLUU
Z LLLL

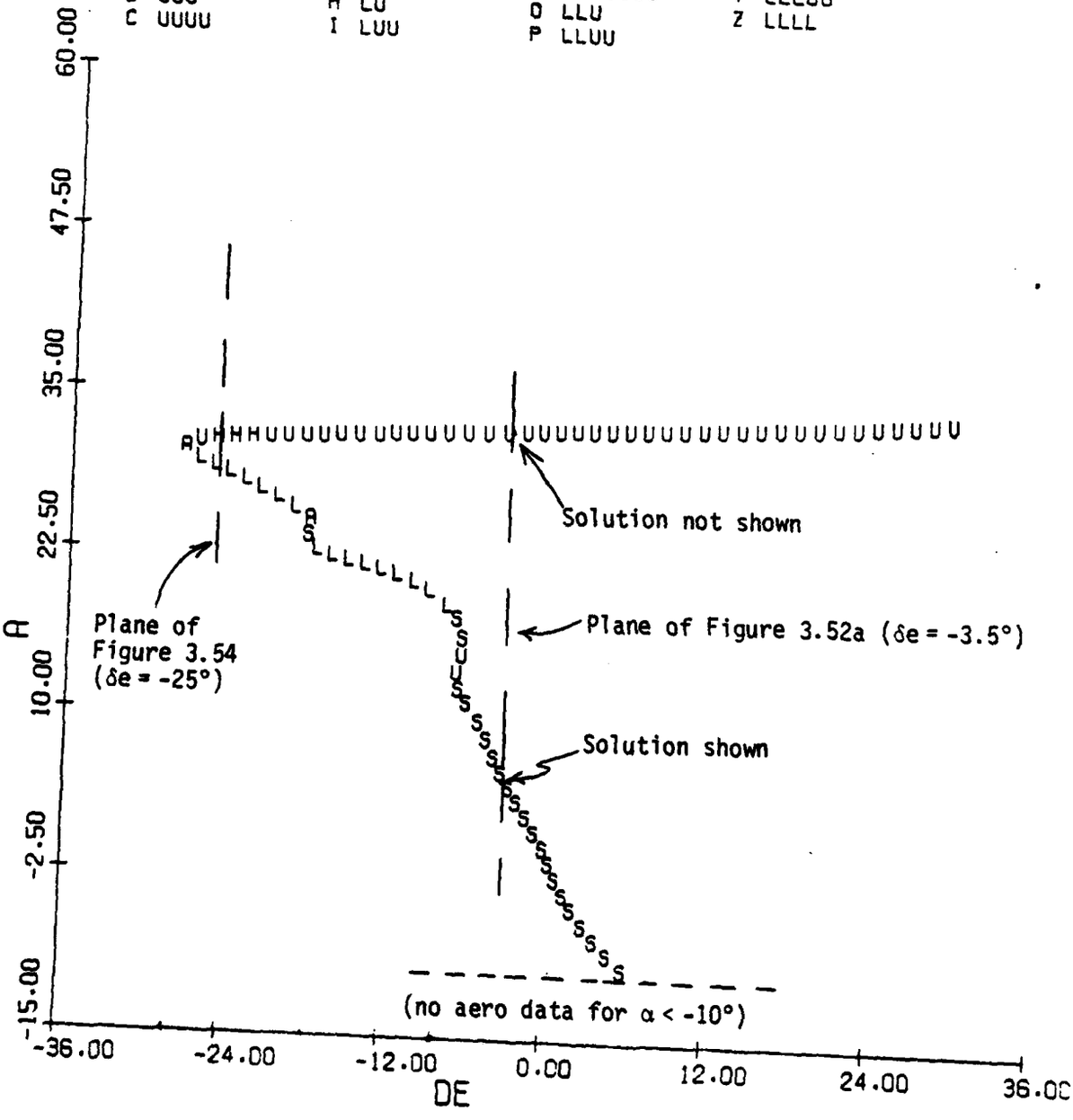

Figure 3.53(b): α vs. δe

DA= -6.0
DR= -6.0

S	D UUUUU	J LUUU	Q LLUUU
U	E UUUUUU	K LUUUU	R LLUUUU
L	F UUUUUUU	M LUUUUU	X LLLU
A UU	G UUUUUUUU	N LUUUUUU	Y LLLUU
B UUU	H LU	O LLU	Z LLLL
C UUUU	I LUU	P LLUU	

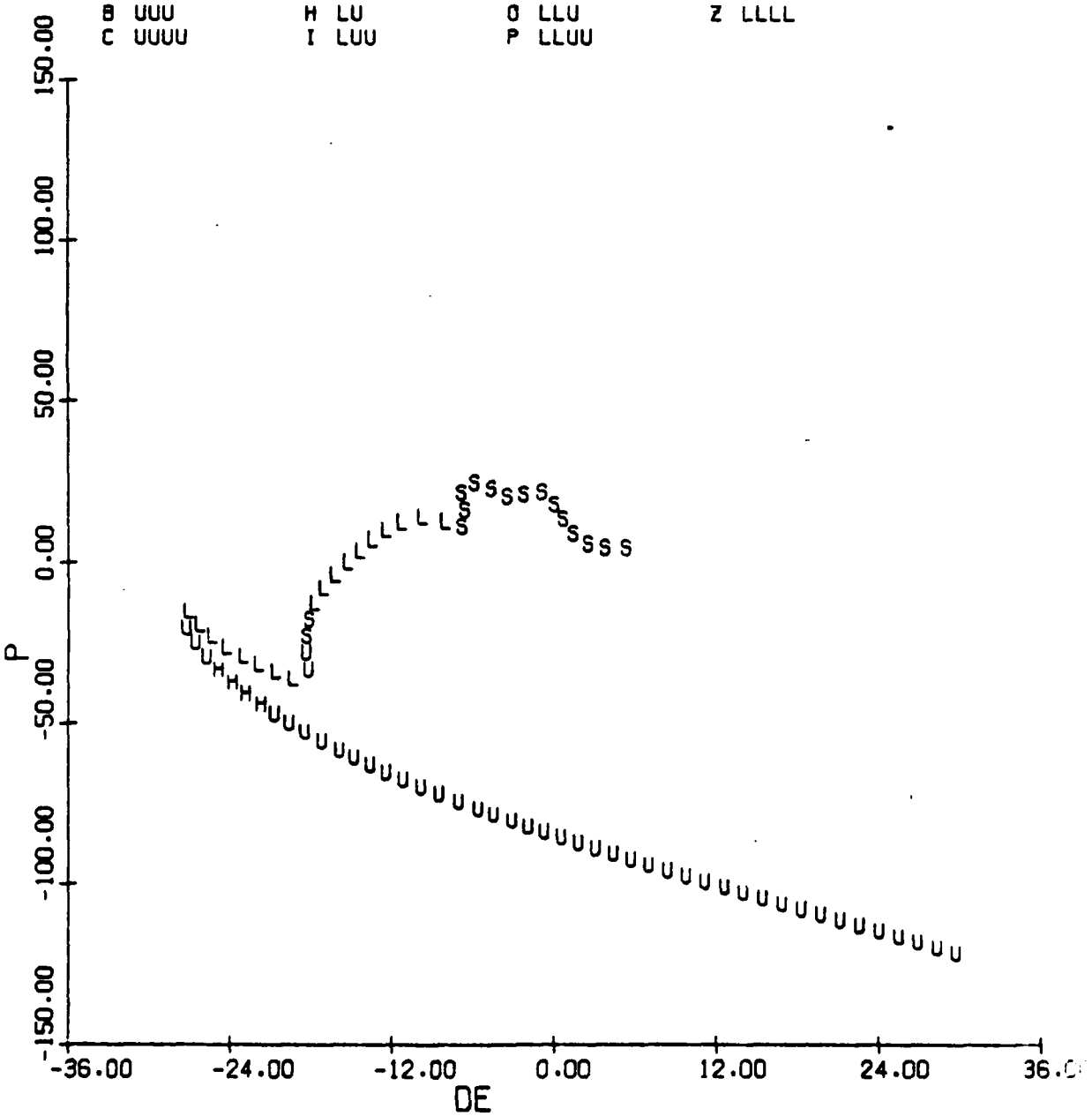

Figure 3.53(c): p vs. δe

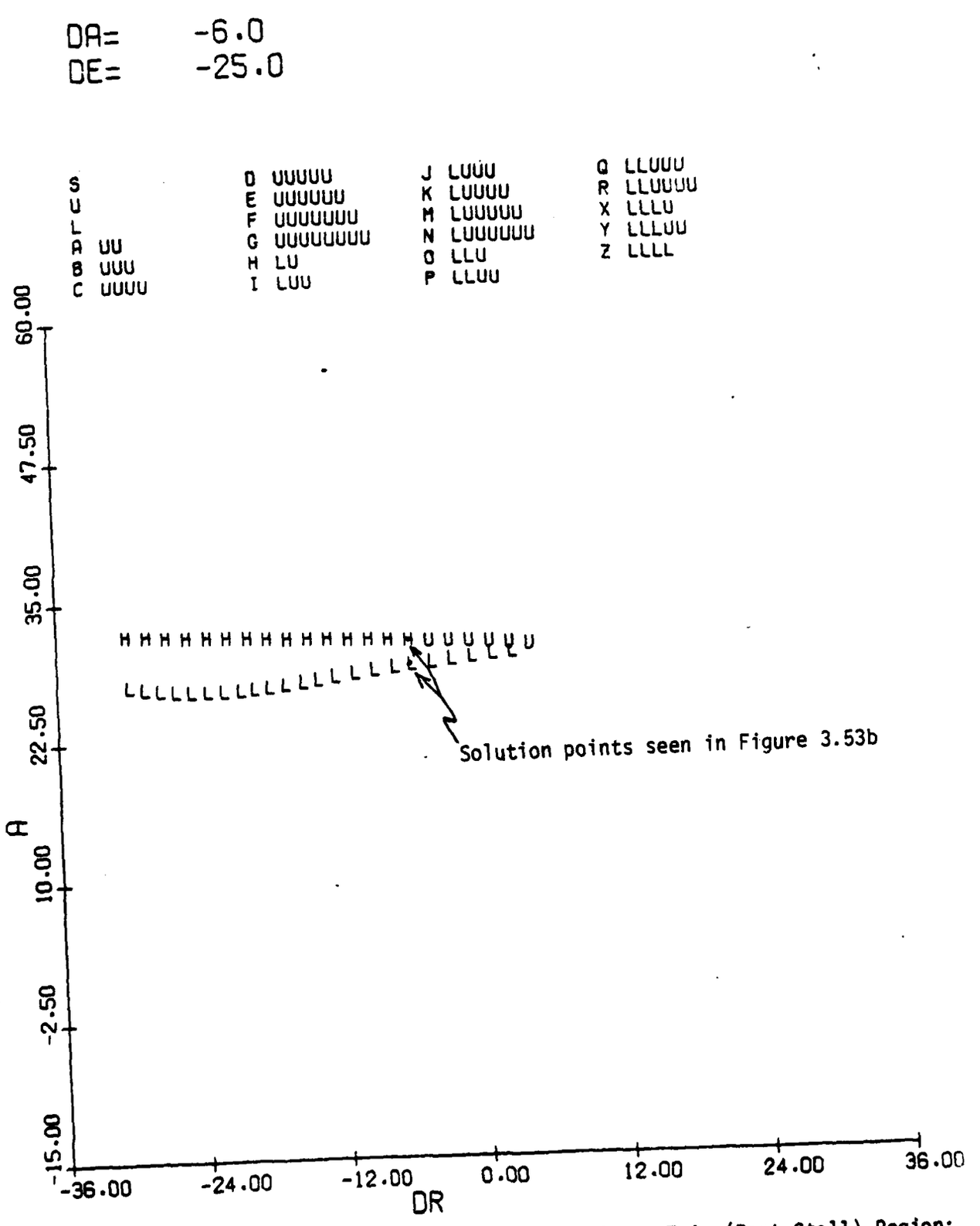

Figure 3.54: F-4 Equilibrium Surface, Trim (Post-Stall) Region; h=5000 ft, V=330 fps, thrust=0; α vs. δr

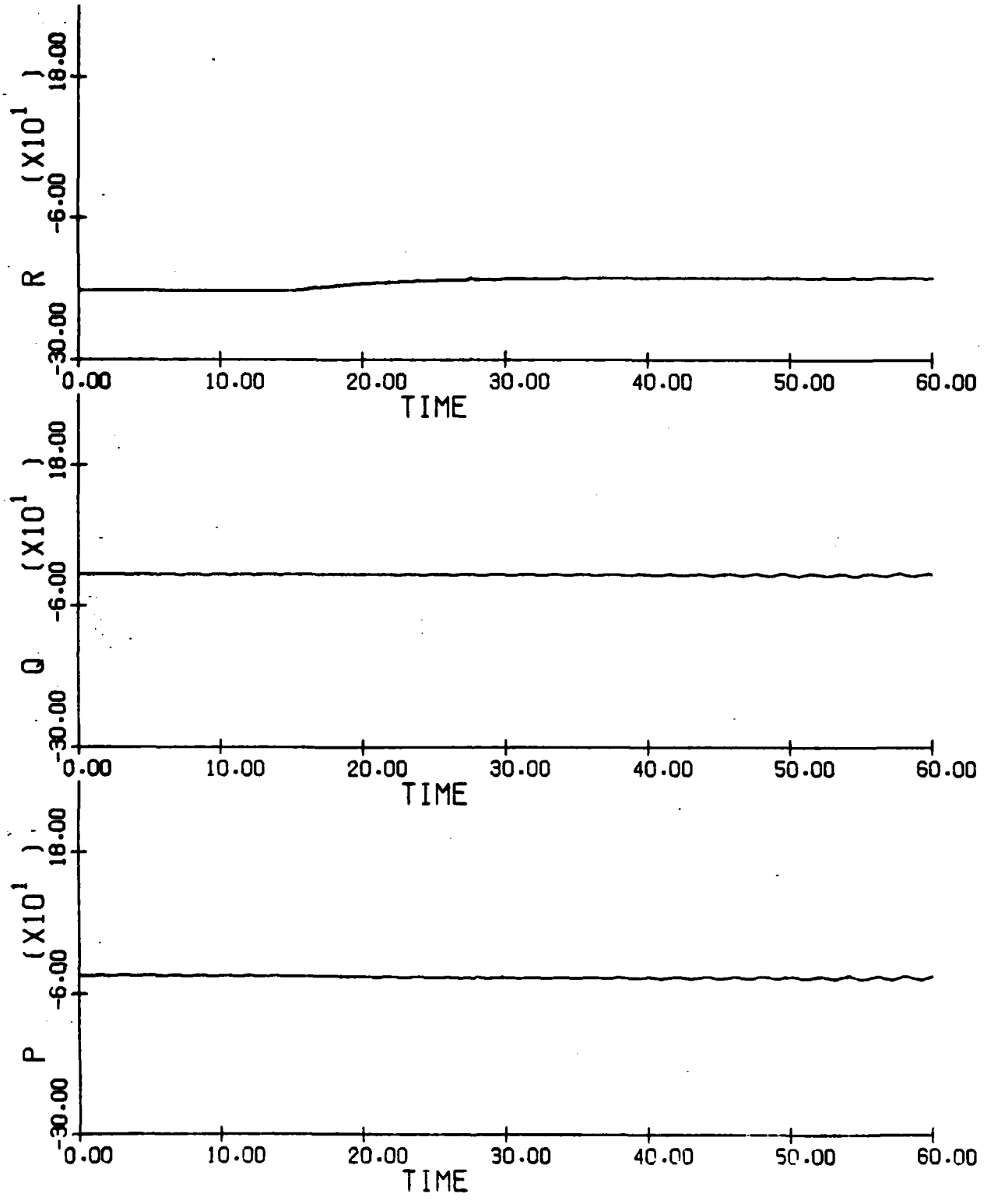

Figure 3.55: F-4 Spin; $\underline{\delta}_0 = (0.,-21.,30.)$; $\delta a = 28°$ at $t = 15$ sec. Initial conditions are flat, equilibrium spin. Linear interpolation is used for rotation balance aero data (a) p,q,r vs. time

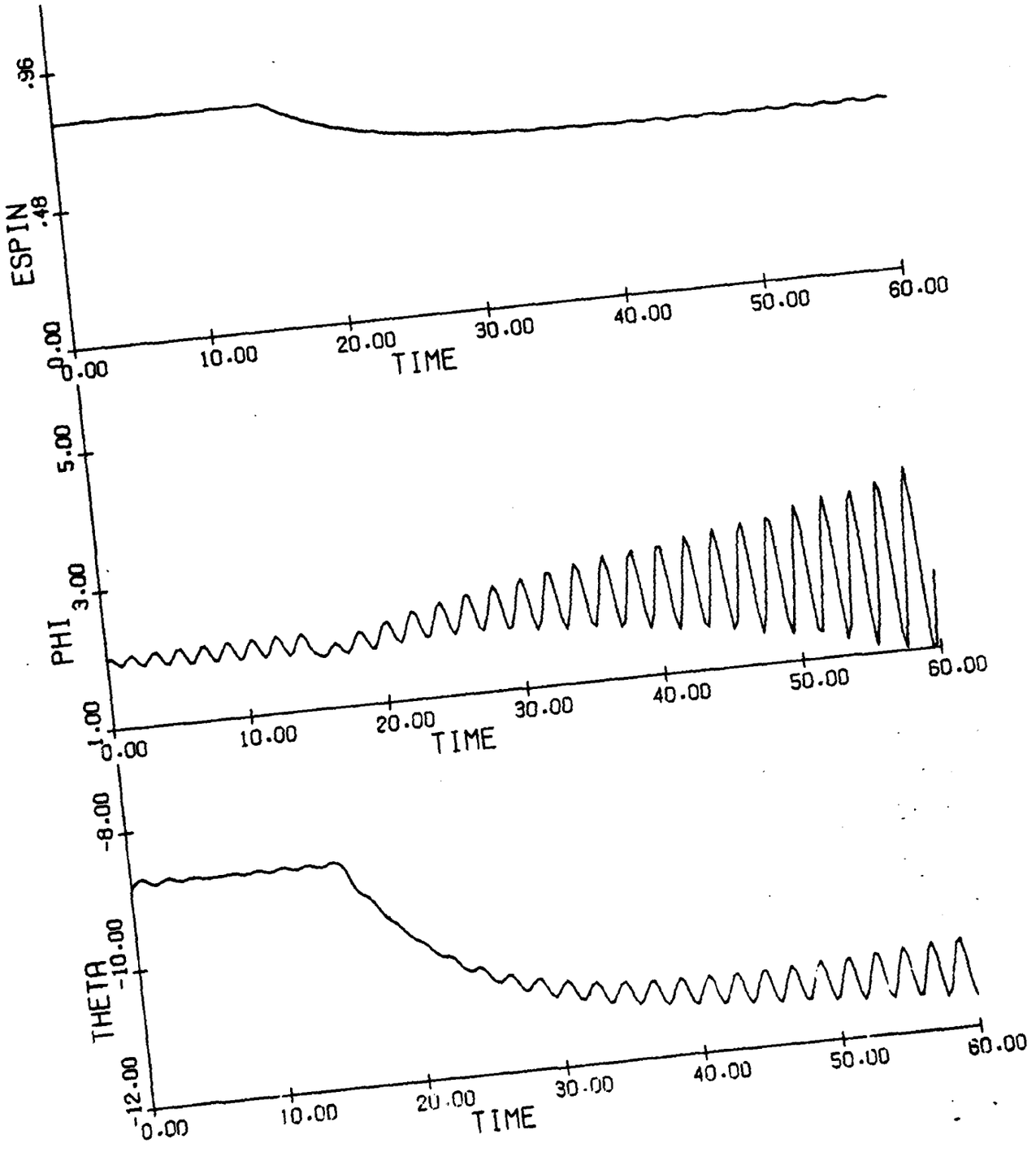

Figure 3.55(b) θ, ϕ, E_{SPIN} vs. time

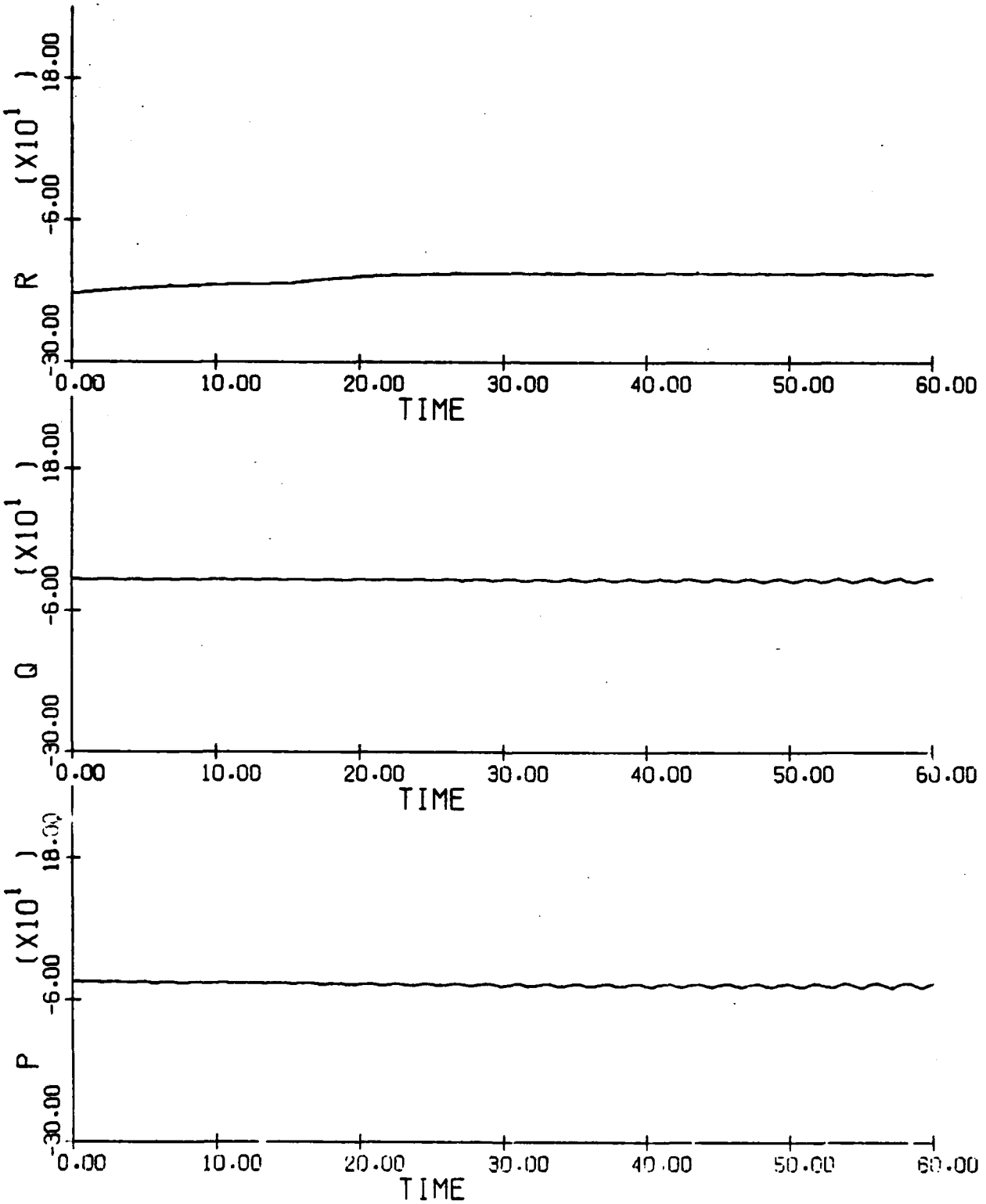

Figure 3.56: F-4 Spin; same trajectory as Figure 3.55, except rotation balance data generated from bicubic splines (a) p,q,r vs. time

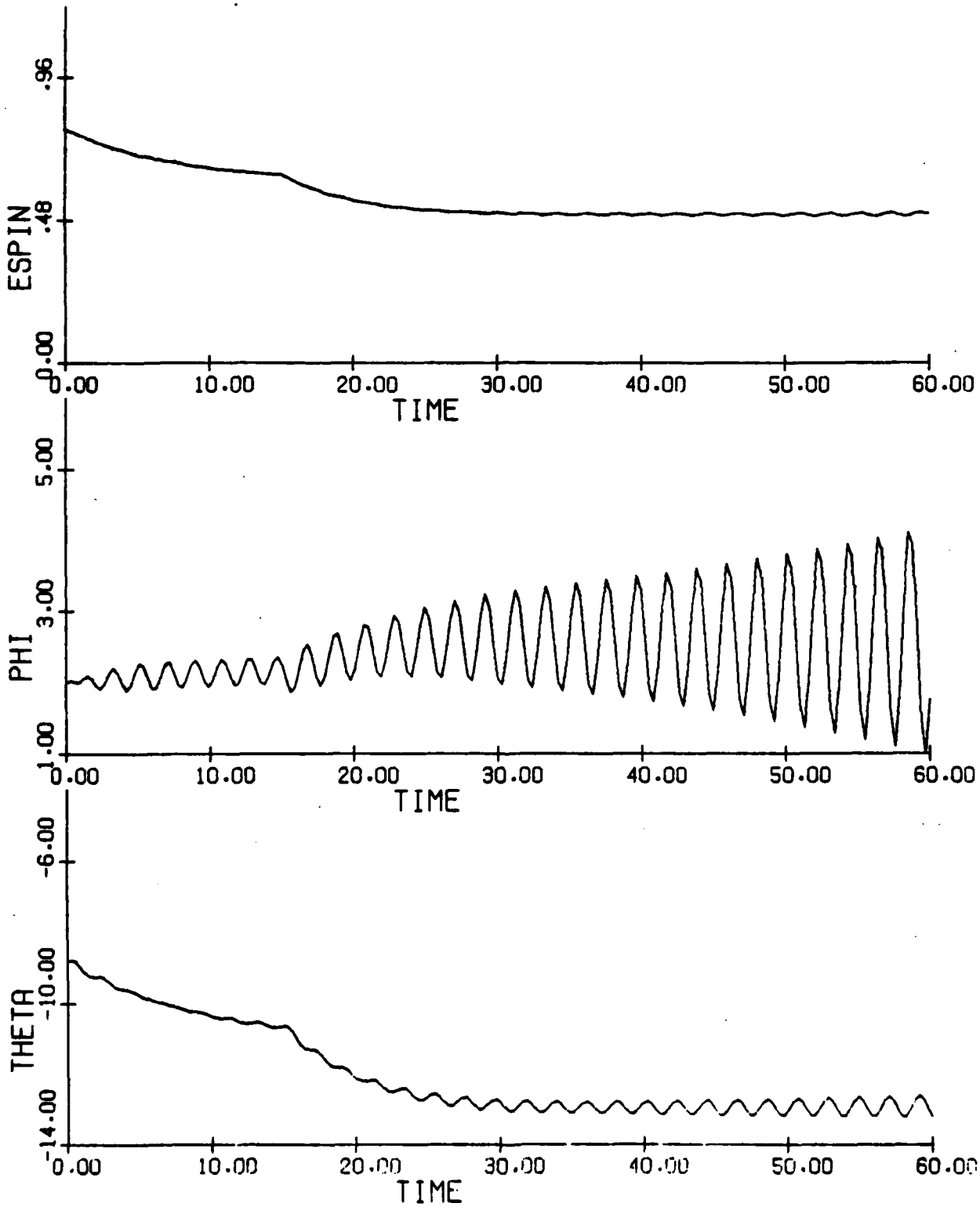

Figure 3.56(b) θ, ϕ, E_{SPIN} vs. time

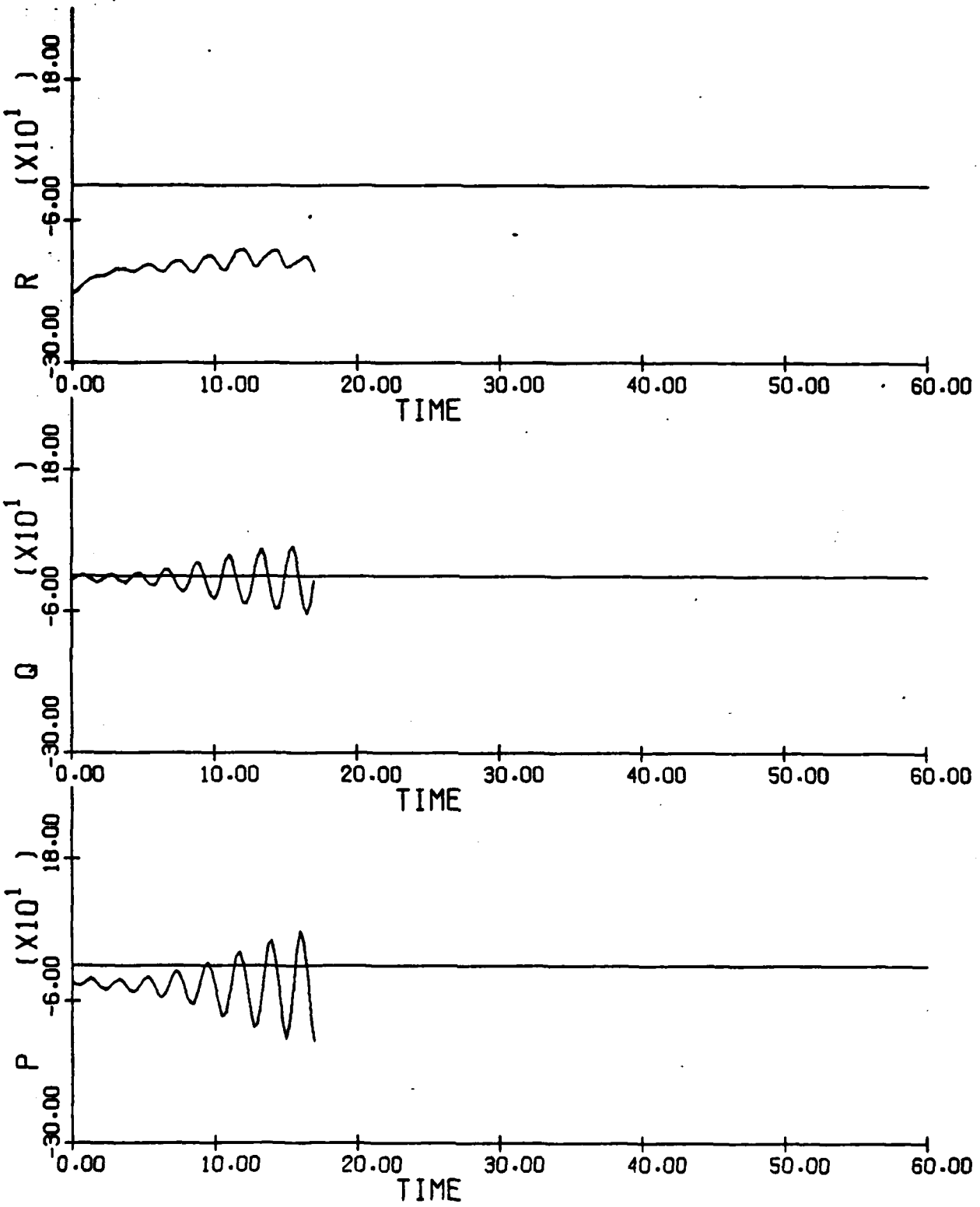

Figure 3.57: F-4 Spin; same trajectory as Figures 3.55 and 3.56, except $\Omega = (p \cos\alpha + r \sin\alpha)$
(a) p,q,r vs. time

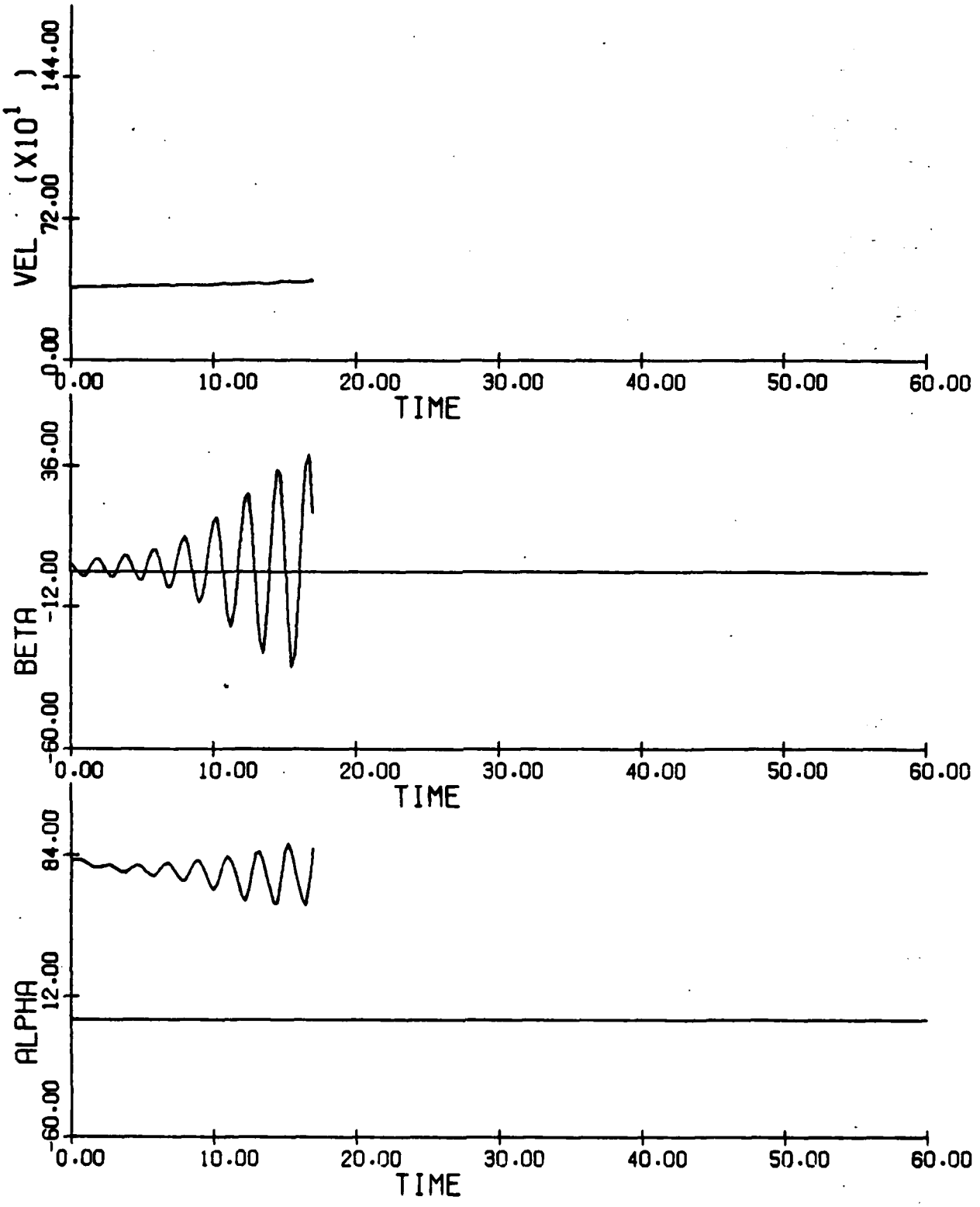

Figure 3.57(b) α,β,V vs. time

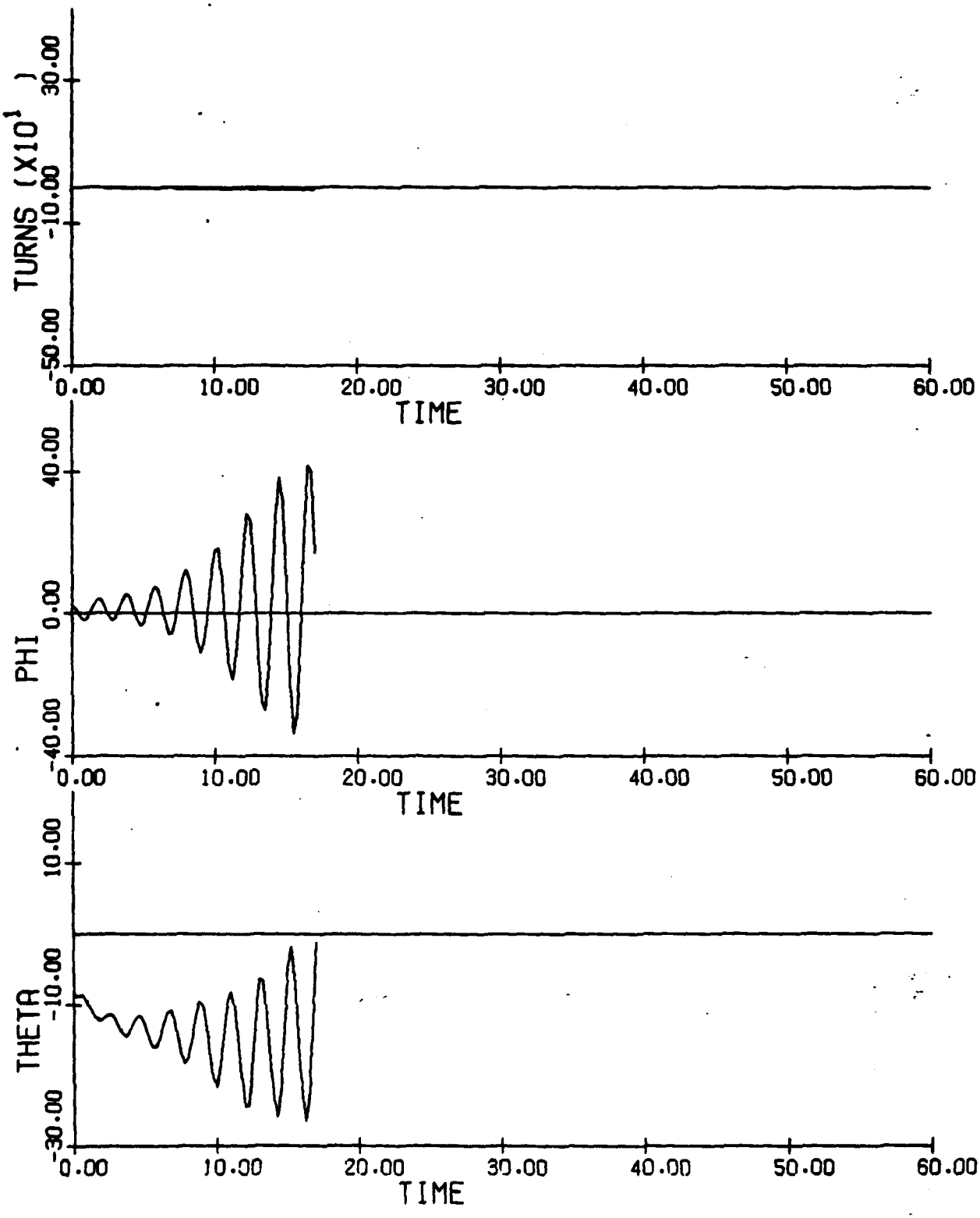

Figure 3.57(c) θ,ϕ,TURNS vs. time

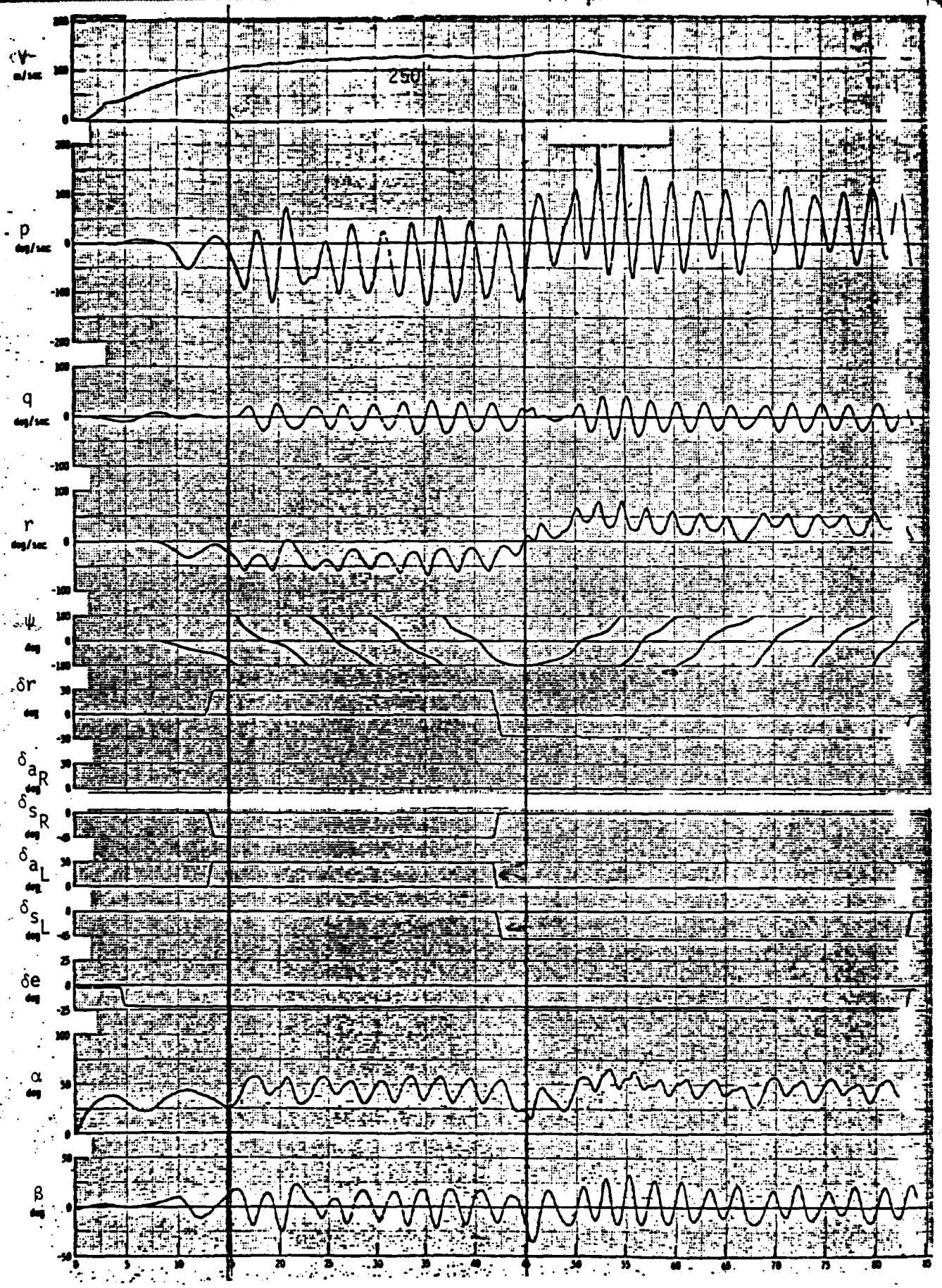

Figure 3.58: F-4 Drop Model Flight Test, conducted at NASA Langley, Flight 6; initial altitude ≈5000 ft. For most of the period $15. \leq t \leq 45$, $\underline{\delta} = (30, -21, 30)$

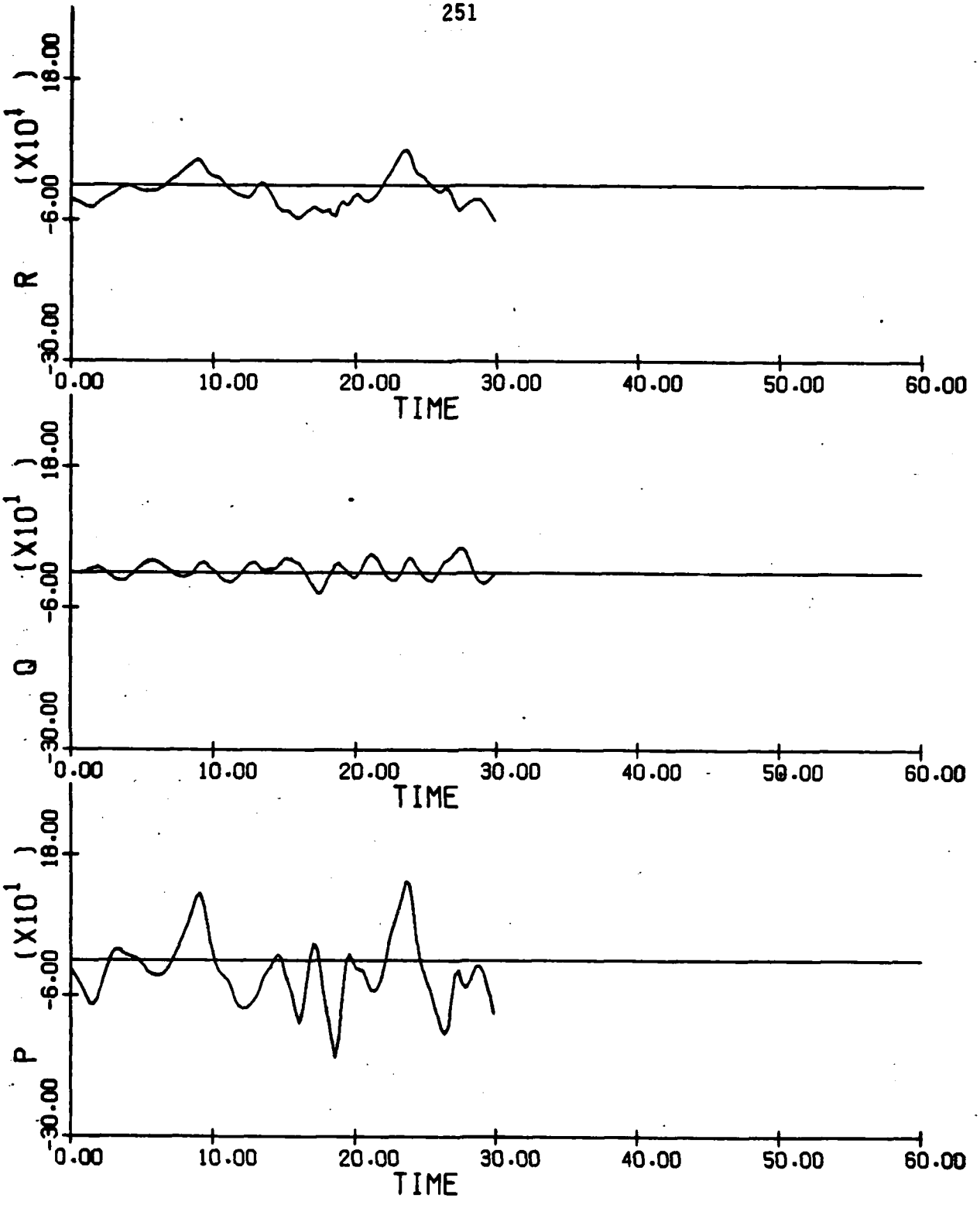

Figure 3.59: F-4 Correlation Run; Comparison with Fig. 3.58 Langley Flight Test; $\delta a = 30°$, $\delta e = -21°$, $\delta r = 30°$; $h(t_0) = 30000$ ft. (a) p,q,r vs. time

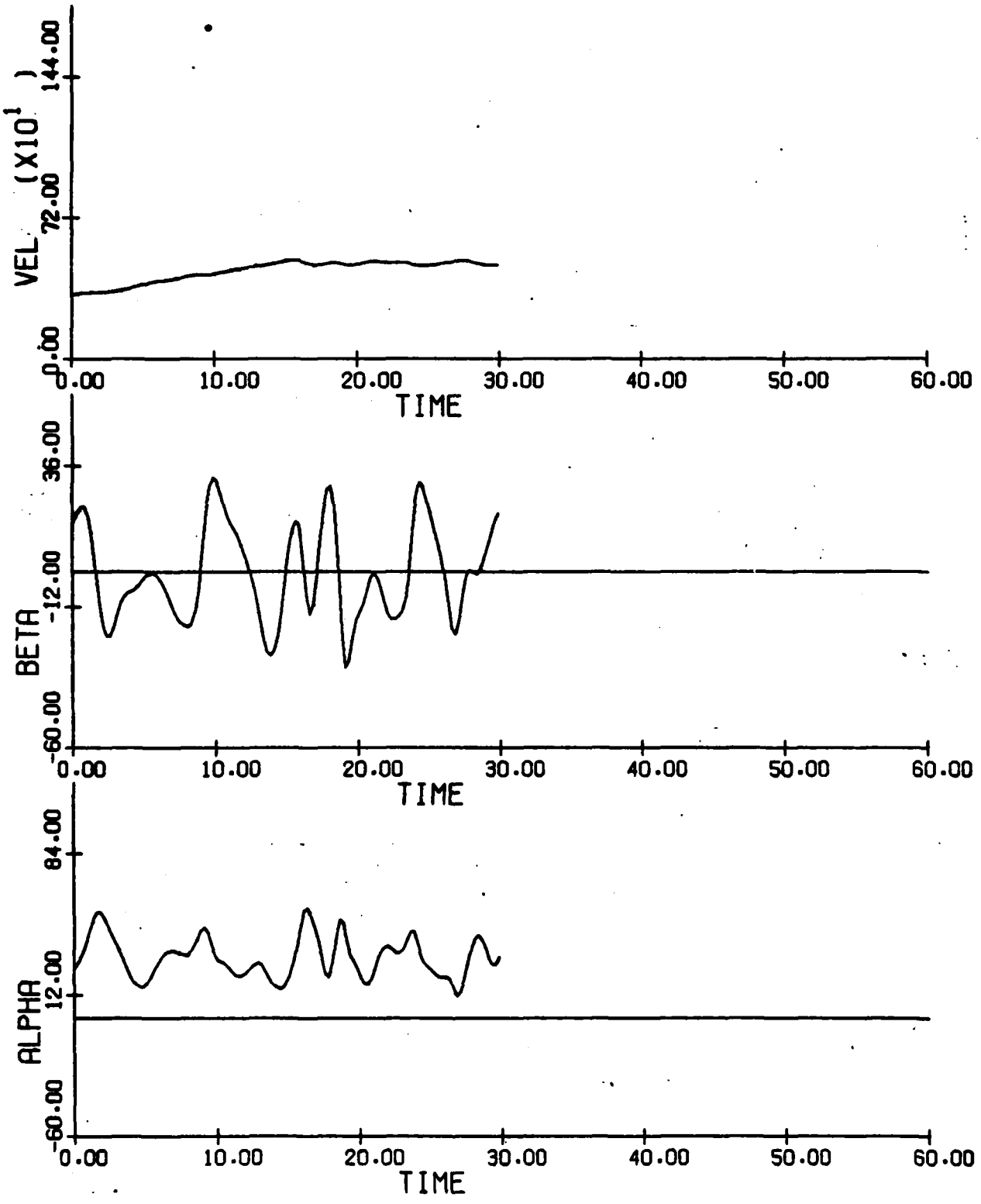

Figure 3.59(b) α, β, V vs. time

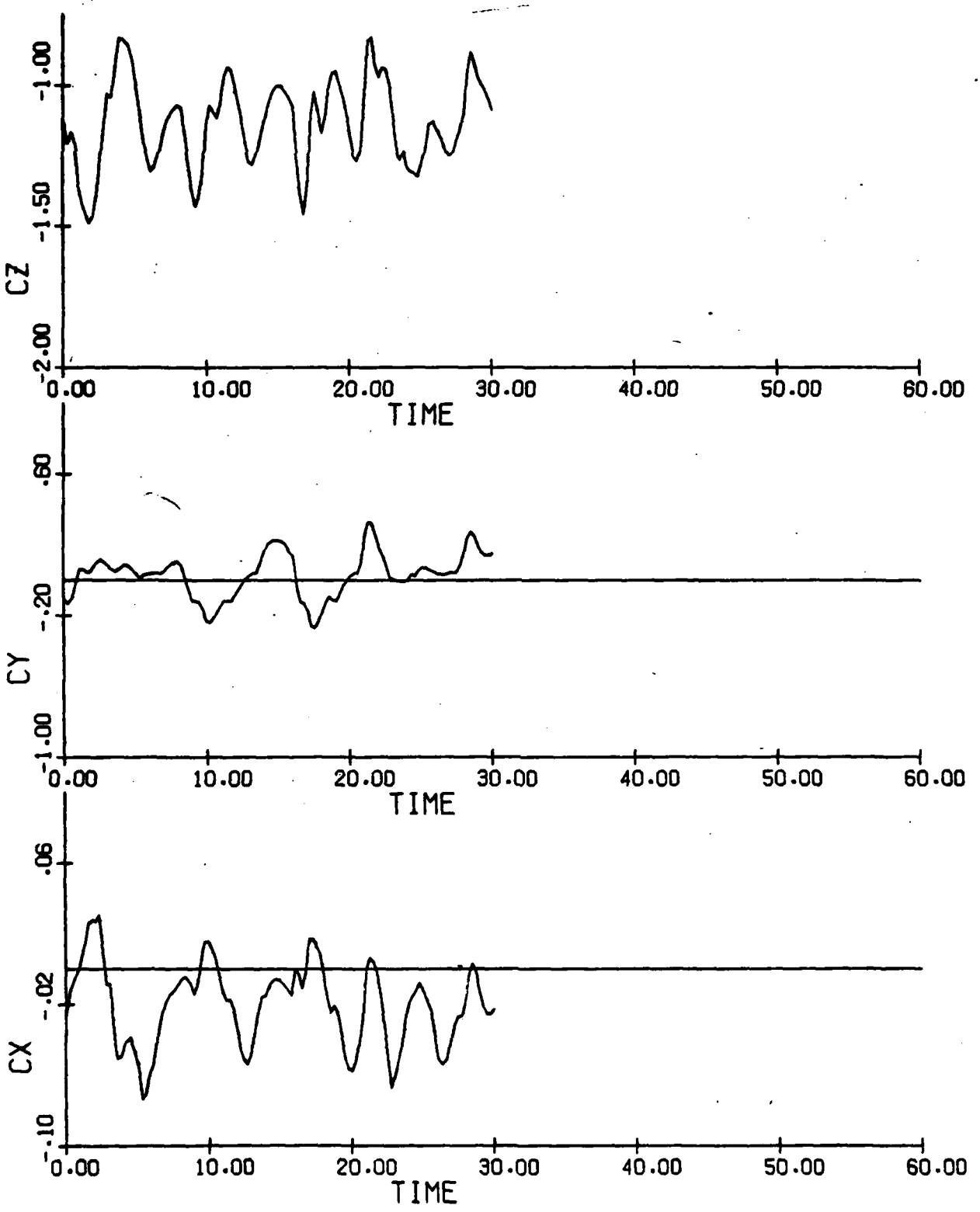

Figure 3.60: F-4 Correlation Run; Taken from Figure 3.59 trajectory
(a) C_x, C_y, C_z vs. time

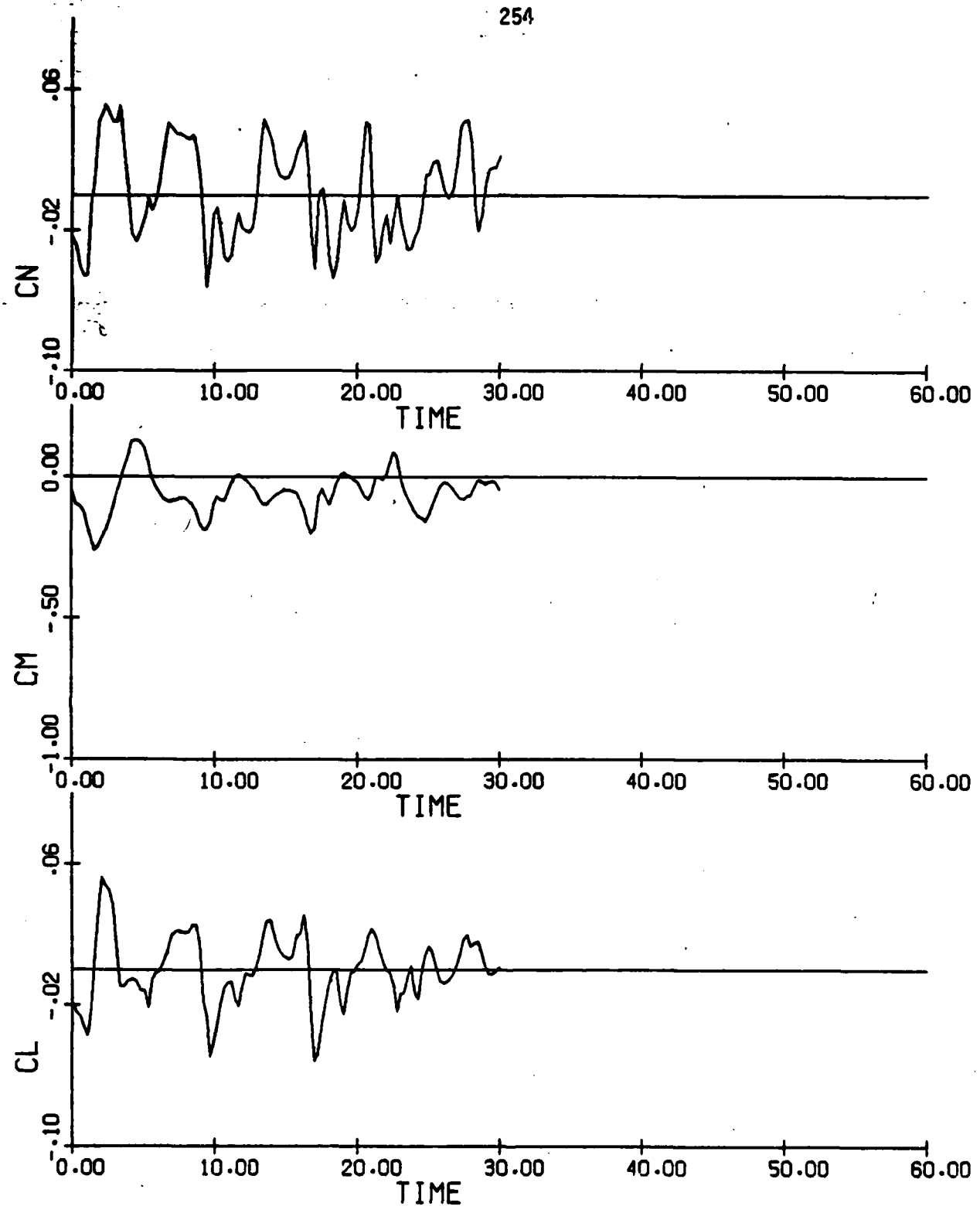

Figure 3.60(b) C_ℓ, C_m, C_n vs. time

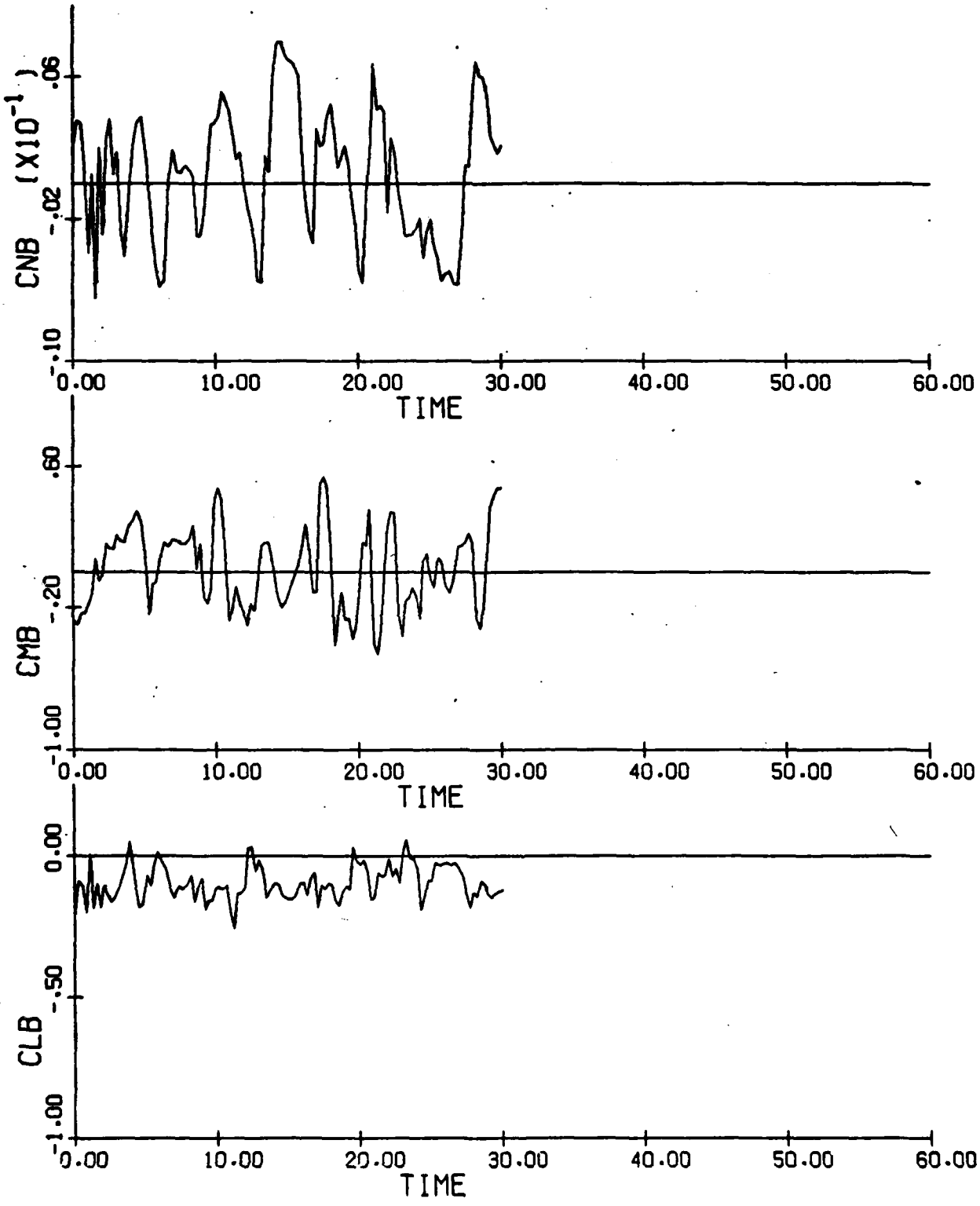

Figure 3.60(c) $C_{\ell_\beta}, C_{m_\beta}, C_{n_\beta}$ vs. time

Figure 3.61: F-4 Correlation Run; Comparison with Figure 3.58
Langley Flight Test; $\delta a = 30°$, $\delta e = -21°$, $\delta r = 30°$,
$h = 30000$ ft

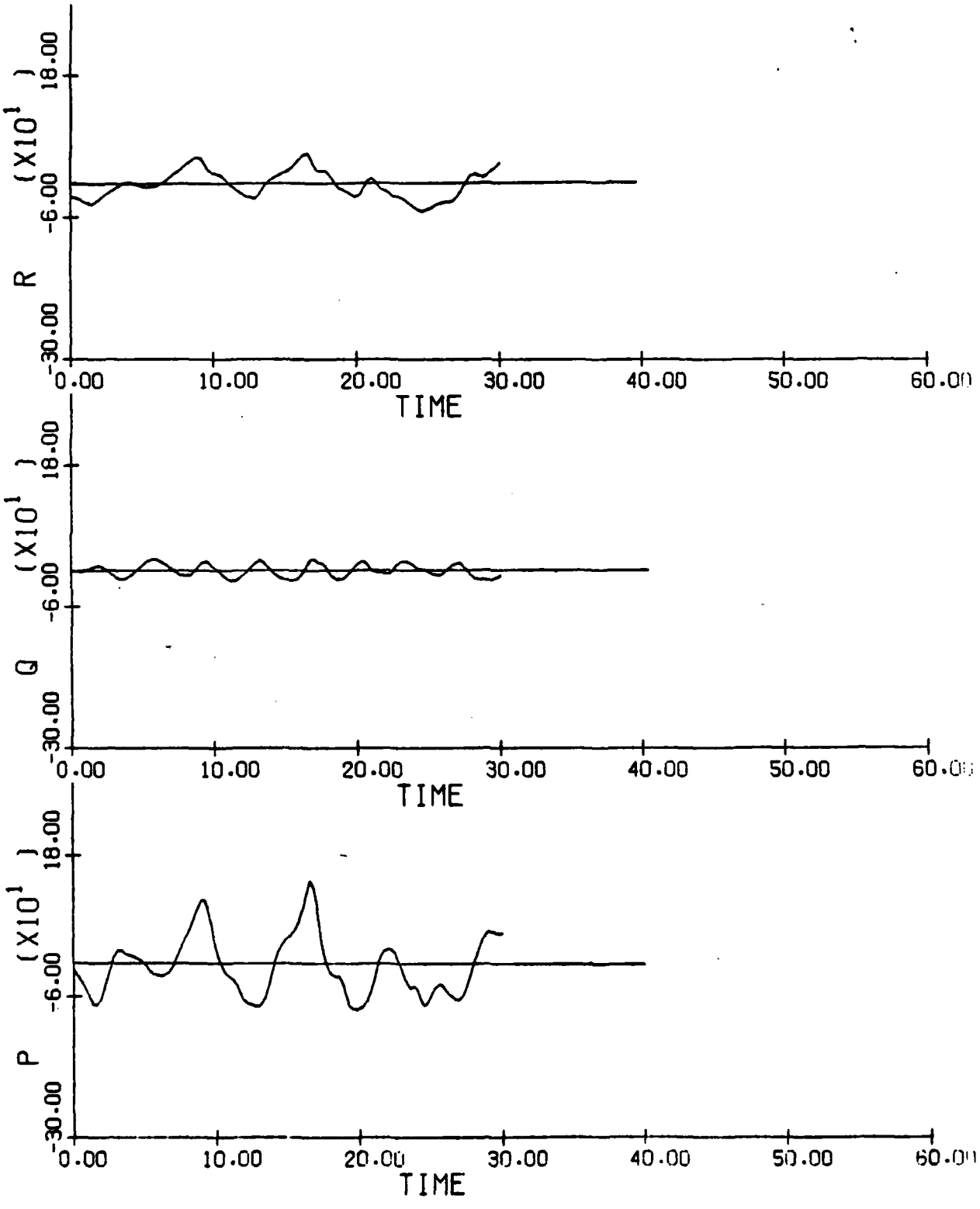

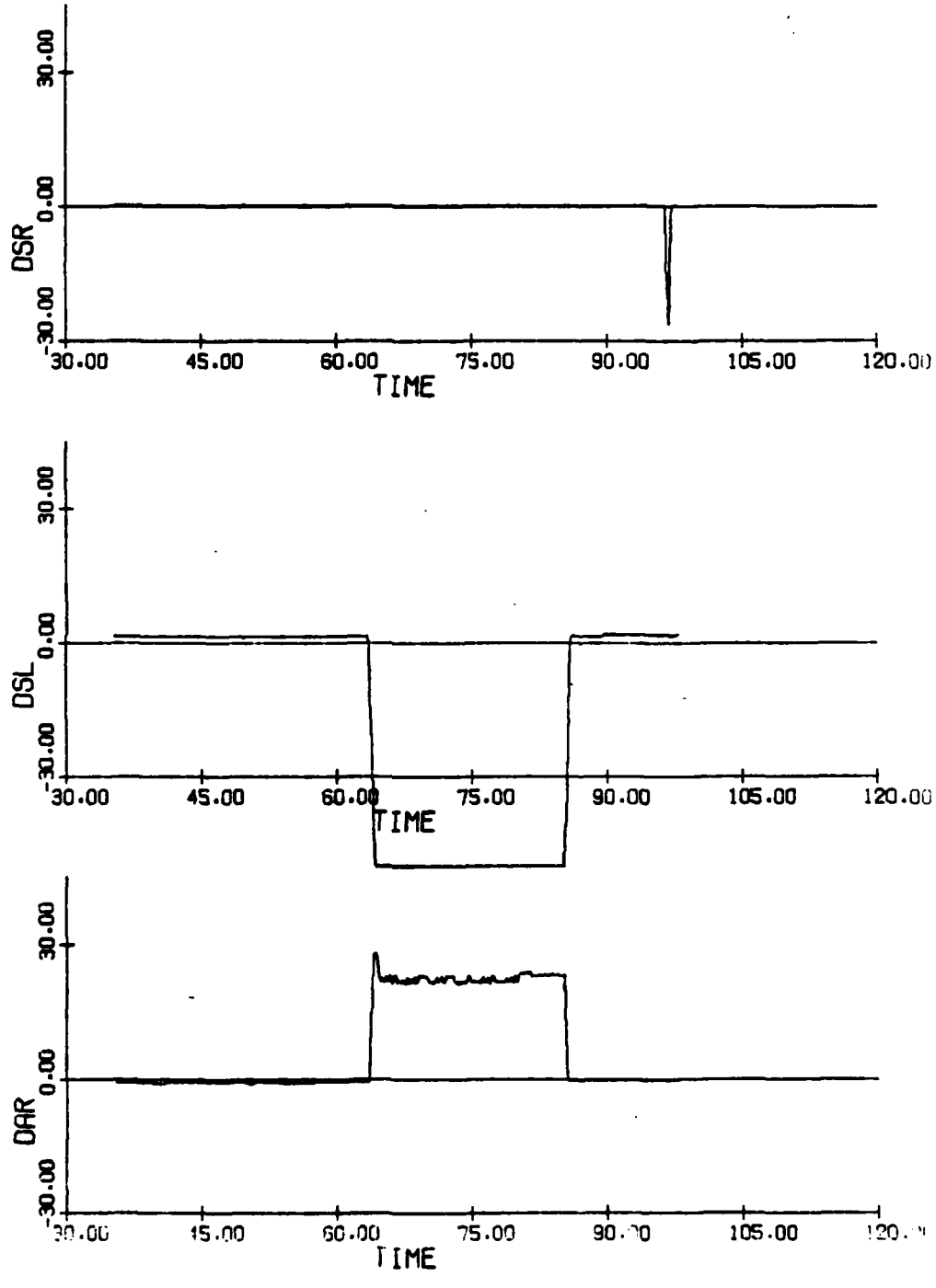

Figure 3.62: F-4 Correlation Run; Langley Flight 1 (parts (a) to (d)) vs. Simulation Model (parts (e) to (g))
(a) Langley Model: δ_{a_R}, δ_{s_L}, δ_{s_R} vs. t

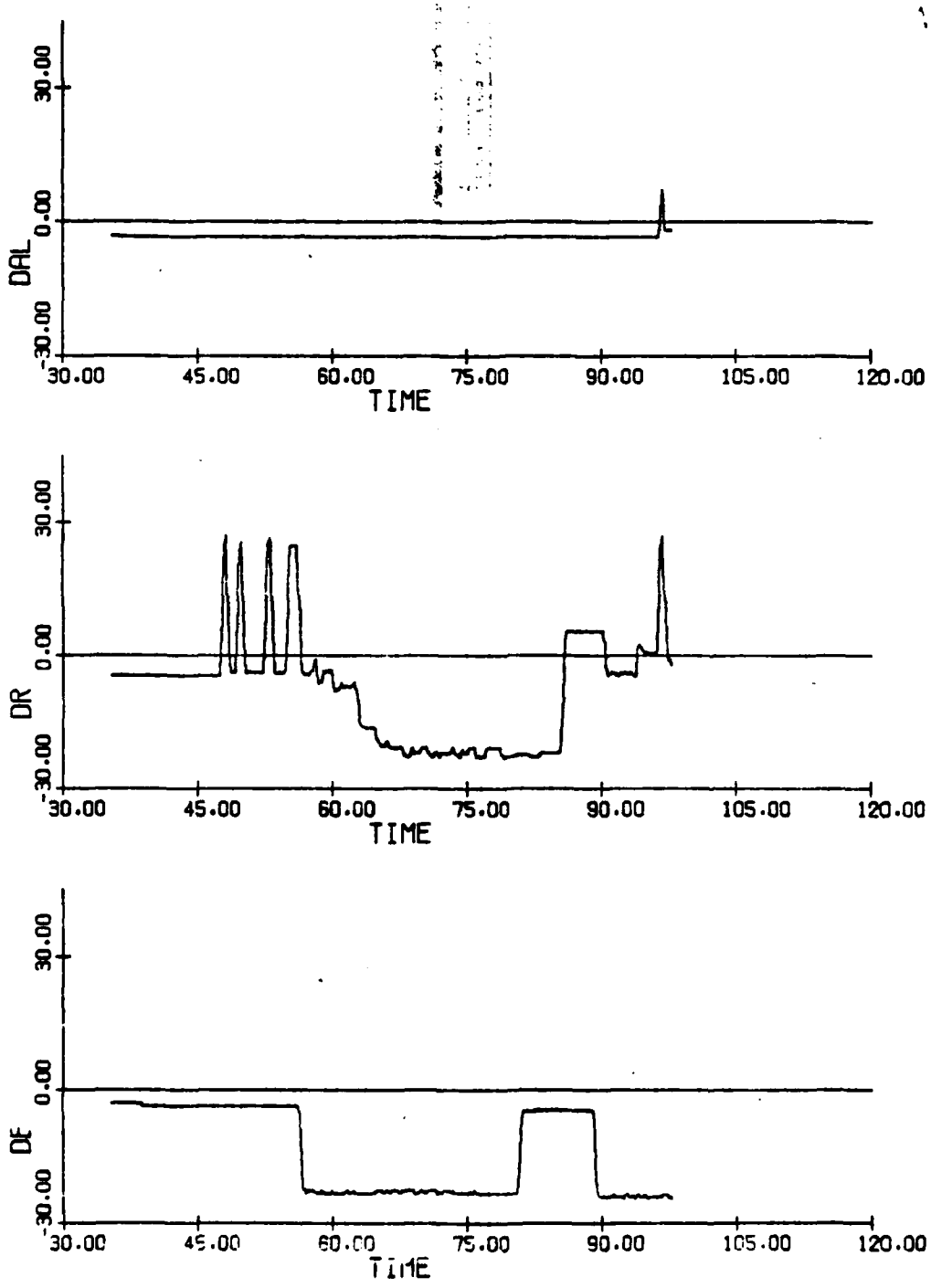

Figure 3.62(b): Langley Model: δe, δr, δ_{a_L} vs. t

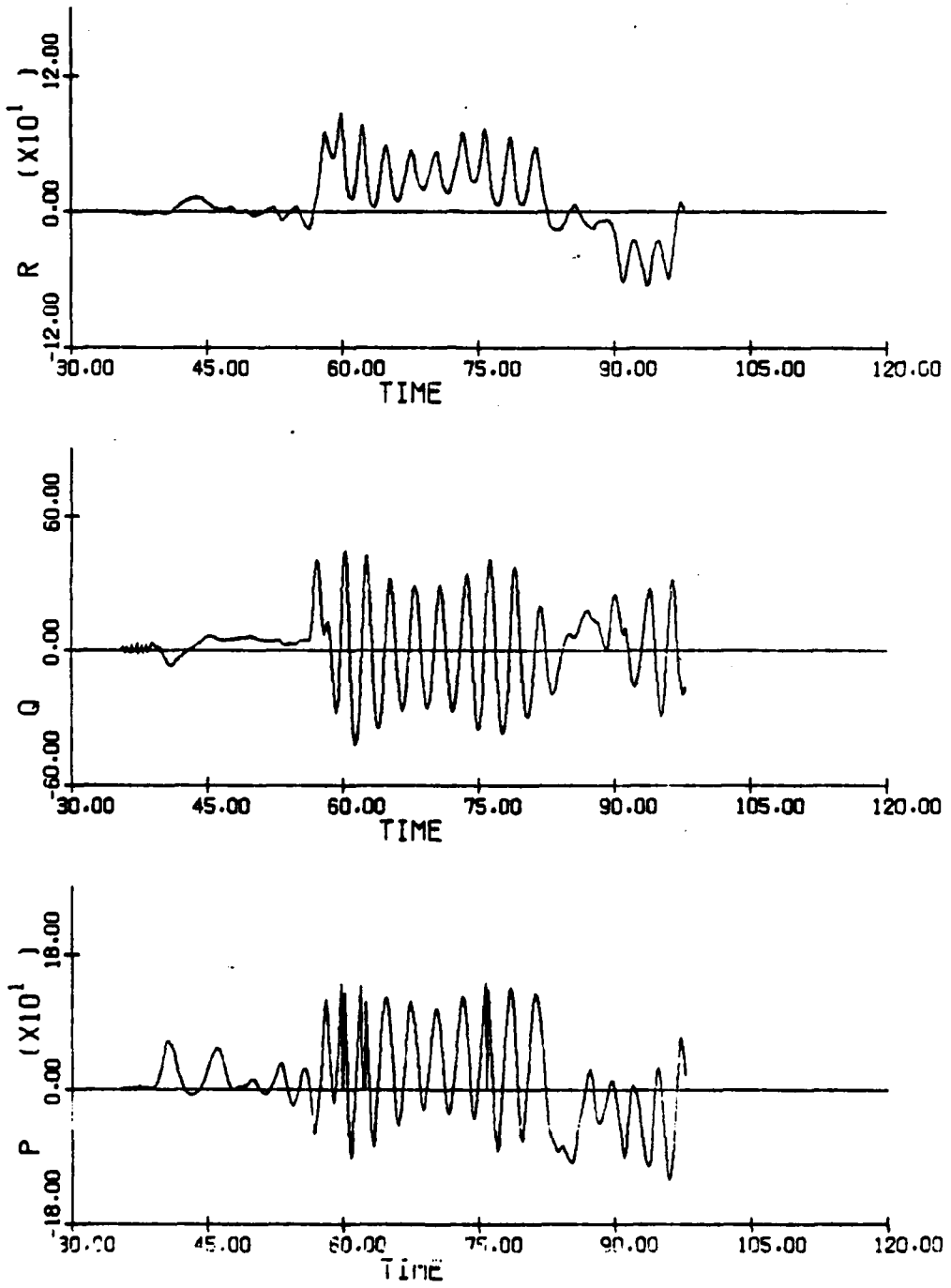

Figure 3.62(c): Langley Model: p, q, r vs. t

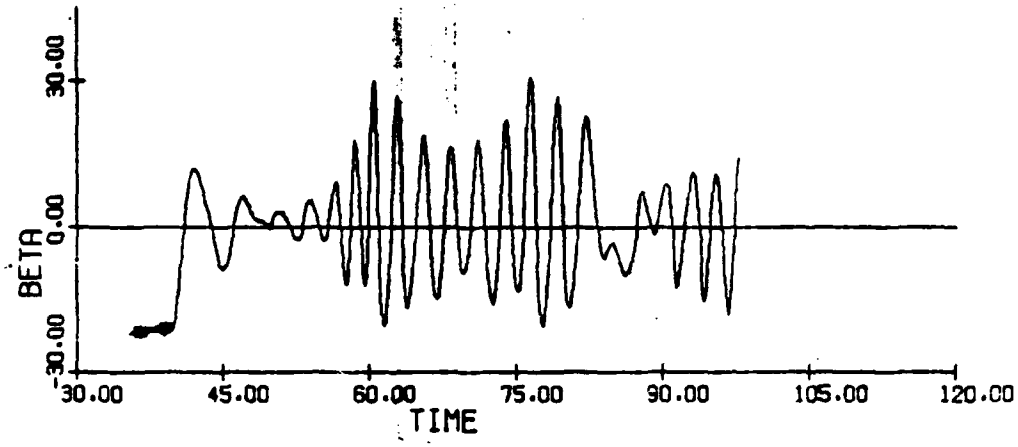

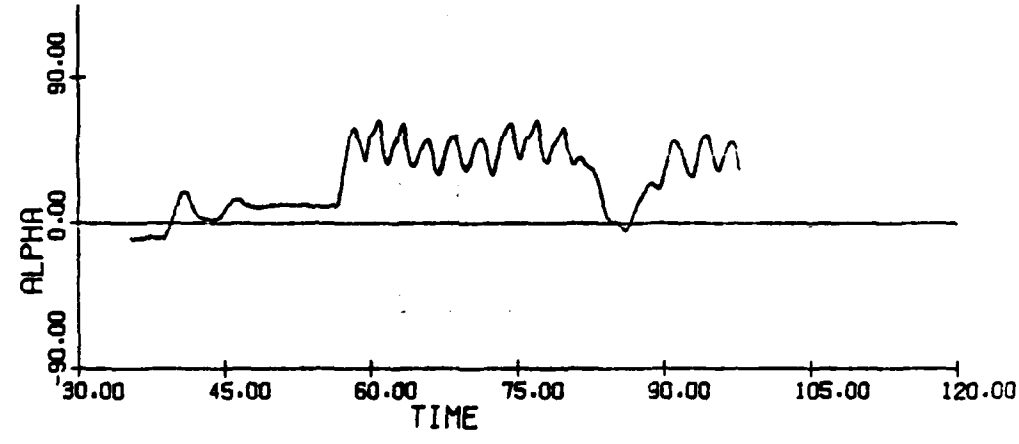

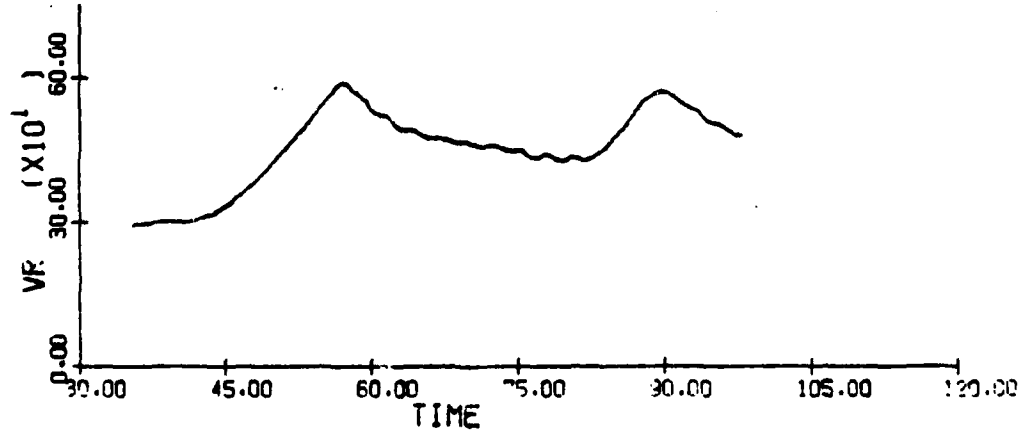

Figure 3.62(d): Langley Model: V, α, β vs. t

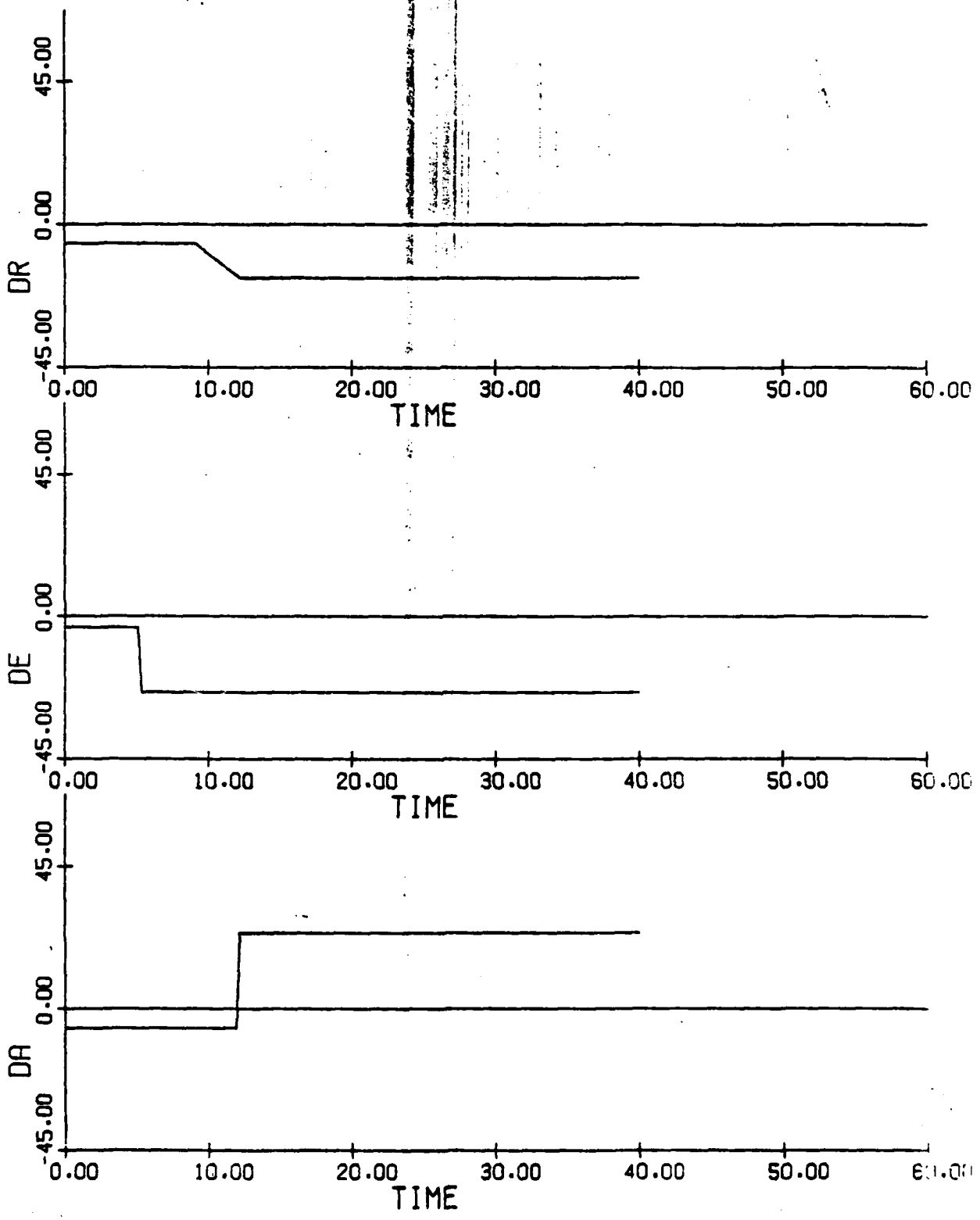

Figure 3.62(e): Simulation Model: δa, δe, δr vs. t

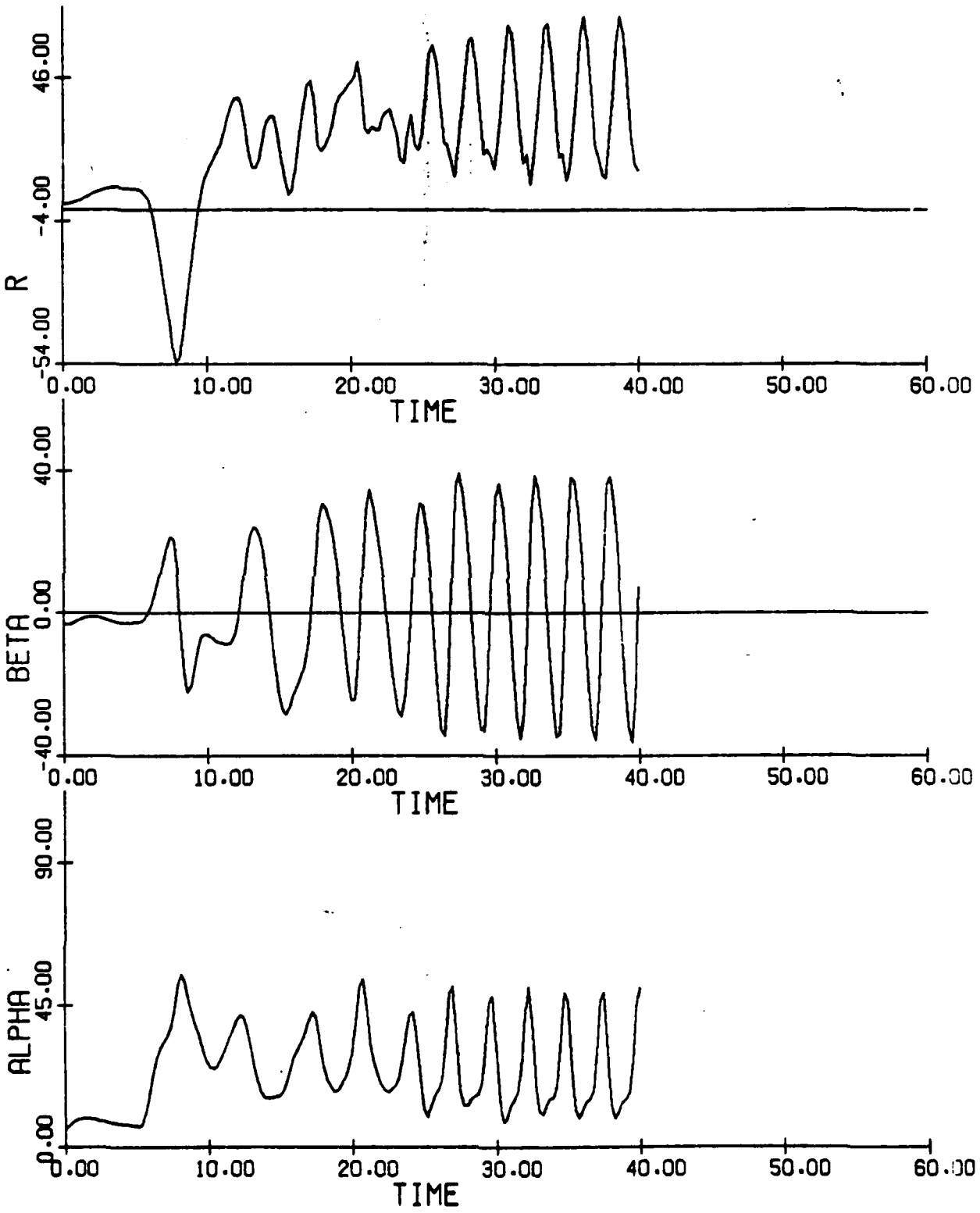

Figure 3.62(f): Simulation Model: α, β, r vs. t

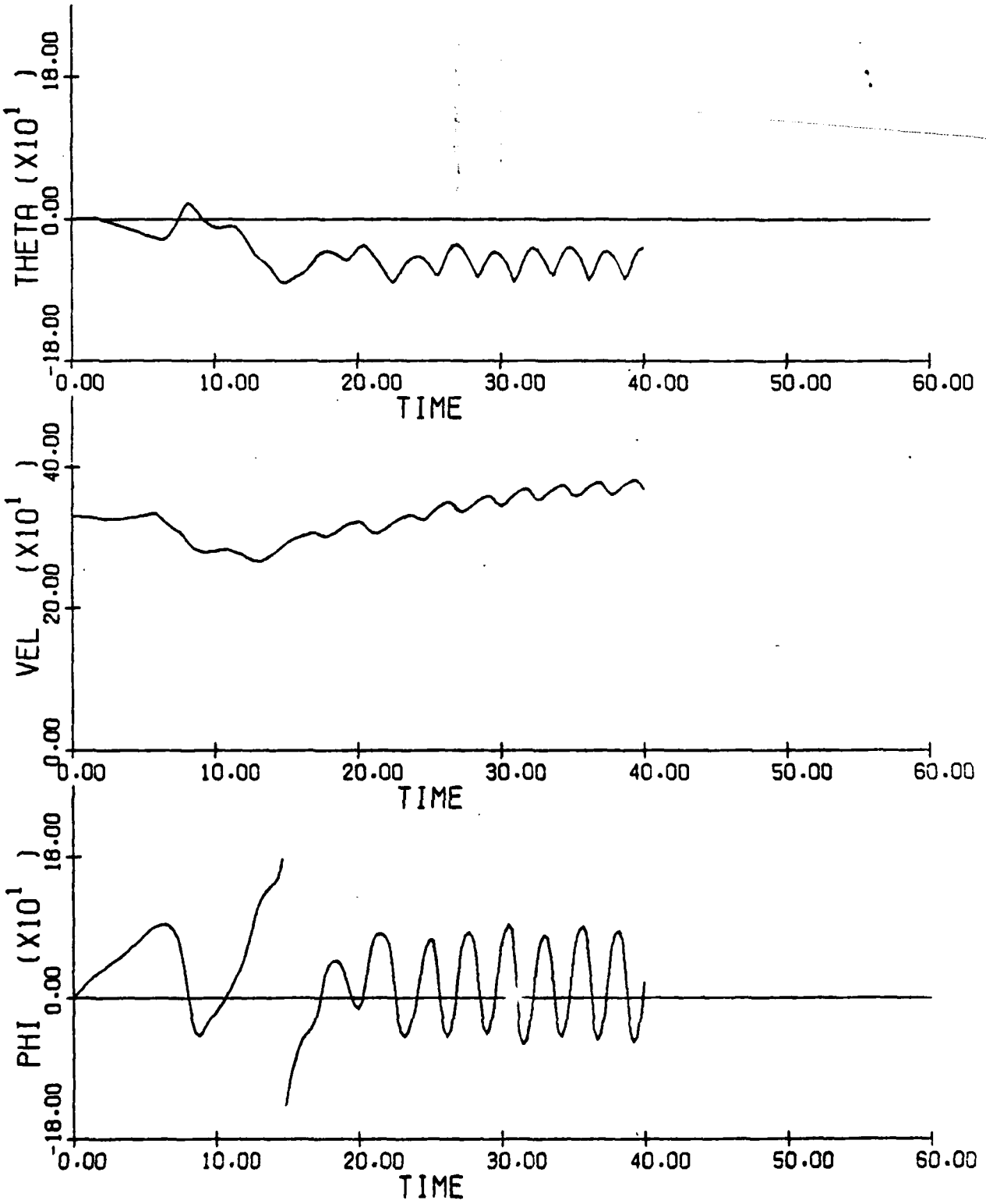

Figure 3.62(g): Simulation Model: ϕ, V, θ vs. t

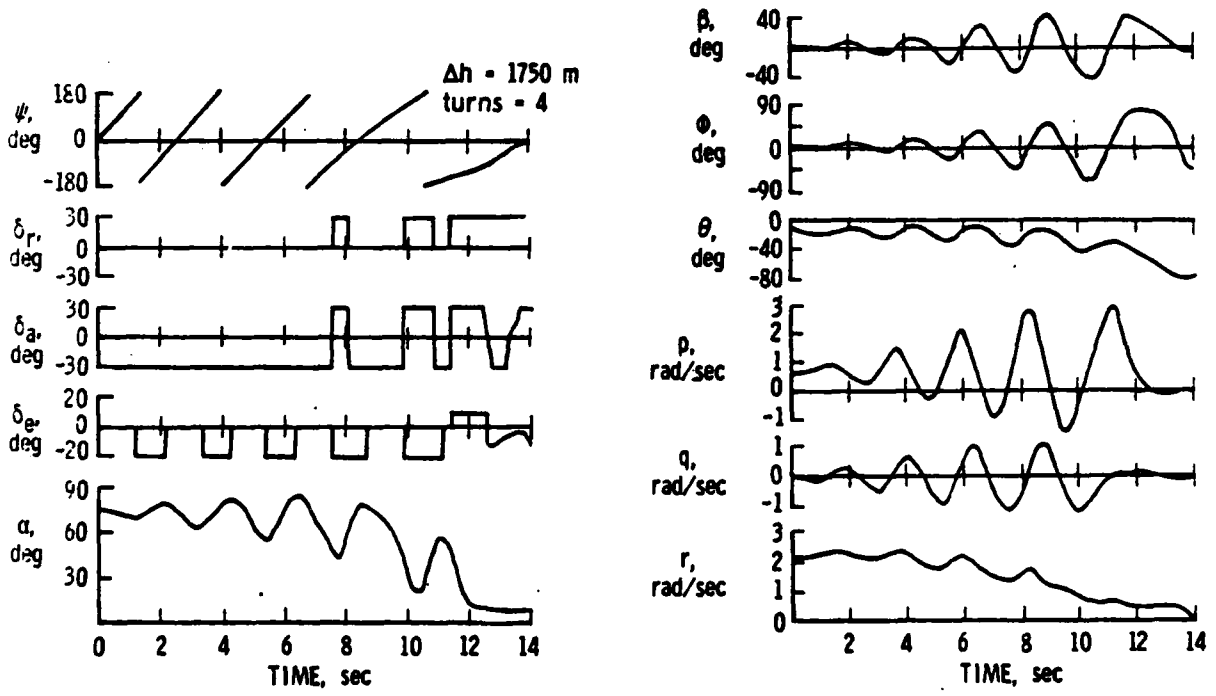

Figure 3.63: Spin Recovery for F-4 Using Pitch Excitation

Figure 3.64: F-4 Correlation Run; Comparison with Young and Adams (1972) result, Figure 3.63; h = 40000 ft. (a) δa, δe, δr vs. t

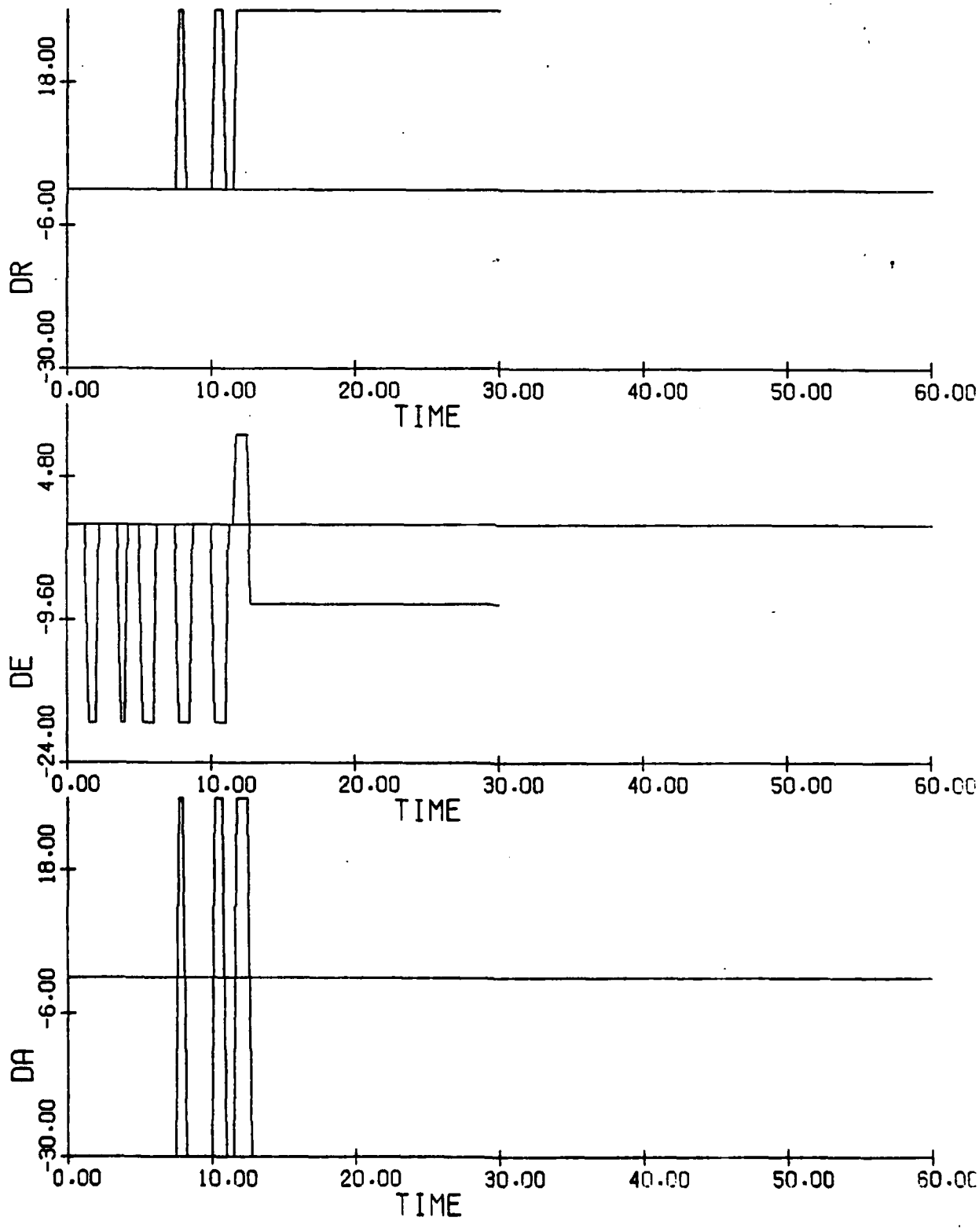

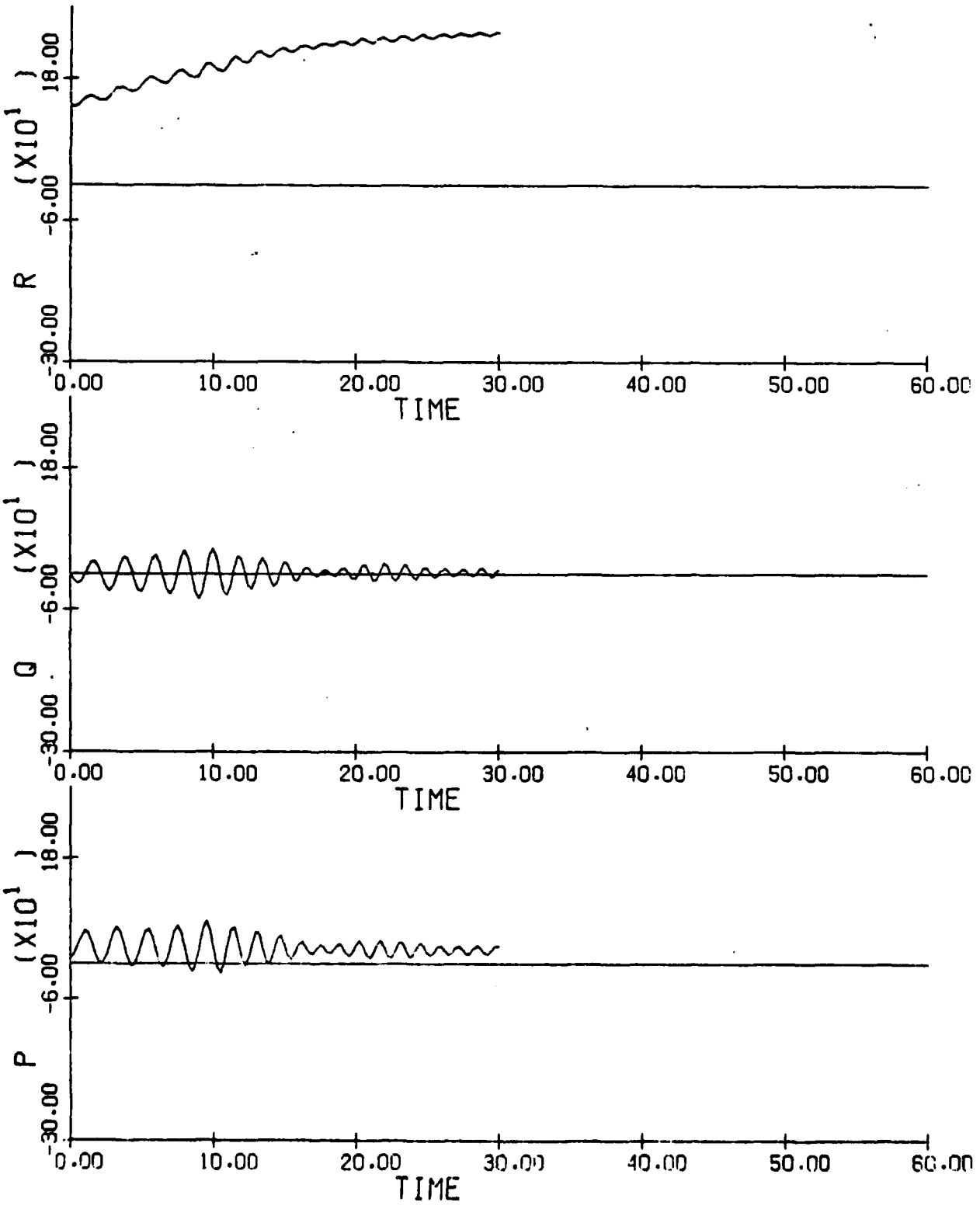

Figure 3.64(b): p, q, r vs. t

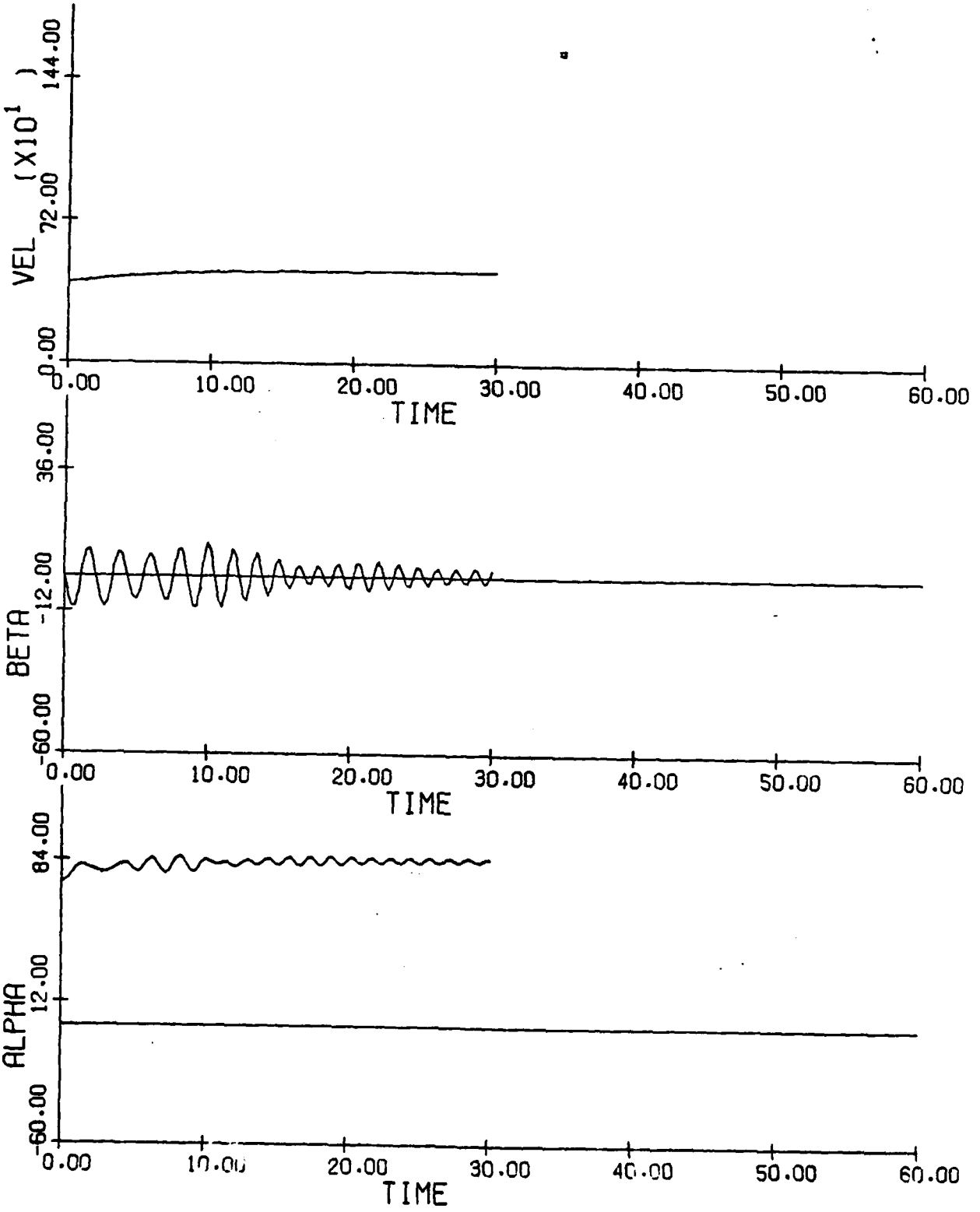

Figure 3.64(c): α, β, V vs. t

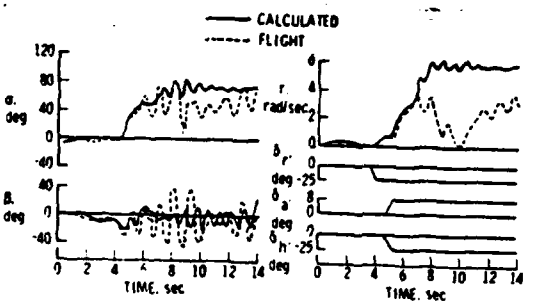

Figure 3.65(a): Comparison of Theoretical Spin Calculations and Free-Flight Model Motions, F-4 Aircraft

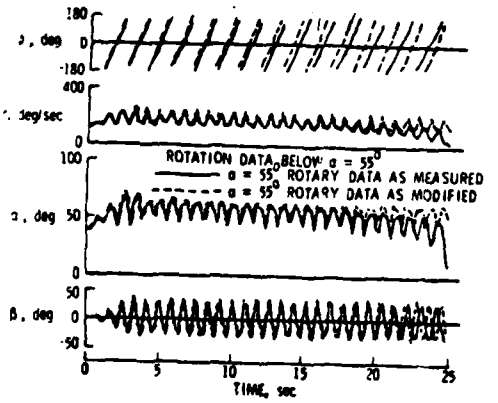

Figure 3.65(b): Prerotated Oscillatory Spins Using the Hybrid Data System Incorporating Rotation-Balance Yawing Moment Data; F-4 Aircraft

Figure 3.66: F-4 Correlation Run; Comparison with Anglin (1978) Figure 8 (Figure 3.65a); h fixed at 30000 ft.
(a) δa, δe, δr vs. t

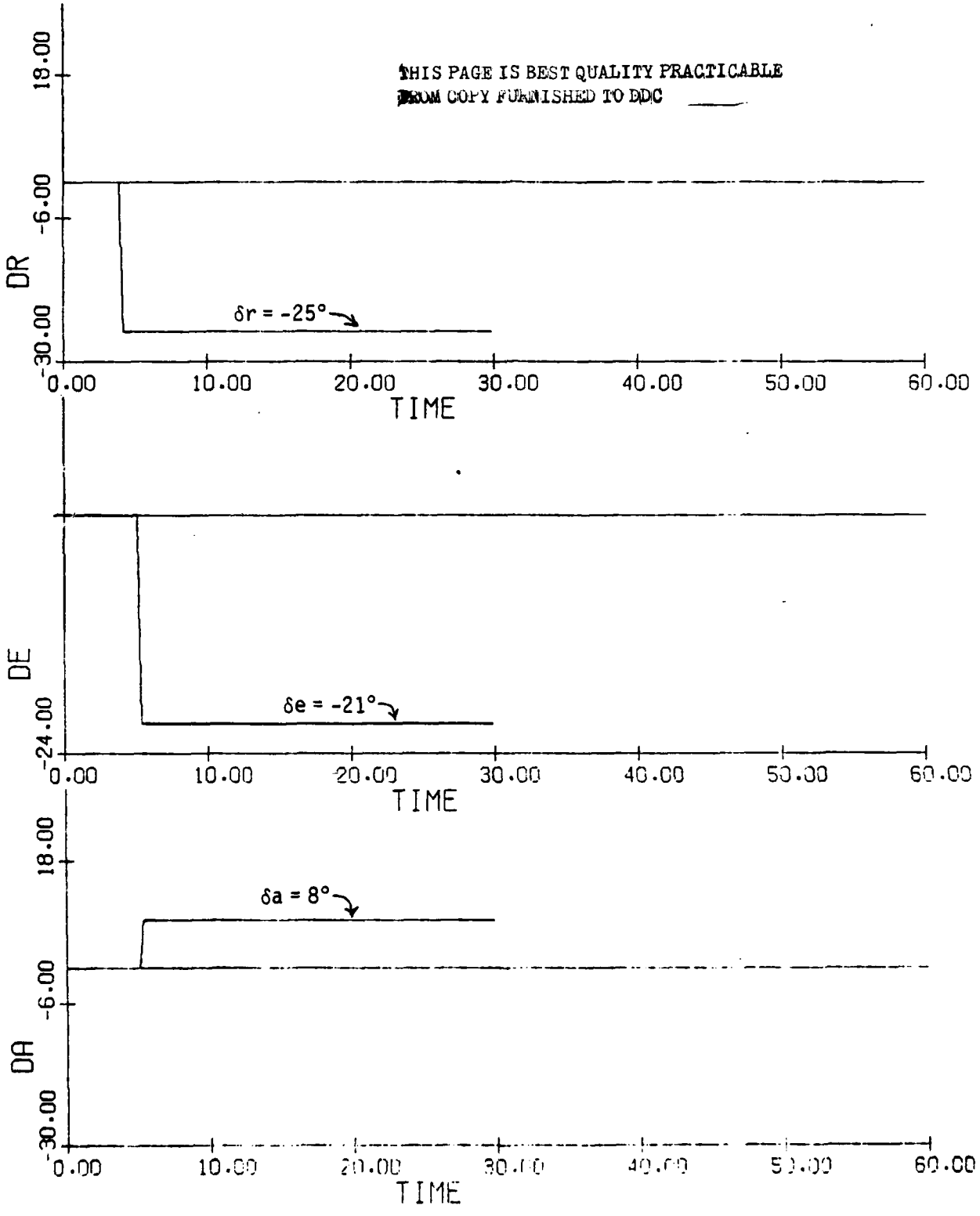

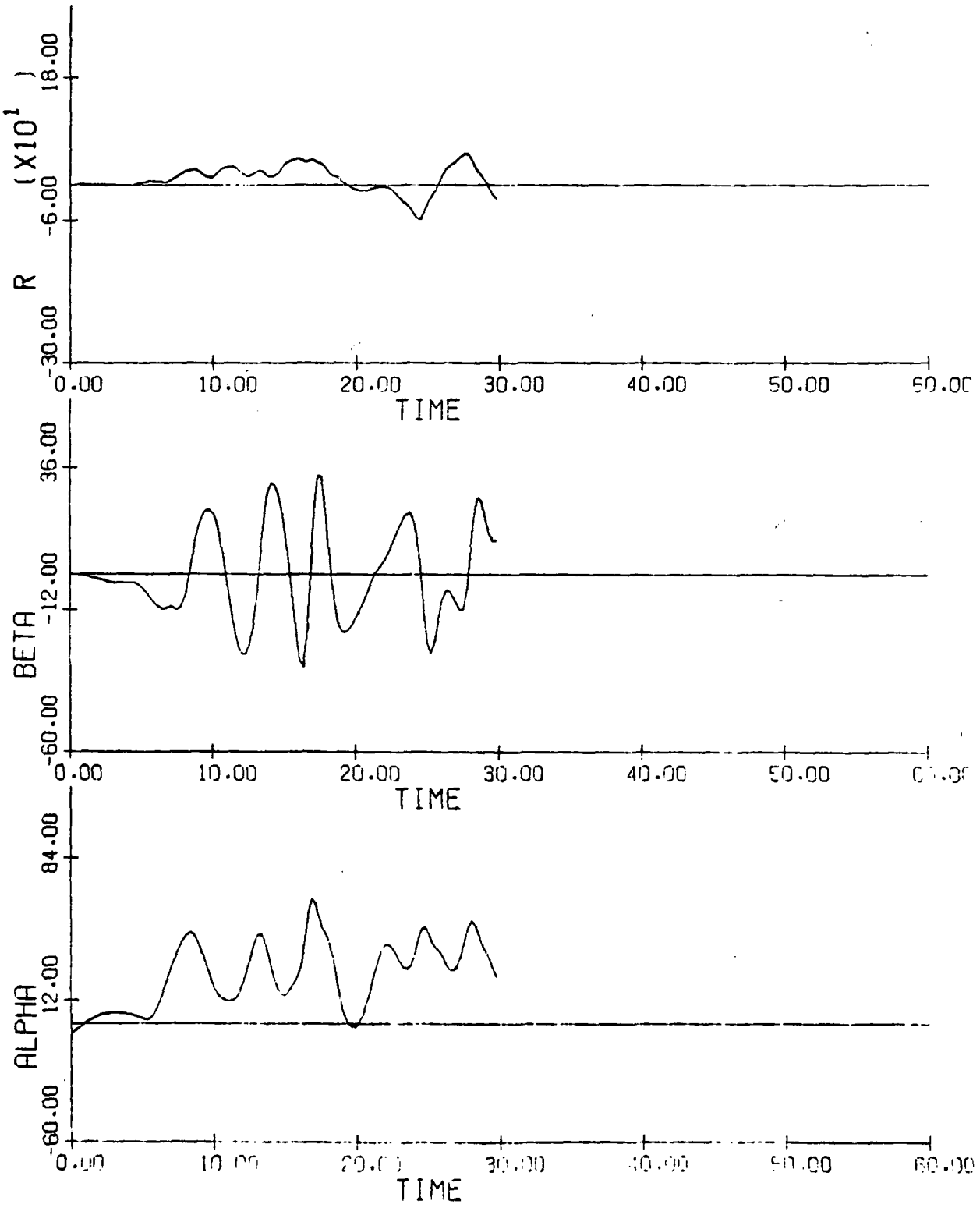

Figure 3.66(b): α, β, r vs. t

Figure 3.67: F-4 Correlation Run; Comparison with Anglin (1978) Figure 13 (Figure 3.65b); h fixed at 30000 ft; $\delta a = 20°$, $\delta e = -21°$, $\delta r = 25°$
(a) α, β, r vs. t

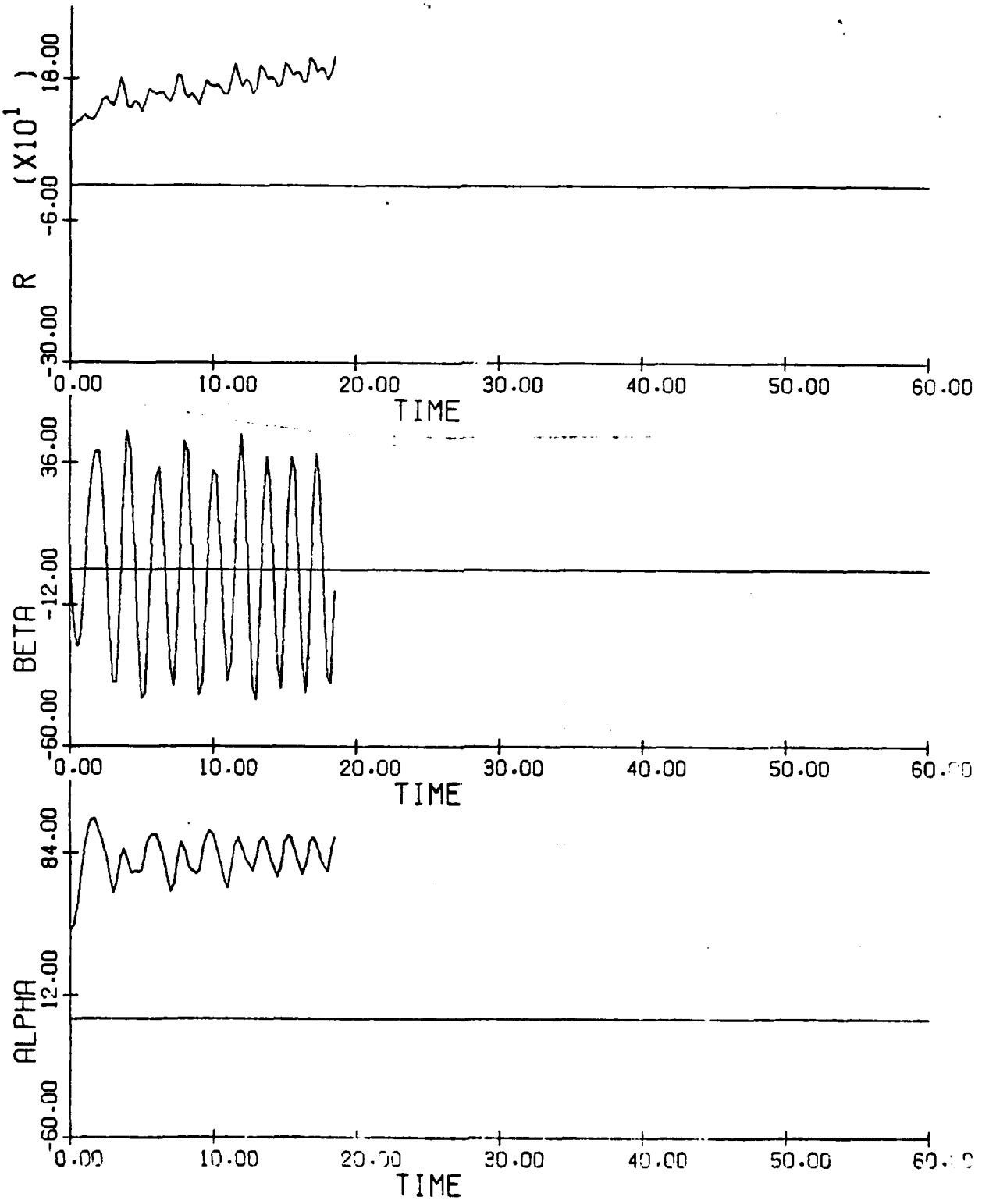

Figure 3.67(b): θ, ϕ, TURNS (= $\psi/360°$) vs. t

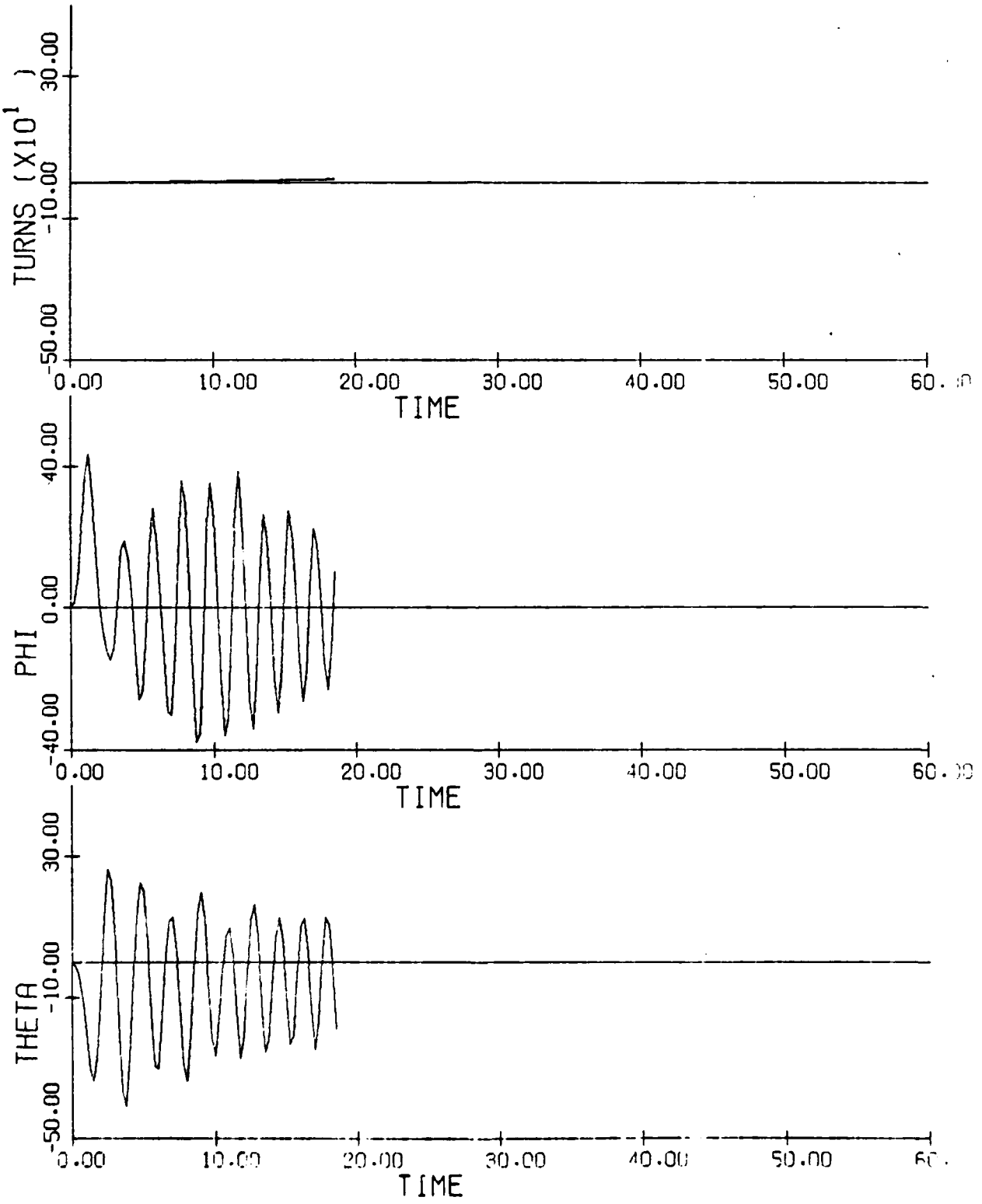

AD-A084 938 SCIENTIFIC SYSTEMS INC CAMBRIDGE MA F/G 20/4
GLOBAL STABILITY AND CONTROL ANALYSIS OF AIRCRAFT AT HIGH ANGLE--ETC(U)
AUG 79 R K MEHRA, J V CARROLL N00014-76-C-0780
UNCLASSIFIED ONR-CR215-245-3 NL

4 OF 4
AD
A084938

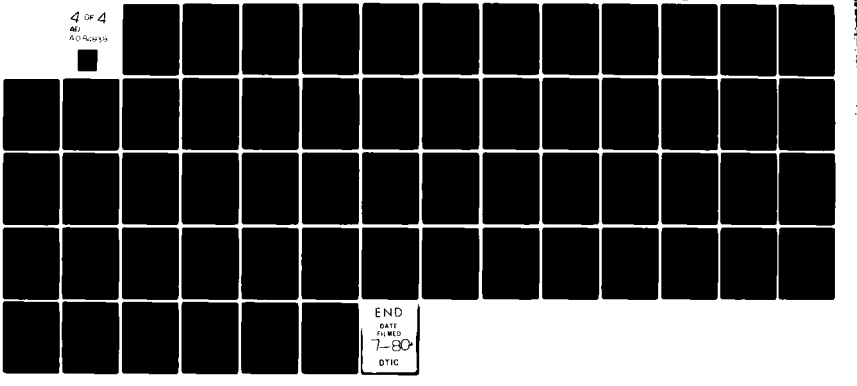

END
DATE FILMED
7-80
DTIC

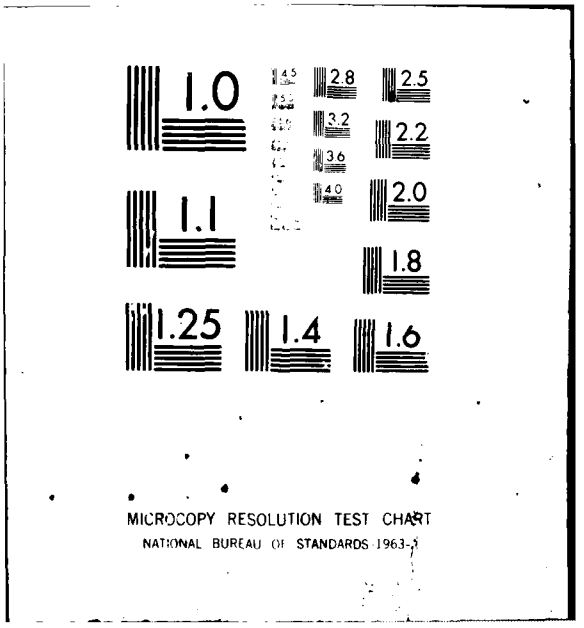
1.0
1.1
1.25
1.4
1.6
1.8
2.0
2.2
2.5
2.8
3.2
3.6
4.0
MICROCOPY RESOLUTION TEST CHART
NATIONAL BUREAU OF STANDARDS 1963-A

Figure 3.68: F-4 Time History; Stall and Spin Entry Study;
$h(t_0) = 40000$ ft; $V(t_0) = 875$ fps
(a) δa, δe, δr vs. t

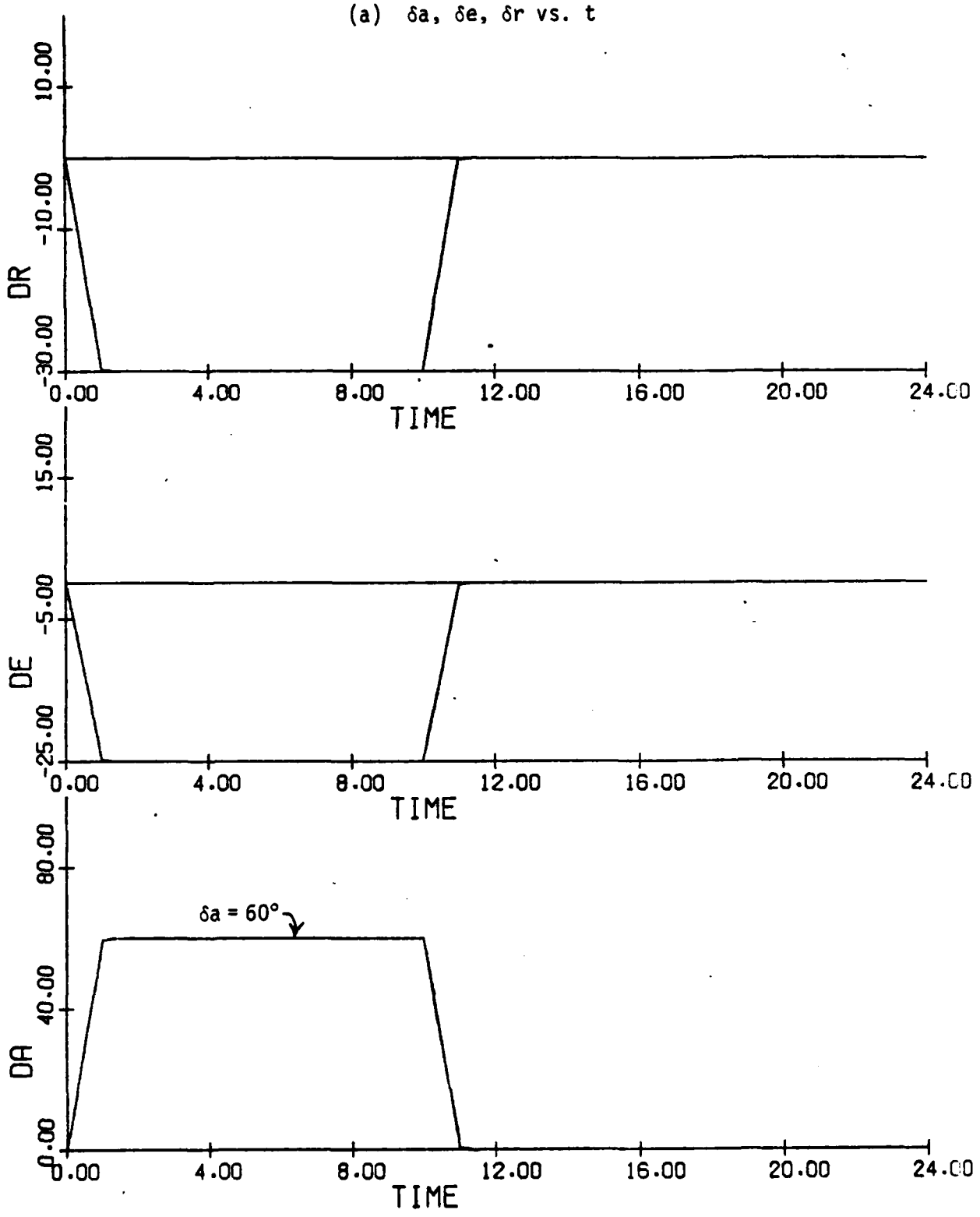

Figure 3.68(b): r, α, ϕ vs. t

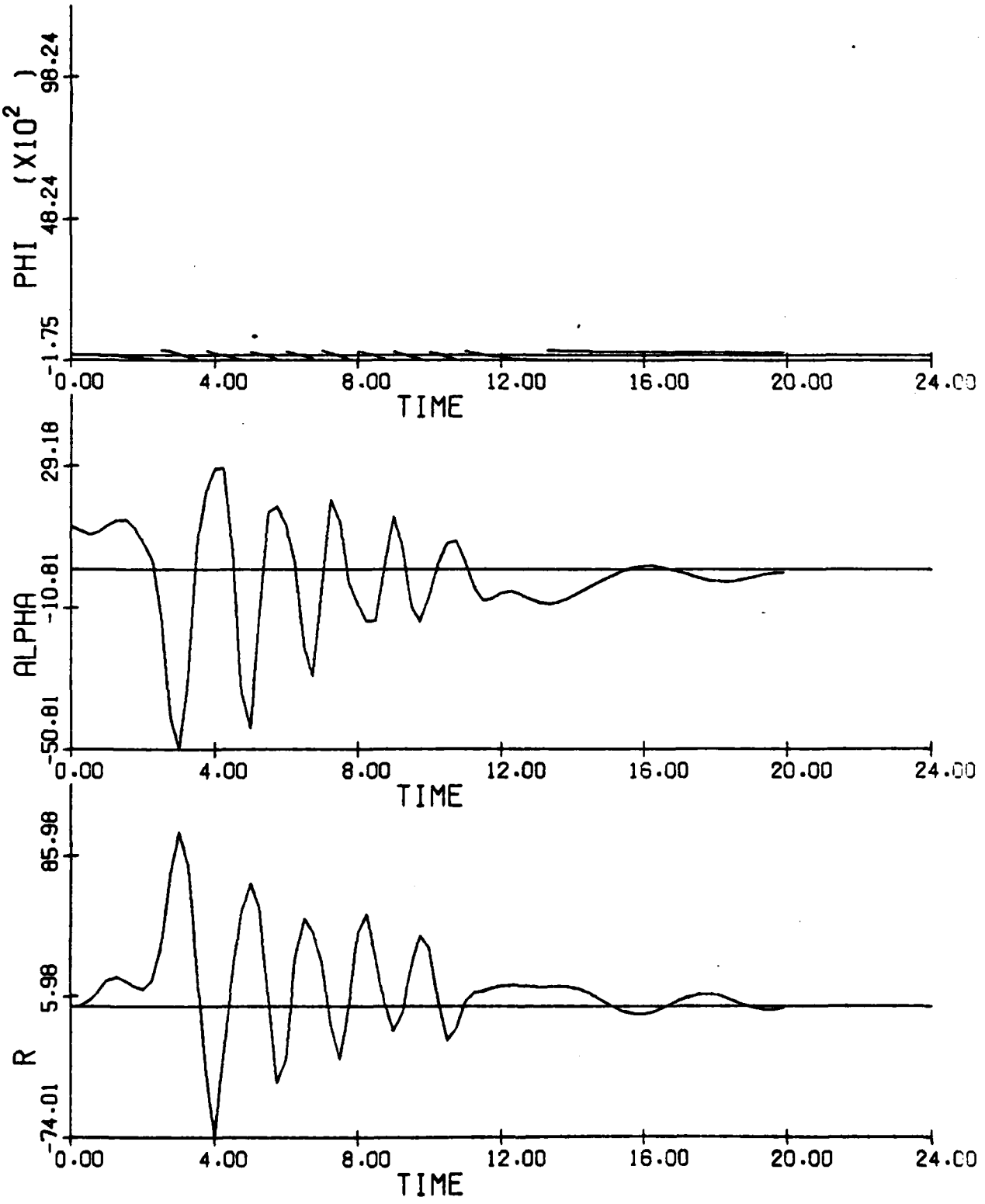

Figure 3.69: F-4 Time History; Stall and Spin Entry Study; $h(t_0) = 40000$ ft; $V(t_0) = 875$ fps; t* represents initial conditions for subsequent runs
(a) δa, δe, δr vs. t

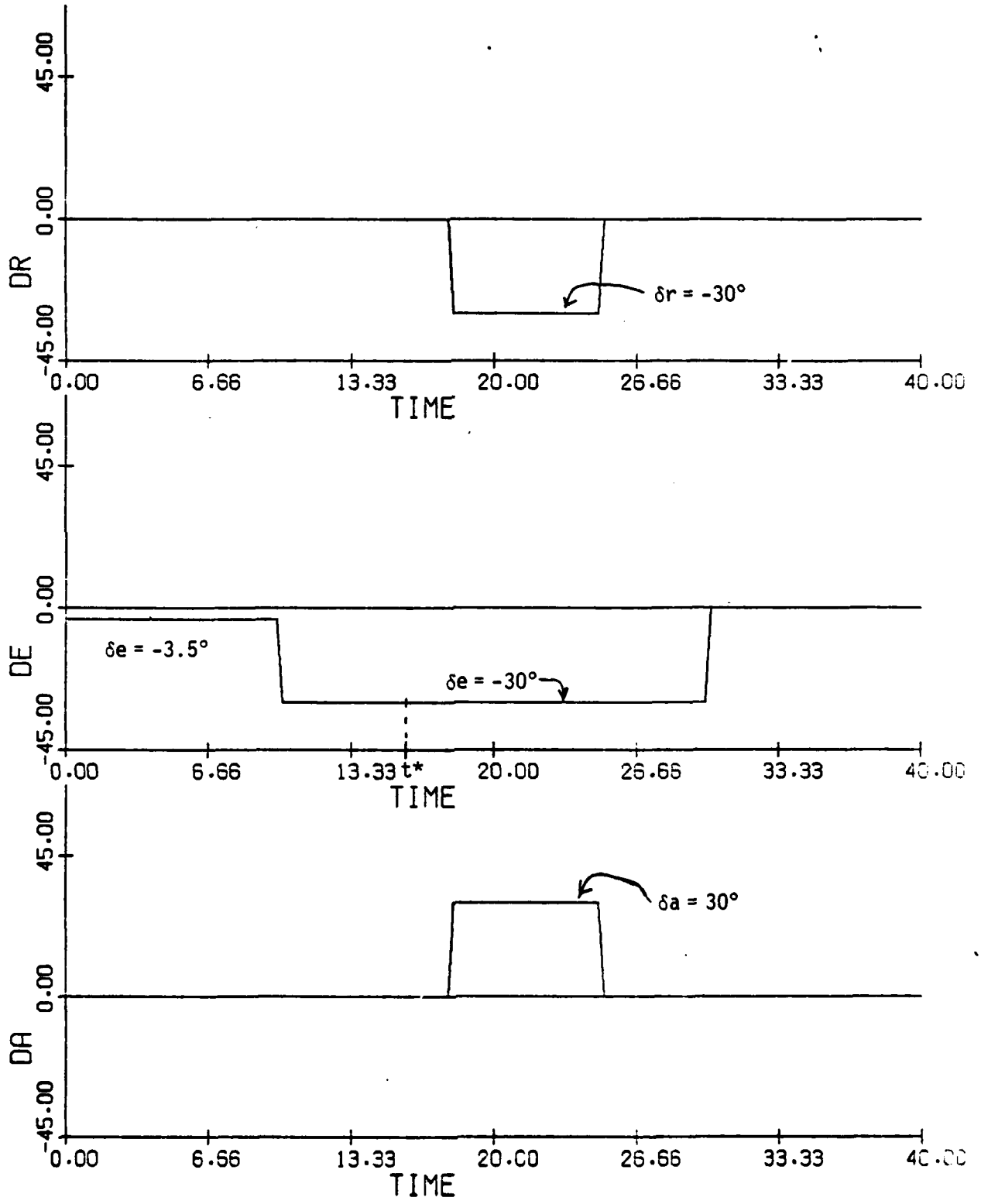

Figure 3.69(b): p, q, r vs. t

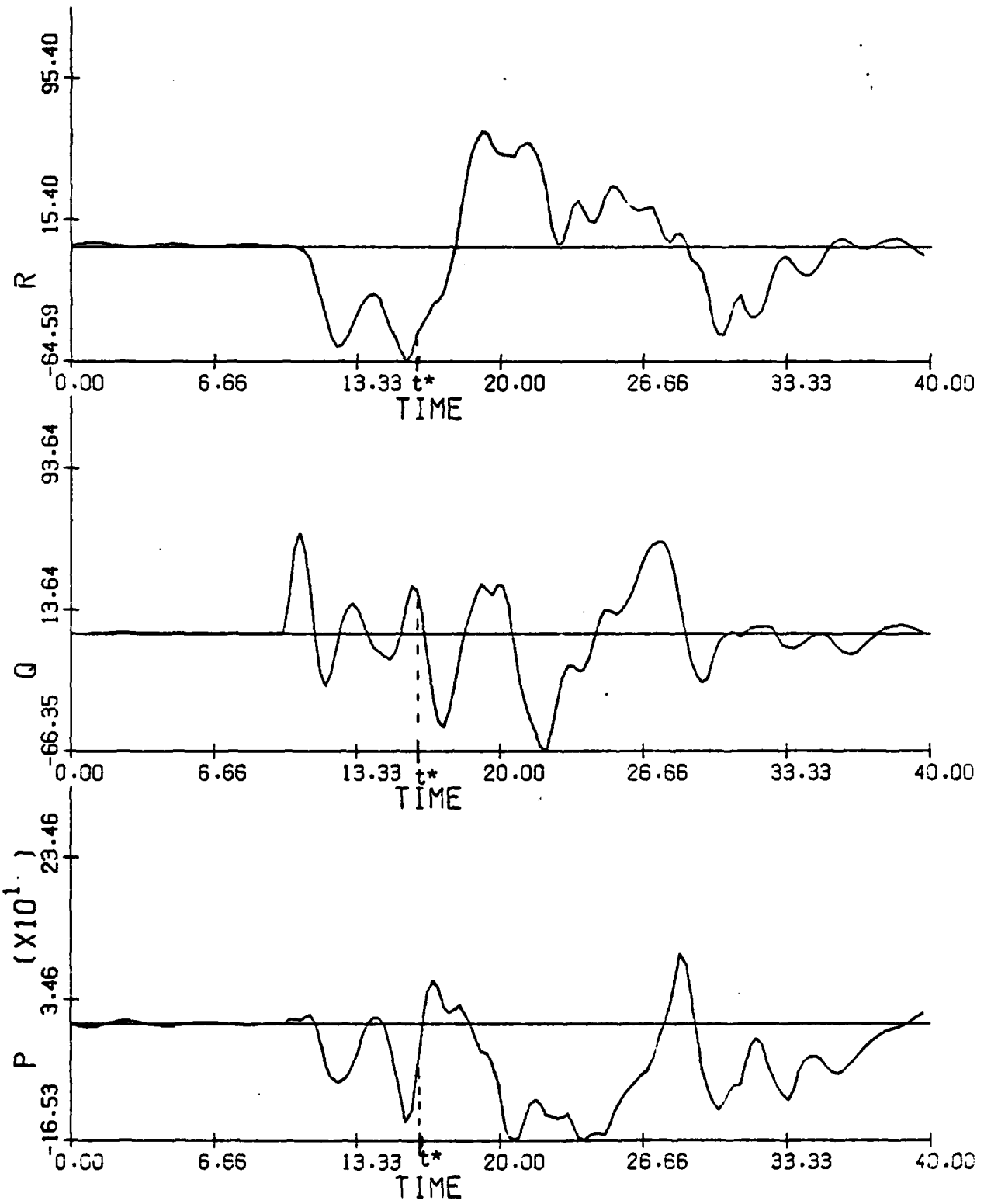

Figure 3.69(c): α, β, V vs. t

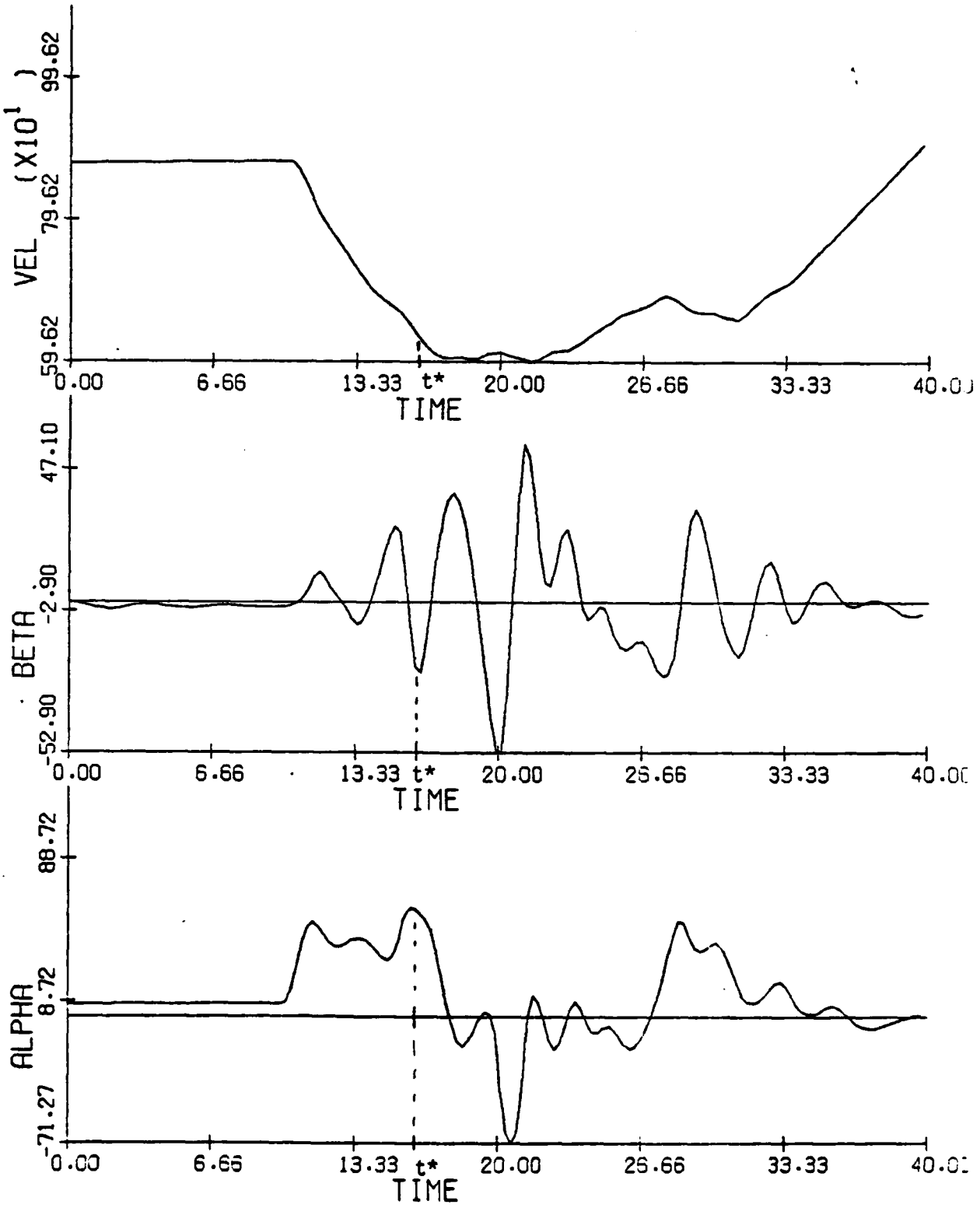

Figure 3.69(d): θ, ϕ, E vs. t

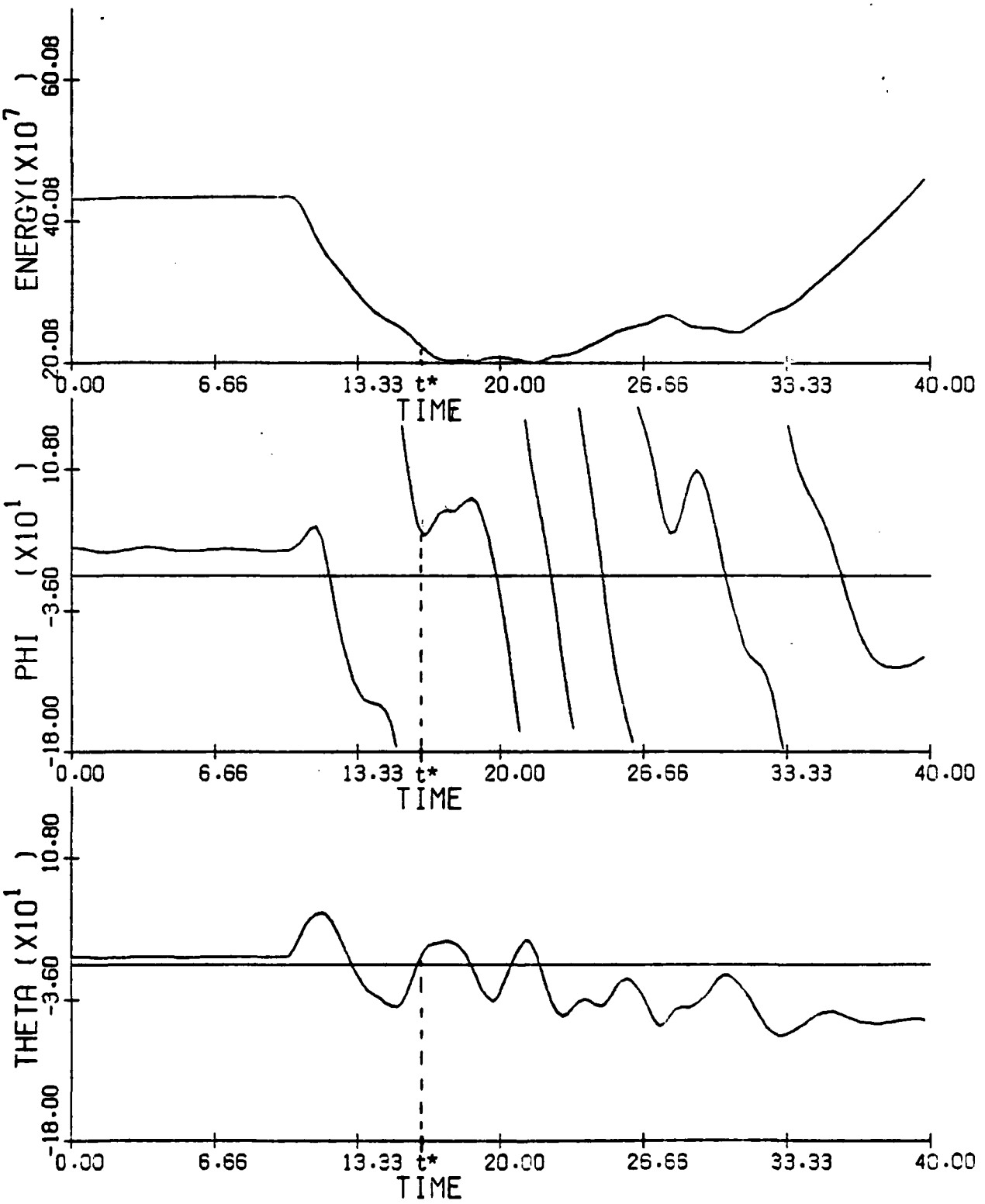

Figure 3.70: F-4 Time History; Spin Entry Study; Initial Conditions from t* of Figure 3.69; $\delta a = 0°$, $\delta e = -30°$, $\delta r = 30°$; h fixed at 30000 feet
(a) α, r, ϕ vs. t

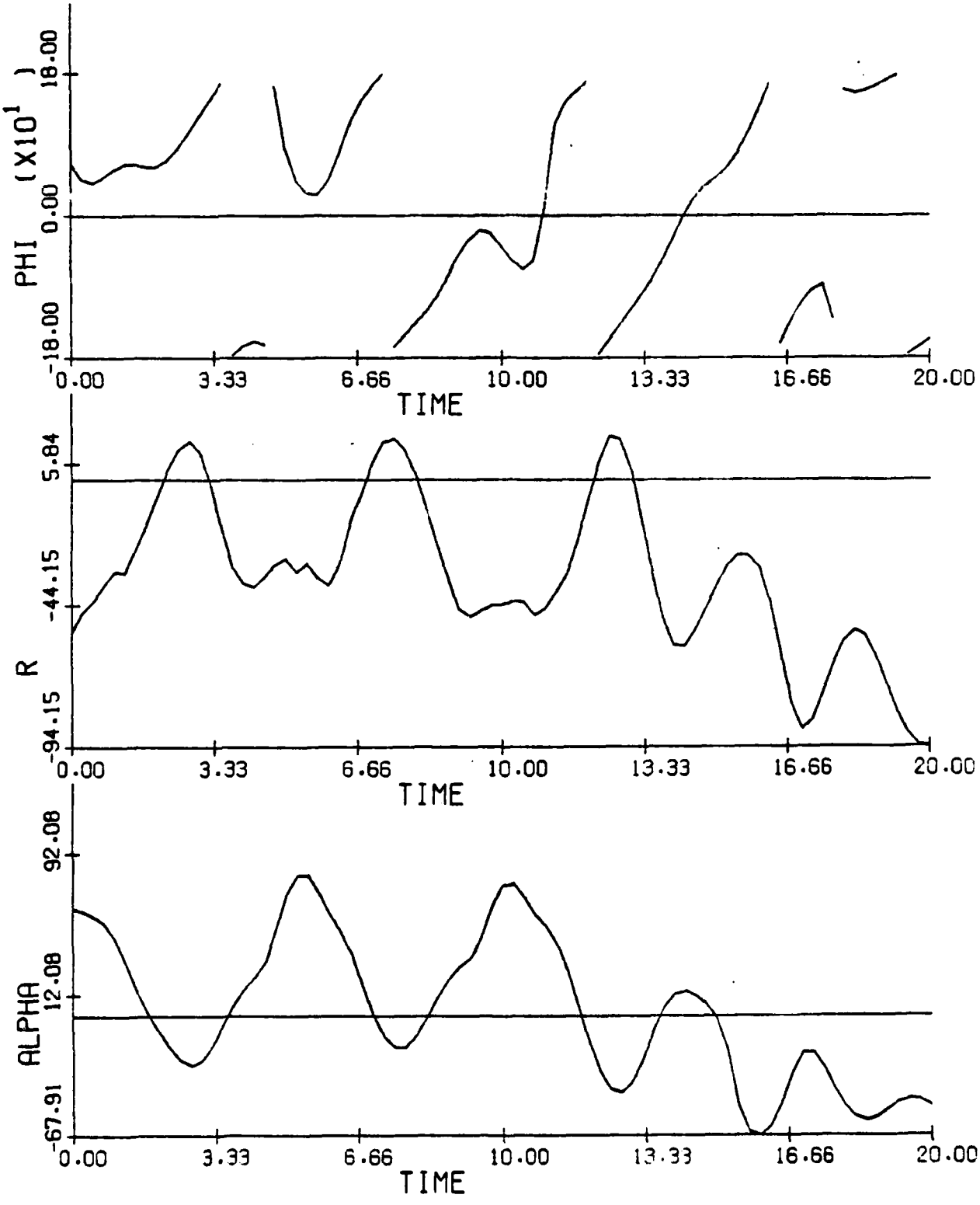

Figure 3.70(b): V, θ, E vs. t

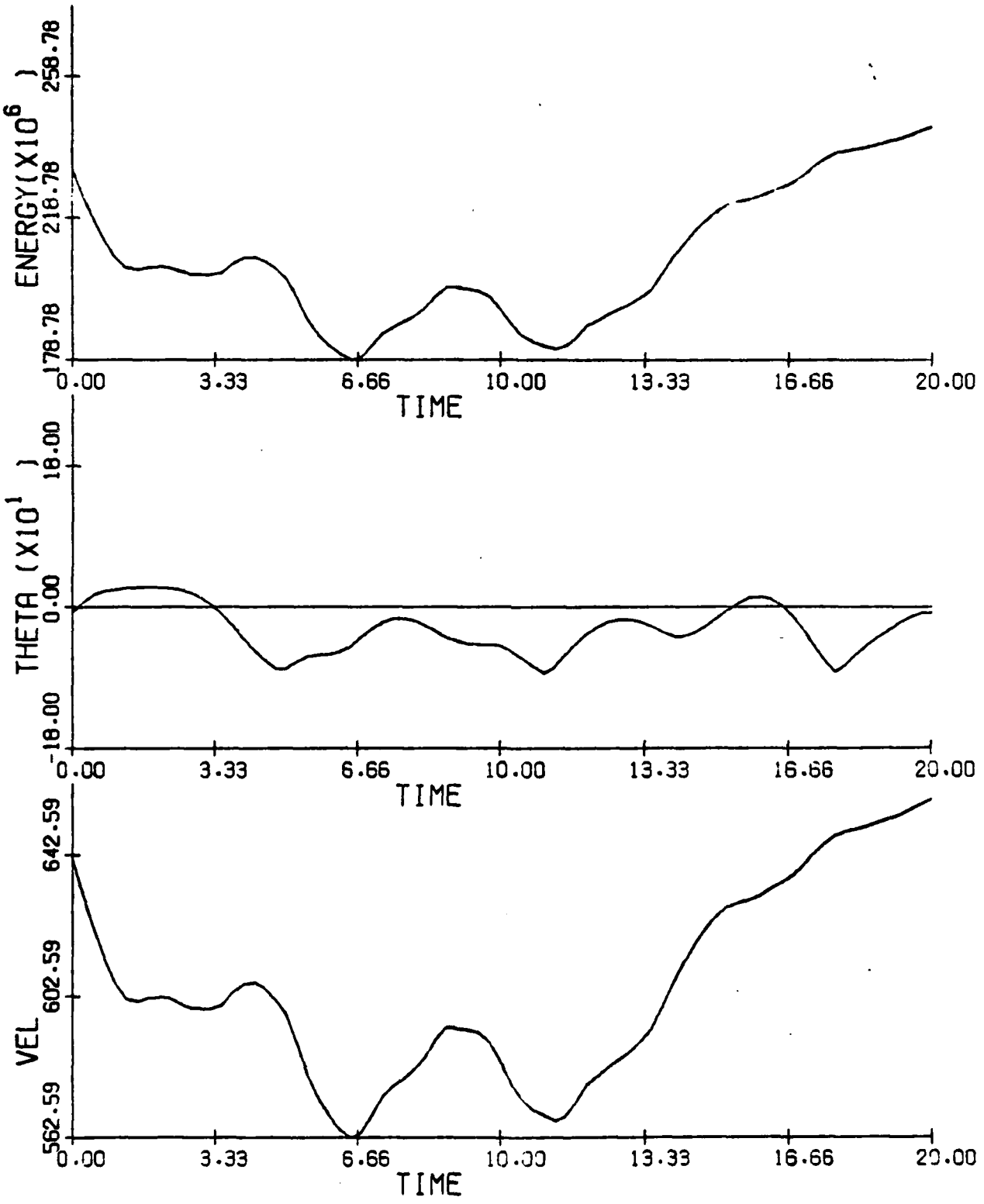

Figure 3.71: F-4 Time History; Spin Entry Study; Initial Conditions from t = t* of Figure 3.69; $\delta a = 30°$, $\delta e = -30°$, $\delta r = 30°$; h ≡ 30K feet; no thrust
(a) α, r, ϕ vs. t

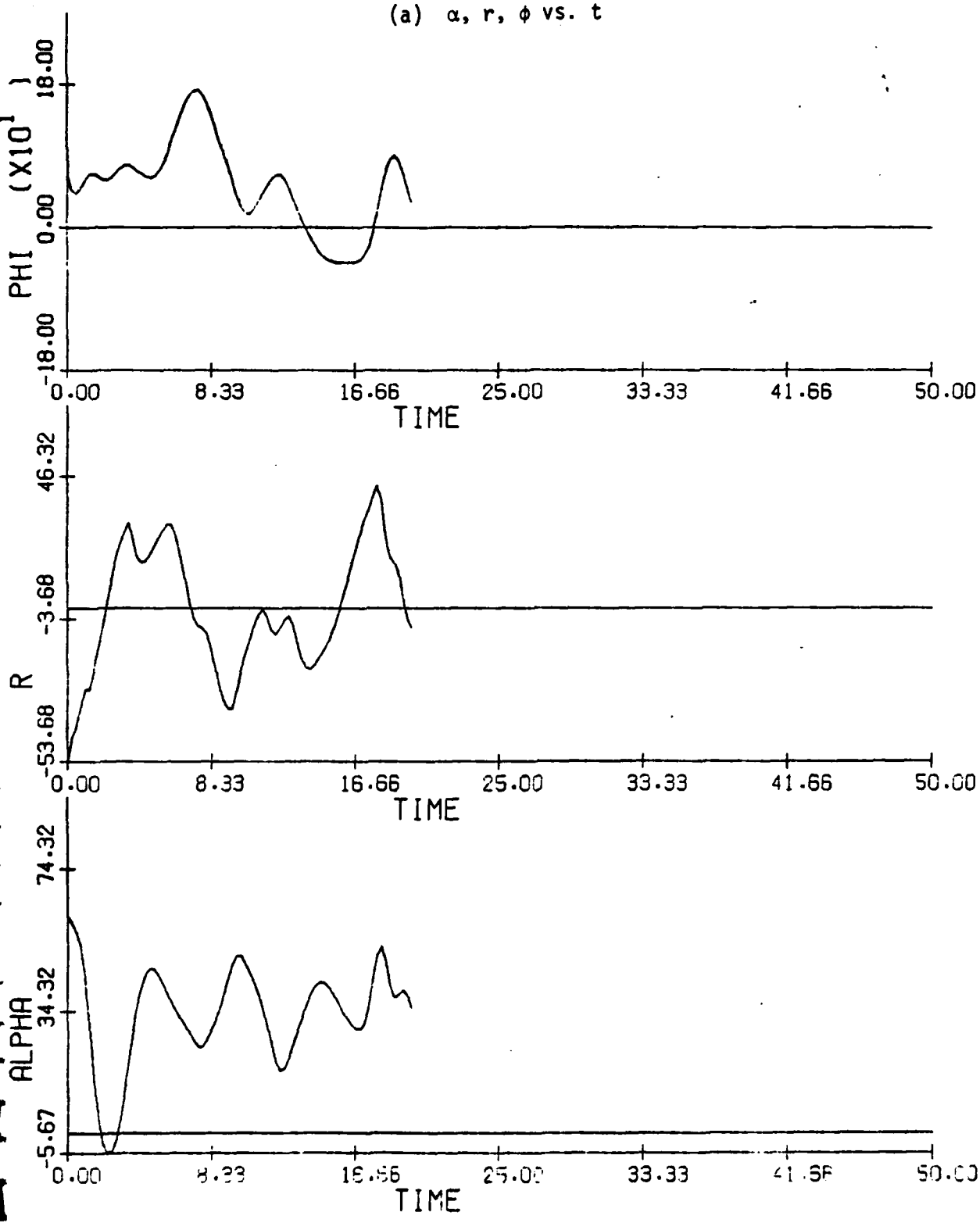

Figure 3.71(b): V, θ, E vs. t

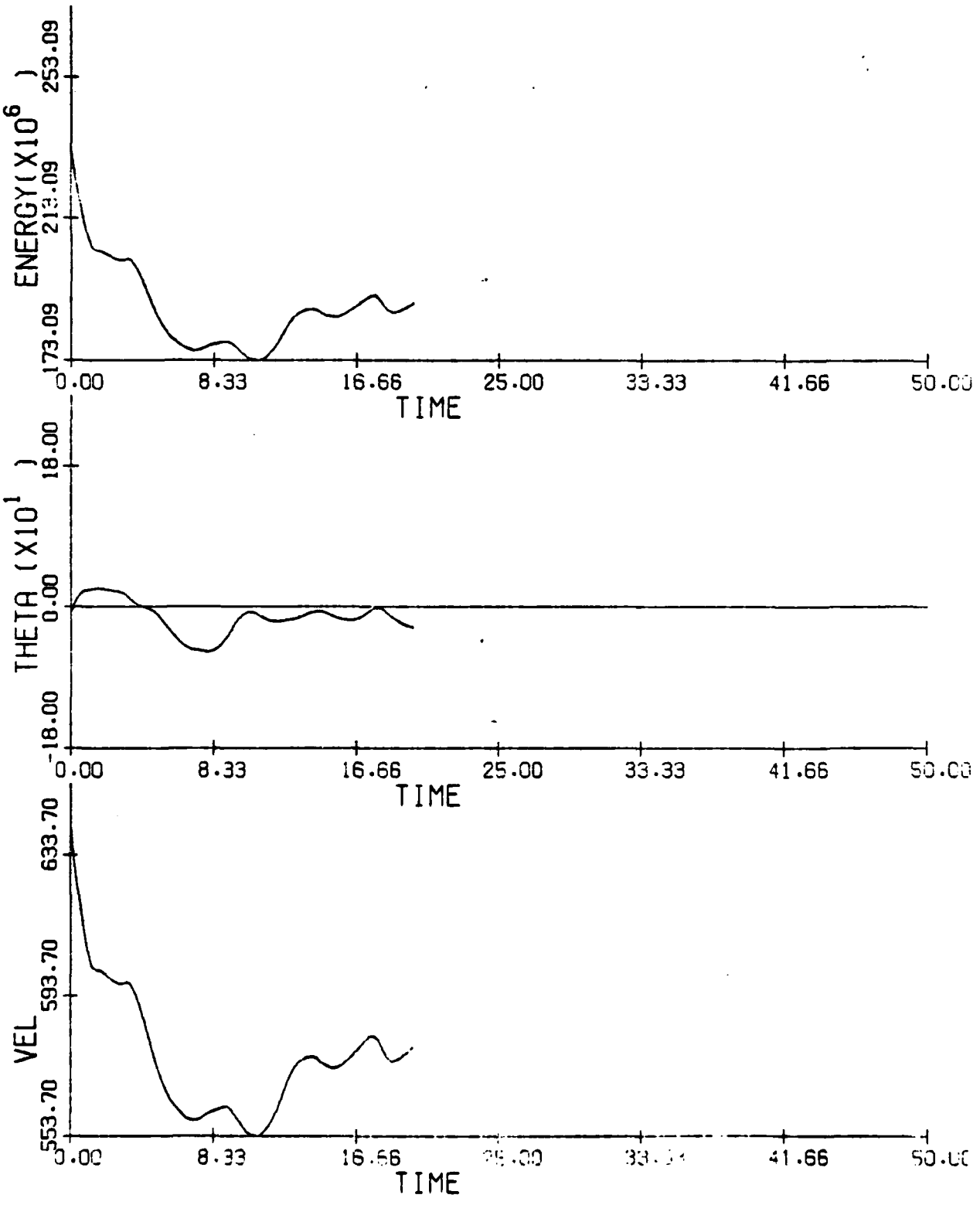

Figure 3.72: F-4 Time History; Spin Entry Study; Initial Conditions from $t = t^*$ of Figure 3.69; $\delta a = 30°$, $\delta e = -30°$, $\delta r = 30°$; $h \equiv 30K$ ft; Thrust for α e (-10°,20°)
(a) α, r, ϕ vs. t

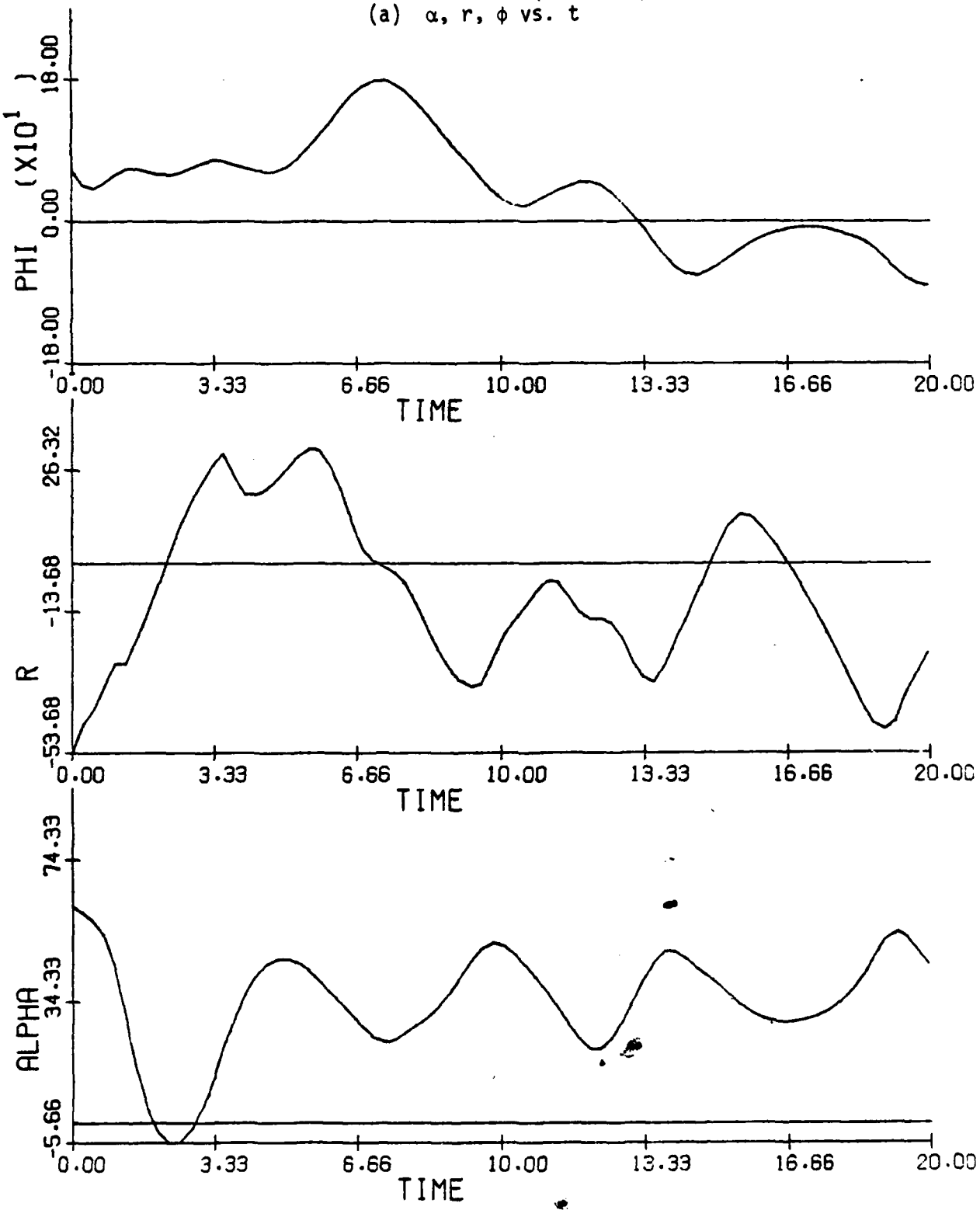

Figure 3.72(b): V, θ, E vs. t

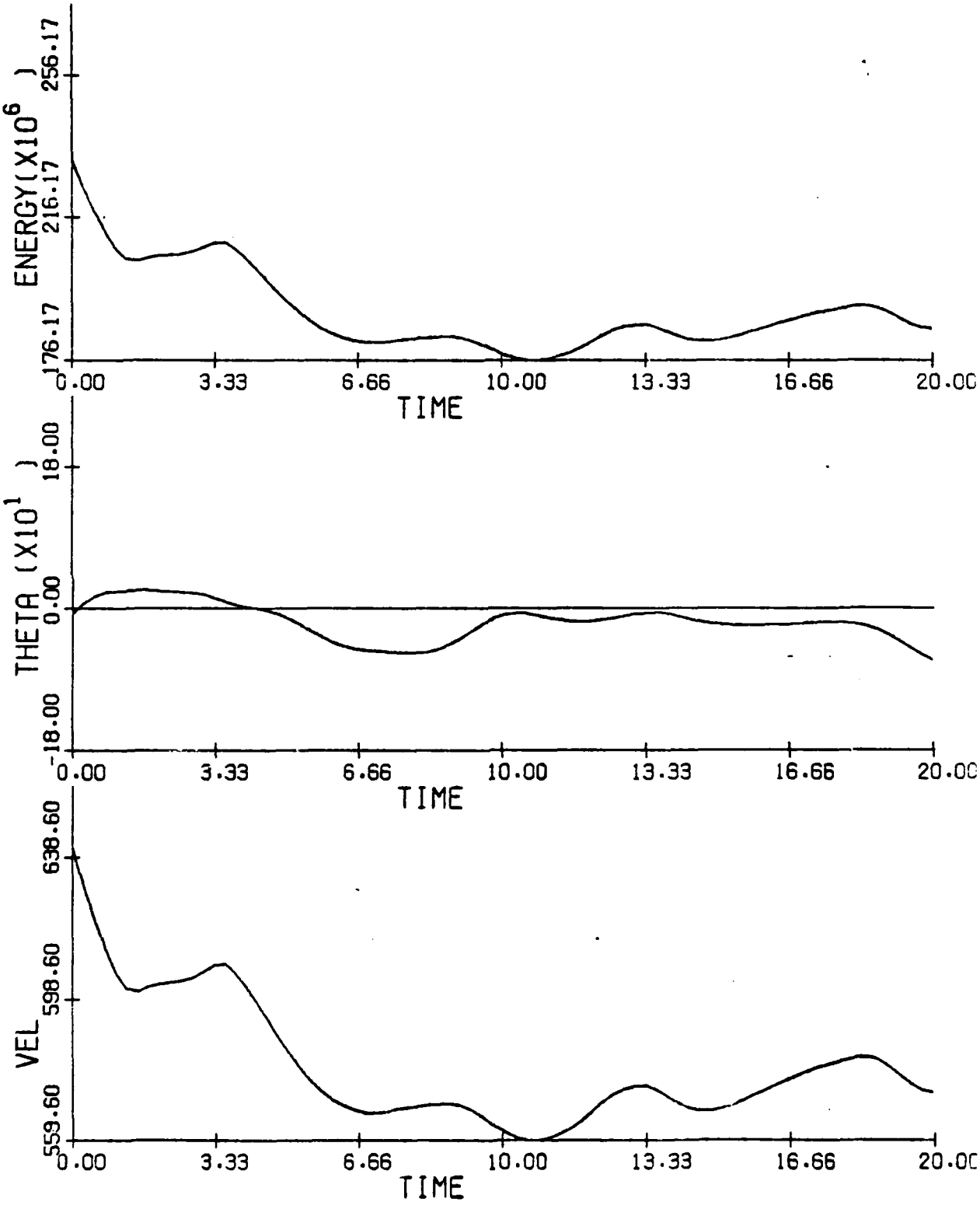

Figure 3.73: F-4 Bifurcation Surface; V = 330 fps; h = 5000 ft; δr vs. δa

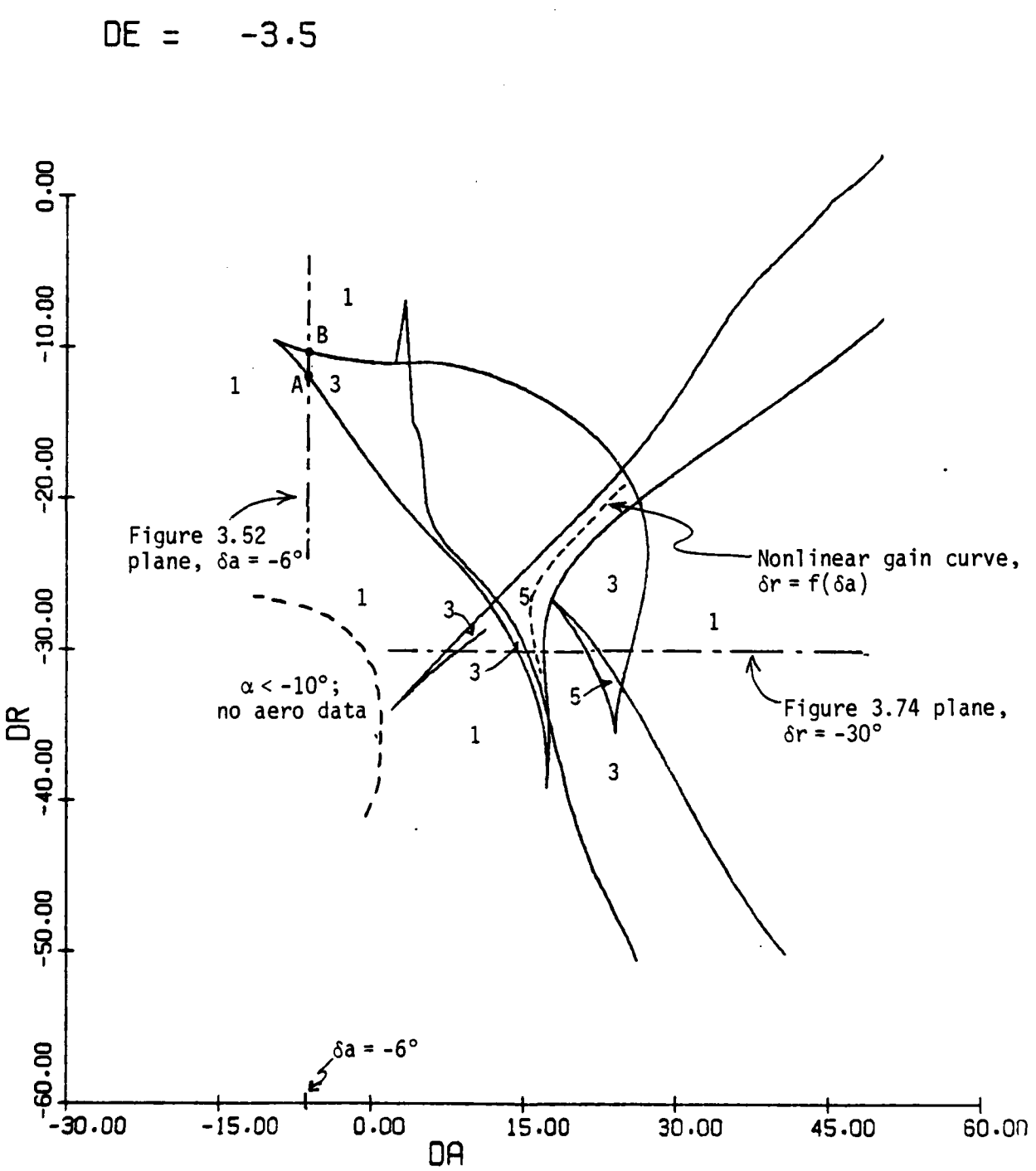

Figure 3.74: F-4 Equilibrium Surface; V = 330 fps;
h = 5000 ft; α vs. δa

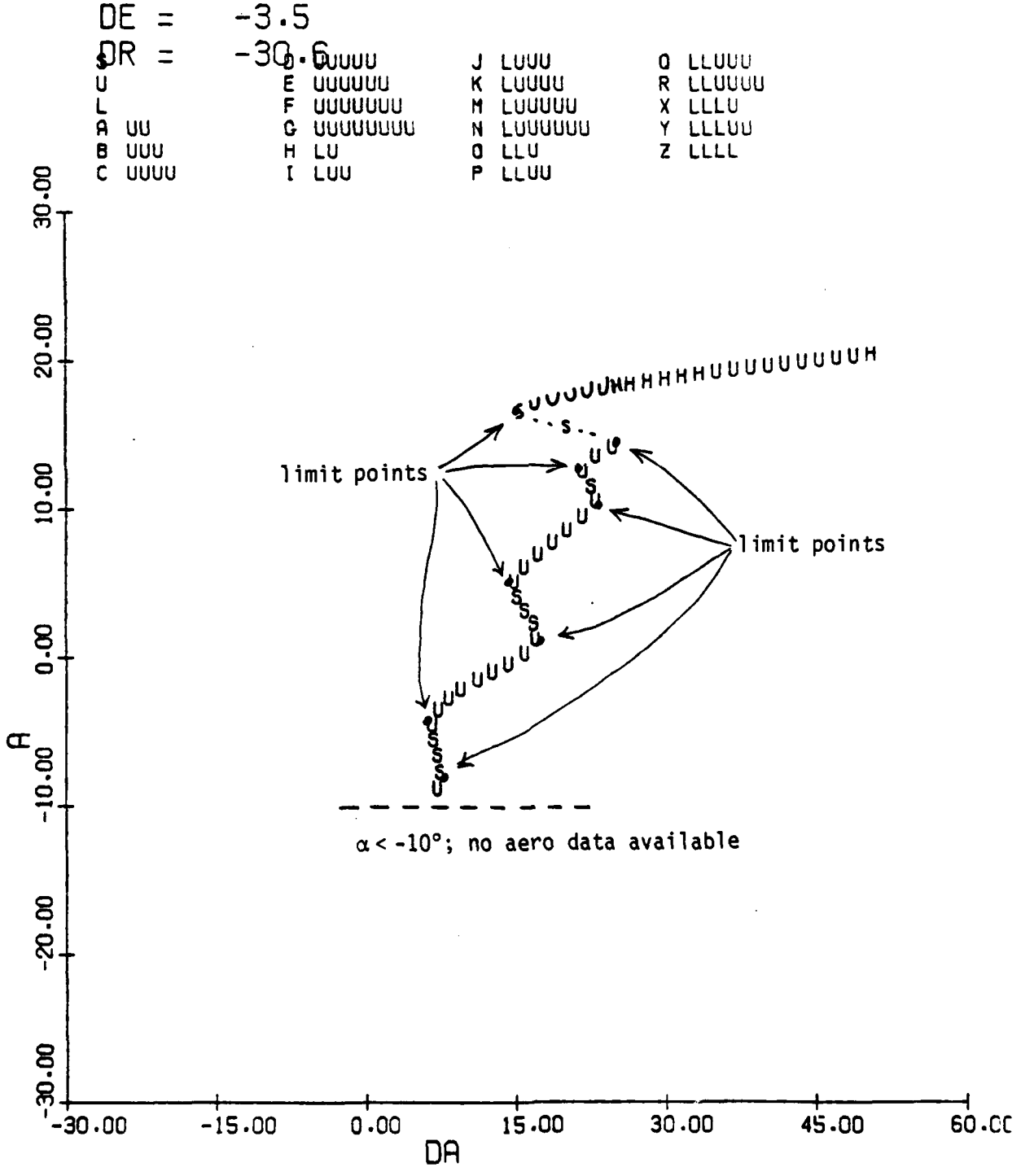

Figure 3.75: F-4 Bifurcation Surfaces; V = 330 fps; h = 5000 ft; δr vs. δa

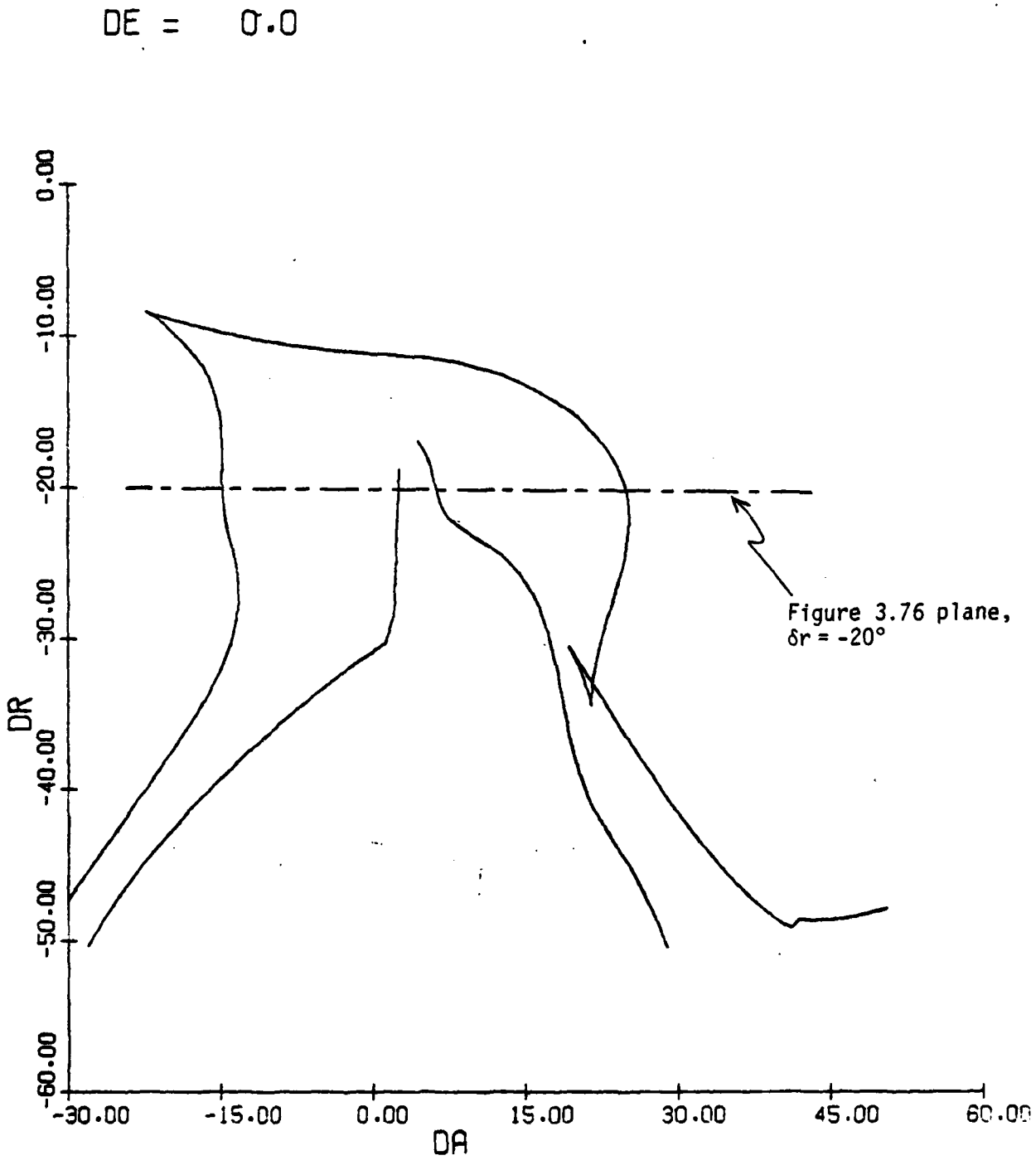

Figure 3.76: F-4 Equilibrium Surface; V = 330 fps; h = 5000 ft; α vs. δa

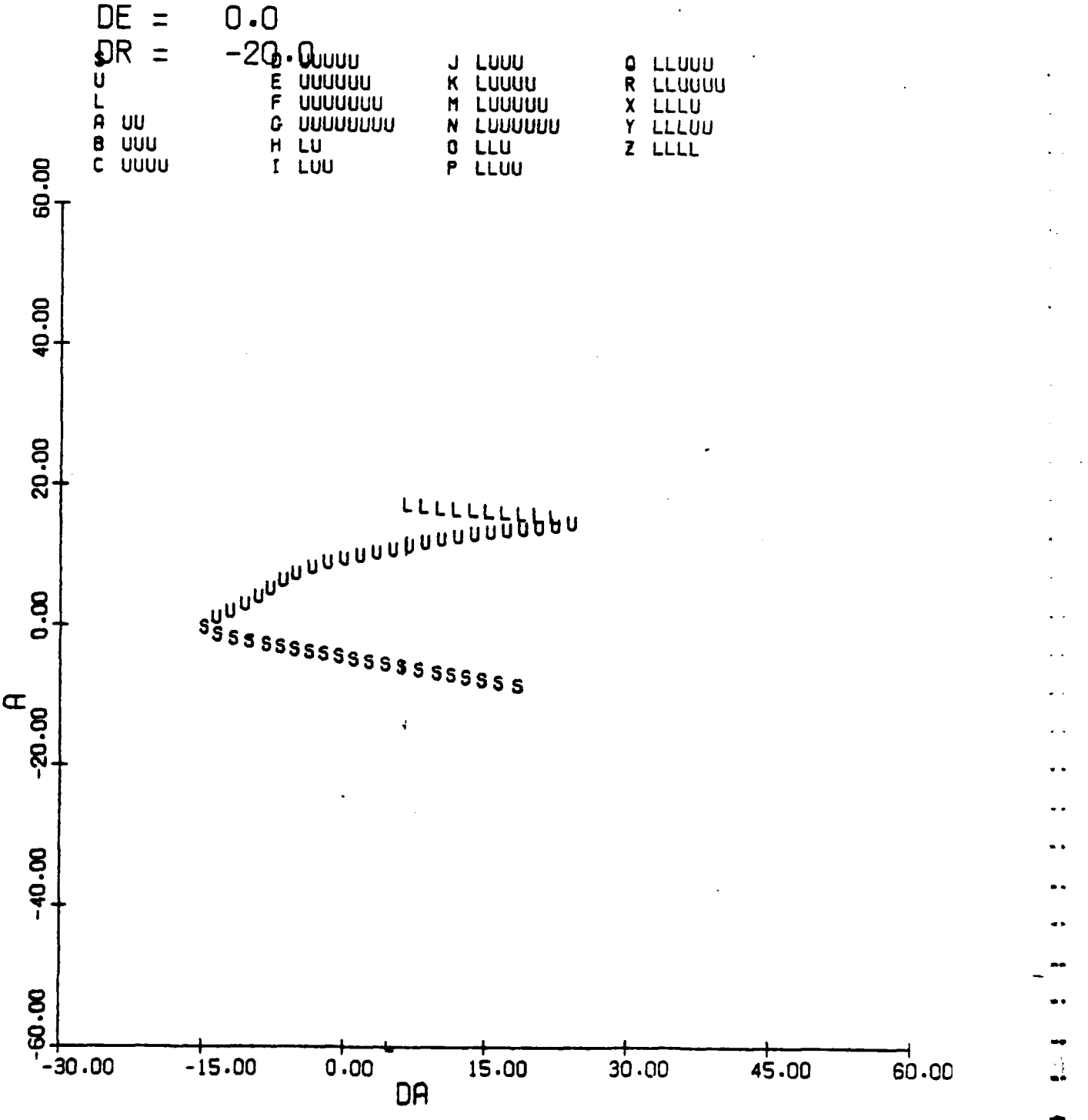

Figure 3.77: F-4 Equilibrium Surface, Trim Condition; h = 40000 ft; Thrust = 900 lbs; Spin Equilibrium System (n = 8)
(a) α vs. δa

DE= -3.5
DR= 0.0

S	D UUUUU	J LUUU	Q LLUUU
U	E UUUUUU	K LUUUU	R LLUUUU
L	F UUUUUUU	M LUUUUU	X LLLU
A UU	G UUUUUUUU	N LUUUUUU	Y LLLUU
B UUU	H LU	O LLU	Z LLLL
C UUUU	I LUU	P LLUU	

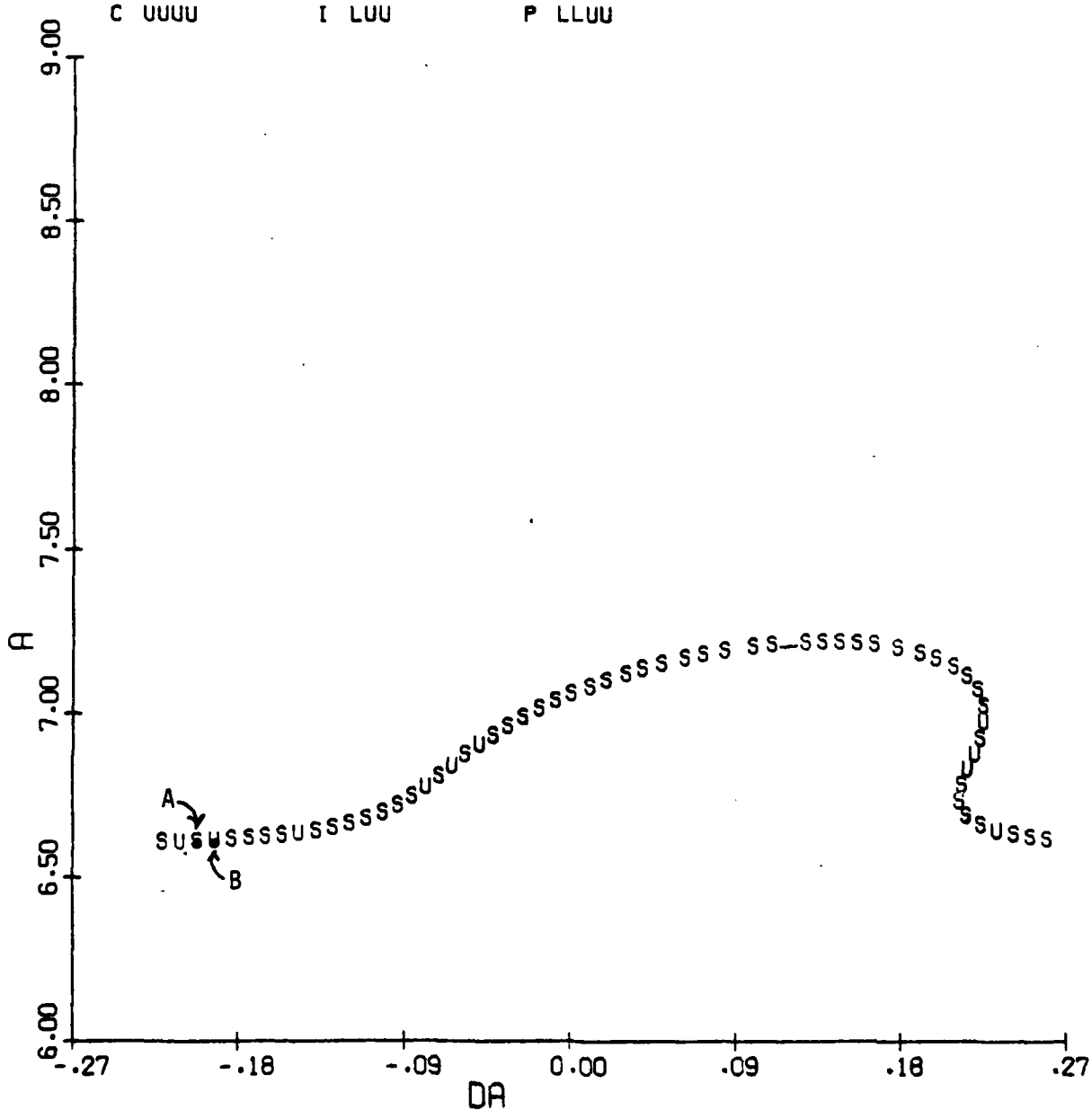

Figure 3.77(b): V vs. δa

DE= -3.5
DR= 0.0

S	D UUUUU	J LUUU	Q LLUUU
U	E UUUUUU	K LUUUU	R LLUUUU
L	F UUUUUUU	M LUUUUU	X LLLU
A UU	G UUUUUUUU	N LUUUUUU	Y LLLUU
B UUU	H LU	O LLU	Z LLLL
C UUUU	I LUU	P LLUU	

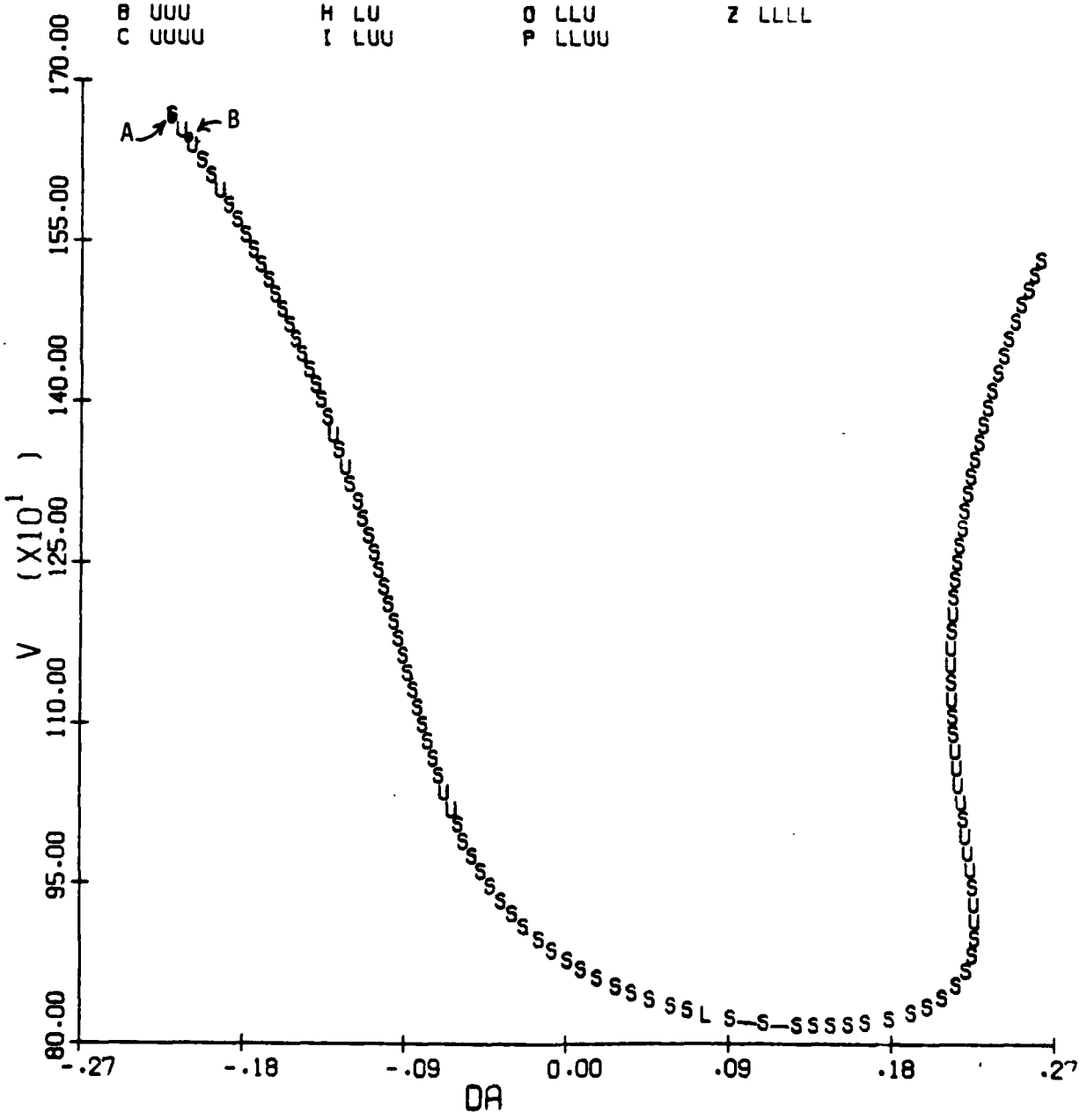

Figure 3.77(c): α vs. V

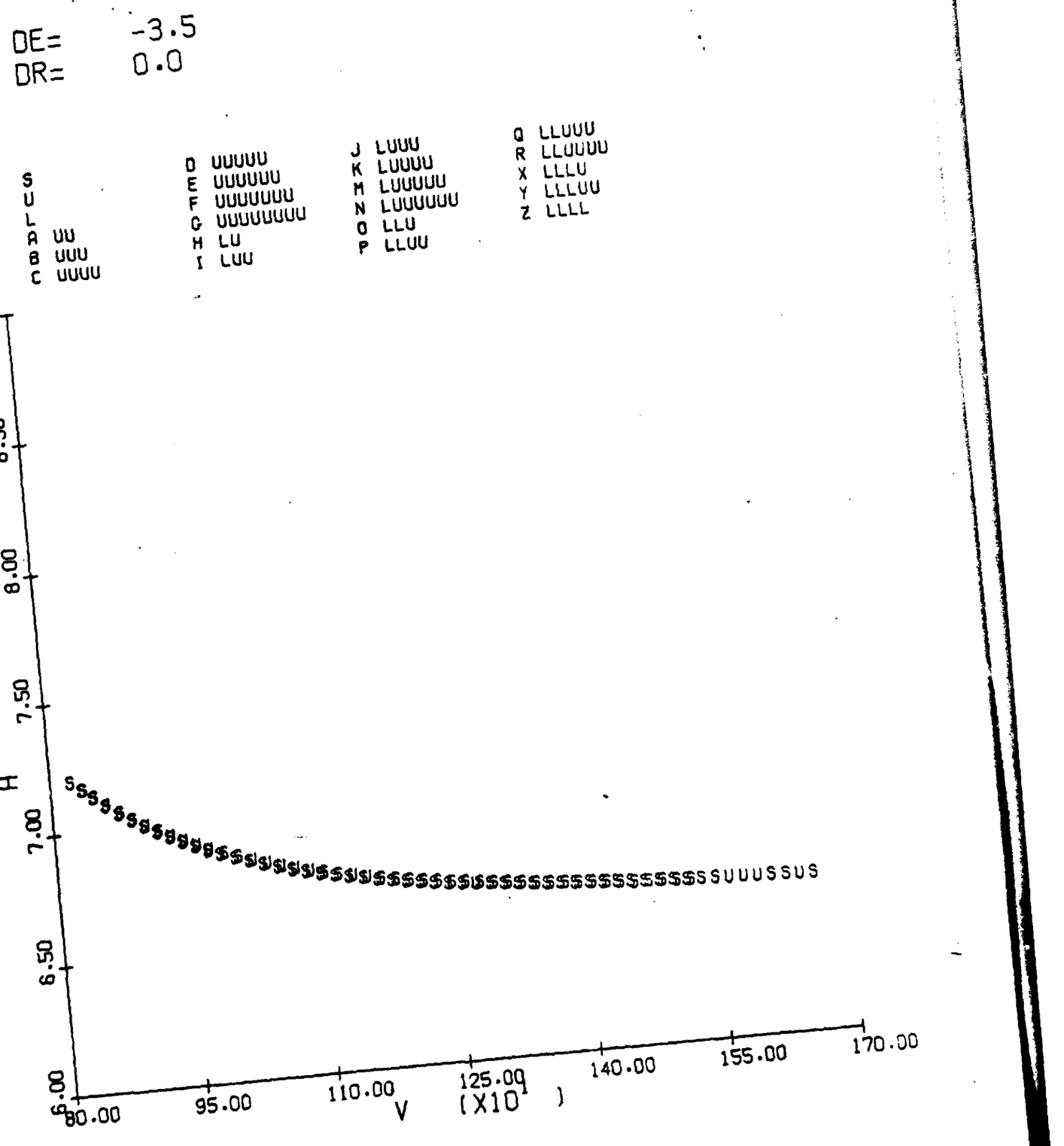

Figure 3.77(d): p vs. V

DE= -3.5
DR= 0.0

S
U
L
A UU
B UUU
C UUUU
D UUUUU
E UUUUUU
F UUUUUUU
G UUUUUUUU
H LU
I LUU
J LUUU
K LUUUU
M LUUUUU
N LUUUUUU
O LLU
P LLUU
Q LLUUU
R LLUUUU
X LLLU
Y LLLUU
Z LLLL

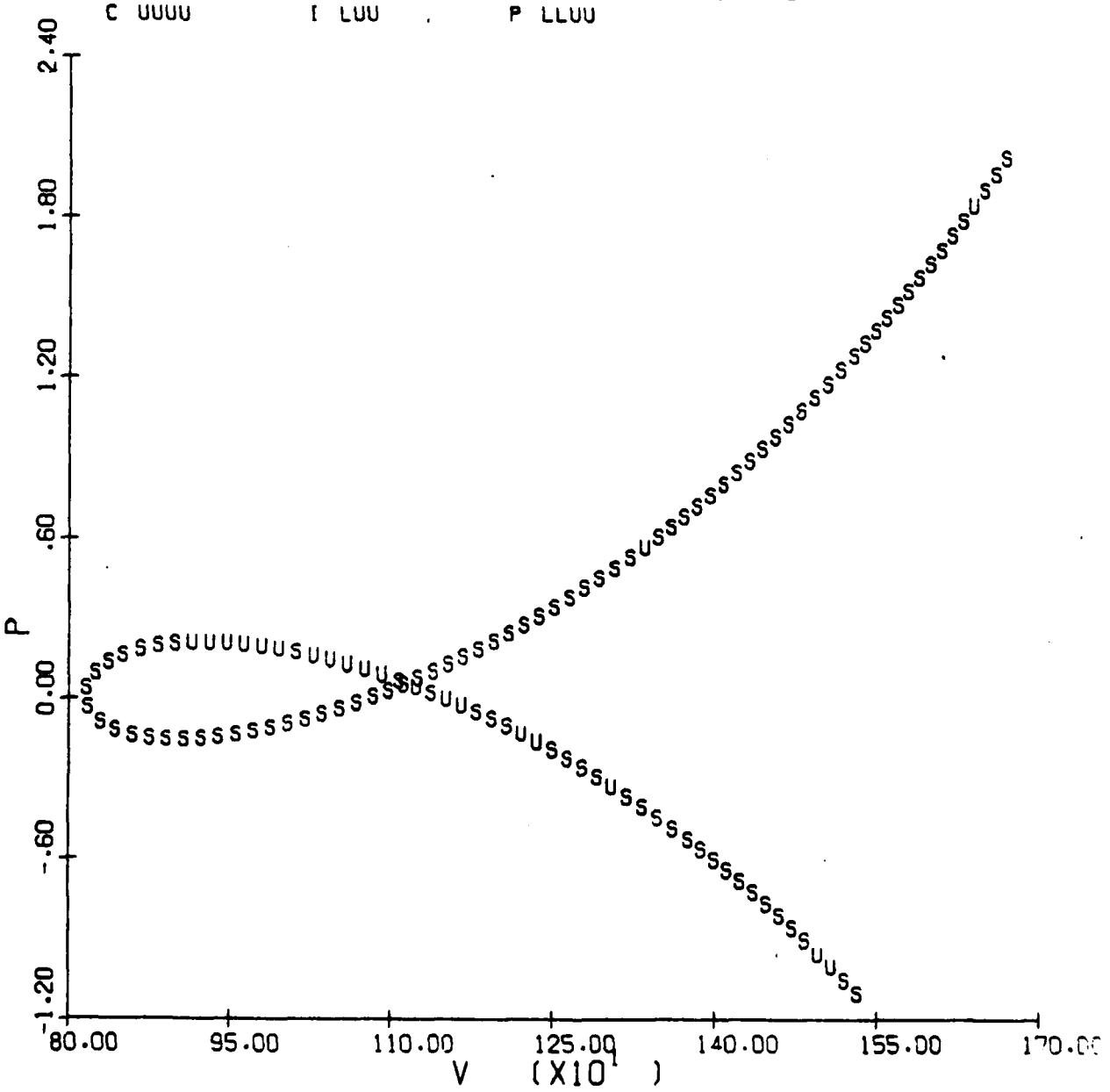

Figure 3.78: F-4 Time History Run; h = 40000 ft; Thrust = 9000 lbs. $\delta a_0 = -0.221°$, $\delta e = -3.5°$, $\delta r = 0°$; $\delta a = -0.215$ for $t > 25$ sec; α, r, V vs. t

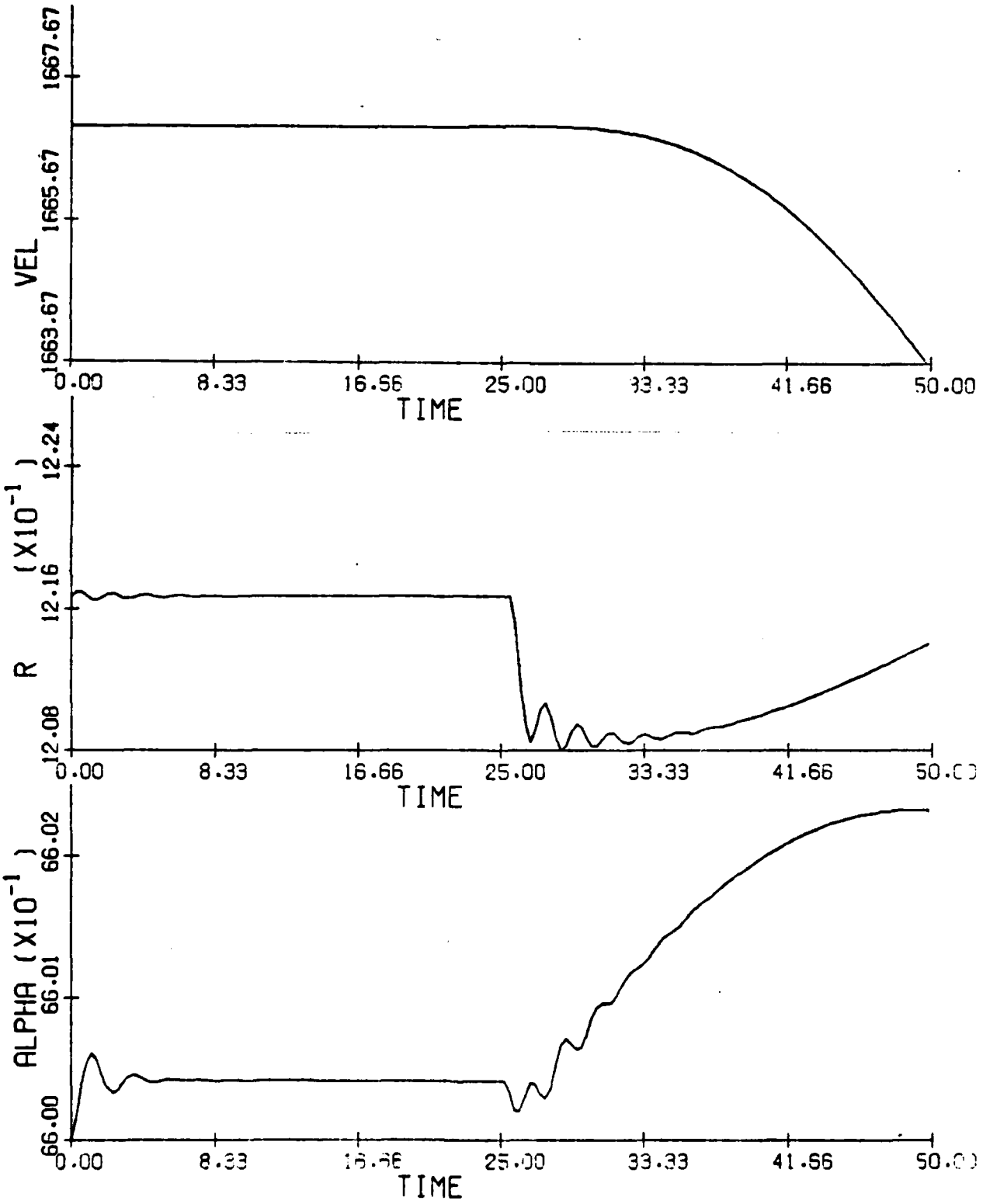

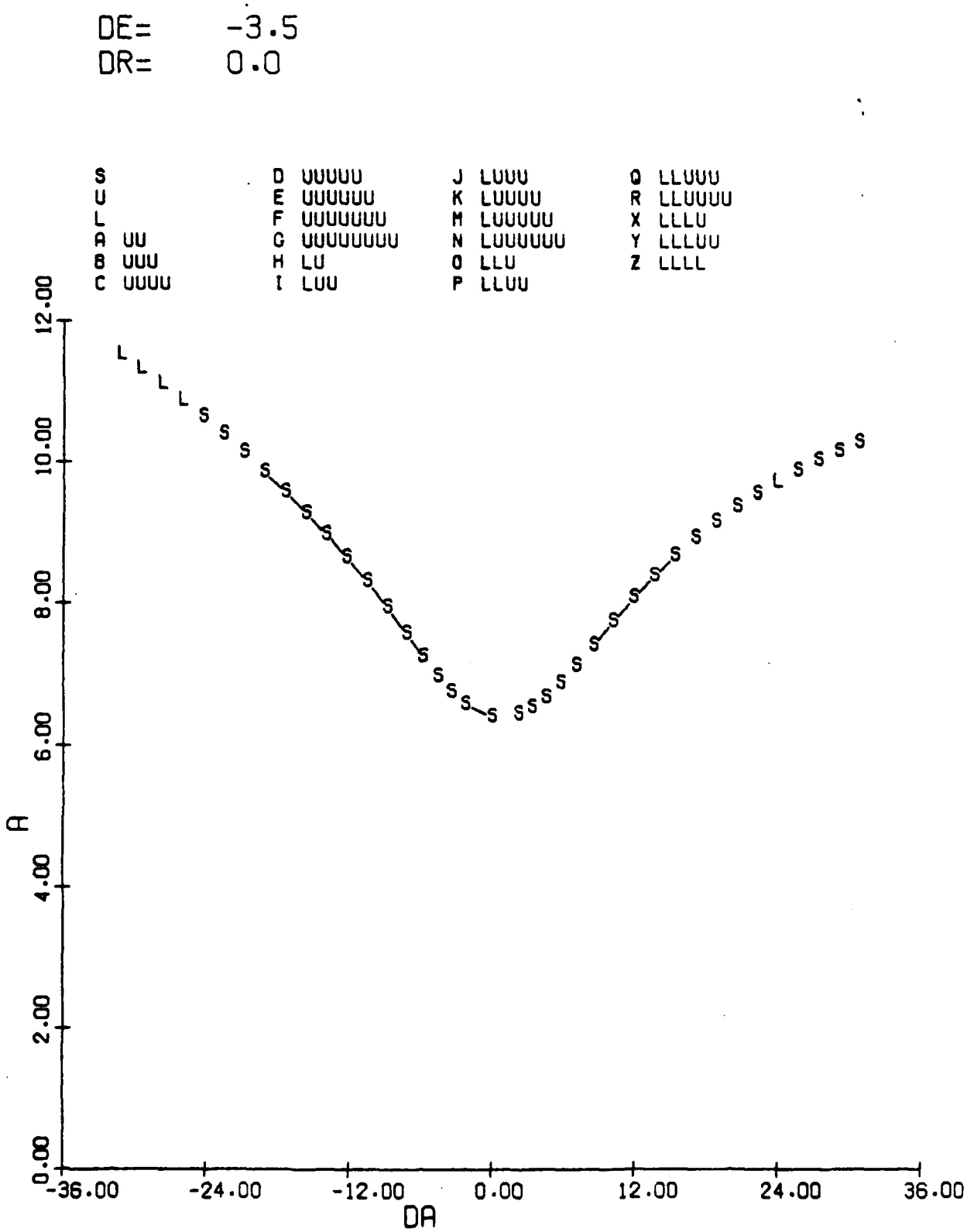

Figure 3.79: F-4 Equilibrium Surface, Trim Condition; h = 40000 ft; Thrust = 9000 lb; V = 875 fps; Trim Equilibrium System (a) α vs. δa

DE= -3.5
DR= 0.0

S	D UUUUU	J LUUU	Q LLUUU
U	E UUUUUU	K LUUUU	R LLUUUU
L	F UUUUUUU	M LUUUUU	X LLLU
A UU	G UUUUUUUU	N LUUUUUU	Y LLLUU
B UUU	H LU	O LLU	Z LLLL
C UUUU	I LUU	P LLUU	

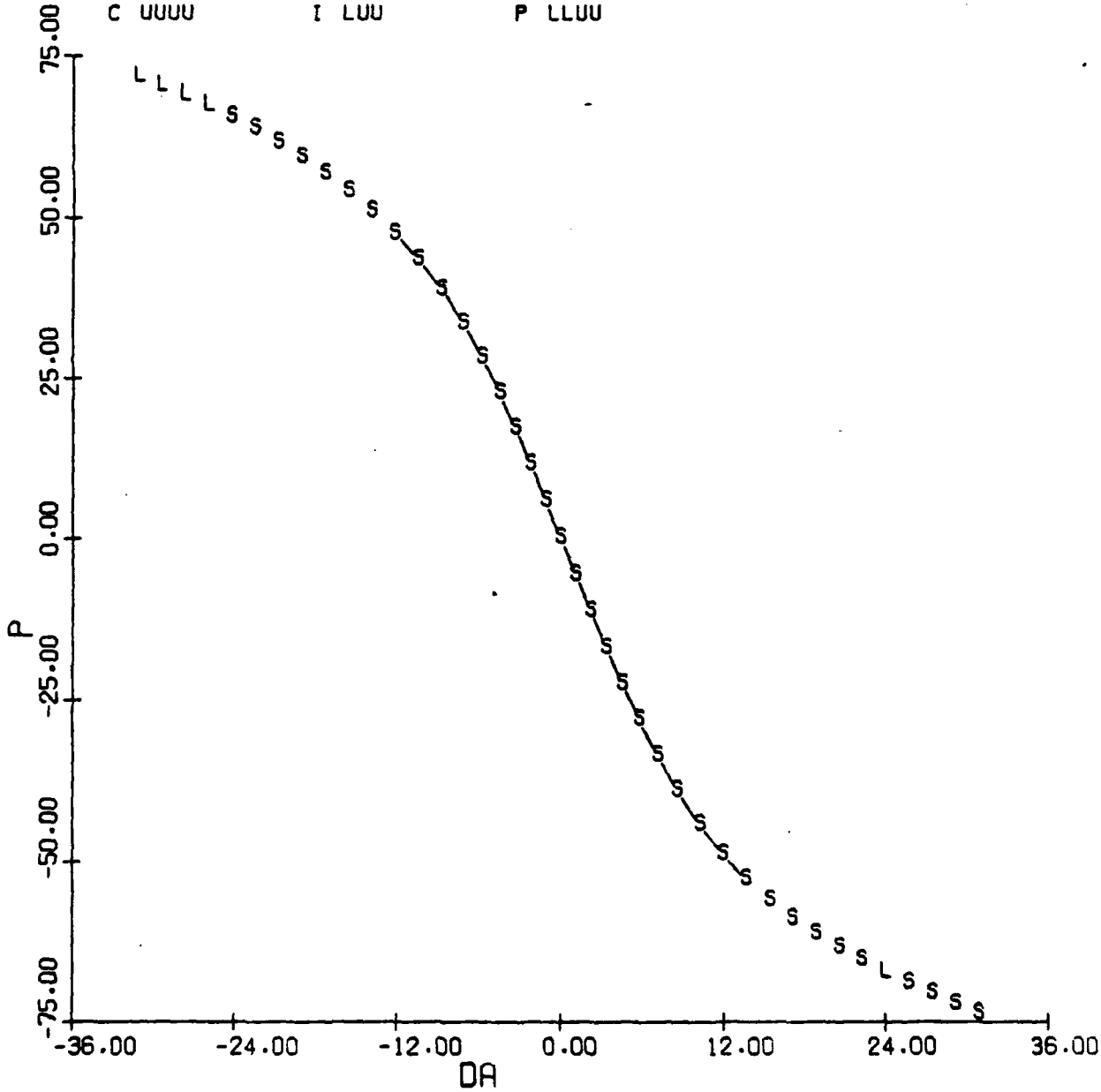

Figure 3.79(b): p vs. δa

DE= -3.5
DR= 0.0

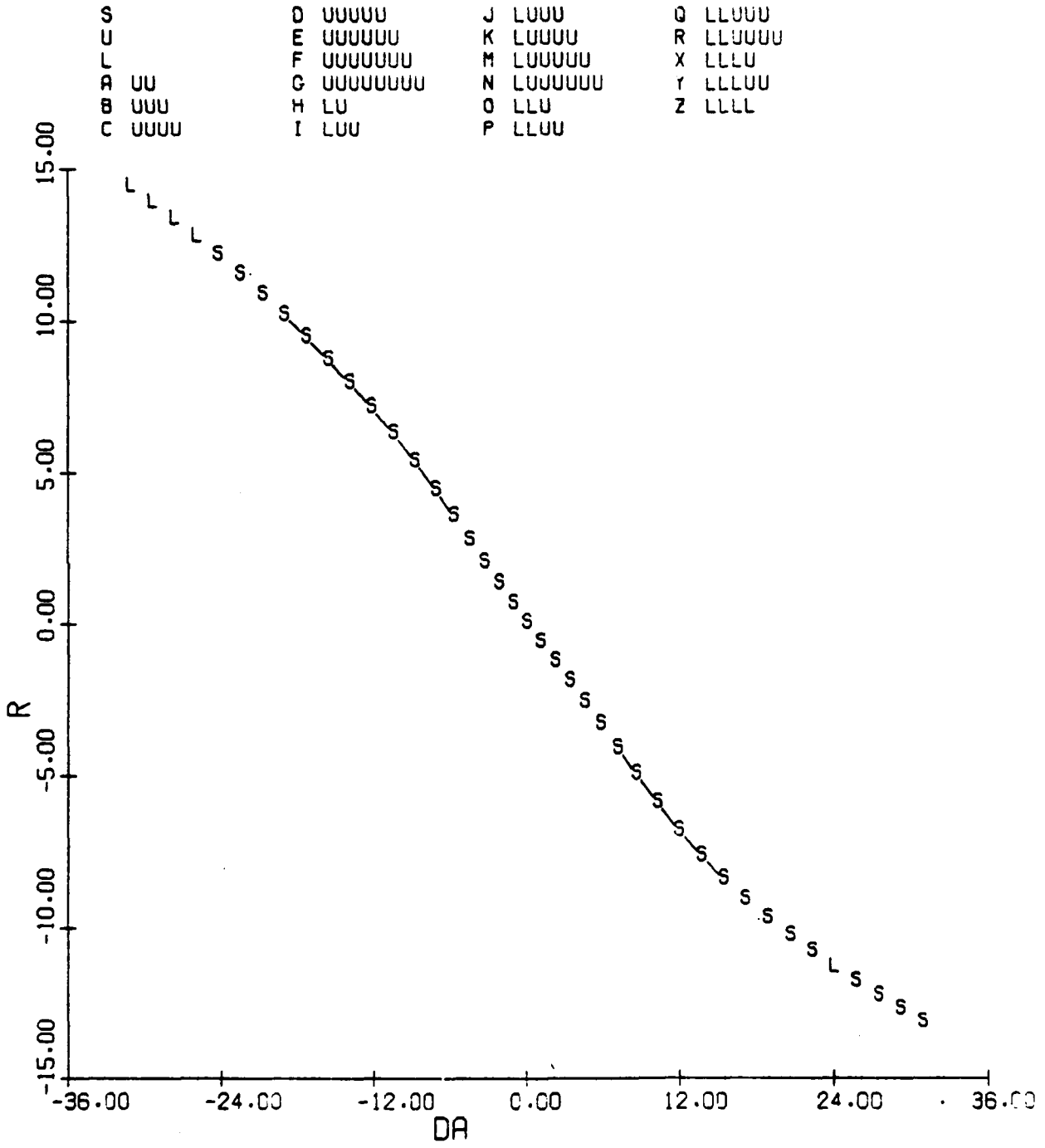

Figure 3.79(c): r vs. δa

Figure 3.80: F-4 Equilibrium Surface, Trim Regime;
h = 40000 ft; V = 875 fps; α vs. δe
(a) Thrust = 9000 lbs.

DA= 0.0
DR= 0.0

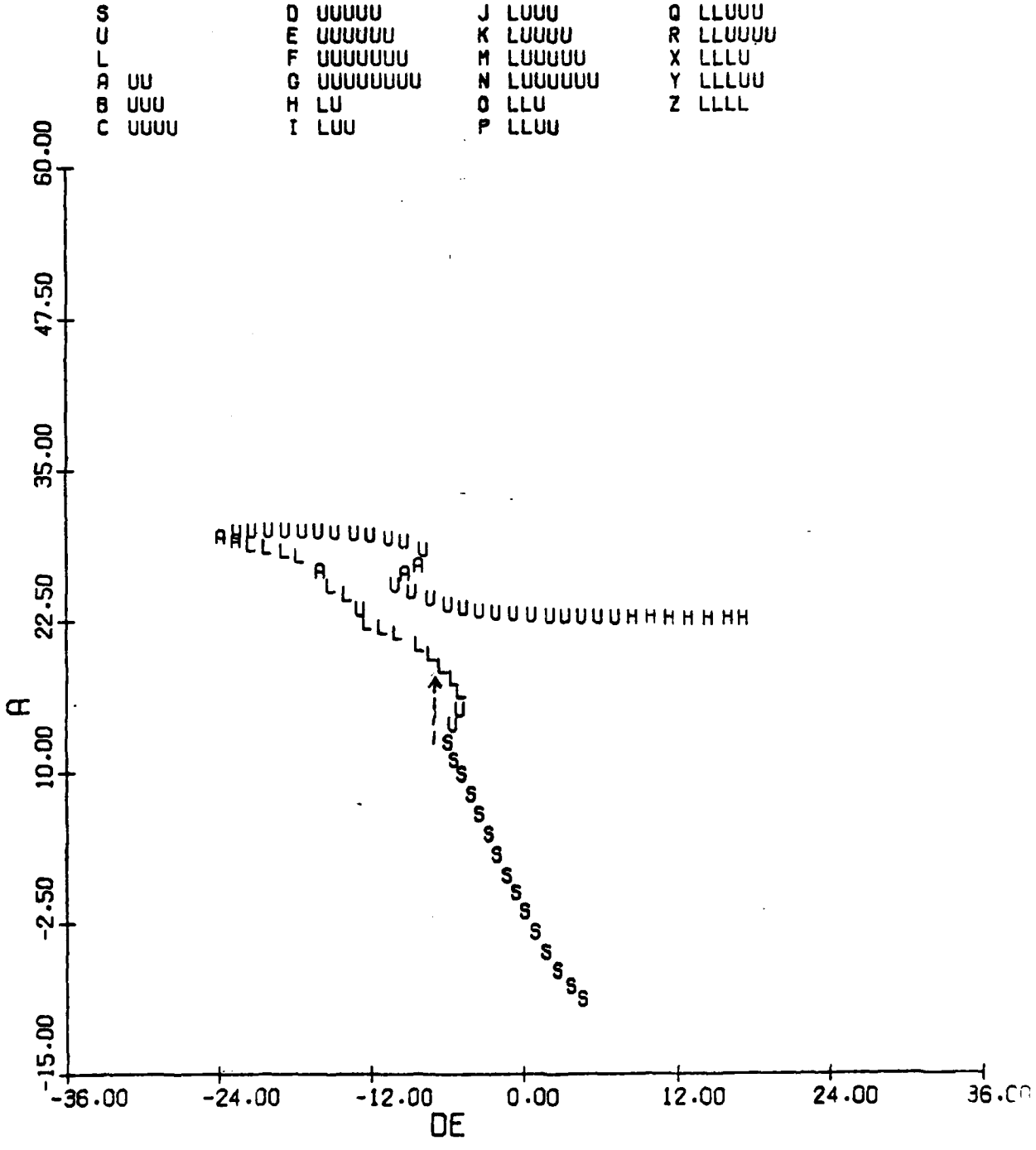

DA= 0.0
DR= 0.0

S	D UUUUU	J LUUU	Q LLUUU
U	E UUUUUU	K LUUUU	R LLUUUU
L	F UUUUUUU	M LUUUUU	X LLLU
A UU	G UUUUUUUU	N LUUUUUU	Y LLLUU
B UUU	H LU	O LLU	Z LLLL
C UUUU	I LUU	P LLUU	

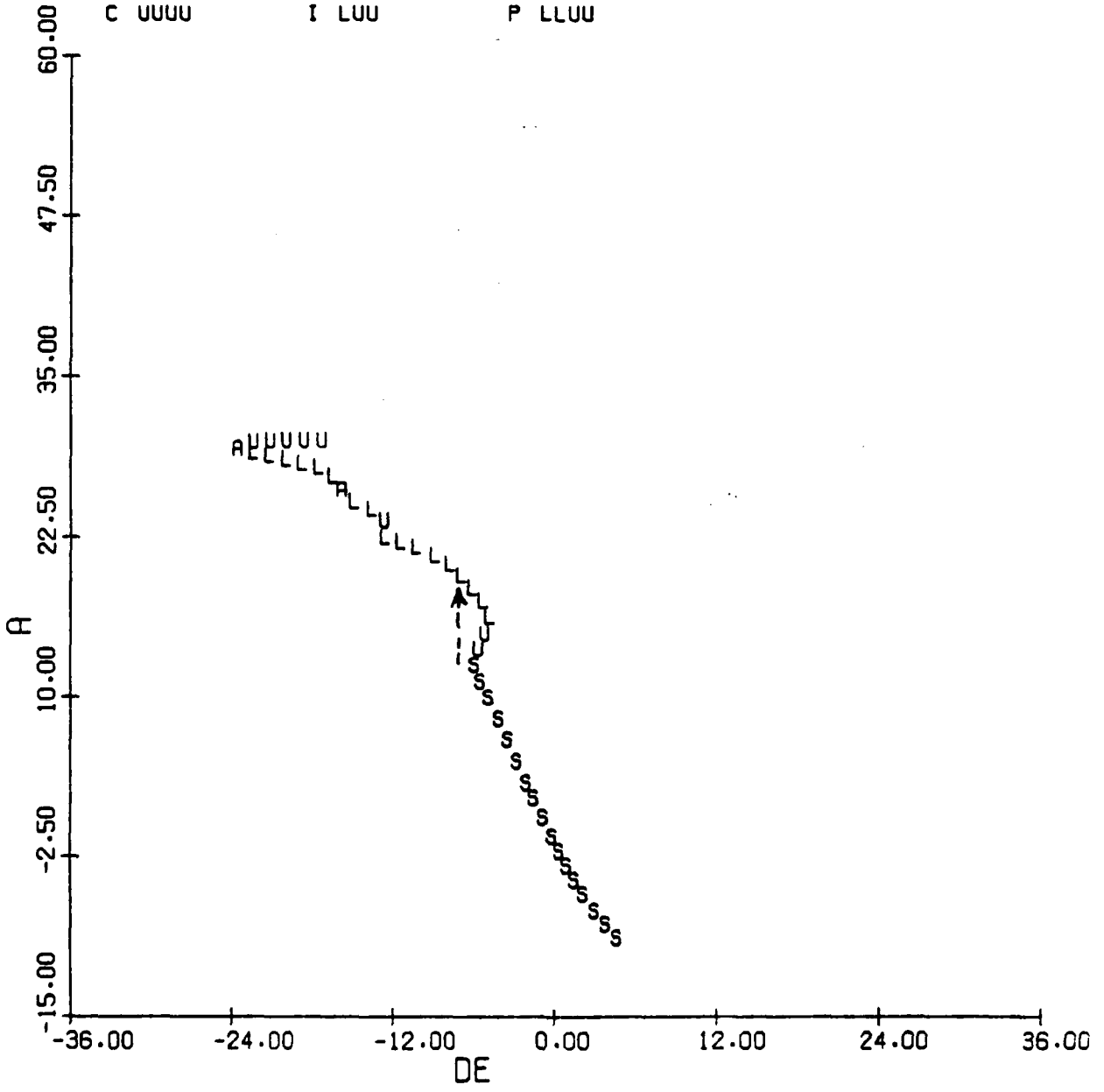

Figure 3.80(b): Thrust = 0.

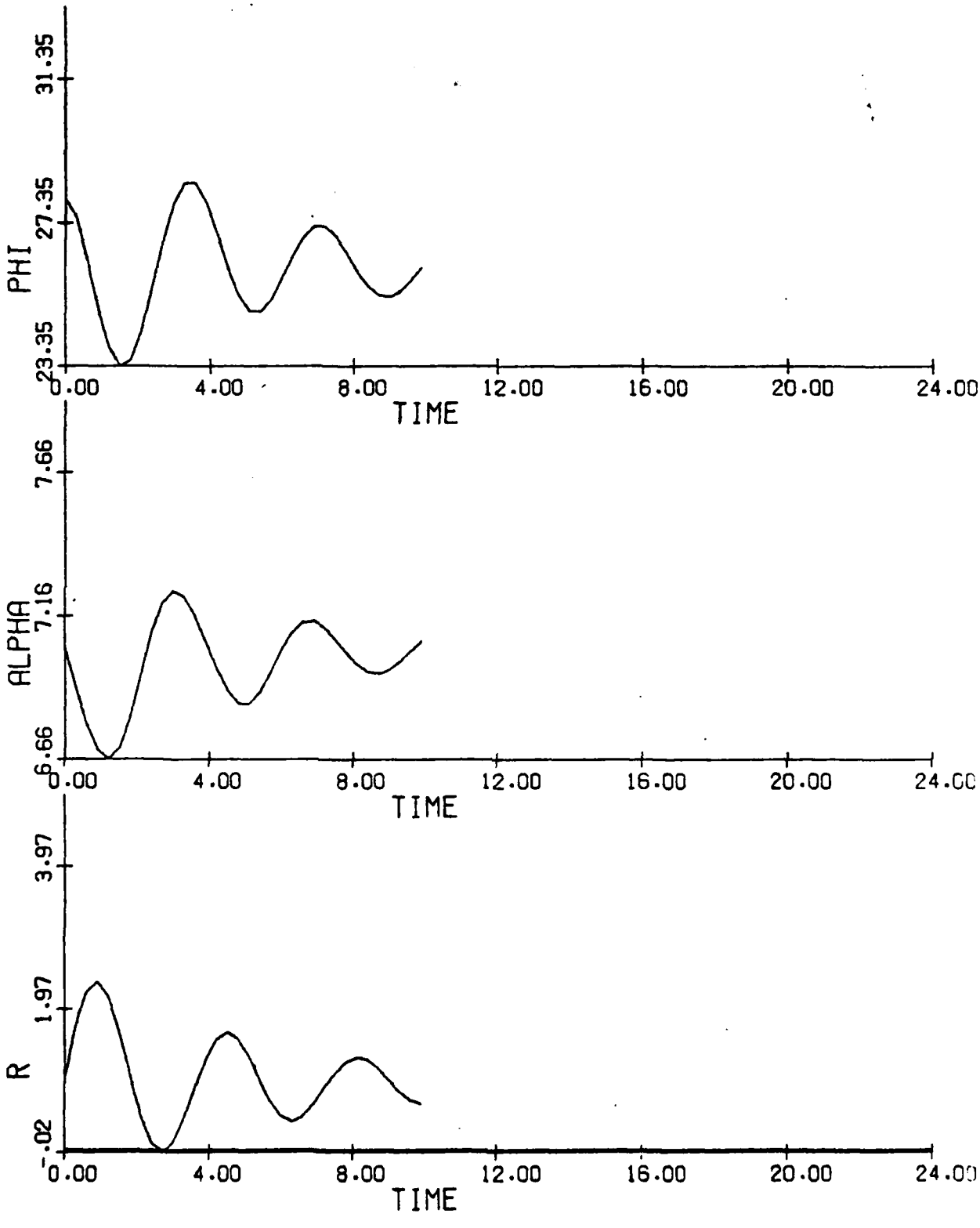

Figure 3.81: F-4 Time History; $h_0 = 40000$ ft; $V_0 = 875$ fps; Thrust = 9000 lbs; r, α, ϕ vs. t; $(\delta a, \delta e, \delta r) = (0., -3.5, 0.)^\circ$

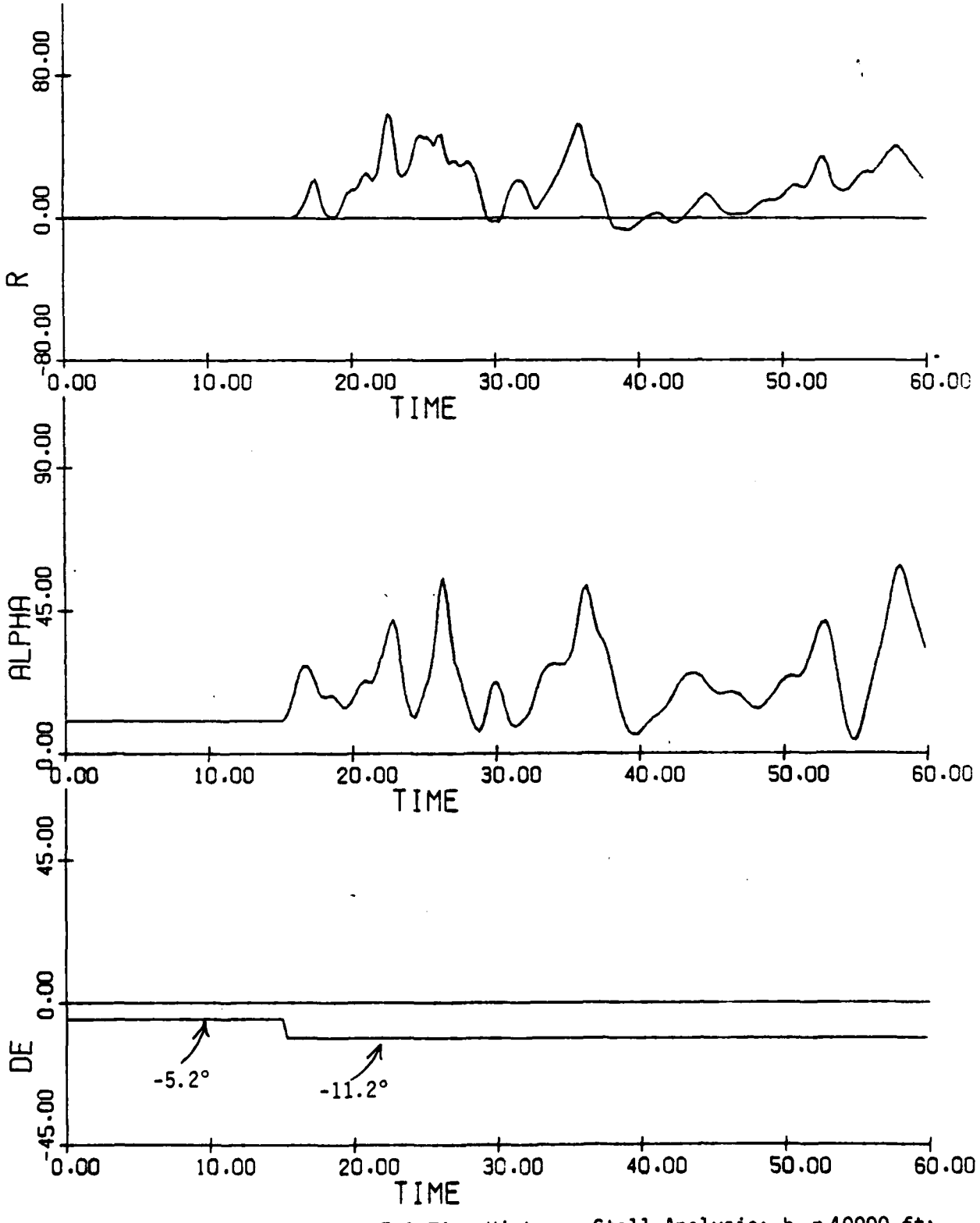

Figure 3.82: F-4 Time History; Stall Analysis; h_0 = 40000 ft; V_0 = 875 fps; Thrust = 0; $\delta a = \delta r = 0$

(a) δe, α, r vs. t

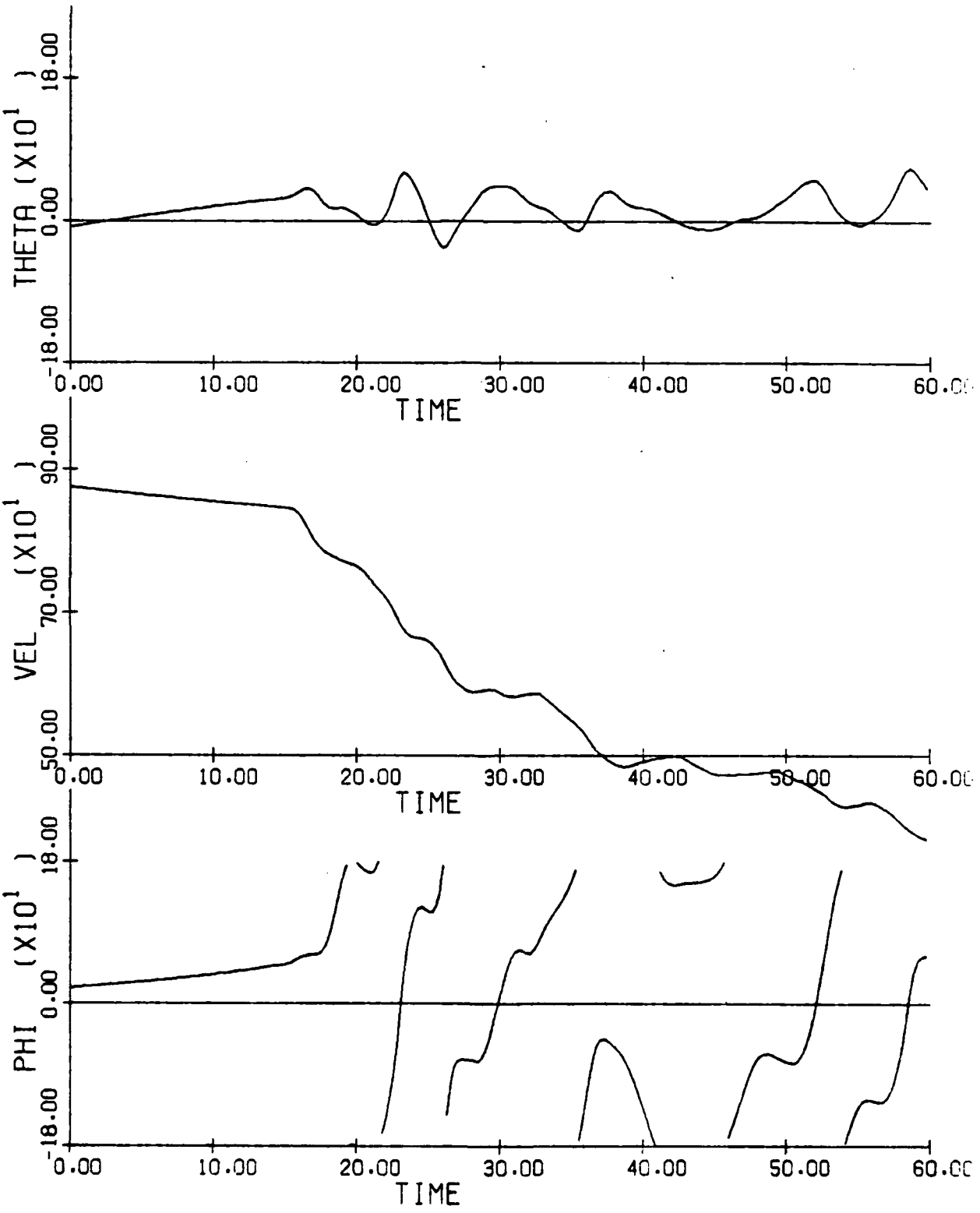

Figure 3.82(b): ϕ, V, θ vs. t

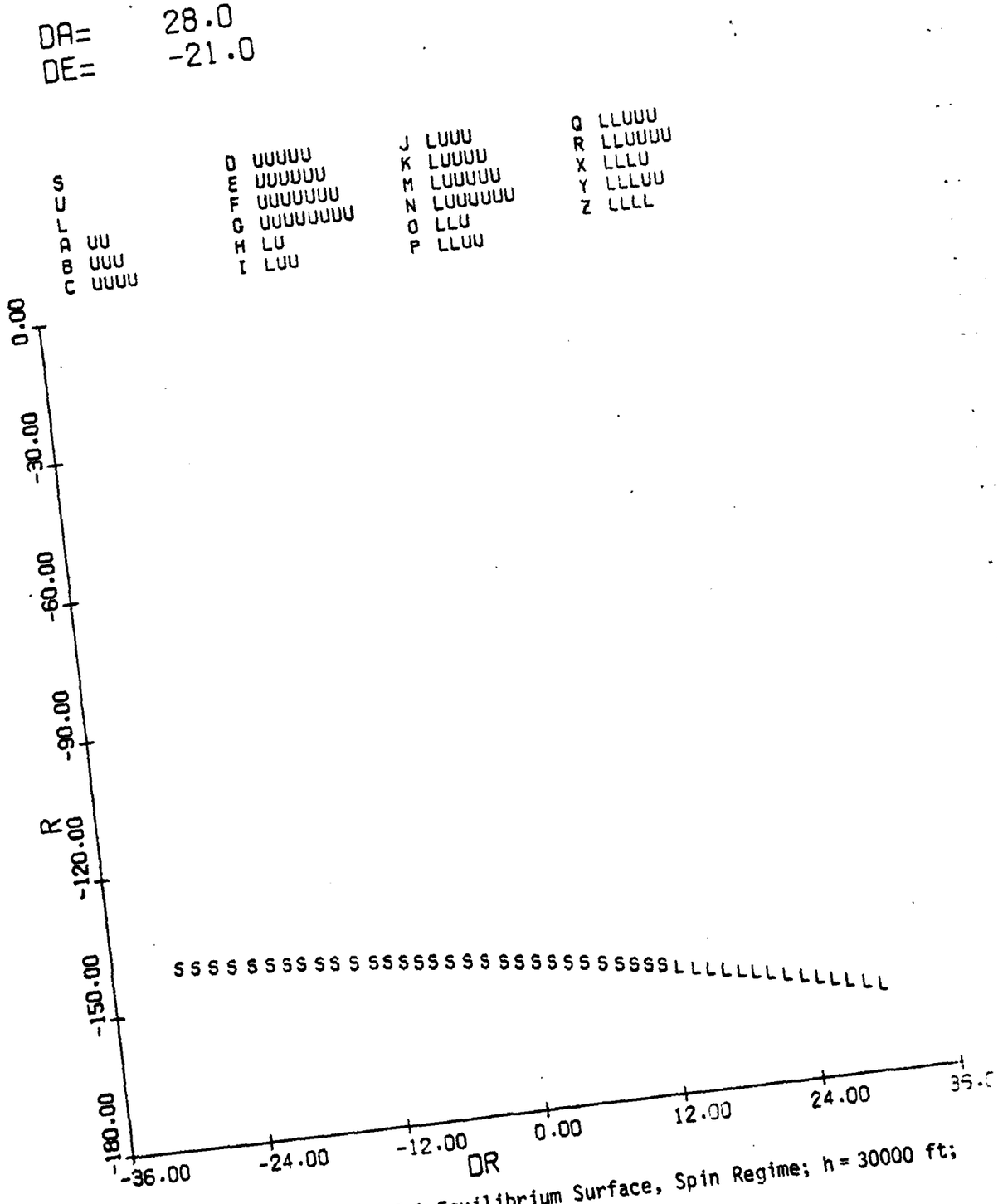

Figure 3.83: F-4 Equilibrium Surface, Spin Regime; h = 30000 ft;
(a) r vs. δr

DA= 28.0
DE= -21.0

S	D UUUUU	J LUUU	Q LLUUU
U	E UUUUUU	K LUUUU	R LLUUUU
L	F UUUUUUU	M LUUUUU	X LLLU
A UU	G UUUUUUUU	N LUUUUUU	Y LLLUU
B UUU	H LU	O LLU	Z LLLL
C UUUU	I LUU	P LLUU	

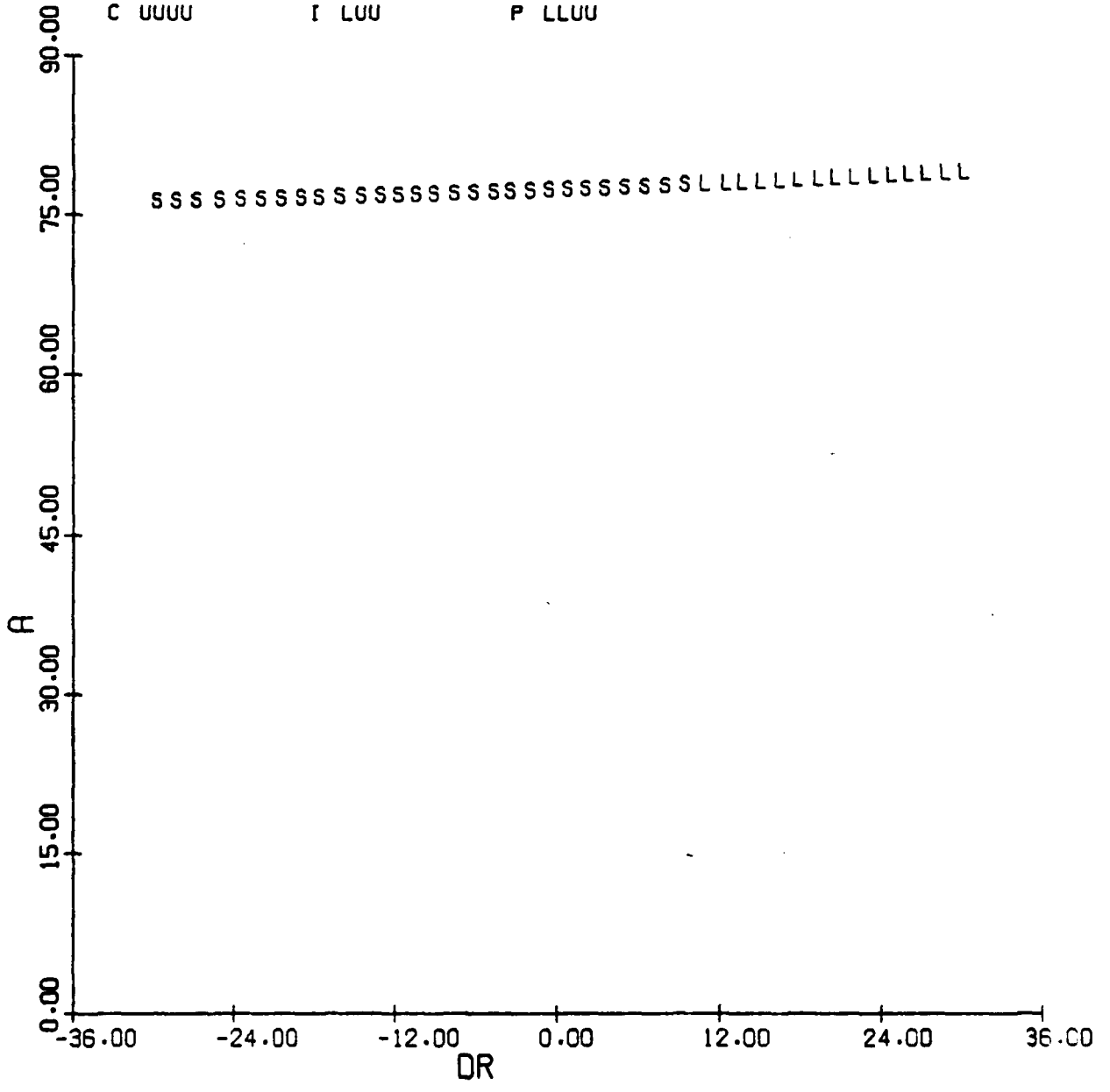

Figure 3.83(b): α vs. δr

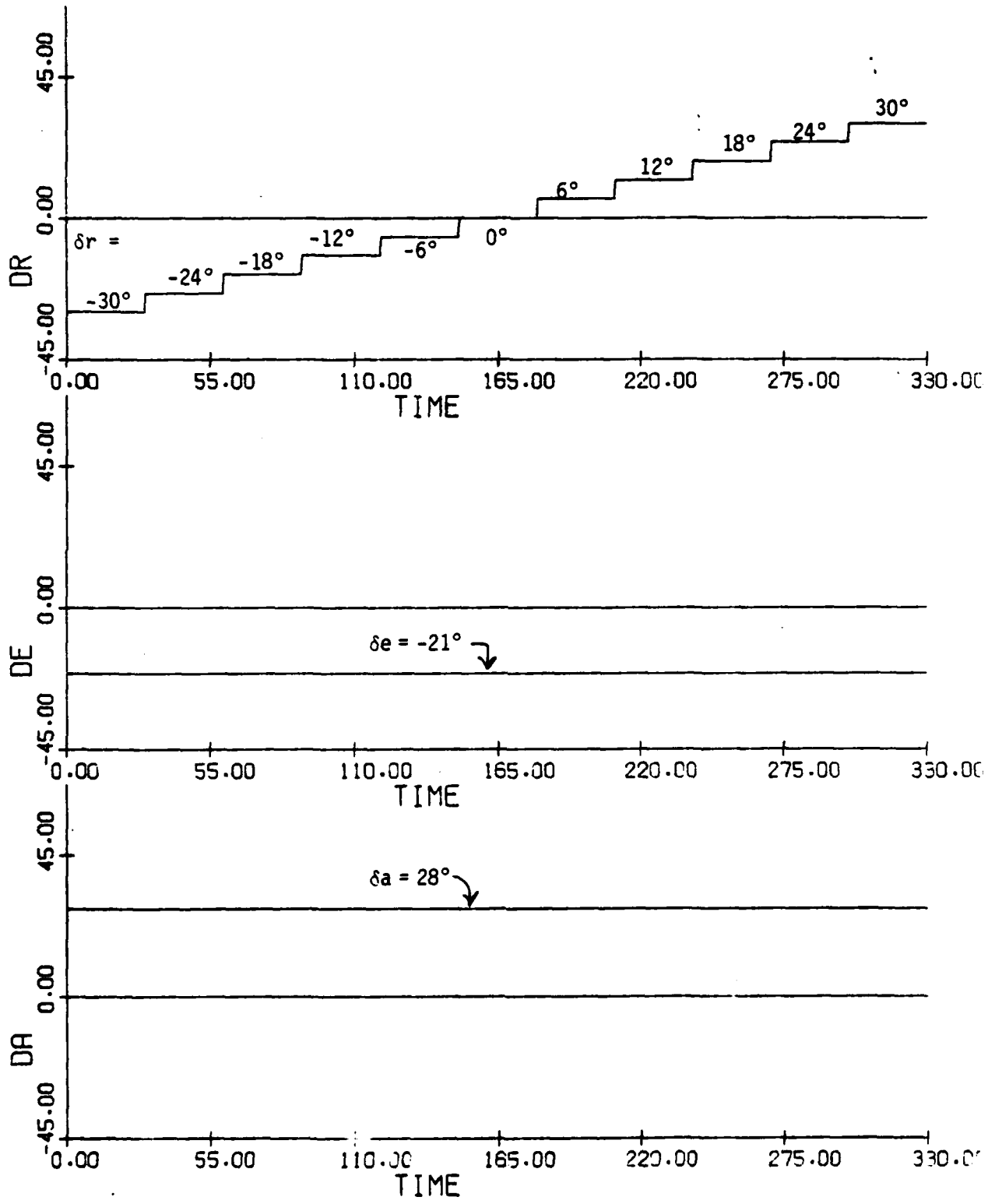

Figure 3.84: F-4 Time History, Limit Cycle Analysis; Spin Regime; h ≅ 30000 ft; (a) δa, δe, δr vs. t

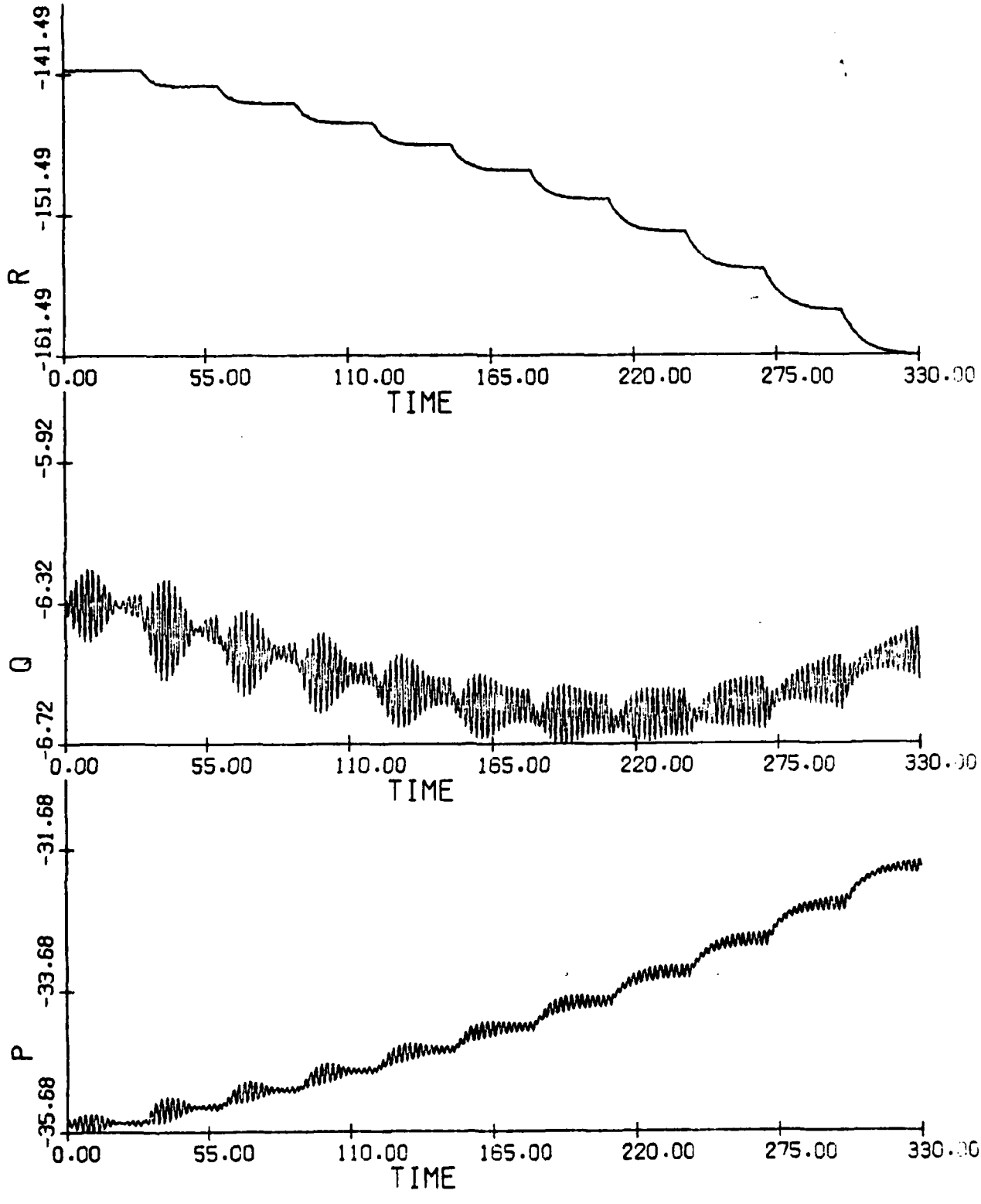

Figure 3.84(b): p, q, r vs. t

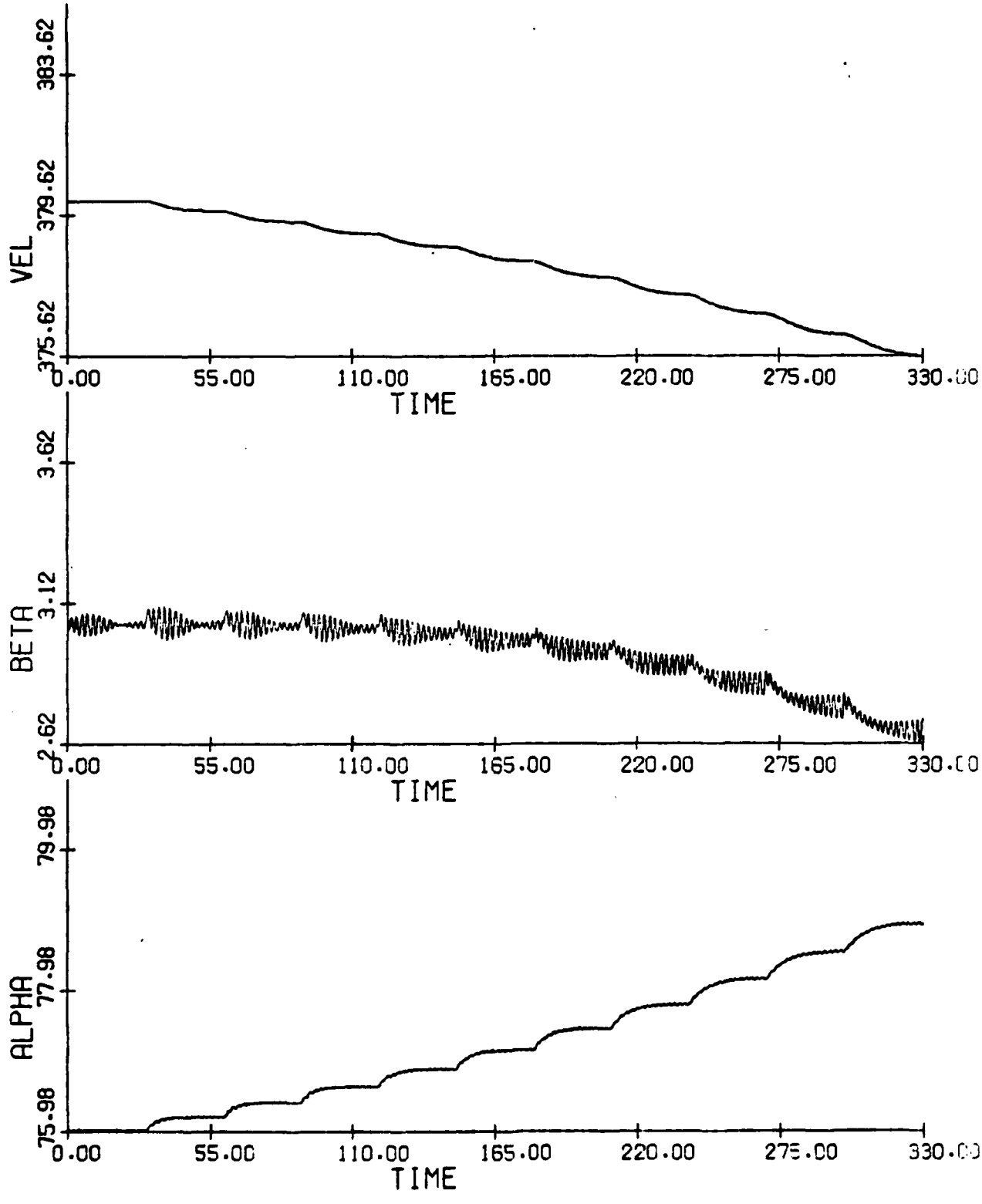

Figure 3.84(c): α, β, V vs. t

Figure 3.85: F-4 Time History, Limit Cycle Analysis, Spin Regime; h = 30000 ft; $\delta a = 28°$, $\delta e = -21°$, $\delta r = -30°$; α, r, ϕ vs. t

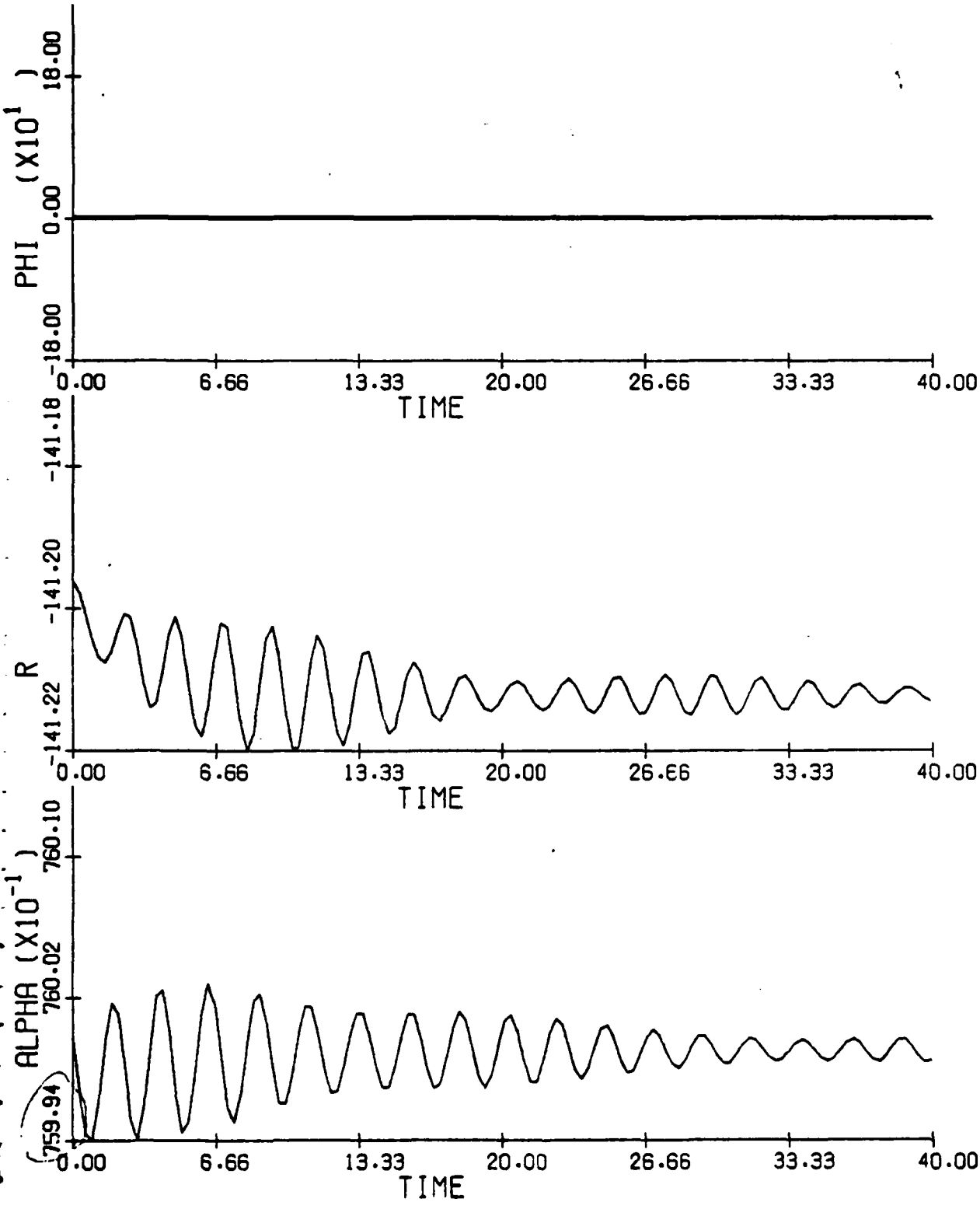

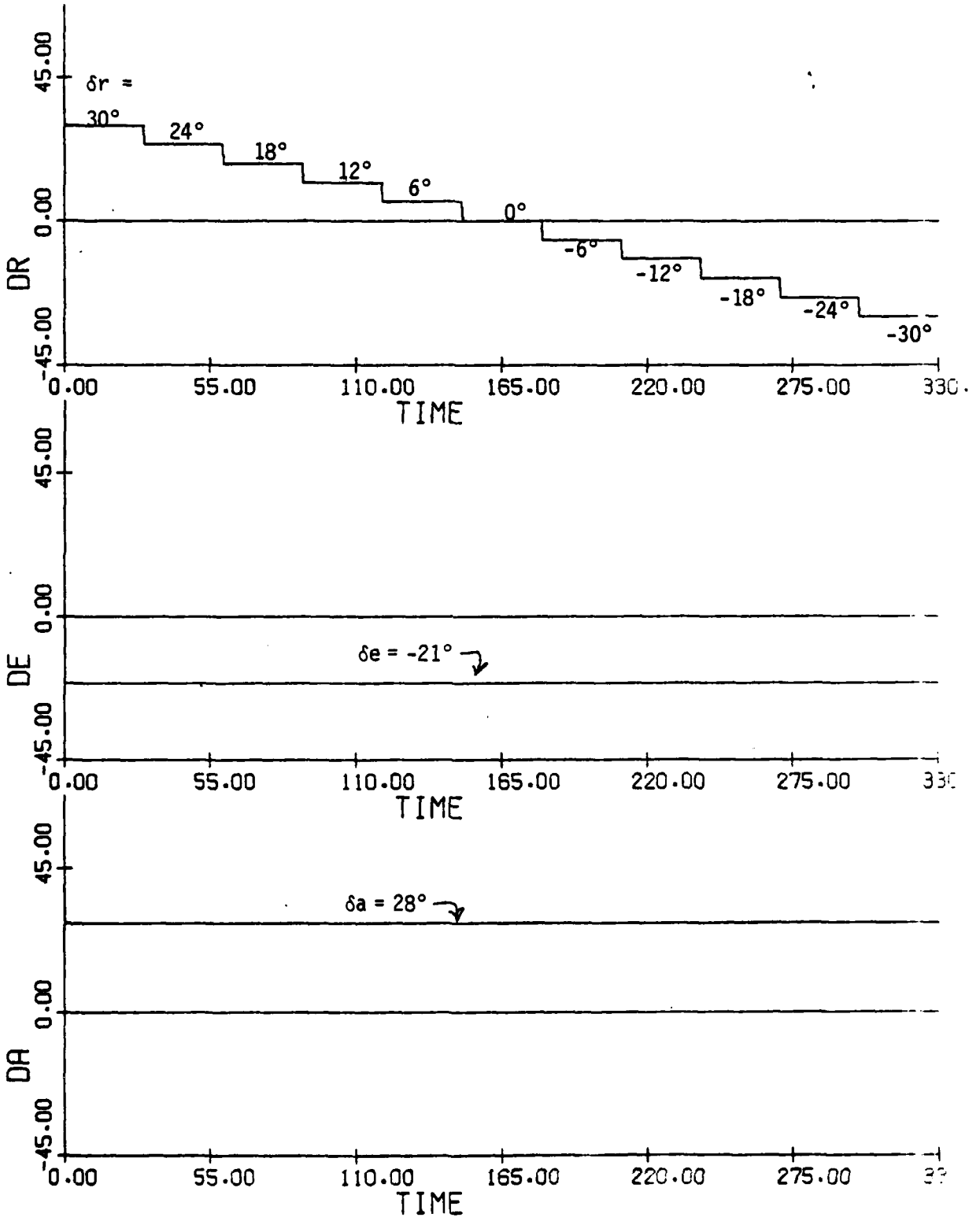

Figure 3.86: F-4 Time History, Limit Cycle Analysis, Spin Regime; h = 30000 ft; (a) δa, δe, δr vs. t

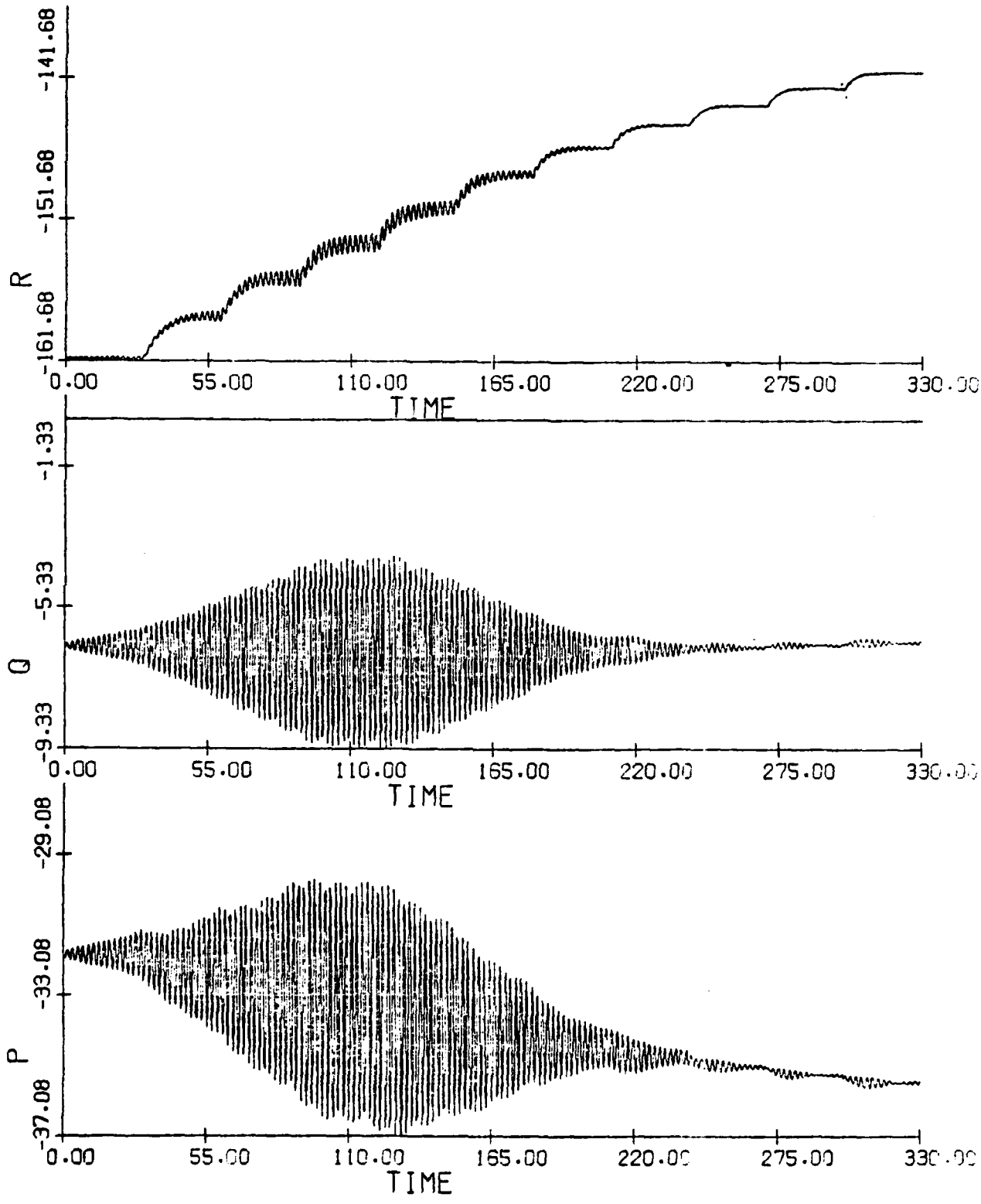

Figure 3.86(b): p, q, r vs. t

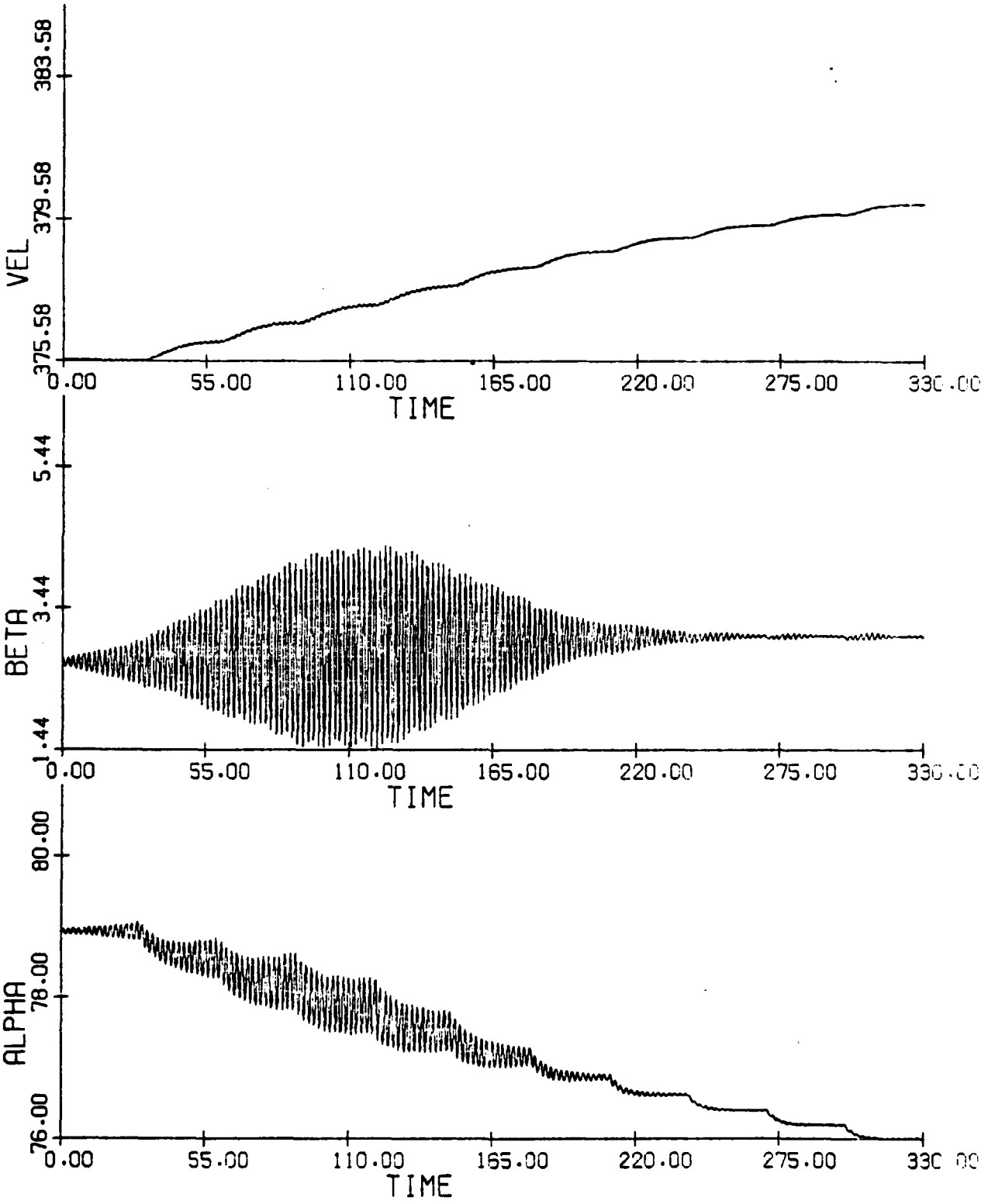

Figure 3.86(c): α, β, V vs. t

Figure 3.87: F-4 Limit Cycle Analysis; h = 40000 ft,
Thrust = 0;
(a) α vs. δe for δe decreasing: -4°, -10°, -15°, -20°, -24°

DA= 0.0
DR= 0.0

S	D UUUUU	J LUUU	Q LLUUU
U	E UUUUUU	K LUUUU	R LLUUUU
L	F UUUUUUU	M LUUUUU	X LLLU
A UU	G UUUUUUUU	N LUUUUUU	Y LLLUU
B UUU	H LU	O LLU	Z LLLL
C UUUU	I LUU	P LLUU	

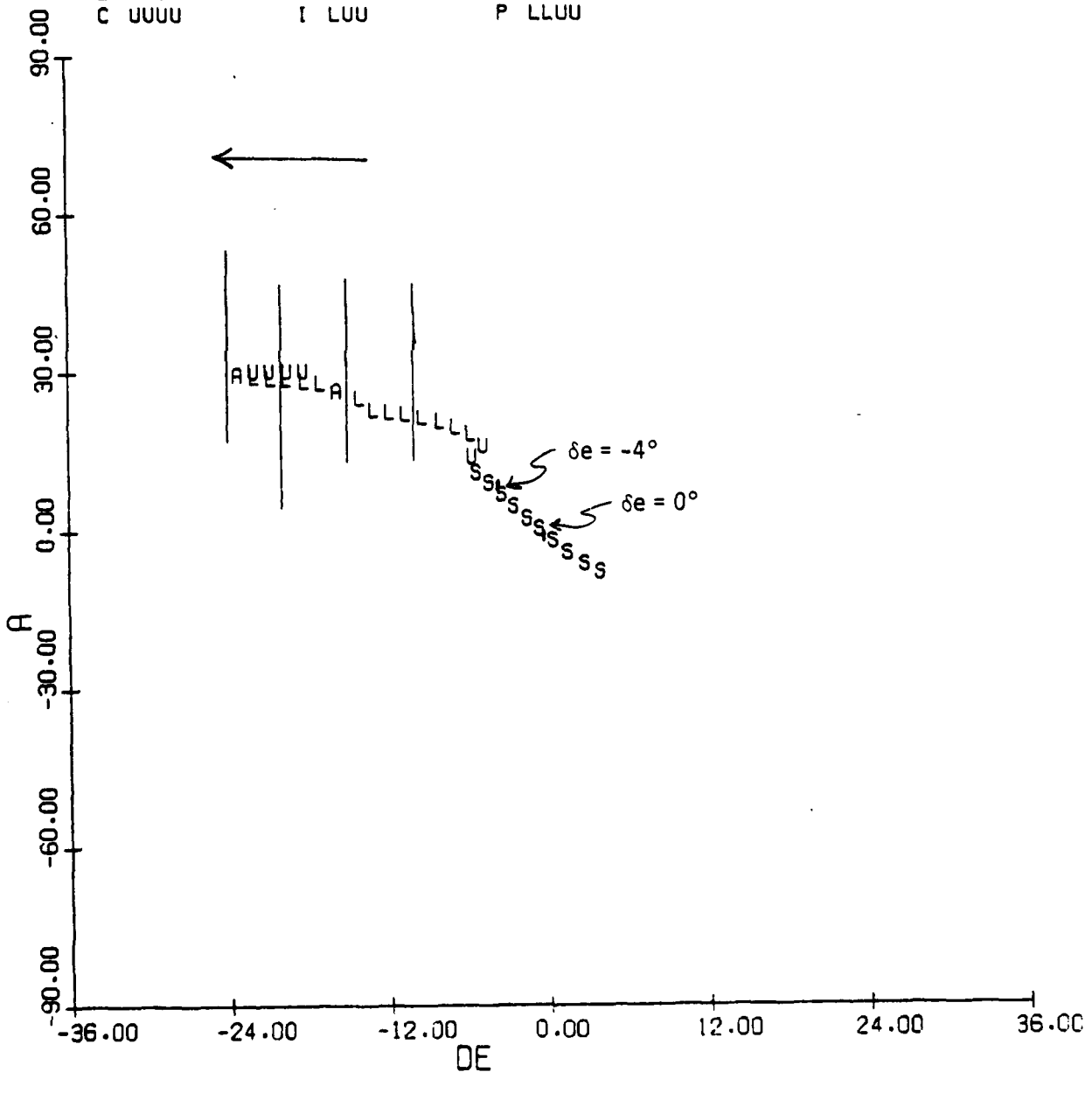

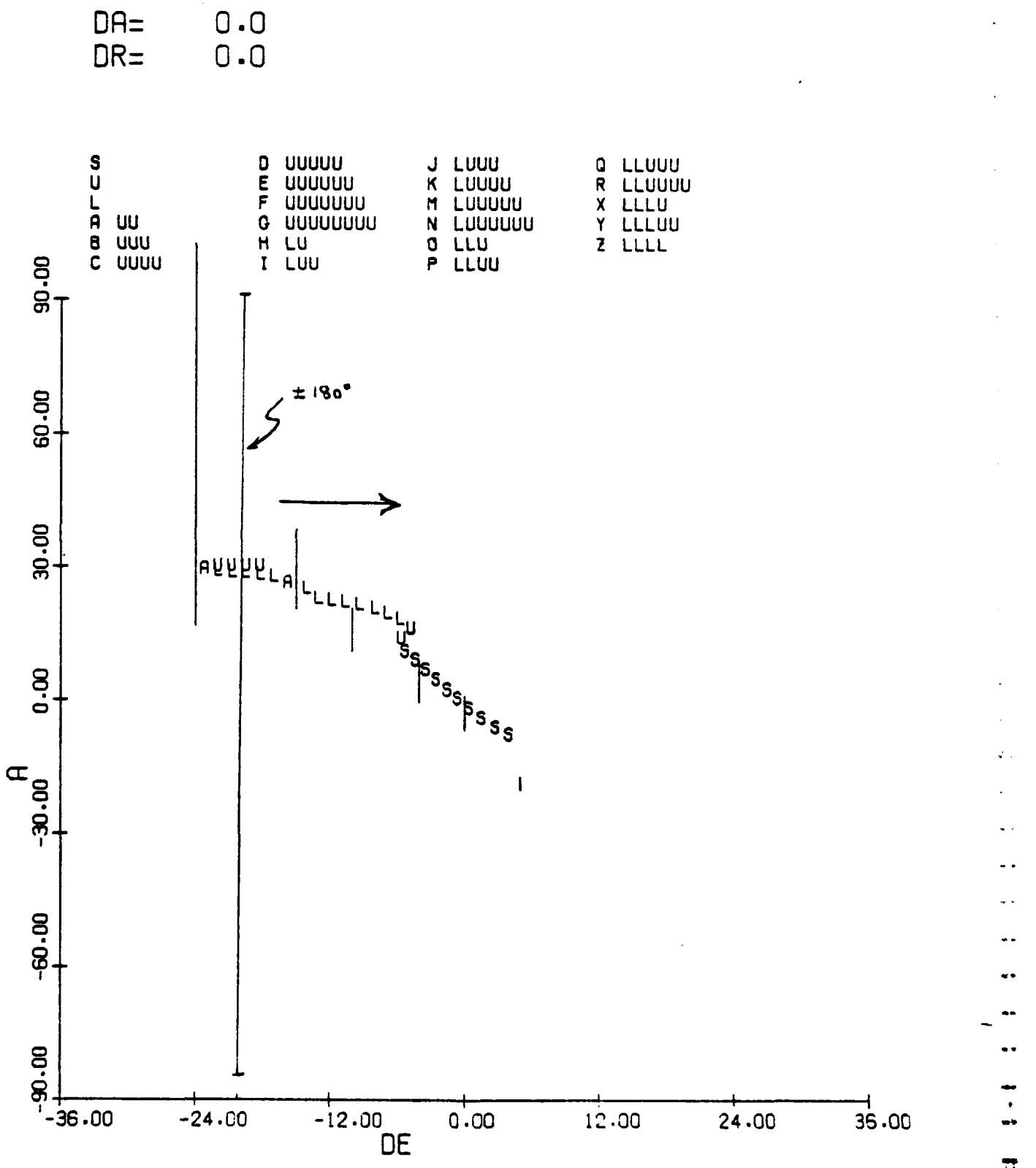

Figure 3.87(b): α vs. δe for δe increasing: -24°, -20°, -15°, -10°, -4°, 0°, 5°

Figure 3.88: F-4 Time History Run, Limit Cycle Analysis, Trim Regime; h = 40000 ft, Thrust = 0; δe, α, β vs. t
(a) δe decreasing

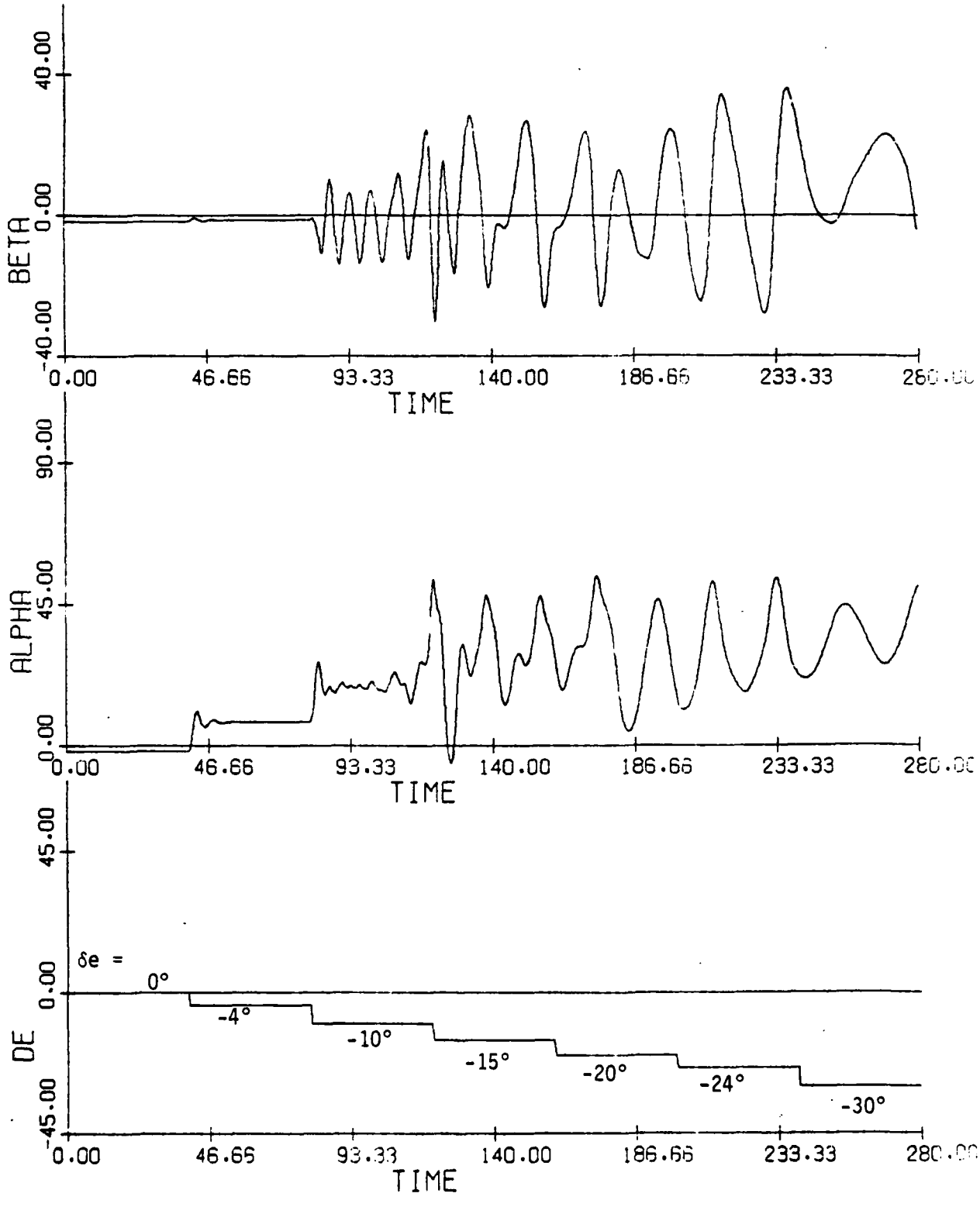

Figure 3.88(b): δe increasing

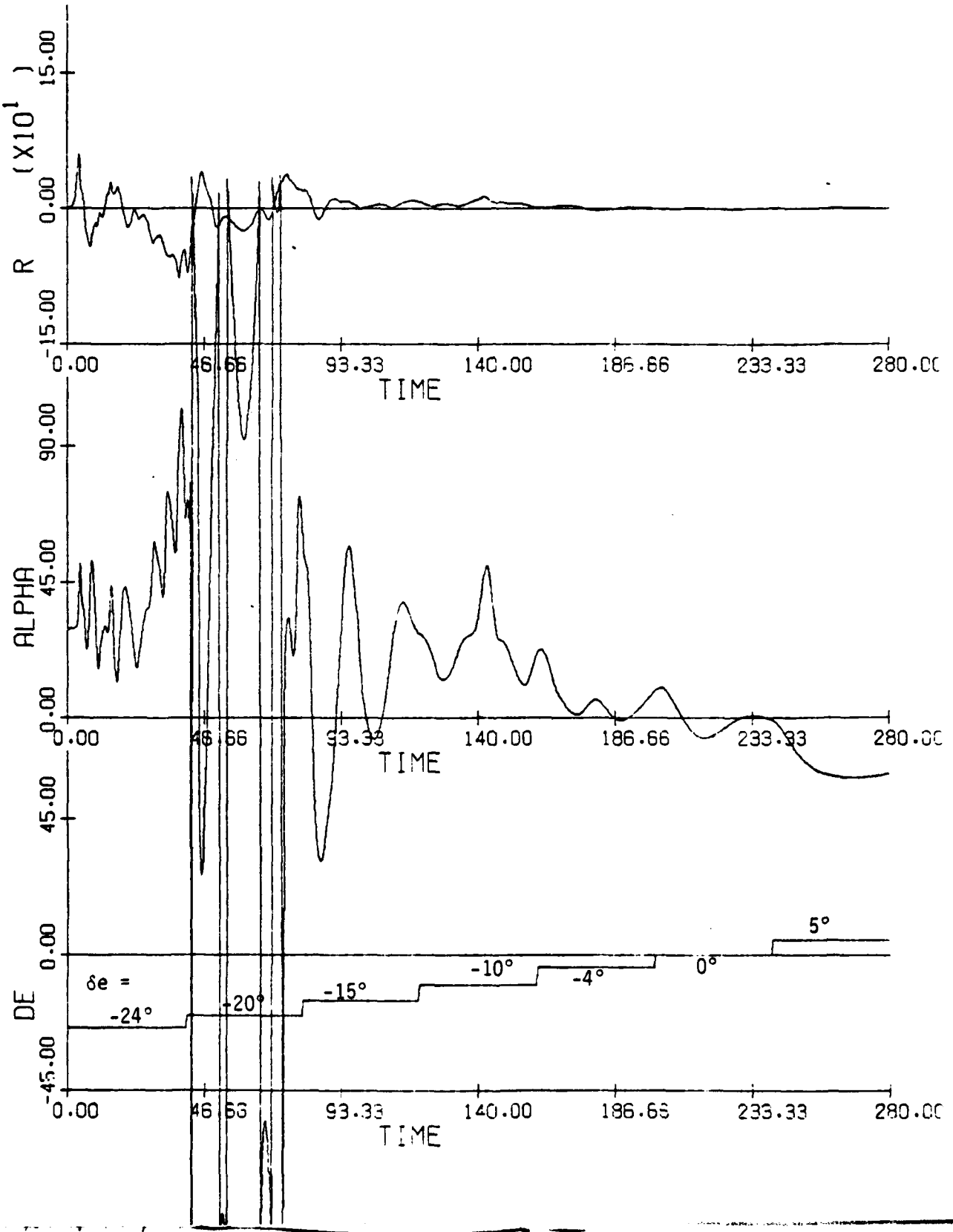

4. CONCLUSIONS AND RECOMMENDATIONS FOR FURTHER RESEARCH

4.1 Conclusions

Based on BACTM analysis of the aircraft F model and the F-4 model, we can conclude that: (i) BACTM is capable of effectively performing analysis of spin behavior, including steep and flat spins, for aircraft modeled with tabular aerodynamic data. This analysis has, in particular, explored the oscillatory and limit cycle phenomena of the steep spin flight regime for aircraft F; from this, spin recovery control strategies have been devised.

(ii) The experience gained from the development and utilization of BACTM on aircraft F has been applied to the F-4 aircraft model. The data for this more realistic aircraft model were supplied in three standard forms of wind-tunnel data: static, forced oscillation and rotary balance. It is the rotary balance data in particular which make the F-4 aero data base a considerably more realistic model for the study of high-α and spin motions. While the aircraft F model was useful as a prototype for the development of BACTM programs which could handle multi-dependent tabular aerodynamic data bases, many of its simulated motions, particularly with regard to the length of time required to effect spin recovery, were not realistic, because this model lacks rotary balance data.

(iii) BACTM was upgraded and expanded in order to develop the tools required to analyze the limit cycle and oscillatory behavior which typifies both aircraft F and F-4 motion in the steep spin flight regime. These

modifications include the development of a limit cycle continuation algorithm, which can find locations in state-control space where limit cycle motion (defined as a motion in which the time history trajectory intersects itself after a finite, non-zero time interval), if any, exists. This algorithm greatly expands the capability to perform quantitative analysis of limit cycles, providing global information on the size of amplitudes and period, and the manner in which control parameter changes affect them. Also, elementary stability information is computed. Also, the development of a third system of variables for the computation of equilibrium and bifurcation surfaces. This new equilibrium system consists of the variables yaw, pitch and roll rate, angles of attack and sideslip, and pitch and roll angles. In this system, velocity is computed independently via a simple algebraic relationship. This system, using one less variable (velocity) than the standard spin system, offers potential for much greater efficiency in computing equilibrium surfaces in the high-α and spin regimes. (The third equilibrium system consists of only five variables, and is used principally in the trim flight regime, although it can be useful in high-α regimes. The reduced number of variables arises from the decoupling caused by neglecting gravity effects, which is possible in those flight regimes where velocity can be held constant.)

(iv) The basic programs in BACTM, in particular the equilibrium surface, time history and bifurcation surface programs, have been modified and expanded extensively, for the purpose of being able to accomodate aircraft models with extensive aerodynamic data bases. There now exist three kinds of equilibrium surface programs, all of which are based on

solution by continuation methods: the full spin system (eight coupled variables), the reduced spin system (seven coupled variables; velocity computed algebraically), and the trim spin system (five coupled variables; velocity constant, zero gravity).

(v) The bifurcation surface algorithm has been modified to reduce as much as possible the requirements for numerical differentiation of the elements of the Jacobian matrix. This has substantially reduced the cost of generating bifurcation surfaces.

(vi) The upgraded and expanded BACTM package has been used extensively on a prototype aircraft model, designated aircraft F in our studies, for the purpose of both validating the soundness of the BACTM approach and of conducting preliminary spin studies on a generically representative aircraft.

(vii) A major goal being the application of BACTM to a modern fighter aircraft for the purpose of analyzing high-α and spin behavior, we have obtained extensive wind tunnel data for the F-4 aircraft. These data are in the form of static, forced oscillation and rotary balance aerodynamic derivatives. They have been implemented on BACTM, and have been used successfully in the various programs which require the F-4 model.

(viii) Spin analysis on aircraft F has concentrated on the spin recovery problem. We have devised a recovery strategy from a flat, equilibrium spin condition which involves only aerosurface control deflections. In addition, while our recovery strategy was derived from an analysis of BACTM simulations, it is seen to be rather similar to recovery strategies developed by test engineers.

(ix) As a consequence of the aircraft F spin recovery analysis, we have found and generated equilibria in the steep, oscillatory spin flight domain. The aircraft behavior in this region, which is intermediate to the trim and flat spin ($\alpha > 80°$) regions, is highly oscillatory. In this region, limit cycle motion is prevalent. Recognizing the need for proper analysis of such motion for nonlinear systems has led us to develop a numerical continuation algorithm which can detect limit cycle motion and compute the period at each such point on a limit cycle branch. Using these curves, control strategies can be found which would recover from limit cycle conditions. We have found situations for aircraft F in which control variations cause the creation and annihilation of stable limit cycles (global bifurcation). An understanding of their behavior leads to the development of recovery control strategies.

Other aircraft F studies have included stall, departure, lateral directional divergence, wing rock and flat equilibrium spin. Using the tools of the BACTM package, we have demonstrated the capability to define in these regions flight envelopes and avoidance and recovery strategies.

(x) F-4 aircraft model analysis has begun with the computation of equilibrium surfaces in the trim and steep spin flight domains. These results have been expanded greatly and supported by time history simulations and bifurcation surface results. Validation of our F-4 model simulations has thus far indicated that the model is properly implemented, insofar as the aero data supplied to us is concerned.

(xi) Extensive time history correlation runs have been made with

the F-4 model. There still is more work to be done before firm correlation is achieved, but a few of the runs show promise.

(xii) A method for adequate and effective control system synthesis utilizing bifurcation surfaces has been demonstrated on the F-4. The method is based on scheduling control deflections in an interdependent manner so as to avoid traversing the boundary lines delineated by the bifurcation curves. These lines are projections of equilibrium surface limit points onto the control subspace, and indicate the occurrence of jump phenomena.

(xiii) A series of equilibrium surface and time studies have been conducted utilizing an F-4 model which incorporates the effects of thrust. In these runs, thrust is held at a fixed value, and then the usual process is applied in generating the surfaces. Only in-plane thrust is simulated, and no thrust moments are modeled. For the time history simulations, thrust is turned off when angle-of-attack is outside the domain (-10°,20°). It was found, for equilibrium surfaces, that thrust effects are negligible when the trim system is used (velocity fixed, gravity equal to zero), but that velocity, pitch, and roll are extremely sensitive to minor control parameter changes, if velocity is allowed to vary and gravity coupling is present (spin equilibrium system). No large differences were noticed between thrust and non-thrust time history results, run at fixed controls.

4.2 Recommendations

Based on our experience during this reporting period, it is suggested that the following areas be investigated in the future:

(i) The F-4 model correlation studies with actual flight data should be continued. The goal of this study would be to assess the adequacy of the aerodynamic data at hand for the high angle-of-attack aircraft analysis of the kind required to render the conclusions arrived at by BACTM as realistic as possible.

(ii) If the aero data on hand were found to be inadequate, a study should be made to indicate what specific needs must be met, e.g., how may more data be taken, in order to develop a data base capable of adequate correlation.

(iii) If the aero data on hand were found to be adequate, a study should be made concerning how explicitly the hybrid aero model ought to be synthesized, in order to enhance correlation. In particular, a comprehensive scheme for incorporating rotation balance data with static and forced oscillation data should be developed. Furthermore, specific, quantitative correlation criteria should be developed, and aero coefficients whose influence is negligible in certain flight regimes should be identified as such.

(iv) Limit cycle analysis should be pursued as soon as possible. Use of the continuation algorithm on the F-4 model will enhance greatly our understanding of high angle-of-attack phenomena in stall and steep spin regimes. The quantization of limit cycles should, if possible, be extended to the establishment of a means to define domains of attraction for stable limit cycles, and the identification of unstable limit cycles.

(v) The use of control system synthesis in high angle-of-attack flight regimes, utilizing results from equilibrium and bifurcation surfaces,

should continue in as comprehensive a manner as time and budget considerations allow.

REFERENCES

1. Abraham, R. and J. E. Marsden (1978), Foundations of Mechanics, Reading, Mass.: Benjamin/Cummings.

2. Adams, W. M. (1972), "Analytic Prediction of Airplane Equilibrium Spin Characteristics," NASA TN D-6926.

3. Anglin, E. and S. Scher (1964), "Analytical Study of Aircraft--Developed Spins and Determination of Moments Required for Satisfactory Spin Recovery," NASA TN D-2181.

4. Anglin, E. (1977), "Recent Research on Aerodynamic Characteristics of Fighter Configuration During Spins," AIAA Atmospheric Flight Mechanics Conf., Hollywood, Fla.

5. Anglin, E. (1978), "Aerodynamic Characteristics of Fighter Configurations During Spin Entries and Developed Spins," AIAA J. Aircraft, Vol. 15, No. 11.

6. Bihrle, W. and B. Barnhart (1974), "Effects of Several Factors on Theoretical Predictions of Airplane Spin Characteristics," NASA DR-132521.

7. Birhle, W. (1976), "Correlation Study of Theoretical and Experimental Results for Spin Tests of a 1/10-Scale Radio Controlled Model," NASA CR-144995.

8. Birhle, W. and B. Barnhart (1978), "Design Charts and Boundaries for Identifying Departure Resistant Fighter Configurations," Report No. NADC-76154-30.

9. Chambers, J. R., J. Bowman and E. L. Anglin (1969), "Analysis of the Flat-Spin Characteristics of a Twin-Jet Swept-Wing Fighter Airplane," NASA TN D-5409.

10. L. O. Chua and P. M. Lin (1975), Computer-Aided Analysis of Electronic Circuits, Englewood Cliffs, N.J.: Prentice-Hall.

11. Kroll, W. B. (1976), "An Analytical Investigation of the Stall, Departure and Spin Entry Characteristics of a Current Fighter Airplane Using Conventional and Rotary Aerodynamic Models," M.S. Thesis, School of Engineering and Applied Sciences, George Washington Univ.

12. Kubicek, M. (1976), "Algorithm 502. Dependence of Solution of Nonlinear Systems on a Parameter," ACM Trans. Math. Software, Vol. 2, No. 1.

13. Mehra, R. K., W. C. Kessel and J. V. Carroll (1977), "Global Stability and Control Analysis of Aircraft at High Angles-of-Attack," Scientific Systems, Inc., Report ONR-CR215-248-1.

14. Mehra, R. K. and J. V. Carroll (1978), "Global Stability and Control Analysis of Aircraft at High Angles-of-Attack," Scientific Systems, Inc., Report ONR-CR215-248-2.

15. Moore, F. L., E. L. Anglin, et al. (1971), "Utilization of a Fixed-Base Simulator to Study the Stall and Spin Characteristics of Fighter Planes," NASA TN D-6117.

16. Williams, D. H. (1976), "The Use of Rotation-Balance Aerodynamic Data in Theoretical Spin Studies," M.S. Thesis, School of Engineering and Applied Sciences, George Washington University.

17. Young, J. W. and W. M. Adams (1972), "Analytic Prediction of Aircraft Spin Characteristics and Analysis of Spin Recovery," AIAA Atmospheric Flight Mechanics Conf., Palo Alto, Calif.

APPENDIX A

Notation

A_v, B_v, C_v	coefficients of quadratic expression for velocity (Eq. (2.37))
b	wing span
$(\ )^B$	signifies quantity in ( ) is coordinatized in B axis system
$[\cdot]$	defines elements of a set, e.g., $[x_i]$
$\bar{c}$	mean aerodynamic chord
$C_\ell = \frac{M_y}{\bar{q}Sb}$	rolling moment coefficient
$C_m = \frac{M_y}{\bar{q}S\bar{c}}$	pitching moment coefficient
$C_n = \frac{M_z}{\bar{q}Sb}$	yawing moment coefficient
$C_x = \frac{(\underline{F} - m\underline{g})\cdot\hat{\underline{x}}}{\bar{q}S}$	longitudinal force coefficient
$C_y = \frac{(\underline{F} - m\underline{g})\cdot\hat{\underline{y}}}{\bar{q}S}$	side force coefficient
$C_z = \frac{(\underline{F} - m\underline{g})\cdot\hat{\underline{z}}}{\bar{q}S}$	normal force coefficient
E	vehicle total kinetic energy
E_{SPIN}	vehicle spin kinetic energy; $I_V\dot{\psi}/2$
$\underline{f}$	force-moment terms in the aircraft
F	Jacobian matrix of partial derivatives, $\left[\frac{\partial f_i}{\partial x_j}\right]$

$\underline{F}$	vector in R^n which measures proximity to limit cycle solution
g	(constant) acceleration due to gravity, 9.8067 m/sec^2 (32.174 ft/sec^2)
$\underline{g}$	algebraic system of terms for generating bifurcation surfaces (Chapter 2)
G	augmented Jacobian matrix of partial derivatives, $\left[\frac{\partial g_i}{\partial y_j}\right]$, for bifurcation surfaces
h	altitude above earth's surface
I_x, I_y, I_z, I_{xz}	body axis moments and product of inertia, taken about the center of mass
I_v	vehicle moment of inertia about current vertical axis
k	index for standard continuation parameter; index for fixed state variable at initial conditions in the limit cycle continuation problem
ℓ	index for limit cycle continuation parameter
M_x, M_y, M_z	rolling, pitching, yawing moments acting about body axes
m	aircraft mass
$\underline{M}$	special vector, Section 2.1.2
n	dimension of vector space of interest, e.g., $\underline{x} \in R^n$
N(·)	null space
P	error tolerance for limit cycle continuation algorithm
p,q,r	angular rates about body axes (roll, pitch, yaw, respectively)
$\bar{q}$	dynamic pressure, $\frac{1}{2}\rho V^2$
R	radius of helical path of airplane; rotation balance parameter ($\Omega b/2V$)

$R(\cdot)$	range space
R^n	n-dimensional space of real numbers
$\hat{\underline{R}}, \hat{\underline{T}}, \hat{\underline{z}}^I$	unit vectors in cylindrical coordinates; $\hat{\underline{z}}^I$ is vertical, directed toward center of earth
$\text{sgn}(\cdot)$	function whose value is +1 if $(\cdot) \geq 0$, and -1 if $(\cdot) < 0$
S	wing area
t	time
t*	time at which equilibrium solution is made
T	limit cycle period
u,v,w	body axis components of $\underline{V}$
V	airspeed, = $\lvert\underline{V}\rvert$
V_H	horizontal component of velocity
V_{VERT}	vertical component of velocity; $\dot{h}$
$\underline{V}$	aircraft center of mass velocity, inertial with respect to local horizontal
W	aircraft weight
W_i	input weighting element used to compute P
$x \in [x_i]$	x is an element of the set $[x_i]$
$\underline{x}$	vector of state variables; e.g., for n = 5 equilibrium system, $\underline{x} = (p,q,r,\alpha,\beta)$
$\underline{x}^{(k)}$	$k^{\underline{th}}$ iterated value of $\underline{x}$
$\underline{x}_0$	$\underline{x}$ at initial conditions, i.e., $\underline{x}(t_0)$
$\underline{x}_R$	reduced state vector for high-α analysis; $\underline{x}_R \in R^7$
$\underline{x}_{SP}$	spin equilibrium states

$\underline{y}$	augmented vector of dependent variables, for bifurcation surfaces; e.g., for n = 5 equilibrium system, $\underline{y} = (x, \delta_i)$, where $\delta_i \in (\delta a, \delta e, \delta r)$; also, augmented continuation vector for limit cycle analysis
$\underline{y}'$	special state vector used in limit cycle continuation; defined by Eq. (2.13)
$\hat{\underline{x}}, \hat{\underline{y}}, \hat{\underline{z}}$	aircraft body axis unit vectors ($\hat{x}$ positive through nose, $\hat{y}$ positive through right wing, $\hat{z}$ positive down)
α	angle of attack, or incidence angle (Chapter 3); also continuation variable (Chapter 2)
β	angle of sideslip
γ_{ij}	element of Γ in the $i^{\underline{th}}$ row, $j^{\underline{th}}$ column
Γ	augmented Jacobian matrix of size $n \times (n+1)$
Γ_k	Γ with $k^{\underline{th}}$ column eliminated
δ	control parameter; either δa, δe, or δr (Chapter 2)
Δ	determinant of the Jacobian matrix; F or G, depending on context
$\underline{\delta}$	control vector, $(\delta a, \delta e, \delta r)$
$\underline{\delta}_{SP}$	spin equilibrium states
$\delta a, \delta e, \delta r$	aileron, elevator, and rudder control deflections (positive δe is trailing edge down, positive δa is right trailing edge down, positive δr is trailing edge left)
ρ	atmospheric density
ψ, θ, ϕ	Euler angles defining orientation of body axes in the inertial reference axes (yaw, pitch, roll, in that sequence)
ω	angular rate about center of mass, $\sqrt{p^2 + q^2 + r^2}$
$\underline{\omega}$	(p,q,r), vehicle angular velocity

Ω	rotation parameter for computing rotary balance aerodynamic coefficients
η	polar angle in cylindrical coordinate system defining aircraft position
$\alpha \in [-1,1]$	α such that $-1 \leqq \alpha \leqq 1$
$\alpha \in (-1,1)$	α such that $-1 < \alpha < 1$

the combinations $[\cdot)$ and $(\cdot]$ are similar, i.e., $\alpha \in [-1,1)$ means $-1 \leqq \alpha < 1$

$\alpha \in A$	α is an element of the set A
$\alpha \notin A$	α is not an element of the set A
$[a_{ij}]$	a matrix array whose elements are designated by a_{ij}, the element at row i, column j
(a_i)	a vector array whose elements are designated by a_i, the i th location element
$\underline{v}^I$	indicates vector $\underline{v}$ is in inertial coordinates
$(\ )^T$	matrix transpose
$(\ )^*$	equilibrium solution, as in Section 2.1.2
$\|\underline{x}\|$	the Euclidean norm of the vector x, i.e., $\|\underline{x}\| = \sqrt{\sum_{i=1}^{n} x_i^2}$ if $\underline{x} \in R^n$
det(•)	the determinant of the argument (which must be a square matrix)
$(\dot{})$	d( )/dt; also d( )/ds in Section 2.1
$\triangleq$	equal by definition

Stability Derivatives (Aerodynamic Coefficients)

$C_{i_\xi} \triangleq \frac{\partial C_i}{\partial \xi}$, for $i = \ell,m,n,x,y,z$
and $\xi = \delta a, \delta e, \delta r$

$$C_{i_\eta} \triangleq \frac{\partial C_i}{\partial(\frac{b}{2V}\eta)}, \text{ for } \eta = p,r,\dot{\beta}$$

$$C_{i_\zeta} \triangleq \frac{\partial C_i}{\partial(\frac{\bar{c}}{2V}\zeta)}, \text{ for } \zeta = q$$

$C_{i_{ROT}} \triangleq C_i$ due to rotary balance effects; a function of α, β, and $(\Omega b/2V)$

In addition, the coefficients C_i and the derivatives $\partial C_i/\partial\{\xi,\eta,\zeta\}$ are functions of α and β, and are usually determined via tabular or graphical look-up.

DISTRIBUTION LIST

Office of Naval Research
800 N. Quincy Street
Arlington, VA 22217
- R. von Husen, Code 211 — 4
- S. L. Brodsky, Code 432 — 1
- David Siegel — 1

Office of Naval Research
Eastern/Central Regional Office
495 Summer Street
Boston, MA 02210 — 1

Office of Naval Research
Western Regional Office
1030 E. Green Street
Pasadena, CA 91106 — 1

Naval Research Laboratory
Washington, DC 20375
- Code 2627 — 3

Naval Air Systems Command
Washington, DC 20361
- D. Kirkpatrick, AIR 320D — 1
- R. C. A'Harrah, AIR 50311 — 1

Naval Air Development Center
Warminster, PA 19874
- C. J. Mazza, Code 6153 — 1
- C. R. Abrams, Code 6072 — 1

Naval Material Command
Washington, DC 20360
- Code 08T23

Naval Weapons Center
China Lake, CA 93555
- B. Hardy, Code 3914 — 1
- R. Hewer — 1

Naval Surface Weapons Center
Silver Spring, MD 20910
- J. Wingate, Code R44 — 1

Naval Air Test Center
Patuxent River, MD 20670
- W. M. Branch, Code SA — 1
- R. E. Detrick, Code AT — 1
- J. McCue, Code TPS — 1

Naval Coastal Systems Center
Hydromechanics Division
Panama City, FL 32407
- D. Humphreys, Code 794 — 1

David Taylor Naval Ship R&D Center
Bethesda, MD 20084
- J. P. Feldman, Code 1564 — 1
- W. E. Smith, Code 1576 — 1

Naval Post Graduate School
Monterey, CA 93940
- Technical Reports Library — 1
- L. Schmidt — 1

Defense Technical Information Center
Building 5
Cameron Station
Alexandria, VA 22314 — 12

Air Force Office of Scientific Research
Building 410
Bolling Air Force Base
Washington, DC 20332
- G. W. McKemie — 1
- R. Buchal — 1

Air Force Flight Dynamics Laboratory
Wright-Patterson Air Force Base
Dayton, OH 45433
- R. Anderson, Control Dyn. Br. — 1
- D. Bowser, Control Dyn. Br. — 1

Air Force Institute of Technology
Wright-Patterson Air Force Base
Dayton, OH 45433
- P. Maybeck — 1
- J. G. Reid — 1

Army Armament R&D Command
Building #18
Dover, NJ 07801
- N. Coleman, DRDAR-SCFCC — 1

NASA Langley Research Center
Hampton, VA 23665
- J. R. Chambers — 1
- E. Anglin — 1
- V. Klein — 1
- A. Schy — 1
- G. Elliot — 1
- R. Dunning — 1

NASA Dryden Research Center
PO Box 273
Edwards, CA 93523
K. Iliff 1

Systems Technology, Inc.
13766 South Hawthorne Blvd.
Hawthorne, CA 90250
R. Whitbeck 1

The Analytic Sciences Corp.
6 Jacob Way
Reading, MA 01867
C. Price 1

Massachusetts Institute of Technology
Lab. for Information and Decision Systems
Cambridge, MA 02139
M. Athans 1

University of Michigan
Dept. of Naval Architecture and Marine Engineering
Ann Arbor, MI 48109
M. G. Parsons 1

Nielsen Engineering and Research, Inc.
510 Clyde Avenue
Mountain View, CA 94043
J. N. Nielsen 1

University of Notre Dame
Dept. of Electrical Engineering
Notre Dame, IN 46556
M. K. Sain 1

The C. S. Draper Laboratory, Inc.
555 Technology Square
Cambridge, MA 02139
R. V. Ramnath 1

Honeywell, Inc.
Systems and Research Center
2600 Ridgway Parkway
Minneapolis, MN 55413
C. A. Harvey 1

Alphatech, Inc.
3 New England Executive Park
Burlington, MA 01803
N. R. Sandell 1

Calspan Corp.
PO Box 400
Buffalo, NY 14225
E. G. Rynaski 1
K. S. Govindaraj 1

Systems Control Inc.
1801 Page Mill Road
Palo Alto, CA 94306
E. Hall 1

Flight Research Laboratory
Dept. of Mechanical and Aerospace Engineering
Princeton University
Princeton, NJ 08544
R. F. Stengel 1

Dynamics Research Corp.
60 Concord Street
Wilmington, MA 01887
H. L. Stalford 1

Oklahoma State University
Dept. of Mechanical and Aerospace Engr.
Stillwater, OK 74074
J. H. Taylor 1

Northrop Corporation
3901 West Broadway
Hawthorne, CA 90250
J. L. Lockenour 1
J. Kalviste 1

NASA Headquarters
Washington, DC 20546
H. Rediess 1

NASA Ames Research Center
Moffet Field, CA 94035
W. Johnson 1
D. Denery 1

Princeton University
Dept. of Mechanical and Aerospace Engr.
Princeton, NJ 08540
E. Dowell 1

University of Texas
Dept. of Aerospace Engineering
Austin, TX 78712
J. Speyer 1

SUNY at Buffalo
Dept. of Mathematics
106 Diefendorf Hall
Buffalo, NY 14216
B. Hassard 1

Stanford University
Dept. of Mechanical Engineering
Stanford, CA 94305
A. E. Bryson 1

National Transportation Safety Board
Bureau of Technology
Laboratory Services Division
800 Independence Ave., S.W.
Washington, DC 20594
R. von Husen 1

University of California
Dept. of Electrical Engineering and
Computer Science
Berkeley, CA 94720
J. Marsden 1
P. Varaiya 1

Stanford University
Dept. of Aeronautics and Astronautics
Stanford, CA 94305
J. V. Breakwell 1